Assessing the structural and alteration controls on gold mineralization at Detour Lake mine, Ontario, Canada

Renelle Dubosq

A thesis submitted to the Faculty of Graduate and Postdoctoral Studies in partial fulfillment of the requirements for the degree of
Master of Science in Earth Sciences

University of Ottawa
Ottawa, Canada
July 2017

Abstract

The giant Detour Lake deposit is a Neoarchean orogenic Au ore body located in the northwestern Abitibi district within the Superior Province. The deposit is situated along the high strain Sunday Lake Deformation Zone (SLDZ) parallel to the broadly E-W trending Abitibi greenstone belt. The lower amphibolite facies assemblage (Act-Bt-Pl-Ep-Alm ±Cal ±Qz ±Ilm) suggests maximum temperatures reaching 550°C, exceeding conditions for pyrite plasticity, an important and ubiquitous Au-bearing phase that may ultimately represent the source for Au at orogenic style Au deposits. The metamorphic assemblage also obscures the relationship between Au and biotite, a visual indicator mineral within Au-rich ore zones. This work combines microstructural, geochemical and geochronological analyses to assess the influence of regional-scale deformation and alteration on Au mineralization. EBSD and LA-ICP-MS analyses on pyrite reveal Au enrichment at microstructures supporting a syn- to post-peak metamorphic and deformation-assisted Au upgrading model. EMPA and $^{40}Ar/^{39}Ar$ analyses on biotite reveal one chemically homogeneous population, which yield variably reset ages that post-date regional metamorphism and Au mineralization.

Sommaire

Le gîte d'or géant de Detour Lake est un dépôt orogénique néoarchéen situé au nordouest de la sous-province de l'Abitibi dans la Province Supérieure. La mine est construite le long de la zone de deformation de Sunday Lake, parallèle à la ceinture des roches vertes de l'Abitibi E-W. L'assemblement metamorphique de faciès amphibolite inférieur (actinolite-biotite-plagioclase-epidote-almandine) suggère une temperature maximum atteignant 550°C, ce qui excède la limite pour le régime plastique de la pyrite, une phase minerale aurifère importante et omniprésente

dans plusieur dépôts orogéniques. L'assemblement métamorphique oscur aussi la relation entre la biotite, un minéral indicateur visuel, et l'or. Ce projet combine des analyses microstructurales, géochimique et géochronologique afin de determiner l'influence de la déformation régionale et l'altération sur la mineralization d'or. Les données des analyses EBSD et LA-ICP-MS sur la pyrite révèles un enrichissement d'or dans les microstructures ce qui supporte un modèle de concentration d'or synmétamorphique entraîné par la déformation. Les données des analyses EMPA et $^{40}Ar/^{39}Ar$ effectués sur la biotite révèles une seule population de biotite avec composition homogène, qui poste-date le métamorphisme régionale ainsi que la mineralization d'or.

Acknowledgements

Foremost, I thank my supervisor, David Schneider, who has guided me through this project over the past two years. Dave has given me great opportunities and pushed me to collaborate with other researchers to try new techniques. Thank you, for being my mentor.

I thank Christopher Lawley, who has been incredibly helpful in the field and was always available for discussions. His enthusiasm has kept me motivated throughout this project.

I thank Anna Rogowitz, who was eager to share her expertise and invited to Vienna to conduct EBSD analyses. She has been a great host and was very patient in the many hours of instructing me on the science behind EBSD analyses.

I am grateful to Jean Francois Metail who has given me the opportunity to gain mining and exploration experience throughout my masters and was very supportive over the last two years. I also extend a thank you to John Florek, Guy MacGuillivray, Adree DeLazzer, and Kelly Malcolm who have been very helpful and accommodating during mine visits.

Table of Contents

CHAPTER 1

Introduction

The Detour Lake mine in the northwestern district within the Abitibi Subprovince hosts Canada's largest Au reserves among producing operations (measured and indicated resource of 530.2 million tonnes at 1 g/t and containing 16.4 Moz). The deposit differs from most well-known Abitibi greenstone belt deposits by possessing a lower amphibolite facies metamorphic mineral assemblage (actinolite-biotite-plagioclase-epidote-almandine ± calcite ± quartz ± ilmenite). These elevated peak metamorphic temperatures and pressures have resulted in an atypical mineral assemblage within and adjacent to Au ore zones and it is not clear whether conventional pathfinder minerals, for example biotite, represent useful exploration vectors at the Detour Lake Au deposit. As a result, this thesis aims to investigate an important sub-type of orogenic Au deposits that are associated with higher grade domains and deeper crustal levels within Neoarchean and predominately greenschist facies greenstone belts. Metamorphism and progressive deformation has also obscured source to sink pathways for Au, features that are typical of the orogenic Au deposit type. This study will address that knowledge gap through a combination of *in situ* structural and geochemical mapping of pyrite, which represents an important pathfinder mineral related to Au. Metamorphosed pyritric sediments and volcanic rocks that host the Detour Lake Au deposit have previously been suggested to represent the ultimate source for Au (Gaboury, 2013), however, the mechanism(s) controlling the retention and release of Au are not well understood. Peak metamorphic temperatures/pressures at the Detour Lake Au deposit exceed the conditions for pyrite plasticity and represents an important study area to investigate the role of syn-metamorphic deformation on Au deposit genesis at the micro to deposit scales.

In Chapter 2, pyrite porphyroblasts from mafic meta-volcanic host rocks and mineralized veins sampled within the hanging wall of the Sunday Lake Deformation Zone (SLDZ) are examined to assess the influence of pyrite plastic deformation during peak-metamorphic conditions on the retention and release of trace elements. Both EBSD mapping and LA-ICP-MS element mapping techniques are used to quantify plastic strain within pyrite porphyroblasts and document the distribution of trace elements within the same crystals. The results have significant ramifications for refining the source to sink pathways of ore deposition. This work will be submitted to Lithos and co-author contributions include guidance and supervision from Christopher Lawley, Anna Rogowitz and David Schneider, and collaboration with Simon Jackson.

Chapter 3 combines petrographical, geochemical, and geochronological data of biotite at the Detour Lake deposit, with the intent of discerning between metamorphic and secondary assemblages within the deposit. Both EMPA WDS chemical mapping and spot analyses were used to identify the different biotite populations. $^{40}Ar/^{39}Ar$ geochronology was also conducted on biotite from different structural settings to potentially document various generations of biotite. The results are consistent with previous $^{40}Ar/^{39}Ar$ studies in the Superior Province, and yield variably reset, Neoarchean to Paleoproterozoic ages that post-date the inferred timing of Au and metamorphism at the Detour Au deposit. This work has contributions including guidance and supervision from David Schneider, and collaboration with Alfredo Camacho.

Both projects described in Chapters 2 and 3 have had significant impacts on better resolving the Au paragenesis at Detour Lake. With most surficial ore bodies discovered and explored across Canada, we need to integrate microscale observations to the district- to deposit-scale and develop more innovative exploration techniques to discover more buried deposits.

CHAPTER 2

Pyrite deformation and connections to gold mobility: insight from micro-structural analysis and trace element mapping

Abstract

Pyrite is an important sulphide mineral phase in many orogenic Au deposits that can release Au and other metals during its metamorphic phase transition to pyrrhotite. This process forms the basis for the metamorphic-driven Au-upgrading model, however the role of pyrite deformation in controlling the retention and release of Au and related pathfinder elements during metamorphism is poorly understood. The lower amphibolite facies metamorphic mineral assemblage (Act-Bt-Pl-Ep-Alm ±Cal ±Qz ±Ilm; 550°C) of the giant Detour Lake deposit (Canada; measured and indicated resource of 530.2 million tonnes at 1 g/t and containing 16.4 Moz) possesses rocks exceeding the conditions for plastic deformation in pyrite (450°C). Thus, Detour Lake is an ideal study area to evaluate the link between pyrite deformation microstructures and Au upgrading through a complementary approach of electron backscatter diffraction (EBSD) mapping and laser ablation inductively coupled plasma mass spectrometry (LA-ICP-MS) 2D element mapping on pyrite. Local misorientation patterns in pyrite exhibit parallel bands that can be described by continuous rotation around one of the <100> axes, whereas higher strain areas reveal more heterogeneous misorientation patterns and the development of low-angle grain boundaries locally accompanied by micro-fractures indicative of dislocation creep and possible strain hardening. LA-ICP-MS element maps document primary, syn-metamorphic oscillatory growth zoning and early, Au-rich sieve textured pyrite domains. These are cut by Au-rich fractures suggesting that remobilization of Au occurred with trace element enrichment of field row transition elements, post-transition metals and metalloids during a late brittle deformation stage. This brittle stage post-dates the main period of syn-metamorphic pyrite crystallization at the margins of pre- to syn-deformation, high-grade auriferous veins. Mass balance calculations at the deposit scale suggest that only a small percentage of Au could

have been sourced from pyrite and instead points to the role of pyrite microstructures as depositional traps for Au during syn-metamorphic, deformation- and fluid-assisted diffusion and associated Au-upgrading. We therefore suggest that the close spatial relationship between pyrite and Au at the microscale, textures typical of orogenic Au deposits, may, in fact, reflect the introduction of Au and associated elements into Au-poor pyrite porphyroblasts syn- to post-peak metamorphism rather than the release of these elements during the metamorphic transition from pyrite to pyrrhotite.

1. Introduction

Pyrite is an important and ubiquitous sulphide phase that accompanies Au in many greenschist to amphibolite facies orogenic Au deposits (Groves et al., 1998; Dubé and Gosselin, 2005). Sulphide minerals can incorporate significant concentrations (≤2 wt%; Reich et al., 2005) of lattice-bound Au and/or ultrafine native Au inclusions (i.e., invisible Au; Cook and Chryssoulis 1990), and may represent the primary mineral host for Au ore at some deposit types. The close spatial relationship between pyrite and Au has led previous workers to suggest that the metamorphic transition of pyrite to pyrrhotite through de-sulphidation processes can liberate lattice-bound and nano-particulate base- and precious-metals hosted within early, Au-rich sulphide minerals, which are then remobilized and concentrated into late, high-grade ore shoots (Craig and Vokes, 1993; Tomkins and Mavrogenes, 2001; Large et al., 2007). As a result, sedimentary successions that possess Au-rich diagenetic pyrite nodules within mafic volcanic rock-dominated greenstone belts are now viewed as possible Au-rich source regions for some classic orogenic Au districts, including many of those within the Abitibi Subprovince of Canada (e.g., Large et al., 2007; Gaboury 2013). Macro- to micro-scale observations at these deposits

suggest that late, Au mineralization is synchronous with deformation (Bleeker, 2015). Although most studies focus on the role metamorphism plays in the (re)mobilization of Au, very few have addressed the relationship between plastic deformation and this Au-upgrading model. Fougerouse et al. (2016) provided insight into crystal plasticity and element mobility in arsenopyrite to test the syn-metamorphic and deformation-driven Au upgrading model. Results from that study reveal folded arsenopyrite crystals with low-angle grain boundary development and brittle fracturing at the fold hinge, which allowed fluids to leach out the lattice-bound Au, consequently resulting in Au-depleted zones within the sulphide phase. Our goal herein is to evaluate this remobilization model in pyritic ores. However, an incomplete understanding of pyrite deformation mechanisms at the brittle-plastic transition, which typifies the deformation conditions at most orogenic Au deposits, presents a challenge in assessing the role that deformation plays in driving and/or facilitating the metamorphic Au-upgrading model.

In this study, we document pyrite micro-structures and a Au paragenesis that are consistent with a syn- to post-peak metamorphic- and deformation-driven Au upgrading model, where Au and other trace elements are, at least locally, introduced and/or remobilized into deformation-induced diffusion pathways within pyrite. Peak metamorphic conditions at the Detour Lake deposit, a giant orogenic Au deposit in the northwestern Abitibi Subprovince, reached 550°C and 3.3 kbar (Oliver et al., 2011), exceeding the range of pressure-temperature conditions expected for pyrite plastic deformation, thus making this deposit an ideal area to test the model. Herein we combine microstructural analysis via electron backscatter diffraction (EBSD) techniques and laser ablation inductively coupled plasma mass spectrometry (LA-ICP-MS) 2D element mapping to further investigate the influence of deformation on the retention and release of Au and other trace elements within deformed, syn-metamorphic pyrite porphyroblasts

and overgrowths. Finally, we combine 2D micro-scale trace element mapping with 3D deposit-scale S and Au concentration maps to model the contribution of sulphide-hosted, invisible Au on the overall Au endowment of the Detour Lake deposit and to test the significance of the Au-upgrading model.

2. Pyrite Deformation Mechanisms

Gold at most ore deposits is paragenetically late and occurs along pyrite grain boundaries and late fractures, suggesting Au mobility is synchronous with a late stage of brittle deformation that post-dates pyrite crystallization (Kerrich and Kyser, 1994; Groves et al., 2000; Tomkins and Mavrogenes, 2001; Large et al., 2007). A variety of other deformation microstructures in metamorphic pyrite has been described including brittle fractures with plastic injection of mobile sulfides, mortar-type brittle fracturing at pyrite margins, elongation of pyrite by pressure solution or mimectic growth, foam texture by annealing/static recrystallization, and recrystallization through grain boundary bulging (e.g. McClay and Ellis, 1983; 1984). Above 450°C, pyrite is thought to deform ductily through a combination of pressure-solution, dislocation-glide and creep mechanisms (Cox et al. 1981; Graf et al. 1981; Levade 1982; Levade et al. 1982). Ductile deformation structures have also been observed in pyrite crystals deformed at temperatures ~260°C, suggesting that pyrite can behave plastically at relatively lower temperatures, as well (Barrie et al., 2011).

Plastic deformation occurs as slip on specific crystallographic planes in certain crystallographic directions. The resulting misorientation of the crystal lattice can be described by the misorientation angle and a rotation axis. Pyrite has a cubic structure belonging to the Pa3 space group with symmetry of 2/m3 and a face-centered-cubic lattice (Levade et al., 1982).

Covalently bonded S–S pairs make up the center of the cubic cell's edges, which increases the critical resolved shear stress for glide on {110} (Cox et al., 1981; Van Goethem et al., 1978; Wyckoff, 1965). Thus, crystal plastic deformation in pyrite is mainly accommodated by slip on {100} and more rarely {110} planes, and rotation about <100> and more rarely <110> axes (Boyle et al., 1998; Barrie et al., 2008). However, the relationship between these plastic and brittle-plastic pyrite deformation mechanisms and their impact on the Au endowment at orogenic Au deposits remains poorly understood.

3. Geological Setting

3.1. Regional geology of the Abitibi Subprovince

The Abitibi Subprovince represents the southernmost region of the Superior Province and is a well-known region in Canada for its abundance in economic base- and precious-metal mineral deposits, including orogenic Au deposits (**Fig. 1**). Neoarchean mafic to ultramafic volcanic and lesser felsic to intermediate volcanic rocks are intruded by syn-volcanic tonalite and gabbrodiorite dikes and plutons, and unconformably overlain by younger sedimentary assemblages such as the Porcupine (2690–2680 Ma) and Timiskaming assemblages (<2676 Ma; Ayer et al., 2002; Daigneault et al., 2004; Goutier and Melançon, 2007). Volcanic and sedimentary assemblages of the subprovince, including the important precious metal-hosting Porcupine and Timiskaming assemblages, are crosscut by east-west trending, variably dipping thrust faults that were reactivated as strike-slip faults during the later stages of tectonic compression (2650– 2600 Ma; e.g., Bleeker, 2010). Some of these faults, such as the Porcupine-Destor and Cadillac fault zones, are well known for hosting world-class Au deposits (Goutier, 1997; Benn and Peschler, 2005; Bateman et al., 2008). Geochronological studies suggest the

Abitibi volcanic episode occurred between 2750–2676 Ma (Ayer et al., 2002, 2005, 2010; Goutier and Melançon, 2007; Oliver et al., 2011). The belt was later subjected to lower-middle greenschist facies metamorphism between 2677–2643 Ma (Thompson, 2003; Powell et al., 1995).

Several major deformation events that resulted in the current structure of the Abitibi Subprovince have been identified: (1) the oldest event corresponds to the collision between the Abitibi and the northern Superior subprovinces. The deformation event is recognized locally as a north-trending cleavage and folds with north-trending axial planes that pre-date the deposition of the Porcupine Assemblage at ca. 2690 Ma (Bateman et al., 2008); (2) pre-Porcupine Assemblage folds are refolded and transposed during a second regional deformation event that pre-dates the ca. 2690 Ma Timiskaming Assemblage. Deformation structures associated with this younger event are observed within the Au-bearing Porcupine-Destor Fault (Ayer et al., 2005); and (3) post-Timiskaming deformation resulted in folding and faulting of the Timiskaming Assemblage and represents an important control on the occurrence and geometry of Au deposits along the auriferous Porcupine-Destor and Cadillac faults (Bateman et al., 2008). The timing of Au is diachronous across the Abitibi with multiple Au events and deposit styles that pre- and post-date the Timiskaming Assemblage (2680–2665 Ma; Ayer et al., 2009; Bleeker, 2010; Dubé and Mercier-Langevin, 2015).

3.2. Detour Lake geology

The Detour Lake deposit is located at the contact between the mafic-volcanic dominated Detour Lake Formation, or Deloro Assemblage (<2725 Ma), and the siliciclastic to volcaniclastic Caopatina Assemblage (ca. 2700 Ma; Fig. 2A; Johns 1982; Marmont 1986, 1987). The

unconformable and faulted contact between the two assemblages also corresponds to the sub-vertical, brittle-plastic, regional-scale deformation zone referred to as the Sunday Lake Deformation Zone (SLDZ). The deformation zone is an important control on Au at the deposit scale and, within the mine stratigraphy, is marked by a felsic volcaniclastic horizon within the Detour Lake Formation, known locally as the Chert Marker Horizon (2725.1 ± 1.4 Ma; Oliver et al., 2011). The Detour Lake Formation and the Caopatina Assemblage are intruded by tonalitic to granodioritritic and gabbroic to dioritic intrusions (2720–2722 Ma; Marmont and Corfu, 1988; Oliver et al., 2011) and at least three main generations of dikes (2743–2699 Ma; Oliver et al., 2011) including: (1) felsic to intermediate dikes; (2) mafic dikes that locally cut the Caopatina Assemblage (Oliver et al., 2011); and (3) late diabasic and gabbroic dikes that are possibly related to the Proterozoic Matachewan dike swarm (Oliver et al., 2011).

The Detour Lake Formation (2730–2724 Ma) comprises the hanging wall of the SLDZ. Geochronology suggests that tholeiitic mafic volcanic rocks and ultramafic flows of the Lower Detour Formation (>2725 Ma; Oliver et al., 2011) pre-date tholeiitic mafic volcanic rocks and related mafic volcaniclastic rocks of the Upper Detour Lake Formation (<2725 Ma; Oliver et al., 2011). Contacts between pillowed mafic lavas, massive lava flows and mafic volcaniclastic rocks of the Upper Detour Lake Formation are important depositional sites for Au in the hanging wall of the deposit (Oliver et al., 2011). However, the highest Au grades are hosted primarily at the faulted contact between the Lower Detour Formation with the younger Caopatina Assemblage (**Fig. 2A**).

The Caopatina Assemblage comprises three main interbedded lithologies including volcaniclastic rocks along with lesser argillaceous siltstones, quartz wackes, and turbidites. The dominant volcaniclastic rocks are laminated with cm-scale quartz-rich bands intercalated with

biotite-actinolite-hornblende bands (Oliver et al., 2011). Auriferous quartz veins cutting the Caopatina Assemblage constrain the timing of Au to ≤2700 Ma, whereas a barren albitite dike dated at 2699 ± 7 Ma, which previous workers have interpreted as a post-ore dike, represents a possible maximum age for Au mineralization (OIiver et al., 2011).

3.3. Deformation and metamorphism of the Detour Lake deposit

The Detour Lake area has undergone at least four major deformation events (D_1-D_4) as recognized by Oliver et al. (2011). The first of these events, D_1, is manifested in the formation of the SLDZ, which juxtaposed the mafic-volcanic dominated Detour Lake Formation and the younger Caopatina Assemblage. The second deformation phase, D_2, formed shallow, west-plunging folds with subvertical, east-west trending axial planes. This deformation event is associated with a pervasive foliation fabric, S_2, which is parallel to D_2 folding. The third deformation event, D_3, produced open, north-northwest trending, shallowly plunging folds, and is associated with a crenulation fabric, S_3, which is best developed within ultramafic flows of the Lower Detour Lake Formation. The last major phase of deformation, D_4, is characterized by a series of southeast fault splays from the main SLDZ.

The metamorphic mineral assemblage of actinolite-biotite-plagioclase-epidote-almandine ± calcite ± quartz ± ilmenite at Detour Lake (Oliver et al., 2011) indicates that, unlike the greenschist facies metamorphic rocks elsewhere in the Abitibi greenstone belt, the region has undergone lower amphibolite facies metamorphism. Peak metamorphic conditions have been estimated to be 550°C at 3.3 kbar using the f_{O2} controlled prograde metamorphic mineral assemblage of actinolite-biotite-plagioclase-epidote-almandine (Oliver et al., 2011). These conditions are also consistent with the compositional range of plagioclase (An^{28-58}) reported by

Mormont (1986) and pressure-temperature conditions that exceeded the stability of pro-grade chlorite (510–540°C; Bouchard, 2015). Sedimentary rocks of the Caopatina Assemblages (ca. 2700 Ma; Fig. 2A; Johns 1982; Marmont 1986, 1987) are metamorphosed, which constrains the timing of regional deformation at Detour Lake to ≤2700 Ma and is broadly consistent with the timing of regional metamorphism in the southern Abitibi between 2670 Ma and 2640 Ma (Oliver et al., 2011; Powell et al., 1995a, 1995b). Inclusions of prograde metamorphic mineral assemblages (discussed below) in pre- to syn-D_2 veins suggests peak metamorphic conditions were reached during D_2 (Oliver et al., 2011).

3.4. Veining and mineralization

The Detour Lake deposit is one of Canada's largest Au deposits hosting 16.4 Moz of Au at 1g/t (Allaire, 2014). Gold and sulphur block models from the mine's assay database show the close, co-spatial relationship between sulphide minerals (predominately pyrite and pyrrhotite) and Au mineralization, following the main, steeply-dipping east-west trending S_2 structure (**Fig. 2B-C; DR1, DR2**). Mineralized, west-plunging D_2 folds are refolded by D_3 (open, north-northwest trending, shallow-dipping folds), however post-D_2 structures do not significantly impact the geometry of Au ore zones and likely post-date mineralization within the main deposit. At the micro-scale, Au is typically free milling and is often associated with clusters of bismuth- and/or tellurium-bearing minerals and inclusions. These precious metal-rich minerals are concentrated within veins (discussed below) and in micro-dilatational sites (e.g., pressure shadows, boudin necks, grain boundaries) along with hydrothermal alteration minerals (e.g., pyrite, chalcopyrite, pyrrhotite, calcite, ankerite(?), chlorite(?), sericite) and their metamorphosed equivalents (e.g., biotitized vein selvages).

Previous studies have associated the Au mineralization at Detour Lake to the presence of D_2 fault-fill and extensional quartz veins in addition to late D_2 sulphide-rich high-grade Au-bearing brecciated veins (Oliveira, 1997). These high-grade, fault-fill veins, known locally as Q veins, are concentrated primarily along the SLDZ and within the historic Campbell pit, which was exploited between 1983 and 1999 (Marmont, 1986; Oliver et al., 2011). The relationship between steeply-dipping, auriferous fault-fill veins and rare flat-dipping extension veins with the SLDZ is consistent with reverse movement along D_2 shear zones during Au deposit genesis. Locally these auriferous veins cut D_2 folds, but are, in turn, transposed parallel to the main S_2 deposit fabric, suggesting that some Au-bearing veins evolved during late-D_2. Extensional veins and the plunge of syn-D_2 Au ore zones within left-stepping portions of the SLDZ, point to the importance of dilational structures during late, sinistral reactivation of D_2 faults. Dextral reactivation of D_2 faults, as demonstrated within mineralized zones north of the Detour Lake open pit, record a poly-phase kinematic evolution during D_2, which is typical of other major, Au-bearing faults in the southern Abitibi Subprovince.

Fault-fill veins are not exposed within the current mine, which is a westward expansion of previous mining operations along the SLDZ. As a result, our study focuses on Au mineralization within the large, but relatively low-grade hanging wall of the Detour Lake deposit. We have identified eight vein types within this part of the deposit. Six of these vein types are interpreted to be pre- to syn-D_2 whereas two are interpreted to post-date D_2. The mineralogy and relative timing of each vein type is summarized in **Table 1**. Pre- to syn-D_2 vein types include: pillow veins (V_1); completely transposed and dismembered Qz veins (V_2); laminated-sulphidized (pyrite-pyrrhotite-chalcopyrite-arsenopyrite) Qz veins (V_3), folded Qz-Cal veins (V_4), folded-sulphidized (pyrite-pyrrhotite-chalcopyrite) Qz-Cal-Chl veins (V_5), and Cal

veinlets (V_6). Post-D_2 veins consist of planar Cal veinlets (V_7), and carbonate breccia veins that locally possess sericitized and carbonatized alteration halos (V_8). The most relevant Au-bearing vein set for this study is the pre- to syn-D_2 folded-sulphidized (pyrite-pyrrhotite-chalcopyrite) Qz-Cal-Chl vein set (V_5; **Fig. 3**), the most common veins in the hanging wall of the deposit. They are mostly composed of quartz and calcite with some chlorite, biotite and sulphides (Py, Po, Cpy) and usually have a biotite alteration halo, or more rarely a sericitized vein margin. Locally, structures common to shear veins include foliated wall rock selvages and dilational jogs between en-echelon isolated veinlets that can be interpreted as pre- to syn-D_2 timing for this vein type. Evidence for plastic deformation consists of folding and pinch and swell structures. V_5 veins are parallel to S_2 or have fold axes parallel to S_2. It is the only vein set containing coarse, visible Au at Detour Lake, as well as clusters of coarse precious-metal mineral inclusions (Au-Ag-Bi-Te) locally associated with pyrite and pyrrhotite (**Fig. 4A**). Pillow veins (V_1) were also documented in high ore grade intervals of drill core, and scanning electron microscope (SEM) imaging confirm the presence of rare 5 μm Au grains adhered to the surface of pyrite crystals within this earliest generation of quartz veining (**Fig. 4B**).

4. Analytical Methods

4.1. Sampling

In an attempt to better understand the internal crystal plasticity of pyrite and its impact on trace element remobilization, we sampled a variety of mineralized host rocks within the hanging wall of the main ore body possessing large (>1 mm) pyrite crystals. These include mafic and ultramafic volcanic samples where pyrite is ubiquitous within the host rock, occasionally aligned

with the main S_2 foliation, and samples where the pyrite is contained within deformed and sulphidized pre- to syn-D_2 veins (V_5).

Multiple pyrite generations were identified within auriferous veins (**Fig. 5A-C**). Pyrite texture types include: (1) sieve-texture, or inclusion-rich, pyrite domains (type-1a) with poorly defined grain boundaries (**Fig. 5B**). These sieve-texture pyrite domains occur as early, anhedral clots within the vein and rock matrix and/or as irregular cores that are wrapped by later pyrite generations; (2) inclusion-free, euhedral pyrite domains (type-2a) and overgrowths (type-2b) that typically wrap early, sieve-textured pyrite domains (**Fig. 5B**). We hypothesize that these euhedral, inclusion-free pyrite crystals and overgrowths are porphyroblasts that grew as part of the metamorphic mineral assemblage within and at the margins of pre- to syn-D_2 veins. However, euhedral pyrite porphyroblasts are also mantled by sieve-textured pyrite (type-1b), documenting a complex pyrite paragenesis that is difficult to resolve with reflected light microscopy alone (discussed below); and (3) sooty, colloform pyrite bands (type-3;**Fig. 5C**). Rare colloform pyrite bands envelop sieve-textured and inclusion-poor pyrite overgrowths and are the youngest pyrite generation within pre- to syn-D_2 veins observed as part of the current study.

Each of the identified pyrite types is wrapped by chalcopyrite and pyrrhotite, which fill late, pyrite fractures and are concentrated in low-strain micro-textural sites along with free Au (e.g., boudin necks, pressure shadows). These textural relationships suggest that the breakdown and de-sulphidation of pyrite may have occurred during prograde metamorphism, features that are consistent with the metamorphic Au-upgrading model (e.g., Tomkins et al., 2006). Pyrite-pyrrhotite-chalcopyrite are also concentrated within the fractures and pressure shadows of porphyroblastic metamorphic minerals (e.g., actinolite), which suggests a syn- to post-peak metamorphic timing for these sulphide phases within pre- to syn-D_2 auriferous veins. Post-D_2

veins are also locally pyrite-bearing, however these veins are devoid of Au (≤2 ppb Au) and sulphide minerals hosted within these late veins are not further considered in this study.

Using petrologic and petrographic observations, we targeted areas of interest (**Fig. 6**) where pyrite appeared to have been deformed. Coarse, inclusion-free pyrite crystals (type-2) were the focus of EBSD mapping because these crystals exhibited the clearest evidence for strain and were the most common pyrite type within pre- to syn-D_2 veins. Pyrite deformation microstructures targeted include late brittle fractures, elongated folded porphyroblasts, pinch and swell structures, high stress regions at grain contacts and apparent annealed foam-textured domains. After noting the deformational microstructures in the surrounding matrix (**Fig. 7**), we conducted orientation contrast (OC) imaging and EBSD analyses on specific pyrite domains from five samples and LA-ICP-MS element mapping on pyrite domains from six samples. Four areas within three of these samples (MV-20, RD16-H, and RD16-I) were analyzed with both complementary techniques.

4.2. OC imaging and EBSD mapping

In order to confirm the presence of plastic strain, we performed forescatter electron orientation contrast (FSE OC) imaging before selecting areas suitable for EBSD mapping. All crystallographic data was collected at the University of Vienna (Vienna, Austria) using a FEI Quanta 3D FEG instrument equipped with an EDAX Pegasus Apex 4 system consisting of a Digiview IV EBSD camera, including a FSE detector and an Apollo XV silicon drift detector for EDX analysis. Thin sections for OC imaging and EBSD mapping were chemomechanically polished with an alkaline colloidal silica suspension (Köstrosol 3530) and afterwards carbon coated to establish conductivity. Analytical conditions were set to a probe current of 4 nA and an acceleration voltage of 15 kV with a spot size of 1 μm in analytical modus. Samples were tilted

to 70° at a working distance of 14 mm. A step size between 0.8 and 1.5 μm was used for EBSD mapping, depending on intensity of crystal plastic deformation and grain size. All collected data (**Fig. 8–11; DR3–DR4**) was processed using the OIM Data Collection and Analysis software.

4.3. LA-ICP-MS mapping

Based on our observations from EBSD mapping, we selected four mapping areas that are representative of the deformation features to conduct 2D LA-ICP-MS element mapping (Cabri and Jackson, 2011). Element mapping was also conducted on pyrite crystals in the absence of EBSD mapping to document the geochemical signature of disparate pyrite textural types (**Fig. DR5–DR8**). Each LA-ICP-MS element map was performed at the Geological Survey of Canada (Ottawa, Canada) using an Agilent Technologies 7700x ICP-MS coupled to a Teledyne Photon Machine Analyte G2 excimer laser ablation system (λ = 193 nm) and processed following the approach of Lawley et al. (2015). Edge to edge spot-mapping with 10 μm square spots (energy density = 5.7 J/cm^2; repetition rate = 30 Hz) was used to produce each ~1 mm^2 map. Each line of spots started with 20–30 s of background data acquisition, or gas blank, which was followed by pre-cleaning each individual spot with several laser bursts (n: 4–6) to minimize surface contamination. Our approach thus differs from conventional continuous line-scanning mapping methods that result in small to significant degrees of contamination between adjacent spots. United States Geological Survey (USGS) glass reference material GSE-1G (Guillong et al., 2005) was used as the primary calibration standard and was analyzed twice every 16 lines. For elemental C and S, which are not present within GSE-1G, Iceland Spar Calcite and synthetically doped pyrrhotite standard Po689 were used to estimate concentrations for these elements based on the C/Ca and S/Fe sensitivity ratios, respectively.

Time-resolved signal intensities for each 2 s spot ablation were first integrated using an in-house Microsoft Excel spreadsheet and then converted to concentrations using a 100% total element normalization routine implemented with LAMTRACE (Jackson, 2008). Our normalization approach is designed for multi-mineral mapping, which otherwise would require prior knowledge and input of a major element concentration for each spot within the mapping area (Jackson, 2015). Quantitative major and trace element concentrations maps are color-coded (**Fig. DR5–DR12**)

5. Results

5.1. Microstructural analysis

As already noted, we sampled a variety of mineralized Lower Detour Formation mafic and ultramafic volcanic rocks with large (>1 mm) type-2 pyrite porphyroblasts. Since the deformation behaviour of pyrite remains poorly understood, it is important to document the deformation of the surrounding matrix minerals to resolve deformation conditions for each pyrite domains. Below, we summarize the deformational microstructures observed in two main rock types (mafic and ultramafic) from five samples (MV-19, MV-20, RD16-H, RD16-I, TC-06).

Mafic volcanic rocks are mainly composed of quartz (~25%), plagioclase (~15%), actinolite (~35%), calcite (~10%), with minor biotite, chlorite and sulphides including pyrite, chalcopyrite and pyrrhotite. Two main structures can be subdivided depending on grain size, both possessing a moderate to strong foliation defined by alternating layers of aligned actinolite, biotite, and chlorite. Deformation structures of coarser grained mafic volcanic rocks show clear evidence of crystal plasticity by the presence of undulatory extinction and low-angle grain boundaries in quartz, plagioclase and actinolite (**Fig. 7A, C, D**), which constrains the timing of

deformation to be syn- to post-peak metamorphism. Locally, bulges can be observed at sutured quartz grain boundaries. The fine-grained (~25 μm) rocks are dominated by polygonal structure in the quartz and plagioclase crystals (**Fig. 7B**) indicating grain size sensitive deformation mechanisms (e.g., grain size sensitive flow) were active. Both, the coarse and fine-grained mafic volcanic rocks are cut by mineralized syn-D_2 Qz-Cal veins, often aligned subparallel to the S_2 foliation. Quartz within these veins can be up to 1500 μm and is enriched in fluid inclusions. Deformation structures in calcite are dominated by mechanical twinning and minor undulatory extinction.

Type-2 pyrite domains located within the mafic volcanic host rock matrix exhibit subhedral to euhedral crystals varying in size between 50 to 250 μm, locally aligned with S_2 foliation (**Fig. 5D)**. These type-2 pyrite grains generally do not appear to have been plastically deformed, whereas elongated type-2 pyrite crystals are folded. More commonly, pyrite seems to occur within and at the margins of syn-D_2 Qz-Cal veins ranging from anhedral sieve-textured type-1 pyrite domains to euhedral, type-2 pyrite crystals between 50-3000 μm. Type-2 pyrite domains reveal evidence of plastic to brittle deformation through the presence of fractures, brecciation, pinch and swell structures, high stress grain contacts and polygonal or foam-textured pyrite domains that likely occurred during high-temperature annealing of finer grained pyrite aggregates (**Fig. 6E**).

Ultramafic samples are strongly foliated and weakly crenulated rocks composed of a talc-chlorite-quartz matrix with pyrite, pyrrhotite and magnetite porphyroblasts. Pyrite porphyroblasts (type-2) occur as anhedral to euhedral crystals varying between 100 and 1000 μm. These crystals are generally undeformed and aligned with the S_2 foliation fabric, however, few porphyroblasts appear folded by the S_3 crenulation fabric (**Fig. 5E**). Deformation in the host rock occurs mostly

as a foliation and crenulation fabric and minor subgrain development of quartz grains. Generally, quartz and plagioclase occur as small polygonal crystals indicating grain size sensitive deformation mechanisms were active.

As mentioned above, the deformation of the surrounding matrix minerals allows us to estimate the deformation conditions of the samples pyrite domains. More specifically, the combination of observed microstructures, including subgrain development within plagioclase and actinolite prophyroplasts, suggests conditions exceeding 500°C (Scholz, 1988; Kurse et al., 2001; Stipp et al., 2002). These conditions are consistent with the peak deformational (D_2) conditions and support the inferred pre- to syn-deformational timing of the sampled veins.

5.2. Intracrystalline behavior and deformation of pyrite

Based on our microstructural observations, we have targeted type-2 pyrite domains within our mafic and ultramafic volcanic samples for EBSD analyses and for quantification of pyrite intracrystalline deformation. The pyrite domains include pinch and swell structures, boudinaged brecciated veins, apparent annealed crystals with triple junctions, folded crystals, and high stress regions at grain contacts.

OC images of type-2 pyrite domains within the ultramafic volcanic host rocks exhibit a homogeneous gray pattern indicative of relatively strain-free crystals (**Fig. DR13**). The absence of plastic deformation microstructures within pyrite is consistent with strain partitioning between the soft talc-chlorite matrix and the relatively rigid behavior of pyrite porphyroblasts. Due to the lack of plastic deformation within the pyrite crystals, we did not conduct further EBSD analyses on samples from ultramafic rocks.

For pyrite domains within the mafic volcanic samples, OC images show a clear variation in gray scale indicating crystal plastic deformation. Gray scale variation of strongly elongated, folded pyrite grains (**Fig. DR4A**) and pyrite layers composed of finer grained crystals with high stress grain contacts (**Fig. DR3A**) reveal linear misorientation patterns, which can be described by a continuous rotation around one of the <100> axes (**Fig. DR3B, DR4B**). Thus our results are consistent with experimental and natural pyrite deformation studies that demonstrate slip is primarily accommodated on <100> axes (e.g., Barrie et al., 2008).

Small recrystallized grains as well as minor low-angle grain boundaries can be observed along the outer arc of the fold hinge and at grain contacts (**Fig. DR4A,C**). Pinch and swell structures (**Fig. 8A,C; 9A,C**) and boudinaged pyrite (**Fig. 10A,C**) exhibit checkerboard to complex heterogeneous misorientation patterns, which can be described by rotation around at least two <100> axes (**Fig. 9B, 10B**). Orientation deviation angle maps from these areas confirm observations from OC imaging and show maximum misorientations of up to 45° (**Fig. 10C**), revealing significant plastic deformation. Within higher strain areas, such as the necks of pinch and swell structures (**Fig. 8, 9**) and boudins (**Fig. 10**), the development of low-angle grain boundaries and new grains likely formed by subgrain rotation recrystallization. Brittle fracturing appears to be localized at such high strain areas (**Fig. 8**) possibly indicating strain hardening. In other areas, such as in the boudinaged sample (MV-20), strain is localized along microfractures in the form of crystal lattice misorientation (**Fig. 10A,C**), suggesting that brecciation and plastic deformation of pyrite in this sample were broadly coeval. For this reason, it is important to note that what appears to be low-angle grain boundaries in the brecciated pyrite domain could potentially be healed fractures, which have slightly rotated the crystal lattice.

OC images of apparently annealed pyrite domains reveal no clear gray scale variation (**Fig. 11A**), however there is some evidence of plastic strain documented by EBSD analyses. Orientation deviation angle maps show misorientations of up to 16° (**Fig. 11C**). These linear patterns occur mostly near grain boundaries and can be described by a rotation around one of the <100> axes (**Fig. 11B**). Little to no evidence of low-angle-grain boundary development is visible in the grain boundary maps (**Fig. 11D**). The absence of plastic strain in this sample could potentially be explained by pyrite annealing during D_2, which likely obscured any evidence for plastic strain within the crystal lattice.

Almost all samples show evidence of relatively late brittle deformation present as fractures crosscutting the misorientation patterns (**Fig. 8C–11C; DR3C, DR4C**). The structures and pyrite textures described above require multiple brittle-plastic deformation mechanisms during and post-dating the crystallization of pyrite porphyroblasts.

5.3. Element mapping

Four EBSD mapping areas from three samples (MV-20, RD16-H, RD16-I) were analyzed with 2D LA-ICP-MS element mapping. The areas of interest represent the deformation features observed in our samples including low-angle grain boundaries, recrystallized grains, linear and more complex misorientation patterns and brittle fractures. The combined EBSD and trace element maps (**Fig. 8–11**) provide an opportunity to evaluate the role of brittle and plastic pyrite deformation mechanisms on the retention and release of trace elements and precious metals. In addition, examples of each pyrite types were mapped (n: 4) without supporting EBSD data to define the chemical signature and metal budget of different pyrite generations (types 1–3; **Fig. DR5-DR8**).

LA-ICP-MS element maps of an inclusion-poor pyrite porphyroblast (type-2a) mantled by sieve-textured pyrite (type-1b) and wrapped by an inclusion-poor pyrite overgrowth (type-2b) clearly demonstrate that each pyrite textural type yield distinct chemical signatures (**Fig. 5B**). Trace element mapping, however, also identifies additional pyrite generations that were difficult, if not impossible, to identify visually and evinces a complex pyrite paragenesis within and adjacent to pre- to syn-D_2 auriferous veins. Some of these type-1 and type-2 pyrite domains are metal rich, and thus identifying the relative timing of Au and its relationship to deformation features is of particular importance to the current study and are discussed below.

Oscillatory-zoned pyrite domains, interpreted as primary growth zones, were mapped within individual, type-2a pyrite porphyroblasts (As map; **Fig. 12A**) and within late, type-2b pyrite overgrowths (**Fig. 12B**). First-row transition metals (Cr-Co-Ni-Cu-Zn) and some post-transition metals (Pb) and metalloids (As-Sb±Se) are particularly effective at discriminating individual growth zones, whereas Au (0.2–100 ppm; max: 184,000 ppm; **Fig. 12A**) and a suite of low melting-point chalcophile elements (Au-Ag-Bi-Te; Frost et al., 2002; Ciobanu et al., 2006) tend to yield complex, clustered, heterogeneous distributions that are concentrated within fractures and along pyrite grain boundaries. These fractures that are delineated by some transition metals, post-transition metals, metalloids, and lithophile elements (Mg-Mn-Al-Si-P-Na-K-Ca-Ti-Y-U-Th), cut pyrite oscillatory zoning (MgO; **Fig. 12A**) and auriferous pre- to syn-D_2 veins, and are mostly oblique to S_2. In most cases, these important metal-rich mineral inclusions were not visible within fractures prior to element mapping.

Sooty, colloform pyrite bands (type-3) that overgrow euhedral, type-2a pyrite porphyroblasts yield unusual Cu-Pb-Zn-Ag-rich concentrations that are devoid of Au (<0.002 ppm; **Fig. DR8**). The mechanism(s) of colloform growth remain poorly understood (Barrie et al.,

2008), but element mapping suggest that late colloform bands are geochemically distinct compared to type-1 and -2 pyrite porphyroblasts. Trace element maps also document zonation within the core of the early, type-2a pyrite porphyroblast that is not clear from reflect light microscopy. These geochemically distinct zones, which include Au-rich cores (0.1–2 ppm; **Fig. 12C**), are cut by fracture-hosted Au (2–30 ppm)-Ag-Te-Bi-rich inclusions.

Combined EBSD and element mapping of the boudinaged pyrite vein (MV-20) and the pinch and swell pyrite vein (RD16-I) reveal that Au (0.2–10 ppm; max: 349 ppm; **Fig. 8E, 10E, 11E**) and other trace elements are relatively enriched at low-angle grain boundaries and brittle fractures. Critically, grain boundaries within this sample are devoid of Au (<0.002 ppm) and thus the pinch and swell pyrite domain (RD16-I) provides the clearest link between plastic pyrite deformation microstructures and Au for our sample suite (**Fig. 8E, 9E**).

A range of metal-rich fractures (Ag-Te-Bi±Au) also cut ductily-deformed pyrite pinch and swell domains and are distinct from the mostly uniform metal distribution within the silicate mineral matrix (**Fig. 8–9**). The contrasting element map patterns between sulphide and silicate minerals reflect, in part, the low-concentration of these elements within the silicate mineral matrix, which are at or below the analytical detection limit, but also highlight the important role of sulphide minerals as micro-structural traps for Au (discussed below).

LA-ICP-MS maps of the sigma-shaped pyrite vein with polygonal or foam-textured pyrite likely reflect high-temperature annealing (RD16-H). Grain boundaries and the interstices between polygonal pyrite crystals are Au-rich (0.1–5 ppm; max: 8070 ppm; **Fig. 11E**) and have a lithophile-element signature, which could be indicative of fluid-mediated high temperature annealing. Zoning patterns of first-row transition metals (Co-Ni) and metalloids (As) within this sample also document that foam-textured pyrite in fact represents the amalgamation of

geochemically distinct pyrite crystals and element diffusion towards migrating grain boundaries during pyrite recrystallization (**Fig. 11**), which are then cut by metal-rich fractures.

Element and EBSD mapping of the boudinaged and brecciated pre- to syn-D_2 vein also document that individual pyrite fragments are geochemically distinct. First-row transition, post-transition and metalloids are enriched along fragmented pyrite grain boundaries and likely signal coupled dissolution-precipitation reactions and/or neocrystallization of pyrite during cataclasis. Fractures, low-angle grain boundaries and fracture-hosted pyrite crystals are relatively Au-rich (0.2–0.5 ppm; max: 157 ppm), which is consistent with metal mobility and the precipitation of fracture-hosted native Au during a late-stage, post-vein phase of plastic-brittle deformation. Fractures hosted entirely within individual pyrite fragments contrast with broader zones of cataclasite that dismembered previously fractured pyrite grains and likely document successive fracture generations.

6. Discussion

6.1. Deformation micro-structures and pressure-temperature conditions

The results of this study indicate evolving conditions in the brittle-plastic to brittle regime at lower amphibolite facies conditions. Observed annealed pyrite textures provide independent evidence that pre- to syn-D_2 auriferous veins reached medium metamorphic grade (≥500°C; McClay and Ellis, 1983). We document pyrite deformation described by rotation about at least one of the <100> axes in the form of linear, checkerboard, and more complex heterogeneous misorientation patterns, low-angle grain boundary development, and foam-textured pyrite domains indicative of dislocation–glide and –creep, and high temperature static recrystallization, respectively. Although the bulk of our work complements previous studies on pyrite plastic

deformation, we also document new grain recrystallization by subgrain rotation within necks of pinch and swell structures and boudinaged domains, which have not been previously observed at such pressure-temperature conditions. In addition, trace element enrichment at these deformation-induced substructures (i.e., low-angle grain boundaries, recrystallized grain boundaries, brittle fractures) suggests that the brittle-plastic to brittle deformation of pyrite is likely concomitant with Au mineralization and/or remobilization at the Detour Lake deposit. Our results, however, differ from those of Fougerouse et al. (2016) as we document Au and trace element enrichment within the low-angle grain boundaries.

6.2. Au paragenesis

Mineralized D_2 faults are concentrated along the W-trending and steeply-dipping SLDZ and support a relative time relationship between D_2 and Au at the district- to deposit-scales. Post-D_2 structures do not significantly impact the Au deposit geometry, suggesting that they post-date the main period of Au mineralization. Moreover, the syn-deformational timing of the mineralized veins within the low-grade, hanging wall are consistent with the syn-D_2 timing of high-grade fault-fill veins along the SLDZ and within the historic mine of the Campbell pit. In contrast, extensive transposition during D_2 has obscured the relationship between Au and pre-D_2 structures, although D_1 unconformities that were reactivated during D_2 (e.g., SLDZ) are clearly an important exploration criterion at the district scale. Ore zones at the deposit scale are also sulphidized suggesting a close spatial- and temporal-relationship between Au and pyrite-pyrrhotite, features that are consistent with the Au-upgrading model.

Here we integrate these district- to deposit-scale observations that constrain the relative timing of Au with new micro-textural observations and element mapping. Primary, oscillatory

growth-zoning within pyrite porphyroblasts are observed within early type-2a pyrite cores and type-2b pyrite overgrowths. Early, Au-rich type-2a pyrite cores are mantled by later, Au-poor type-2b pyrite overgrowths (**Fig. 12B**), suggesting that lattice-bound Au locally represents an early-stage of Au mineralization.

The vast majority of Au-rich domains, however, yield complex chemical map patterns and clustered distributions along grain boundaries and/or fractures, which is consistent with the textural setting of coarse fracture-hosted native Au at the decimeter scale and dilatant Au-rich ore zones at the kilometer scale (e.g., such as left-stepping ore shoots along the SLDZ; **Fig. 2B; DR1**). These domains likely reflect sub-micron Au inclusions within the majority of samples, which is also consistent with the extreme Au concentrations for some individual spot analyses (e.g., 18 wt% Au; **Fig. DR6**). In most cases these native Au inclusions were not observed prior to mapping, which suggest that they occur as ultrafine inclusions and/or inclusions that were buried within a few microns of the polished pyrite surface.

Primary pyrite porphyroblast growth features (e.g., oscillatory zoning) are cut by late metal-rich fractures suggesting that Au remobilization was coupled with the redistribution of other metals (Ag-Bi-Te±Cu±Pb) and lithophile elements. Dissolution-precipitation reactions and/or element diffusion adjacent to fractures also modified pyrite compositions during brittle fracturing and locally led to Au-enrichment along new, pyrite grain-boundaries. The close paragenetic relationship at the micro-scale between Au enrichment, fracturing and dissolution-precipitation suggests that auriferous fluids and deformation were concomitant and that high ore grade veins were re-worked during Au remobilization. Some of the most Au-rich examples yield anomalous As-rich concentrations (100s of ppm to wt%), suggesting that As-S substitution reactions likely distort the pyrite crystal lattice and facilitate the incorporation of Au and the

adsorption of Au onto arsenian pyrite surfaces (discussed below). A similar model has been invoked for other trace elements, which highlights that early- and late-stage pyrite-hosted Au enrichment may be dependent on the spatial distribution of impurities and the distribution of impurities within disparate pyrite generations (e.g., Cook et al., 2006; discussed below).

Field relationships and element maps also document a complex, relative timing for Au remobilization. Metal-rich fractures that cut syn-metamorphic growth zones and polygonal pyrite crystals clearly demonstrate a late-stage, brittle-dominated deformation phase during the youngest Au remobilization event. However, lattice-bound Au and ultrafine Au inclusions hosted within early type-2a pyrite and later type-2b pyrite overgrowths, which coupled with multiple generations of Au-rich fractures, likely document multiple, successive stages of Au remobilization during re-working of pre- to syn-D_2 auriferous veins.

The absolute timing of Au remobilization also remains poorly constrained. Whereas barren, post-D_2 veins provide the clearest evidence that the introduction and subsequent remobilization of Au occurred during D_2, small-scale Au remobilization may have also occurred post-D_2. However, any late-stage, Au remobilization did not disrupt the E-W trending-geometry of ore zones at the deposit scale and is not associated with any macro-scale deformation fabrics. Moreover, the absolute age of D_2 remains poorly constrained. Despite the uncertain age for the introduction and subsequent remobilization of Au, the relationships documented above are broadly consistent with the Au-upgrading model where early, lattice-bound Au is re-distributed and concentrated as free Au during a younger remobilization event. The possible mechanisms controlling Au-remobilization within pyrite are evaluated within the context of our EBSD results below.

6.3. Syn-metamorphic deformation-driven Au-upgrading

In this section, we define the relationship between pyrite deformation and Au by integrating our microstructural and geochemical observations. The syn-metamorphic and deformation-driven Au-upgrading model predicts that Au is introduced, remobilized or both during metamorphism and then concentrated into deformation-induced microstructural settings (i.e., low-angle grain boundaries, fractures) possibly through intragrain diffusion mechanisms (cf. Vukmanovic et al., 2014). Herein, we discuss how lattice-bound Au or Au inclusions introduced by vein forming fluids can move with other trace elements into the deformation-induced microstructures through intragrain diffusion processes during syn-D_2 recovery and recrystallization of pyrite. Such a process would help to explain the spatial relationship between Au and pyrite microstructures observed in each of our samples. There are three types of intragrain diffusion: 1) volume diffusion, 2) high-diffusivity "pipe" pathways, and 3) dislocation-impurity pair (DIP) diffusion. Below, we discuss each of these mechanisms.

Volume diffusion is a mechanism through which components (e.g., Au, Bi, Te) are displaced within the crystal lattice following a chemical potential gradient at high temperatures (Klinger and Rabkin, 1999; Vukmanovic et al., 2014). This process has been studied under the assumption of a homogeneous crystal lattice that is likely unrealistic (Fisher, 1951). In most cases, crystals host dislocation networks that are rearranged into low-angle grain boundaries during plastic deformation. Since the diffusion coefficient along dislocation arrays is significantly higher than the diffusion coefficient for volume diffusion (Klinger and Rabkin, 1999), it is unlikely that the trace element concentrations at crystal defects within our samples are due to volume diffusion.

High diffusivity pathways consists of the preferential migration of components along dislocation arrays (i.e., low-angle grain boundaries), commonly referred to as "pipes" (e.g., Vukmanovic et al., 2014). This model requires a chemical potential gradient and a source for the components. We propose two possible sources: 1) a syn-D_2 Au-rich intergranular fluid; and 2) Au nanoparticules and Au-pyrite solid solution. In the first case, a syn-D_2 vein-forming intergranular fluid introduces Au and other trace elements into the system. This scenario establishes a chemical potential gradient between the fluid and the trace element-depleted pyrite along the low-angle grain boundaries, which behave as "pipes." In the second case, Au is included in pyrite during crystallization. The oscillatory crystal growth recorded in As chemical maps (**Fig. 9**) suggests zoning of Au due to the correlation between As content and Au solubility (Reich et al., 2005). The chemical potential gradient created by that zoning could potentially be the driving force behind "pipe" diffusion.

Dislocation-impurity pair (DIP) diffusion is the entrainment of components or impurities within migrating dislocations (Vukmanovic et al., 2014). Although impurities have previously been thought to act as barriers for migrating dislocations, Imai and Sumino (1983) have suggested that, at high temperature and stress conditions, the activation energy for dislocations decreases with increasing impurity concentrations, thus facilitating their mobility. Although the increased impurity concentration of dislocations may reduce their velocity, slower moving dislocations capture impurities more efficiently, creating a positive feedback between the distribution of dislocations and impurities (Petukhov and Klyuchnik, 2012). The migration of these dislocations results in higher impurities concentration in dislocation arrays such as low-angle grain boundaries. Though this model does not necessitate a chemical potential gradient, it does require impurities with large ionic radii (Vukmanovik et al., 2014). Since Au in pyrite

crystal lattices most likely exists in a negative valence state (Cabri et al., 2000), it is possible that the ionic radius of Au in pyrite is sufficiently large to migrate along with dislocations.

The absence of Au-rich grain boundaries in the pinch and swell and boudinaged pyrite domains (RD16-I, MV-20) provides the clearest evidence of Au-upgrading related to intragrain diffusion. In both of these domains, low-angle pyrite grain boundaries are relatively Au-rich (0.1–0.5 ppm), which we suspect could have resulted from either "pipe" or DIP diffusion. However, we cannot explain the Au and trace element enrichment along fractures in the boudinaged domain (MV-20) without invoking fluids. In addition, first-row transition metals, post-transition metals, and low melting-point chalcophile elements (Ag-Te-Bi) are concentrated within the same low-angle grain boundaries in addition to grain boundaries and fractures. The complex, micro-structural distribution of these elements is likely related to the late-D_2, overprinting of fluid-assisted fracturing of pre- to syn-D_2 veins, which obscure the relationship between element-enrichment and diffusion models. Thus, DIP diffusion is unlikely to be the only diffusion mechanism active and most likely occurs with "pipe" diffusion.

The late-D_2 brittle phase of deformation is likely responsible for a significant amount of Au-rich domains within each of the pyrite element maps. In most cases, these Au-rich fractures, which based on the heterogeneous distribution of Au likely contain inclusions of native Au, exceed the concentration of lattice-bound Au within early metal-rich type-1 and type-2 pyrite porphyroblasts (0.2–1 ppm). The composition of these fractures indicates a complex assemblage of micro- to nano-scale mineral inclusions that contrast with the quartz-dominated mineral assemblage observed during petrography. Healed pyrite fractures support the notion of multiple episodes of coupled dissolution-precipitation reactions that ultimately led to a complex, metal-rich network at the micro-scale.

Our data demonstrate that pyrite microstructures are favourable mechanical traps for Au at the micro-scale. Grain boundaries and fracture surfaces are key micro-textural sites for the Au adsorption during a late, brittle-dominated deformation phase concomitant with the youngest stage of Au remobilization. The scattered and clumped distribution of metals within the silicate mineral rock matrix is due, in part, to the low concentration of these elements within the silicate minerals, whereas the association between Au and pyrite fractures partially supports the electrochemical-deposition, or adsorption, of Au on sulphide mineral surfaces. In this model, silicate mineral surfaces and fractures are less favorable depositional sites, which help to explain why Au-rich fractures within pyrite do not extend into the surround rock matrix. Some of this Au may have been locally derived from early, lattice-bound Au within type-1 and type-2 pyrite porphyroblasts. Gold adsorption, however, does not explain the occurrence of coarse, native Au hosted within hydrothermal alteration minerals (e.g., calcite and chlorite) or high ore grade Au veins devoid of sulphides. These observations likely require multiple depositional mechanisms, locally within the same vein. Below we further explore the contribution of the observed sulphide-hosted Au on the overall Au endowment of the Detour Lake deposit through a series of mass balance calculations at the deposit scale.

6.4. Testing the impact of the Au-upgrading model

We have presented textural, geochemical and structural evidence for Au mineralization and remobilization during pyrite (re)crystallization and structural reworking of auriferous veins. However, the relative contribution of lattice-bound Au within pyrite versus free Au remains unclear. Assay data and 3D block models acquired by Detour Gold Corp. suggest that 4,088,650 tonnes of S were hosted within 327,016,000 tonnes of rock that has currently been mined from

the open pit at the Detour Lake deposit: calculations are based on assays for S that were above the analytical detection limit and block models were divided into 0.5 ppm S intervals up to >3.5 wt% S (**Table 2**). An equal volume of mined rock contained 8,694,669 oz of Au and assuming that 1) all of the S is related to pyrite and 2) pyrite was the only source of Au in this deposit, concentrations of lattice-bound pyrite hosted Au would need to exceed 32 ppm Au to account for the Au endowment of the Detour Lake deposit. This value is improbable. More realistic concentrations of primary, lattice-bound Au, would be 1 ppm, 0.1 ppm, or even 1 ppb. Calculations using these concentrations for the same volume or rocks yield values of 269,814 oz, 26,981 oz, and 270 oz of Au, respectively. At most, lattice-bound Au contained in pyrite can only account for 3.1% of the known Au resources at the Detour Lake deposit.

These mass balance calculations suggest that the Detour Lake deposit is too Au-rich, S-poor, or both to allow for lattice-bound Au to contribute significantly to the Au endowment. Sulphide minerals outside of the open pit operations were not included within these calculations and it is possible that lattice-bound Au within these sulphide minerals may have also contributed to Au. However, mafic volcanic and sedimentary rocks outside of the open pit are generally sulphide-poor and a large volume of rock would be required to account for the exceptional amount of Au within the Detour Lake deposit (Gaboury, 2013).

After evaluating these calculations, the "pipe" diffusion model invoking an external source of Au remains the most convincing and consistent model to explain our observations of a link between deformation and trace element distribution. We have summarized and illustrated the deformation and mineralization history of the Detour Lake mine in a synoptic model (**Fig. 13**) based on four major steps: (1) pre-D_2, a possible pyrite-bearing massive mafic volcanic host rock with quartz veining; (2) early syn-D_2, development of a foliation structure, S_2, and

transposition of quartz vein and pyrite mineralization with possible incorporation of Au as nanoparticles by adsorbtion or solid solution; (3) late syn-D_2, crystal plastic deformation of pyrite and development of low-angle grain boundaries and brittle fractures followed by Au enrichment at deformation substructures though "pipe" diffusion; and (4) syn-D_3, development of a crenulation fabric, S_3. The important takeaway from this model is that the progressive brittle and brittle-plastic deformation history of pyrite plays a key role in the micro-scale distribution of Au mineralization at lower amphibolite facies conditions. Although this is still considered a syn-metamorphic and deformation-driven model, it significantly differs from the model introduced by Fougerouse et al. (2016) where lattice-bound Au is leached-out and remobilized through deformation induced pathways (i.e., low-angle grain boundaries).

6.5 Transport mediums

Although "pipe" diffusion can drive Au to migrate into low-angle grain boundaries and fractures, the medium of transport for Au remains unclear. There are various mediums by which Au and other trace elements could have been introduced to then be concentrated into deformation induced substructures including: 1) solid-state Au 2) metal-rich melts, and 3) aqueous solutions.

Solid-state mobilization occurs in deforming multiphase materials, where some phases are less competent than others. During deformation, such phases become weaker and deform more easily than others and thus become more mobile. The deformation of more competent phases creates dilational regions and structures developing a hydraulic gradient, which drives the more ductile phases to concentrate in those dilational sites (Tomkins et al., 2004; Marshall et al., 2000). In the case of Detour Lake, the strain partitioning between Au and more competent sulphides (i.e., pyrite) in mineralized pre- to syn-D_2 veins could potentially explain the

mobilization of Au into the low-angle grain boundaries within the sulphide crystals. This mobilization mechanism is consistent with our deposit-scale observations noting the importance of dilational structures such as mineralized extensional veins and left-stepping ore shoots.

Moreover, the association between Au and other low melting-point elements (Ag-Bi-Te) has also been used as evidence to support the role of metal-rich melts as a transport medium during Au remobilization (Frost et al., 2002). Ciabanu et al. (2006) suggested that these melts can operate at relatively low temperatures that are typical of greenschist facies metamorphic conditions (400°C) and are well below the high temperatures that are inferred for the Detour Lake deposit during Au deposit genesis (500-550°C). However, in this case, coarse native Au is co-spatial with hydrothermal alteration minerals at the hand-sample scale (calcite-chlorite) and Au-rich fractures are filled with lithophile elements at the micro-scale, suggesting that any metal-rich melts were likely transported, at least locally, by syn-deformation hydrothermal fluids. It is possible that these auriferous fluids may have also facilitated solid-state remobilization of other precious- and base-metal rich minerals (e.g., chalcopyrite, galena, pyrrhotite) during deformation, although the relative contribution of fluids, melts and solid-state mechanisms during remobilization remains unclear.

The association of Au with hydrothermal alteration minerals and lithophile elements could also suggest mobilization of Au by aqueous solution. For example, sulfur radical ions (S_3^-) strongly bind Au in aqueous solution at middle to high metamorphic conditions (Pokrovski et al., 2015). When temperatures cool below 500°C, pyrite begins to precipitate, which causes the decay of S_3^- and the decrease of Au solubility. This decrease in solubility could cause the Au to precipitate in the low-angle grain boundaries of the deforming pyrite crystals.

7. Summary

Our data can be summarized in five major points: (1) Pyrite can deform plastically under lower amphibolite facies conditions, which can be described by rotation about at least one of the <100> axes. (2) Crystal plastic deformation in pyrite is present as linear, checkerboard and complex heterogeneous misorientation patterns, low-angle boundary development and recrystallization indicating the activity of dislocation glide and creep at moderate metamorphic conditions. (3) Deformational substructures (i.e., low-angle grain boundaries, micro-cracks) in pyrite may act as traps for Au and other trace elements at the micro-scale. (4) Pyrite textures and trace element mapping are consistent with Au mineralization during the dominant phase of deformation at the Detour Lake deposit (D_2) and syn- to post-peak metamorphism. Gold mineralization locally occurred via intragrain diffusion mechanisms that concentrated trace elements into deformation-induced substructures. However, the vast majority of micro-scale Au is hosted within late, brittle fractures that cut syn-metamorphic pyrite porphyroblasts. (5) Deposit scale mass balance calculations suggest that lattice-bound Au within pyrite porphyroblasts could have supplied a tiny fraction of the known Au (~3%) within the Detour Lake open pit, suggesting that an external source of Au is required for this giant deposit and raise questions surrounding the efficacy of the metamorphic-driven Au upgrading model.

Acknowledgements

This project was funded by Detour Gold Corp., an SEGF student research grant (to RD), a NSERC Discovery grant (to DAS), and NRCan's Targeted Geoscience Initiative (TGI)-5 program (to CJML). We would like to thank Detour Gold Corp. for their cooperation and assistance throughout our project, David Diekrup and Glenn Poirier for help with SEM and

EPMA analyses, Gerlinde Habler for assistance with OC and EBSD analyses and Zhaoping Yang for guidance with LA-ICP-MS analyses. Discussions with Bernhard Grasemann and Mark Hannington are also greatly appreciated.

References

Allaire, 2014. Detour Lake Mine–NI 43-101 technical report.

Ayer, J.A., Amelin, Y., Corfu, F., Kamo, S., Ketchum, J., Kwok, K., Trowell, N., 2002. Evolution of the southern Abitibi greenstone belt based on U-Pb geochronology: autochtonous volcanic construction followed by plutonism, regional deformation, and sedimentation. Precambrian Research 115, 63–95.

Ayer, J.A., Thurston, P.C., Batemen, R., Dubé, B., Gibson, H.L., Hamilton, M.A., Hathway, B., Hocker, S.M., Houle, M.G., Hudak, G., Ispolatov, V.O., Lafrance, B., Lesher, C.M., MacDonald, P.J., Peloquin, A.S., Piercey, S.J., Reed, L.E., Thompson, P.H., 2005. Overview of results from the Greenstone Architecture Project: Discover Abitibi Initiative, Ontario Geological Survey, Open File Report 6154, 146 p.

Ayer, J.A., Trowell, N.F., Dubé, B., 2009. Project Unit 95-024. A Stratigraphic and Metallogenic Comparison of the Detour–Burntbush Area with the Southern Abitibi Greenstone Belt and Its Implications for Exploration. Ontario Geological Survey Open File Report 6240, Summary of Field Work and Other Activities, p. 3.1–3.7.

Ayer, J.A., Goutier, J., Thurston, P.C., Dubé, B., Kamber, B.S., 2010. Tectonic and metallogenic evolution of the Abitibi and Wawa sub-provinces. Summary of Fieldwork and Other Activities 2010: Ontario Geological Survey Open File Report 6260, p. 3.1–3.6.

Barrie, C.D., Boyle, A.P., Cox, S.F., Prior, D.J., 2008. Slip systems and critical resolved shear stress in pyrite: an electron backscatter diffraction (EBSD) investigation. Mineralogical Magazine 72(6), 1181-1199.

Barrie, C.D., Boyle, A.P., Salter, M., 2009. How low can you go? — Extending downwards the limits of plastic deformation in pyrite. Mineralogical Magazine 73, 895–913.

Barrie, C.D., Boyce, A.J., Williams, P.J., Blake, K., Ogawara, T., Akai, J., Prior, D.J., 2009. Growth controls in colloform pyrite. American Mineralogist 94, 415–429.

Barrie, C.D., Cook, N.J., Boyle, A.P., 2010. Textural variation in the pyrite-rich ore deposits of the Røros district, Trondheim Region, Norway: Implications for pyrite deformation mechanisms. Mineralium Deposita 45, 51–68.

Barrie, C.D., Pearce, M.A., Boyle, A.P., 2011. Reconstructing the pyrite deformation mechanism map. Ore Geology Reviews. 39(4), 265–276.

Bateman, R., Ayer, J.A., Dubé, B., 2008. The Timmins-Porcupine gold camp, Ontario: anatomy of an Archean greenstone belt and ontogeny of gold mineralization. Economic Geology 103, 1285–1308.

Bleeker, W., 2015. Synorogenic gold mineralization in granite-greenstone terranes: the deep connection between extension, major faults, synorogenic clastic basins, magmatism, thrust inversion, and long-term preservation. In: Dubé, B., Mercier-Langevin, P., (eds.) Targeted Geoscience Initiative 4: Contributions to the Understanding of Precambrian Lode Gold Deposits and Implications for Exploration, Geological Survey of Canada, Open File 7852, p. 25–47.

Bleeker, W., 2010, Targeted Geoscience Initiative 4. Lode Gold Deposits in Ancient Deformed and Metamorphosed Terranes: The Role of Extension in the Formation of Timiskaming Basins and Large Gold Deposits, Abitibi Greenstone Belt—A Discussion. Summary of Field Work and Other Activities 2012, Ontario Geological Survey Open File Report 6280, p. 47.1–47.12.

Benn, K., Peschler, A.P., 2005. A detachment fold model for fault zones in the Late Archean Abitibi greenstone belt. Tectonophysics. 400, 85-104.

Bouchard, M., 2015. Predicting stable metamorphic assemblages in P-T space using phase equilibria modelling and characterization of mafic metavolcanic rocks South of Detour Lake mine, Ontario, Canada. Unpublished BSc thesis, Laurentian University, Sudbury, Ontario, Canada.

Boyle, A.P., Prior, D.J., Banham, M.H., Timms, N.E., 1998. Plastic deformation of metamorphic pyrite: new evidence from electron-backscatter diffraction and forescatter orientation-contrast imaging. Mineralium Deposita 34, 71–81.

Cabri, L., Newville, M., Gordon, R., Crozier, D., Sutton, S., McMahon, G., Jiang, D. 2000. Chemical speciation of gold in arsenopyrite. Canadian Mineralogist 38, 1265–1281.

Cabri, L., and Jackson, S., 2011. New developments in characterization of sulfide refractory Au ores: MetSoc, World Gold 2011, 50th Conference of Metallurgists, Montreal, Quebec, 2011, Proceedings, 51–62.

Ciobanu, C.L., Cook, N.J., Damian, F., Damian, G., 2006. Gold scavenged by bismuth melts: An example from Alpine shear-remobilizates in the Highiş Massif, Romania. Mineralogy and Petrology 87, 351–384.

Cook, N.J., Chryssoulis, S.L., 1990. Concentrations of “invisible gold” in the common sulphides. Canadian Mineralogist 28, 1–16.

Cook, N.J., Ciobanu, C.L., Mao, J., 2009. Textural control on gold distribution in As-free pyrite from the Dongping, Huangtuliang and Hougo gold deposits, North China Craton. Chemical Geology 264, 101–121.

Cox, S.F., Etheridge, M.A., Hobbs, B.E., 1981. The experimental ductile deformation of polycrystalline and single- crystal pyrite. Economic Geology 76, 2105–2117.

Craig, J.R., Vokes, F.M., 1993. The metamorphism of pyrite and pyritic ores: an overview. Mineralogical Magazine 57, 3–18.

Daigneault, R., Mueller, W.U., Chown, E.H., 2004. Abitibi greenstone belt plate tectonics: A history of a chronic arc development, accretion and collision. In: Eriksson, K.A., Altermann, W., Nelson, D.R., Mueller, W., Catuneanu, O., Strand, K., (Eds.) The Precambrian Earth: Tempos and Events: Elsevier, Amsterdam, 88–103.

Dubé, B., Gosselin, P., 2007. Greenstone-hosted quartz-carbonate vein deposits. Geological Association of Canada, Mineral Deposits Division, Special Publication no. 5, 49–83.

Dubé, B., Mercier-Langevin, P., 2015. Targeted Geoscience Initiative 4: Contributions to the Understanding of Precambrian Lode Gold Deposits and Implications for Exploration. Geological Survey of Canada Open File 7852, 297 p. doi:10.4095/296624.

Fisher, J.C., 1951. Calculation of diffusion penetration curves for surface and grain boundary diffusion. Journal of Applied Physics 22(1), 74–77.

Frost, R.B., Mavrogenes, J.A., Tomkins, A.G., 2002. Partial melting of sulfide ore deposits during medium- and high-grade metamorphism. Canadian Mineralogist, 40, 1–18.

Gaboury, D., 2013. Does gold in orogenic deposits come from pyrite in deeply buried carbon-rich sediments?: Insight from volatiles in fluid inclusions. Geology 41, 1207–1210.

Goutier, J., 1997. Géologie de la région de Destor (SNRC 32D/07): Ministère des ressources naturelles du Québec, report RG96-13, 37 p.

Goutier, J., Melançon, M., 2007. Compilation géologique de la Sous-province de l'Abitibi (version préliminaire): Ministère des Ressources naturelles et de la Faune, Québec, échelle 1/500 000. http://www.mrn.gouv.qc.ca/mines/geologie/geologie-projets.jsp.

Graf, J.L., Skinner, B.J., Bras, J., Fagot, M., Levade, C., Couderc, J.J., 1981. Transmission electron-microscopic observation of plastic-deformation in experimentally deformed pyrite. Economic Geology 76, 738-742.

Groves, D.I., Goldfarb, R.J., Gebre-Mariam, M., Hagemann, S.G., Robert, F., 1998. Orogenic gold deposits: A proposed classification in the context of their crustal distribution and relationship to other gold deposit types. Ore Geology Reviews 13, 7–27.

Groves, D.I., Goldfarb, R.J., Knox-Robinson, C.M., Ojala, J., Gardoll, S., Yun, G.Y., Holyland, P., 2000. Late-kinematic timing of orogenic gold deposits and significance for computer-based exploration techniques with emphasis on the Yilgarn Block, Western Australia. Ore Geology Reviews 17, 1–38.

Guillong, M., Hametner, K., Reusser, E., Wilson, S.A., Günther, D., 2005. Preliminary characterisation of new glass reference materials (GSA-1G, GSC-1G, GSD-1G and GSE-1G) by laser ablation-inductively coupled plasma-mass spectrometry using 193 nm, 213 nm and 266 nm wavelengths. Geostandards and Geoanalytical Research 29, 315–331.

Imai, M., Sumino, K., 1983. In situ x-ray topographic study of the dislocation mobility in high-purity and impurity-doped silicon crystals. Philosophical Magazine A 47, 599–621.

Jackson, S.E., 2008. LAMTRACE data reduction software for LA-ICP-MS. Mineralogical Association of Canada Short Course Series 40, 305–307.

Jackson, S.E., 2015. Application of LA-ICP-MS for mapping of trace element concentrations and isotope ratios in geochemistry. In: Montaser, A., (ed.) Inductively coupled plasma mass spectrometry, 2nd edition: 1, 200 p.

Johns, G.W., 1982. Geology of the Burntbush-Detour Lakes area, District of Cochrane: Ontario Geological Survey, Report 199, 82 p.

Kerrich, R., Kyser, K.T., 1994. 100 Ma timing paradox of Archean gold, Abitibi greenstone belt (Canada): New evidence from U-Pb and Pb-Pb evaporation ages of hydrothermal zircons. Geology 22, 1131–1134.

Klinger, L., Rabkin, E., 1999. Beyond the Fisher model of grain boundary diffusion: effect of structural inhomogeneity in the bulk. Acta Materialia 47, 725–734.

Knipe, R.J., 1997. Juxtaposition and seal diagrams to help analyze fault seals in hydrocarbon reservoirs. American Association of Petroleum Geologists Bulletin 81, 187–195.

Knott, S.D., 1993. Fault seal analysis in the North Sea. American Association of Petroleum Geologists Bulletin 77, 778–792.

Kurse, R., Stünitz, H., Kunze, K., 2001. Dynamic recrystallization processes in plagioclase porphyroclasts. Journal of Structural Geology 23, 1781–1802.

Large, R.R., Maslennikov, V.V., Robert, F., Danyushevsky, L.V., Chang, Z., 2007. Multistage sedimentary and metamorphic origin of pyrite and gold in the Giant Sukhoi log deposit, Lena Gold Province, Russia. Economic Geology 102, 1233–1267.

Lawley, C.J.M., Creaser, R., Jackson, S., Yang, Z., Davis, B., Pehrsson, S., Dubé, B., Mercier-Langevin, P., Vaillancourt, D., 2015. Unravelling the Western Churchill Province Paleoproterozoic Gold Metallotect: Constraints from Re-Os arsenopyrite and U-Pb

xenotime geochronology and LA-ICP-MS arsenopyrite geochemistry at the BIF-hosted Meliadine Gold District, Nunavut, Canada. Economic Geology 110, 1425–1454.

Levade, C., 1982. Dissociated dislocations in pyrites deformed at a high-temperature. J. Microsc. Spectrosc. Elect. 7, A21–A21.

Levade, C., Couderc, J.J., Bras, J., Fagot, M., 1982. Transmission electron-microscopy study of experimentally deformed pyrite. Philosophical Magazine A: Defects and Mechanical Properties 46, 307–325.

Marmont, S., 1986. The geological setting of the Detour Lake Gold Mine, Ontario. Canada. In: MacDonald, A.J., (ed.) Proceedings of Gold '86, an International Symposium on the geology of Gold, 3–22.

Marmont, S., 1987. Geology of the Lower Detour Lake-Hopper-Sunday Lakes area, north-eastern Ontario. Ontario Geological Survey. Miscellaneous Paper No. 137, 175–180.

Marmont, S., Corfu, F., 1988. Timing of gold introduction in the late Archean framework of the Canadian Shield: Evidence from U-Pb zircon geochronology of the Abitibi Subprovince. In: Keays, R.R., Ramsay, W.R.H., Groves, D.I., (eds.) The Geology of Gold Deposits: The Perspective in 1988. Economic Geology Monograph 6, 101–111.

Marshall, B., Vokes, F.M., Larocque, A.C.L., 2000. Regional metamorphic remobilization: Upgrading and formation of ore deposits: Reviews in Economic Geology 16, 19–38.

McClay, K.R., Ellis, P.G., 1983. Deformation and recrystallization of pyrite. Mineralogical Magazine 47, 527–538.

McClay, K.R., Ellis, P.G., 1984. Deformation of pyrite. Economic Geology 79, 400–403.

Miller, A.R., 2005. A contribution of petrography, petrology and mineralogy of wall rocks and gold-bismuth tellurium bearing carbonate veins, West Pit Extension Mine Option Land, Detour Lake Property Abitibi Gold Belt Ontario, utilizing petrography-ore microscopy scanning microscopy – geochemistry, Internal corporate report by Miller and Associates for High River Mines Limited and Pelangio Mines Inc., 82 p.

Oliveira, J.F., 1997. Sulphide breccia veins at Detour Lake Mine, northeastern Ontario. Unpublished BSc thesis, Laurentian University, Sudbury, Ontario, Canada.

Oliver, J., Ayer, J., Dubé, B., Aubertin, R., Burson, M., Panneton, G., Friedman, R. Hamilton, M., 2011. Structure, stratigraphy, U-Pb geochronology and alteration characteristics of gold mineralization at the Detour Lake deposit, Ontario, Canada. Exploration and Mining Geology 20, 1–30.

Owona, S., Ondoa, J.M., Ekodeck, G.E., 2013. Evidence of quartz, feldspar, and amphibole crystal plastic deformations in the Paleoproterozoic Nyong Comples shear zones under amphibolite to granulite conditions (West Central African fold belt, SW Cameroon. Journal of Geography and Geology 5(3), 186–201.

Palenik, C.S., Utsunomiya, S., Reich, M., Kesler, S.E., Wang, L., Ewing, R.C., 2004. “Invisible” gold revealed; direct imaging of gold nanoparticles in a Carlin-type deposit. American Mineralogist 89, 1359–1366.

Passchier, C.W., Trouw, R.A.J., 2005. Microtectonics. Springer.

Petukhov, B.V., Klyuchnik, P.A., 2012. Dynamic interaction of dislocations with impurity subsystem in crystalline materials. Crystallography Reports 57, 388–392.

Pokrovski, G.S., Kokh, M.A., Guillaume, D., Borisova, A.Y., Gisquet, P., Hazemann, J., Lahera, E., Del Net, W., Proux, O., Testemale, D., Haigis, V. Jonchière, R., Seitsonen, A.P., Ferlat, G., Vuilleumier, R., Saitta, A.M., Boiron, M.C., Dubessy, J., 2015. Sulfur radical species form gold deposits on Earth. Proceedings of the National Academy of Sciences 112(44), 13484–13489.

Powell, W.G., Carmichael, D.M., Hodgson, C.J., 1995a. Conditions and timing of metamorphism in the southern Abitibi greenstone belt Quebec. Canadian Journal of Earth Sciences 32, 787–805.

Powell, W.G., Hodgson, C.J., Hanes, J.A., Carmichael, D.M., McBride, S. Farrar, E., 1995b. $^{40}Ar/^{39}Ar$ geochronological evidence for multiple postmetamorphic hydrothermal events focused along faults in the southern Abitibi greenstone belt. Canadian Journal of Earth Sciences 32, 768–786.

Reich, M., Kesler, S., Utsunomiya, S., Palenik, C., Chryssoulis, S., Ewing, R. 2005. Solubility of gold in arsenian pyrite. Geochimica et Cosmochimica Acta 69(11), 2781–2796.

Scholz, C.H., 1988. The brittle-plastic transition and the depth of seismic faulting. Geologische Rundschau. 77(1), 319–328.

Stipp, M., Stünitz, H., Heilbronner, R., Schmid, S.M., 2002. The eastern Tonale fault zone: a ‘natural laboratory’ for crystal plastic deformation of quartz over a temperature range from 250 to 700 °C. Journal of Structural Geology 24(3), 1861–1884.

Tomkins, A.G., Mavrogenes, J.A., 2001. Redistriubtion of gold within arsenopyrite and löllingite during pro- and retrograde metamorphism: Application to timing of mineralization. Economic Geology 96, 525–534.

Tomkins, A. G., et al., 2004. The Hemlo Gold Deposit, Ontario,: An Example of Melting and Mobilization of a Precious Metal-Sulfosalt Assemblage during Amphibolite Facies Metamorphism and Deformation. Economic Geology 99, 1033–1084.

Thompson, P.H., 2003, Discover Abitibi. Metamorphic subproject. Metamorphism and its relationships to gold deposits in the Timmins-Kirkland Lake area, western Abitibi greenstone belt, Ontario: Report 1: Ontario Geological Survey Open File Report 6120, p. 37.1–37.8.

Thurston, P.C., Ayer, J.A., Goutier, J., Hamilton, M.A., 2008. Depositional gaps in Abitibi greenstone belt stratigraphy: a key to exploration for syngenetic mineralization. Economic Geology 103, 1097–1134.

Tolhurst, J., 2014. Detour Lake Mine Geology. Detour Gold Corp., Ontario, scale 1/5 000.

Van Goethem, L., Van Landuyt, J., Amelinckx, S., 1978. Study of the glide elements in pyrite by means of electron microscopy and electron diffraction. American Mineralogist 63, 548-550.

Vukmanovic, Z., Reddy, S., Godel, B., Barnes, S., Fiorentini, M., Barnes, S.J., Kilburn, M., 2014. Relationship between microstructures and grain-scale trace element distribution in komatiite hosted magmatic sulphide ores. Lithos. 184-187, 42-61.

Wyckoff, R. W. G., 1965. Crystal structures. Volume 1, Wiley, New York, 467 pp.

Table 1. Description and composition of veins hosted at the Detour Lake deposit

relative timing	vein name	mineralogy										width (cm)	description
		Qz	Cal	Ksp	Chl	Bt	Py	Po	Cpy	Apy	Au		
pre- to syn-D_2	V_1 pillow	✓	✓		✓		✓	✓			✓	1-15	Folded veins between pillow chill margins with Bt alteration haloes; vein fold axes are transposed parallel to the main S_2 foliation fabric
	V_2 dismembered	✓										0.5-1	Transposed and isoclinaly folded veins with diffuse margins
	V_3 laminated (Po, Py, Cpy, Apy) sulphidized	✓	✓		✓	✓	✓	✓	✓	✓		2-10	Laminated veins with foliated wall rock inclusion, Chl-Cal-Ms slip surfaces, and Bt alteration haloes.
	V_4 folded Qz-Cal	✓	✓									1-3	Folded and boudinaged Qz-Cal veins
	V_5 folded (Po, Py, Cpy) sulphidized	✓	✓		✓	✓	✓	✓	✓		✓	1-5	Folded and transposed sulphide-rich veins with Bt and/or Ser alteration haloes and visible Au
	V_6 Cal veinlets		✓									0.05-0.5	Cal veins with occasional Cal and sericite alteration haloes
post-D_2	V_7 planar Cal veinlets		✓	✓			✓	✓	✓			0.05-0.5	Cal veins with rare Ksp; veinlets have spotty Cal-Ser-Amp alteration halo and are oblique to the main S_2 foliation fabric, overprinting all previous vein types
	V_8 Qz-Cal breccia		✓									0.5-2	Stockwork Qz-Cal veins brecciated wall-rock inclusions; veins have spotty Cal-Ser-Amp alteration halo and overprint the main S_2 foliation fabric

Table 2. Mass balance calculations from Detour Lake mine assay data

S (ppm)	rock (tonnes)	S (tonnes)	Au (oz)	Au in S (ppm)	Au in Py (ppm)
0-0.5	161,469,138	1,843,771	4,444,913	68.34	36.53
0.5-1.0	116,577,881	1,426,856	2,858,805	56.80	30.36
1.0-1.5	39,633,093	618,562	1,067,087	48.91	26.14
1.5-2.0	7,889,083	159,857	261,213	46.32	24.76
2.0-2.5	1,224,380	32,109	55,014	48.57	25.96
2.5-3.0	180,735	5,600	6,913	34.99	18.70
3.0-3.5	15,660	1,211	374	8.76	4.68
>3.5	26,100	683	350	14.51	7.75
Total	327,016,070	4,088,650	8,694,669	60.29	32.22

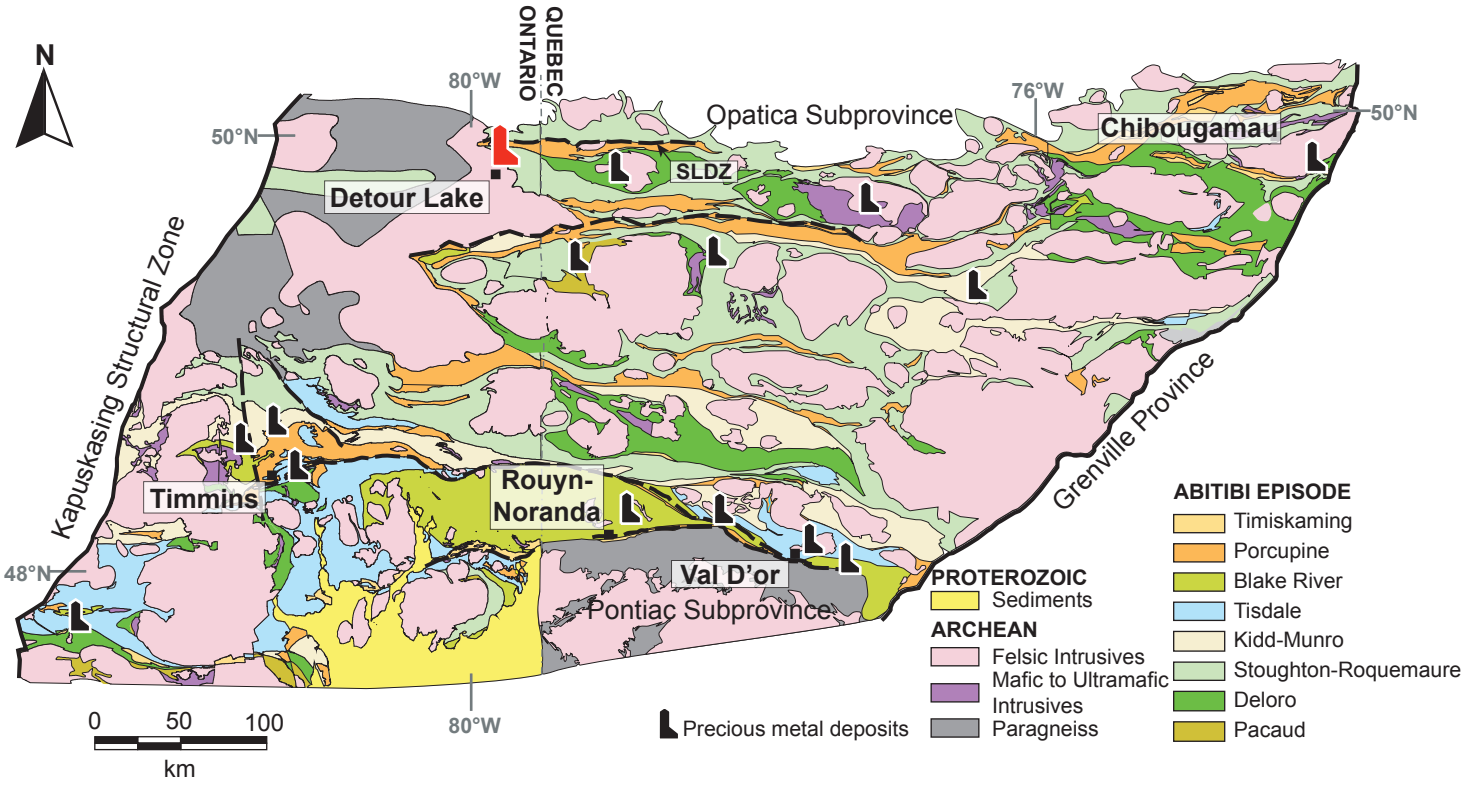

Figure 1. Geological map of the Abitibi Subprovince of eastern Canada showing the location of the Detour Lake mine along an east-west trending high-strain deformation zone (SLDZ) north of the wellknown Abitibi greenstone belt (modified from Thurston et al., 2008).

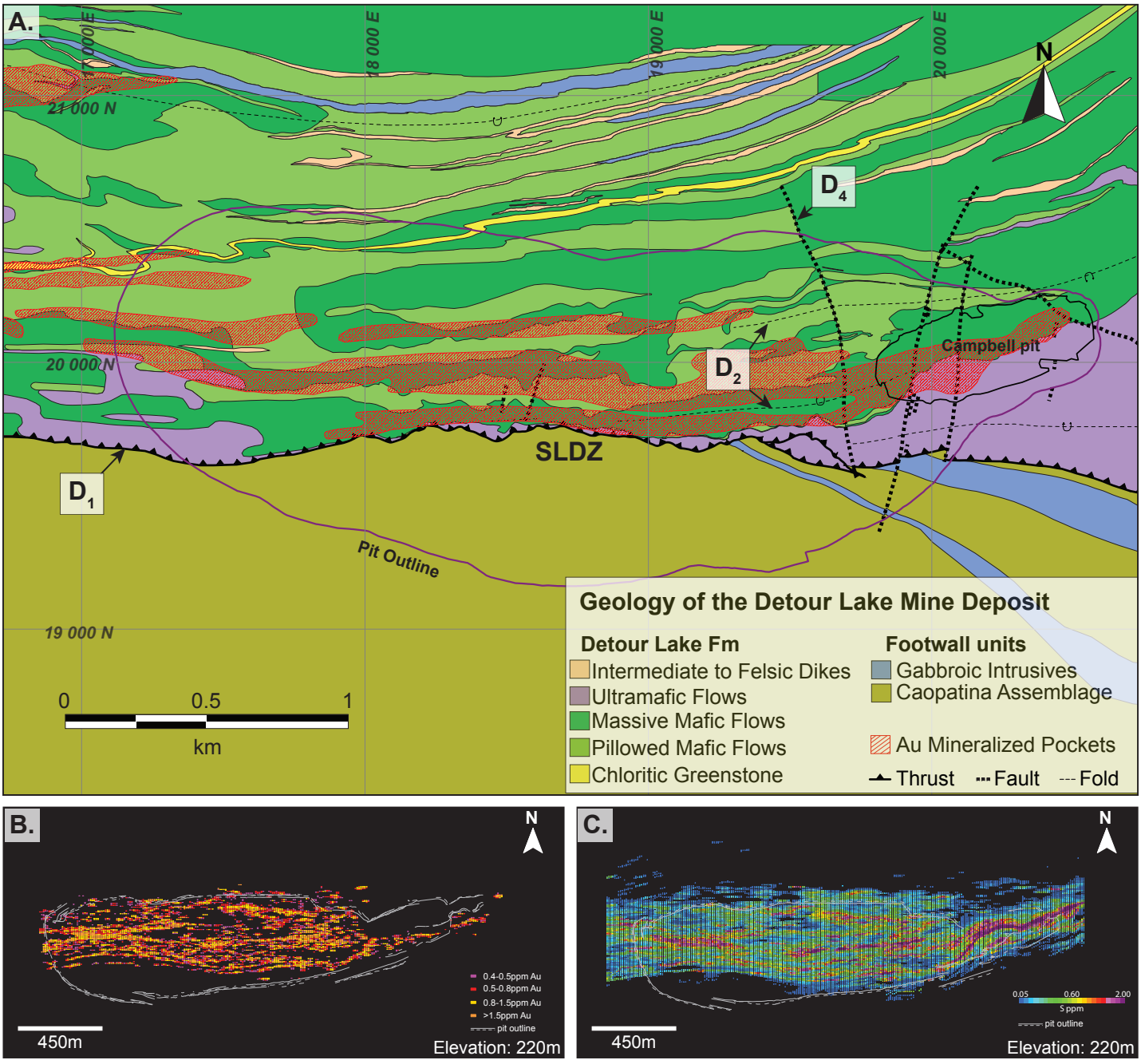

Figure 2. A. Geological map of the Detour Lake deposit showing the outline of the modern open pit mine and historic Campbell pit located along the E-W trending SLDZ, dividing the mafic volcanic rock of the Detour Lake Formation and the sedimentary rocks of the Caopatina Assemblage (modified from Tolhurst, 2014). **B.** and **C.** Lateral section of Au and S block models at an elevation 220 m showing the dominant east-west mineralization and co-spatial relationship.

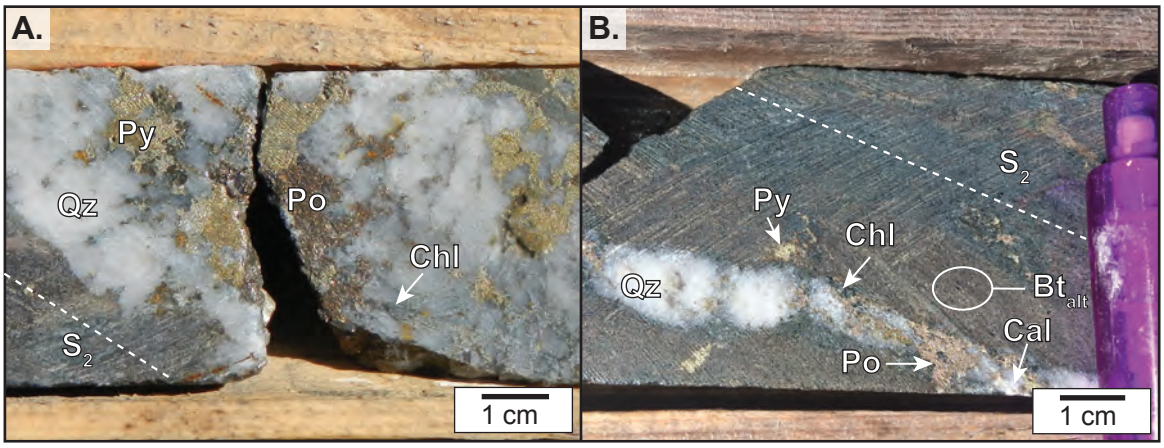

Figure 3. Photographs of drill core showing mineralized pre-syn D_2 folded-sulfidized Qz-Cal-Chl veins (V_5).

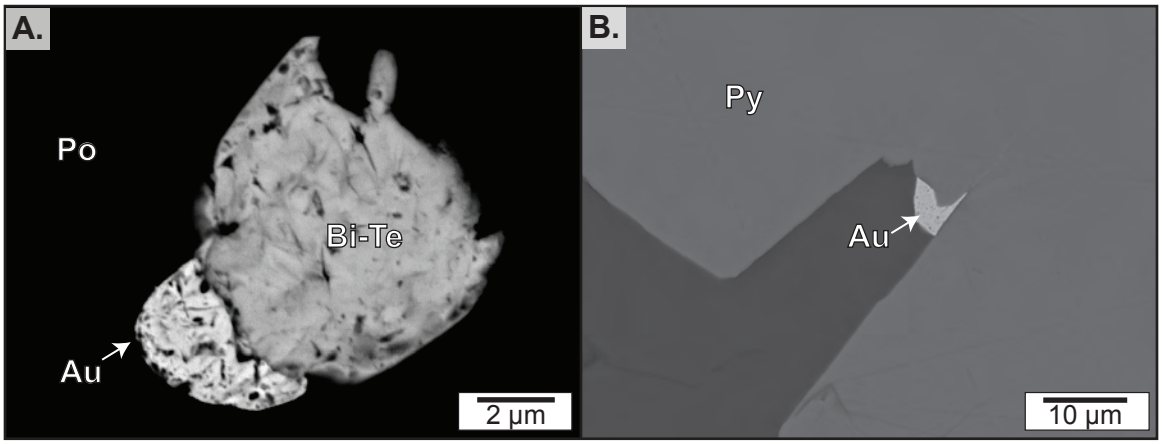

Figure 4. SEM images of Au mineralization from the Detour Lake deposit. **A.** Precious-metal mineral inclusion (Au-Bi-Te) in pyrrhotite crystal from a pre-syn D_2 folded-sulfidized Qz-Cal-Chl vein (V_5). **B**. Au particle adhered to the surface of a pyrite crystal in a pillow vein (V_1).

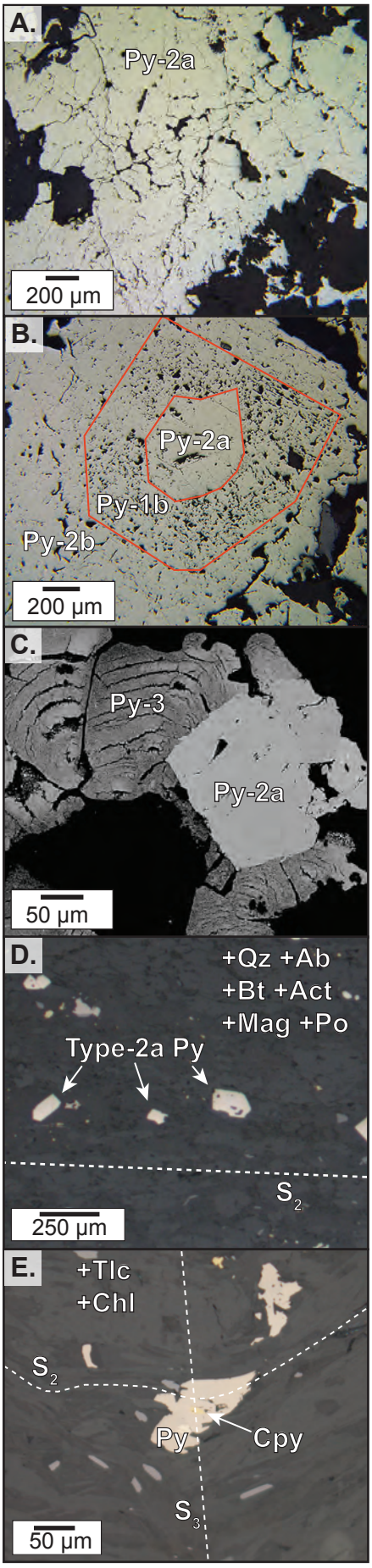
A.
Py-2a
200 µm
B.
Py-2a
Py-1b
Py-2b
200 µm
C.
Py-3
Py-2a
50 µm
D.
+Qz +Ab
+Bt +Act
+Mag +Po
Type-2a Py
S2
250 µm
E.
+Tlc
+Chl
S2
Py
Cpy
S3
50 µm

Figure 5. (previous page) A. Reflected light photomicrograph of type-2a pyrite showing poorly defined grain boundaries and sieved texture. **B.** Reflected light photomicrograph showing a euhedral pyrite crystal (type-2a) with an inclusion-rich overgrowth (type-1b), which is also overgrown by an inclusion-poor type-2b pyrite. **C.** BSE SEM image showing a euhedral pyrite crystal (type-2a) overgrown by collorform bands of pyrite (type-3). **D.** Reflected light photomicrograph of type-2a euhedral pyrite porphyroblasts, locally aligned with the S_2 foliation fabric, in a Qz-Ab-Bt-Act-Mag-Po matrix within a mafic volcanic sample (MV-19). **E.** Reflected light photomicrograph of a deformed anhedral pyrite grain in a Tlc-Chl matrix within an ultramafic sample (TC-07) folded by the S_3 crenulation fabric.

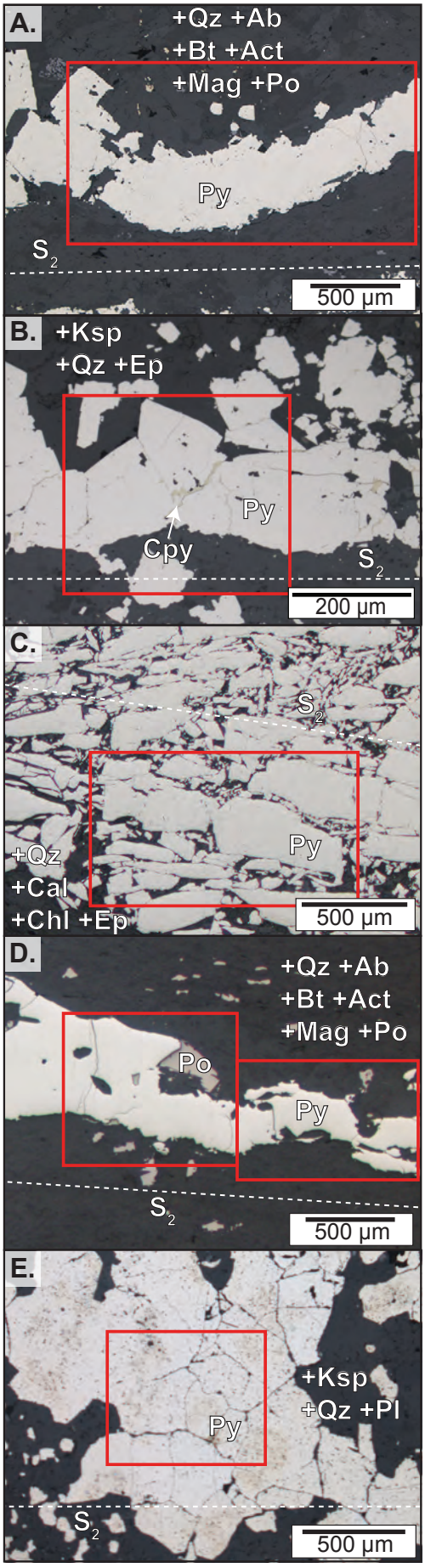
A.
+Qz +Ab
+Bt +Act
+Mag +Po
Py
S2
500 µm
B.
+Ksp
+Qz +Ep
Py
Cpy
S2
200 µm
C.
S2
Py
+Qz
+Cal
+Chl +Ep
500 µm
D.
+Qz +Ab
+Bt +Act
+Mag +Po
Po
Py
S2
500 µm
E.
Py
+Ksp
+Qz +Pl
S2
500 µm

Figure 6. (previous page) Reflected light photomicrographs of pre-syn D_2 folded-sulfidized Qz-Cal-Chl veins (V_5). Dashed lines represent the trace of S_2. Red rectangles show the locations of EBSD maps. **A.** Folded pyrite grain from a V_5 vein within a mafic volcanic rock (sample MV-19). **B.** Subhedral pyrite grains showing collided pyrite grains (sample MV-19). **C.** Pyrite fragments from a boudinaged pyrite-rich vein (sample MV-20). **D.** Pinch and swell structure in a pyrite-rich vein (sample RD16-I) **E.** Recrystallized pyrite from a sigma-shaped pyrite vein possessing foam texture (sample RD16-H).

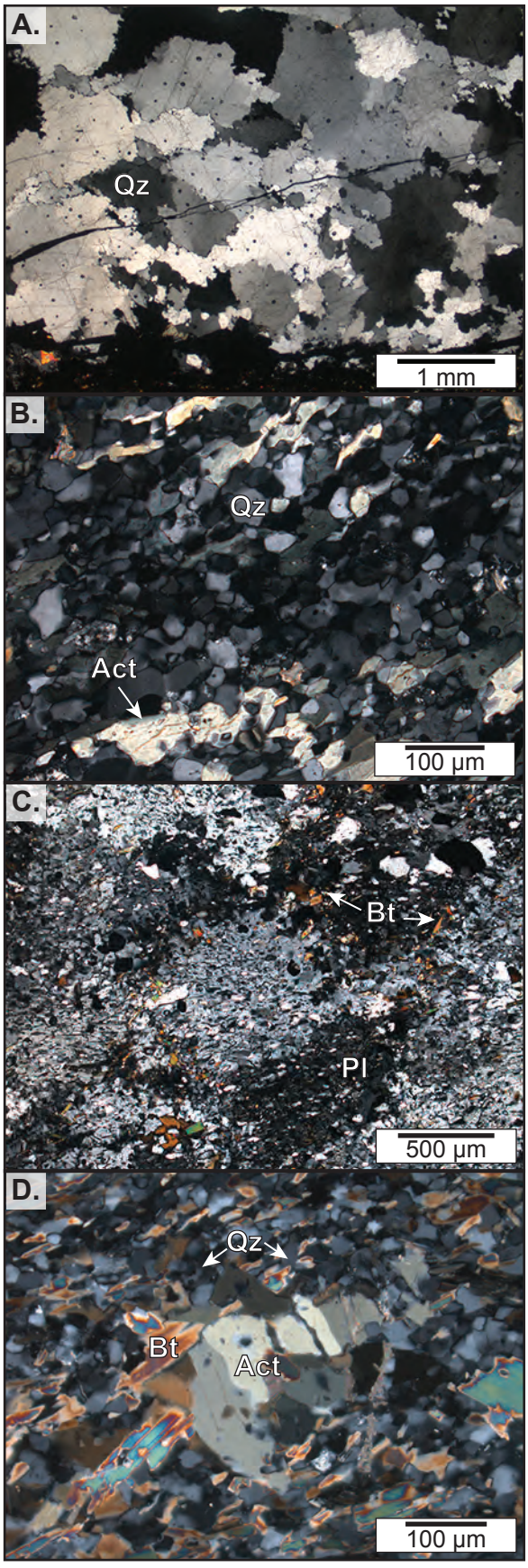
A.
Qz
1 mm
B.
Qz
Act
100 µm
C.
Bt
Pl
500 µm
D.
Qz
Bt
Act
100 µm

Figure 7. (previous page) Optical photomicrographs of host rock deformational microstructures (crossed polarizers). **A.** Grain boundary migration of quartz in a V_5 vein (sample MV-19). **B.** Small polygonal quartz and plagioclase crystals indicative of grain-size sensitive deformation mechanisms (sample MV-20). **C.** Subgrain development in large inclusion-rich plagioclase crystals (sample RD16-H). **D.** Subgrain development in actinolite porphyroblast (sample RD16-I).

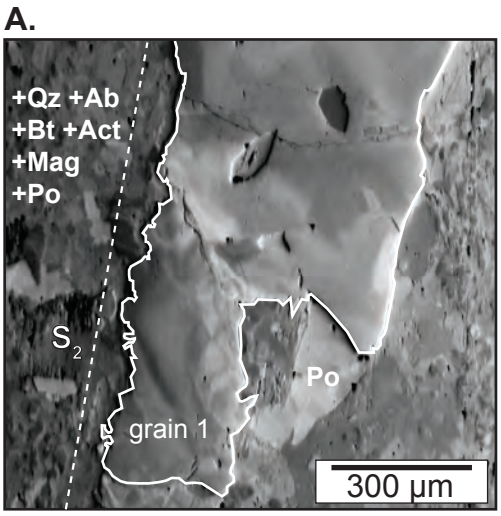
A.
+Qz +Ab
+Bt +Act
+Mag
+Po
S2
Po
grain 1
300 µm

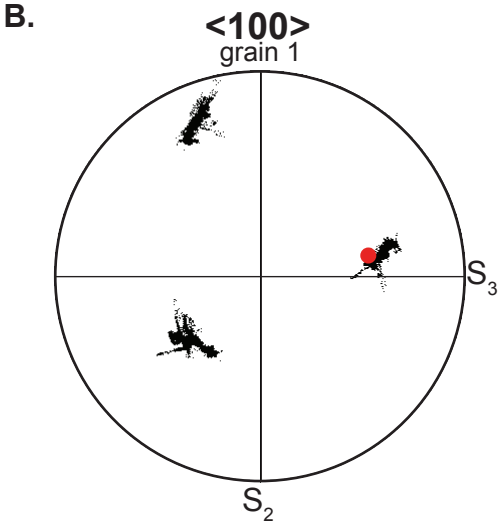
B.
<100>
grain 1
S3
S2

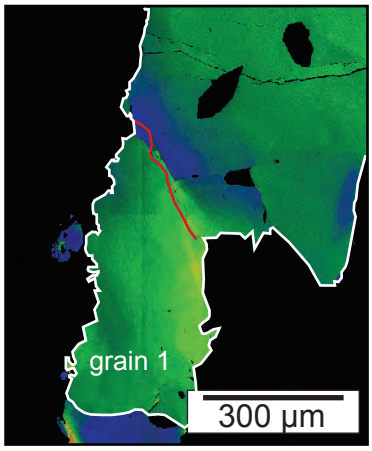
C.
grain 1
300 µm
Misorientation:
0°
30°

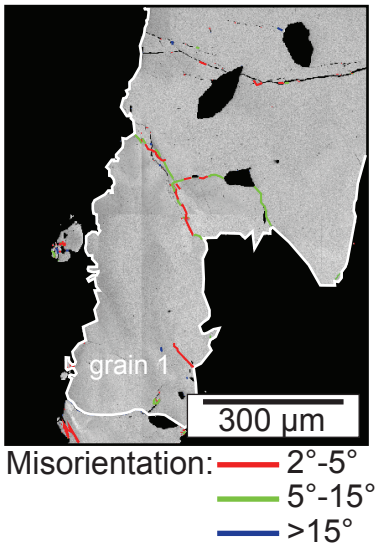
D.
grain 1
300 µm
Misorientation:
2°-5°
5°-15°
>15°

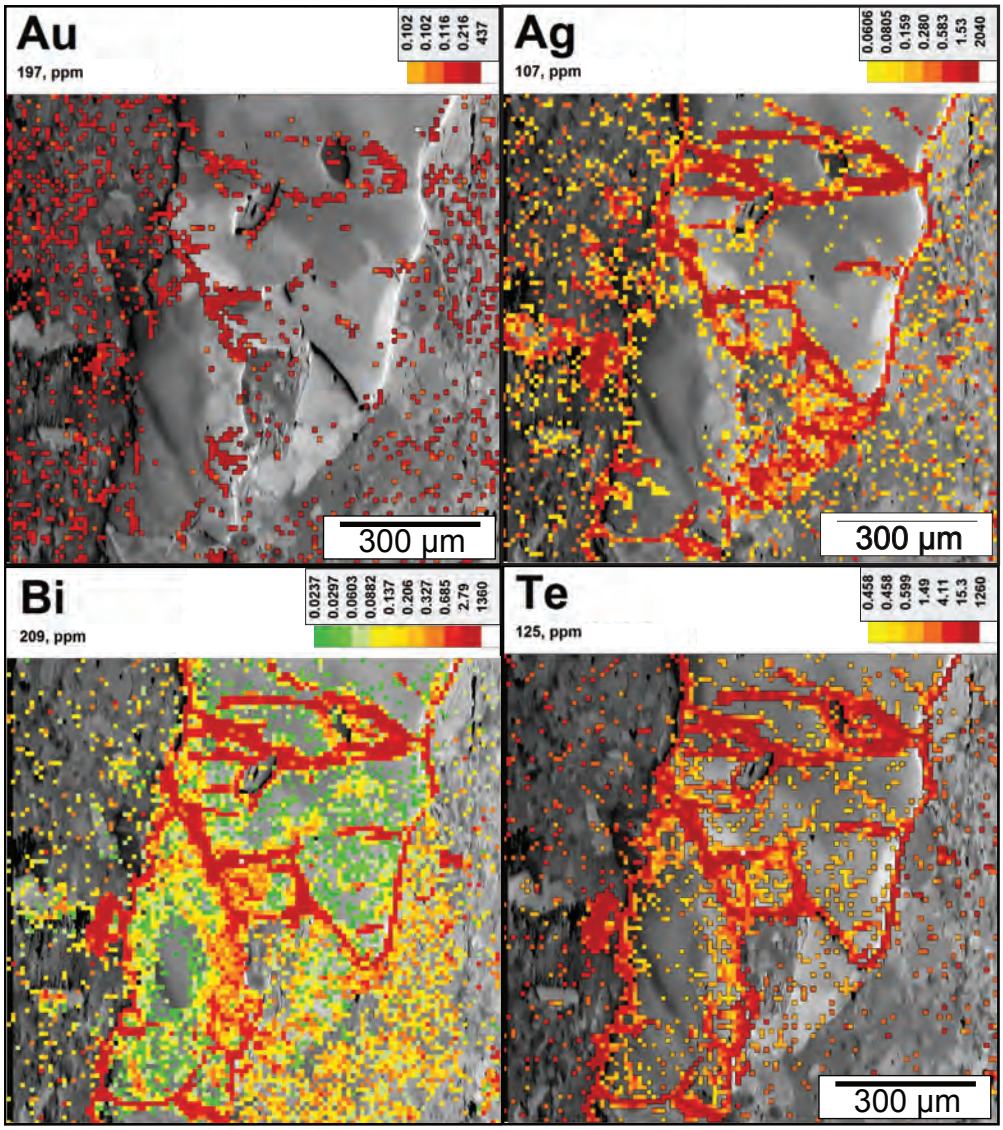
E.
Au
197, ppm
0.102 0.102 0.116 0.216 437
Ag
107, ppm
0.0606 0.0805 0.159 0.280 0.583 1.53 2040
Bi
209, ppm
0.0237 0.0297 0.0603 0.0882 0.137 0.206 0.327 0.685 2.79 1360
Te
125, ppm
0.458 0.458 0.599 1.49 4.11 15.3 1260
300 µm

Figure 8. (previous page) EBSD and LA-ICP-MS results of a pinch and swell pyrite domain (sample RD16-I). **A.** OC image of a pinch and swell Py vein with Act inclusions in a Qz-Ab-Bt-Act-Mag-Po matrix showing a heterogeneous misorientation pattern. **B.** Pole figure representing the <100> axes of grain 1 showing rotation about at least one axis marked by the red circle (lower hemisphere, equal angle projection). **C.** Orientation deviation angle map Py vein showing a heterogeneous misorientation pattern with a maximum misorientation of 30° and a late brittle fracture (shown with a red line) in high strain area indicative of strain hardening. **D.** Grain boundary map of Py revealing low-angle grain boundary development in high strain areas indicative of dislocation creep. **E.** 2D LA-ICP-MS trace element maps of Py vein revealing Au, Ag, Bi, and Te enrichment at grain and low-angle grain boundaries and in late fractures.

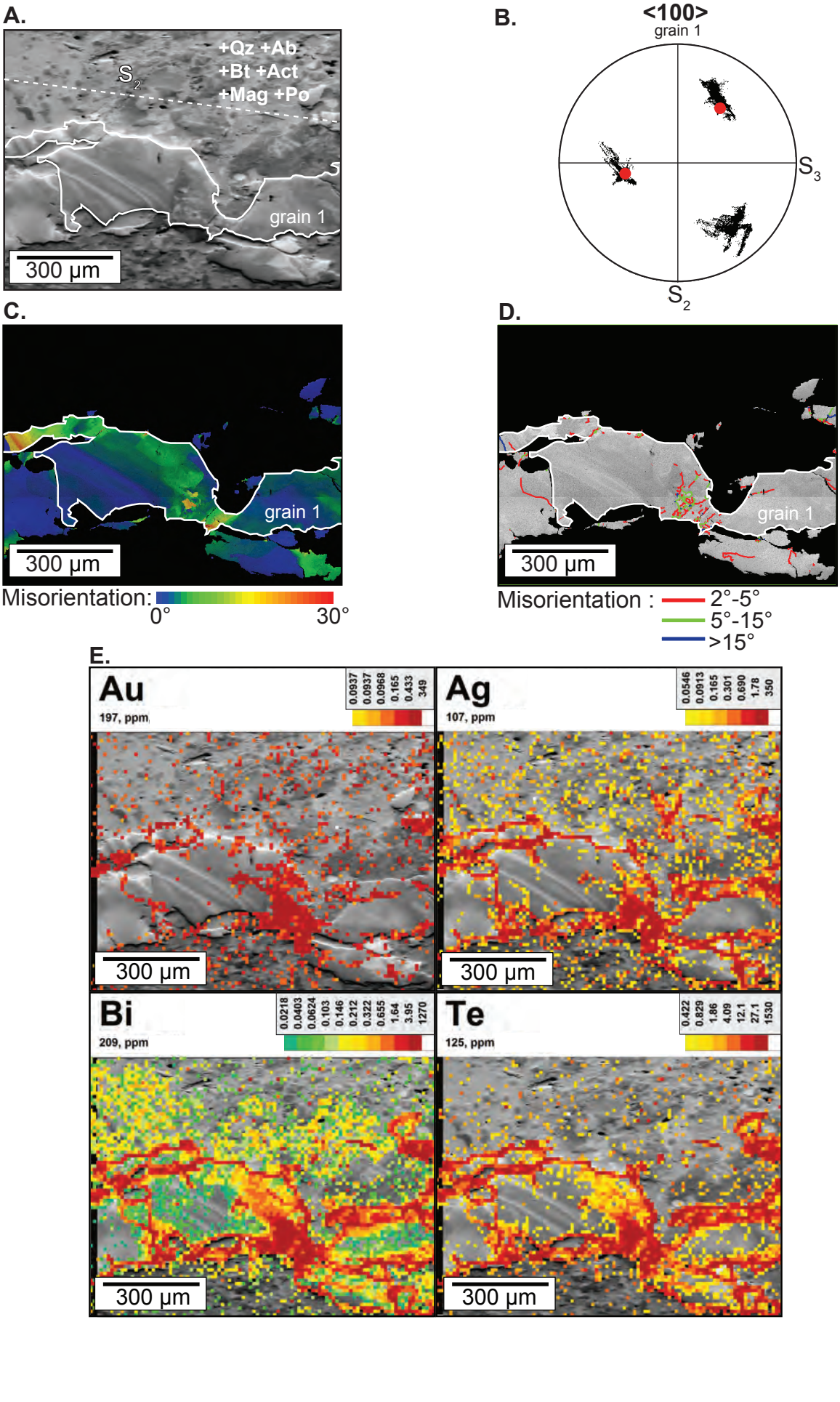
A.
+Qz +Ab
+Bt +Act
+Mag +Po
S2
grain 1
300 µm
B.
<100>
grain 1
S3
S2
C.
grain 1
300 µm
Misorientation:
0°
30°
D.
grain 1
300 µm
Misorientation :
2°-5°
5°-15°
>15°
E.
Au
197, ppm
0.0937 0.0937 0.0968 0.165 0.433 349
300 µm
Ag
107, ppm
0.0546 0.0913 0.165 0.301 0.690 1.78 350
300 µm
Bi
209, ppm
0.0218 0.0403 0.0624 0.103 0.146 0.212 0.322 0.655 1.64 3.95 1270
300 µm
Te
125, ppm
0.422 0.829 1.86 4.09 12.1 27.1 1530
300 µm

Figure 9. (previous page) EBSD and LA-ICP-MS results of a pinch and swell pyrite domain (sample RD16-I). **A.** OC image of a deformed Py vein in a Qz-Ab-Bt-Act-Mag-Po matrix showing a linear misorientation pattern and a more heterogeneous checkerboard misorientation pattern in the neck of a pinch and swell structure. **B.** Pole figure representing the orientation of <100> axes of grain 1 exhibiting rotation about at least two axes marked by the red circles (lower hemisphere, equal angle projection). **C.** Orientation deviation angle map of Py showing a linear misorientation pattern and a heterogeneous misorientation pattern in the neck of the pinch and swell structure with a maximum misorientation of 30°. **D.** Grain boundary map of Py reveal low-angle grain boundary development in high strain areas indicative of dislocation creep. **E.** 2D LA-ICP-MS trace element maps of Py vein revealing Au, Ag, Bi, and Te enrichment at grain and low-angle grain boundaries and in late fractures.

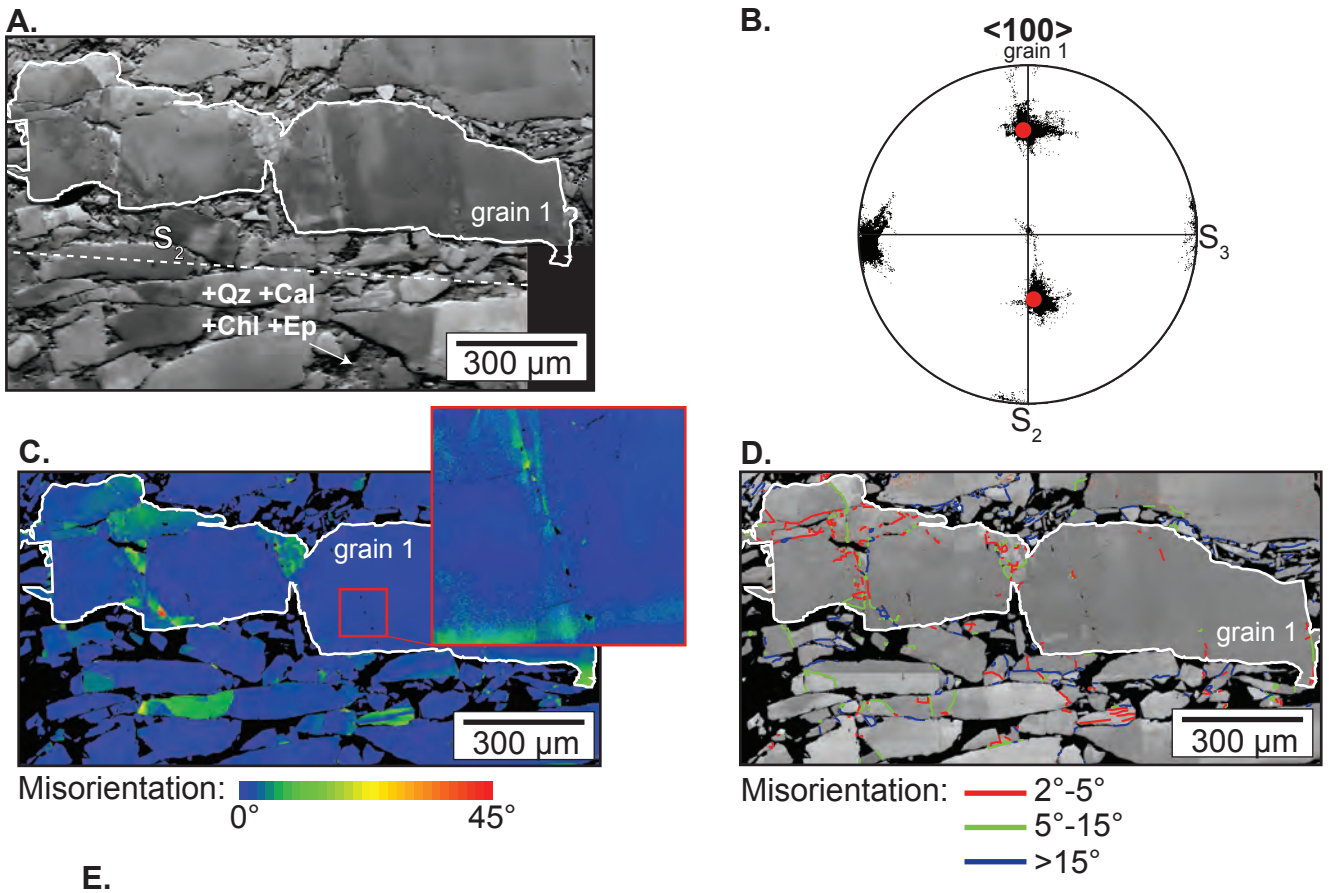
A.
grain 1
S2
+Qz +Cal
+Chl +Ep
300 µm
B.
<100>
grain 1
S3
S2
C.
grain 1
300 µm
Misorientation:
0°
45°
D.
grain 1
300 µm
Misorientation:
2°-5°
5°-15°
>15°

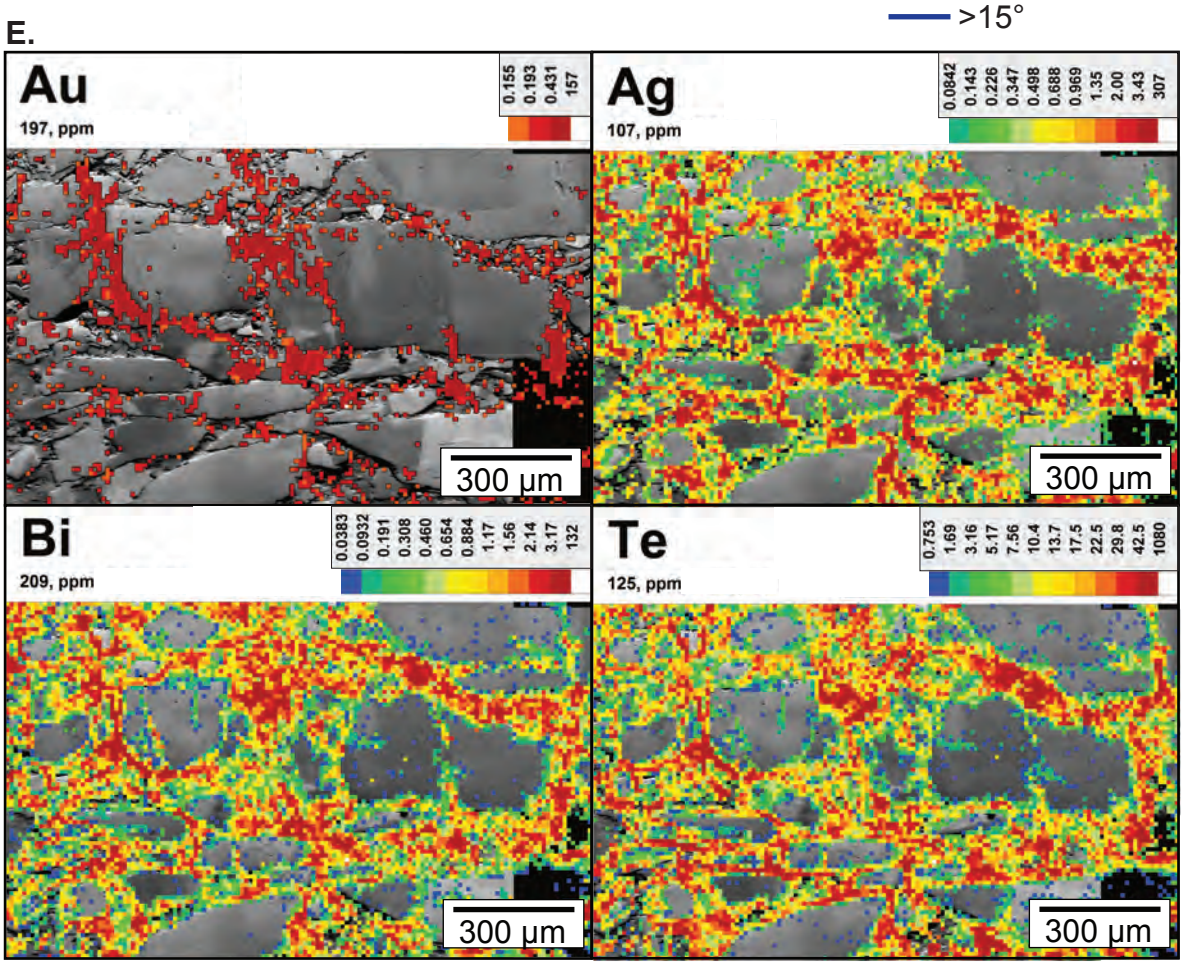
E.
Au
197, ppm
0.155 0.193 0.431 157
300 µm
Ag
107, ppm
0.0842 0.143 0.226 0.347 0.498 0.688 0.969 1.35 2.00 3.43 307
300 µm
Bi
209, ppm
0.0383 0.0932 0.191 0.308 0.460 0.654 0.884 1.17 1.56 2.14 3.17 132
300 µm
Te
125, ppm
0.753 1.69 3.16 5.17 7.56 10.4 13.7 17.5 22.5 29.8 42.5 1080
300 µm

Figure 10. (previous page) EBSD and LA-ICP-MS results of a boudinaged pyrite domain (sample MV-20). **A.** OC image of a boudinaged and brecciated Py vein showing checkerboard misorientation pattern at boudin necks. **B.** Pole figure representing the orientation of <100> axes showing rotation about at least two axes, marked by red circles (lower hemisphere, equal angle projection). **C.** Orientation deviation angle map of Py vein showing a heterogeneous misorientation pattern at boudin necks with a maximum misorientation of 45° and strain localization at microcracks (inset). **D.** Grain boundary map of Py revealing minor low-angle grain boundary development in high-strain areas. **E.** 2D LA-ICP-MS trace element maps of Py revealing enrichment at low-angle grain boundaries and fractures.

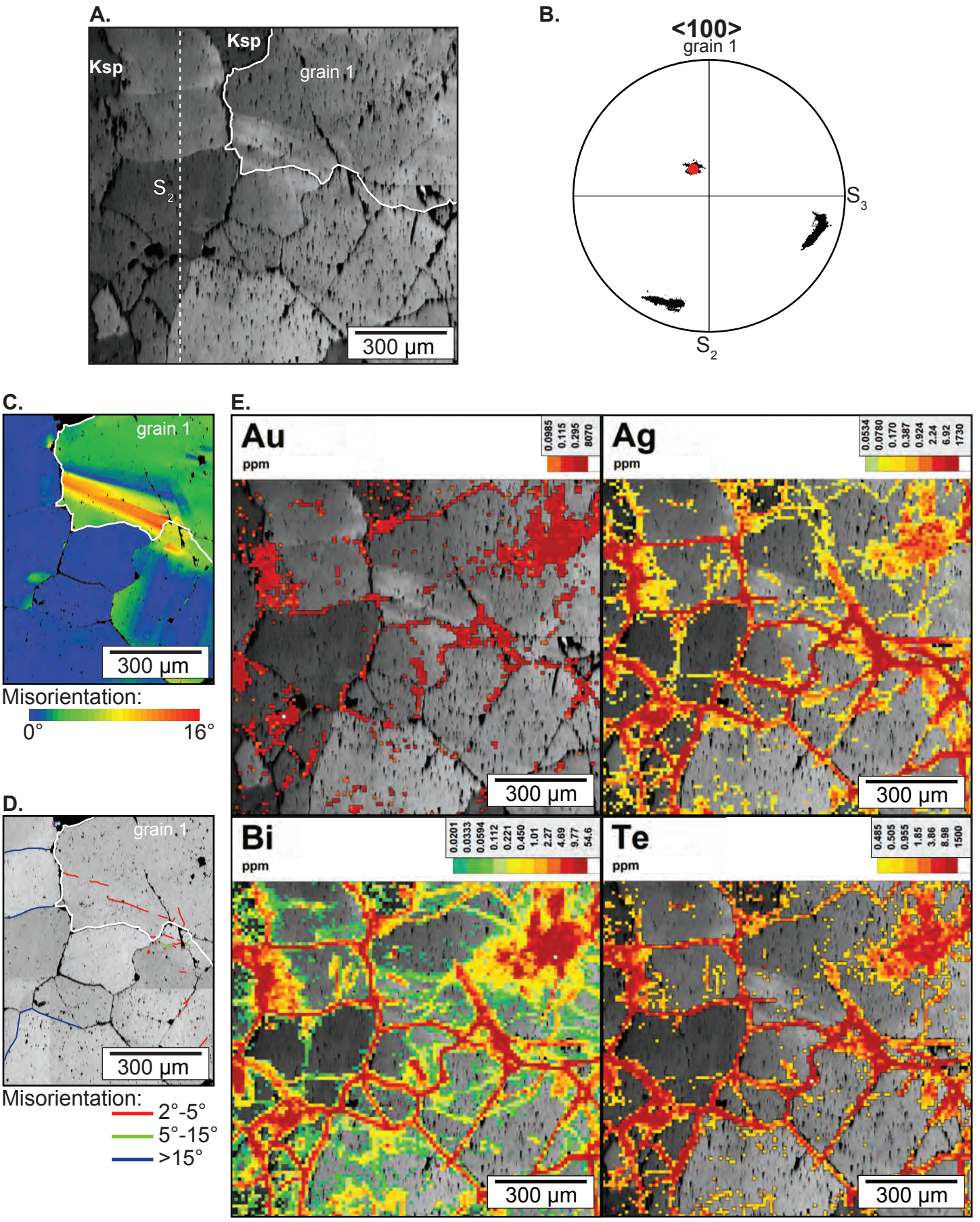
A.
Ksp
Ksp
grain 1
S2
300 µm
B.
<100>
grain 1
S3
S2
C.
grain 1
300 µm
Misorientation:
0°
16°
D.
grain 1
300 µm
Misorientation:
2°-5°
5°-15°
>15°
E.
Au
ppm
0.0985 0.115 0.295 8070
300 µm
Ag
ppm
0.0534 0.0780 0.170 0.387 0.924 2.24 6.92 1730
300 µm
Bi
ppm
0.0201 0.0333 0.0594 0.112 0.221 0.450 1.01 2.27 4.69 9.77 54.6
300 µm
Te
ppm
0.485 0.505 0.955 1.85 3.86 8.98 1500
300 µm

Figure 11. (previous page) EBSD and LA-ICP-MS results of an annealed pyrite domain (sample RD16-H). **A.** OC image of a foam-texture Py vein showing linear misorientation pattern cut by late brittle fractures. **B.** Pole figure representing the orientation of <100> axes of grain 1 showing rotation about one axis marked by the red circle (lower hemisphere, equal angle projection). **C.** Orientation deviation angle map of Py showing a linear misorientation pattern with a maximum misorientation of 16°. **D.** Grain boundary map of Py revealing minor low-angle grain boundary development and recrystallization. **E.** 2D LA-ICP-MS trace element maps of Py vein revealing Au, Ag, Bi, and Te enrichment at grain boundaries and late fractures.

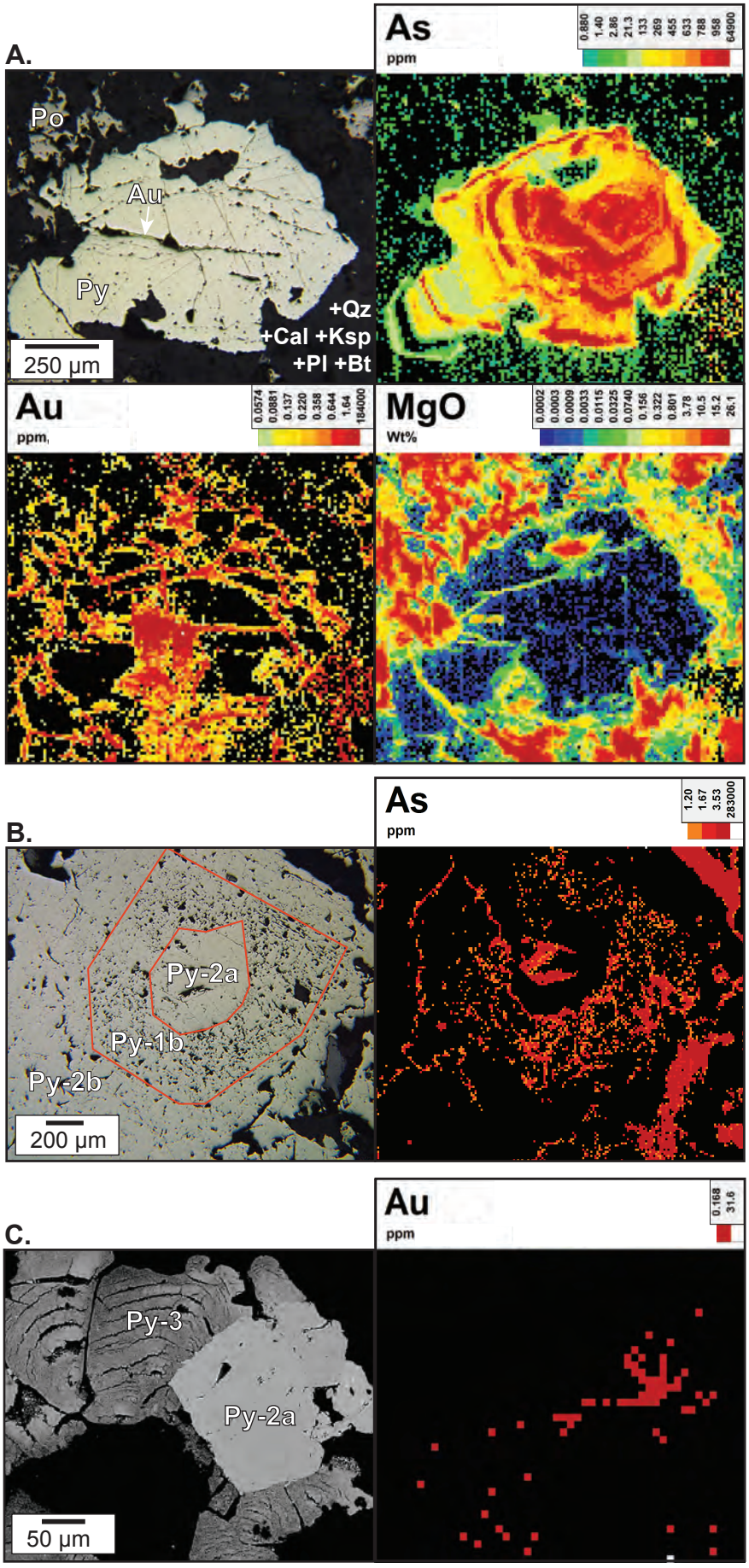
A.
Po
Au
Py
+Qz
+Cal +Ksp
+Pl +Bt
250 µm
As
ppm
0.880
1.40
2.86
21.3
133
269
455
633
788
958
64900
Au
ppm
0.0574
0.0881
0.137
0.220
0.358
0.644
1.64
184000
MgO
Wt%
0.0002
0.0003
0.0009
0.0033
0.0115
0.0325
0.0740
0.156
0.322
0.801
3.78
10.5
15.2
26.1
B.
Py-2a
Py-1b
Py-2b
200 µm
As
ppm
1.20
1.67
3.53
283000
C.
Py-3
Py-2a
50 µm
Au
ppm
0.168
31.6

Figure 12. (previous page) A. Reflected light photomicrograph and LA-ICP-MS element maps (As, Au, MgO) of type-2a pyrite porphyroblast (sample RD15-118-251). Imaging reveals oscillatory growth zoning of a metalloid (As), heterogeneous distribution of Au within fractures and along pyrite grain boundaries, and delineation of fractures by metals (Mg). **B.** Reflected light photomicrograph and LA-ICP-MS element map of type-2b pyrite overgrowth (sample RD15-118-238B). Imaging shows oscillatory growth zoning through a metalloid element (As). **C.** BSE image and LA-ICP-MS element map (Au) of colloform pyrite bands overgrowing a type-2 pyrite porphyroblast (sample RD15-265-353) showing a Au-rich core within the euhedral pyrite crystal.

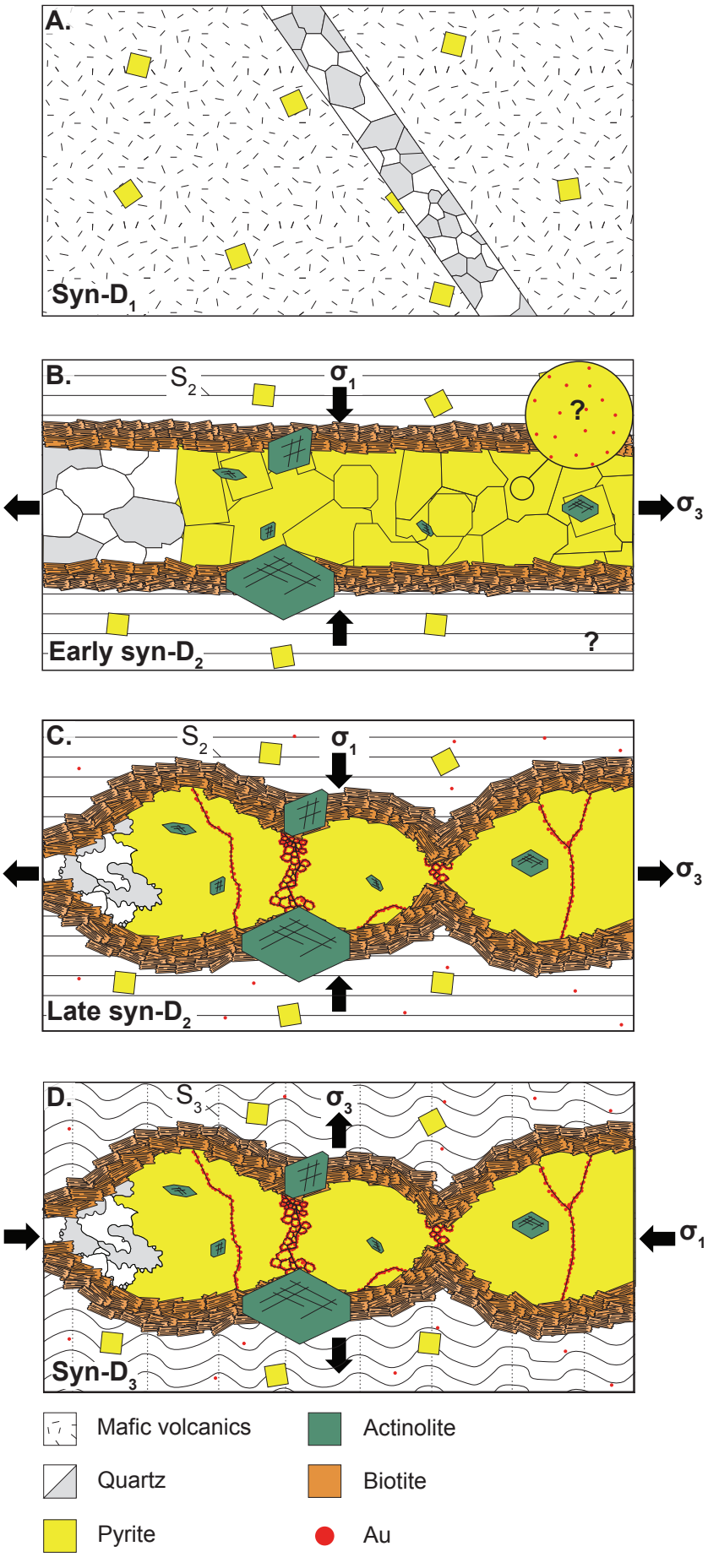
A.
Syn-D1
B.
S2
σ1
?
σ3
Early syn-D2
?
C.
S2
σ1
σ3
Late syn-D2
D.
S3
σ3
σ1
Syn-D3
Mafic volcanics
Actinolite
Quartz
Biotite
Pyrite
Au

Figure 13. (previous page) Synoptic Detour Lake deposit deformation and mineralization model. **A.** Possible Py-bearing massive mafic volcanic host rock with Qz veining. **B.** Development of a foliation fabric and transposition of Qz veins with Py mineralization and biotite alteration haloes. Pyrite may incorporate Au as nanoparticules by adsorbtion or solid-solution. **C.** Crystal plastic deformation of pyrite represented as pinch and swell of the Qz-Py vein. The development of low-angle grain boundaries and brittle fractures necks and in contact with stronger matrix minerals (Act). Au enrichment at low-angle grain boundaries and fractures through DIP diffusion or PIPE diffusion facilitated by intergranular fluids introduced during late-stage brittle deformation. Au is also introduced within the host-rock matrix. **D.** Development of a crenulation fabric.

CHAPTER 3

Geochemical and geochronological analysis of biotite at Detour Lake mine, Canada

Abstract

The 16.4 Moz Detour Lake deposit located in the northwestern district of the Abitibi Subprovince and is hosted at the faulted contact between the volcaniclastic rocks of the Caopatina assemblage and the mafic to ultramafic rocks of the Detour Lake Formation. The deposit differs from other classic ore deposits in the dominantly greenschist facies Abitibi Subprovince by possessing an amphibolite facies metamorphic assemblage of actinolite-biotite-plagioclase-epidote-almandine ± calcite ± quartz ± ilmenite. Consequently, the typical indicator minerals used to identify alteration and mineralization, such as secondary biotite, may not be useful due to the challenge of distinguishing hydrothermal versus metamorphic biotite. Petrological and geochemical analyses have revealed at least three types of biotite: 1) fine- to coarse-grained, subhedral to euhedral vein biotite hosted in syn-D_2 vein sets (V_5); 2) medium-grained euhedral halo biotite at the margins of syn-D_2 veins; and 3) very fine-grained to coarse-grained, anhedral to euhedral host rock biotite within mafic volcanic rocks. EMPA major element mapping and spot analyses reveal chemically homogeneous compositions on ternary biotite plots (~25% Fe, 30% Mg, 55% Al and 35% Fe, 50% Mg, 15% K) for all three biotite types, with the exception of occasional Fe-Mg rich and K-poor rims on halo biotite. $^{40}Ar/^{39}Ar$ analyses yield overlapping ages ranging between 2600–2400 Ma, post-dating regional deformation, metamorphism, and Au mineralization.

1. Introduction

Previous studies of orogenic Au deposits in the Superior Province, including the Canadian Malartic deposit (i.e. De Souza et al., 2015) and the Mouska deposit (Belkabir et al., 2004), have highlighted the importance of biotite as an indicator mineral for Au mineralization. At the Detour

Lake deposit, northeastern Ontario, Marmont (1986) identified a late, post-metamorphic stage of hydrothermal biotite comprising the hydrothermal alteration mineral assemblage related to auriferous veins and broader mineralized zones with disseminated Au. Oliver et al. (2011) observed an extensively biotitized halo surrounding the main mineralized zone in the hanging wall of the Detour Lake deposit, giving the mafic volcanic host rocks a purple-maroon appearance. On the basis of these field relationships, hydrothermal biotite was suggested to be an important visual indicator mineral for the exploration and production geology teams to target and delineate Au ore zones. However, mafic volcanic host rocks at the Detour Lake deposit are metamorphosed to lower amphibolite facies and comprise a prograde, biotite-bearing metamorphic mineral assemblage (actinolite-biotite-plagioclase-epidote-almandine ± calcite ± quartz ± ilmenite; Oliver et al., 2011), which obscures the relationship between biotite and Au. Differentiating metamorphic and secondary hydrothermal biotite is particularly challenging within low-grade disseminated Au ore zones, which are typically devoid of quartz veins and other visual Au indicators. Herein we attempt to identify and document different biotite generations and discern between metamorphic and hydrothermal biotite through a combination of petrographical, geochemical, and geochronological data.

2. Analytical Methods

Biotite-bearing samples were collected from drill core intersecting the main Detour Lake ore body and from exposures within the active open-pit mining operation. Sampling criteria consisted of large visible biotite crystals across a range of lithotypes in both hanging wall and footwall of the Sunday Lake Deformation Zone (SLDZ). This included samples where biotite

was ubiquitous in the host rock defining the main S_2 foliation fabric, forming a halo around mineralized veins, and samples where the biotite was within the pre- to syn-D_2 vein sets.

Petrographical observations were collected before conducting geochemical and geochronological analyses to identify potential biotite types (**Fig 14**). Sample names, rock types, structural positioning, mineralogy, and conducted analyses are reported in **Table 3**. Eight samples were targeted for electron microprobe analyses (EMPA; **Table 4, Fig. 15**), five samples were selected for in situ chemical mapping (WDS; **Fig. 16**), and ten samples were analysed for $^{40}Ar/^{39}Ar$ dating (**Table 5, Fig. 17**).

Eight biotite samples were selected for geochemical analyses in order to characterize geochemical differences between biotite types. Biotite samples were initially imaged with the scanning electron microscope (SEM) at the University of Ottawa to target the most representative biotite crystals for further geochemical analyses Mineral chemical compositions were determined in eight samples (FW-03, FW-10, FW-11, FW-13, MV-02, MV-13, RD15-429-92, RD15-429-27) using the JEOL JXA-8230 SuperProbe at the University of Ottawa (Ottawa, Canada). Analyses were conducted with an accelerating voltage of 20 kV and probe current of 20 nA to focus and concentrate the beam to a minimum of 1 μm. A total of 2–6 grains of biotite per polished section were analyzed by probing 3–4 points per single mica grain to explore possible chemical variations within the grains and between biotite types. Cation site distribution was calculated according to Vidal et al. (2001) and Parra et al. (2002). Analytical results are reported in **Table 4** and presented in **Fig. 15**.

In addition to electron microprobe spot analyses, chemical maps of biotite types from five samples (FW-03, FW-11, FW-13, MV-02, MV-13) have been produced to test for any chemical variation within individual biotite crystals. Mapping was conducted using both the wavelength

dispersive spectrometer (WDS) and the energy dispersive spectrometer (EDS) of the JEOL JXA-8230 SuperProbe at the University of Ottawa (Ottawa, Canada). An accelerating voltage of 20 kV and a beam current of 20–40 nA were combined with a spot size of 1 μm to produce maps ranging from 100 x 150 to 400 x 400 pixels with a 1 μm pixel size and 150–200 ms dwell time on each pixel. Analyzed elements include Fe, Mg, Mn, Na, Ca, Si, O, P, S, C, Cl, Ti, K and Al. The maps for Al, K, Fe and Mg of each biotite type are presented in **Fig. 16**.

After collecting petrographical and geochemical data on the biotite types, $^{40}Ar/^{39}Ar$ analyses were carried out to explore the timing of biotite crystallization and cooling. Mineral separates were prepared from one vein-hosted biotite sample; four halo biotite samples; five host rock biotite samples; and two host rock muscovite samples. All $^{40}Ar/^{39}Ar$ analytical work was performed at the University of Manitoba (Winnipeg, Canada) using a multi-collector Thermo Fisher Scientific ARGUS VI mass spectrometer, linked to a stainless steel Thermo Fisher Scientific extraction/purification line and Photon Machines (55 W) Fusions 10.6 CO_2 laser. Argon isotopes (from mass 40 to 37) were measured using Faraday detectors with low noise 1 x 10^{12} Ω resistors and mass 36 was measured using a compact discrete dynode (CDD) detector. The sensitivity for argon measurements is ~6.312 x 10^{17} moles/fA as determined from measured aliquots of Fish Canyon Sanidine (Dazé et al., 2003; Kuiper et al., 2008). Standards and unknowns were placed in 2 mm deep wells in 18 mm diameter aluminium disks, with standards placed strategically so that the lateral neutron flux gradients across the disk could be evaluated. Planar regressions were fit to the standard data, and the $^{40}Ar/^{39}Ar$ neutron fluence parameter, J, interpolated for the unknowns. Uncertainties in J are estimated at 0.1-0.2% (1σ), based on Monte Carlo error analysis of the planar regressions (Best et al., 1995). All specimens were irradiated in the Cadmium-lined, in-core CLICIT facility of the Oregon State University TRIGA reactor. The

duration of irradiation was 70 h with HB3GR amphibole (1073.6 Ma; Jourdan et al., 2006) as the flux monitor. Irradiated samples were placed in a Cu sample tray, with a KBr cover slip, in a stainless steel high vacuum extraction line and baked with an infrared lamp for 24 h. Single crystals were fused using the laser, and reactive gases were removed, after ~3 m, by three GP-50 SAES getters (two at room temperature and one at 450°C) prior to being admitted to an ARGUS VI mass spectrometer by expansion. Five argon isotopes were measured simultaneously over a period of 6 m. Measured isotope abundances were corrected for extraction-line blanks averaging ~2 fA for mass 40 and ~0.009 fA for mass 36. Mass discrimination was monitored by online analysis of air pipettes and gave a mean D = 1.0083 ± 0.0019 per amu, based on 53 aliquots interspersed with the unknowns. A value of 295.5 was used for the atmospheric $^{40}Ar/^{36}Ar$ ratio (Steiger and Jaëger, 1977) for the purposes of routine measurement of mass spectrometer discrimination using air aliquots, and correction for atmospheric argon in the $^{40}Ar/^{39}Ar$ age calculation. Corrections are made for neutron-induced ^{40}Ar from potassium, ^{39}Ar and ^{36}Ar from calcium, and ^{36}Ar from chlorine (Roddick, 1983; Renne et al., 1998; Renne and Norman, 2001). Overall, single grain analysis of 5-10 biotite or muscovite grains per sample has been conducted. Analytical results are reported in **Table 5** and presented in **Fig. 17**.

3. Petrography

Three potential biotite types were identified from petrologic and petrographic observations: (1) vein; (2) halo; and (3) host rock (**Fig. 14**). Vein biotite samples consist of vein-hosted biotite crystals from pre- to syn-D_2 sulphidized (py, cpy, and po) Qz-Cal-Chl veins (V_5). Vein biotite was observed in two samples (MV-02, FW-13). MV-02 is a moderately foliated mafic volcanic host rock from the hanging wall of the deposit cut by a pre- to syn-D_2 sulfidized (Py, Cpy, and

Po) Qz-Cal-Chl vein that is transposed parallel to the main deposit fabric (S_2; Oliver et al., 2011). Biotite crystals within this vein are very coarse-grained (0.5-2 mm), euhedral and elongated sub-parallel to the S_2 foliation fabric. These biotite crystals are also intergown with actinolite porphyroblasts within the vein. Sample FW-13 is a strongly foliated biotite schist (volcaniclastic protolith) from the footwall of the SLDZ, also cut by a pre- to syn-D_2 quartz veins. Vein-hosted biotite crystals in this sample are fine- to medium-grained (0.2-0.5 mm), subhedral to euhedral crystals, and are randomly oriented within the vein. Chlorite crystals overprint the vein-hosted biotite. Biotitized hydrothermal alteration halos are also associated with these biotite-bearing pre- to syn-D_2 veins. Halo biotite crystals are fine- to medium-grained and euhedral in both samples and are generally elongated parallel to the vein margins. In sample MV-02 the halo biotite crystals surround a primary actinolite halo and are overprinted by actinolite porphyroblasts, similar to the vein-hosted biotite samples. Geochronology was also conducted on halo biotite sampled from pre- to syn-D_2 veins (RD15-265-43, RD15-118-225.2 and RD15-118-10.2) that cut mafic volcanic rocks within the Detour Lake hanging wall; however, the sample preparation process consumed the entire rock and no petrographical data could be collected. Halo biotite from sample MV-02 were also dated; therefore, observations on this sample can likely be extended to the previous three samples of halo biotite. Based on these observations, vein and halo biotite appear to have a pre- to syn-metamorphic timing.

Nine biotite bearing samples were also collected from the mafic volcanic host rocks (MV-02, FW-13, FW-11, MV-04, FW-03, FW-10, MV-13, RD15-429-27, RD15-429-92). In the mafic volcanic sample, MV-02, biotite crystals are very fine-grained (~0.1 mm), anhedral, and defining the main S_2 deposit fabric. Actinolite, which defines the peak-metamorphic minerals assemblage, typically overgrows host-rock biotite, suggesting that biotite is pre- to syn-metamorphic.

However, rare, finer grained (30-50 μm) euhedral biotite crystals also overprint actinolite, which points to multiple generations of biotite crystallization. Biotite crystals from biotite schist (volcaniclastic protolith) sample FW-13 are very fine-grained (0.1-0.2 mm), subhedral to euhedral crystals and are elongated parallel to S_2. These pre- to syn-S_2 biotite crystals are intergrown with coeval, fine-grained muscovite, which are overprinted by a younger, randomly oriented, post-S_2 generation of muscovite. Biotite schist samples, such as FW-11, from the footwall unit at Detour Lake are fine-grained (0.2-0.3 mm), anhedral to euhedral, are elongated parallel to the S_2 foliation. Pre- to syn-S_2 biotite crystals from these samples are overprinted by late, fine-grained, euhedral muscovite crystals, which are also oriented sub-parallel to the main deposit fabric. Sample MV-04 is a weakly-foliated, mafic volcanic rock collected from the Detour Lake hanging wall unit. Biotite crystals within MV-04 are subhedral to euhedral, range in grain size from very fine (0.1 mm)- to medium-grained (0.3 mm) and are weakly aligned with the S_2 foliation. Medium-grained biotite crystals are overprinted by actinolite; whereas the finer grained (<0.1 mm) biotite grains overprint pre- to syn-S_2 actinolite crystals, further suggesting multiple biotite generations are hosted within biotite schist samples. Sample FW-03 is a strongly foliated and weakly crenulated biotite schist from the footwall unit of the deposit. The host rock biotite are coarse-grained subhedral to euhedral crystals defining 0.5-1.0 mm bands. Finer grained anhedral biotite crystals are also observed in the Qz-rich bands. Sample FW-10 is a strongly foliated biotite schist, also from the footwall unit of the deposit, with coarse-grained euhedral host rock biotite crystals defining the main foliation. These biotite are overprinted by alternating bands of wispy chlorite and finer grained actinolite. MV-13 is a coarse-grained meta-gabbro sample from the hanging wall of the deposit with anhedral to subhedral medium-grained host rock biotite crystals. These biotite are randomly oriented in the finer matrix in between the

larger hornblende phenocrysts overprinted by actinolite. Chlorite, muscovite, and actinolite overprint these biotite crystals. The host rock biotite in sample RD15-429-27, a weakly foliated mafic volcanic sampled from the hanging wall unit, are fine-grained and subhedral crystals dispersed in 200-300 μm knots throughout the host rock. Biotite in these clusters are sub-parallel to the weak foliation and are also overprinted by actinolite. Host rock biotite in sample RD15-429-92, also a weakly foliated mafic volcanic sample from the hanging wall, range from anhedral to subhedral fine-grained crystals weakly aligned with the rock structure. These biotite are also overprinted by actinolite. Based on these observations, host rock biotite appear to have a pre- to syn- metamorphic timing.

In addition to biotite, host rock muscovite was also studied from two samples (FW-13, MV-12). The host rock muscovites in the FW-13 biotite schist are very fine-grained, subhedral to euhedral defining the S_2 foliation, suggesting a syn-metamorphic timing. These muscovite are intergrown with the host rock biotite in the sample. A second, coarser-grained muscovite generation overprints the S_2 defining biotite and muscovite. Sample MV-12 is a massive mafic volcanic unit from the hanging wall with very coarse-grained muscovite in the host rock. The entirety of the sample was consumed during sample preparation for $^{40}Ar/^{39}Ar$ dating; therefore no petrographical data was collected.

To summarize, there are three potential types of biotite: (1) vein biotite in syn-D_2 vein sets (V_5) ranging from fine- to coarse-grained, subhedral to euhedral crystals; (2) halo biotite are medium-grained euhedral crystals that are parallel to the syn-D_2 vein margins; and (3) host rock biotite ranging from very fine-grained to coarse-grained, anhedral to euhedral crystals. Biotite from all three types define the S_2 foliation structure when present and are either intergrown with or overprinted by chlorite, actinolite, and muscovite suggesting a pre- to syn-metamorphic

timing. The similar timing of these three types makes it difficult to distinguish between metamorphic and hydrothermal biotite. Based on the structural location of halo biotite, it is safe to assume a hydrothermal source, possibly related to the mineralizing event, but it appears that these biotite were subsequently metamorphosed. For this reason, we further analysed the geochemistry of these samples targeting all three of the identified biotite types.

4. Mineral Geochemistry

Overall, all three biotite types yield overlapping Fe-Mg-K-Al compositions on ternary plots of ~25% Fe, 30% Mg, 55% Al and 35% Fe, 50% Mg, 15% K (**Fig. 15**), which suggests that each biotite type is homogeneous and that different biotite generations are geochemically similar. Rare geochemically anomalous analyses include Mg-rich biotite crystals from a gabbroic intrusive unit (sample MV-13) and slightly Fe-Mg enriched vein-hosted biotite from sample MV-02. The Fe-rich nature of these anomalous analyses may be due to nearby pyrite crystals that may have been included within the sample volume during analysis. The data also shows a linear trend towards K depletion and Al enrichment in the alteration halo biotite type (**Fig. 15**). These compositional trends are also observed in hydrothermal biotite from the Mouska deposit, where the proximal alteration is defined by the progressive replacement of biotite by quartz and white micas, (Belkabir et al, 2004). The similarity of the geochemical composition of the different biotite types is also evident when comparing the averages of the wt% oxides and the cations of each biotite type reported in **Table 4**. Previous studies including Imeokeparia (1984) and Kesler et al. (1975), have used the variations in the Mg# in biotite to discern between mineralized and barren zones, with mineralized zones yielding higher Mg#s. However, in the case of Detour Lake

deposit, all three biotite types yield similar Mg# values (**Table 4**). Vein-hosted, halo and host-rock biotite yield Mg# of 0.52±0.04), 0.53±0.02) and 0.56±0.09), respectively.

Results from the WDS geochemical maps (**Fig. 16**) also demonstrate broad compositional overlap between biotite types. Vein-hosted biotite (MV-02, FW-13), reveal chemically homogeneous crystals whereas the chemical maps of the halo biotite from the same samples show chemical zonation in the form of 2-5 μm Fe-Mg rich and K-poor rims. The halo biotite in sample MV-02 also reveal the intergrowth of the biotite with a Ca-Al rich and Fe-Mg-K poor mineral phase, which could explain the linear trend of K depletion and Al enrichment in halo biotite. As for the host rock biotite, the chemical maps of samples FW-11, MV-13, MV-02, and FW-03 show very little intra-grain chemical variation with the exception of a very thin 1-2 μm Fe-Mg-K poor rim in sample FW-11 and a slightly Fe-Mg rich rim in sample FW-03.

To summarize, biotite from all three potential type yield ternary biotite plot compositions of approximately 25% Fe, 30% Mg, 55% Al and 35% Fe, 50% Mg, 15% K. Vein-hosted biotite and host rock biotite are generally chemically homogeneous, whereas halo biotite have Fe-Mg rich and K-poor rims. Our results suggest that all three biotite types are indistinguishable based on their major and minor elements compositions alone.

5. $^{40}Ar/^{39}Ar$ Geochronology

In another attempt to discern between metamorphic and secondary biotite, each of the identified biotite types were analyze using $^{40}Ar/^{39}Ar$ geochronology (**Table 5; Fig.17**) The biotite crystals from the vein biotite in sample MV-02 yielded ages of 2550–2460 Ma with most of the dates overlapping at ca. 2525 Ma. For the halo biotite, sample RD15-118-265.43 yielded ages of 2420–2260 Ma and one younger anomalous date of 2510 Ma. Ages from sample RD15-

118-225.2 vary from 2530 to 2140 Ma. Biotite from sample RD15-118-10.2 also yield ages over a large range between 2650 Ma and 2230 Ma with most of the dates at 2650–2545 Ma. Sample MV-02 revealed dates ranging from 2610 Ma to 2530 Ma. The host rock type of biotite and muscovite also yielded similar ages. Biotite from sample FW-13 are 2500–2410 Ma with outliers at 2350 Ma and 2550 Ma whereas muscovite from the same sample yielded ages of 2540–-2410 Ma with a few outlying dates <2325 Ma. Biotite from samples FW-11, MV-04, FW-03 and FW-10 yielded ages of 2500-2440 Ma, 2560–2500 Ma, 2550–2500 Ma and 2610–2530 Ma, respectively. Muscovite from sample MV-12 revealed dates ranging between 2600 Ma and 2560 Ma. These data show that all three types of biotite yield very similar ages with single grain halo biotite ages that are dispersed over a 500 m.y. window. Overall, the vein biotite yield ages in the range of 2550–2460 Ma; the halo biotite yield ages ranging between 2650–2150 Ma; and the host rock type yield ages of 2610–2410 Ma.

6. Discussion and Summary

These new $^{40}Ar/^{39}Ar$ ages do not resolve distinct phases of biotite cooling or deformation. Biotite ages post-date the main deformation events at the Detour Lake deposit (D_1 and D_2; dated at 2696–2690 Ma and 2676–2670 Ma, respectively) and the timing of regional metamorphism, (2670–2640 Ma; Oliver et al., 2011), except for two analyses from one halo-hosted sample. Powell et al. (1995) reported $^{40}Ar/^{39}Ar$ data from white micas and amphiboles to resolve the thermal history in the southern Abitibi and Pontiac subprovinces. These previously reported ages were divided into five stages: 2543 ± 8 Ma, 2578 ± 10 Ma, 2421 ± 15 Ma, 2414 ± 9 Ma and >2594 Ma. Each stage was interpreted to date multiple, post-metamorphic hydrothermal events along fault zones. New Detour Lake biotite ages are also complex, but broadly coincide with the

timing of the widespread Neaoarchean to Paleoproterozoic Matachewan, Irsuaq Hearst, and Maguire dike swarms (2480 Ma, 2507.5 ± 5.8 Ma 2430 Ma, 2229+35/−20Ma repectively; Heaman, 1997; Buchan et al., 1998; Maurice et al., 2009). Kerrich and Ludden (2000) interpreted such post-metamorphic and deformational ages to be the result of a $^{40}Ar/^{39}Ar$ spectra resetting from 2550 Ma to 2200 Ma caused by tectonic pumping of fluids along Archean structures reactivated during the accretion of 200 km thick mantle lithosphere to Archean crust. These fluids are a product of hypersaline $CaCl_2$ brines, derived from Paleoproterozoic glaciogenic sediments, penetrating the Archean basement where they were driven to higher temperatures by the Matachewan and Hearst dike swarms leading to advection and redistribution of Au.

Our petrographical observations suggest three distinct types of syn-D_2 biotite: (1) vein biotite in syn-D_2 vein sets ranging from fine- to coarse-grained, subhedral to euhedral crystals; (2) medium-grained euhedral halo biotite that parallel the syn-D_2 vein margins; and (3) host rock biotite ranging from very fine-grained to coarse-grained, anhedral to euhedral crystals. However, our geochemical and geochronological data do not unequivocally support distinct biotite types. All biotite are generally chemically homogeneous with a composition of approximately 25% Fe, 30% Mg, 55% Al and 35% Fe, 50% Mg, 15% K and yield dispersed ages in the range of 2600–2450 Ma. Based on these data, metamorphic biotite and secondary hydrothermal biotite cannot be easily discerned. The $^{40}Ar/^{39}Ar$ ages may likely be a result of regional resetting in the Abitibi Subprovince and are not linked to the Au mineralization. For these reasons, we do not recommend the use of biotite as an indicator mineral for targeting ore pockets at the Detour Lake deposit. The same conclusions may also be relevant to other lower to middle amphibolite facies orogenic Au deposits around the world.

Acknowledgements

This project was funded by Detour Gold Corp and an NSERC Discovery grant (to DAS). We would like to thank Detour Gold Corp. for their cooperation and assistance throughout our project, David Diekrup and Glenn Poirier for help with SEM and EPMA analyses and Alfredo Camacho for the Ar-Ar analyses. Discussions with Patrick Mercier-Langevin (NRCan) were also greatly appreciated. CJML acknowledges support from the Targeted Geoscience Initiative (TGI)-5 program.

References

Belkabir, A., Hubert, C., Hoy, L., 2004. Gold emplacement and hydrothermal alteration in metabasic rocks at the Mouska mine, Bousquet district, Abitibi, Quebec, Canada. The Canadian Mineralogist 42, 1079–1096.

Best, M.G., Christiansen, E.H., Deino, A.L., Grommé, C.S., Tingey, D.G., 1995. Correlation and emplacement of a large, zoned, discontinuously exposed ash flow sheet; the $^{40}Ar/^{39}Ar$ chronology, paleomagnetism, and petrology of the Pahranagat Formation, Nevada. Journal of Geophysical Research 100, 24593–24609.

Buchan, K.L., Mortensen, J.K., Card, K.D., Percival, J.A., 1998. Paleomagnetism and U–Pb geochronology of diabase dyke swarms of Minto block, Superior Province, Quebec, Canada. Canadian Journal of Earth Sciences 35(9), 1054–1069.

Craig, J.R, Vokes, F.M., 1993. The metamorphism of pyrite and pyritic ores: an overview. Mineralogical Magazine 57, 3–18.

Dazé, A., Lee, J.K.W., Villeneuve, M., 2003. An intercalibration study of the Fish Canyon sanidine and biotite $^{40}Ar/^{39}Ar$ standards and some comments on the age of the Fish Canyon Tuff. Chemical Geology 199, 111–127.

De Souza, S., Dubé, B., McNicoll, V., Dupuis, C., Mercier-Langevin, P., Creaser, R., Kjarsgaard, I., 2015. Targeted Geoscience Initiative 4: Contributions to the understanding of Precambrian lode gold deposits and implications for exploration. Geological Survey of Canada, Open File Report 7852, 115–123.

Heaman, L., 1997. Global mafic magmatism at 2.45 Ga: Remnants of an ancient large igneous province? Geology 25, 299–302.

Imeokparia, E., 1984. Chemical variations in biotites-an exploration tool to distinguish between mineralized and barren rocks in the Nigerian tin bearing province. Journal of African Earth Sciences 2, 327–331.

Jourdan, F., Verati, C., Fe´raud, G., 2006. Intercalibration of the HB3GR $^{40}Ar/^{39}Ar$ dating standard. Chemical Geology 231, 77–189.

Kesler, S., Issigonis, M., Brownlow, A., Damon, P., Moore, W., Northcote, K., Preto, V. 1975. Geochemistry of biotites from mineralized and barren intrusive systems. Economic Geology 70, 559–567.

Kuiper, K.F., Deino, A., Hilgen, F.J., Krijgsman, W., Renne, R., Wijbrans, J.R., 2008. Synchronizing Rock Clocks of Earth History. Science, 320, 500–504.

Marmont, S., 1986. The geological setting of the Detour Lake Gold Mine, Ontarion, Canada. A.J. Macdonald (ed.), Proceedings of Gold '86, an International Symposium on the Geology of Gold: Toronto, 3–22.

Maurice, C., David, J., O'Neil, J., Francis, D., 2009. Age and tectonic implications of Paleoproterozoic mafic dyke swarms for the origin of 2.2 Ga enriched lithosphere beneath the Ungava Peninsula, Canada. Precambrian Research 174, 163–180.

Oliver, J., Ayer, J., Dubé, B., Aubertin, R., Burson, M., Panneton, G., Friedman, R., Hamilton, M., 2011. Structure, stratigraphy, U-Pb geochronology and alteration characteristics of gold mineralization at the Detour Lake deposit, Ontario, Canada. Exploration and Mining Geology 20, 1–30.

Parra, T., Vidal, O., and Agard, P., 2002. A thermodynamic model for Fe-Mg dioctahedral K white micas using data from phase-equilibrium experiments and natural pelitic assemblages. Contributions to Mineralogy and Petrology 143, 706–732.

Powell, W., Hodgson, C., Hanes, J., Carmichael, D., McBride, S., Farrar, E., 1995. $^{40}Ar/^{39}Ar$ geochronological evidence for multiple postmetamorphic hydrothermal events focused along faults in the southern Abitibi greenstone belt. Canadian Journal of Earth Sciences 32, 768–786.

Renne, P.R., Cassata, W.S., Morgan, L.E., 2009. The isotopic composition of atmospheric argon and $^{40}Ar/^{39}Ar$ geochronology: time for a change? Quaternary Geochronology 4, 288–298.

Renne, P.R., Norman, E.B., 2001. Determination of the half-life of ^{40}Ar by mass spectrometry. Physics Reviews C63 (047302), 3.

Renne P.R., Swisher C.C., Deino A.L., Karner D.B., Owens T.L., DePaolo D.J., 1998. Intercalibration of standards, absolute ages and uncertainties in $^{40}Ar/^{39}Ar$ dating. Chemical Geology 145, 117–152.

Roddick, J.C., 1983. High precision intercalibration of $^{40}Ar/^{39}Ar$ standards. Geochimica et Cosmochimica Acta 47, 887–898.

Steiger R.H., Jäger E., 1977. Subcommission on geochronology: convention on the use of decay constants in geo- and cosmochronology. Earth and Planetary Science Letters 36, 359–362.

Vidal, O., Parra, T., Trotet, F., 2001. A thermodynamic model for Fe-Mg aluminous chlorite using data from phase equilibrium experiments and natural politic assemblages in the 100° to 600°C, 1 to 25 kb range. American Journal of Science 301, 557–559

Table 3. Mineralogy, structural position, and conducted analyses of each sample from Detour Lake mine

		Structural position			Mineralogy							Analyses		
Sample name	**Rock type**	**vein**	**halo**	**host rock**	**Qz**	**Cal**	**Ab**	**Chl**	**Bt**	**Ms**	**Act**	**EMPA**	**WDS**	**$^{40}Ar/^{39}Ar$**
FW-03	biotite schist			✓	✓	✓	✓	✓	✓			✓	✓	✓
FW-10	biotite schist			✓	✓			✓	✓		✓	✓		✓
FW-11	biotite schist			✓	✓				✓	✓		✓	✓	✓
FW-13	biotite schist	✓	✓	✓	✓		✓	✓	✓	✓		✓	✓	✓
MV-02	mafic volcanic	✓	✓	✓	✓	✓			✓		✓	✓	✓	✓
MV-04	mafic volcanic			✓	✓	✓			✓		✓			✓
MV-12	mafic volcanic			✓	✓				✓	✓	✓			✓
MV-13	meta-gabbro			✓	✓		✓	✓	✓	✓	✓	✓	✓	
RD15-118-10.2	mafic volcanic		✓		✓				✓		✓			✓
RD15-118-255.2	mafic volcanic		✓		✓				✓		✓			✓
RD15-265-43.0	mafic volcanic		✓		✓				✓		✓			✓
RD15-429-27	mafic volcanic			✓	✓				✓		✓	✓		
RD15-429-92	mafic volcanic			✓	✓	✓			✓		✓	✓		

Table 4. Representative EMP analysesof biotite at the Detour Lake deposit

	Vein				Halo				Host rock			
	min	**mean**	**max**	**std**	**min**	**mean**	**max**	**std**	**min**	**mean**	**max**	**std**
Wt%												
SiO_2	28.89	38.36	40.68	3.48	31.36	36.23	40.04	2.67	32.54	37.77	55.00	3.98
TiO_2	0.03	1.38	1.99	0.55	0.22	1.51	1.98	0.51	0.02	1.26	2.14	0.69
Al_2O_3	17.16	18.68	23.98	1.97	15.93	17.79	21.65	1.47	12.43	17.93	22.75	2.09
FeO	15.92	18.23	20.91	1.48	16.65	18.85	22.48	1.69	12.14	17.02	21.46	2.54
Fe_2O_3												
MnO	0.07	0.11	0.23	0.05	0.12	0.15	0.22	0.03	0.06	0.17	0.27	0.05
MgO	9.03	11.29	16.09	1.99	10.10	12.48	16.47	1.63	9.05	12.73	21.52	3.65
CaO	0.00	0.02	0.04	0.01	0.00	0.16	2.28	0.44	0.00	0.08	1.72	0.25
Na_2O	0.01	0.12	0.18	0.05	0.00	0.09	0.20	0.06	0.00	0.07	0.27	0.06
K_2O	0.04	8.31	9.90	3.01	0.81	6.93	9.99	2.95	0.00	7.59	10.31	3.31
F	0.00	0.04	0.15	0.05	0.00	0.04	0.16	0.05	0.00	0.04	0.19	0.05
Cl	0.00	0.02	0.04	0.01	0.00	0.02	0.03	0.01	0.00	0.02	0.06	0.02
H_2O												
Total	90.18	96.56	98.58	2.44	89.31	94.26	97.86	2.29	88.70	94.69	99.63	2.83
Structural formulae calculation on 22 cations												
Si	2.24	2.82	2.95	0.21	2.39	2.74	2.92	0.15	2.43	2.81	3.67	0.22
Ti	0.00	0.08	0.11	0.03	0.01	0.09	0.11	0.03	0.00	0.07	0.12	0.04
Al	1.47	1.62	2.19	0.21	1.42	1.59	1.95	0.14	0.98	1.58	2.00	0.19
Fe^{2+}	0.97	1.12	1.36	0.11	1.03	1.19	1.46	0.13	0.76	1.06	1.41	0.17
Fe^{3+}												
Mn	0.00	0.01	0.02	0.00	0.01	0.01	0.01	0.00	0.00	0.01	0.02	0.00
Mg	0.99	1.24	1.86	0.25	1.11	1.41	1.87	0.21	0.90	1.42	2.39	0.41
Ca	0.00	0.00	0.00	0.00	0.00	0.01	0.19	0.04	0.00	0.01	0.12	0.02
Na	0.00	0.02	0.03	0.01	0.00	0.01	0.03	0.01	0.00	0.01	0.04	0.01
K	0.00	0.77	0.92	0.28	0.08	0.67	0.94	0.28	0.00	0.72	0.96	0.32
F	0.00	0.01	0.03	0.01	0.00	0.01	0.04	0.01	0.00	0.01	0.05	0.01
Cl	0.00	0.00	0.00	0.00	0.00	0.00	0.00	0.00	0.00	0.00	0.01	0.00
Mg#	0.45	0.52	0.58	0.04	0.49	0.53	0.59	0.02	0.48	0.56	0.76	0.09

Table 5. $^{40}Ar/^{39}Ar$ data of biotite and muscovite from the Detour Lake deposit

	Sample	Mineral	J-value	Ar^{40} ±(1σ)	Ar^{39} ±(1σ)	Ar^{38} ±(1σ)	Ar^{37} ±(1σ)	Ar^{36} ±(1σ)	Ca/K ±(1σ)	Cl/K ±(1σ)	$^{40}Ar^*/^{39}Ar_{(K)}$ ±(1σ)	$^{40}Ar^*$ (%)	Age (Ma) ±(1σ)
Vein	**MV-02**												
	Grain 1	biotite	J=0.0186157 ± 1.62E-05	1965.0 0.2	12.3 0.1	0.1 0.0	-0.1 0.0	0.1 0.0	-0.3 0.1	0.0 0.0	158.2 0.9	98.9	2476.4 7.7
	Grain 2			1629.5 0.2	9.8 0.1	0.1 0.0	0.1 0.0	0.1 0.0	0.3 0.2	0.0 0.0	164.0 1.1	98.8	2524.8 8.8
	Grain 3			3081.6 0.3	19.3 0.1	0.3 0.0	0.0 0.0	0.1 0.0	0.1 0.1	0.0 0.0	158.0 0.6	99.0	2474.6 4.9
	Grain 4			6385.3 0.4	38.9 0.1	0.5 0.0	0.0 0.0	0.1 0.0	0.0 0.0	0.0 0.0	163.3 0.4	99.6	2519.2 3.5
	Grain 5			1874.6 0.2	11.3 0.1	0.1 0.0	0.0 0.0	0.0 0.0	-0.1 0.1	0.0 0.0	165.1 0.9	99.3	2533.9 7.8
	Grain 6			5714.7 0.3	34.1 0.1	0.4 0.0	0.0 0.0	0.2 0.0	0.1 0.0	0.0 0.0	165.5 0.5	98.9	2536.8 3.8
	RD15-118-265.43												
	Grain 1	biotite	J=0.018621 ±1.81E-05	1633.0 0.2	11.6 0.1	0.1 0.0	0.3 0.0	0.0 0.0	1.3 0.1	0.0 0.0	140.6 0.9	99.7	2319.6 7.9
	Grain 2			970.0 0.2	7.1 0.1	0.0 0.0	0.1 0.0	0.0 0.0	0.8 0.2	0.0 0.0	136.7 1.3	99.8	2283.2 12.0
	Grain 3			818.1 0.2	5.5 0.1	0.0 0.0	0.1 0.0	0.0 0.0	0.6 0.3	0.0 0.0	148.2 1.6	99.7	2388.8 14.4
	Grain 4			4391.3 0.3	26.9 0.1	0.3 0.0	0.1 0.0	0.1 0.0	0.1 0.1	0.0 0.0	162.4 0.5	99.5	2511.9 4.3
	Grain 5			2253.9 0.2	15.5 0.1	0.2 0.0	0.0 0.0	0.0 0.0	0.3 0.1	0.0 0.0	144.3 0.6	99.5	2354.1 5.2
	RD15-118-225.2												
	Grain 1	biotite	J=0.0185578±2.77E-05	1936.7 0.2	11.7 0.1	0.1 0.0	0.0 0.0	0.1 0.0	0.2 0.1	0.0 0.0	162.8 0.9	98.6	2510.6 7.6
	Grain 2			3196.2 0.3	19.3 0.1	0.2 0.0	0.0 0.0	0.1 0.0	-0.1 0.1	0.0 0.0	164.2 0.5	99.2	2521.8 4.4
	Grain 3			19518.2 0.9	190.5 0.1	2.3 0.0	0.0 0.0	0.5 0.0	0.0 0.0	0.0 0.0	101.6 0.1	99.3	1911.8 1.2
	Grain 4			11241.1 0.4	86.0 0.1	1.1 0.0	0.1 0.0	0.6 0.0	0.1 0.0	0.0 0.0	128.6 0.2	98.6	2200.7 1.6
	Grain 5			2752.4 0.2	18.0 0.1	0.2 0.0	0.0 0.0	0.1 0.0	0.2 0.1	0.0 0.0	150.3 0.6	98.5	2403.7 5.0
	Grain 6			6470.4 0.3	42.6 0.1	0.6 0.0	0.1 0.0	0.2 0.0	0.1 0.1	0.0 0.0	150.5 0.3	99.2	2404.9 2.5
	Grain 7			3930.1 0.3	30.0 0.1	0.4 0.0	0.5 0.0	0.4 0.0	1.4 0.1	0.0 0.0	127.6 0.3	97.3	2190.5 3.1
	Grain 8			5281.0 0.3	42.3 0.1	0.4 0.0	0.4 0.0	0.2 0.0	0.7 0.1	0.0 0.0	123.3 0.2	99.0	2147.9 2.3
Halo	**RD15-118-10.2**												
	Grain 1	biotite	J=0.0185385±2.66E-05	1417.8 0.2	8.1 0.1	0.1 0.0	0.1 0.0	0.0 0.0	0.4 0.2	0.0 0.0	174.2 1.5	99.9	2601.4 11.8
				4861.8 0.3	27.9 0.1	0.4 0.0	-0.1 0.0	0.1 0.0	-0.1 0.1	0.0 0.0	172.8 0.4	99.5	2590.7 3.6
	Grain 2			2233.5 0.3	12.5 0.1	0.1 0.0	0.0 0.0	0.0 0.0	0.2 0.1	0.0 0.0	178.4 1.0	99.9	2634.9 7.9
				2533.6 0.3	15.9 0.1	0.3 0.0	0.0 0.0	0.1 0.0	0.2 0.1	0.0 0.0	158.2 0.7	99.3	2470.3 5.6
	Grain 3			1619.9 0.2	9.1 0.1	0.1 0.0	0.1 0.0	0.0 0.0	0.4 0.2	0.0 0.0	177.4 1.3	99.9	2626.9 10.5
				3113.8 0.3	20.2 0.1	0.2 0.0	0.0 0.0	0.1 0.0	0.1 0.1	0.0 0.0	153.4 0.5	99.4	2428.8 4.4
	Grain 4			1569.5 0.2	9.2 0.1	0.1 0.0	0.0 0.0	0.0 0.0	0.1 0.2	0.0 0.0	169.5 1.3	99.9	2563.8 10.8
				1344.8 0.2	9.7 0.1	0.2 0.0	0.1 0.0	0.0 0.0	0.4 0.2	0.0 0.0	138.1 0.9	99.2	2290.6 8.1
	Grain 5			7355.9 0.4	42.5 0.1	0.5 0.0	0.0 0.0	0.0 0.0	0.0 0.1	0.0 0.0	172.7 0.3	99.9	2589.8 2.2
	Grain 6			6966.3 0.4	52.1 0.1	0.6 0.0	0.2 0.0	0.2 0.0	0.3 0.0	0.0 0.0	132.4 0.2	99.2	2236.7 2.1
	MV-02												
	Grain 1	biotite	J=0.0186664 ±1.63E-05	5306.4 0.4	31.5 0.1	0.4 0.0	0.0 0.0	0.1 0.0	0.0 0.0	0.0 0.0	167.6 0.4	99.6	2557.0 3.0
	Grain 2			3045.7 0.3	17.4 0.1	0.2 0.0	0.1 0.0	0.1 0.0	0.2 0.1	0.0 0.0	172.6 0.7	98.9	2597.0 5.0
	Grain 3			3659.5 0.3	21.6 0.1	0.3 0.0	0.0 0.0	0.1 0.0	0.1 0.1	0.0 0.0	168.6 0.5	99.6	2565.0 4.0
	Grain 4			3365.6 0.3	19.7 0.1	0.3 0.0	0.0 0.0	0.1 0.0	-0.1 0.1	0.0 0.0	169.8 0.6	99.4	2575.0 5.0
	Grain 5			6053.0 0.4	36.5 0.1	0.4 0.0	0.0 0.0	0.2 0.0	0.0 0.0	0.0 0.0	164.5 0.4	99.3	2532.0 3.0
	FW-13												
	Grain 1	biotite	J=0.0186608±1.90E-05	1177.2 0.2	7.1 0.1	0.1 0.0	0.1 0.0	0.0 0.0	0.7 0.2	0.0 0.0	166.3 1.6	99.9	2547.0 13.0
				5363.8 0.3	33.3 0.1	0.3 0.0	0.0 0.0	0.1 0.0	-0.1 0.0	0.0 0.0	160.3 0.4	99.6	2497.0 3.0
	Grain 2			2647.1 0.3	16.6 0.1	0.2 0.0	0.1 0.0	0.0 0.0	0.2 0.1	0.0 0.0	159.2 0.7	100.0	2487.0 6.0
				5422.2 0.4	35.1 0.1	0.4 0.0	0.0 0.0	0.0 0.0	0.0 0.0	0.0 0.0	154.0 0.3	99.8	2443.0 3.0
	Grain 3			2238.8 0.2	14.0 0.1	0.2 0.0	0.0 0.0	0.0 0.0	0.0 0.1	0.0 0.0	159.2 0.8	99.9	2488.0 7.0
				7394.6 0.4	46.6 0.1	0.5 0.0	0.0 0.0	0.1 0.0	0.0 0.0	0.0 0.0	157.9 0.3	99.7	2477.0 2.0
	Grain 4			3328.7 0.3	21.3 0.1	0.2 0.0	0.1 0.0	0.0 0.0	0.2 0.1	0.0 0.0	156.3 0.6	100.0	2463.0 6.0
				6830.2 0.4	43.9 0.1	0.5 0.0	0.0 0.0	0.1 0.0	0.0 0.0	0.0 0.0	155.2 0.3	99.7	2453.0 2.0
	Grain 5			1624.3 0.2	11.3 0.1	0.1 0.0	0.0 0.0	0.0 0.0	0.0 0.1	0.0 0.0	143.5 0.9	100.0	2349.0 8.0

			6430.4 0.4	42.5 0.1	0.5 0.0	0.0 0.0	0.1 0.0	0.0 0.0	0.0 0.0	150.6 0.3	99.8	2414.0 2.0
FW-13												
Grain 1			5831.5 0.4	37.1 0.1	0.4 0.0	0.0 0.0	0.0 0.0	0.0 0.0	0.0 0.0	156.9 0.3	100.0	2463.8 2.8
			1385.5 0.2	8.5 0.1	0.1 0.0	-0.1 0.0	0.0 0.0	-0.4 0.2	0.0 0.0	163.2 1.3	100.0	2517.1 11.2
Grain 2			3204.9 0.2	20.0 0.1	0.2 0.0	0.1 0.0	0.0 0.0	0.2 0.1	0.0 0.0	159.7 0.5	100.0	2487.9 4.3
Grain 3	muscovite	J=0.0186031±4.22E-05	10038.0 0.6	66.1 0.1	0.8 0.0	0.1 0.0	0.0 0.0	0.1 0.0	0.0 0.0	151.6 0.2	99.9	2417.8 1.8
			3208.4 0.3	22.9 0.1	0.3 0.0	0.1 0.0	0.0 0.0	0.3 0.1	0.0 0.0	140.0 0.5	100.0	2313.4 4.9
Grain 4			8583.4 0.5	71.0 0.1	0.9 0.0	0.1 0.0	0.0 0.0	0.1 0.0	0.0 0.0	120.7 0.2	100.0	2123.5 1.7
			2745.9 0.2	35.0 0.1	0.4 0.0	0.0 0.0	0.0 0.0	0.0 0.0	0.0 0.0	78.4 0.3	100.0	1623.1 3.6
Grain 5			10010.6 0.5	63.7 0.1	0.8 0.0	0.0 0.0	0.0 0.0	0.1 0.0	0.0 0.0	157.0 0.2	100.0	2464.5 2.0
Grain 6			1735.7 0.2	13.2 0.1	0.1 0.0	0.0 0.0	0.0 0.0	-0.3 0.2	0.0 0.0	131.4 0.6	100.0	2230.9 6.3
Grain 7			14345.7 0.6	89.9 0.1	1.1 0.0	0.0 0.0	0.0 0.0	0.0 0.0	0.0 0.0	159.2 0.2	100.0	2483.9 1.6
FW-11												
Grain 1			10742.4 0.5	68.0 0.1	0.8 0.0	0.2 0.0	0.1 0.0	0.1 0.0	0.0 0.0	157.5 0.3	99.8	2474.0 3.0
Grain 2		J=0.0186688	9097.2 0.4	58.7 0.1	0.8 0.0	0.1 0.0	0.1 0.0	0.1 0.0	0.0 0.0	154.3 0.3	99.7	2446.0 3.0
Grain 3	biotite	±1.36E-05	14488.1 0.6	91.6 0.1	1.1 0.0	0.2 0.0	0.1 0.0	0.1 0.0	0.0 0.0	157.6 0.3	99.8	2474.0 3.0
Grain 4			4445.0 0.3	28.1 0.1	0.4 0.0	0.0 0.0	0.0 0.0	-0.1 0.1	0.0 0.0	157.6 0.5	99.9	2475.0 4.0
Grain 5			18689.4 0.7	116.7 0.1	1.4 0.0	0.1 0.0	0.1 0.0	0.1 0.0	0.0 0.0	159.6 0.2	99.8	2492.0 1.0
Grain 6			28522.3 0.9	183.0 0.1	2.2 0.0	0.2 0.0	0.1 0.0	0.1 0.0	0.0 0.0	155.5 0.2	99.9	2457.0 1.0
MV-04												
Grain 1			3631.8 0.3	21.8 0.1	0.3 0.0	0.1 0.0	0.1 0.0	0.2 0.1	0.0 0.0	166.1 0.6	165.1	2535.0 5.0
Grain 2		J=0.0186538	8673.4 0.5	52.3 0.1	0.6 0.0	0.1 0.0	0.1 0.0	0.1 0.0	0.0 0.0	164.9 0.4	99.6	2535.0 3.0
Grain 3	biotite	±4.29E-05	5581.1 0.4	33.3 0.1	0.4 0.0	0.0 0.0	0.0 0.0	-0.1 0.0	0.0 0.0	166.9 0.5	99.7	2552.0 4.0
Grain 4			3558.5 0.3	21.1 0.1	0.2 0.0	0.0 0.0	0.1 0.0	-0.1 0.1	0.0 0.0	166.9 0.6	98.9	2551.0 5.0
Grain 5			5792.3 0.3	35.9 0.1	0.5 0.0	0.1 0.0	0.0 0.0	0.1 0.0	0.0 0.0	161.1 0.4	99.9	2503.0 3.0
FW-03												
Grain 1			7608.7 0.4	46.4 0.1	0.6 0.0	0.0 0.0	0.0 0.0	0.0 0.0	0.0 0.0	163.8 0.3	99.9	2525.0 2.0
Grain 2		J=0.0186482	20294.8 0.8	122.3 0.1	1.6 0.0	0.0 0.0	0.1 0.0	0.0 0.0	0.0 0.0	165.6 0.2	99.9	2540.0 2.0
Grain 3	biotite	±1.98E-05	10323.4 0.6	62.9 0.1	0.7 0.0	0.0 0.0	0.1 0.0	0.0 0.0	0.0 0.0	163.7 0.2	99.8	2524.0 2.0
Grain 4			5816.5 0.3	35.7 0.1	0.4 0.0	-0.1 0.0	0.0 0.0	-0.1 0.0	0.0 0.0	162.6 0.3	99.8	2516.0 3.0
Grain 5			3071.0 0.3	19.0 0.1	0.2 0.0	0.0 0.0	0.0 0.0	0.0 0.1	0.0 0.0	161.5 0.7	99.8	2506.0 6.0
Grain 6			6796.4 0.4	40.7 0.1	0.4 0.0	0.0 0.0	0.0 0.0	0.0 0.0	0.0 0.0	166.5 0.3	99.9	2548.0 3.0
FW-10												
Grain 1			9458.9 0.5	54.2 0.1	0.7 0.0	0.0 0.0	0.1 0.0	0.0 0.0	0.0 0.0	173.7 0.4	99.7	2606.0 3.0
Grain 2			6317.2 0.4	37.3 0.1	0.5 0.0	0.0 0.0	0.0 0.0	0.0 0.0	0.0 0.0	168.9 0.4	99.8	2568.0 3.0
Grain 3	biotite	J=0.0186562	3227.2 0.3	19.2 0.1	0.2 0.0	0.0 0.0	0.0 0.0	0.0 0.1	0.0 0.0	167.8 0.7	99.8	2559.0 5.0
Grain 4		±1.45E-05	4037.6 0.3	24.0 0.1	0.2 0.0	0.0 0.0	0.0 0.0	0.0 0.1	0.0 0.0	168.0 0.6	99.8	2560.0 5.0
Grain 5			5439.2 0.3	31.5 0.1	0.3 0.0	0.0 0.0	0.1 0.0	0.0 0.1	0.0 0.0	171.9 0.5	99.7	2592.0 4.0
Grain 6			7362.3 0.4	44.5 0.1	0.5 0.0	0.0 0.0	0.1 0.0	0.0 0.0	0.0 0.0	164.4 0.3	99.5	2531.0 2.0
Grain 7			15978.9 0.5	93.0 0.1	1.3 0.0	0.0 0.0	0.1 0.0	0.0 0.0	0.0 0.0	171.1 0.2	99.8	2586.0 2.0
MV-12												
Grain 1			4771.8 0.3	28.1 0.1	0.3 0.0	0.0 0.0	0.0 0.0	0.0 0.1	0.0 0.0	169.6 0.4	99.9	2570.0 4.0
Grain 2		J=0.0186017	4863.4 0.3	28.4 0.1	0.3 0.0	0.0 0.0	0.0 0.0	-0.1 0.1	0.0 0.0	170.7 0.4	99.8	2579.0 3.0
Grain 3	muscovite	±1.73E-05	2913.9 0.3	17.0 0.1	0.2 0.0	0.0 0.0	0.0 0.0	0.1 0.1	0.0 0.0	171.0 0.7	99.9	2580.0 5.0
Grain 4			4215.8 0.3	24.4 0.1	0.3 0.0	0.0 0.0	0.0 0.0	0.0 0.1	0.0 0.0	172.3 0.5	100.0	2591.0 4.0
Grain 5			7173.9 0.4	41.9 0.1	0.5 0.0	0.0 0.0	0.0 0.0	0.0 0.0	0.0 0.0	170.9 0.3	99.9	2580.0 3.0

Host rock

* Corrected for blank, mass discrimination, and radioactive decay
Sensitivity: 6.312E-17 ± 1.047E-18 (mol/fAmp)

A. vein biotite

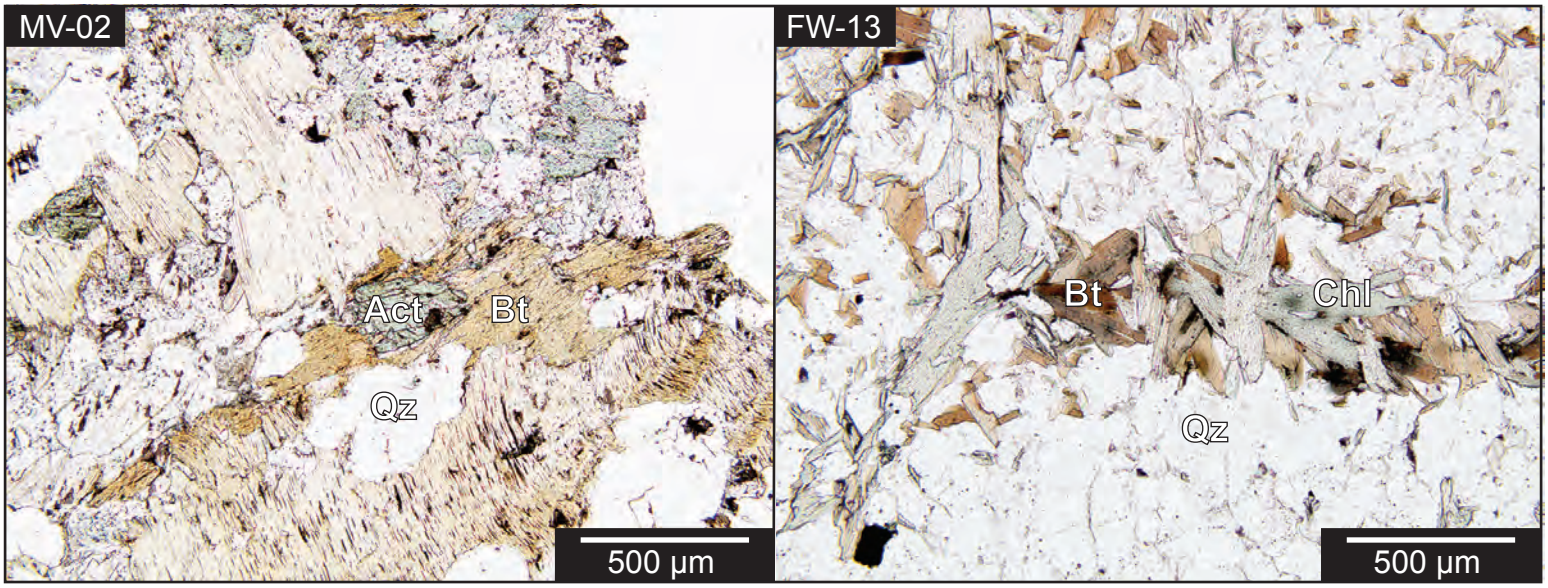

B. halo biotite

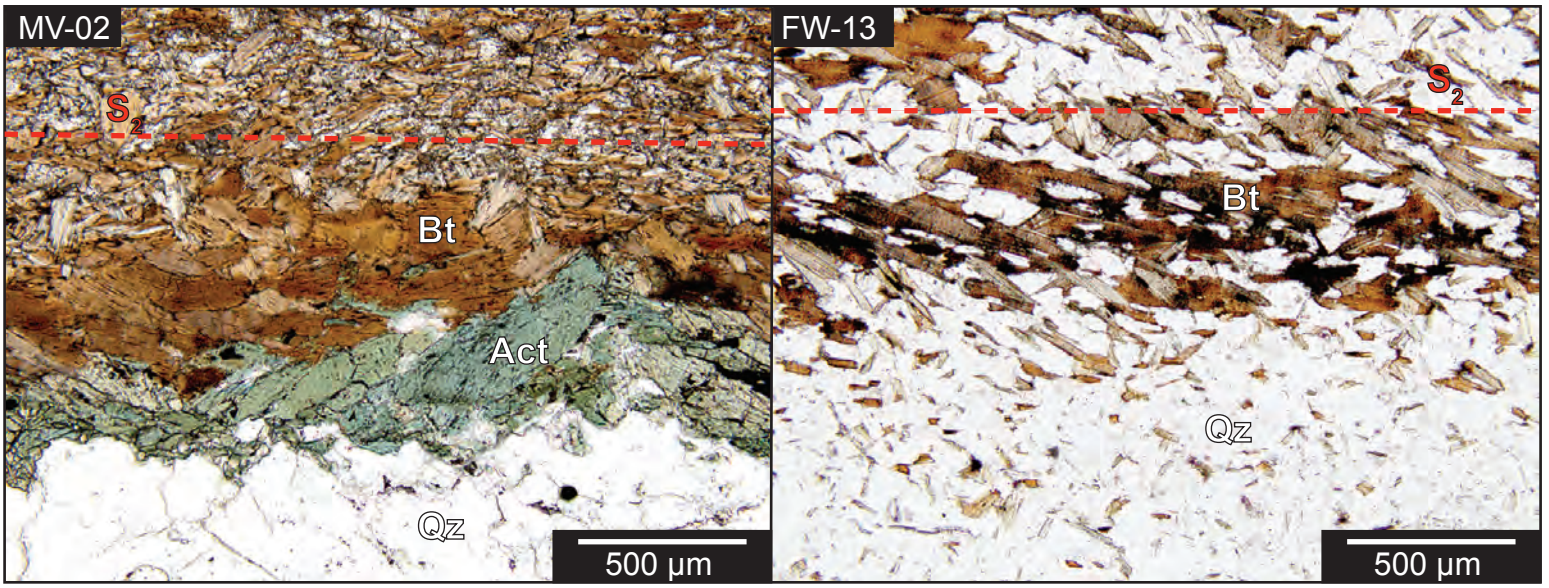

C. host rock biotite

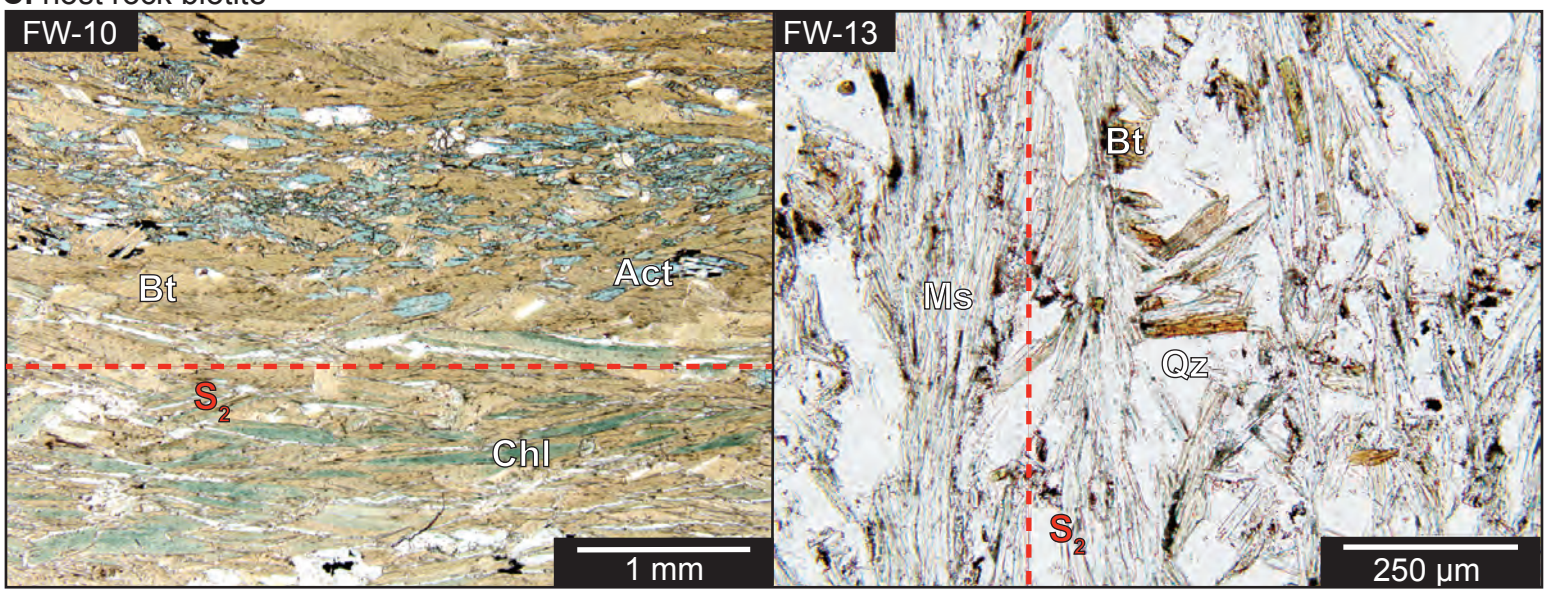

Figure 14. (previous page) Photomicrographs of the three biotite types of the Detour Lake deposit. **A.** Very coarse-grained and fine-grained subhedral-euhedral vein biotite in pre- to syn-D_2 veins from samples MV-02 and FW-13, overprinted by actinolite and chlorite. **B.** Medium-grained, euhedral halo biotite that are parallel to the pre- to syn-D_2 vein margins from samples MV-02 and FW-13. Biotite in MV-02 are overprinted by actinolite. **C.** Coarse-grained and very fine-grained euhedral host rock biotite from biotite schist samples FW-10 and FW-13, respectively. Biotite in FW-10 are overprinted by alternating bands of chlorite and actinolite, and biotite from sample FW-13 are overprinted by muscovite.

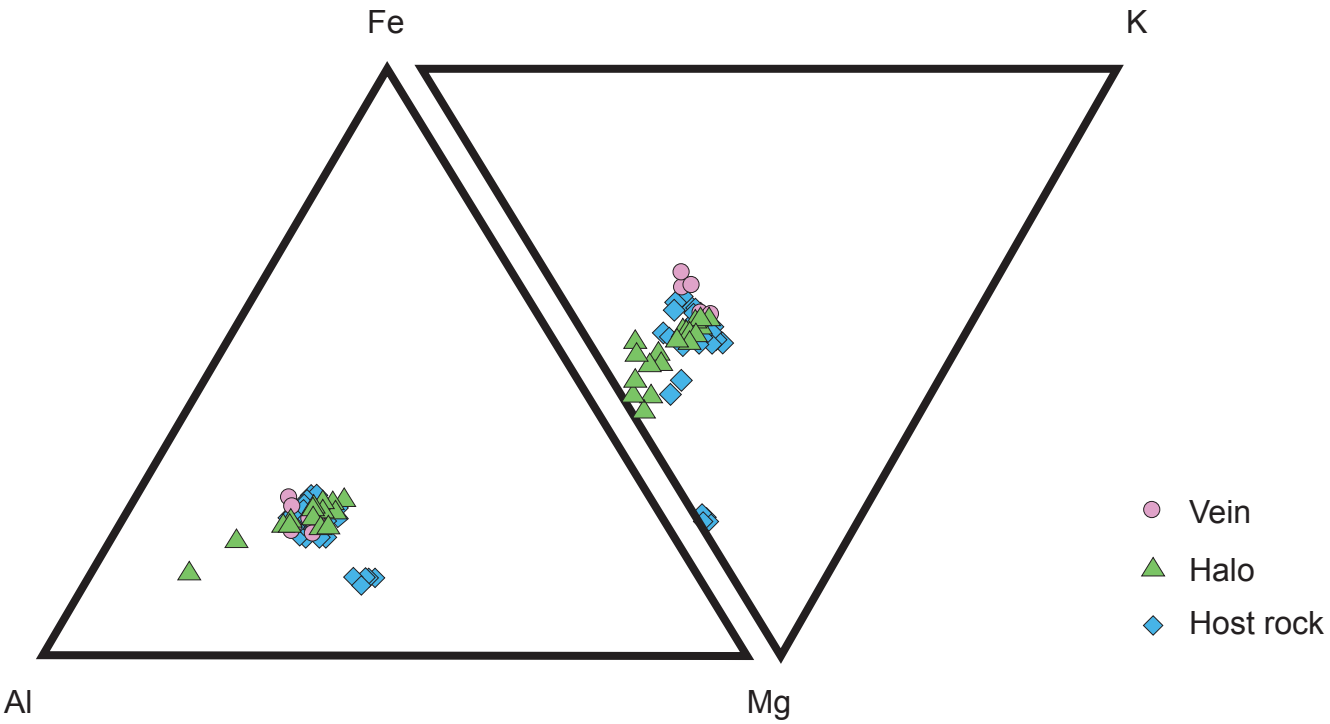

Figure 15. Fe-Mg-Al and Fe-Mg-K ternary diagrams of the vein, halo, and host rock types of biotite of the Detour Lake deposit. Note all three biotite types are geochemically similar. Biotite crystals from sample MV-13, a gabbroic intrusive unit, yield Fe-poor compositions that plot away from the main cluster of analyses.

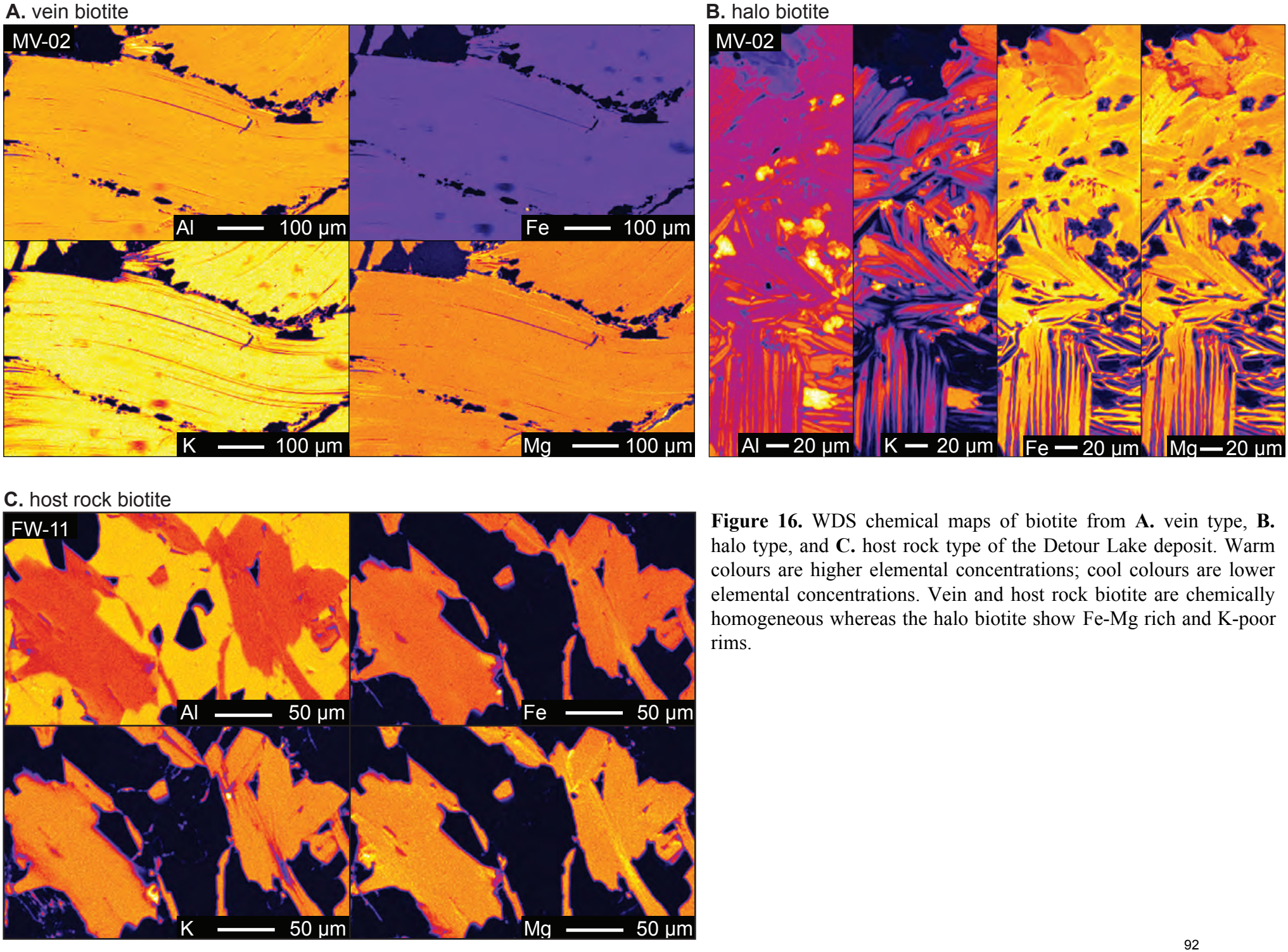

Figure 16. WDS chemical maps of biotite from **A.** vein type, **B.** halo type, and **C.** host rock type of the Detour Lake deposit. Warm colours are higher elemental concentrations; cool colours are lower elemental concentrations. Vein and host rock biotite are chemically homogeneous whereas the halo biotite show Fe-Mg rich and K-poor rims.

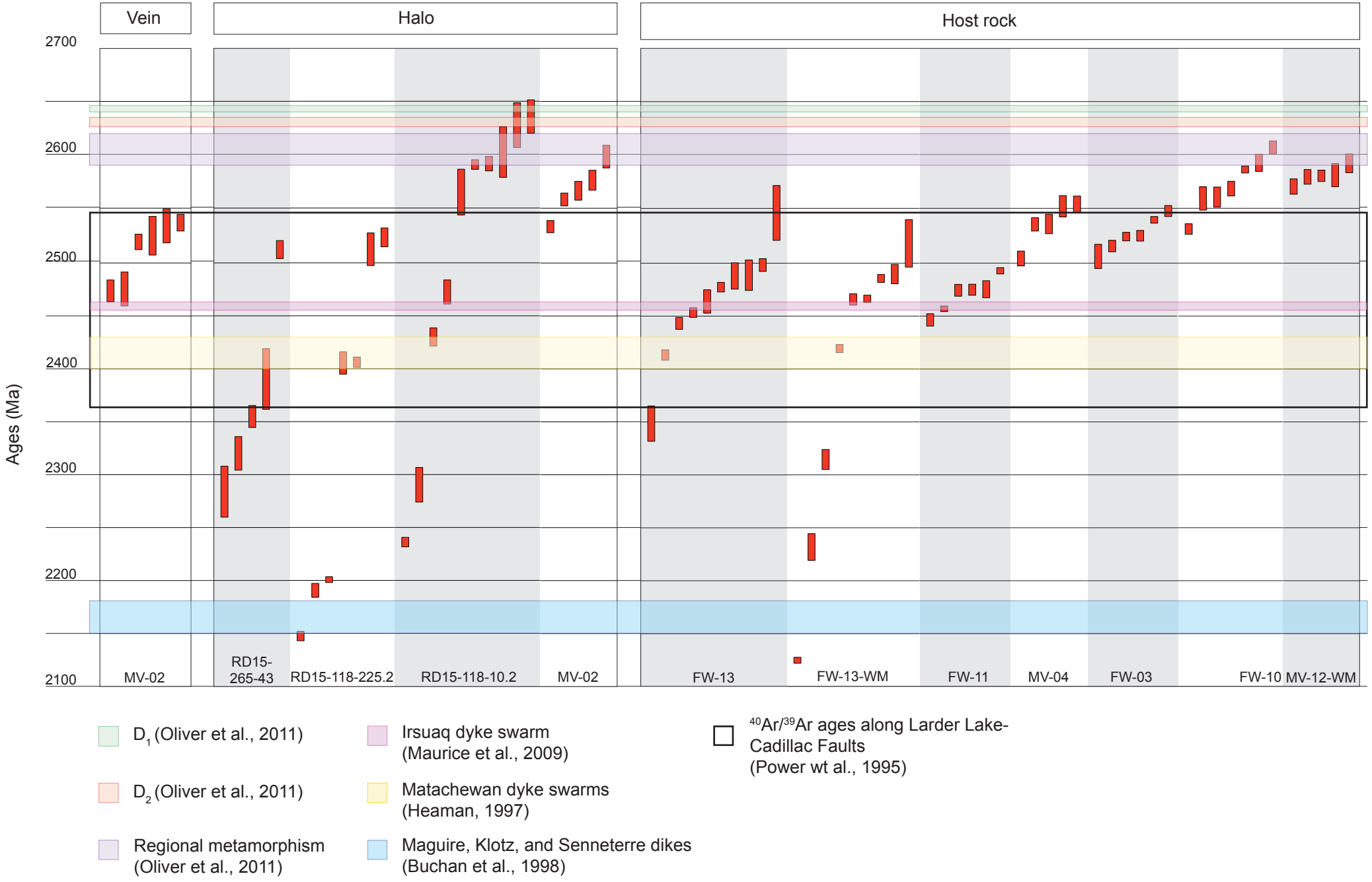

Figure 17. Diagram showing single crystal $^{40}Ar/^{39}Ar$ ages from biotite and muscovite from ten samples representing the three mica types. The height of each red bar represents the 2 sigma uncertainty of the apparent age. Note that all three biotite types yield similar ages significantly post-dating the timing of major deformation events, regional metamorphism and gold mineralization.

CHAPTER 4

Conclusions

EBSD and LA-ICP-MS data presented in Chapter 2 significantly improves our understanding of the role pyrite deformation plays in the formation of a giant ore body such as the Detour Lake gold deposit. Textural, microstructural, and geochemical observations reported in this study support a syn-metamorphic deformation-driven Au-upgrading model. This model suggests that plastic deformation microstructures (i.e., low-angle grain boundaries) develop in pyrite subjected to high strains during lower amphibolite facies metamorphism. Metamorphic fluids then introduce Au into the vein, which is remobilized and concentrating into the microstructures through high diffusivity pathways ("pipe").

Results from EMPA and $^{40}Ar/^{39}Ar$ analyses on biotite presented in Chapter 3 reveal only a single, indistinguishable chemical population of biotite at Detour Lake. The similar homogeneous geochemical compositions and the overlapping ages suggest that the vein, halo, and host rock biotite types may be from the same generation. These results do not successfully allow us discern between metamorphic and potentially Au-associated secondary biotite. The young biotite ages (2600–2400 Ma) post-date the regional metamorphism and deformation and the Au mineralization at Detour Lake, thus making it even more difficult to associate Au with biotite alteration. Consequently, biotite is not an effective indicator mineral for Au mineralization at the Detour Lake deposit.

The results from both projects could have a significant impact on developing exploration techniques for finding high metamorphic grade deposits similar to Detour Lake. Since Au can be trapped within deformation-induced microstructures in sulphides, conducting geomagnetic surveys in terranes that have been subjected to high strain and high metamorphic grade would most likely be an efficient way to discover a deposit. Now that we have a better understanding of

the microstructural setting of Au, we could maybe also develop more efficient techniques to extract the Au and maximize recovery.

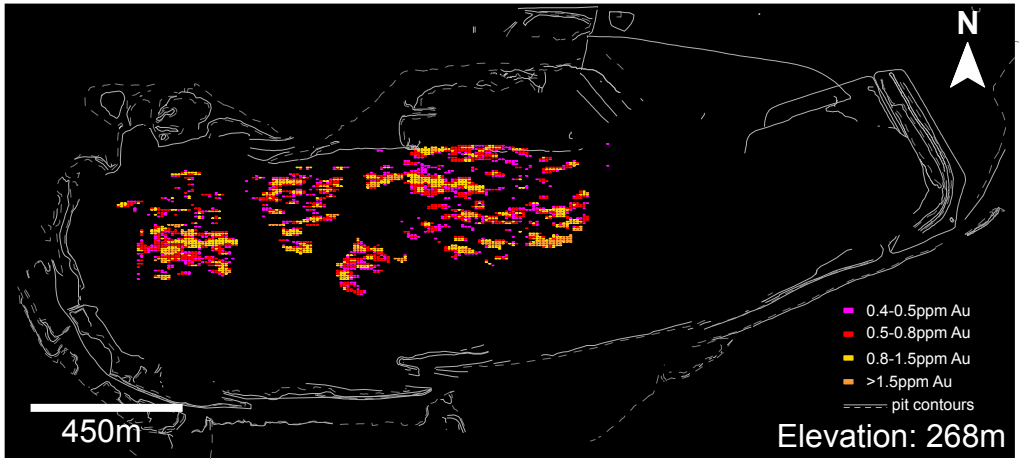
N
0.4-0.5ppm Au
0.5-0.8ppm Au
0.8-1.5ppm Au
>1.5ppm Au
pit contours
450m
Elevation: 268m

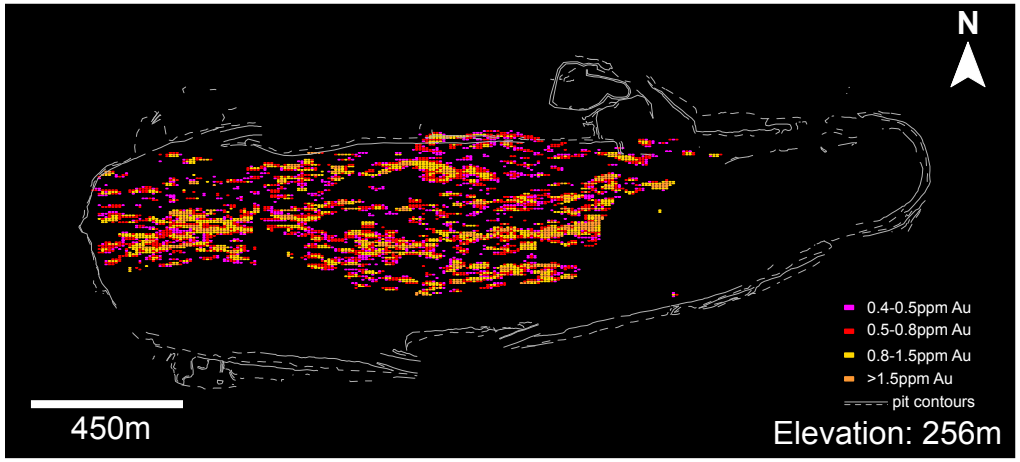
N
0.4-0.5ppm Au
0.5-0.8ppm Au
0.8-1.5ppm Au
>1.5ppm Au
pit contours
450m
Elevation: 256m

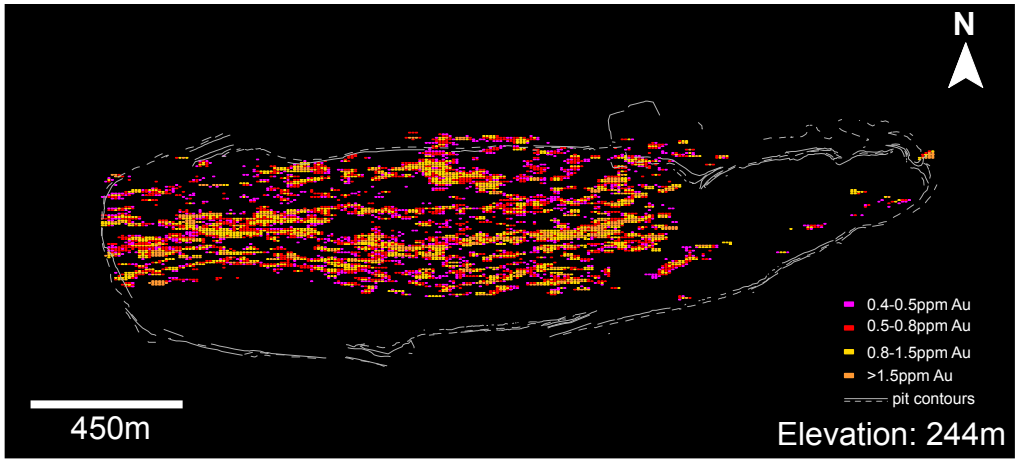
N
0.4-0.5ppm Au
0.5-0.8ppm Au
0.8-1.5ppm Au
>1.5ppm Au
pit contours
450m
Elevation: 244m

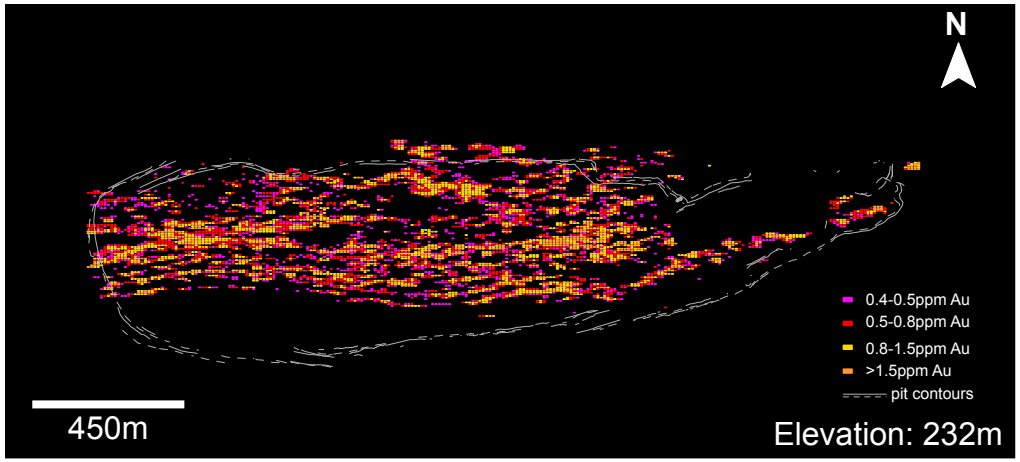
N
0.4-0.5ppm Au
0.5-0.8ppm Au
0.8-1.5ppm Au
>1.5ppm Au
pit contours
450m
Elevation: 232m

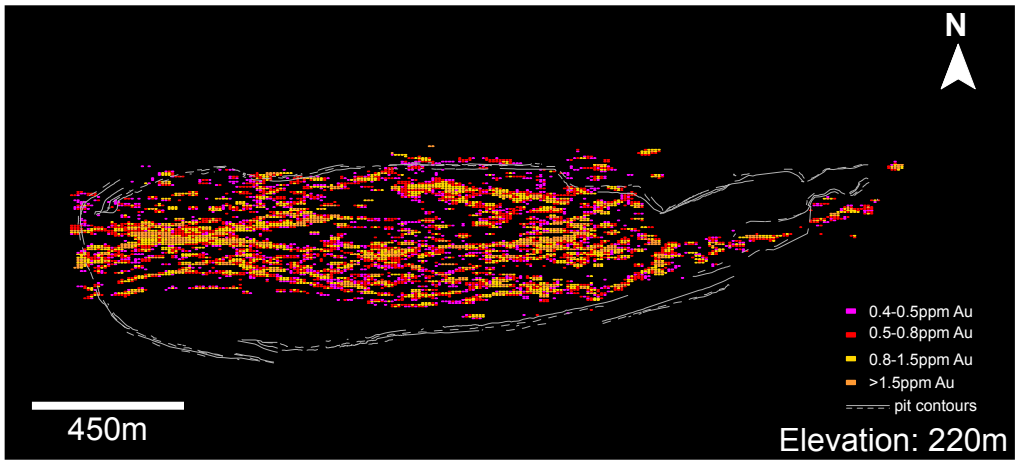
N
0.4-0.5ppm Au
0.5-0.8ppm Au
0.8-1.5ppm Au
>1.5ppm Au
pit contours
450m
Elevation: 220m

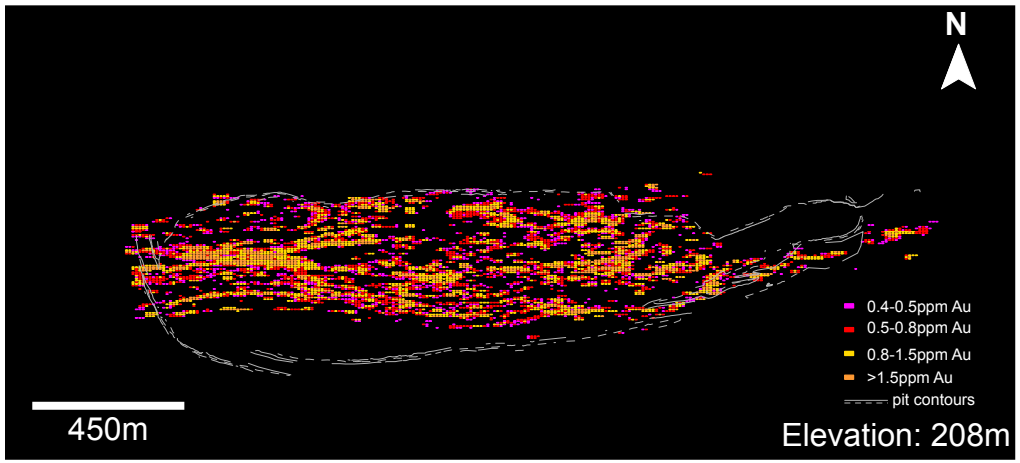
N
0.4-0.5ppm Au
0.5-0.8ppm Au
0.8-1.5ppm Au
>1.5ppm Au
pit contours
450m
Elevation: 208m

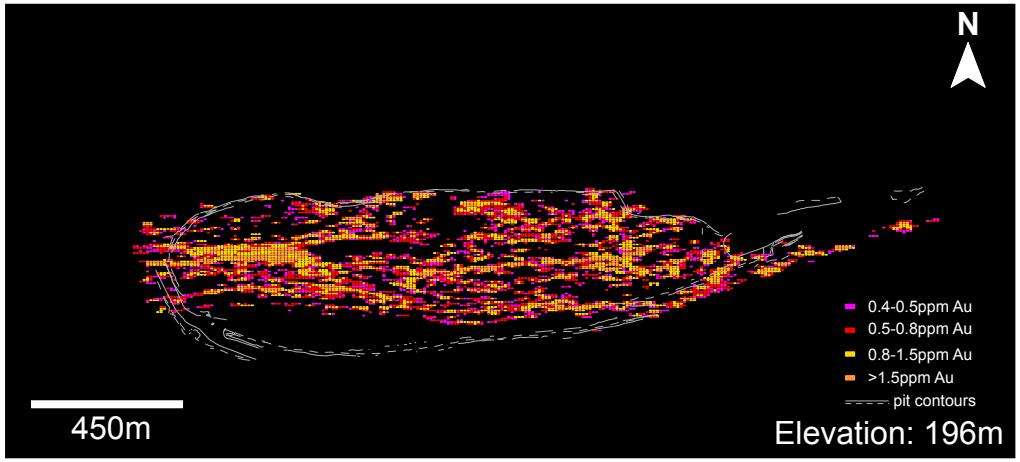
N
0.4-0.5ppm Au
0.5-0.8ppm Au
0.8-1.5ppm Au
>1.5ppm Au
pit contours
450m
Elevation: 196m

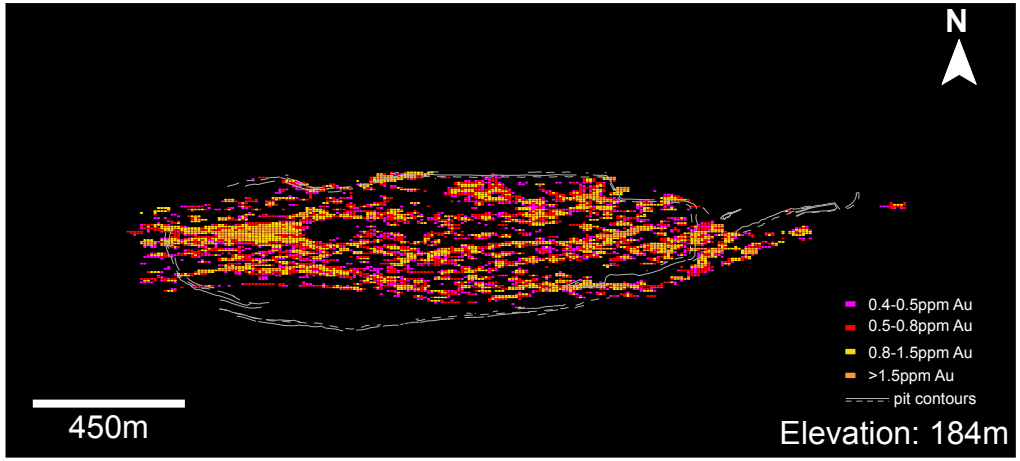
N
0.4-0.5ppm Au
0.5-0.8ppm Au
0.8-1.5ppm Au
>1.5ppm Au
pit contours
450m
Elevation: 184m

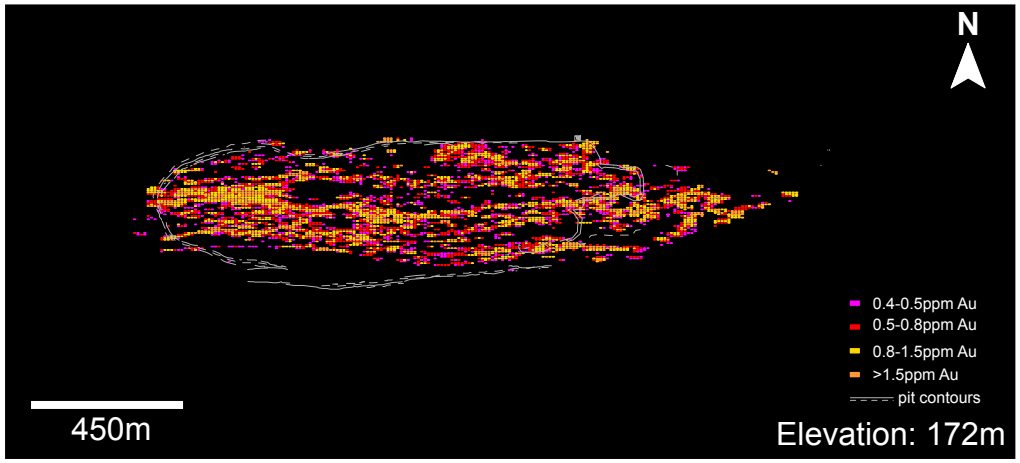
N
0.4-0.5ppm Au
0.5-0.8ppm Au
0.8-1.5ppm Au
>1.5ppm Au
pit contours
450m
Elevation: 172m

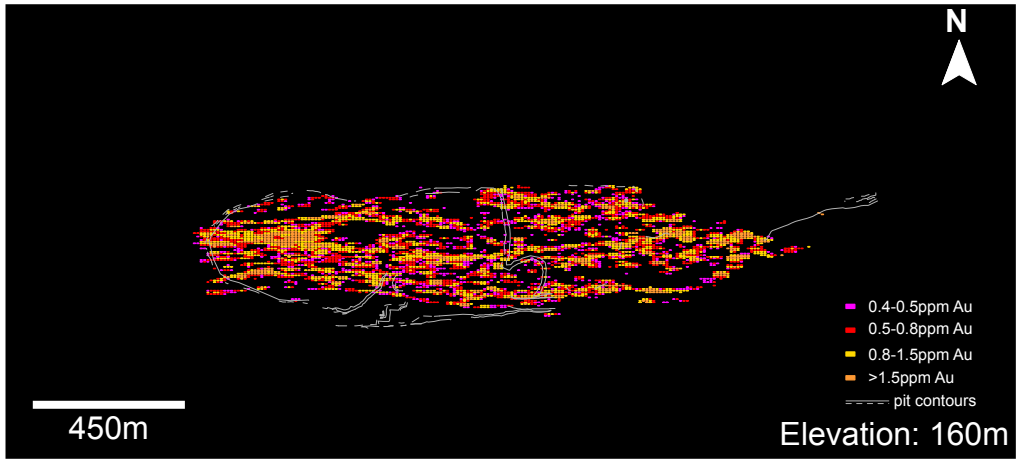
N
0.4-0.5ppm Au
0.5-0.8ppm Au
0.8-1.5ppm Au
>1.5ppm Au
pit contours
450m
Elevation: 160m

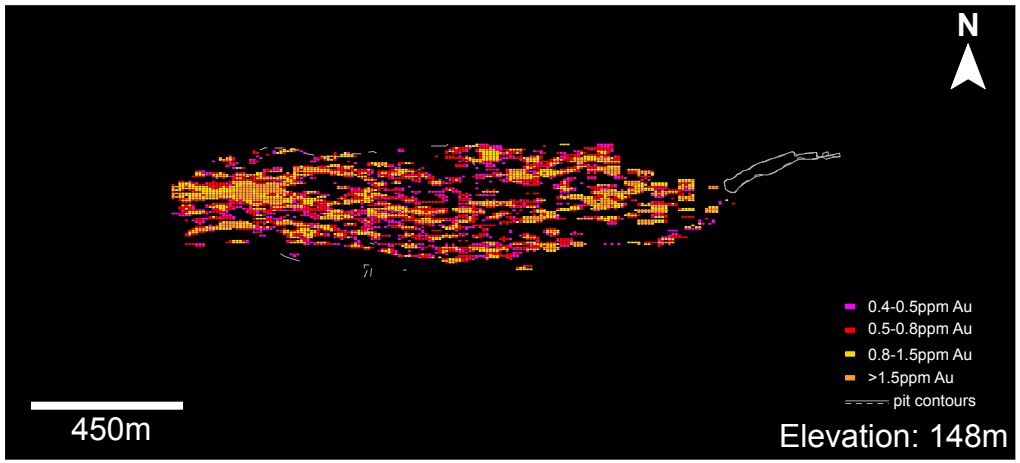
N
0.4-0.5ppm Au
0.5-0.8ppm Au
0.8-1.5ppm Au
>1.5ppm Au
pit contours
450m
Elevation: 148m

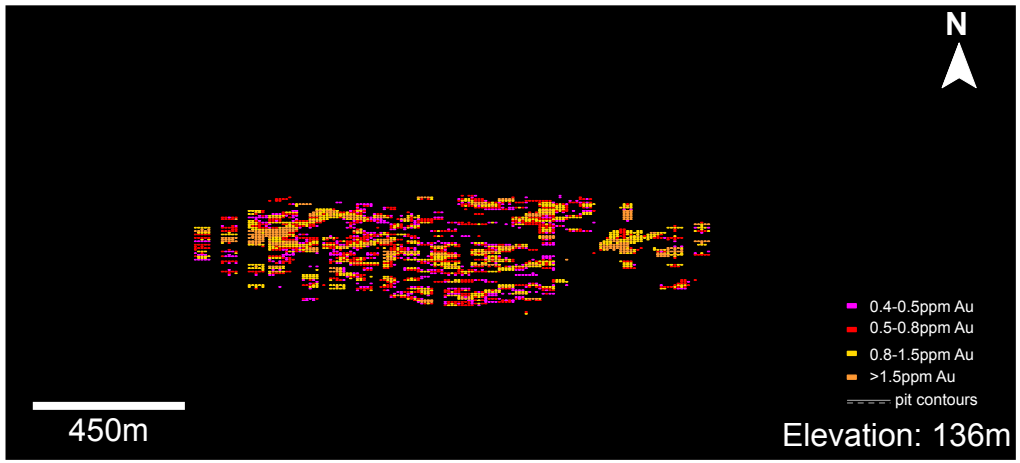
N
0.4-0.5ppm Au
0.5-0.8ppm Au
0.8-1.5ppm Au
>1.5ppm Au
pit contours
450m
Elevation: 136m

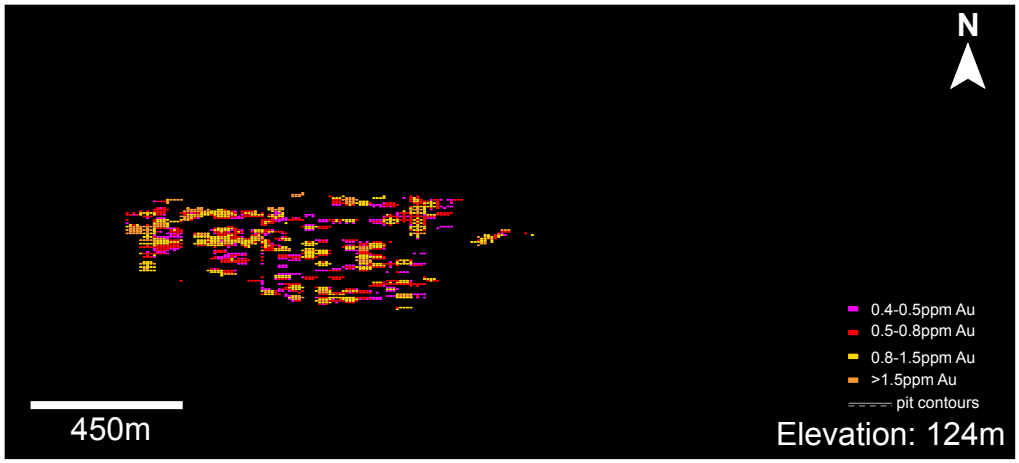

Figure DR1. (pages 98–99) Lateral sections of a Au block model of the Detour Lake deposit at different elevations designed from mine assay data showing east-west trending Au mineralization. Dashed line is the outline of the modern open pit.

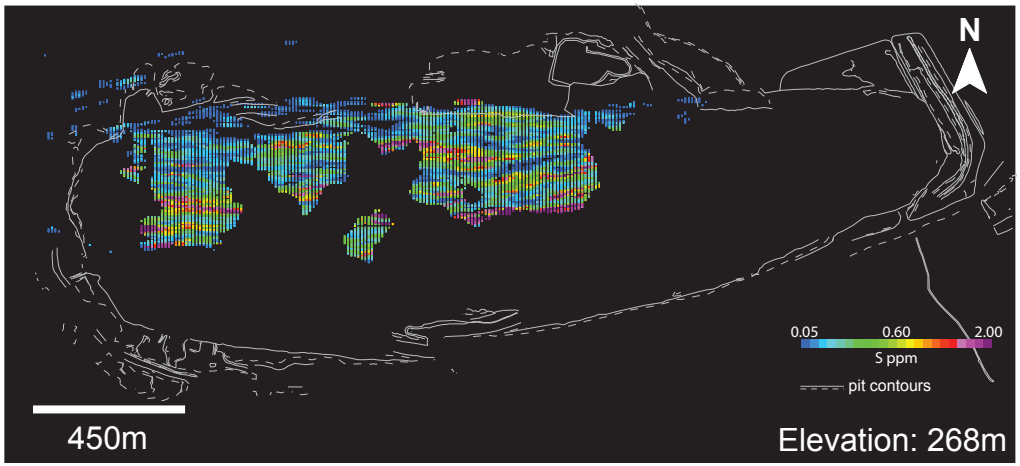
N
0.05
0.60
2.00
S ppm
pit contours
450m
Elevation: 268m

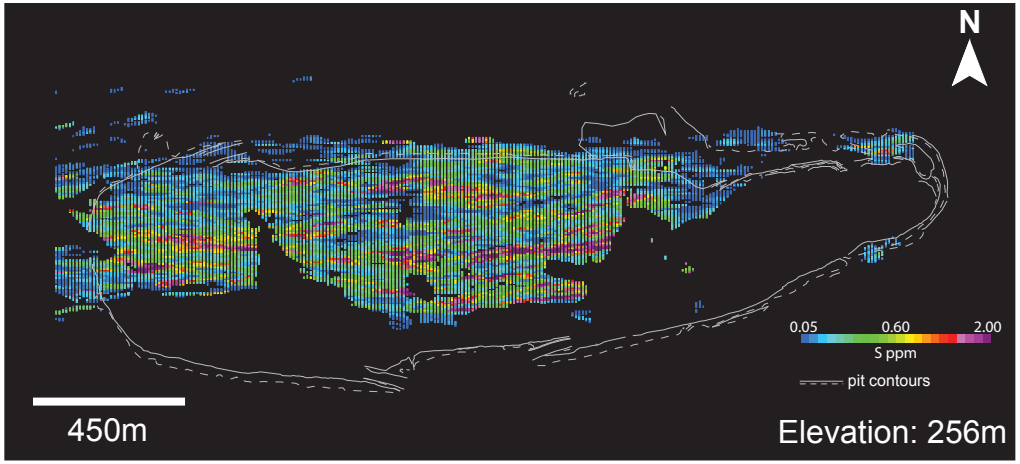
N
0.05
0.60
2.00
S ppm
pit contours
450m
Elevation: 256m

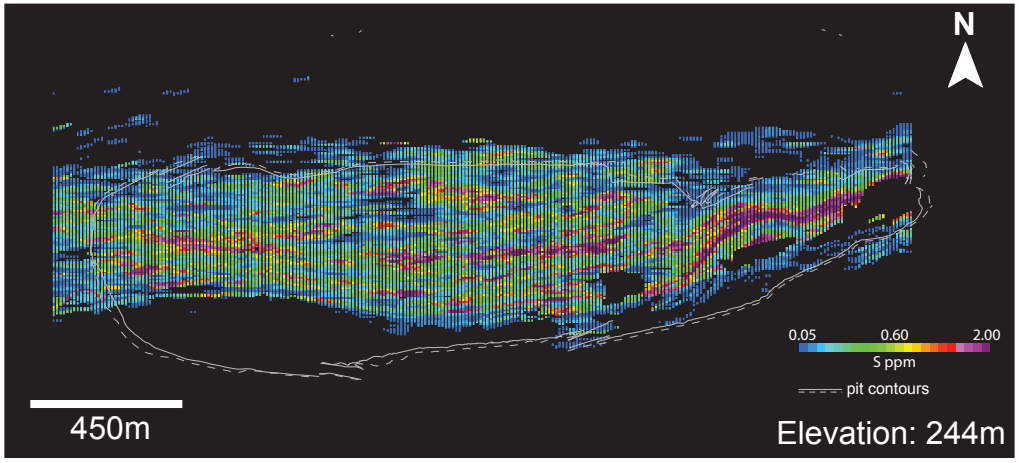
N
0.05
0.60
2.00
S ppm
pit contours
450m
Elevation: 244m

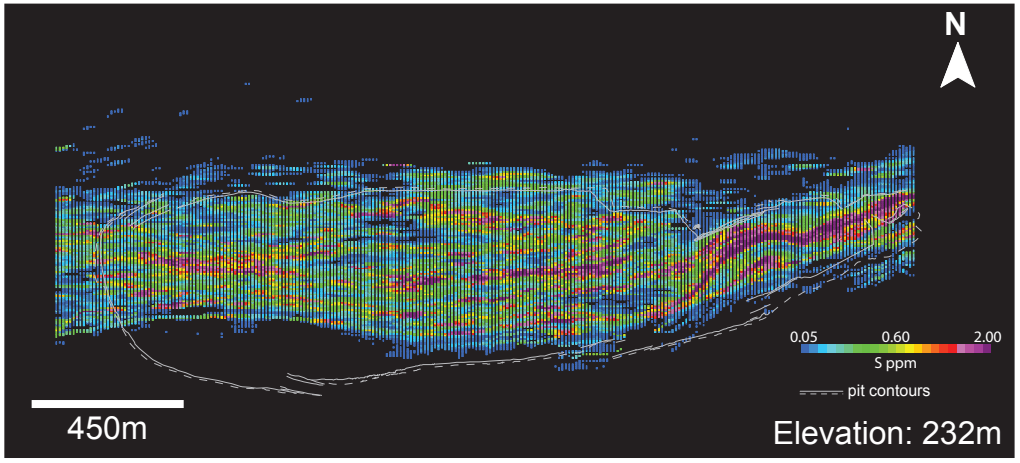
N
0.05
0.60
2.00
S ppm
pit contours
450m
Elevation: 232m

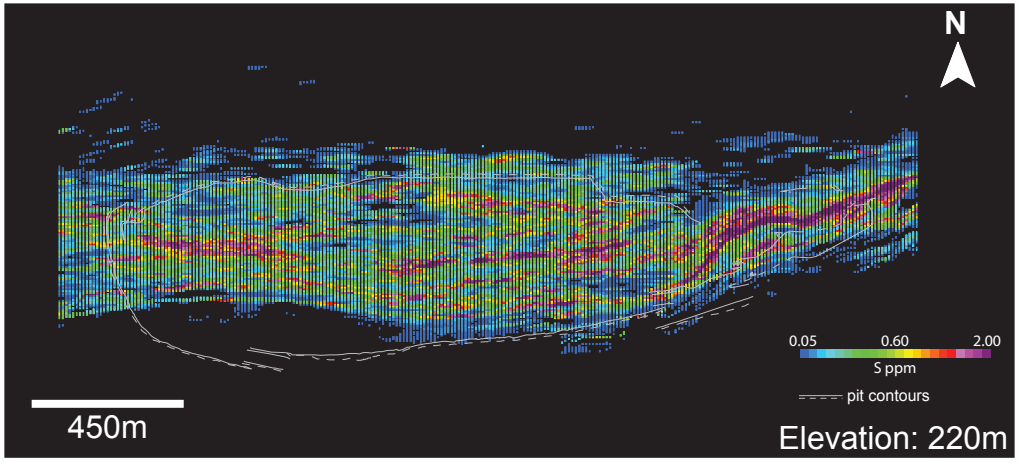
N
0.05
0.60
2.00
S ppm
pit contours
450m
Elevation: 220m

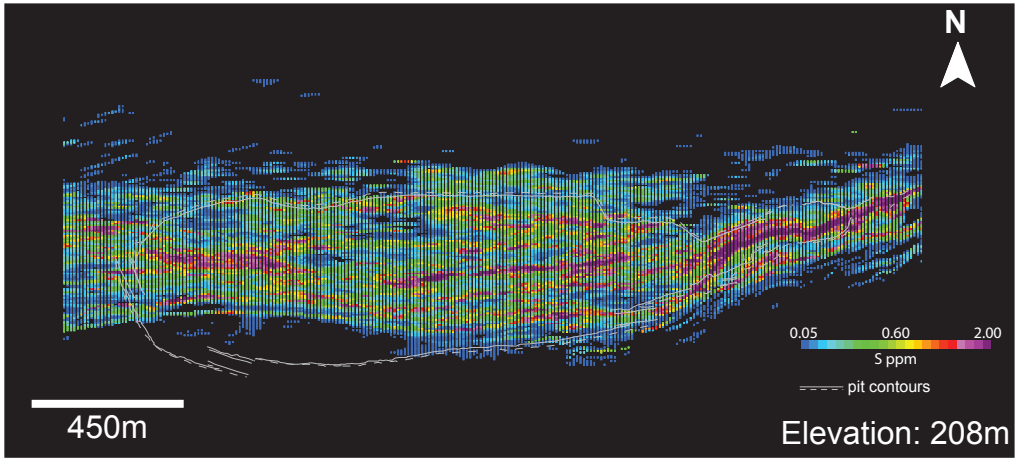
N
0.05
0.60
2.00
S ppm
pit contours
450m
Elevation: 208m

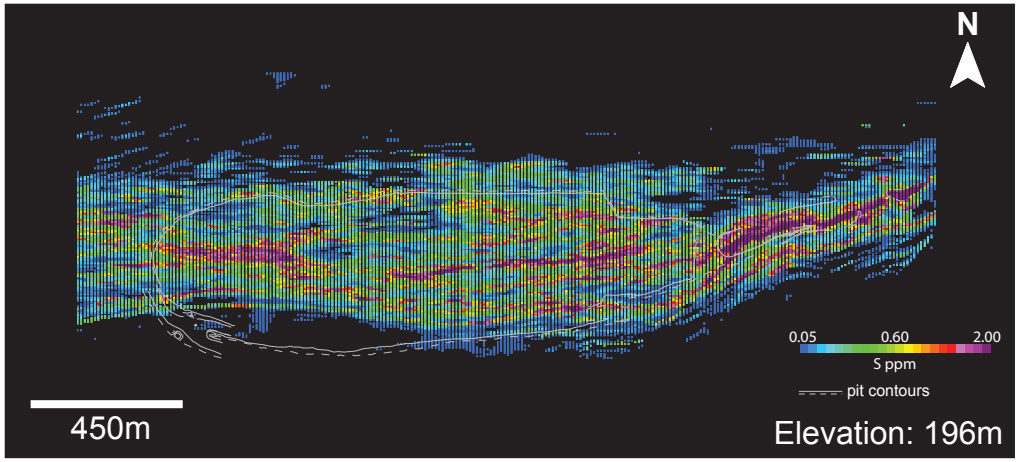
N
0.05
0.60
2.00
S ppm
pit contours
450m
Elevation: 196m

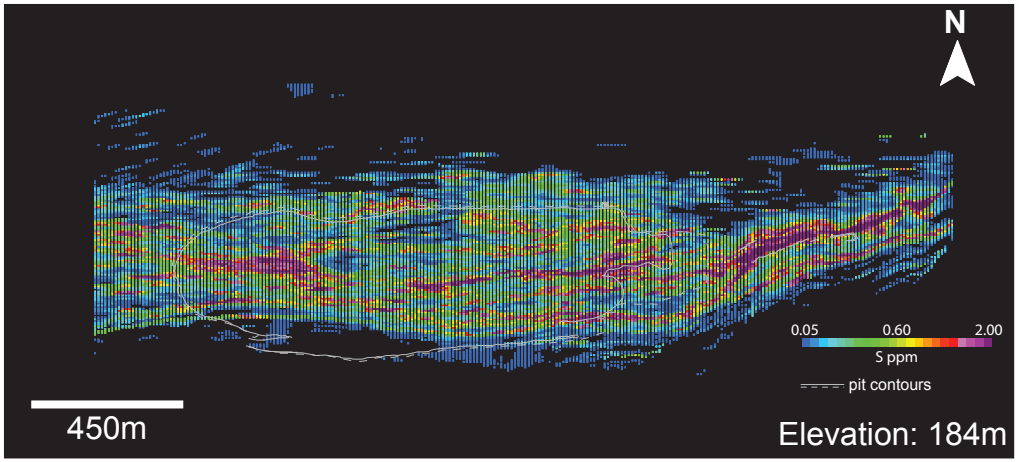
N
0.05
0.60
2.00
S ppm
pit contours
450m
Elevation: 184m

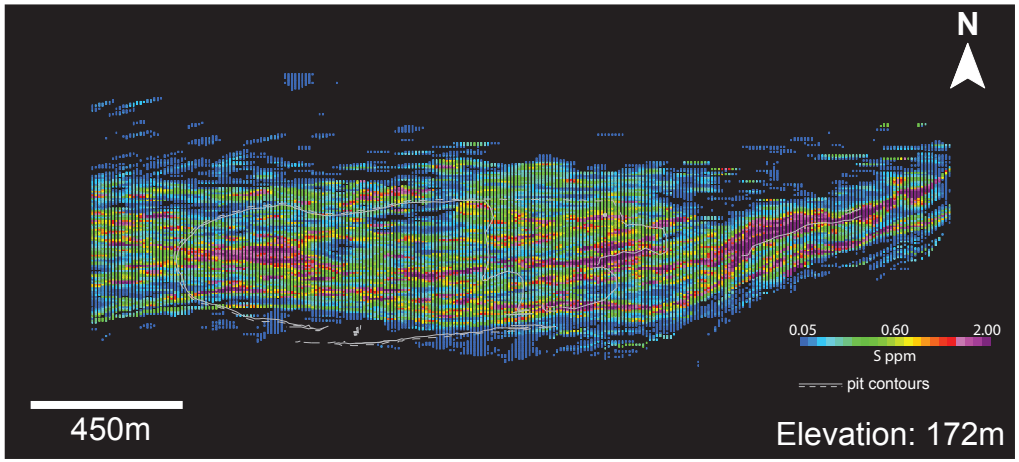
N
0.05
0.60
2.00
S ppm
pit contours
450m
Elevation: 172m

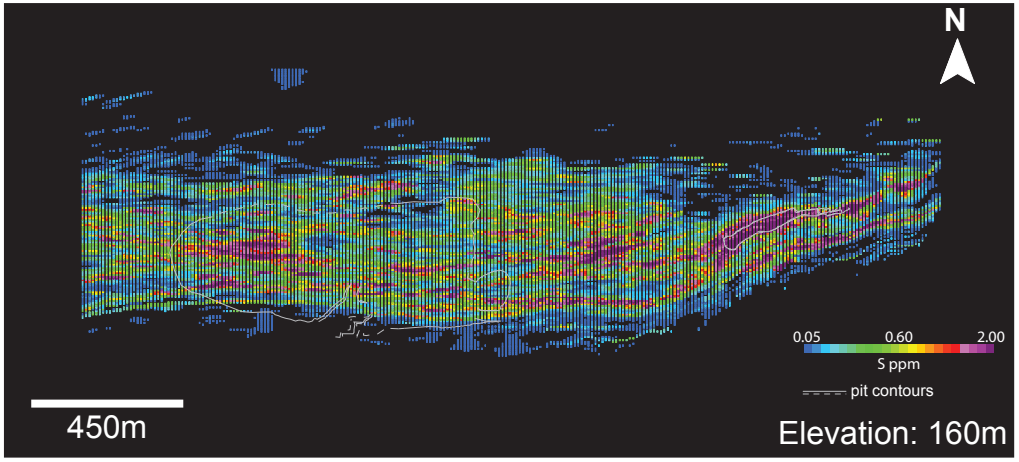
N
0.05
0.60
2.00
S ppm
pit contours
450m
Elevation: 160m

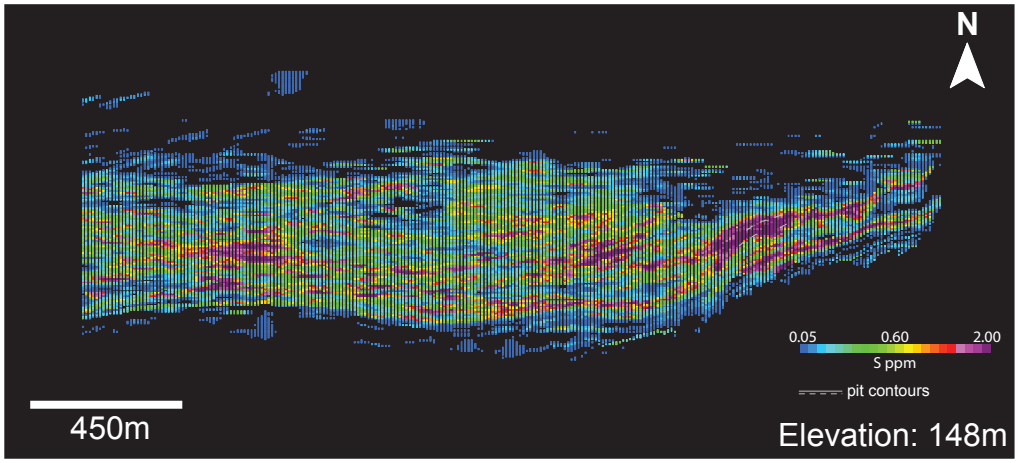
N
0.05
0.60
2.00
S ppm
pit contours
450m
Elevation: 148m

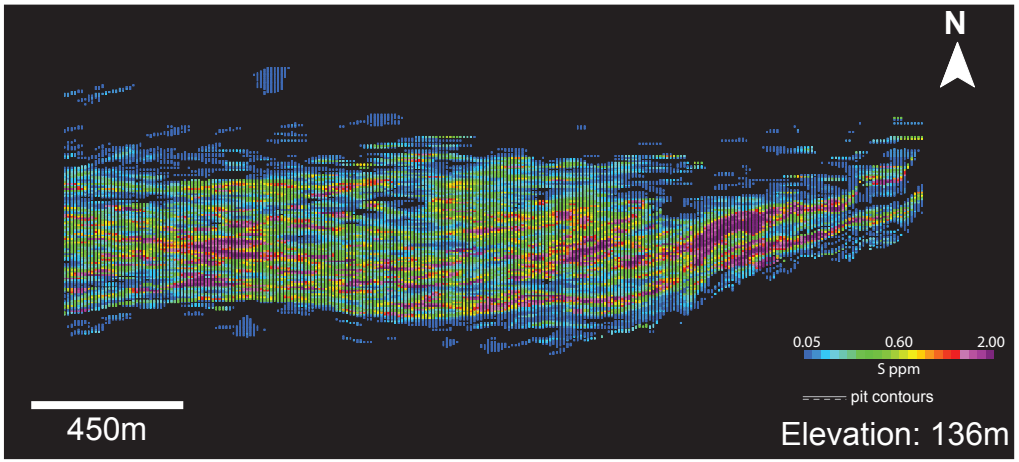
N
0.05
0.60
2.00
S ppm
pit contours
450m
Elevation: 136m

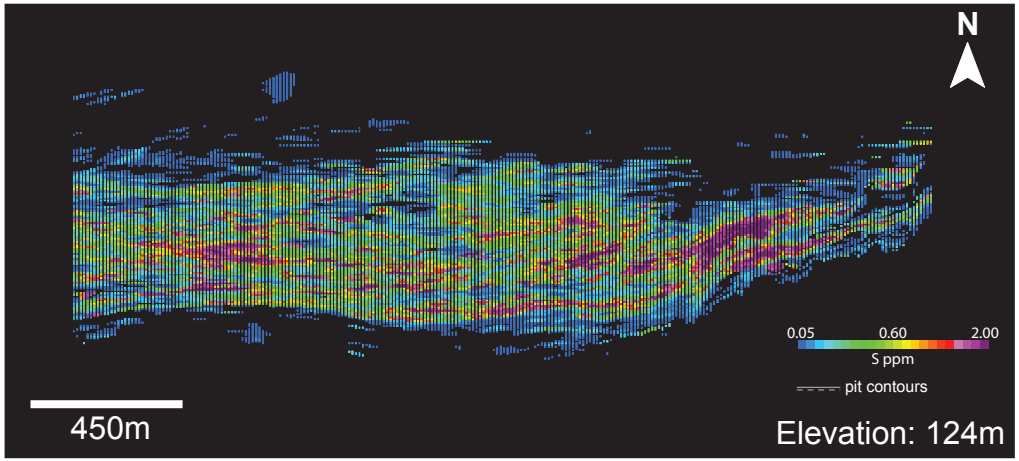

Figure DR2. (pages 100–102) Lateral sections of a S block model from the Detour Lake deposit at different elevations designed from mine assay data show east-west trending sulphide mineralization. Note the co-spatial relationship with Au mineralization shown in Fig. DR1. Dashed line is the outline of the modern open pit.

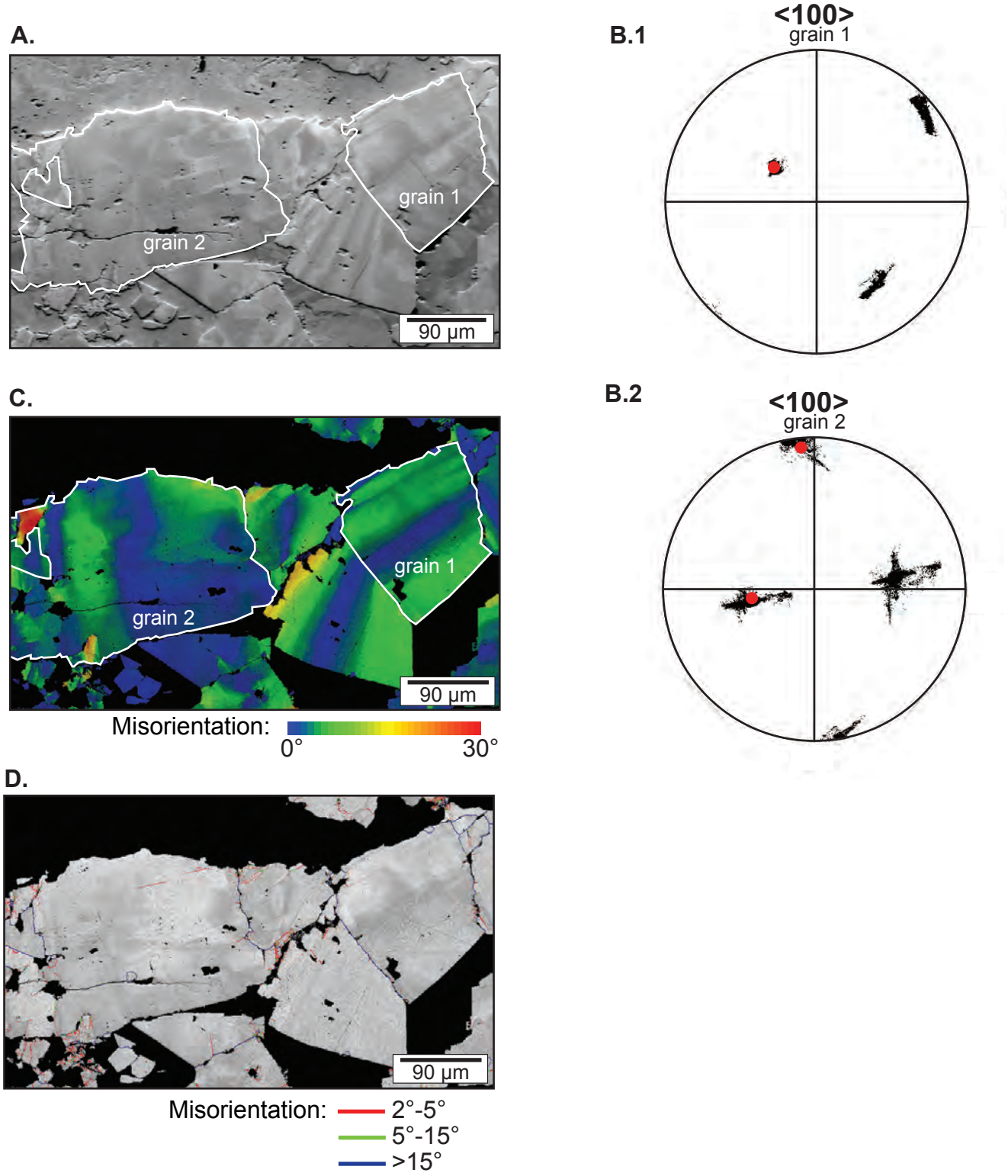

Figure DR3. EBSD results from high stress regions at type-2a pyrite grain contacts from a mafic volcanic sample (MV-19). **A.** Orientation contrast image of pyrite grains showing evidence of low strain intracrystalline plastic deformation through linear gray-scale variations in grain 1 and higher strain plastic deformation through a checkerboard pattern in grain 2. **B.1.** Pole figure representing the <100> axes of grain 1 showing rotation about at least one axis marked by the red circle (lower hemisphere, equal angle projection). **B.2.** Pole figure representing the <100> axes of grain 2 showing rotation about at least one axis marked by the red circles (lower hemisphere, equal angle projection). **C.** Orientation deviation angle map of pyrite grains revealing a linear misorientation pattern in grain 1 and a checkerboard misorientation pattern in grain 2 with a maximum misorientation angle of 30°. **D.** Grain boundary map of pyrite grains showing minor low-angle grain boundary development at high-stress regions between grain contacts.

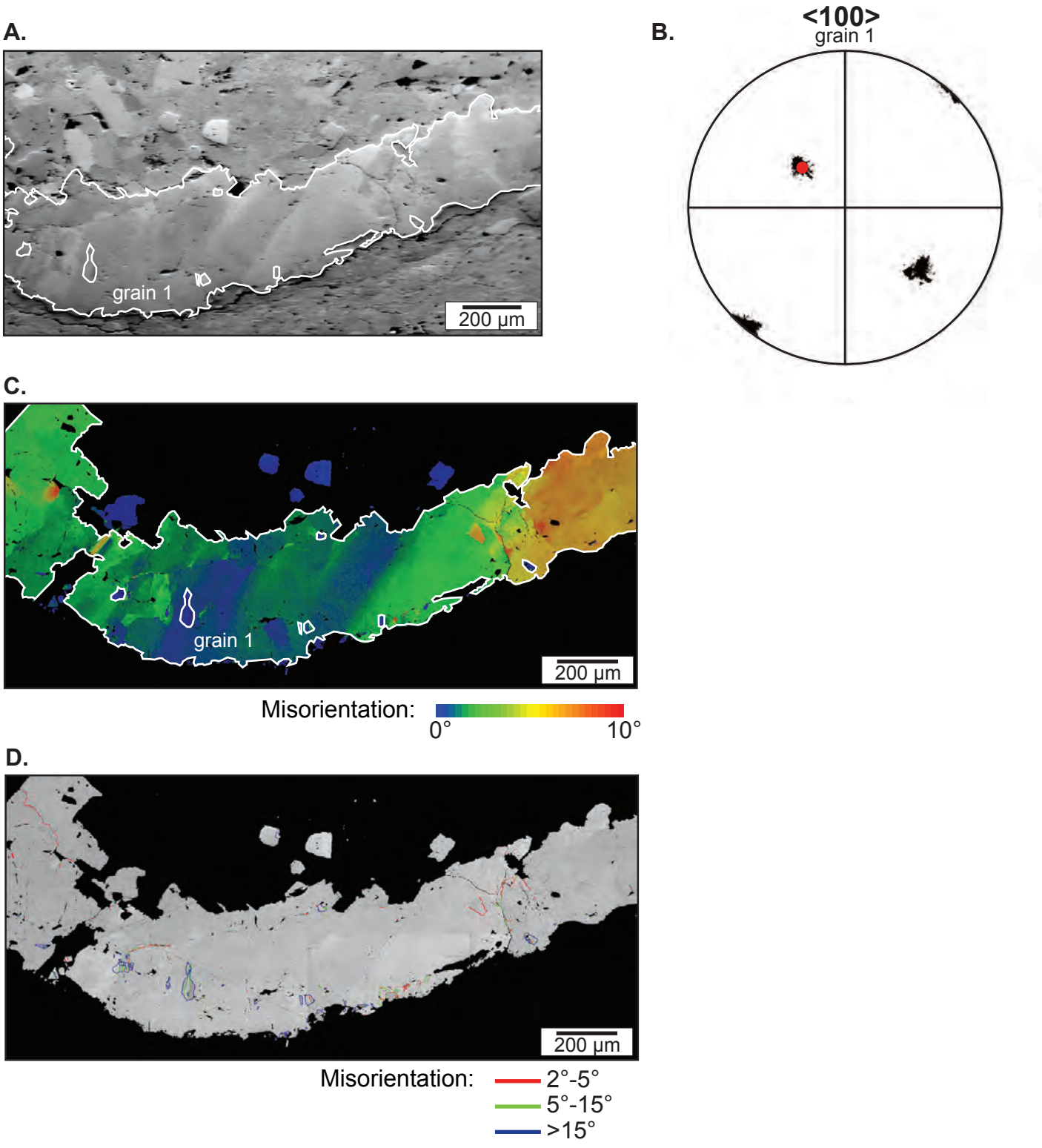

Figure DR4. EBSD results from folded elongated type-2a pyrite grain within a syn-D2 vein (V5) from a mafic volcanic sample (MV-19). **A.** Orientation contrast image of pyrite grain showing evidence of low strain intracrystalline plastic deformation through linear gray-scale variations. **B.** Pole figure representing the <100> axes of grain 1 showing rotation about at least one axis marked by the red circle (lower hemisphere, equal angle projection). **C.** Orientation deviation angle map of pyrite grain revealing a linear misorientation pattern with a maximum misorientation angle of 10°. **D.** Grain boundary map of pyrite grain showing minor low-angle grain boundary development and recrystallization.

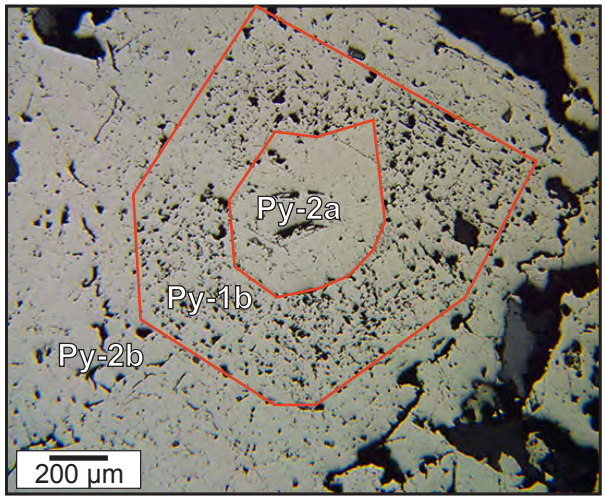
Py-2a
Py-1b
Py-2b
200 µm

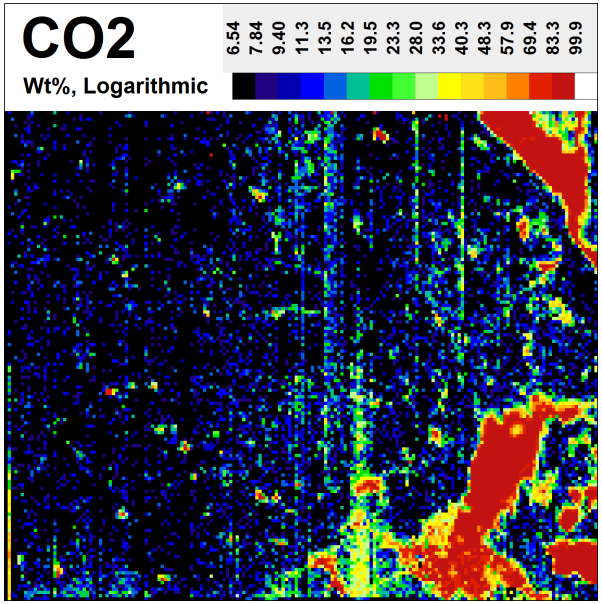
CO2
Wt%, Logarithmic
6.54 7.84 9.40 11.3 13.5 16.2 19.5 23.3 28.0 33.6 40.3 48.3 57.9 69.4 83.3 99.9

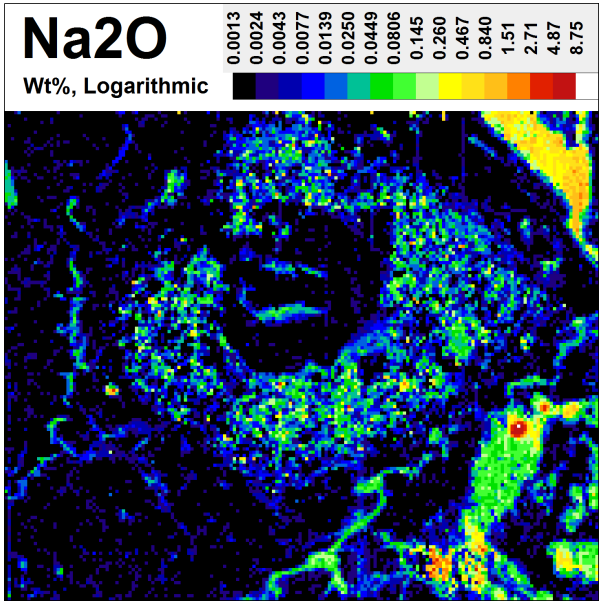
Na2O
Wt%, Logarithmic
0.0013 0.0024 0.0043 0.0077 0.0139 0.0250 0.0449 0.0806 0.145 0.260 0.467 0.840 1.51 2.71 4.87 8.75

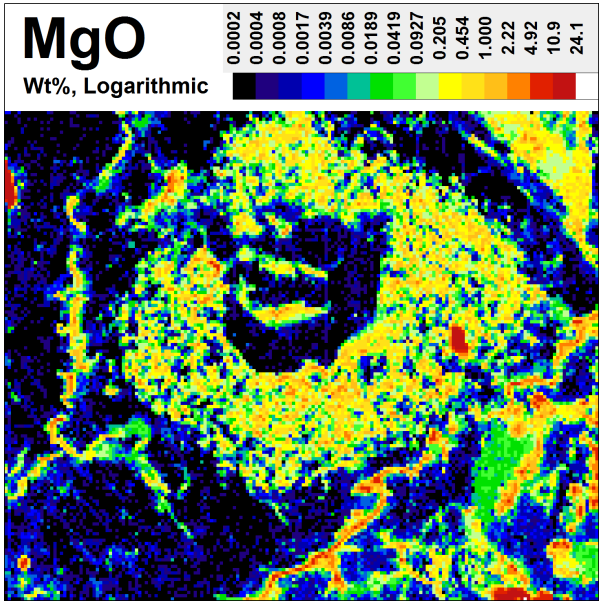
MgO
Wt%, Logarithmic
0.0002 0.0004 0.0008 0.0017 0.0039 0.0086 0.0189 0.0419 0.0927 0.205 0.454 1.000 2.22 4.92 10.9 24.1

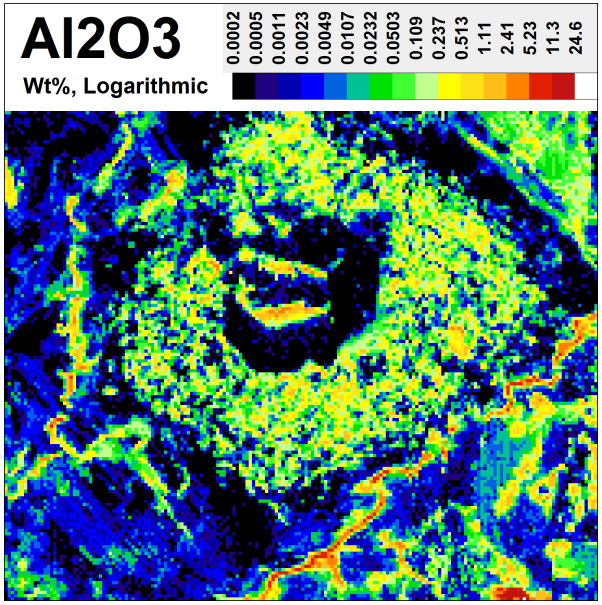
Al2O3
Wt%, Logarithmic
0.0002 0.0005 0.0011 0.0023 0.0049 0.0107 0.0232 0.0503 0.109 0.237 0.513 1.11 2.41 5.23 11.3 24.6

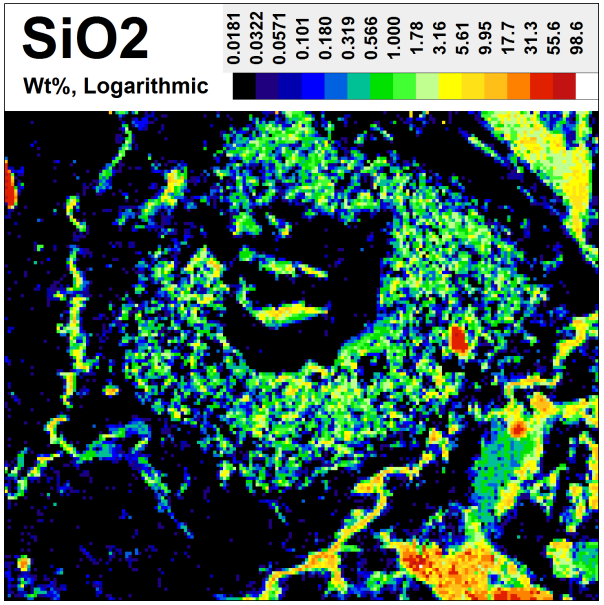
SiO2
Wt%, Logarithmic
0.0181 0.0322 0.0571 0.101 0.180 0.319 0.566 1.000 1.78 3.16 5.61 9.95 17.7 31.3 55.6 98.6

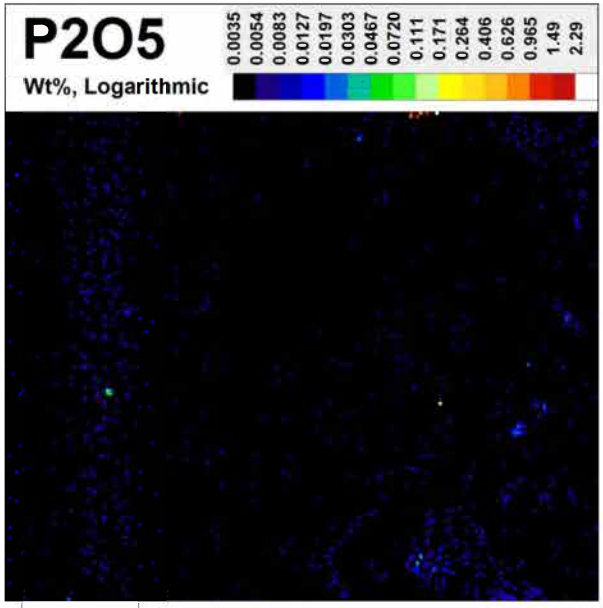
P2O5
Wt%, Logarithmic
0.0035 0.0054 0.0083 0.0127 0.0197 0.0303 0.0467 0.0720 0.111 0.171 0.264 0.406 0.626 0.965 1.49 2.29

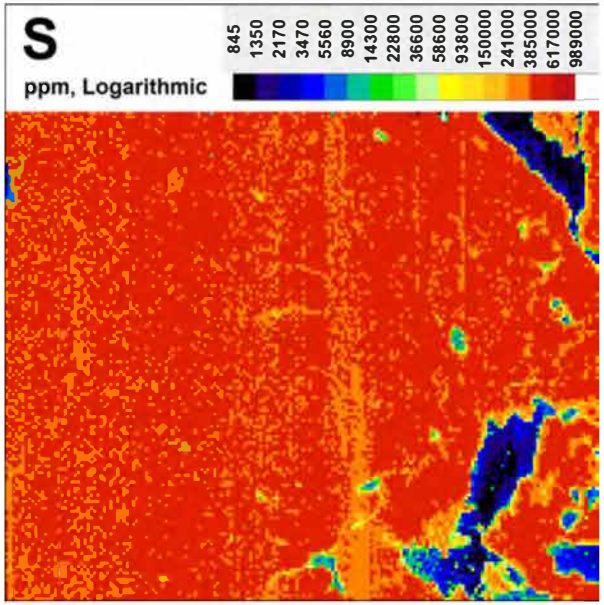
S
ppm, Logarithmic
845 1350 2170 3470 5560 8900 14300 22800 36600 58600 93800 150000 241000 385000 617000 989000

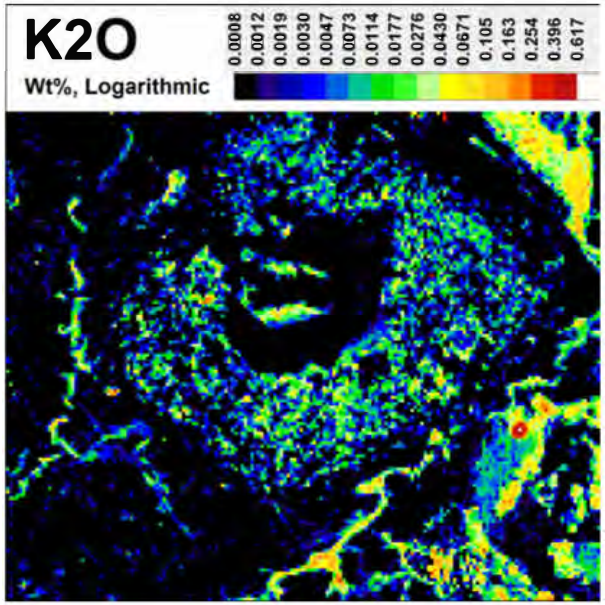
K2O
Wt%, Logarithmic
0.0008 0.0012 0.0019 0.0030 0.0047 0.0073 0.0114 0.0177 0.0276 0.0430 0.0671 0.105 0.163 0.254 0.396 0.617

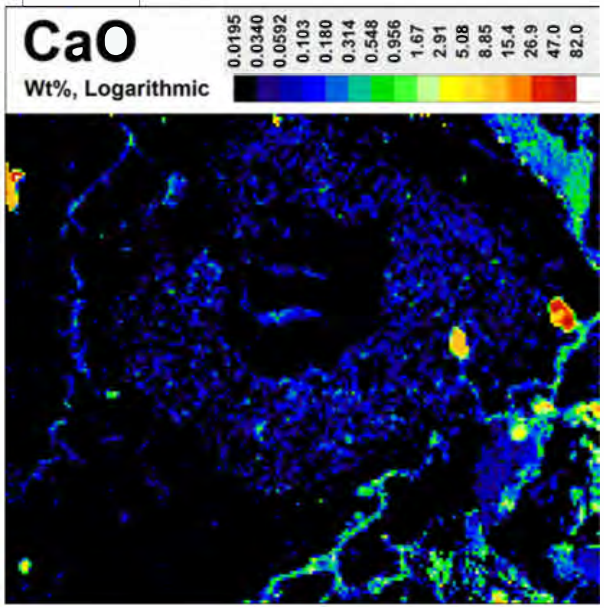
CaO
Wt%, Logarithmic
0.0195 0.0340 0.0592 0.103 0.180 0.314 0.548 0.956 1.67 2.91 5.08 8.85 15.4 26.9 47.0 82.0

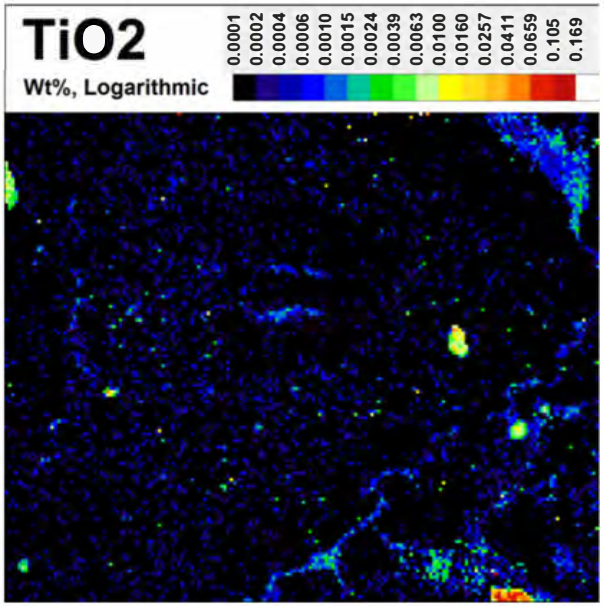
TiO2
Wt%, Logarithmic
0.0001 0.0002 0.0004 0.0006 0.0010 0.0015 0.0024 0.0039 0.0063 0.0100 0.0160 0.0257 0.0411 0.0659 0.105 0.169

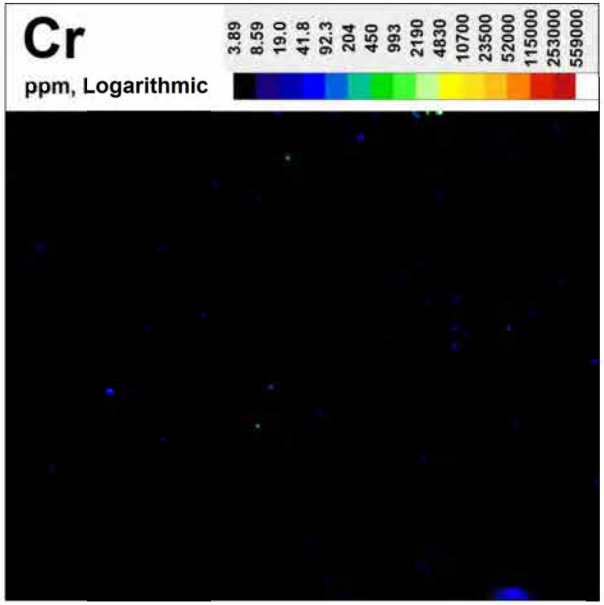
Cr
ppm, Logarithmic
3.89
8.59
19.0
41.8
92.3
204
450
993
2190
4830
10700
23500
52000
115000
253000
559000

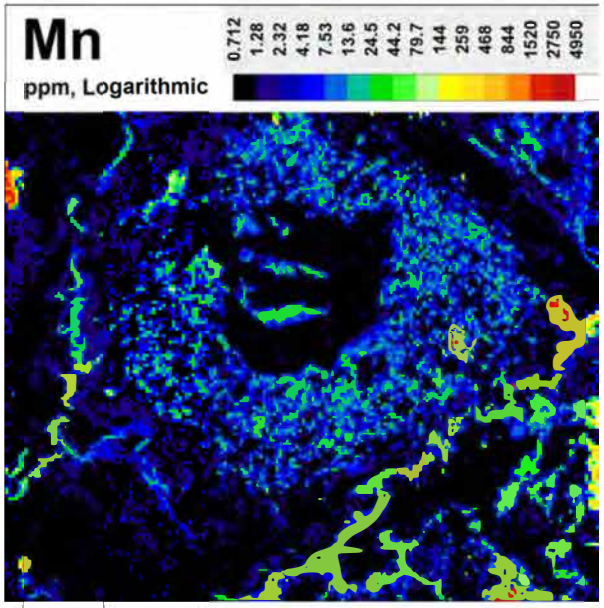
Mn
ppm, Logarithmic
0.712
1.28
2.32
4.18
7.53
13.6
24.5
44.2
79.7
144
259
468
844
1520
2750
4950

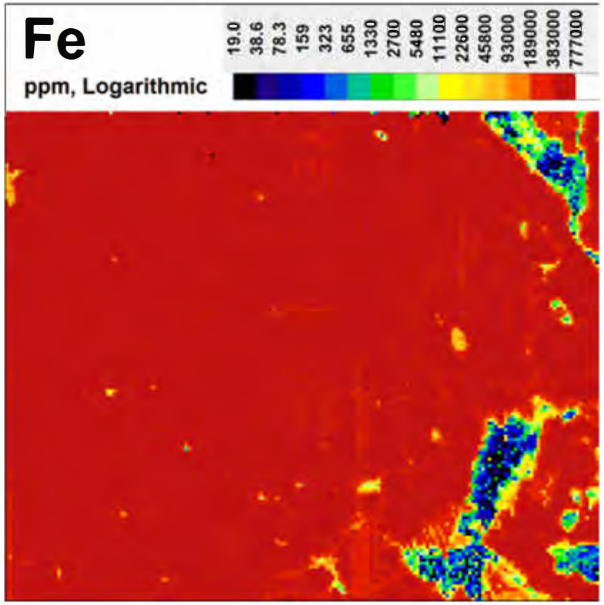
Fe
ppm, Logarithmic
19.0
38.6
78.3
159
323
655
1330
2700
5480
11100
22600
45800
93000
189000
383000
777000

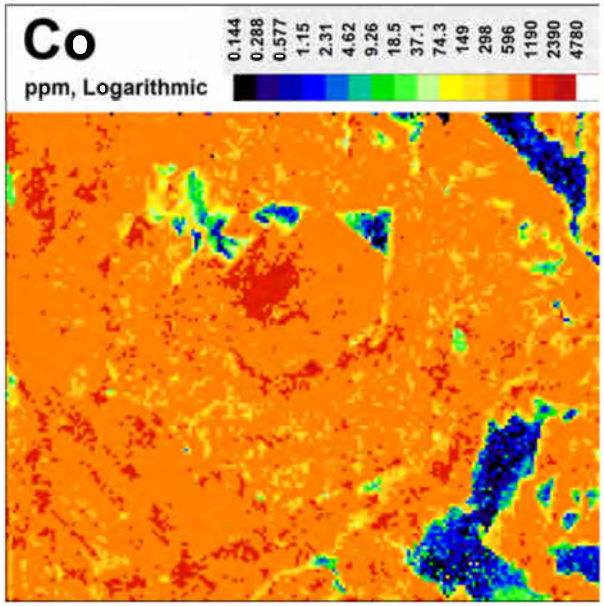
Co
ppm, Logarithmic
0.144
0.288
0.577
1.15
2.31
4.62
9.26
18.5
37.1
74.3
149
298
596
1190
2390
4780

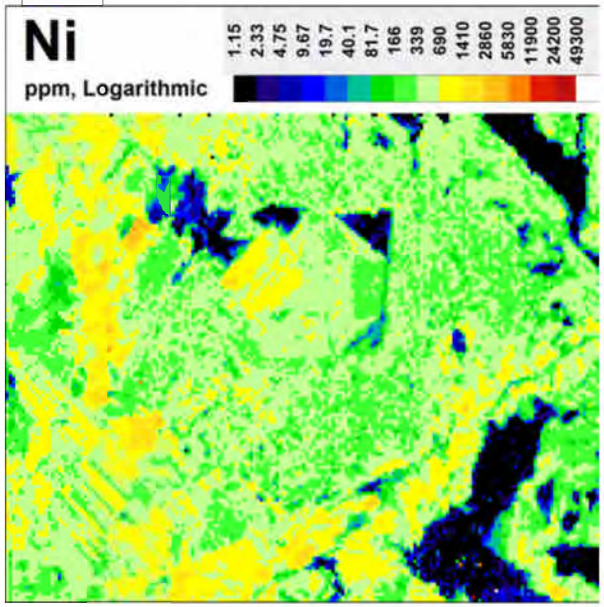
Ni
ppm, Logarithmic
1.15
2.33
4.75
9.67
19.7
40.1
81.7
166
339
690
1410
2860
5830
11900
24200
49300

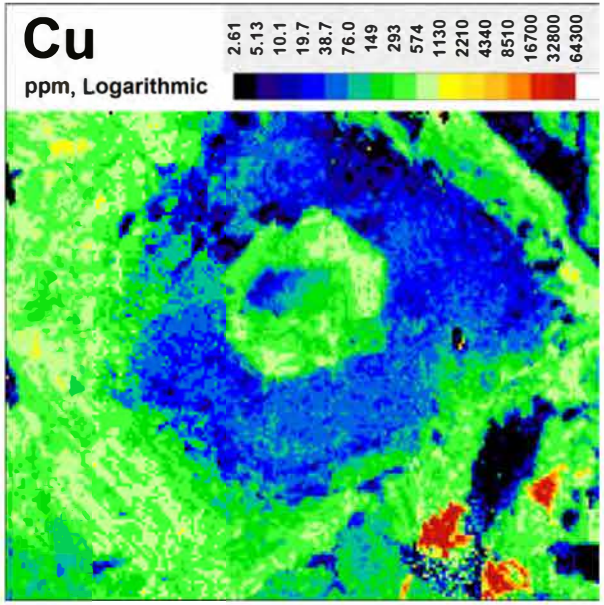
Cu
ppm, Logarithmic
2.61 5.13 10.1 19.7 38.7 76.0 149 293 574 1130 2210 4340 8510 16700 32800 64300

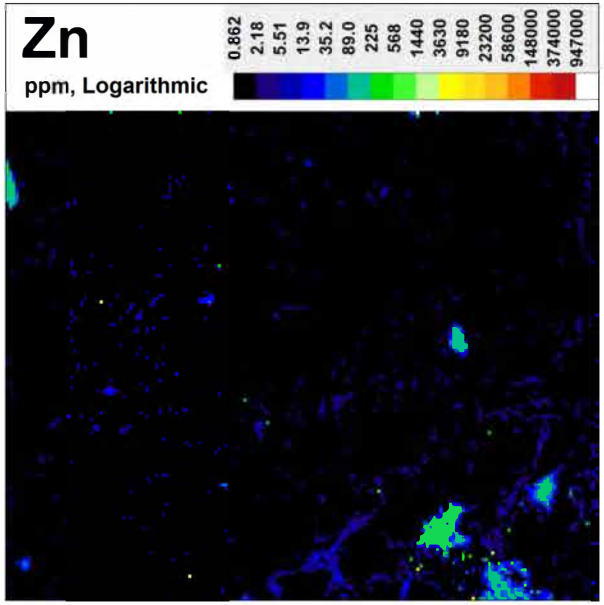
Zn
ppm, Logarithmic
0.862 2.18 5.51 13.9 35.2 89.0 225 568 1440 3630 9180 23200 58600 148000 374000 947000

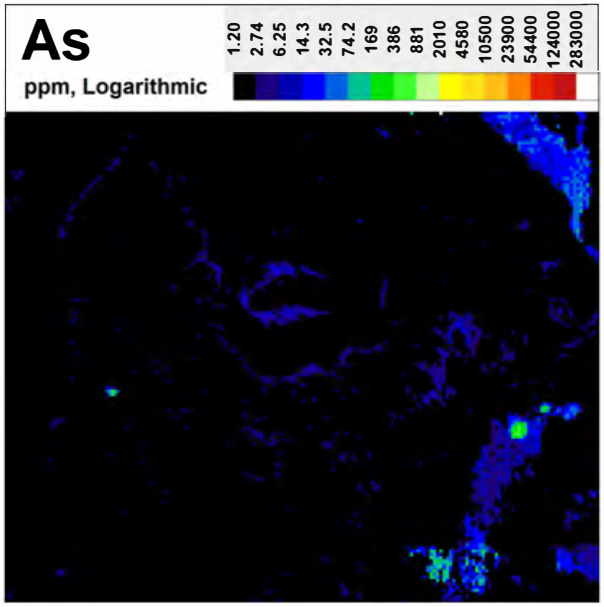
As
ppm, Logarithmic
1.20 2.74 6.25 14.3 32.5 74.2 169 386 881 2010 4580 10500 23900 54400 124000 283000

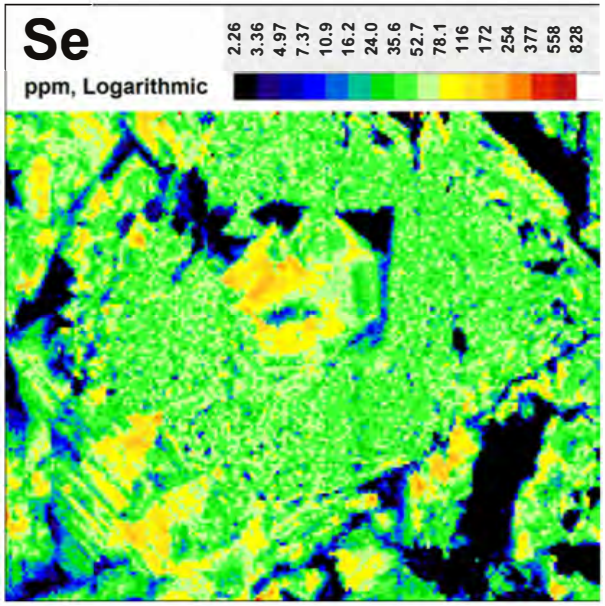
Se
ppm, Logarithmic
2.26 3.36 4.97 7.37 10.9 16.2 24.0 35.6 52.7 78.1 116 172 254 377 558 828

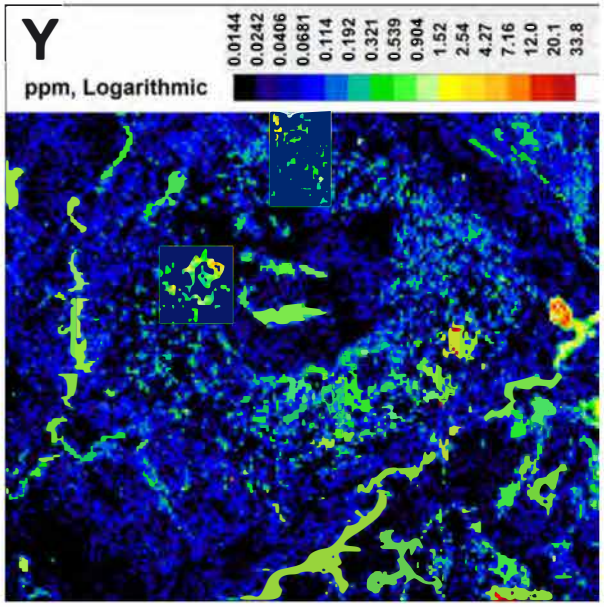
Y
ppm, Logarithmic
0.0144 0.0242 0.0406 0.0681 0.114 0.192 0.321 0.539 0.904 1.52 2.54 4.27 7.16 12.0 20.1 33.8

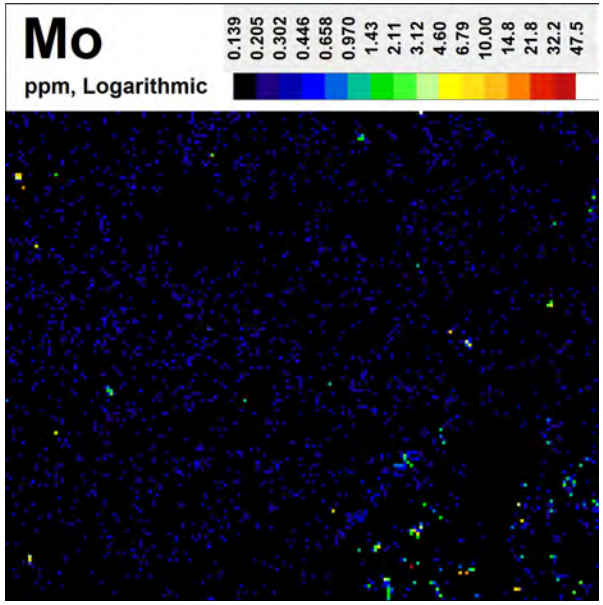
Mo
ppm, Logarithmic
0.139 0.205 0.302 0.446 0.658 0.970 1.43 2.11 3.12 4.60 6.79 10.00 14.8 21.8 32.2 47.5

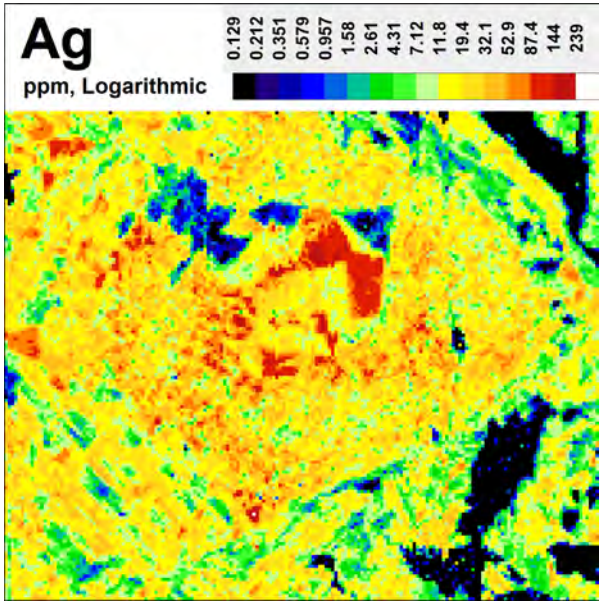
Ag
ppm, Logarithmic
0.129 0.212 0.351 0.579 0.957 1.58 2.61 4.31 7.12 11.8 19.4 32.1 52.9 87.4 144 239

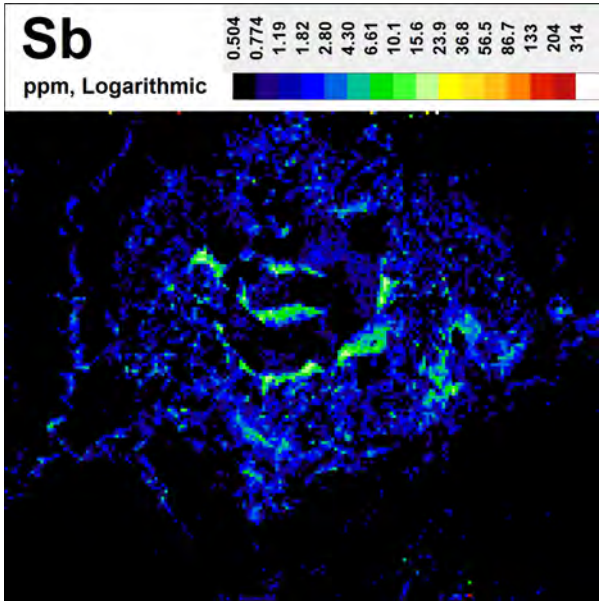
Sb
ppm, Logarithmic
0.504 0.774 1.19 1.82 2.80 4.30 6.61 10.1 15.6 23.9 36.8 56.5 86.7 133 204 314

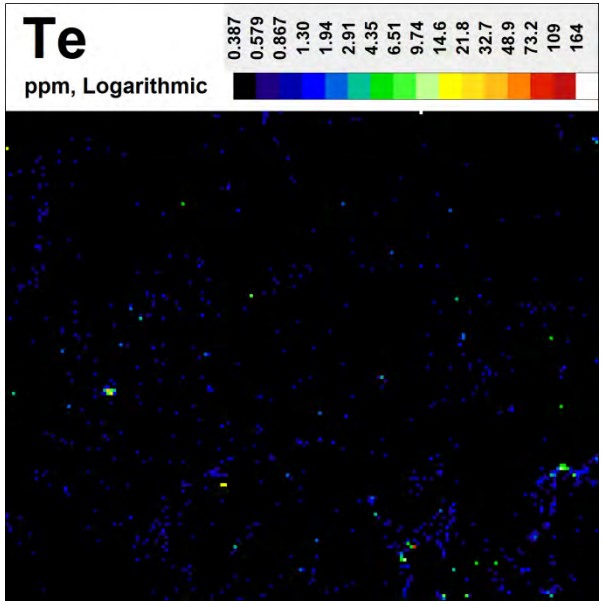
Te
ppm, Logarithmic
0.387 0.579 0.867 1.30 1.94 2.91 4.35 6.51 9.74 14.6 21.8 32.7 48.9 73.2 109 164

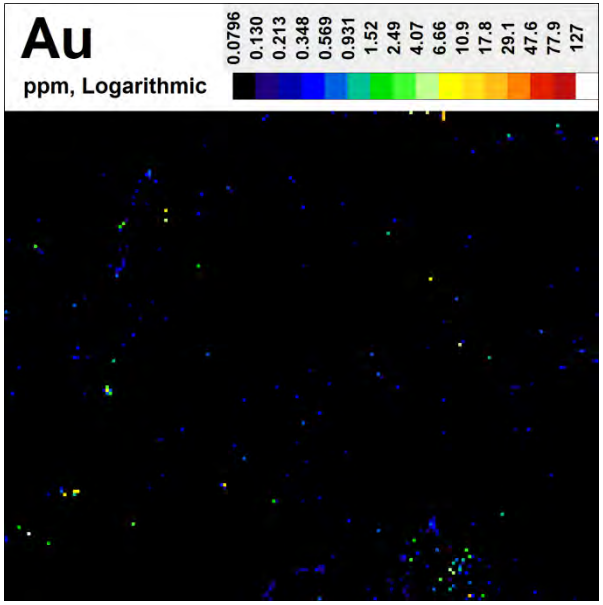
Au
ppm, Logarithmic
0.0796 0.130 0.213 0.348 0.569 0.931 1.52 2.49 4.07 6.66 10.9 17.8 29.1 47.6 77.9 127

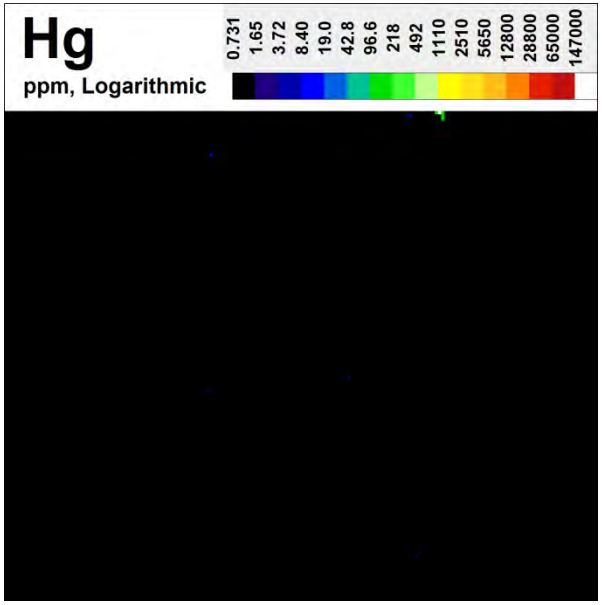
Hg
ppm, Logarithmic
0.731
1.65
3.72
8.40
19.0
42.8
96.6
218
492
1110
2510
5650
12800
28800
65000
147000

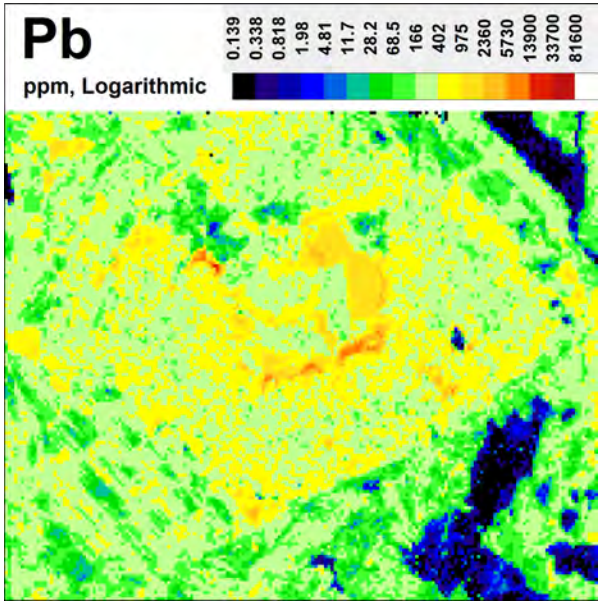
Pb
ppm, Logarithmic
0.139
0.338
0.818
1.98
4.81
11.7
28.2
68.5
166
402
975
2360
5730
13900
33700
81600

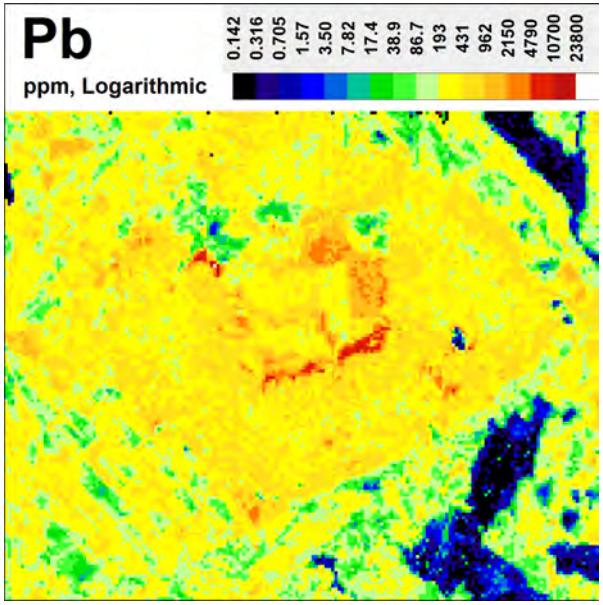
Pb
ppm, Logarithmic
0.142
0.316
0.705
1.57
3.50
7.82
17.4
38.9
86.7
193
431
962
2150
4790
10700
23800

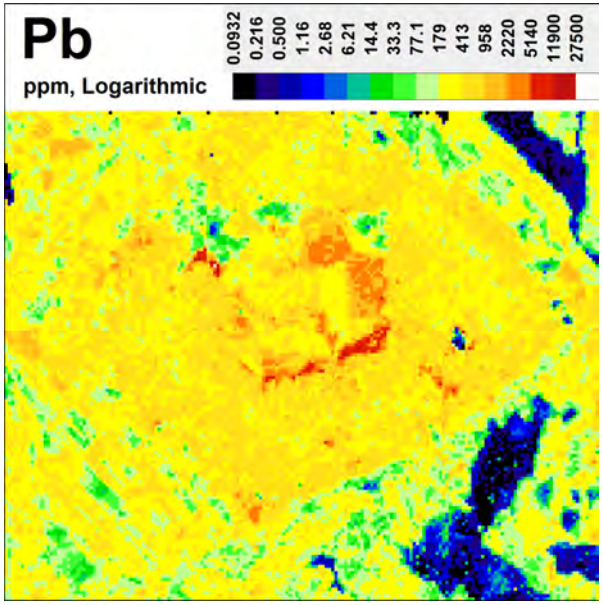
Pb
ppm, Logarithmic
0.0932
0.216
0.500
1.16
2.68
6.21
14.4
33.3
77.1
179
413
958
2220
5140
11900
27500

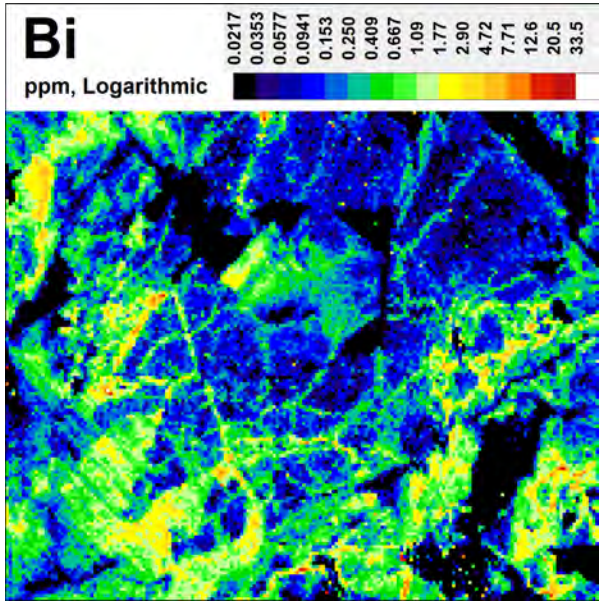
Bi
ppm, Logarithmic
0.0217
0.0353
0.0577
0.0941
0.153
0.250
0.409
0.667
1.09
1.77
2.90
4.72
7.71
12.6
20.5
33.5

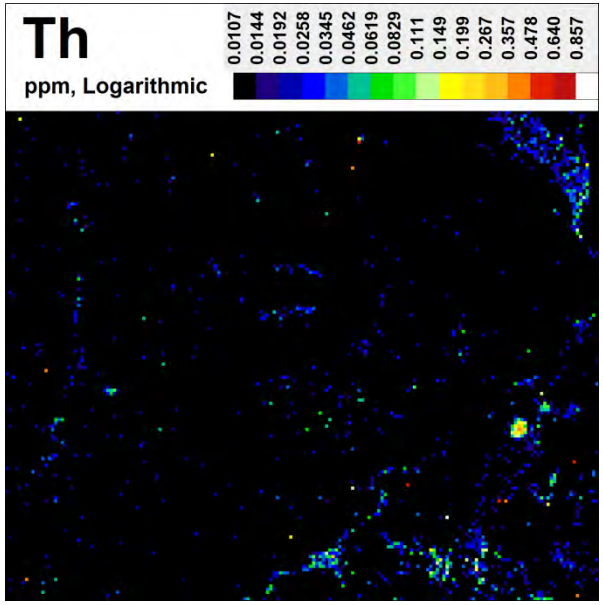
Th
ppm, Logarithmic
0.0107
0.0144
0.0192
0.0258
0.0345
0.0462
0.0619
0.0829
0.111
0.149
0.199
0.267
0.357
0.478
0.640
0.857

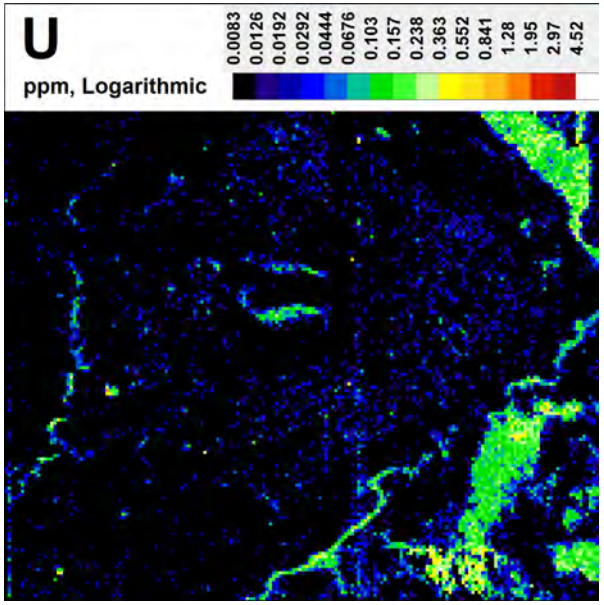
U
ppm, Logarithmic
0.0083
0.0126
0.0192
0.0292
0.0444
0.0676
0.103
0.157
0.238
0.363
0.552
0.841
1.28
1.95
2.97
4.52

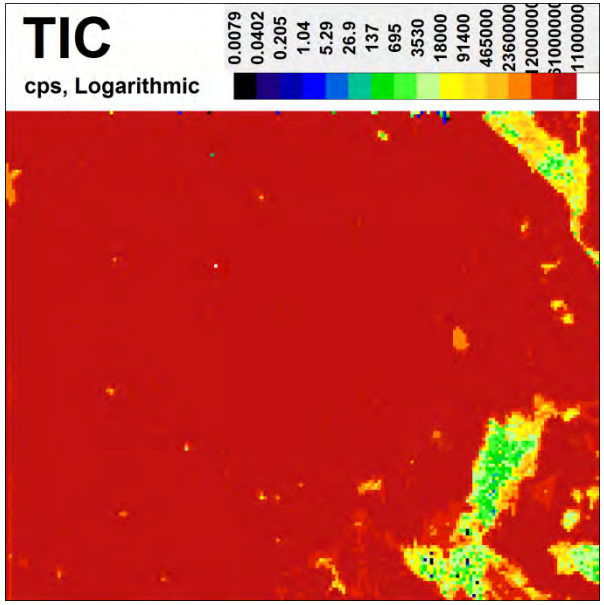
TIC
cps, Logarithmic
0.0079
0.0402
0.205
1.04
5.29
26.9
137
695
3530
18000
91400
465000
2360000
1100000

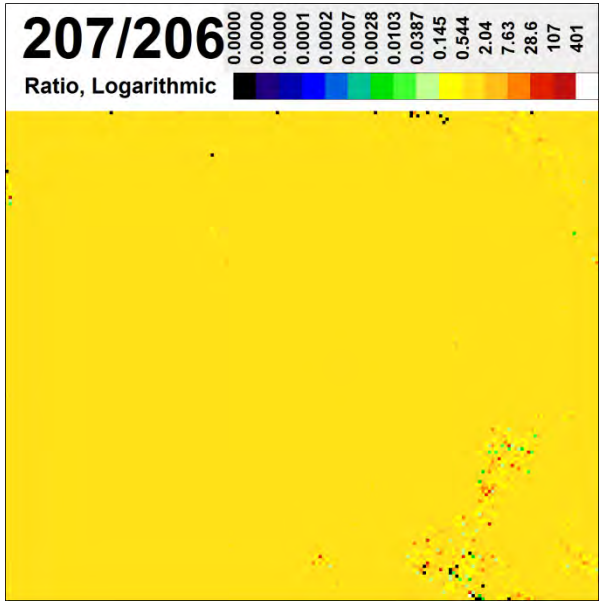
207/206
Ratio, Logarithmic
0.0000
0.0000
0.0000
0.0001
0.0002
0.0007
0.0028
0.0103
0.0387
0.145
0.544
2.04
7.63
28.6
107
401

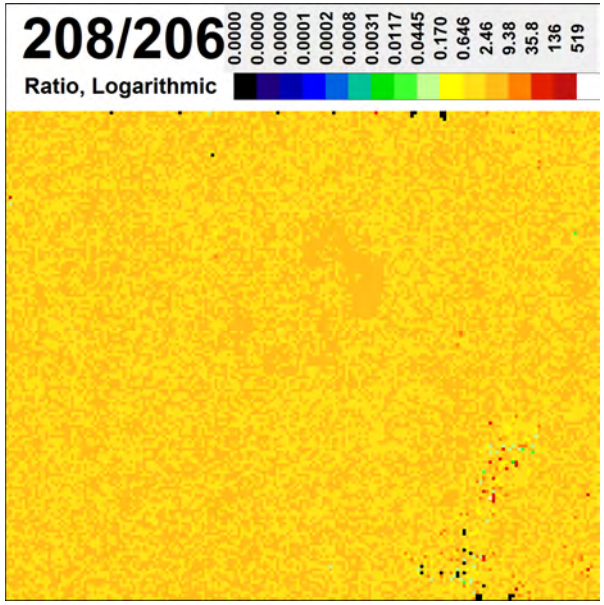
208/206
Ratio, Logarithmic
0.0000
0.0000
0.0000
0.0001
0.0002
0.0008
0.0031
0.0117
0.0445
0.170
0.646
2.46
9.38
35.8
136
519

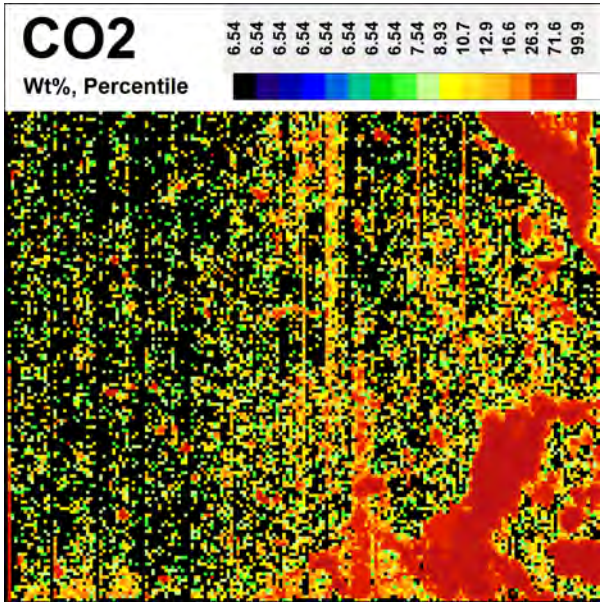
CO2
Wt%, Percentile
6.54 6.54 6.54 6.54 6.54 6.54 6.54 7.54 8.93 10.7 12.9 16.6 26.3 71.6 99.9

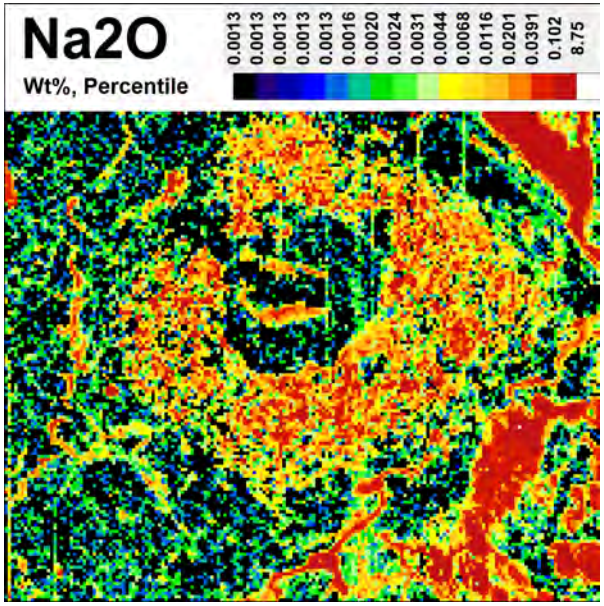
Na2O
Wt%, Percentile
0.0013 0.0013 0.0013 0.0013 0.0016 0.0020 0.0024 0.0031 0.0044 0.0068 0.0116 0.0201 0.0391 0.102 8.75

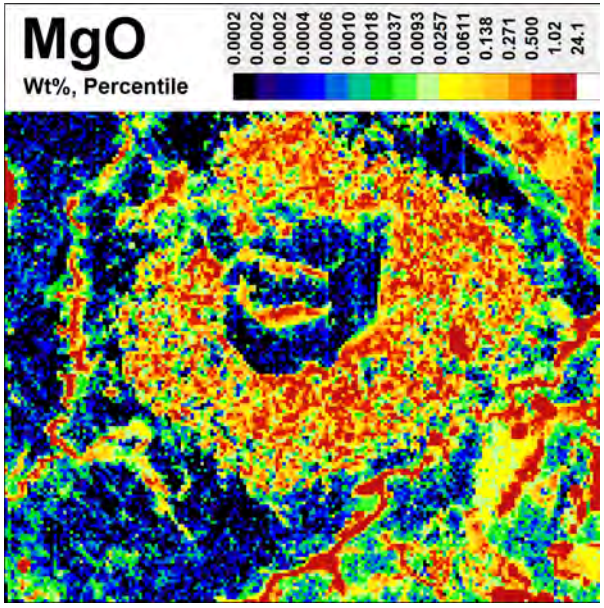
MgO
Wt%, Percentile
0.0002 0.0002 0.0002 0.0004 0.0006 0.0010 0.0018 0.0037 0.0093 0.0257 0.0611 0.138 0.271 0.500 1.02 24.1

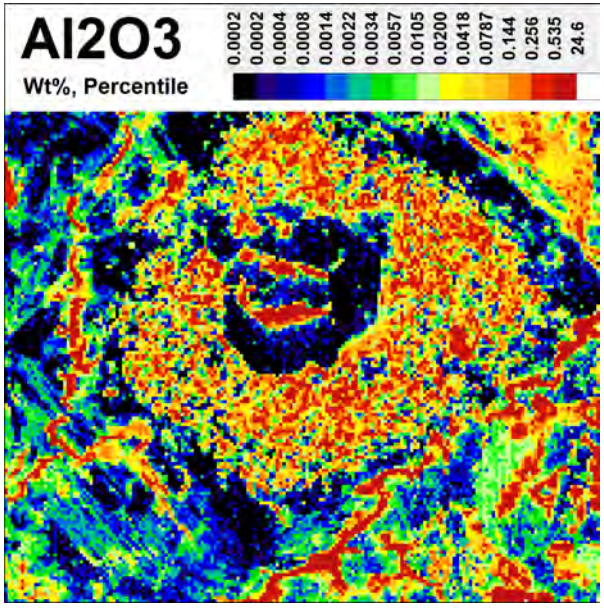
Al2O3
Wt%, Percentile
0.0002 0.0002 0.0004 0.0008 0.0014 0.0022 0.0034 0.0057 0.0105 0.0200 0.0418 0.0787 0.144 0.256 0.535 24.6

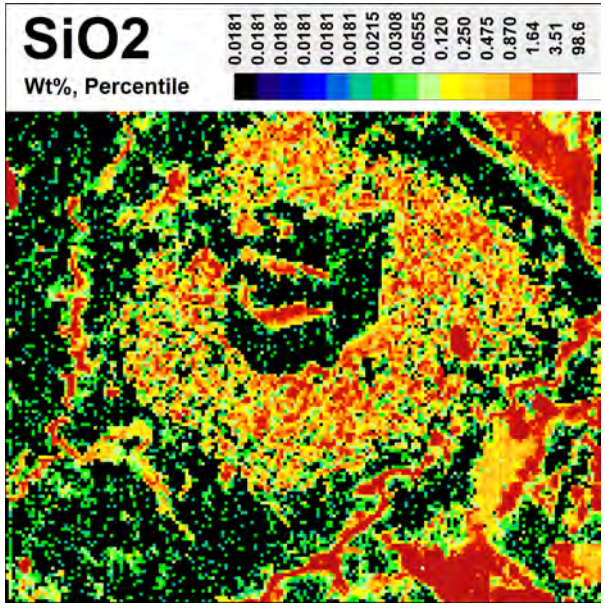
SiO2
Wt%, Percentile
0.0181 0.0181 0.0181 0.0181 0.0181 0.0181 0.0215 0.0308 0.0555 0.120 0.250 0.475 0.870 1.64 3.51 98.6

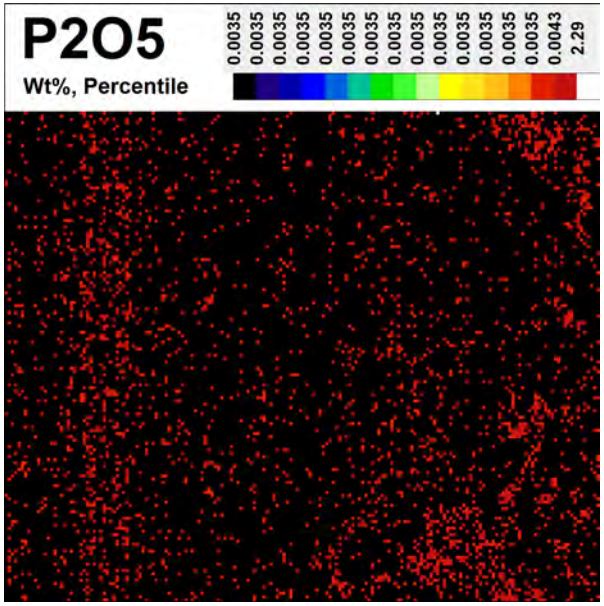
P2O5
Wt%, Percentile
0.0035 0.0035 0.0035 0.0035 0.0035 0.0035 0.0035 0.0035 0.0035 0.0035 0.0035 0.0035 0.0043 2.29

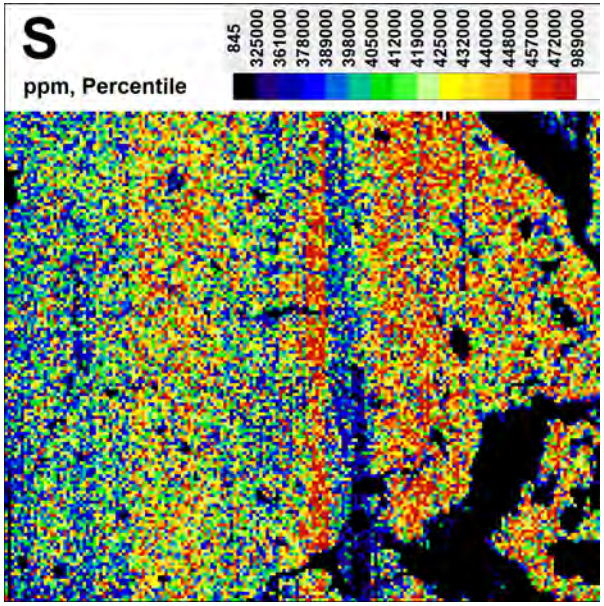
S
ppm, Percentile
845 325000 361000 378000 389000 398000 405000 412000 419000 425000 432000 440000 448000 457000 472000 989000

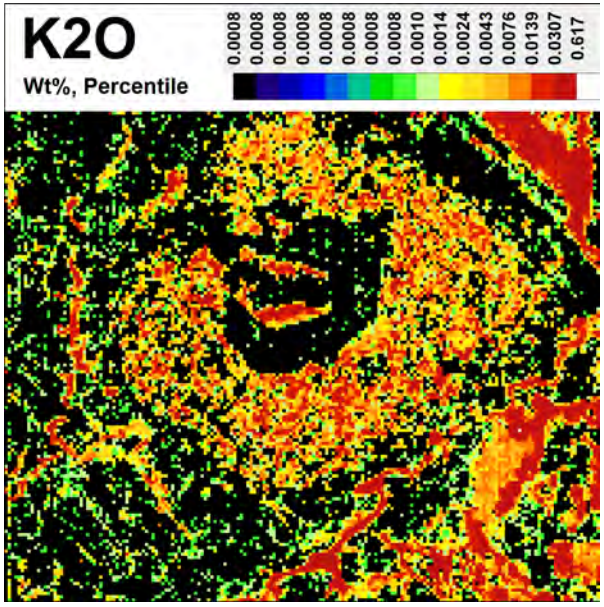
K2O
Wt%, Percentile
0.0008 0.0008 0.0008 0.0008 0.0008 0.0008 0.0008 0.0008 0.0010 0.0014 0.0024 0.0043 0.0076 0.0139 0.0307 0.617

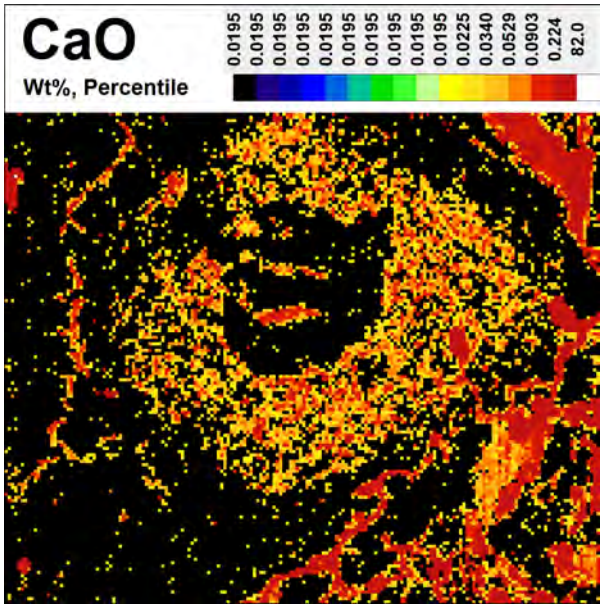
CaO
Wt%, Percentile
0.0195 0.0195 0.0195 0.0195 0.0195 0.0195 0.0195 0.0195 0.0195 0.0225 0.0340 0.0529 0.0903 0.224 82.0

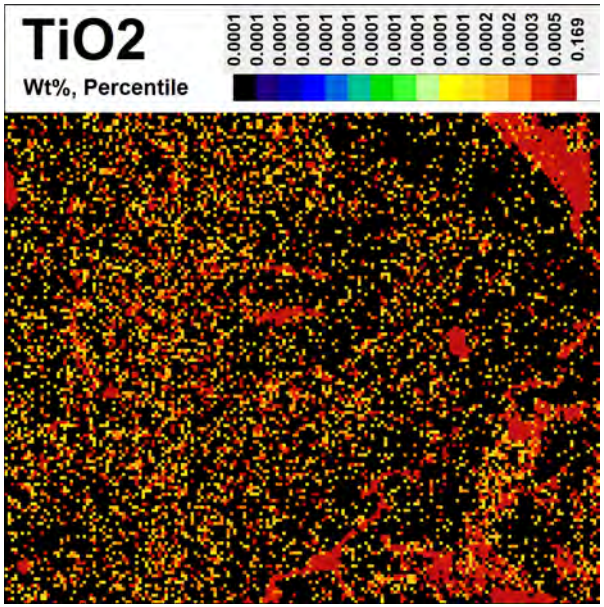
TiO2
Wt%, Percentile
0.0001 0.0001 0.0001 0.0001 0.0001 0.0001 0.0001 0.0001 0.0001 0.0001 0.0001 0.0002 0.0002 0.0003 0.0005 0.169

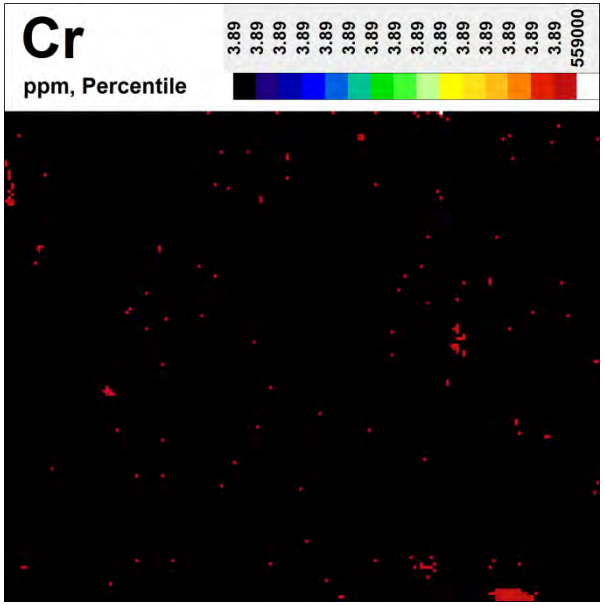
Cr
ppm, Percentile
3.89 3.89 3.89 3.89 3.89 3.89 3.89 3.89 3.89 3.89 3.89 3.89 559000

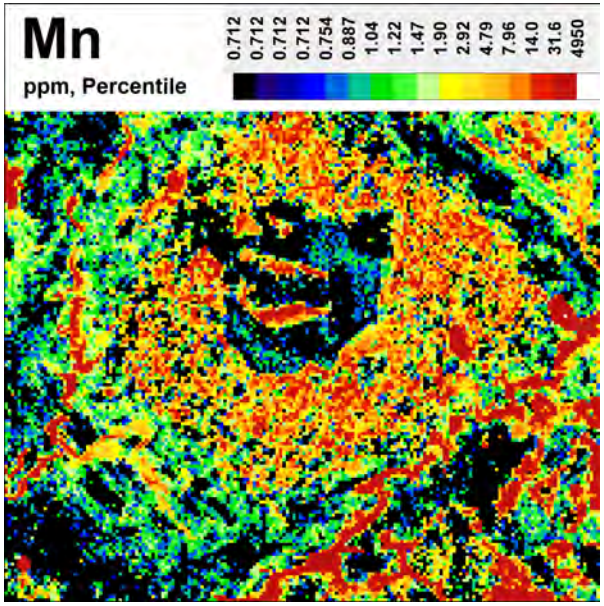
Mn
ppm, Percentile
0.712 0.712 0.712 0.712 0.754 0.887 1.04 1.22 1.47 1.90 2.92 4.79 7.96 14.0 31.6 4950

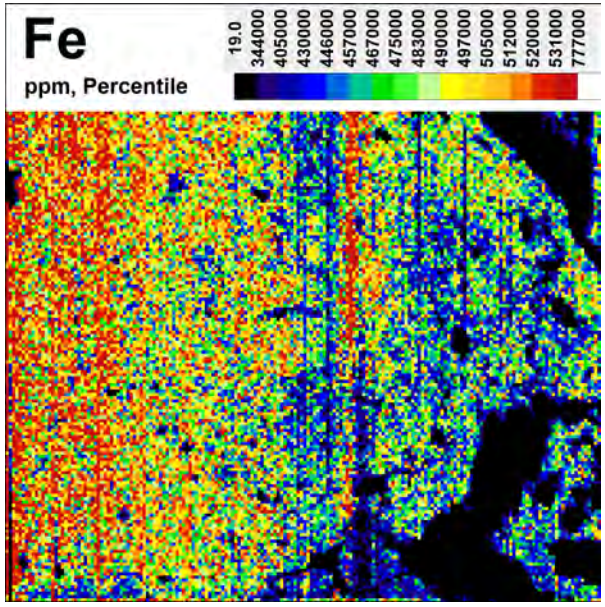
Fe
ppm, Percentile
19.0 344000 405000 430000 446000 457000 467000 475000 483000 490000 497000 505000 512000 520000 531000 777000

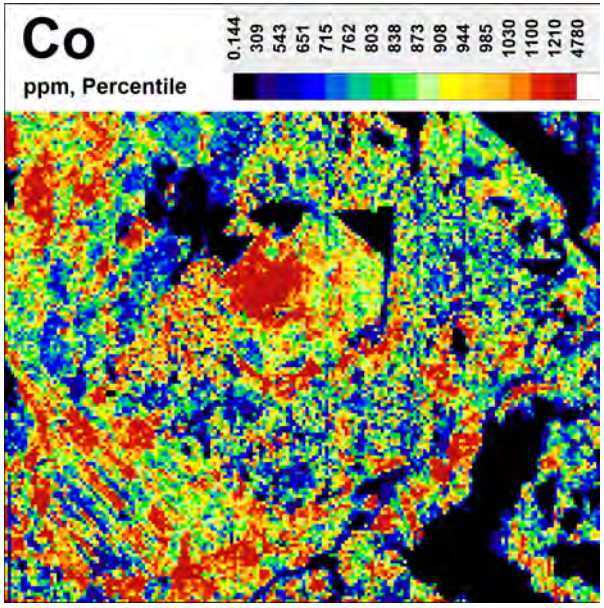
Co
ppm, Percentile
0.144 309 543 651 715 762 803 838 873 908 944 985 1030 1100 1210 4780

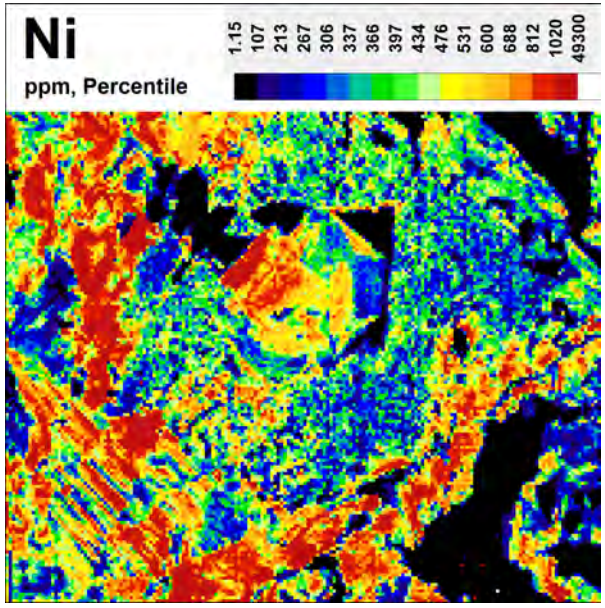
Ni
ppm, Percentile
1.15 107 213 267 306 337 366 397 434 476 531 600 688 812 1020 49300

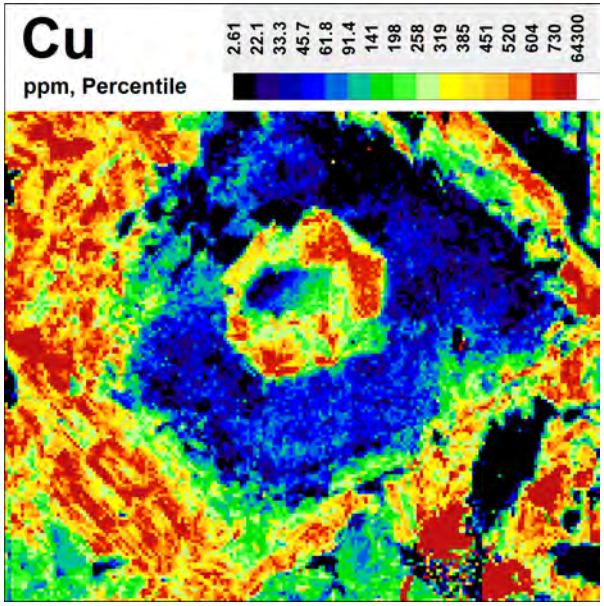
Cu
ppm, Percentile
2.61 22.1 33.3 45.7 61.8 91.4 141 198 258 319 385 451 520 604 730 64300

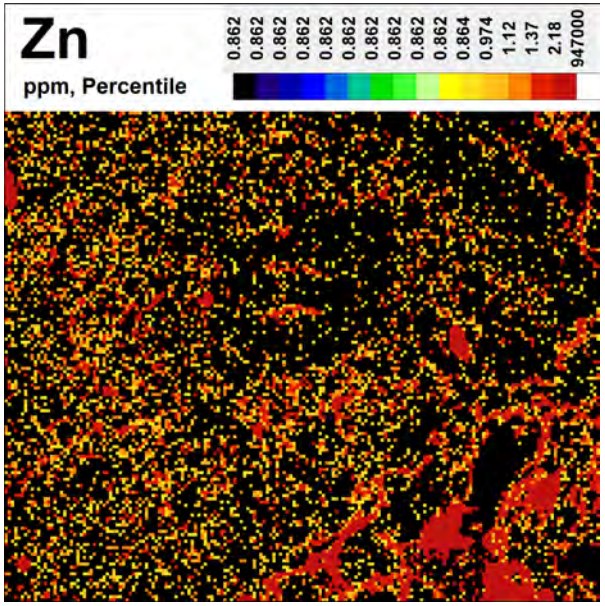
Zn
ppm, Percentile
0.862 0.862 0.862 0.862 0.862 0.862 0.862 0.862 0.862 0.862 0.864 0.974 1.12 1.37 2.18 947000

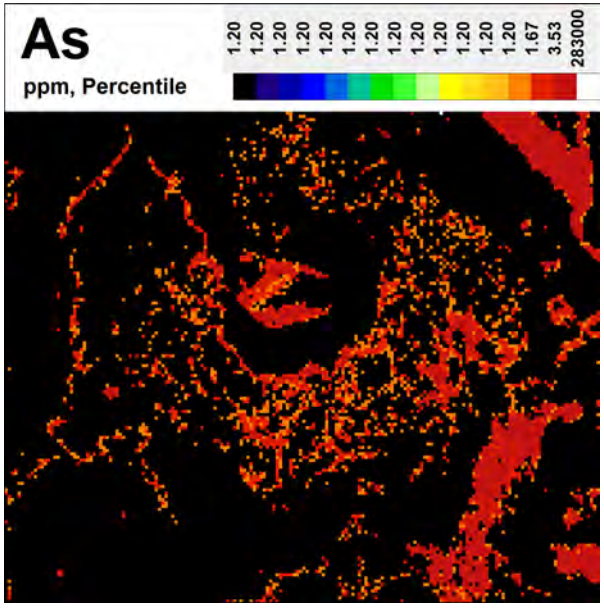
As
ppm, Percentile
1.20 1.20 1.20 1.20 1.20 1.20 1.20 1.20 1.20 1.20 1.20 1.20 1.67 3.53 283000

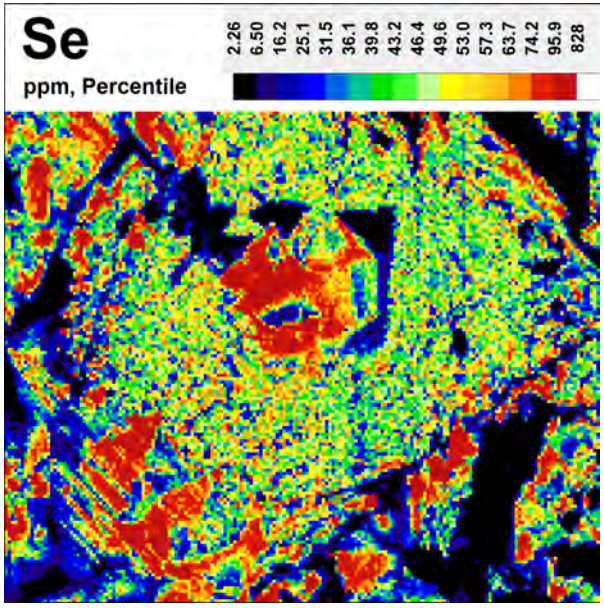
Se
ppm, Percentile
2.26 6.50 16.2 25.1 31.5 36.1 39.8 43.2 46.4 49.6 53.0 57.3 63.7 74.2 95.9 828

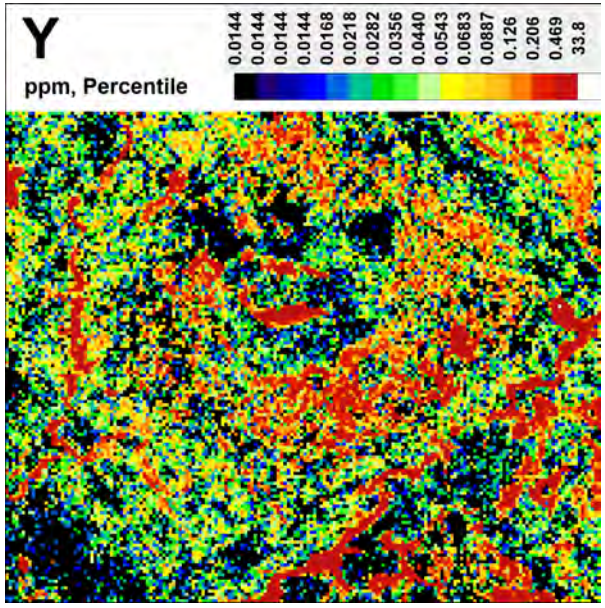
Y
ppm, Percentile
0.0144 0.0144 0.0144 0.0144 0.0168 0.0218 0.0282 0.0356 0.0440 0.0543 0.0683 0.0887 0.126 0.206 0.469 33.8

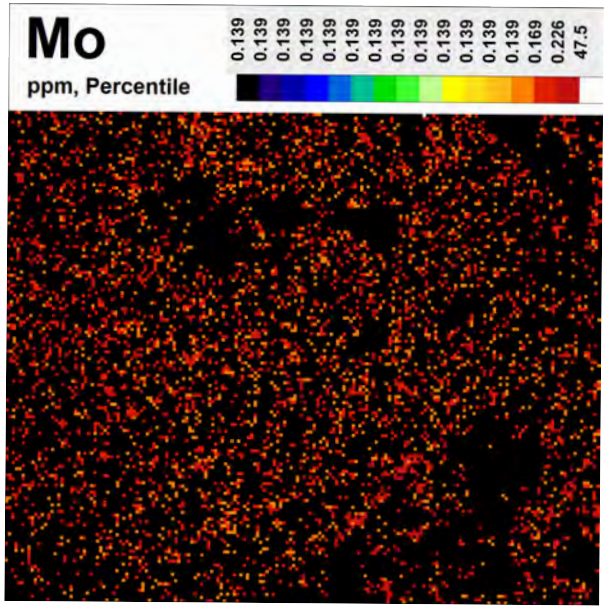
Mo
ppm, Percentile
0.139 0.139 0.139 0.139 0.139 0.139 0.139 0.139 0.139 0.139 0.139 0.169 0.226 47.5

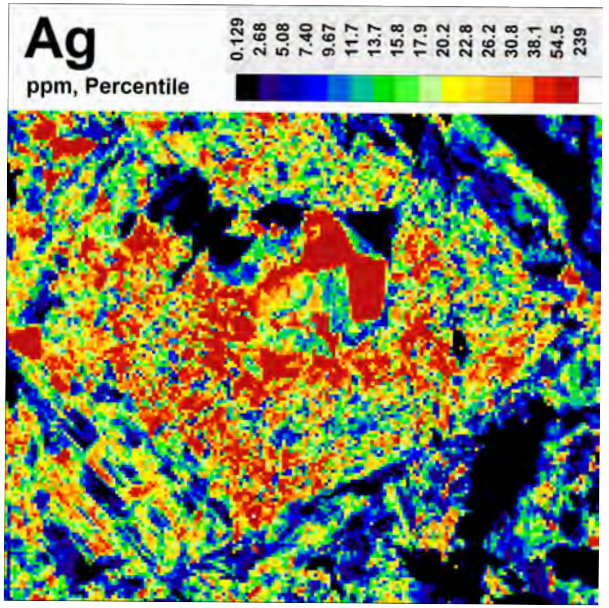
Ag
ppm, Percentile
0.129 2.68 5.08 7.40 9.67 11.7 13.7 15.8 17.9 20.2 22.8 26.2 30.8 38.1 54.5 239

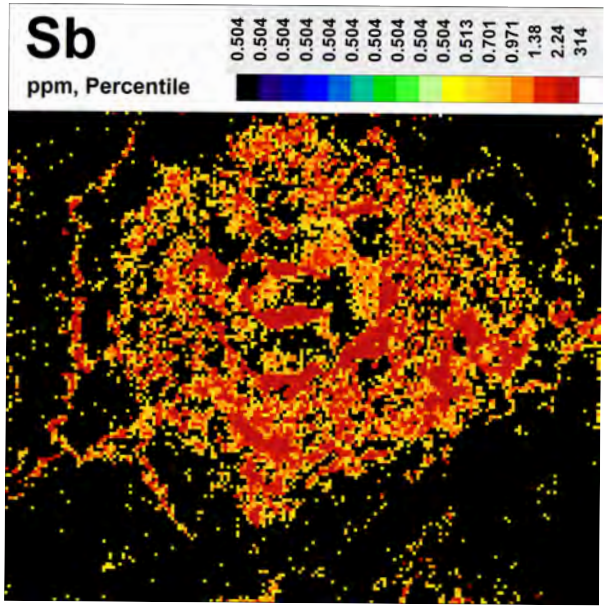
Sb
ppm, Percentile
0.504 0.504 0.504 0.504 0.504 0.504 0.504 0.504 0.504 0.513 0.701 0.971 1.38 2.24 314

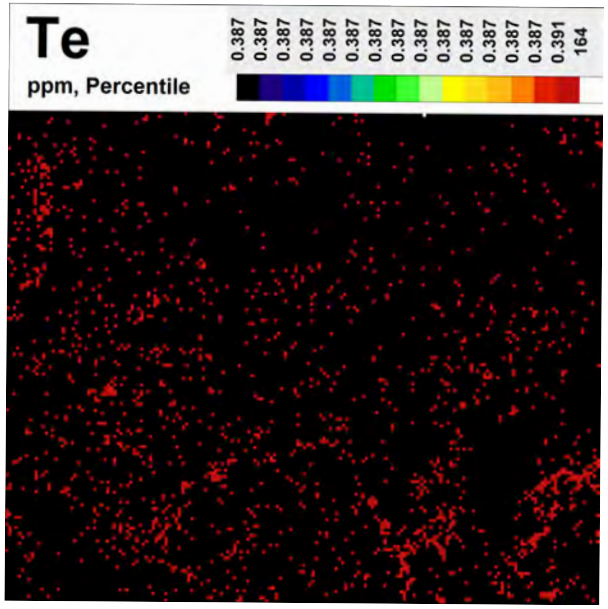
Te
ppm, Percentile
0.387 0.387 0.387 0.387 0.387 0.387 0.387 0.387 0.387 0.387 0.387 0.391 164

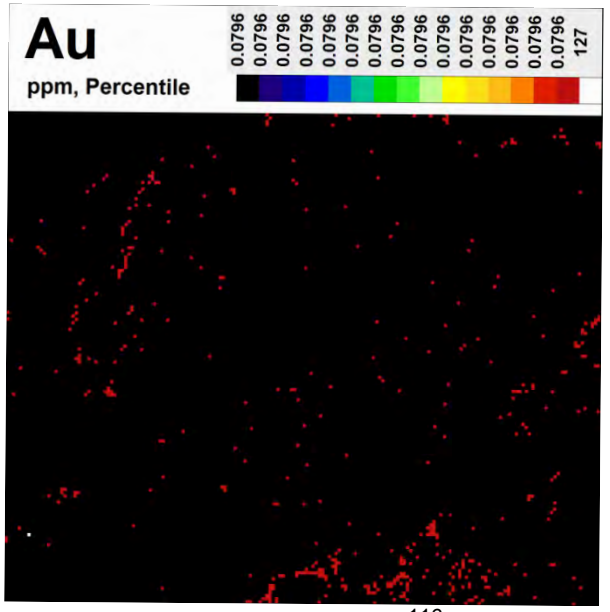
Au
ppm, Percentile
0.0796 0.0796 0.0796 0.0796 0.0796 0.0796 0.0796 0.0796 0.0796 0.0796 0.0796 0.0796 0.0796 127

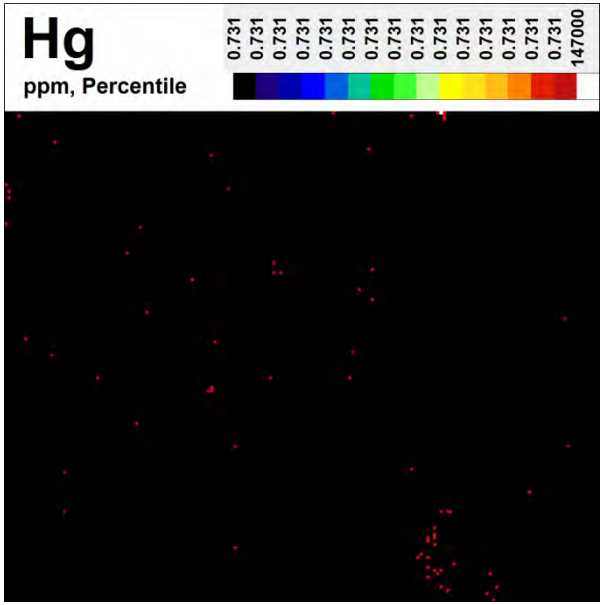
Hg
ppm, Percentile
0.731
0.731
0.731
0.731
0.731
0.731
0.731
0.731
0.731
0.731
0.731
0.731
147000

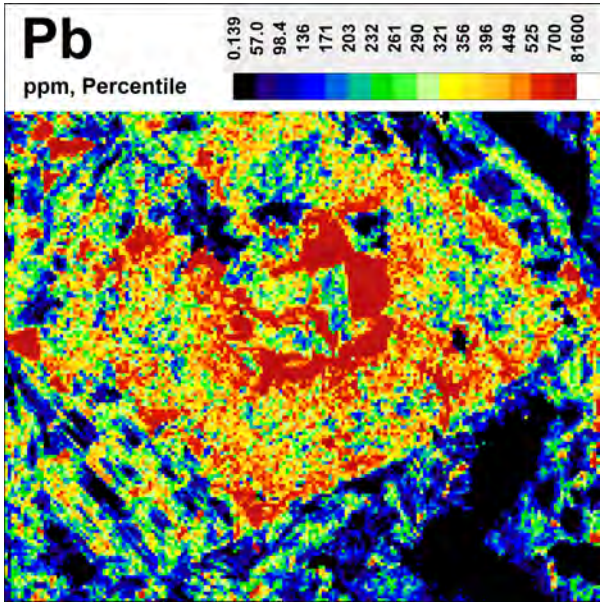
Pb
ppm, Percentile
0.139
57.0
98.4
136
171
203
232
261
290
321
356
396
449
525
700
81600

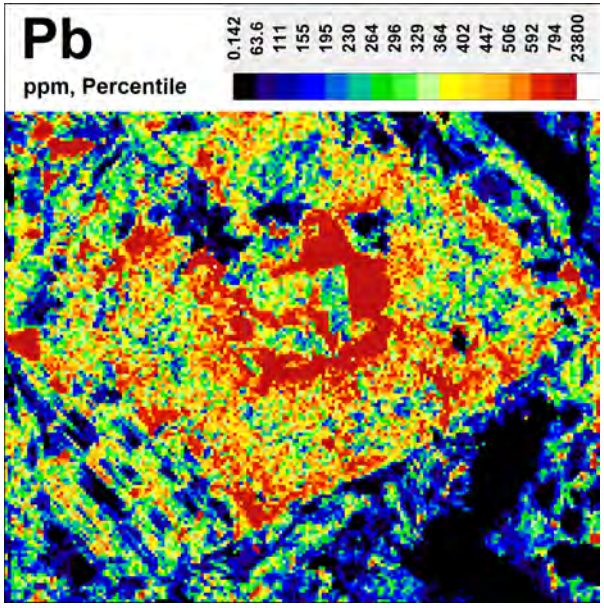
Pb
ppm, Percentile
0.142
63.6
111
155
195
230
264
296
329
364
402
447
506
592
794
23800

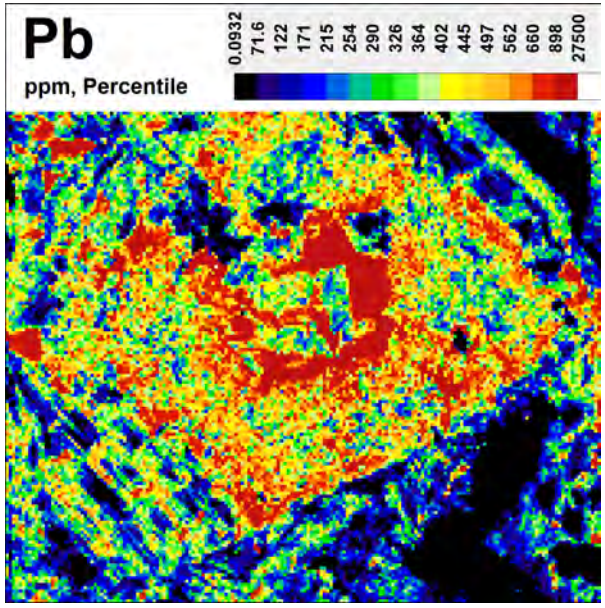
Pb
ppm, Percentile
0.0932
71.6
122
171
215
254
290
326
364
402
445
497
562
660
898
27500

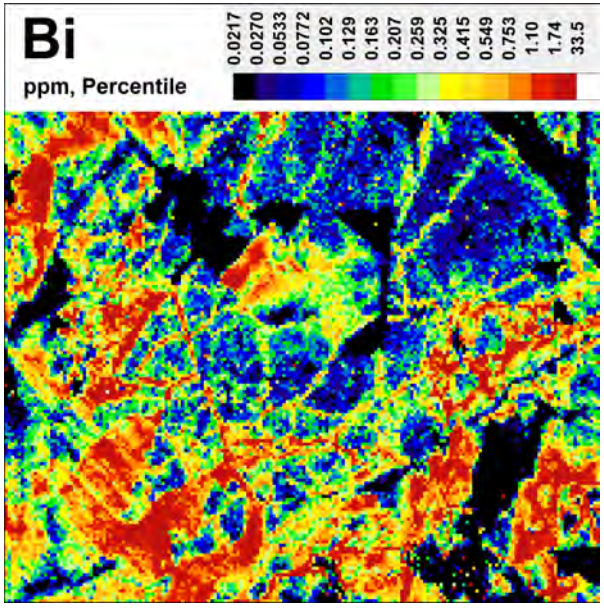
Bi
ppm, Percentile
0.0217
0.0270
0.0533
0.0772
0.102
0.129
0.163
0.207
0.259
0.325
0.415
0.549
0.753
1.10
1.74
33.5

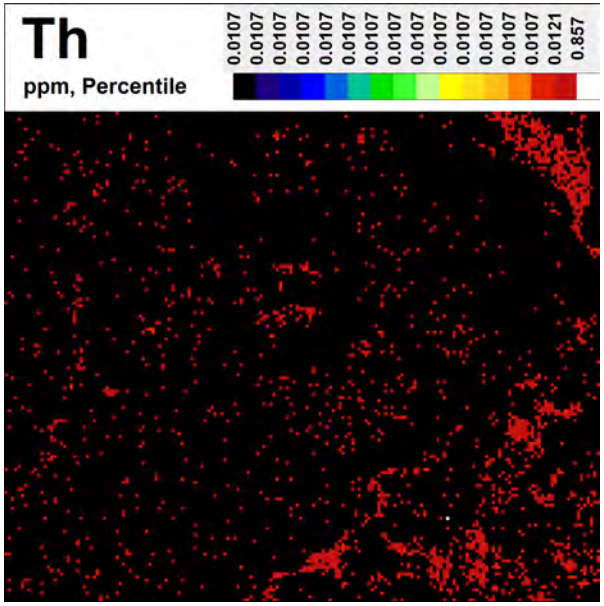
Th
ppm, Percentile
0.0107
0.0107
0.0107
0.0107
0.0107
0.0107
0.0107
0.0107
0.0107
0.0107
0.0107
0.0107
0.0121
0.857

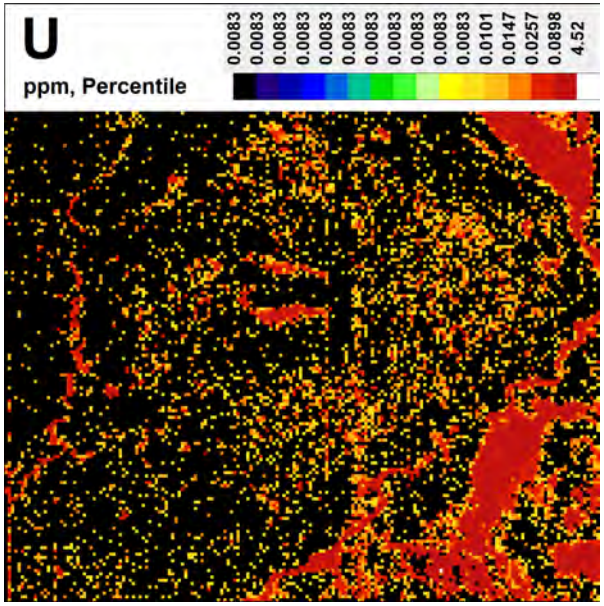
U
ppm, Percentile
0.0083
0.0083
0.0083
0.0083
0.0083
0.0083
0.0083
0.0083
0.0083
0.0083
0.0101
0.0147
0.0257
0.0898
4.52

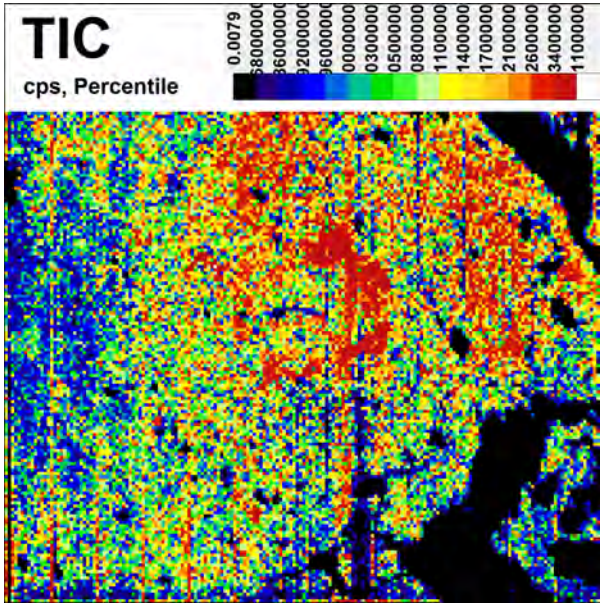
TIC
cps, Percentile
0.0079

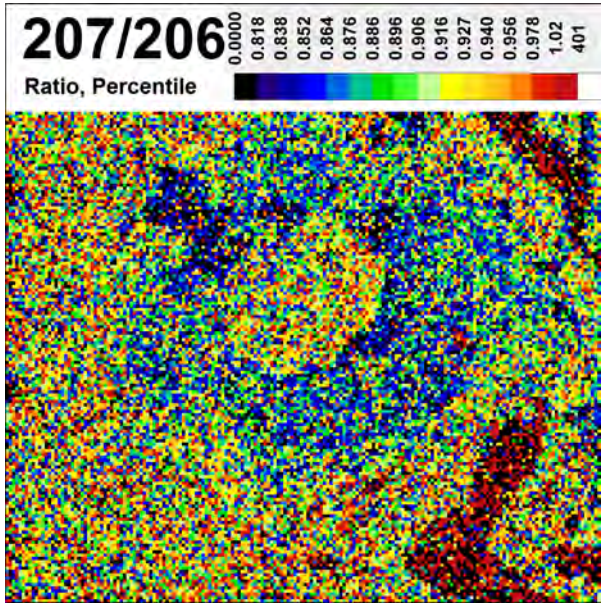
207/206
Ratio, Percentile
0.0000
0.818
0.838
0.852
0.864
0.876
0.886
0.896
0.906
0.916
0.927
0.940
0.956
0.978
1.02
401

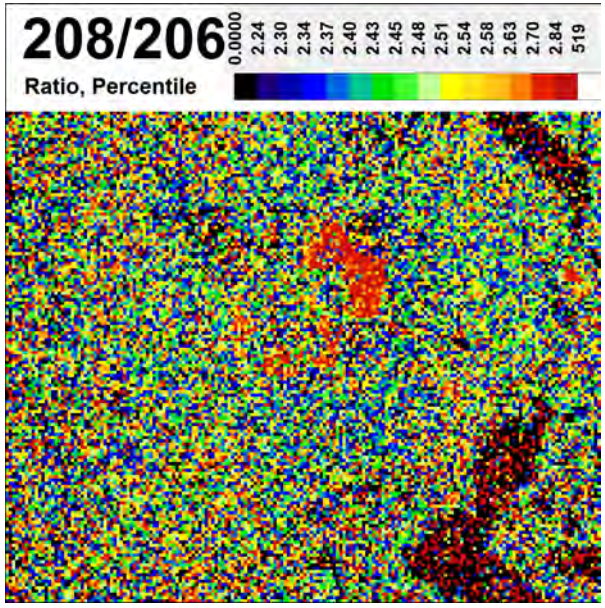
208/206
Ratio, Percentile
0.0000
2.24
2.30
2.34
2.37
2.40
2.43
2.45
2.48
2.51
2.54
2.58
2.63
2.70
2.84
519

Figure DR5. (pages 105–118) LA-ICP-MS results of a euhedral pyrite crystal (type-2a) with an inclusion-rich overgrowth (type-1b), which is also overgrown by an inclusion-poor type-2b pyrite within a syn-D2 vein (V5) from a mafic volcanic sample (RD15-118-238B) showing a reflected light photomicrograph of the mapping area and 32 major and trace maps. LA-ICP-MS maps revealing additional pyrite generations through oscillatory growth zoning of first-row transition metals (Cr-Co-Ni-Cu-Zn) and some post-transition metals (Pb) and metalloids (As-Sb ± Se). Growth zones are cut by metal-rich (Bi) brittle fractures.

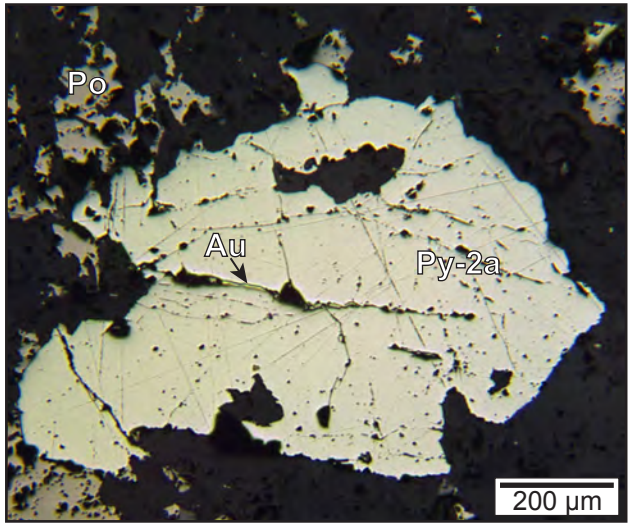
Po
Au
Py-2a
200 µm

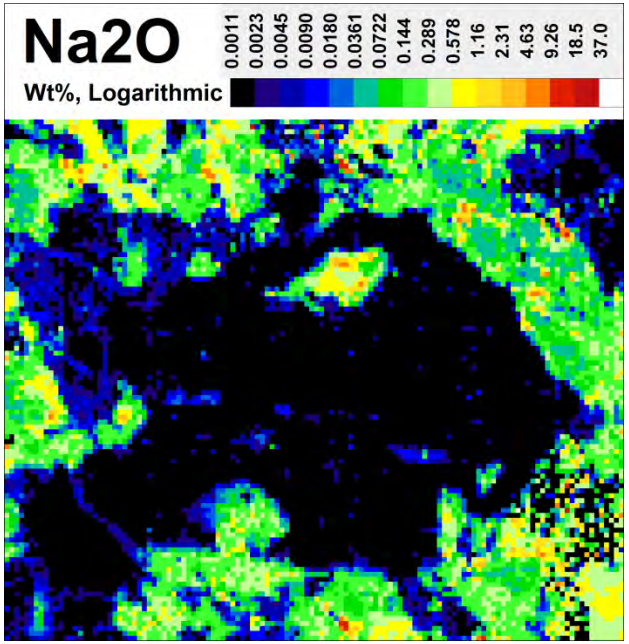
Na2O
Wt%, Logarithmic
0.0011 0.0023 0.0045 0.0090 0.0180 0.0361 0.0722 0.144 0.289 0.578 1.16 2.31 4.63 9.26 18.5 37.0

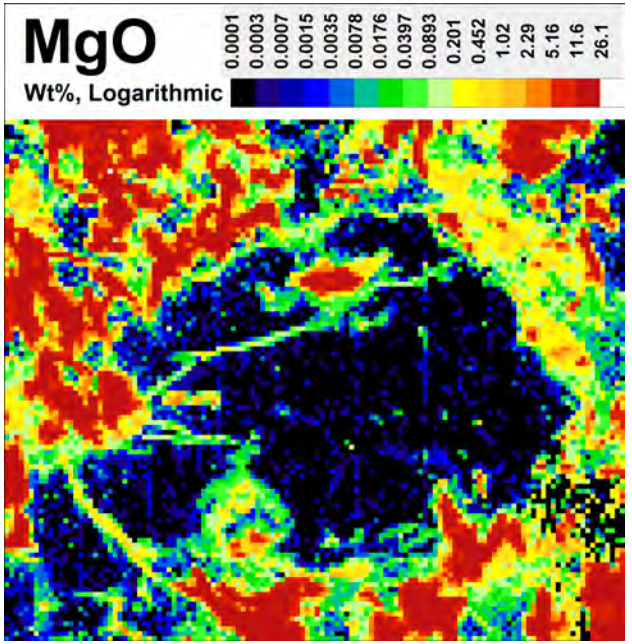
MgO
Wt%, Logarithmic
0.0001 0.0003 0.0007 0.0015 0.0035 0.0078 0.0176 0.0397 0.0893 0.201 0.452 1.02 2.29 5.16 11.6 26.1

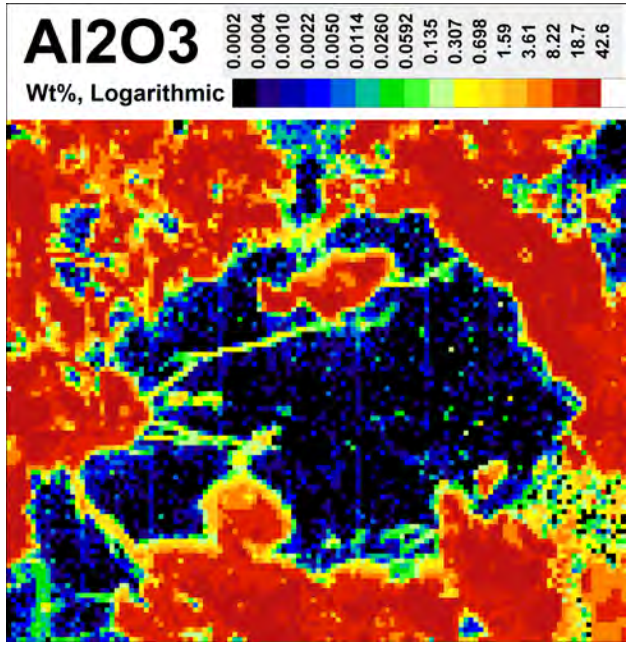
Al2O3
Wt%, Logarithmic
0.0002 0.0004 0.0010 0.0022 0.0050 0.0114 0.0260 0.0592 0.135 0.307 0.698 1.59 3.61 8.22 18.7 42.6

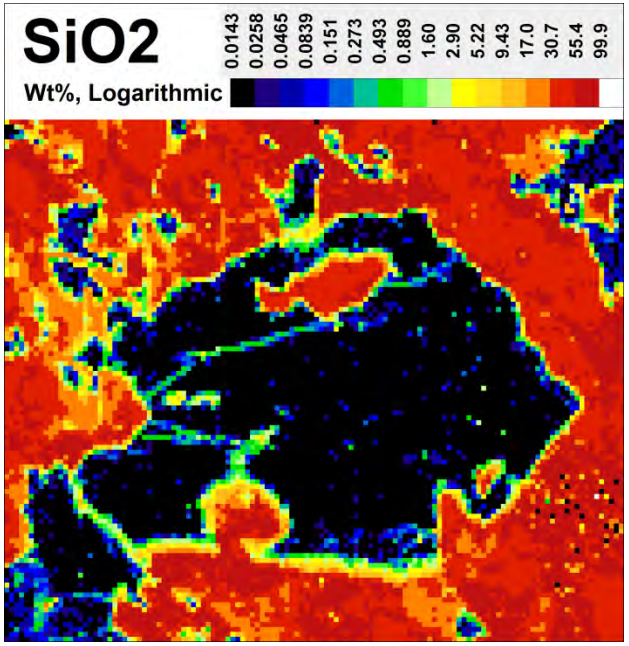
SiO2
Wt%, Logarithmic
0.0143 0.0258 0.0465 0.0839 0.151 0.273 0.493 0.889 1.60 2.90 5.22 9.43 17.0 30.7 55.4 99.9

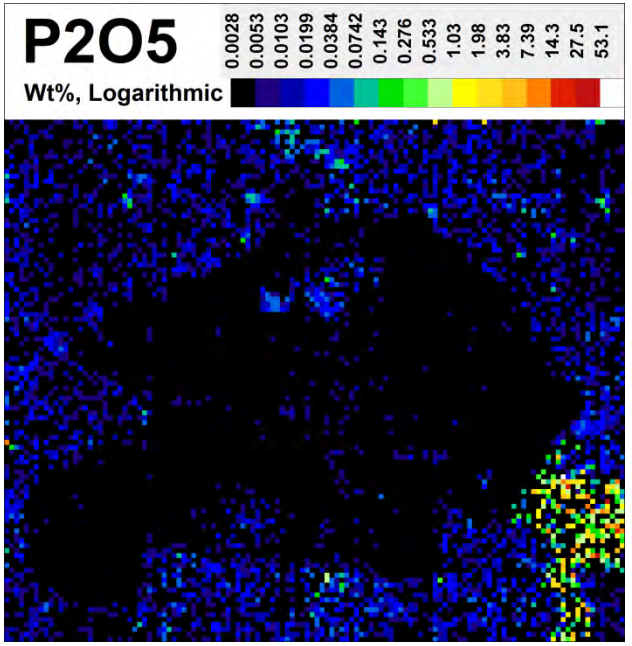
P2O5
Wt%, Logarithmic
0.0028 0.0053 0.0103 0.0199 0.0384 0.0742 0.143 0.276 0.533 1.03 1.98 3.83 7.39 14.3 27.5 53.1

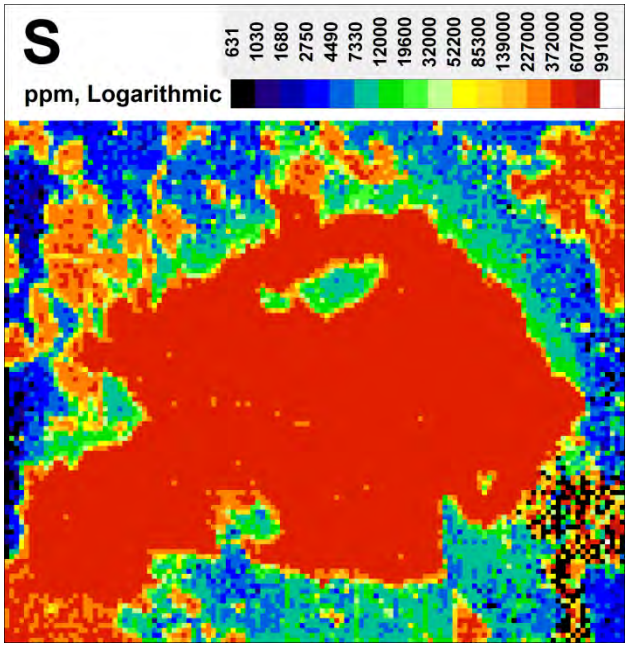
S
ppm, Logarithmic
631 1030 1680 2750 4490 7330 12000 19600 32000 52200 85300 139000 227000 372000 607000 991000

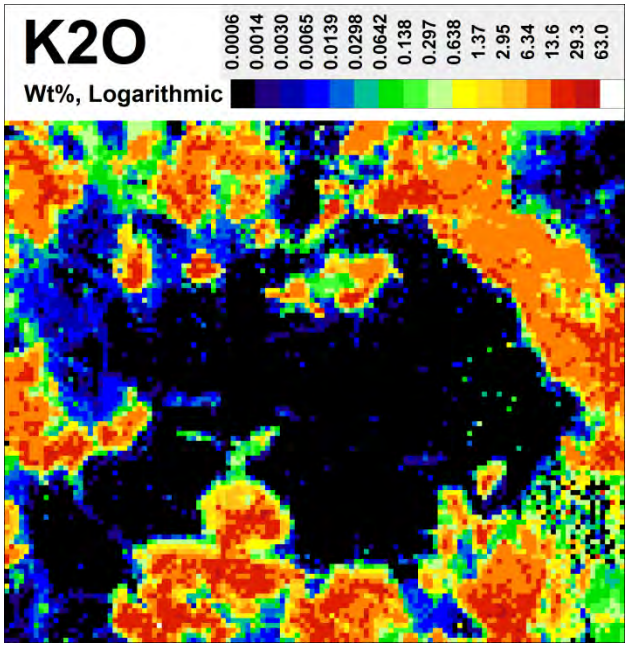
K2O
Wt%, Logarithmic
0.0006 0.0014 0.0030 0.0065 0.0139 0.0298 0.0642 0.138 0.297 0.638 1.37 2.95 6.34 13.6 29.3 63.0

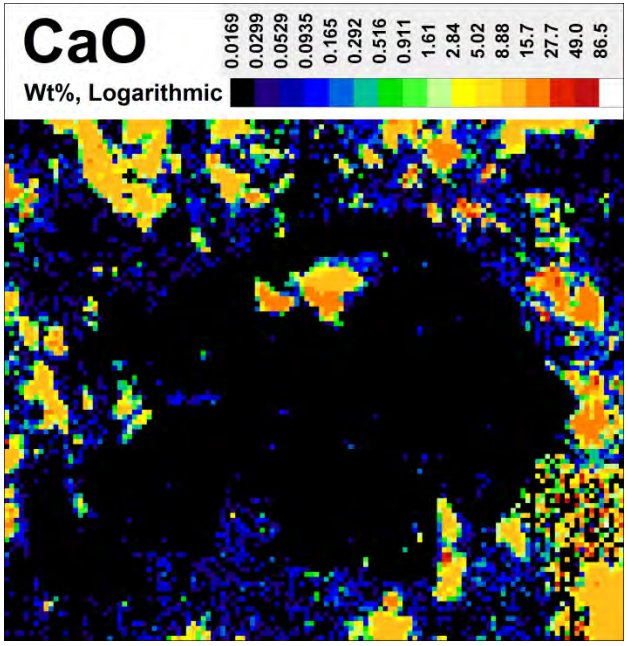
CaO
Wt%, Logarithmic
0.0169 0.0299 0.0529 0.0935 0.165 0.292 0.516 0.911 1.61 2.84 5.02 8.88 15.7 27.7 49.0 86.5

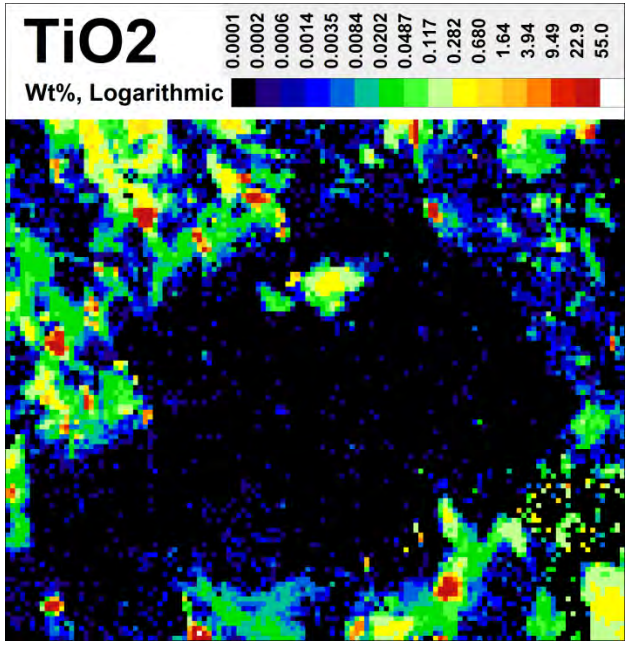
TiO2
Wt%, Logarithmic
0.0001 0.0002 0.0006 0.0014 0.0035 0.0084 0.0202 0.0487 0.117 0.282 0.680 1.64 3.94 9.49 22.9 55.0

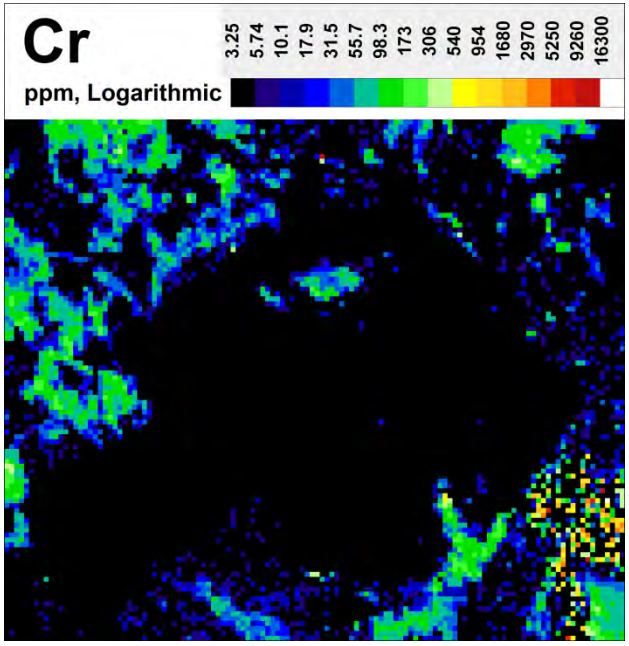
Cr
ppm, Logarithmic
3.25 5.74 10.1 17.9 31.5 55.7 98.3 173 306 540 954 1680 2970 5250 9260 16300

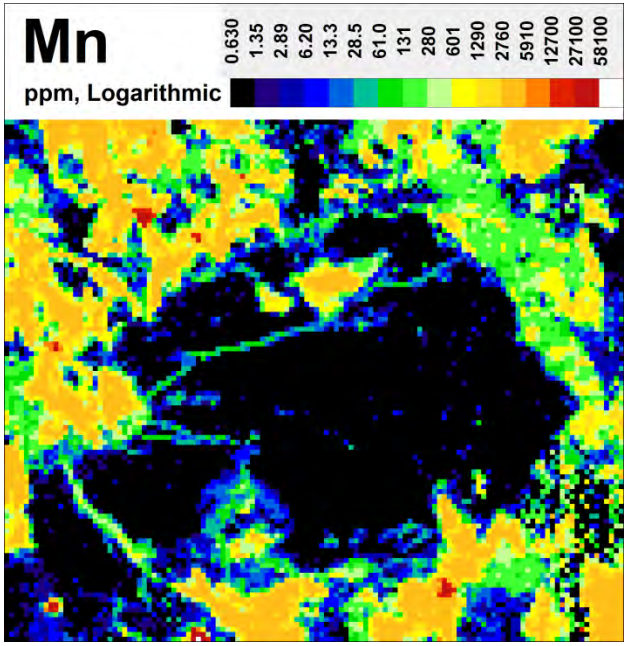
Mn
ppm, Logarithmic
0.630
1.35
2.89
6.20
13.3
28.5
61.0
131
280
601
1290
2760
5910
12700
27100
58100

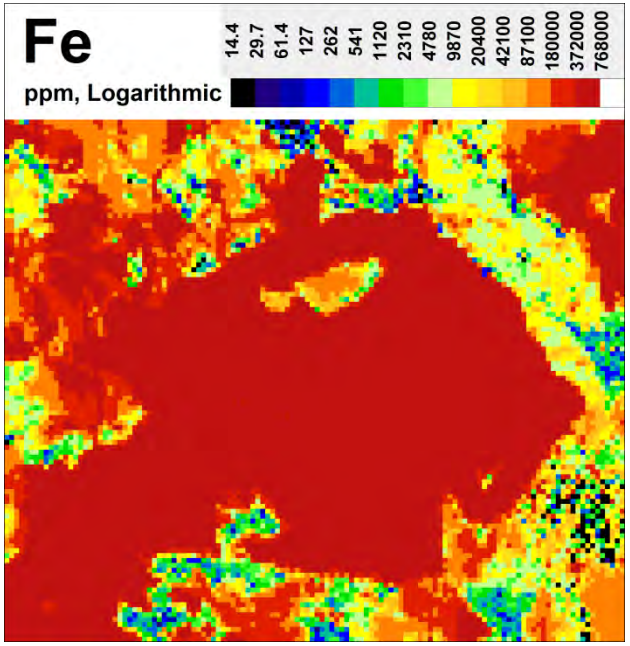
Fe
ppm, Logarithmic
14.4
29.7
61.4
127
262
541
1120
2310
4780
9870
20400
42100
87100
180000
372000
768000

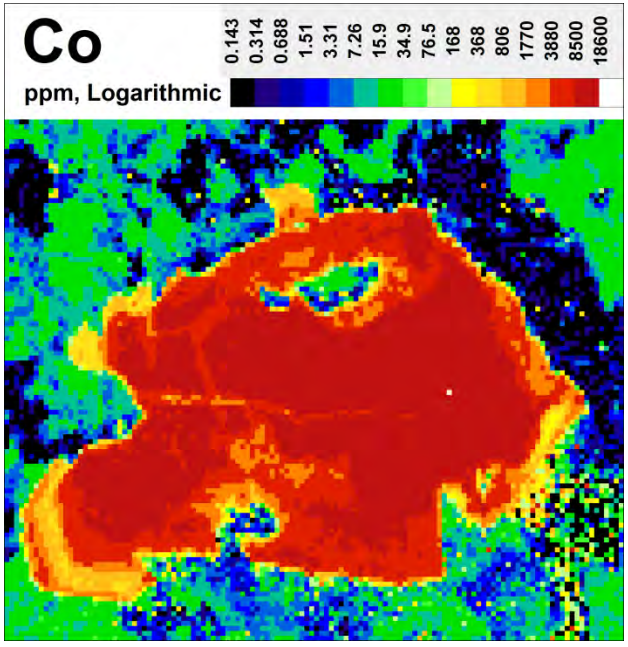
Co
ppm, Logarithmic
0.143
0.314
0.688
1.51
3.31
7.26
15.9
34.9
76.5
168
368
806
1770
3880
8500
18600

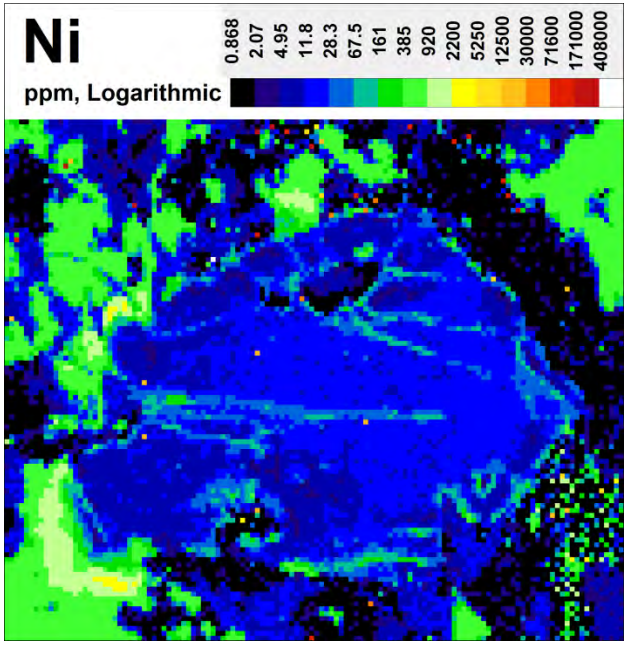
Ni
ppm, Logarithmic
0.868
2.07
4.95
11.8
28.3
67.5
161
385
920
2200
5250
12500
30000
71600
171000
408000

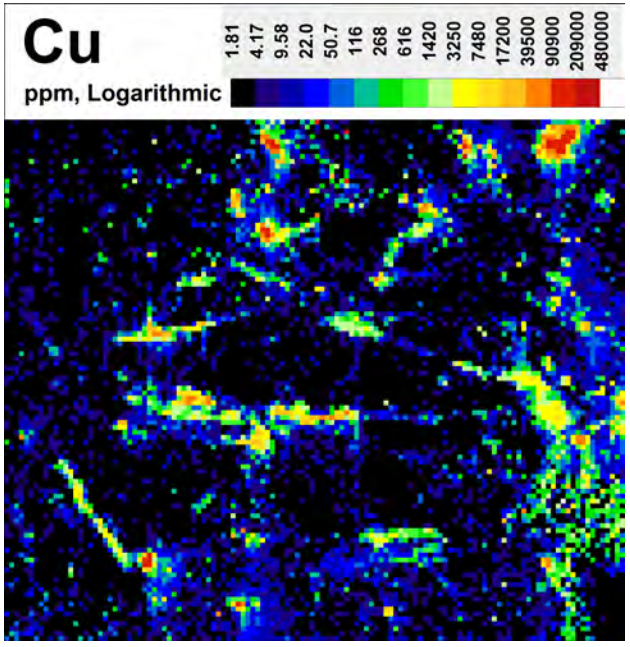
Cu
ppm, Logarithmic
1.81
4.17
9.58
22.0
50.7
116
268
616
1420
3250
7480
17200
39500
90900
209000
480000

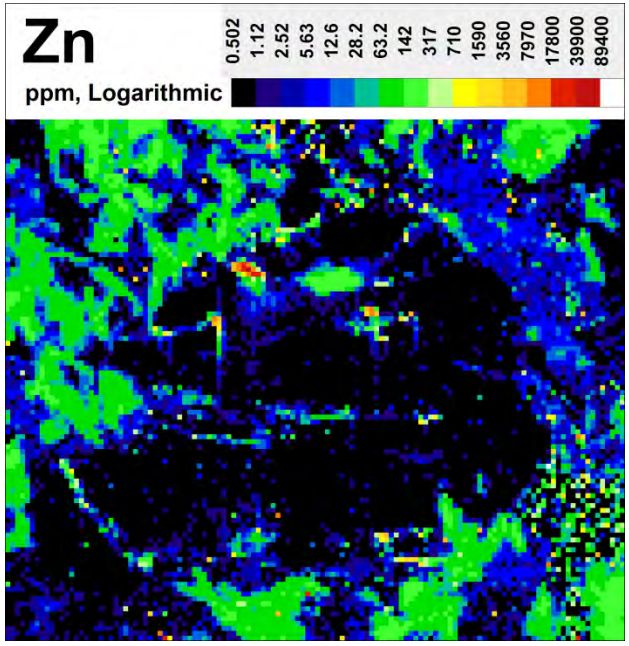
Zn
ppm, Logarithmic
0.502 1.12 2.52 5.63 12.6 28.2 63.2 142 317 710 1590 3560 7970 17800 39900 89400

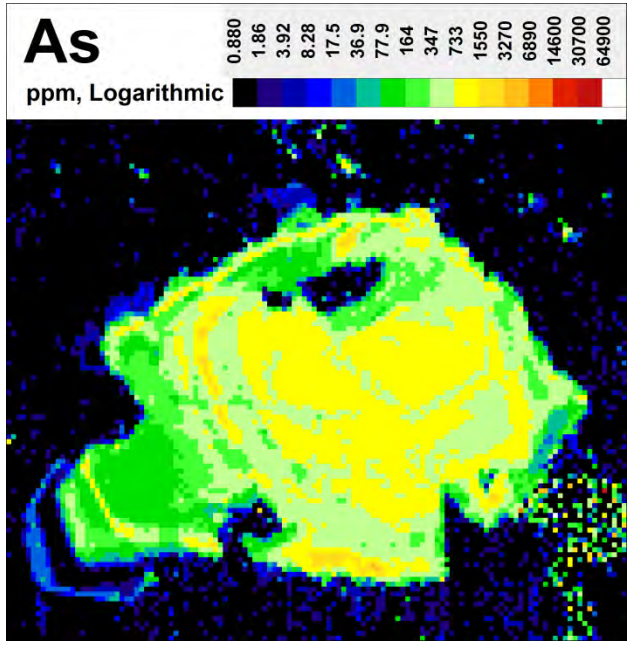
As
ppm, Logarithmic
0.880 1.86 3.92 8.28 17.5 36.9 77.9 164 347 733 1550 3270 6890 14600 30700 64900

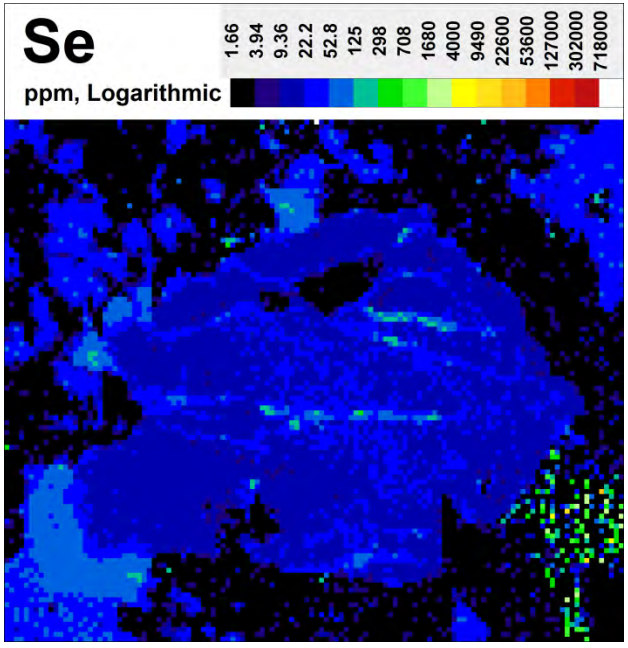
Se
ppm, Logarithmic
1.66 3.94 9.36 22.2 52.8 125 298 708 1680 4000 9490 22600 53600 127000 302000 718000

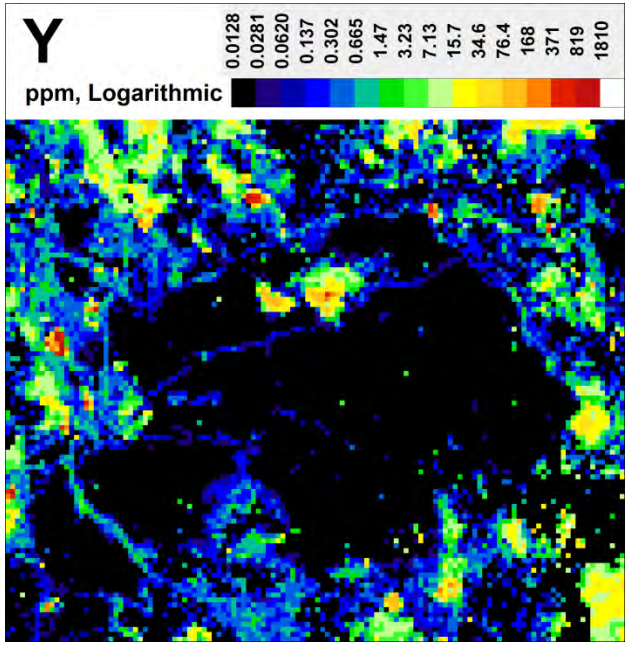
Y
ppm, Logarithmic
0.0128 0.0281 0.0620 0.137 0.302 0.665 1.47 3.23 7.13 15.7 34.6 76.4 168 371 819 1810

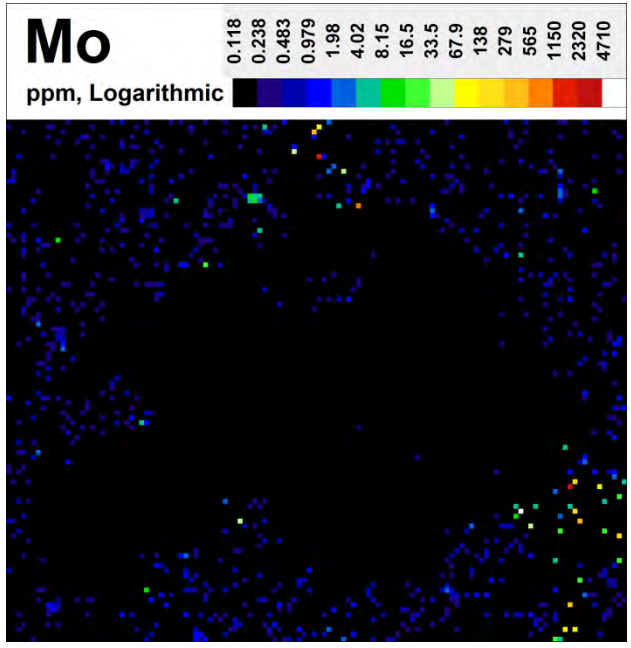
Mo
ppm, Logarithmic
0.118 0.238 0.483 0.979 1.98 4.02 8.15 16.5 33.5 67.9 138 279 565 1150 2320 4710

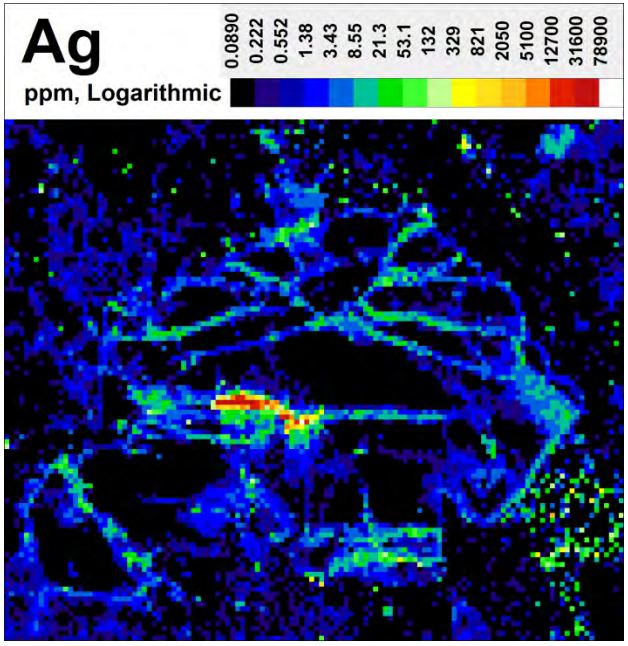
Ag
ppm, Logarithmic
0.0890
0.222
0.552
1.38
3.43
8.55
21.3
53.1
132
329
821
2050
5100
12700
31600
78900

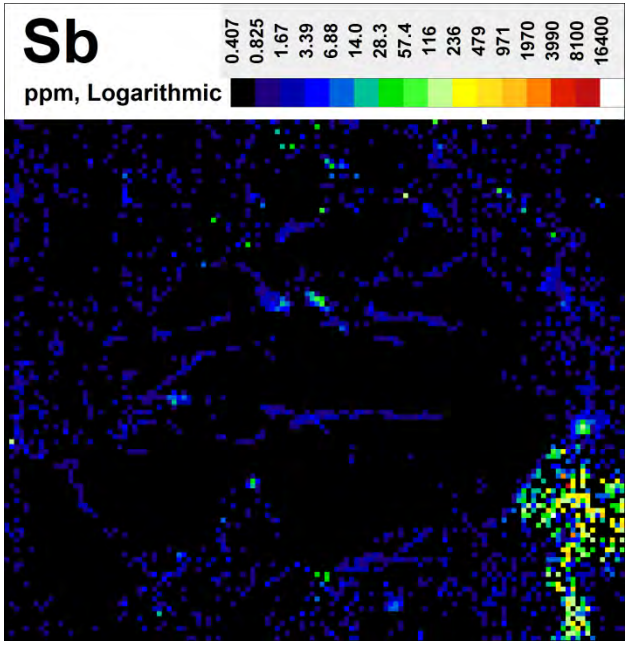
Sb
ppm, Logarithmic
0.407
0.825
1.67
3.39
6.88
14.0
28.3
57.4
116
236
479
971
1970
3990
8100
16400

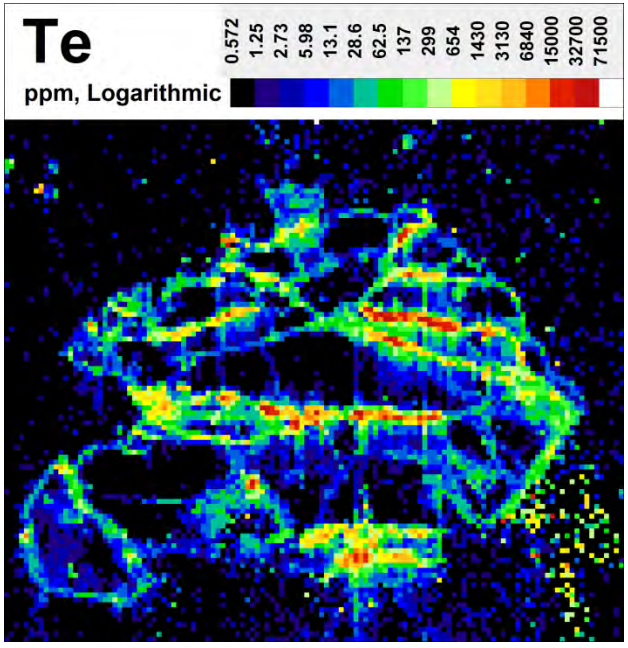
Te
ppm, Logarithmic
0.572
1.25
2.73
5.98
13.1
28.6
62.5
137
299
654
1430
3130
6840
15000
32700
71500

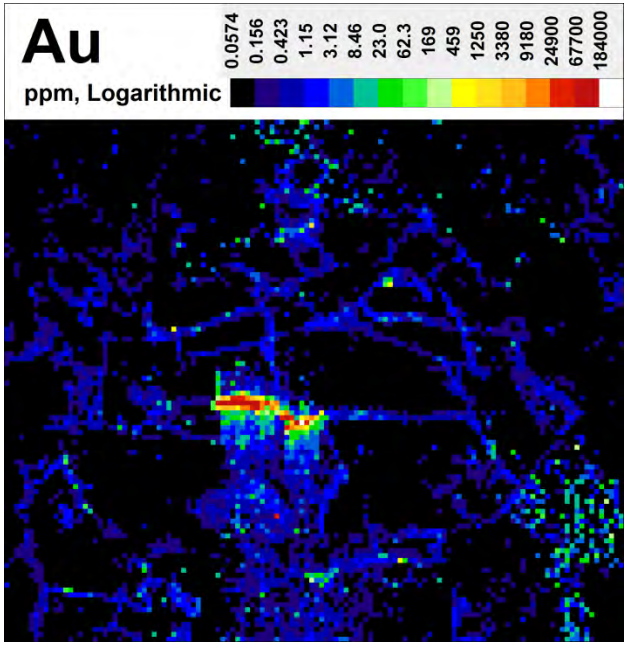
Au
ppm, Logarithmic
0.0574
0.156
0.423
1.15
3.12
8.46
23.0
62.3
169
459
1250
3380
9180
24900
67700
184000

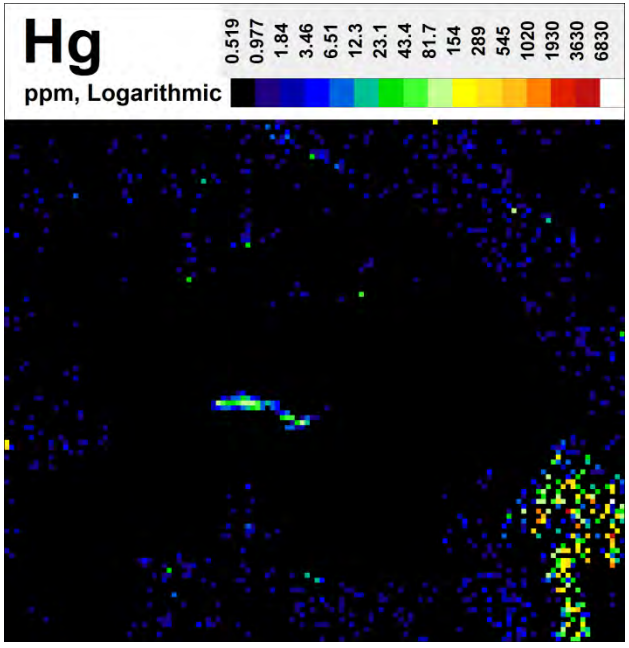
Hg
ppm, Logarithmic
0.519
0.977
1.84
3.46
6.51
12.3
23.1
43.4
81.7
154
289
545
1020
1930
3630
6830

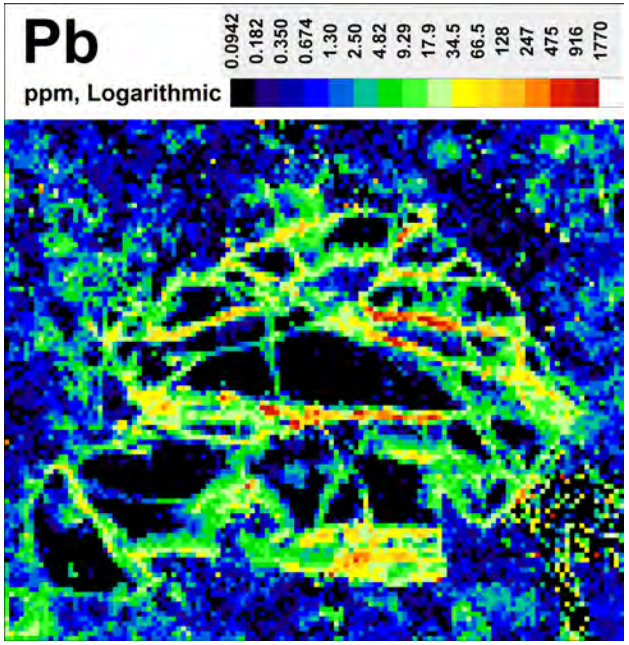
Pb
ppm, Logarithmic
0.0942
0.182
0.350
0.674
1.30
2.50
4.82
9.29
17.9
34.5
66.5
128
247
475
916
1770

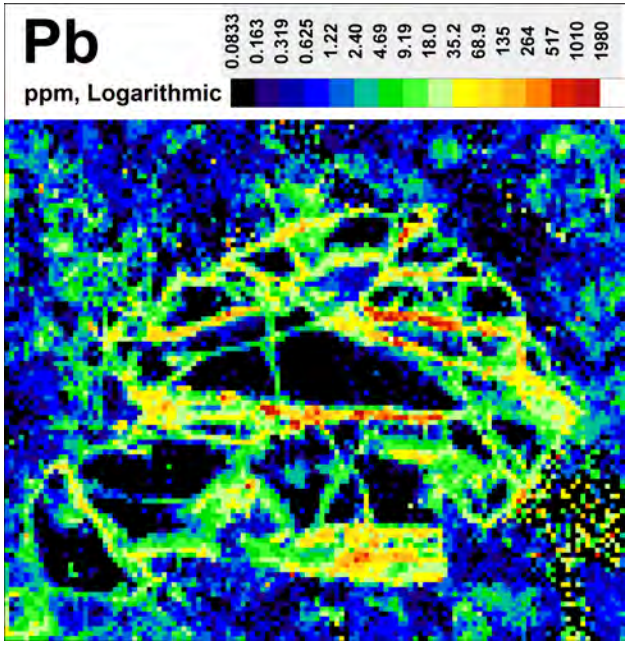
Pb
ppm, Logarithmic
0.0833
0.163
0.319
0.625
1.22
2.40
4.69
9.19
18.0
35.2
68.9
135
264
517
1010
1980

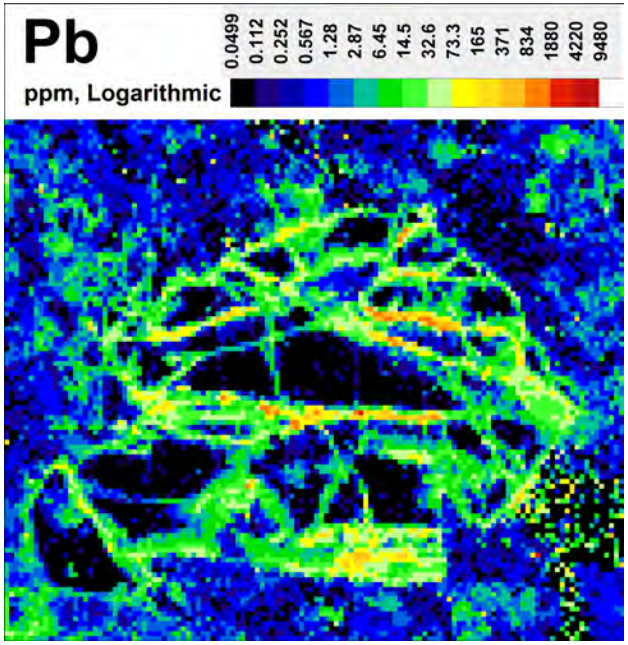
Pb
ppm, Logarithmic
0.0499
0.112
0.252
0.567
1.28
2.87
6.45
14.5
32.6
73.3
165
371
834
1880
4220
9480

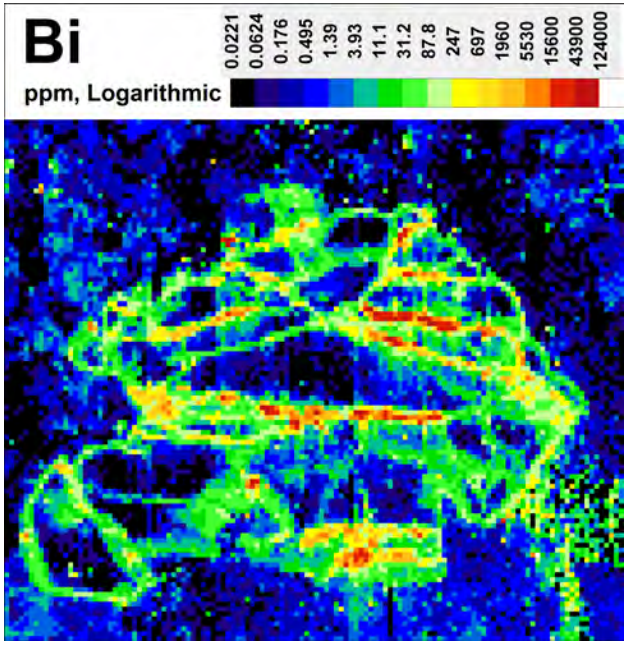
Bi
ppm, Logarithmic
0.0221
0.0624
0.176
0.495
1.39
3.93
11.1
31.2
87.8
247
697
1960
5530
15600
43900
124000

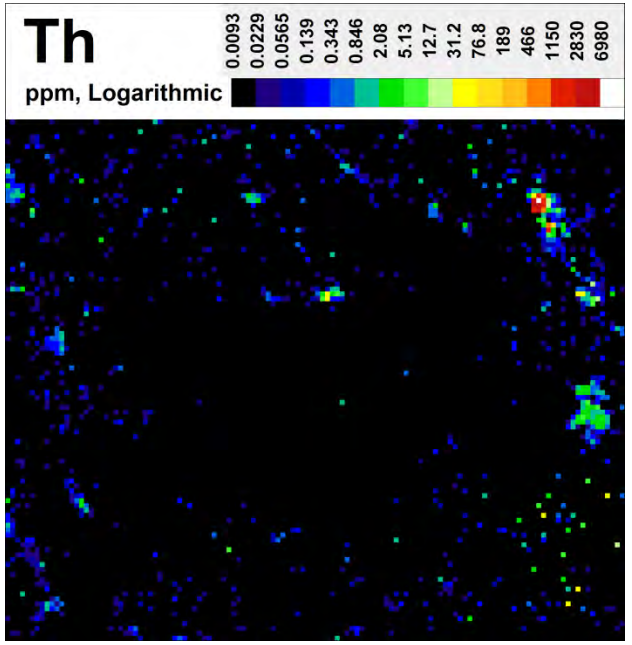
Th
ppm, Logarithmic
0.0093
0.0229
0.0565
0.139
0.343
0.846
2.08
5.13
12.7
31.2
76.8
189
466
1150
2830
6980

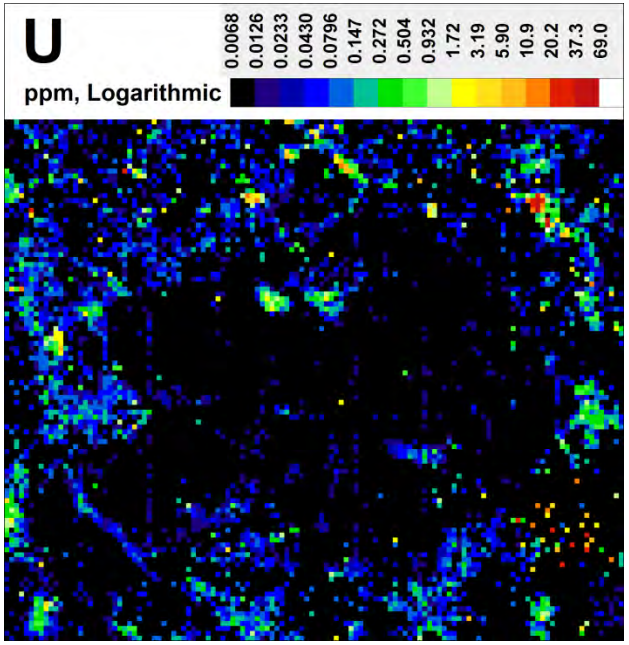
U
ppm, Logarithmic
0.0068
0.0126
0.0233
0.0430
0.0796
0.147
0.272
0.504
0.932
1.72
3.19
5.90
10.9
20.2
37.3
69.0

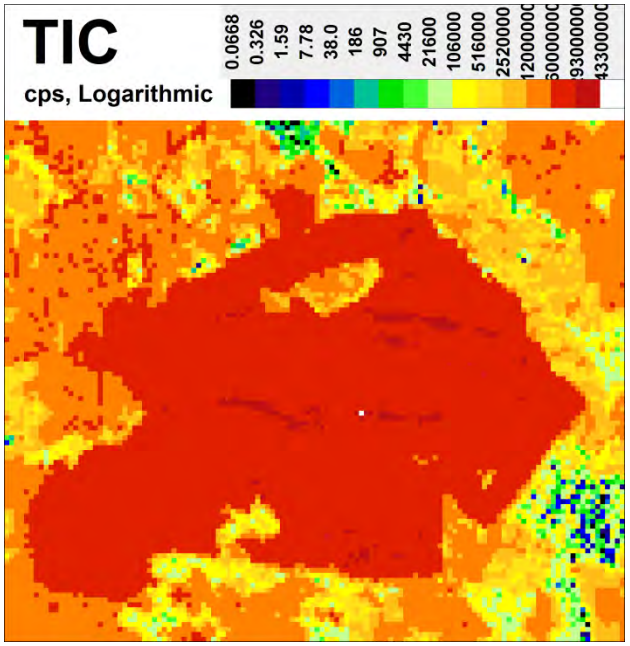
TIC
cps, Logarithmic
0.0668
0.326
1.59
7.78
38.0
186
907
4430
21600
106000
516000
2520000

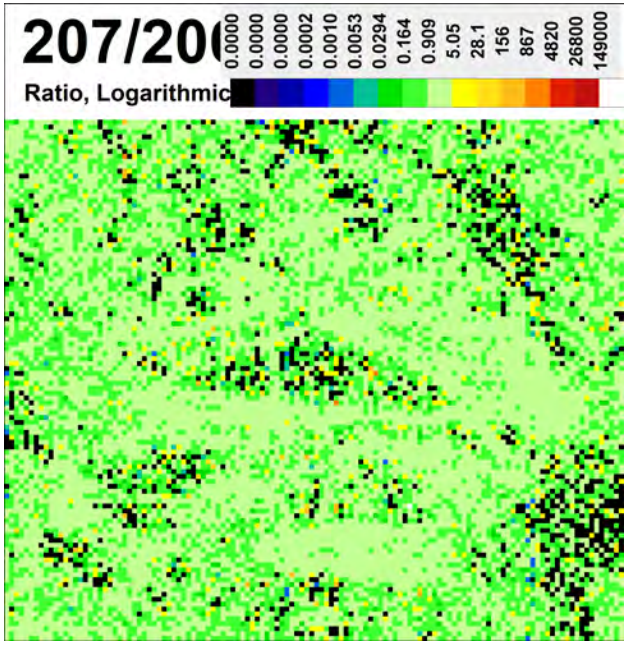
207/20(
Ratio, Logarithmic
0.0000
0.0000
0.0000
0.0002
0.0010
0.0053
0.0294
0.164
0.909
5.05
28.1
156
867
4820
26800
149000

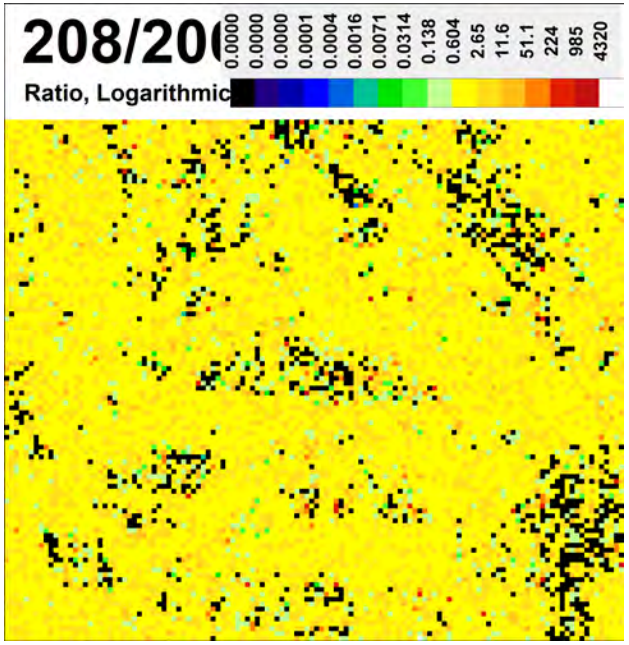
208/20(
Ratio, Logarithmic
0.0000
0.0000
0.0000
0.0001
0.0004
0.0016
0.0071
0.0314
0.138
0.604
2.65
11.6
51.1
224
985
4320

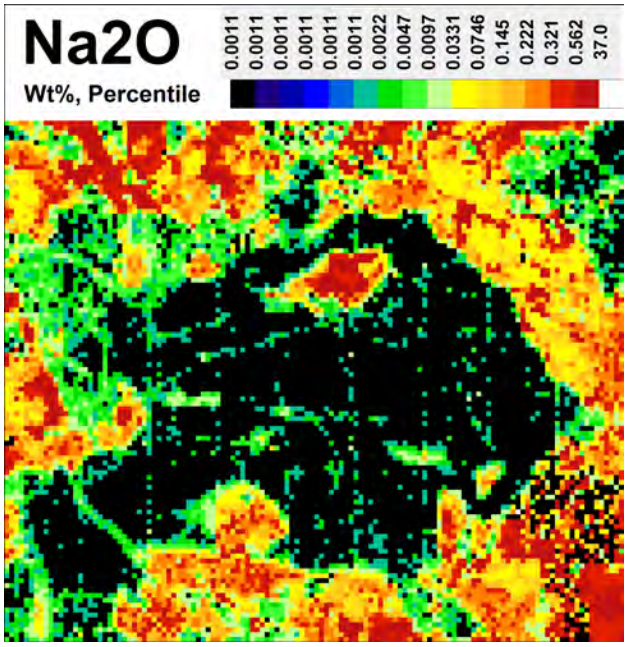
Na2O
Wt%, Percentile
0.0011 0.0011 0.0011 0.0011 0.0011 0.0011 0.0022 0.0047 0.0097 0.0331 0.0746 0.145 0.222 0.321 0.562 37.0

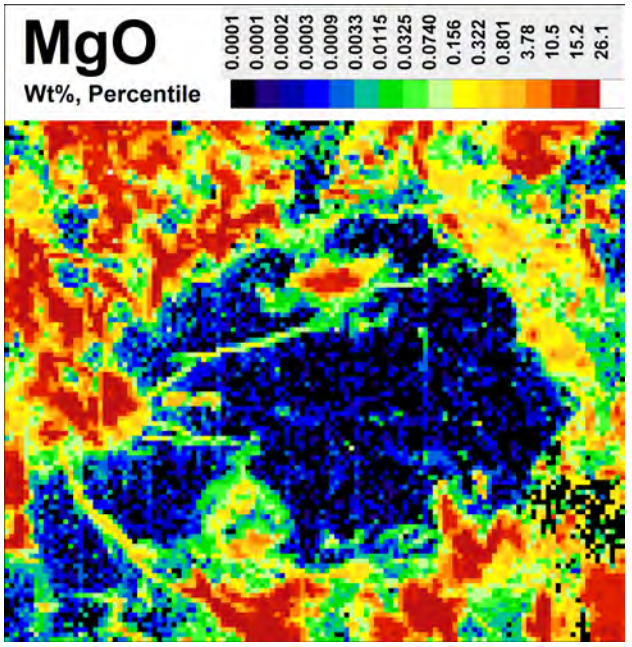
MgO
Wt%, Percentile
0.0001 0.0001 0.0002 0.0003 0.0009 0.0033 0.0115 0.0325 0.0740 0.156 0.322 0.801 3.78 10.5 15.2 26.1

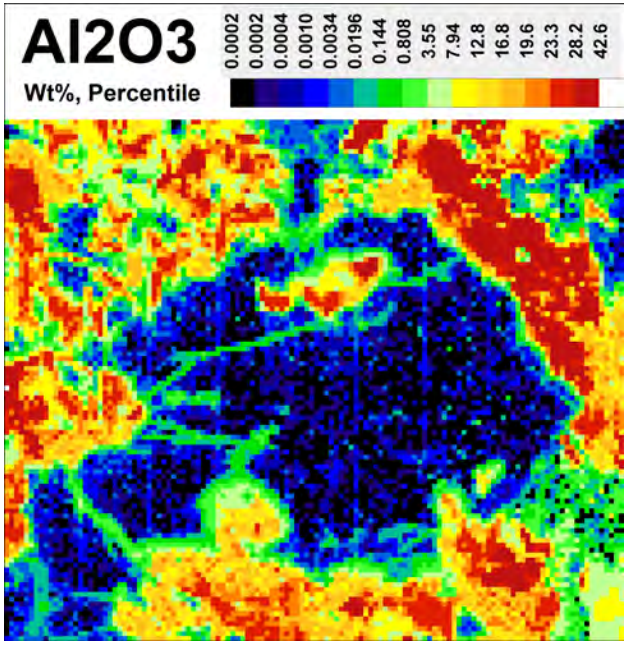
Al2O3
Wt%, Percentile
0.0002 0.0002 0.0004 0.0010 0.0034 0.0196 0.144 0.808 3.55 7.94 12.8 16.8 19.6 23.3 28.2 42.6

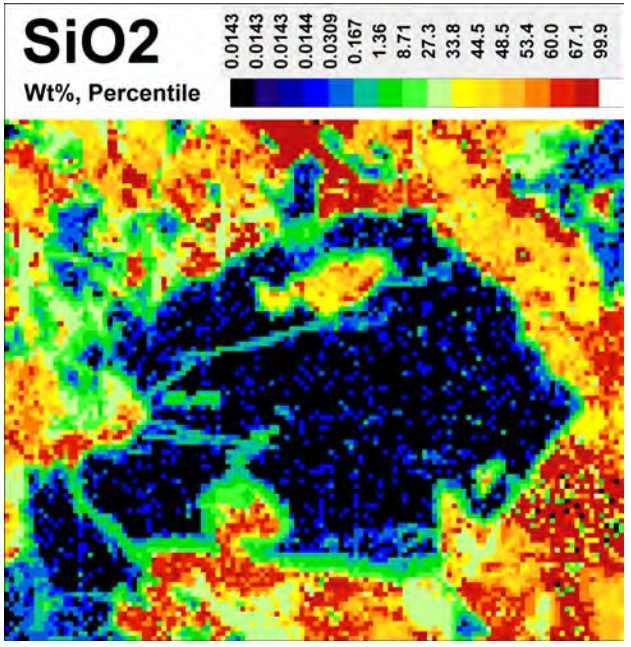
SiO2
Wt%, Percentile
0.0143 0.0143 0.0143 0.0144 0.0309 0.167 1.36 8.71 27.3 33.8 44.5 48.5 53.4 60.0 67.1 99.9

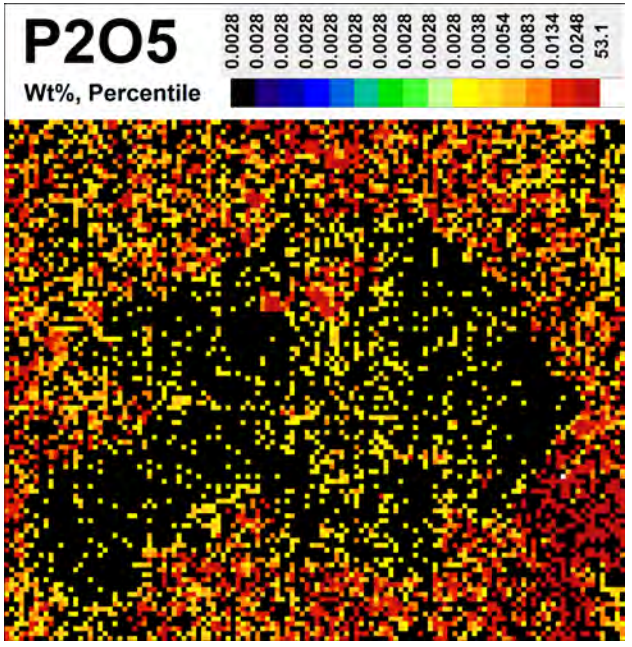
P2O5
Wt%, Percentile
0.0028 0.0028 0.0028 0.0028 0.0028 0.0028 0.0028 0.0028 0.0028 0.0038 0.0054 0.0083 0.0134 0.0248 53.1

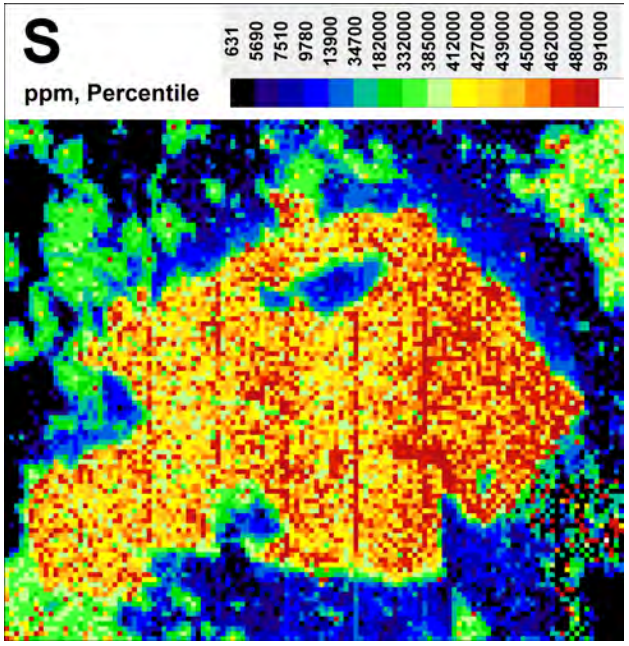
S
ppm, Percentile
631 5690 7510 9780 13900 34700 182000 332000 385000 412000 427000 439000 450000 462000 480000 991000

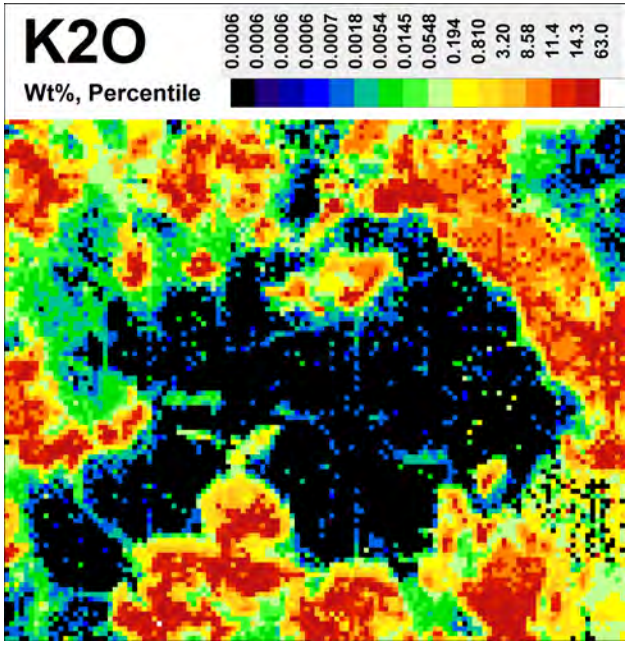
K2O
Wt%, Percentile
0.0006 0.0006 0.0006 0.0006 0.0007 0.0018 0.0054 0.0145 0.0548 0.194 0.810 3.20 8.58 11.4 14.3 63.0

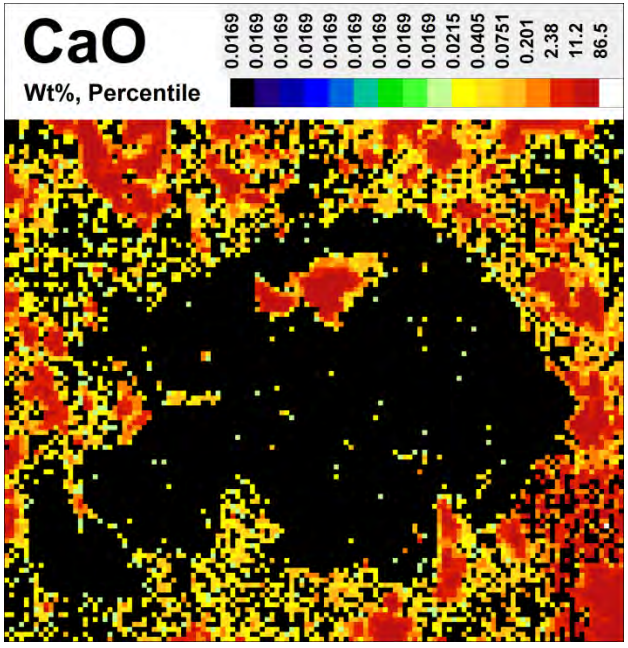
CaO
Wt%, Percentile
0.0169 0.0169 0.0169 0.0169 0.0169 0.0169 0.0169 0.0169 0.0215 0.0405 0.0751 0.201 2.38 11.2 86.5

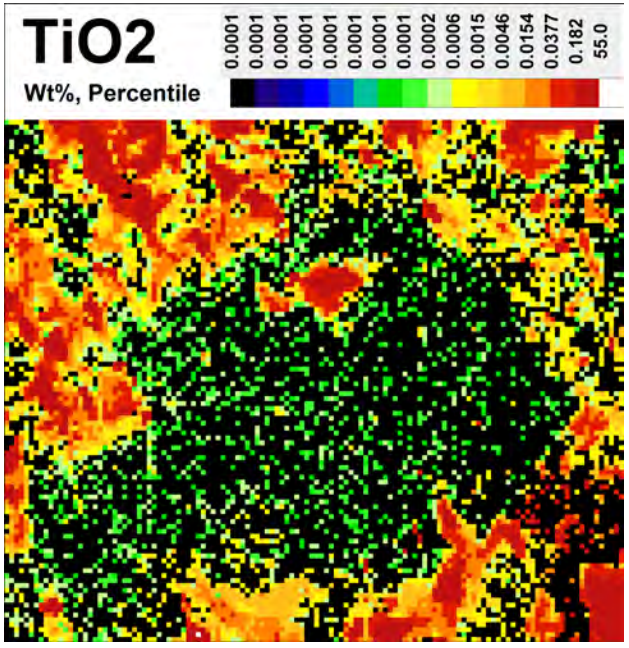
TiO2
Wt%, Percentile
0.0001 0.0001 0.0001 0.0001 0.0001 0.0001 0.0001 0.0002 0.0006 0.0015 0.0046 0.0154 0.0377 0.182 55.0

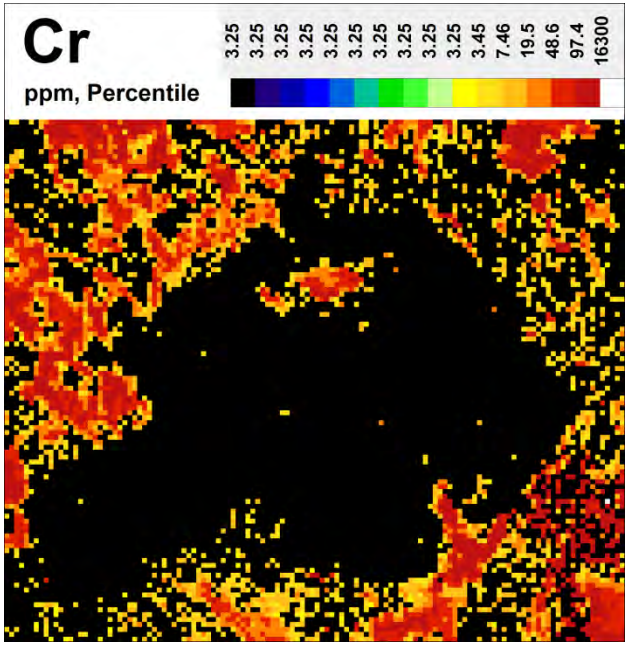
Cr
ppm, Percentile
3.25 3.25 3.25 3.25 3.25 3.25 3.25 3.25 3.25 3.25 3.45 7.46 19.5 48.6 97.4 16300

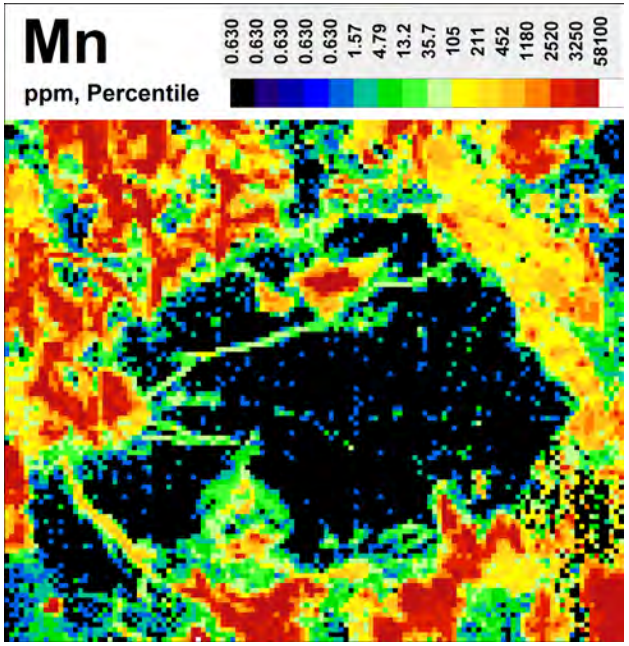
Mn
ppm, Percentile
0.630
0.630
0.630
0.630
0.630
1.57
4.79
13.2
35.7
105
211
452
1180
2520
3250
58100

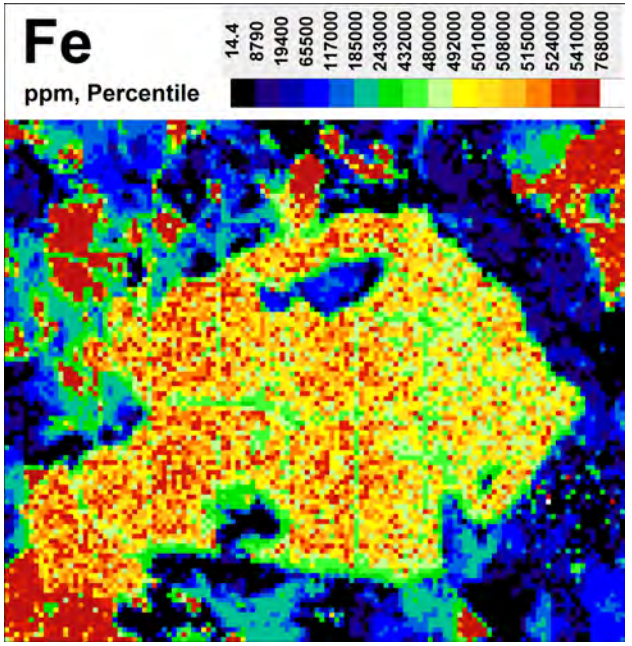
Fe
ppm, Percentile
14.4
8790
19400
65500
117000
185000
243000
432000
480000
492000
501000
508000
515000
524000
541000
768000

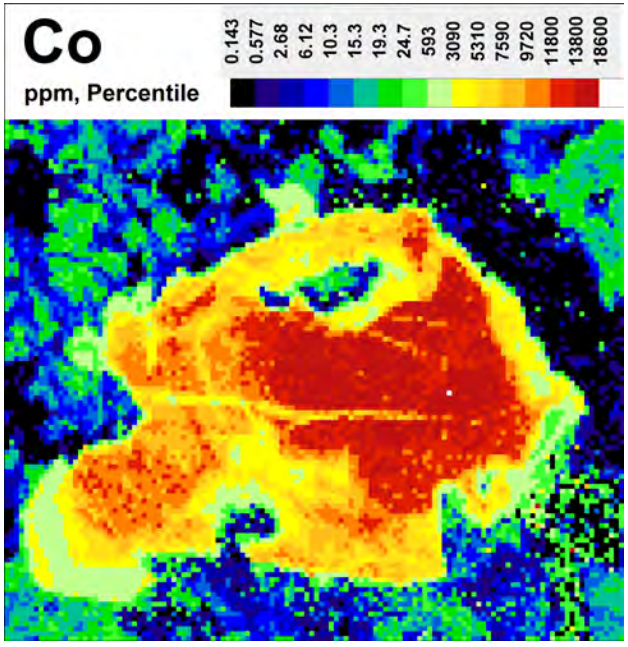
Co
ppm, Percentile
0.143
0.577
2.68
6.12
10.3
15.3
19.3
24.7
593
3090
5310
7590
9720
11800
13800
18600

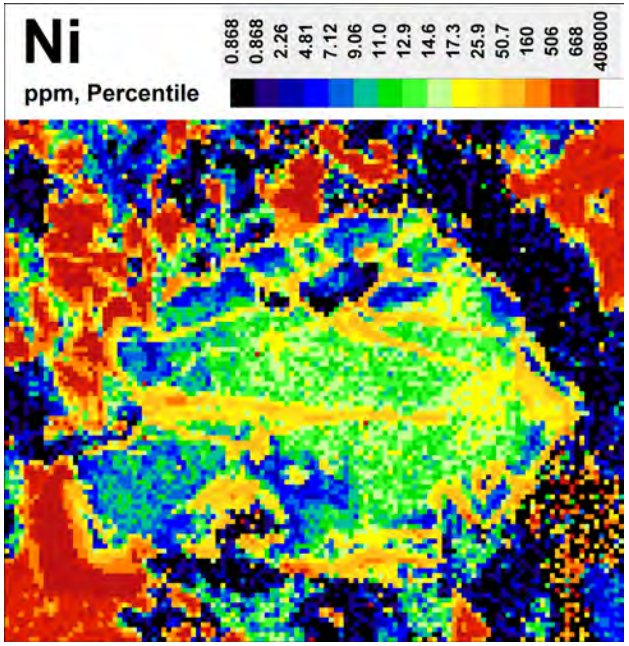
Ni
ppm, Percentile
0.868
0.868
2.26
4.81
7.12
9.06
11.0
12.9
14.6
17.3
25.9
50.7
160
506
668
408000

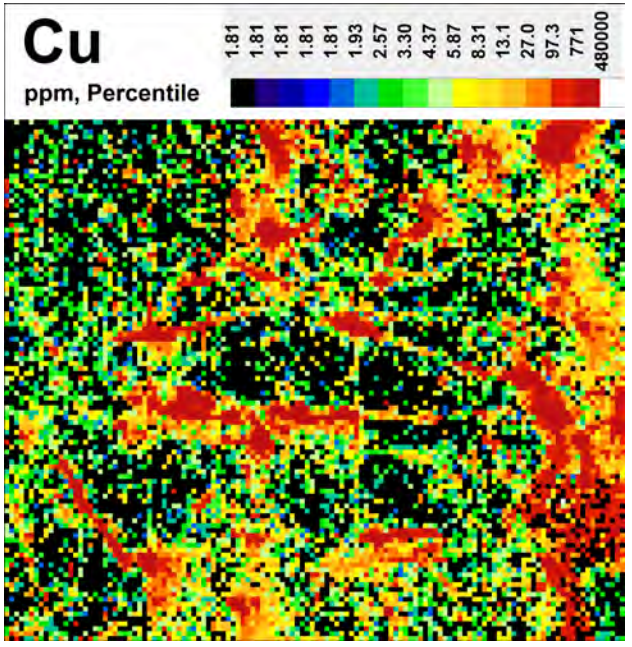
Cu
ppm, Percentile
1.81
1.81
1.81
1.81
1.81
1.93
2.57
3.30
4.37
5.87
8.31
13.1
27.0
97.3
771
480000

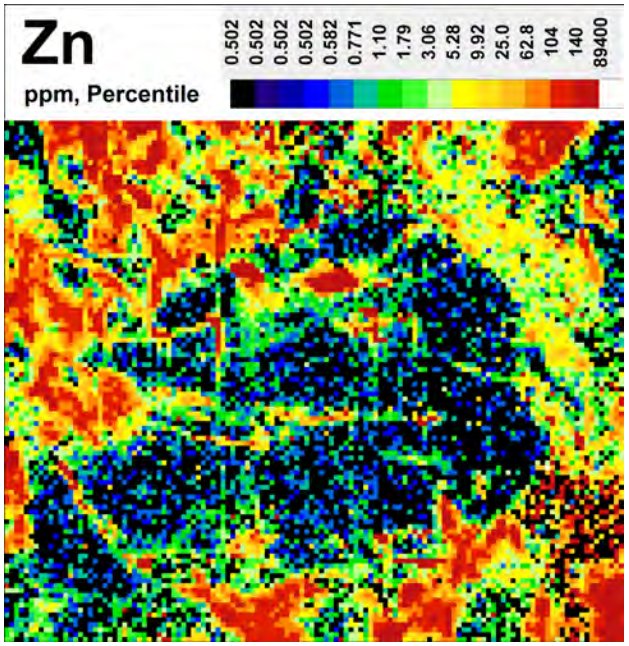
Zn
ppm, Percentile
0.502 0.502 0.502 0.502 0.582 0.771 1.10 1.79 3.06 5.28 9.92 25.0 62.8 104 140 89400

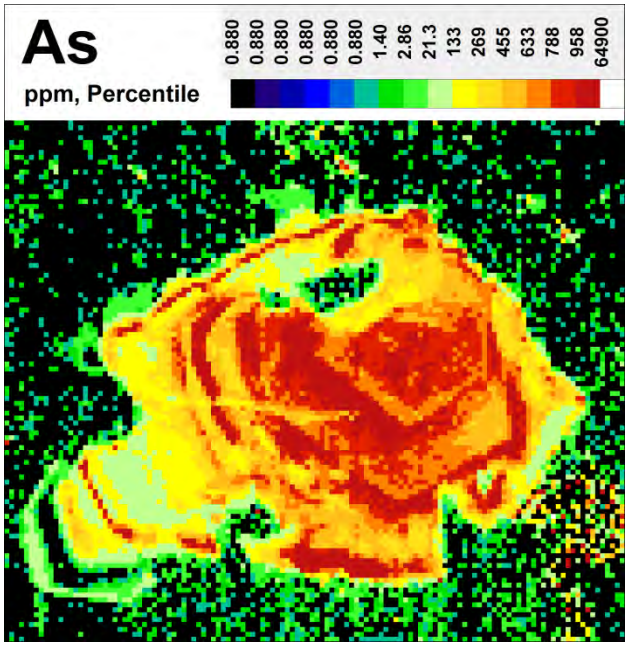
As
ppm, Percentile
0.880 0.880 0.880 0.880 0.880 0.880 1.40 2.86 21.3 133 269 455 633 788 958 64900

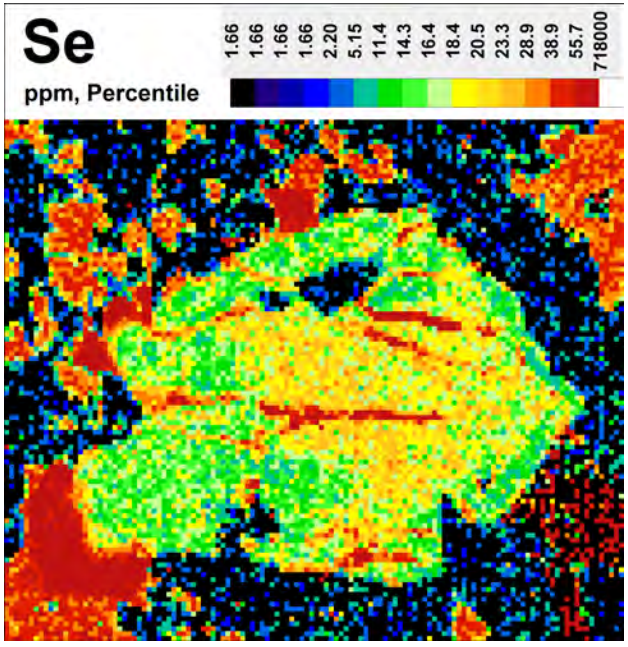
Se
ppm, Percentile
1.66 1.66 1.66 1.66 2.20 5.15 11.4 14.3 16.4 18.4 20.5 23.3 28.9 38.9 55.7 718000

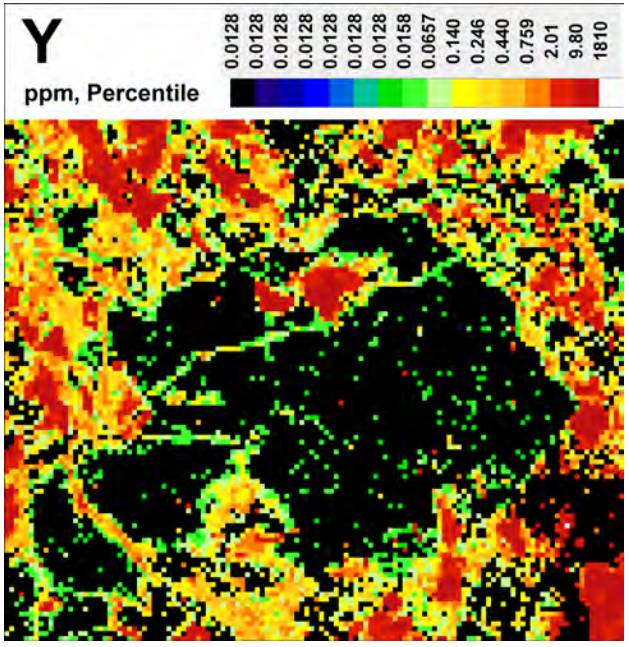
Y
ppm, Percentile
0.0128 0.0128 0.0128 0.0128 0.0128 0.0128 0.0128 0.0158 0.0657 0.140 0.246 0.440 0.759 2.01 9.80 1810

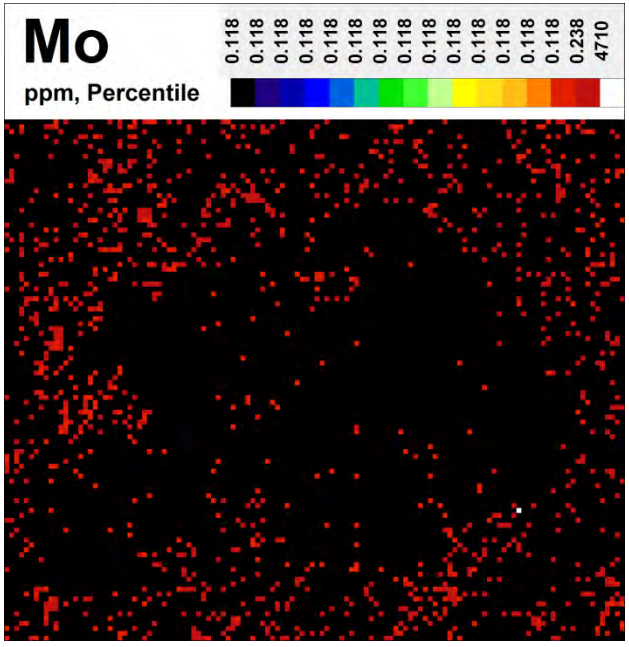
Mo
ppm, Percentile
0.118 0.118 0.118 0.118 0.118 0.118 0.118 0.118 0.118 0.118 0.118 0.118 0.118 0.238 4710

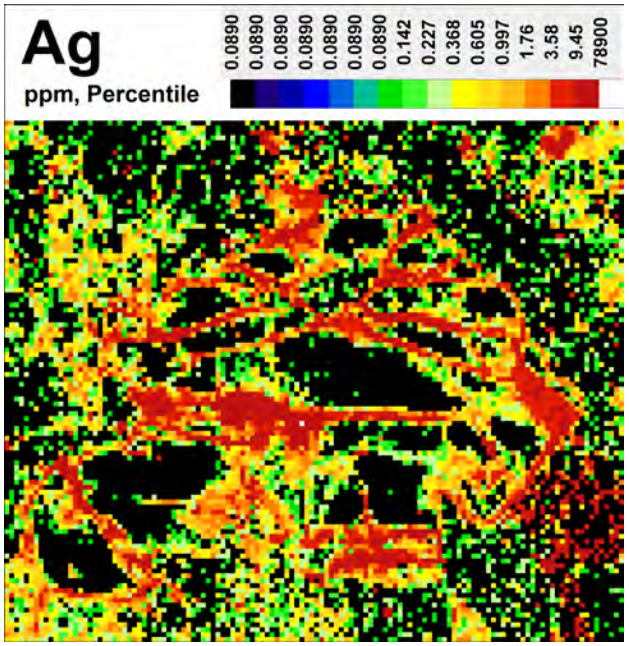
Ag
ppm, Percentile
0.0890 0.0890 0.0890 0.0890 0.0890 0.0890 0.0890 0.142 0.227 0.368 0.605 0.997 1.76 3.58 9.45 78900

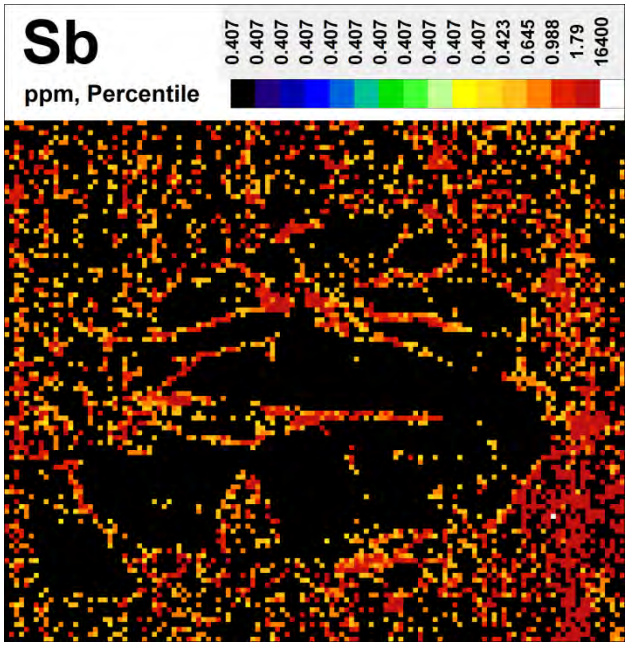
Sb
ppm, Percentile
0.407 0.407 0.407 0.407 0.407 0.407 0.407 0.407 0.407 0.407 0.423 0.645 0.988 1.79 16400

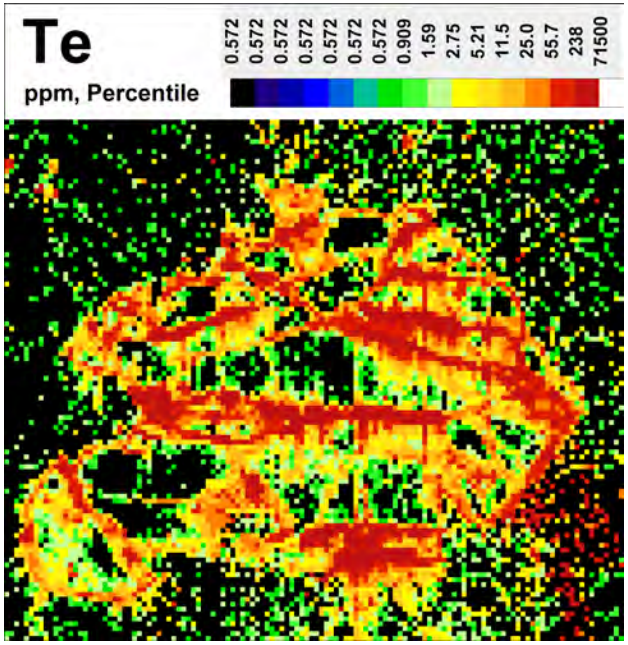
Te
ppm, Percentile
0.572 0.572 0.572 0.572 0.572 0.572 0.572 0.909 1.59 2.75 5.21 11.5 25.0 55.7 238 71500

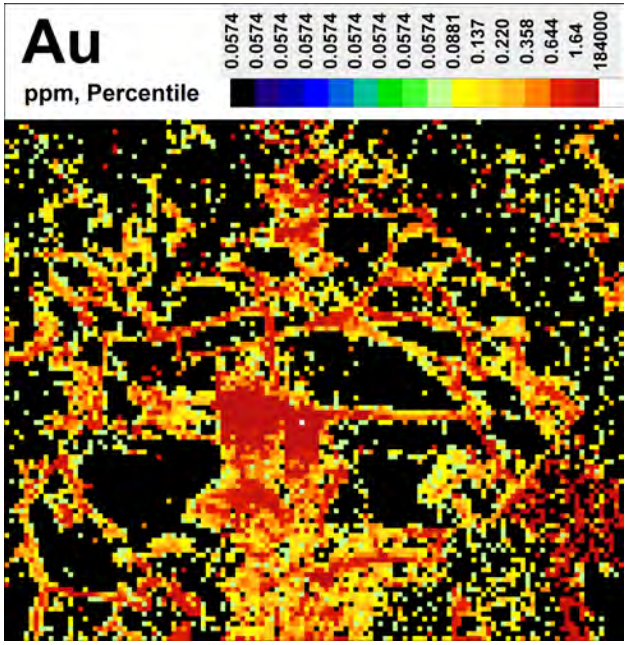
Au
ppm, Percentile
0.0574 0.0574 0.0574 0.0574 0.0574 0.0574 0.0574 0.0574 0.0574 0.0881 0.137 0.220 0.358 0.644 1.64 184000

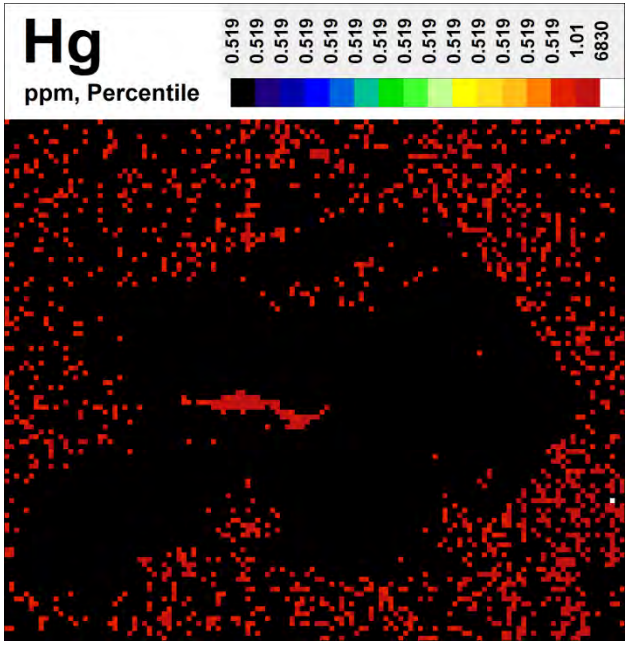
Hg
ppm, Percentile
0.519 0.519 0.519 0.519 0.519 0.519 0.519 0.519 0.519 0.519 0.519 0.519 0.519 1.01 6830

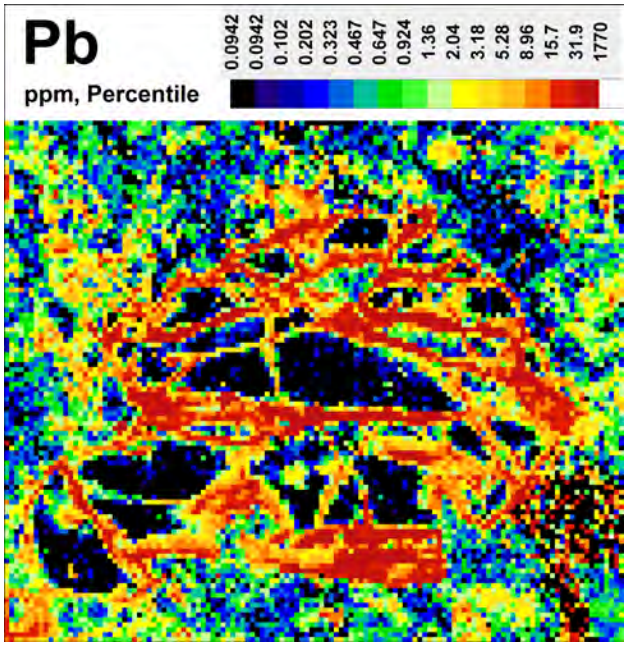
Pb
ppm, Percentile
0.0942
0.0942
0.102
0.202
0.323
0.467
0.647
0.924
1.36
2.04
3.18
5.28
8.96
15.7
31.9
1770

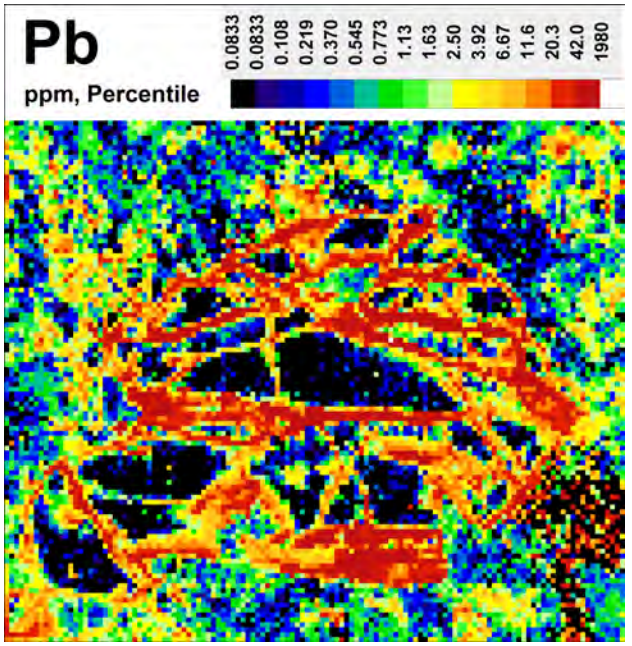
Pb
ppm, Percentile
0.0833
0.0833
0.108
0.219
0.370
0.545
0.773
1.13
1.63
2.50
3.92
6.67
11.6
20.3
42.0
1980

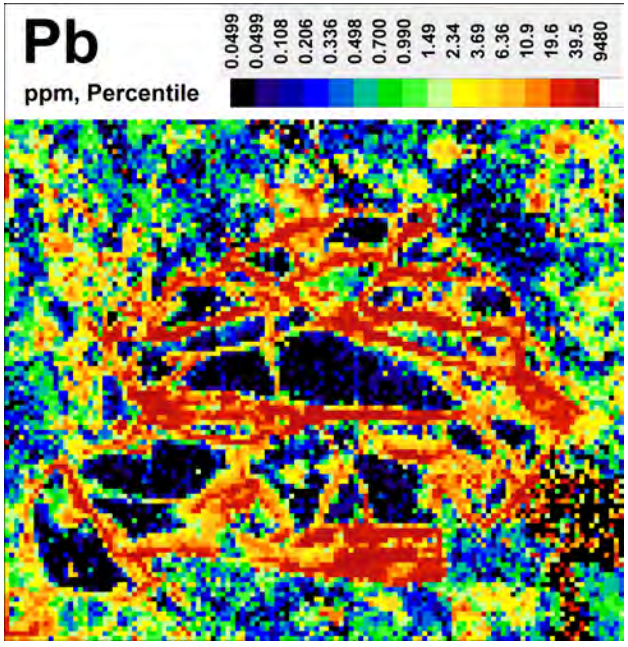
Pb
ppm, Percentile
0.0499
0.0499
0.108
0.206
0.336
0.498
0.700
0.990
1.49
2.34
3.69
6.36
10.9
19.6
39.5
9480

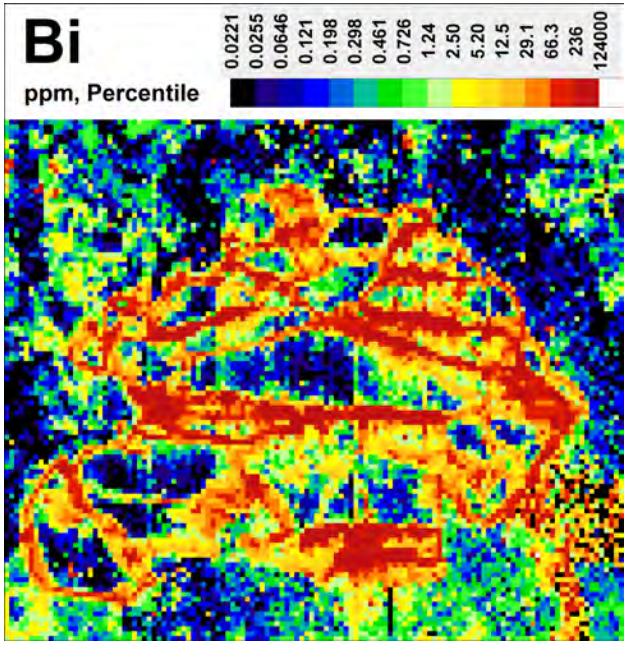
Bi
ppm, Percentile
0.0221
0.0255
0.0646
0.121
0.198
0.298
0.461
0.726
1.24
2.50
5.20
12.5
29.1
66.3
236
124000

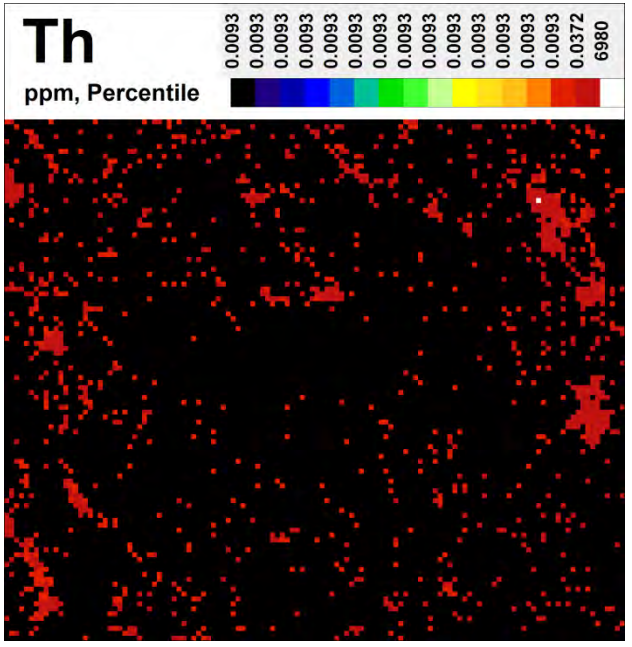
Th
ppm, Percentile
0.0093
0.0093
0.0093
0.0093
0.0093
0.0093
0.0093
0.0093
0.0093
0.0093
0.0093
0.0093
0.0093
0.0372
6980

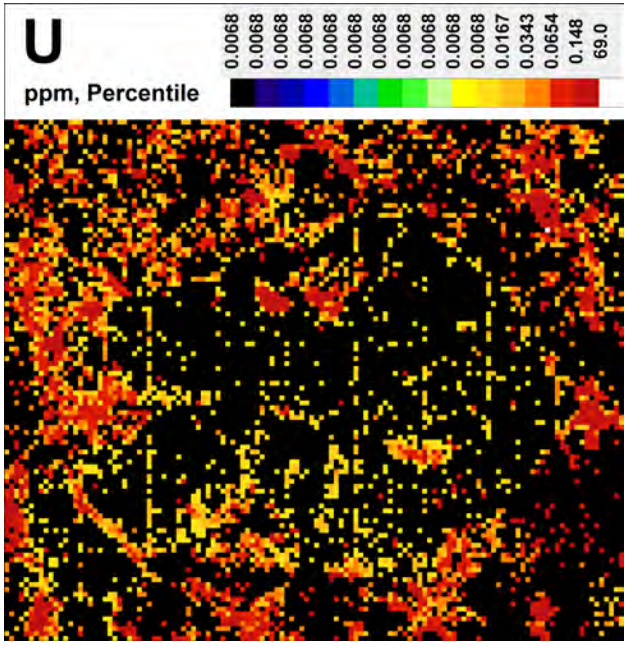
U
ppm, Percentile
0.0068
0.0068
0.0068
0.0068
0.0068
0.0068
0.0068
0.0068
0.0068
0.0068
0.0167
0.0343
0.0654
0.148
69.0

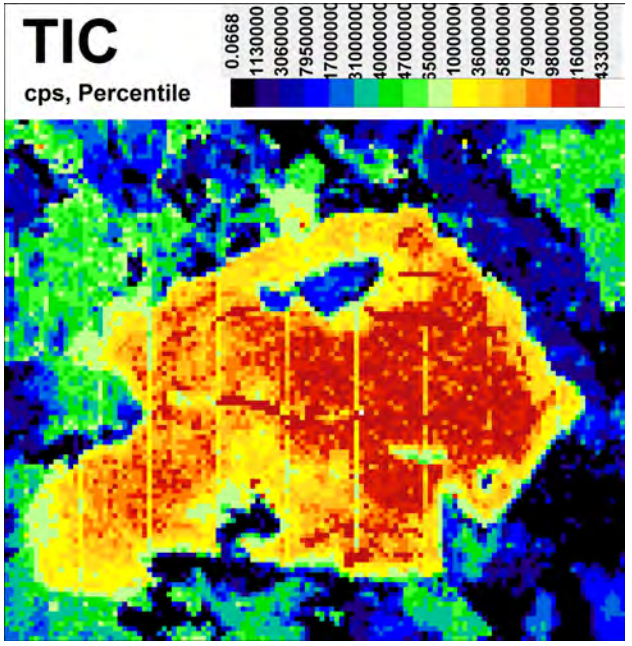
TIC
cps, Percentile
0.0668
1130000
3060000
7950000
17000000
31000000
40000000
47000000
55000000
1000000
36000000
58000000
79000000
98000000
16000000
43300000

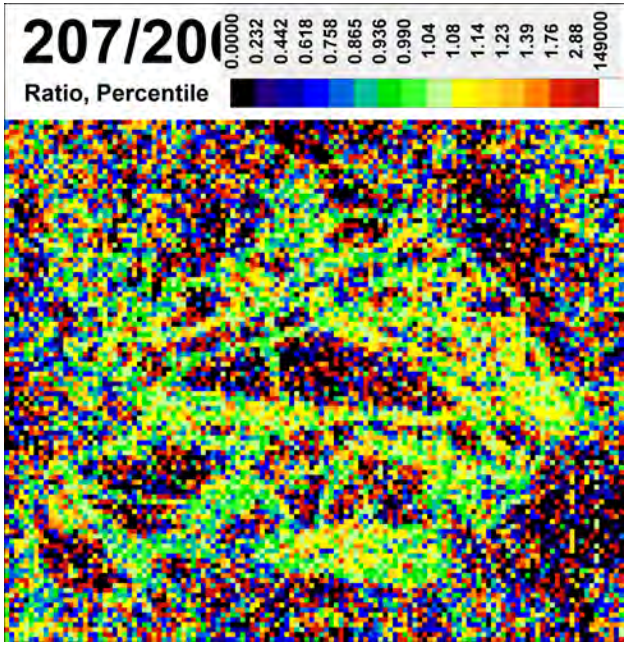
207/20(
Ratio, Percentile
0.0000
0.232
0.442
0.618
0.758
0.865
0.936
0.990
1.04
1.08
1.14
1.23
1.39
1.76
2.88
149000

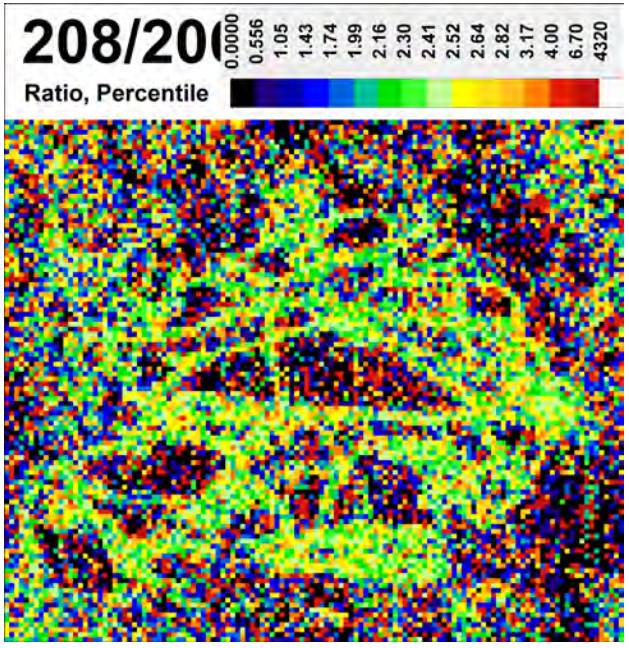
208/20(
Ratio, Percentile
0.0000
0.556
1.05
1.43
1.74
1.99
2.16
2.30
2.41
2.52
2.64
2.82
3.17
4.00
6.70
4320

Figure DR6. (pages 120–133) LA-ICP-MS results of a type-2a pyrite porphyroblast within a mafic volcanic sample (RD15-118-251) showing a reflected light photomicrograph of the mapping area and 32 major and trace maps. LA-ICP-MS maps reveal oscillatory growth zoning of first-row transition metals (Cr-Co-Ni-Cu-Zn) and some post-transition metals (Pb) and metalloids (As-Sb ± Se) and trace element enrichment (Zn-Y-Ag-Sb-Te-Au-Pb-Bi) in brittle fractures.

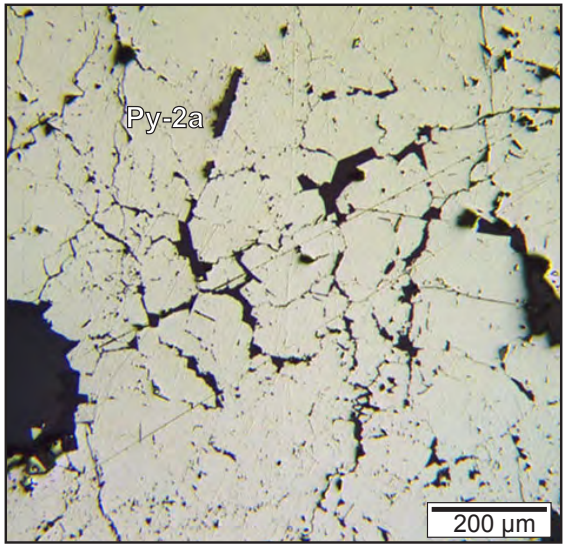
Py-2a
200 µm

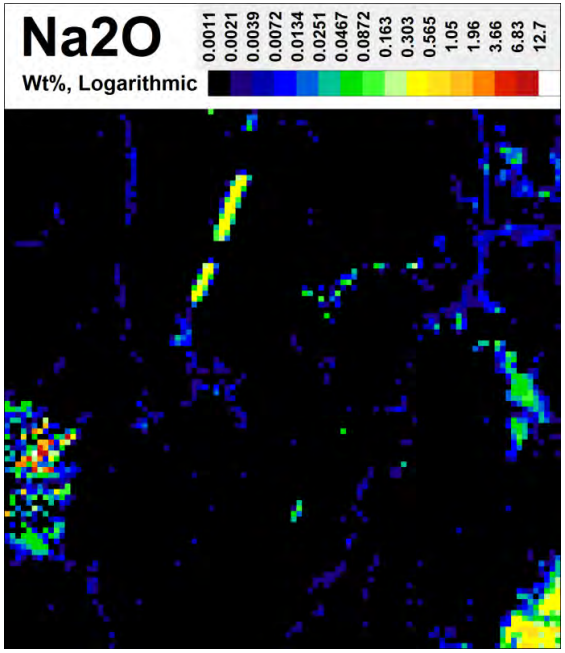
Na2O
Wt%, Logarithmic
0.0011 0.0021 0.0039 0.0072 0.0134 0.0251 0.0467 0.0872 0.163 0.303 0.565 1.05 1.96 3.66 6.83 12.7

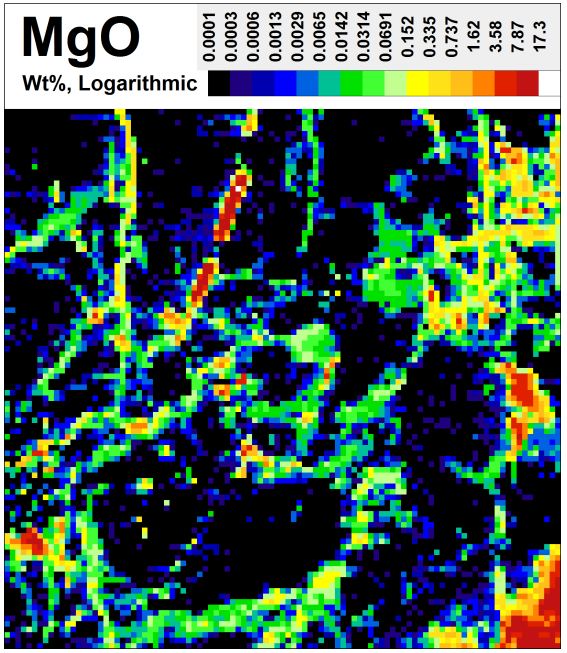
MgO
Wt%, Logarithmic
0.0001 0.0003 0.0006 0.0013 0.0029 0.0065 0.0142 0.0314 0.0691 0.152 0.335 0.737 1.62 3.58 7.87 17.3

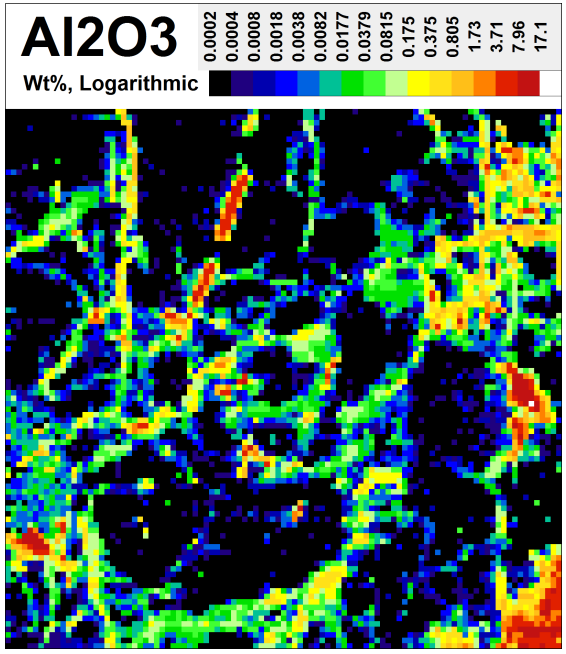
Al2O3
Wt%, Logarithmic
0.0002 0.0004 0.0008 0.0018 0.0038 0.0082 0.0177 0.0379 0.0815 0.175 0.375 0.805 1.73 3.71 7.96 17.1

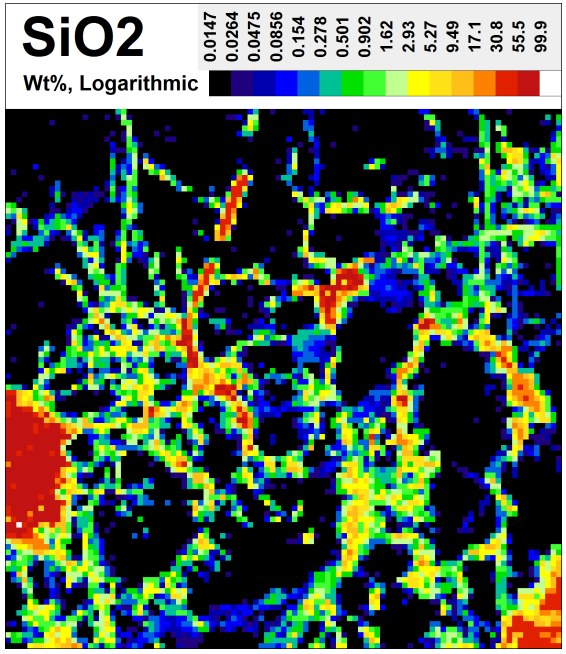
SiO2
Wt%, Logarithmic
0.0147 0.0264 0.0475 0.0856 0.154 0.278 0.501 0.902 1.62 2.93 5.27 9.49 17.1 30.8 55.5 99.9

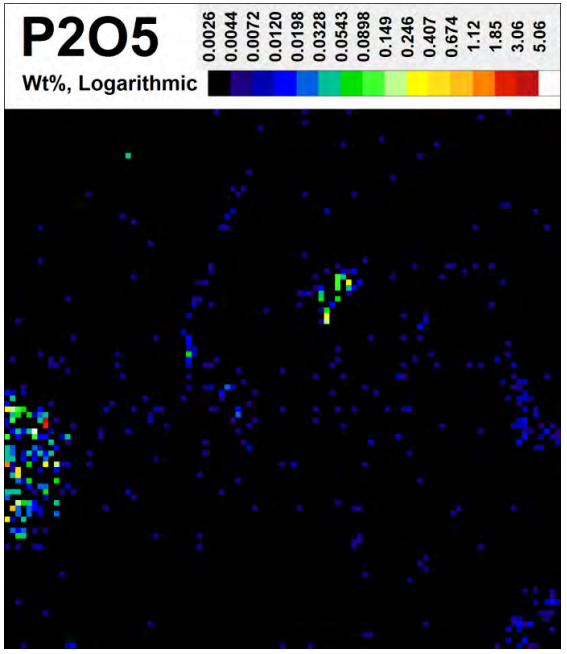
P2O5
Wt%, Logarithmic
0.0026 0.0044 0.0072 0.0120 0.0198 0.0328 0.0543 0.0898 0.149 0.246 0.407 0.674 1.12 1.85 3.06 5.06

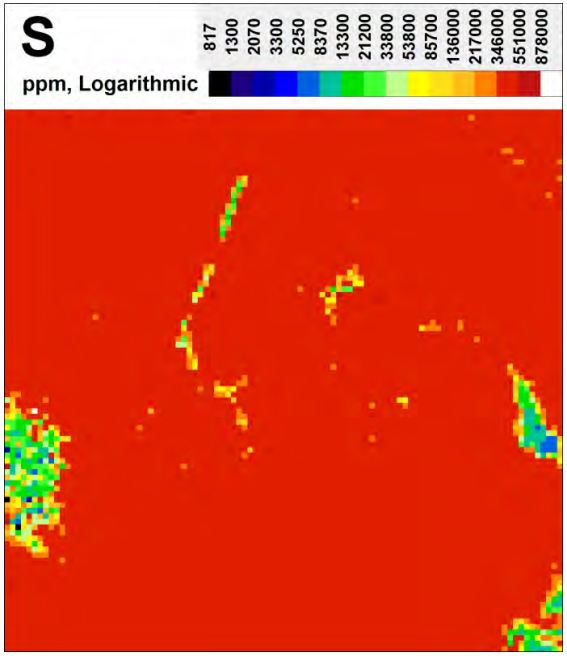
S
ppm, Logarithmic
817 1300 2070 3300 5250 8370 13300 21200 33800 53800 85700 136000 217000 346000 551000 878000

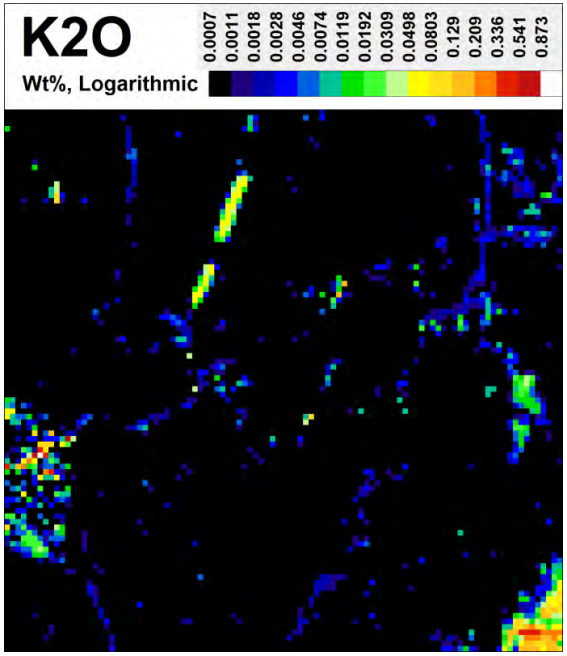
K2O
Wt%, Logarithmic
0.0007 0.0011 0.0018 0.0028 0.0046 0.0074 0.0119 0.0192 0.0309 0.0498 0.0803 0.129 0.209 0.336 0.541 0.873

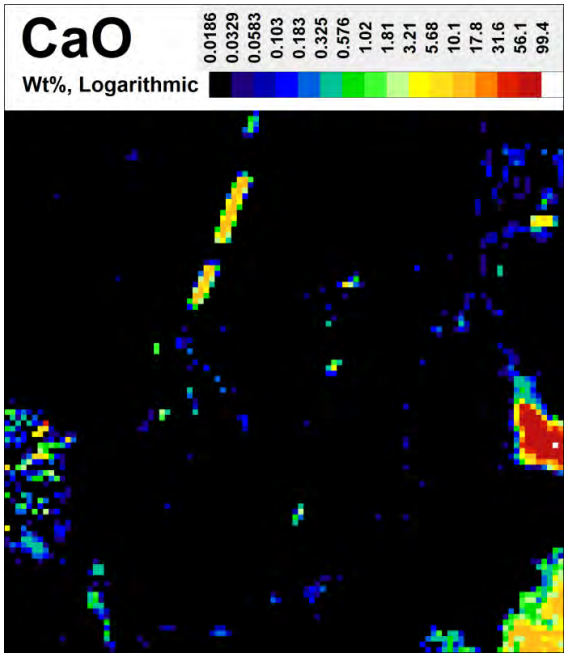
CaO
Wt%, Logarithmic
0.0186 0.0329 0.0583 0.103 0.183 0.325 0.576 1.02 1.81 3.21 5.68 10.1 17.8 31.6 56.1 99.4

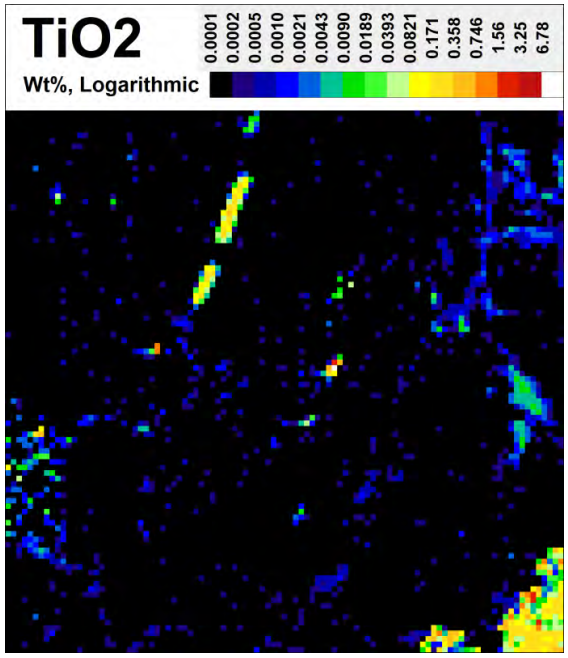
TiO2
Wt%, Logarithmic
0.0001 0.0002 0.0005 0.0010 0.0021 0.0043 0.0090 0.0189 0.0393 0.0821 0.171 0.358 0.746 1.56 3.25 6.78

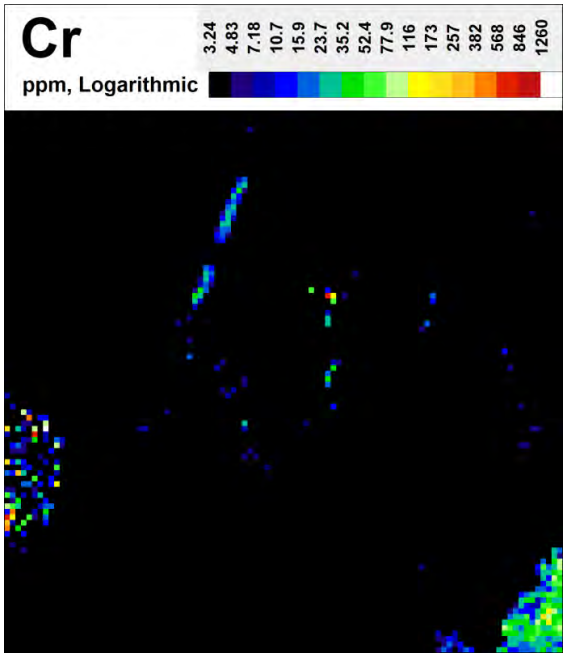
Cr
ppm, Logarithmic
3.24 4.83 7.18 10.7 15.9 23.7 35.2 52.4 77.9 116 173 257 382 568 846 1260

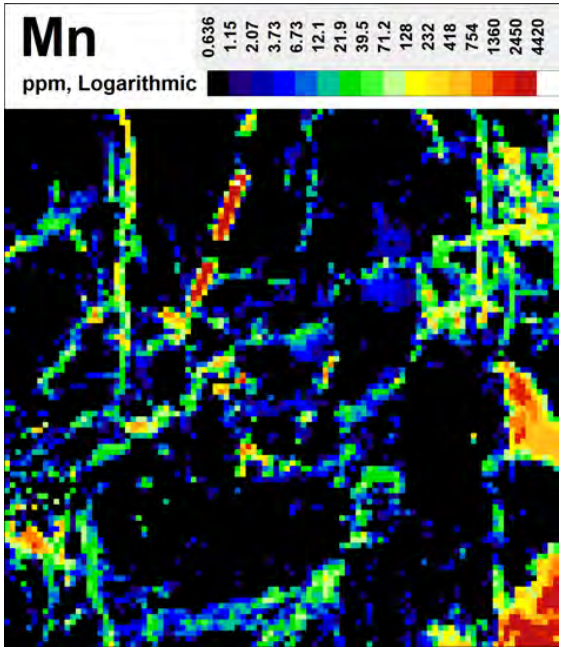
Mn
ppm, Logarithmic
0.636 1.15 2.07 3.73 6.73 12.1 21.9 39.5 71.2 128 232 418 754 1360 2450 4420

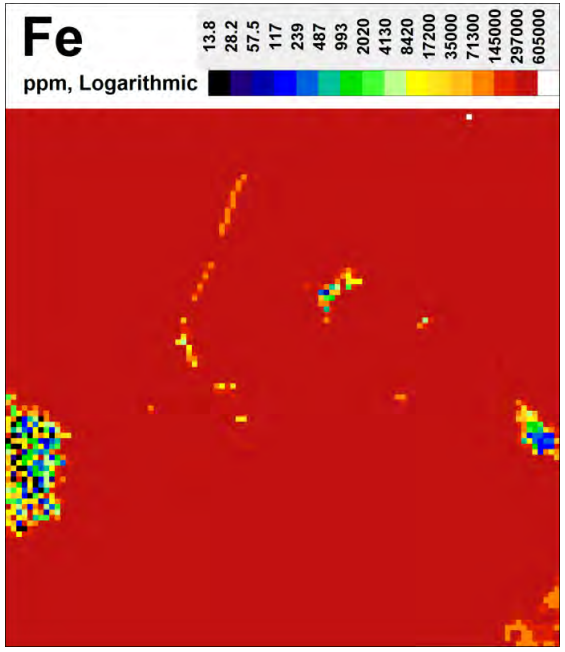
Fe
ppm, Logarithmic
13.8 28.2 57.5 117 239 487 993 2020 4130 8420 17200 35000 71300 145000 297000 605000

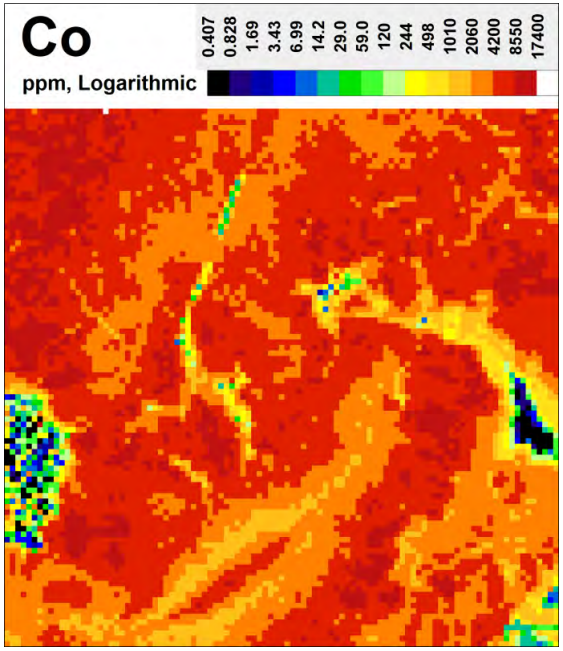
Co
ppm, Logarithmic
0.407 0.828 1.69 3.43 6.99 14.2 29.0 59.0 120 244 498 1010 2060 4200 8550 17400

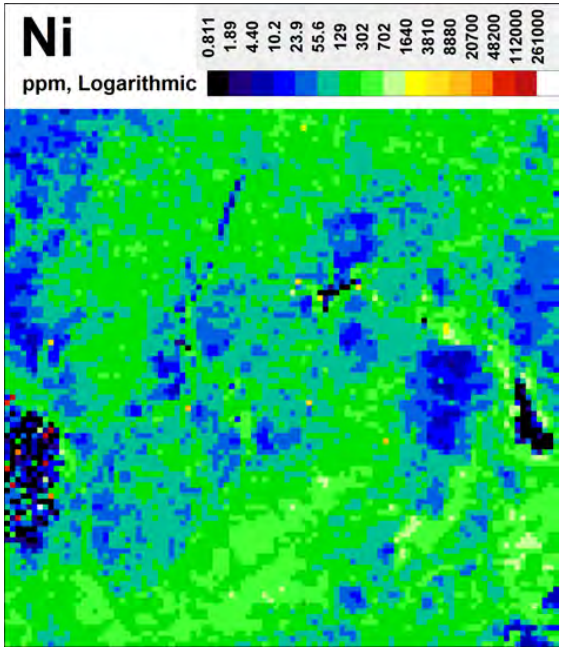
Ni
ppm, Logarithmic
0.811 1.89 4.40 10.2 23.9 55.6 129 302 702 1640 3810 8880 20700 48200 112000 261000

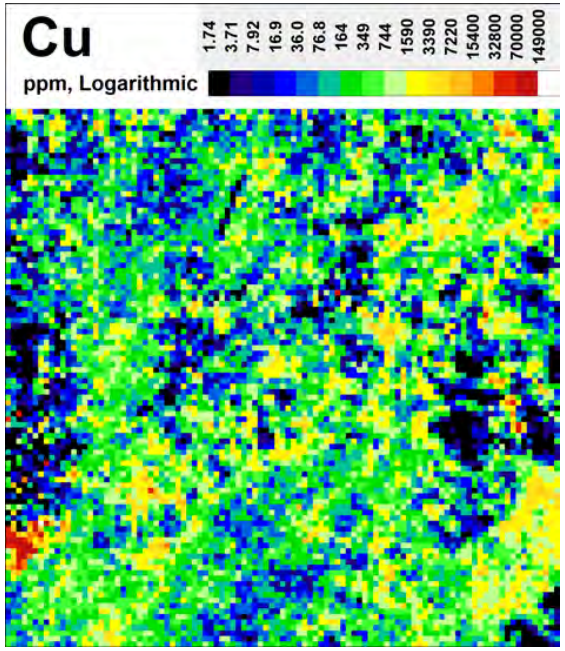
Cu
ppm, Logarithmic
1.74 3.71 7.92 16.9 36.0 76.8 164 349 744 1590 3390 7220 15400 32800 70000 149000

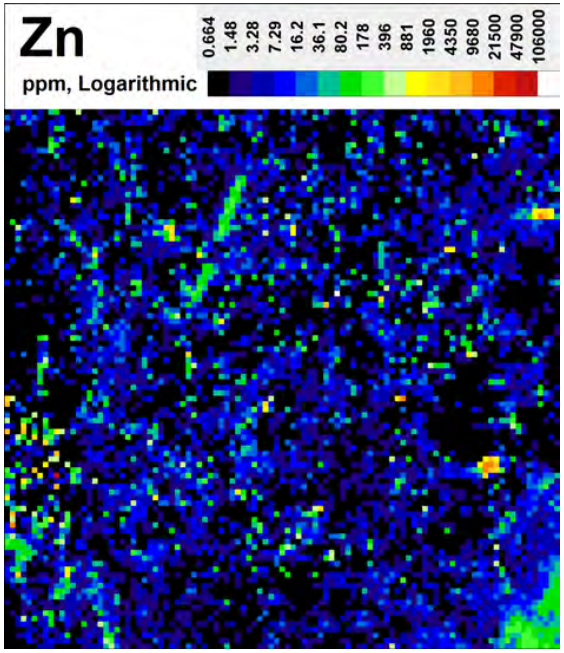
Zn
ppm, Logarithmic
0.664 1.48 3.28 7.29 16.2 36.1 80.2 178 396 881 1960 4350 9680 21500 47900 106000

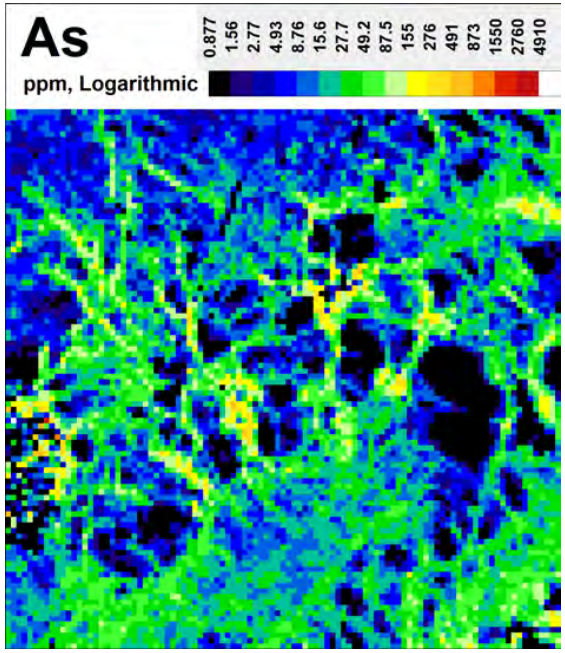
As
ppm, Logarithmic
0.877 1.56 2.77 4.93 8.76 15.6 27.7 49.2 87.5 155 276 491 873 1550 2760 4910

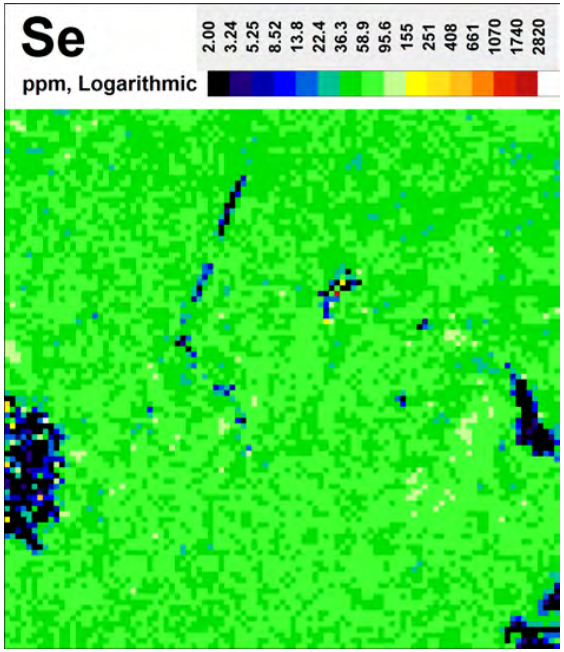
Se
ppm, Logarithmic
2.00 3.24 5.25 8.52 13.8 22.4 36.3 58.9 95.6 155 251 408 661 1070 1740 2820

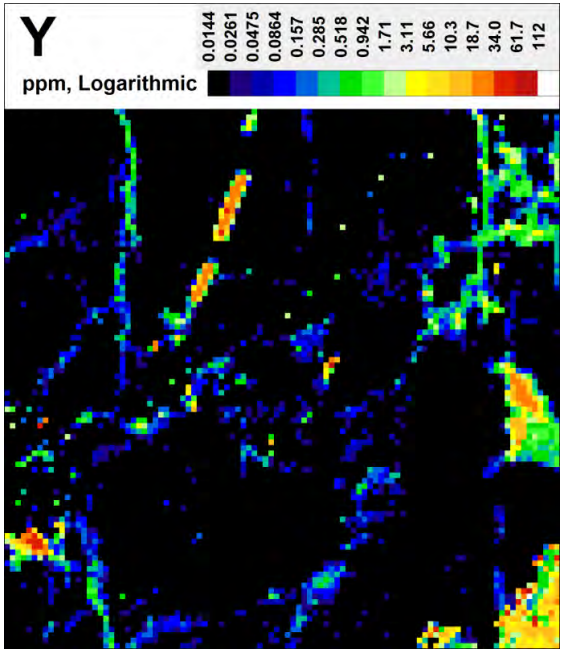
Y
ppm, Logarithmic
0.0144 0.0261 0.0475 0.0864 0.157 0.285 0.518 0.942 1.71 3.11 5.66 10.3 18.7 34.0 61.7 112

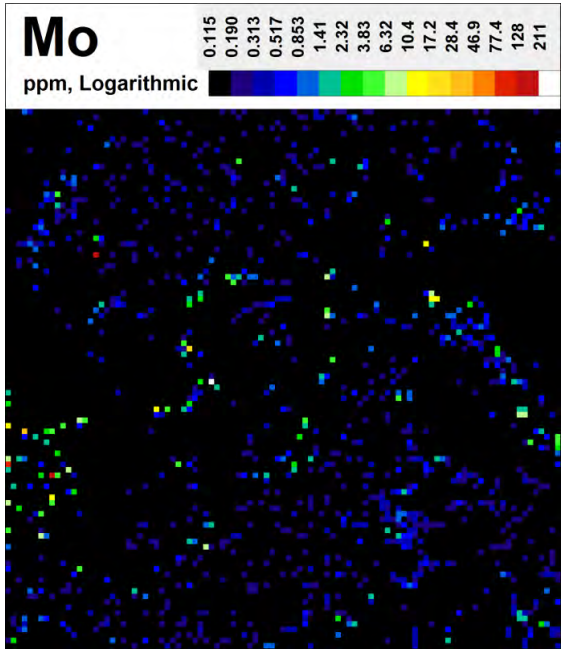
Mo
ppm, Logarithmic
0.115 0.190 0.313 0.517 0.853 1.41 2.32 3.83 6.32 10.4 17.2 28.4 46.9 77.4 128 211

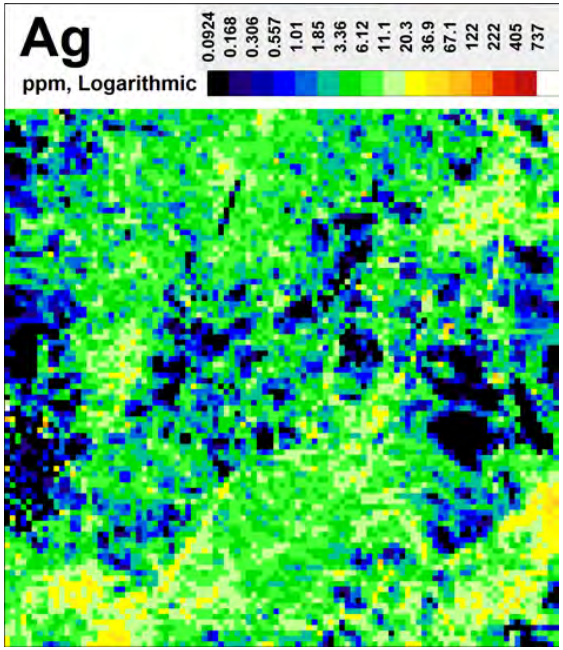
Ag
ppm, Logarithmic
0.0924 0.168 0.306 0.557 1.01 1.85 3.36 6.12 11.1 20.3 36.9 67.1 122 222 405 737

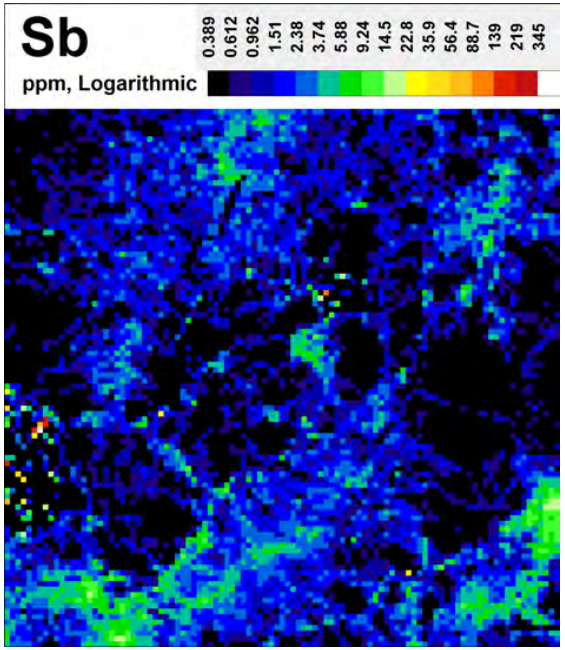
Sb
ppm, Logarithmic
0.389 0.612 0.962 1.51 2.38 3.74 5.88 9.24 14.5 22.8 35.9 56.4 88.7 139 219 345

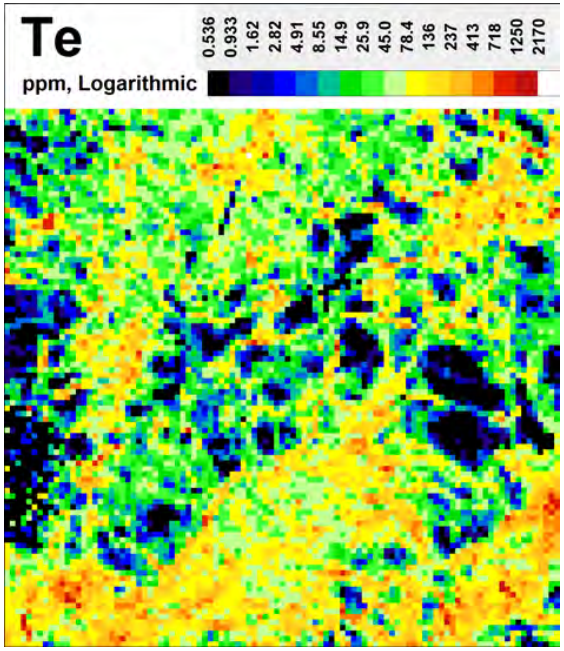
Te
ppm, Logarithmic
0.536 0.933 1.62 2.82 4.91 8.55 14.9 25.9 45.0 78.4 136 237 413 718 1250 2170

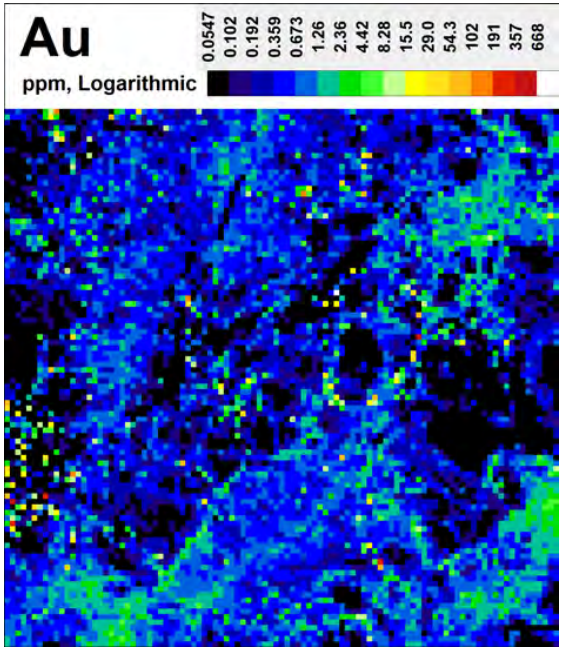
Au
ppm, Logarithmic
0.0547 0.102 0.192 0.359 0.673 1.26 2.36 4.42 8.28 15.5 29.0 54.3 102 191 357 668

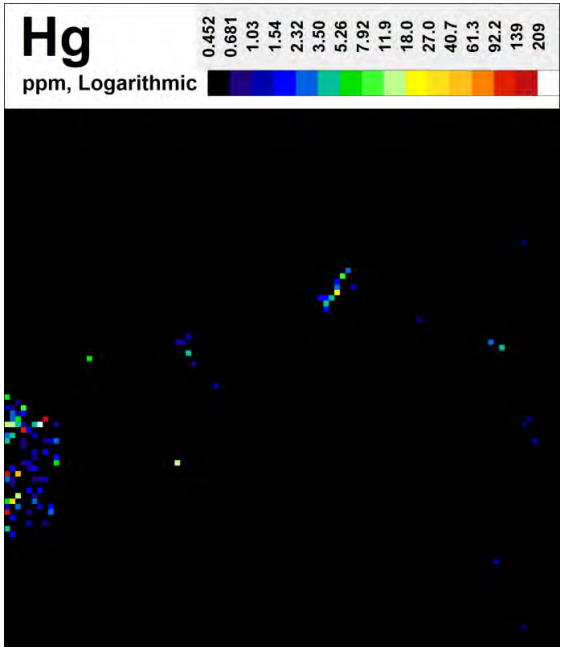
Hg
ppm, Logarithmic
0.452 0.681 1.03 1.54 2.32 3.50 5.26 7.92 11.9 18.0 27.0 40.7 61.3 92.2 139 209

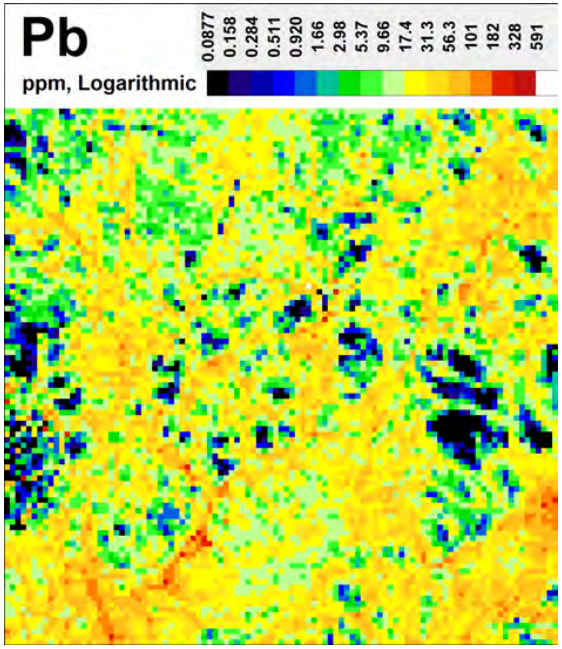
Pb
ppm, Logarithmic
0.0877 0.158 0.284 0.511 0.920 1.66 2.98 5.37 9.66 17.4 31.3 56.3 101 182 328 591

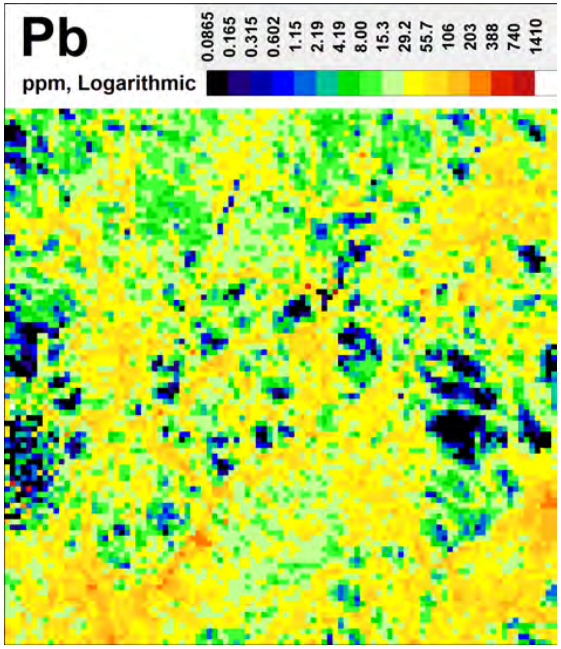
Pb
ppm, Logarithmic
0.0865 0.165 0.315 0.602 1.15 2.19 4.19 8.00 15.3 29.2 55.7 106 203 388 740 1410

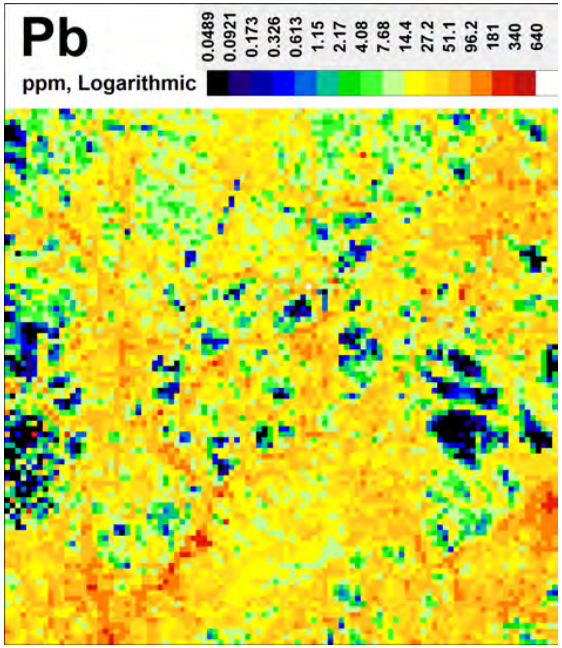
Pb
ppm, Logarithmic
0.0489 0.0921 0.173 0.326 0.613 1.15 2.17 4.08 7.68 14.4 27.2 51.1 96.2 181 340 640

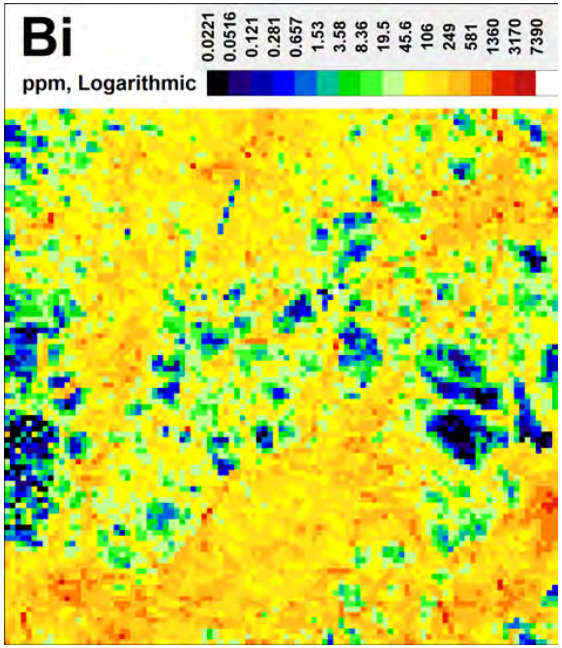
Bi
ppm, Logarithmic
0.0221 0.0516 0.121 0.281 0.657 1.53 3.58 8.36 19.5 45.6 106 249 581 1360 3170 7390

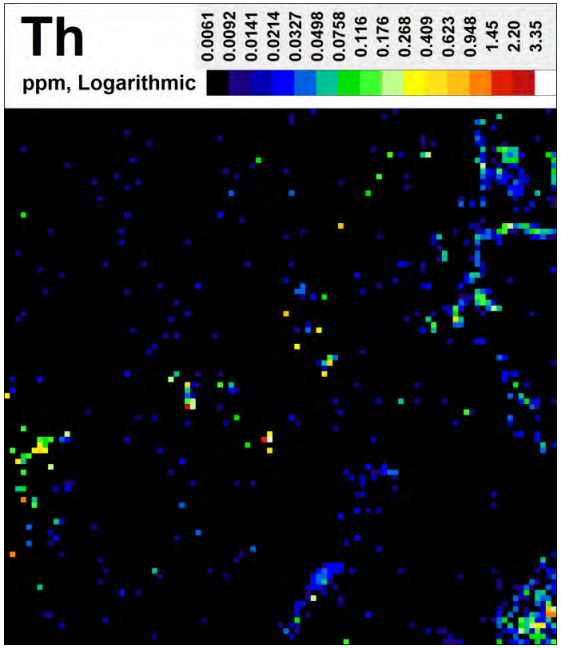
Th
ppm, Logarithmic
0.0061 0.0092 0.0141 0.0214 0.0327 0.0498 0.0758 0.116 0.176 0.268 0.409 0.623 0.948 1.45 2.20 3.35

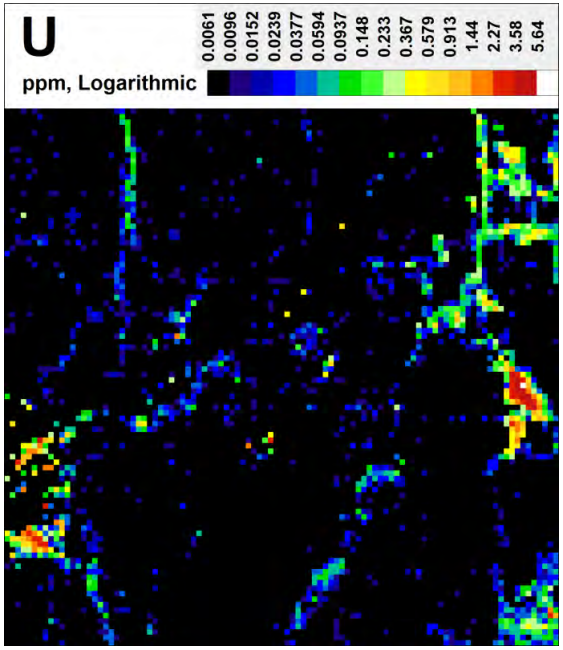
U
ppm, Logarithmic
0.0061
0.0096
0.0152
0.0239
0.0377
0.0594
0.0937
0.148
0.233
0.367
0.579
0.913
1.44
2.27
3.58
5.64

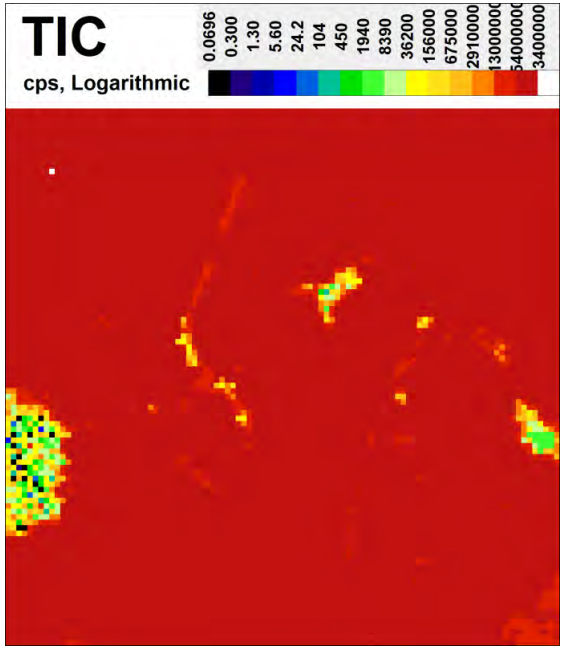
TIC
cps, Logarithmic
0.0696
0.300
1.30
5.60
24.2
104
450
1940
8390
36200
156000
675000
2910000
13000000
54000000
3400000

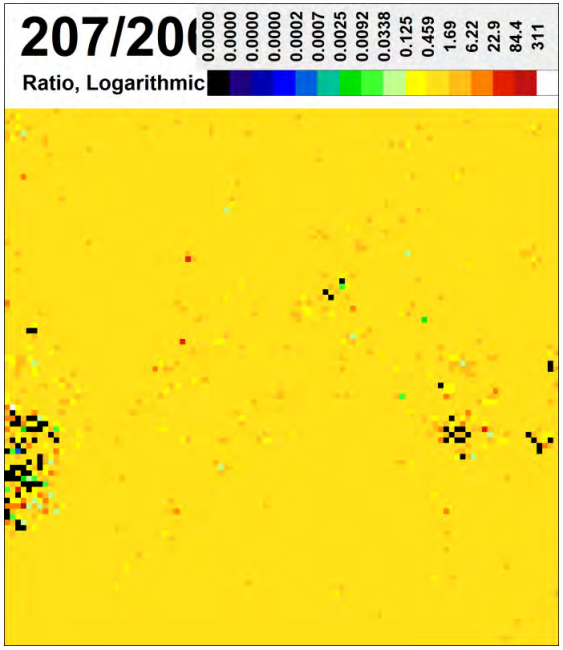
207/20(
Ratio, Logarithmic
0.0000
0.0000
0.0000
0.0000
0.0002
0.0007
0.0025
0.0092
0.0338
0.125
0.459
1.69
6.22
22.9
84.4
311

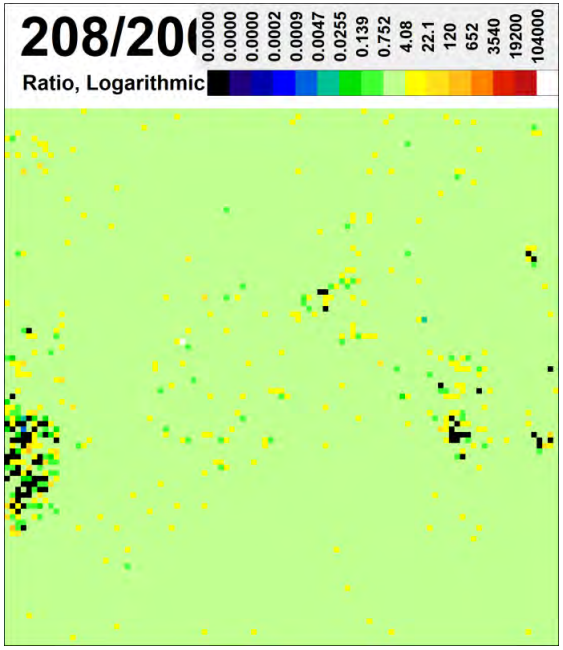
208/20(
Ratio, Logarithmic
0.0000
0.0000
0.0000
0.0002
0.0009
0.0047
0.0255
0.139
0.752
4.08
22.1
120
652
3540
19200
104000

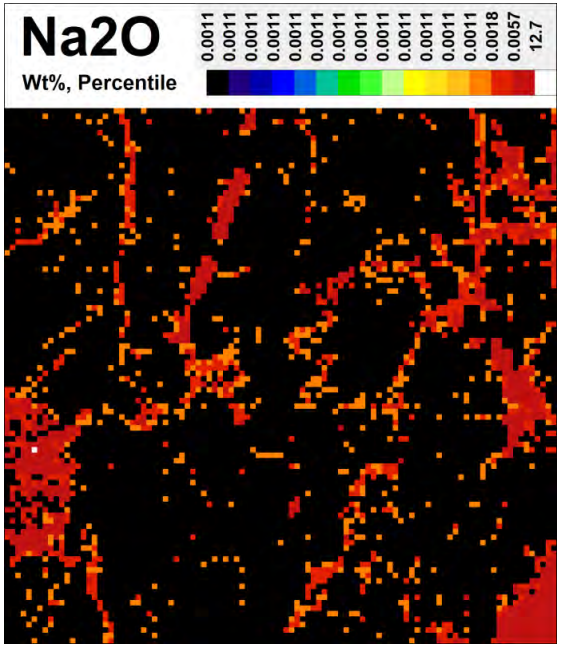
Na2O
Wt%, Percentile
0.0011 0.0011 0.0011 0.0011 0.0011 0.0011 0.0011 0.0011 0.0011 0.0011 0.0011 0.0011 0.0018 0.0057 12.7

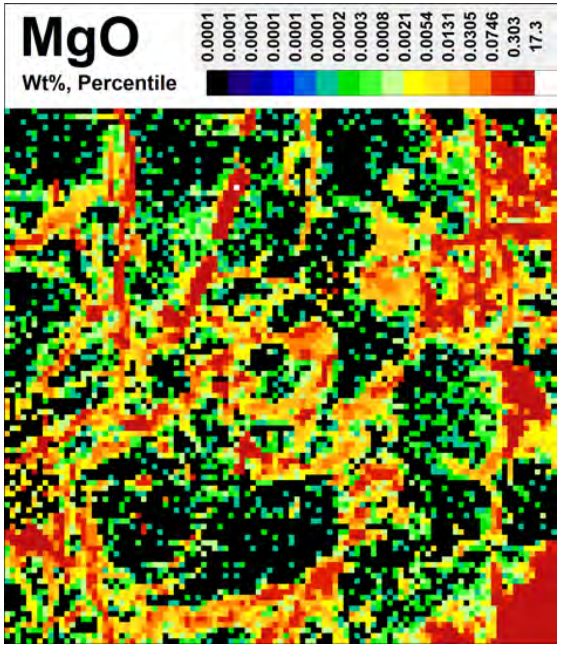
MgO
Wt%, Percentile
0.0001 0.0001 0.0001 0.0001 0.0001 0.0001 0.0002 0.0003 0.0008 0.0021 0.0054 0.0131 0.0305 0.0746 0.303 17.3

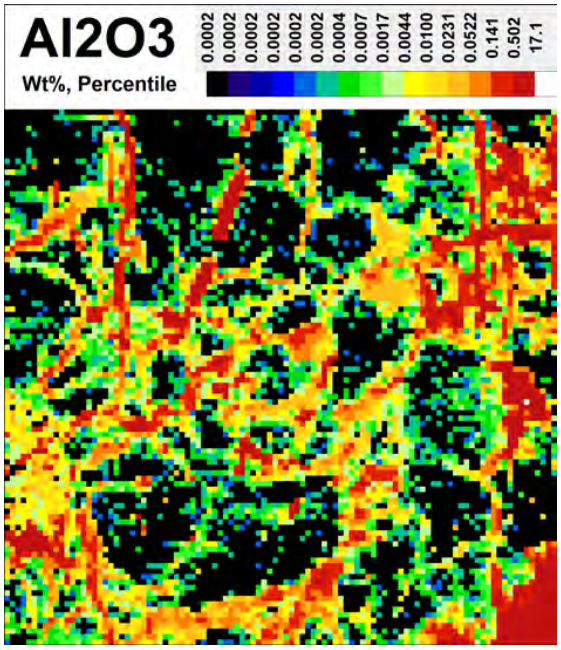
Al2O3
Wt%, Percentile
0.0002 0.0002 0.0002 0.0002 0.0002 0.0002 0.0004 0.0007 0.0017 0.0044 0.0100 0.0231 0.0522 0.141 0.502 17.1

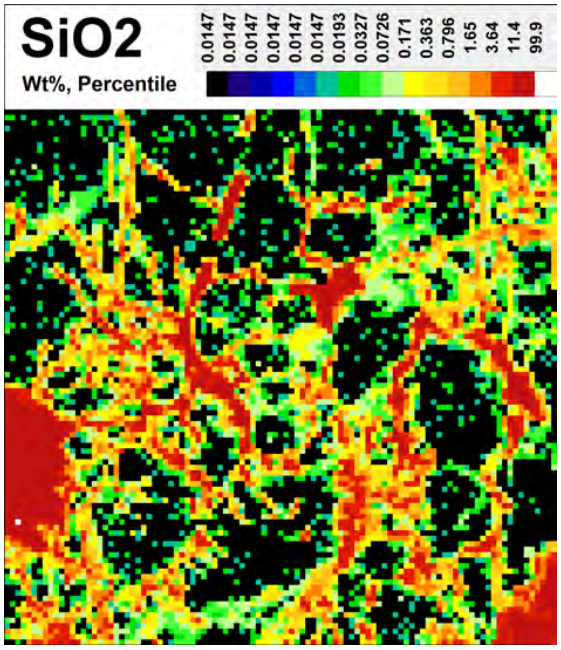
SiO2
Wt%, Percentile
0.0147 0.0147 0.0147 0.0147 0.0147 0.0147 0.0193 0.0327 0.0726 0.171 0.363 0.796 1.65 3.64 11.4 99.9

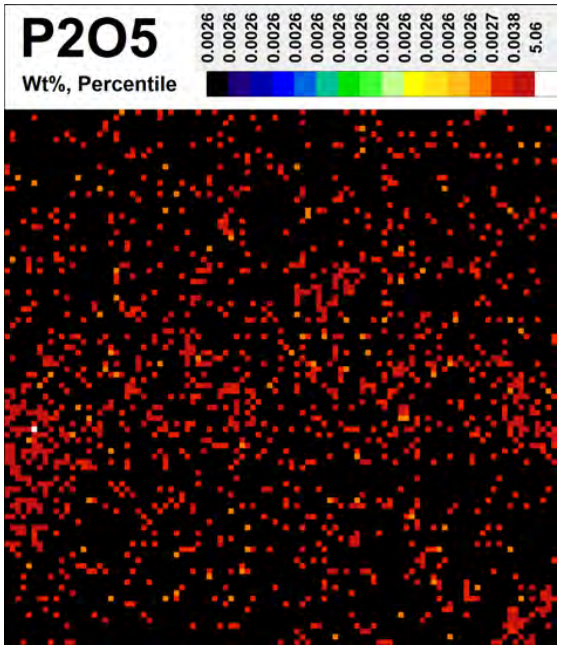
P2O5
Wt%, Percentile
0.0026 0.0026 0.0026 0.0026 0.0026 0.0026 0.0026 0.0026 0.0026 0.0026 0.0026 0.0026 0.0027 0.0038 5.06

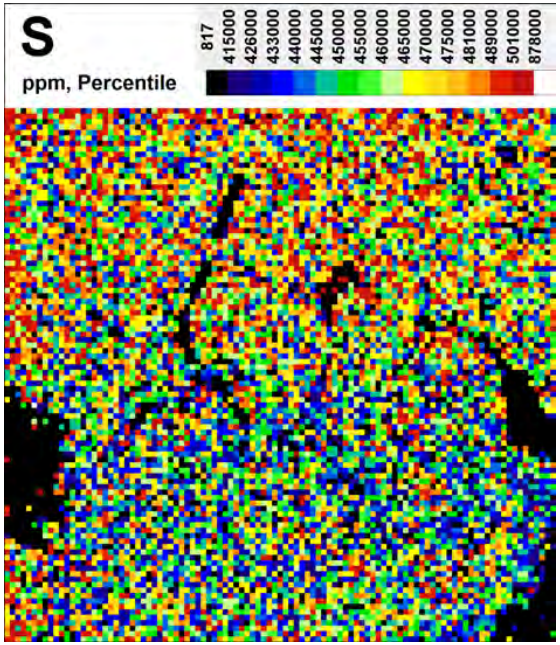
S
ppm, Percentile
817
415000
426000
433000
440000
445000
450000
455000
460000
465000
470000
475000
481000
489000
501000
878000

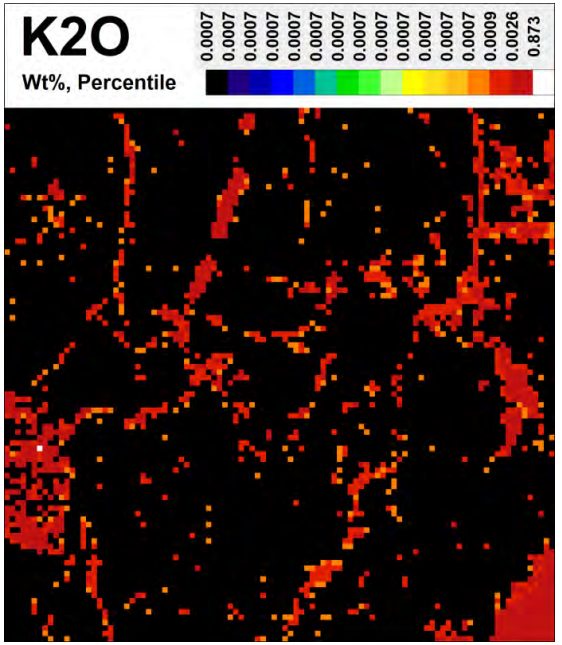
K2O
Wt%, Percentile
0.0007
0.0007
0.0007
0.0007
0.0007
0.0007
0.0007
0.0007
0.0007
0.0007
0.0007
0.0009
0.0026
0.873

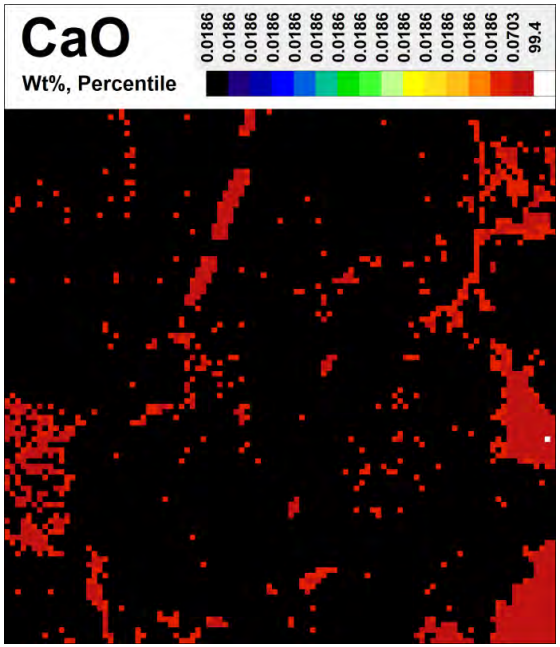
CaO
Wt%, Percentile
0.0186
0.0186
0.0186
0.0186
0.0186
0.0186
0.0186
0.0186
0.0186
0.0186
0.0186
0.0186
0.0703
99.4

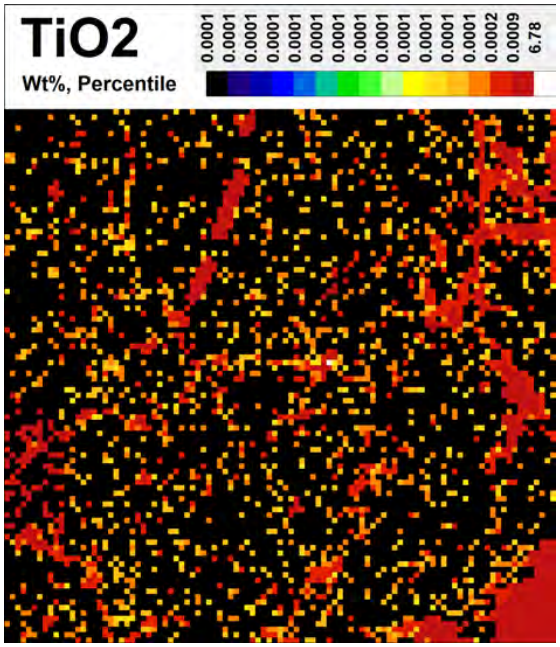
TiO2
Wt%, Percentile
0.0001
0.0001
0.0001
0.0001
0.0001
0.0001
0.0001
0.0001
0.0001
0.0001
0.0001
0.0002
0.0009
6.78

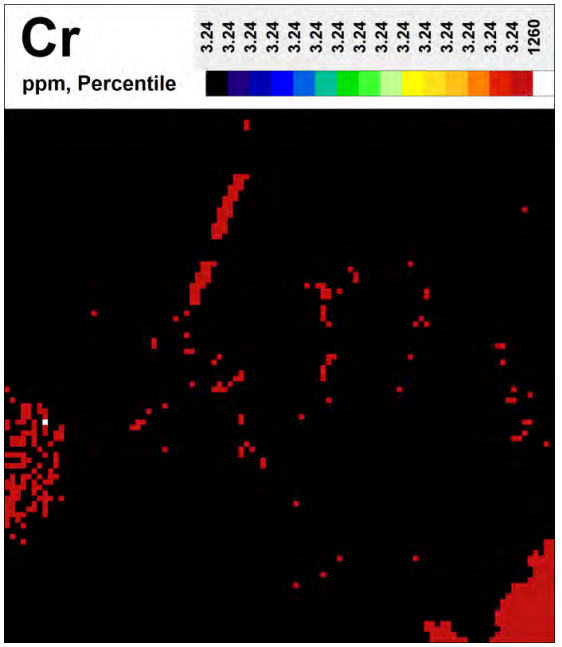
Cr
ppm, Percentile
3.24
3.24
3.24
3.24
3.24
3.24
3.24
3.24
3.24
3.24
3.24
3.24
3.24
1260

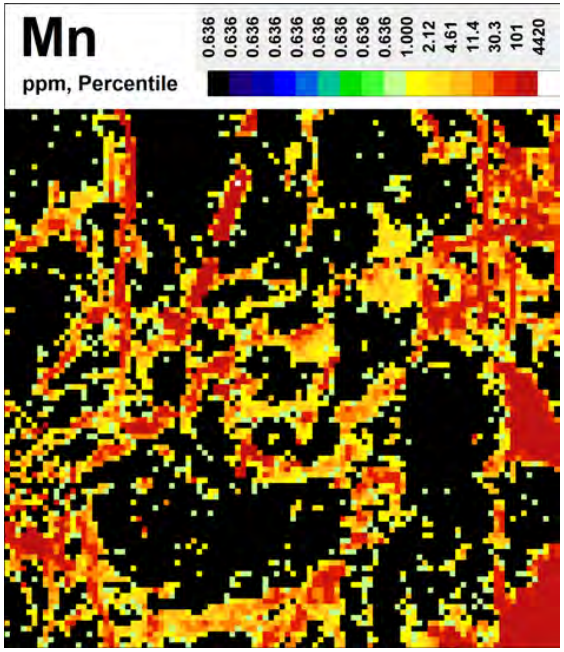
Mn
ppm, Percentile
0.636 0.636 0.636 0.636 0.636 0.636 0.636 0.636 1.000 2.12 4.61 11.4 30.3 101 4420

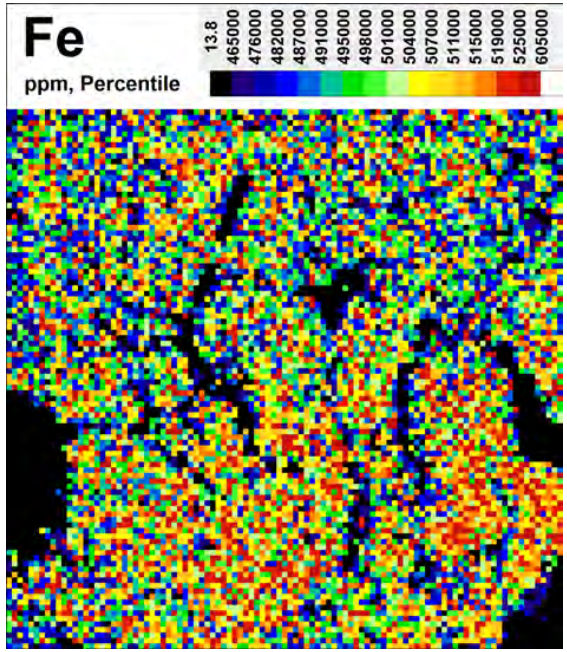
Fe
ppm, Percentile
13.8 465000 476000 482000 487000 491000 495000 498000 501000 504000 507000 511000 515000 519000 525000 605000

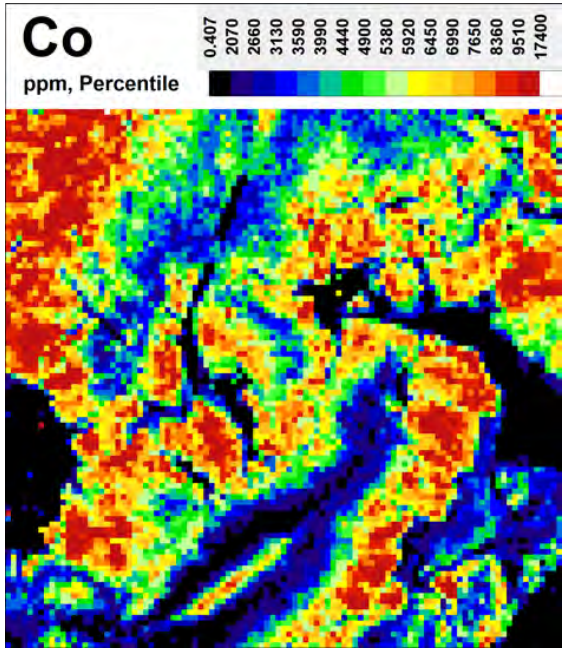
Co
ppm, Percentile
0.407 2070 2660 3130 3590 3990 4440 4900 5380 5920 6450 6990 7650 8360 9510 17400

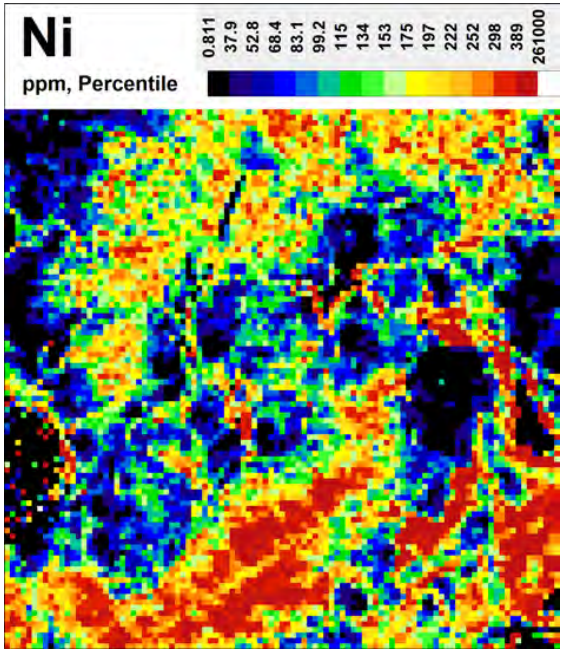
Ni
ppm, Percentile
0.811 37.9 52.8 68.4 83.1 99.2 115 134 153 175 197 222 252 298 389 261000

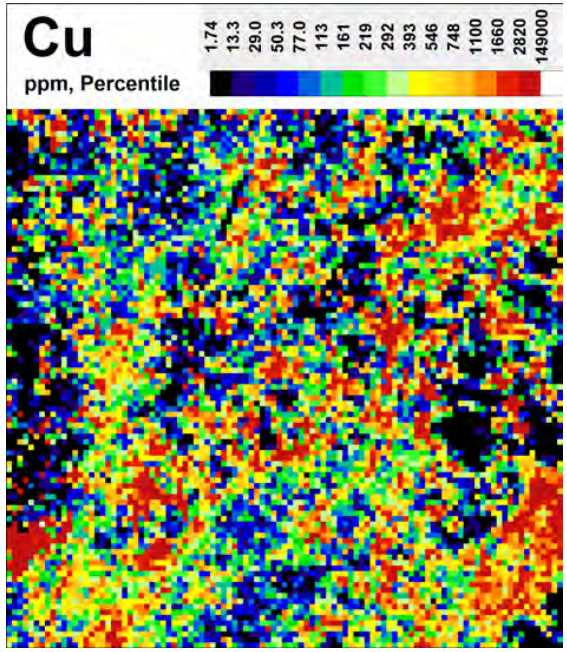
Cu
ppm, Percentile
1.74 13.3 29.0 50.3 77.0 113 161 219 292 393 546 748 1100 1660 2820 149000

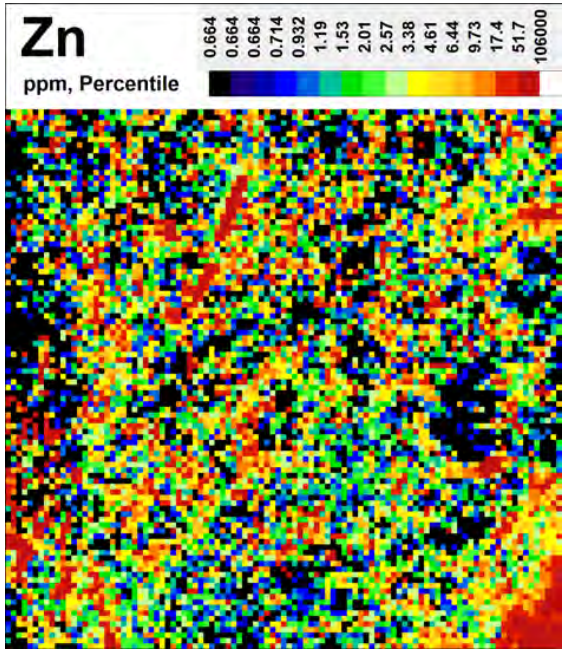
Zn
ppm, Percentile
0.664 0.664 0.664 0.714 0.932 1.19 1.53 2.01 2.57 3.38 4.61 6.44 9.73 17.4 51.7 106000

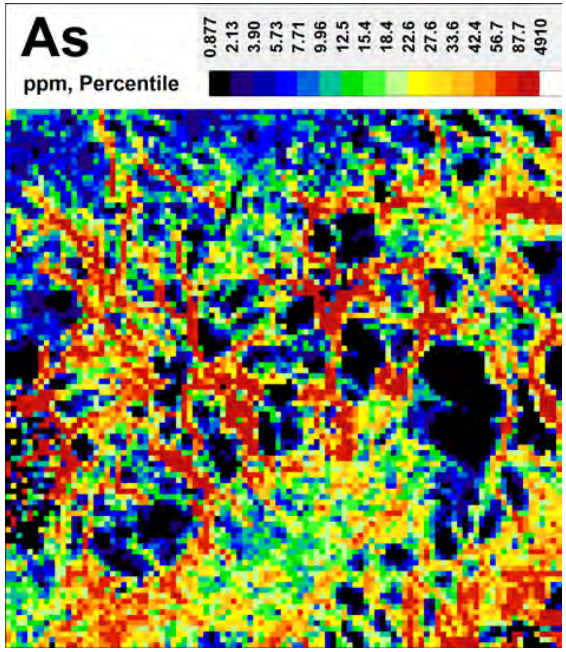
As
ppm, Percentile
0.877 2.13 3.90 5.73 7.71 9.96 12.5 15.4 18.4 22.6 27.6 33.6 42.4 56.7 87.7 4910

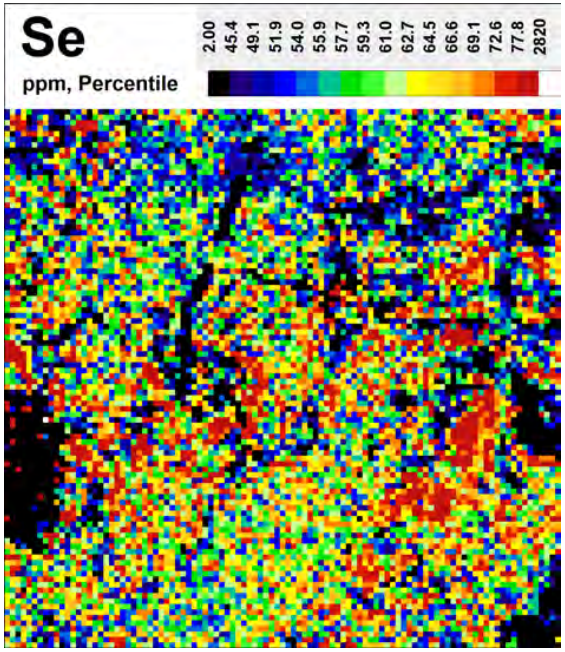
Se
ppm, Percentile
2.00 45.4 49.1 51.9 54.0 55.9 57.7 59.3 61.0 62.7 64.5 66.6 69.1 72.6 77.8 2820

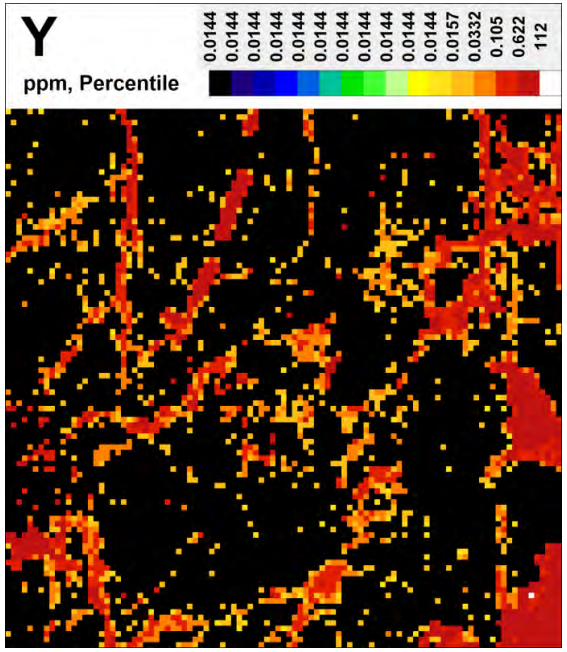
Y
ppm, Percentile
0.0144 0.0144 0.0144 0.0144 0.0144 0.0144 0.0144 0.0144 0.0144 0.0144 0.0144 0.0157 0.0332 0.105 0.622 112

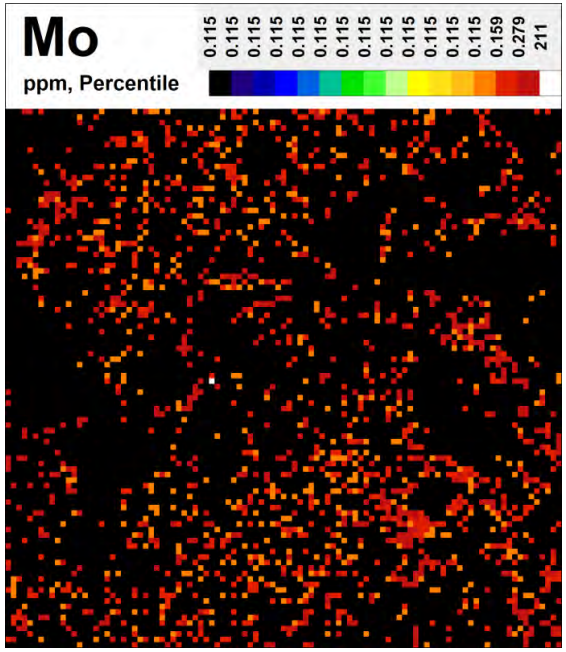
Mo
ppm, Percentile
0.115 0.115 0.115 0.115 0.115 0.115 0.115 0.115 0.115 0.115 0.115 0.115 0.115 0.159 0.279 211

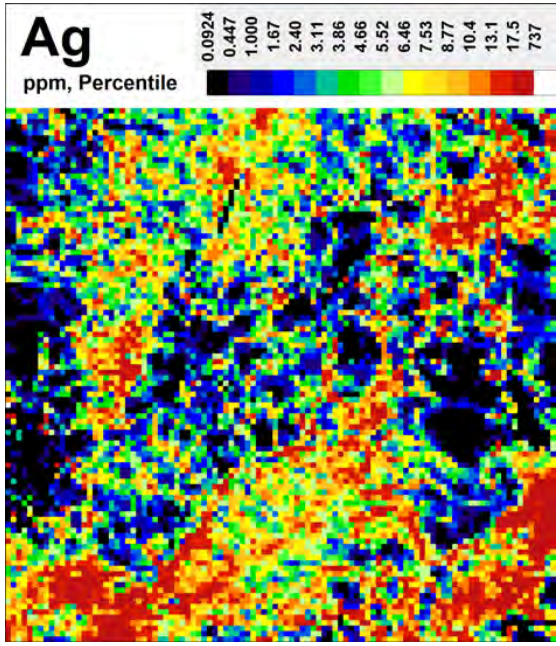
Ag
ppm, Percentile
0.0924 0.447 1.000 1.67 2.40 3.11 3.86 4.66 5.52 6.46 7.53 8.77 10.4 13.1 17.5 737

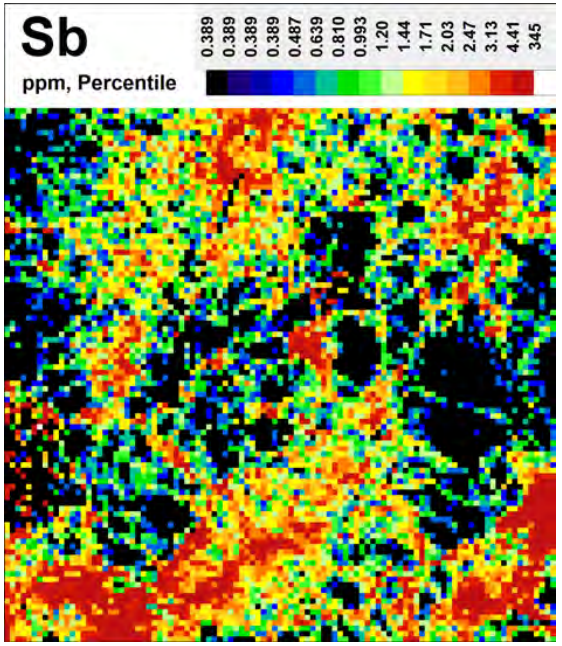
Sb
ppm, Percentile
0.389 0.389 0.389 0.389 0.487 0.639 0.810 0.993 1.20 1.44 1.71 2.03 2.47 3.13 4.41 345

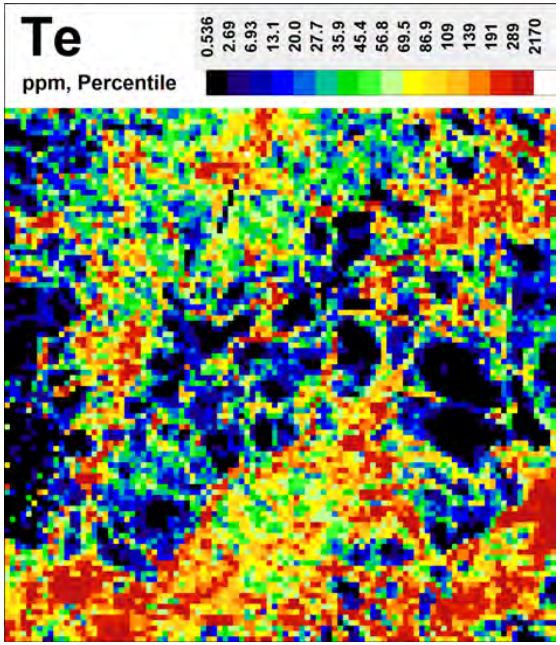
Te
ppm, Percentile
0.536 2.69 6.93 13.1 20.0 27.7 35.9 45.4 56.8 69.5 86.9 109 139 191 289 2170

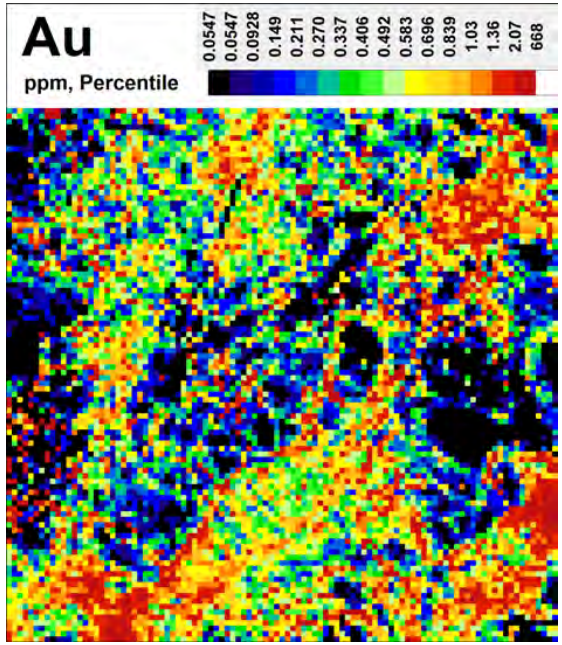
Au
ppm, Percentile
0.0547 0.0547 0.0928 0.149 0.211 0.270 0.337 0.406 0.492 0.583 0.696 0.839 1.03 1.36 2.07 668

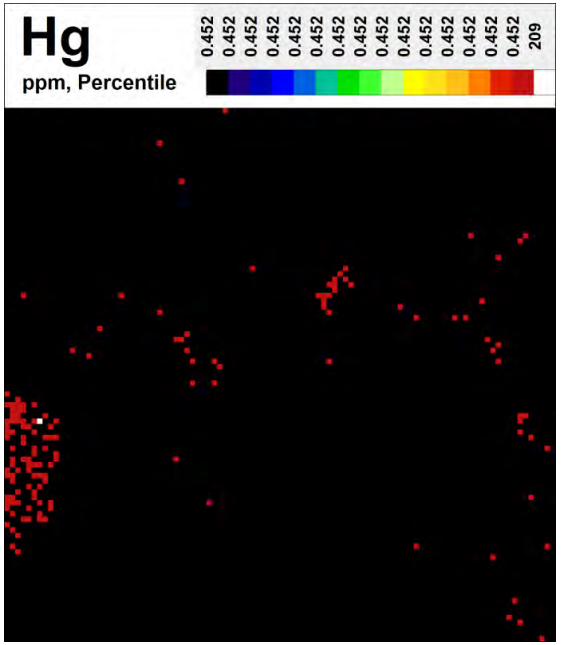
Hg
ppm, Percentile
0.452 0.452 0.452 0.452 0.452 0.452 0.452 0.452 0.452 0.452 0.452 0.452 0.452 0.452 209

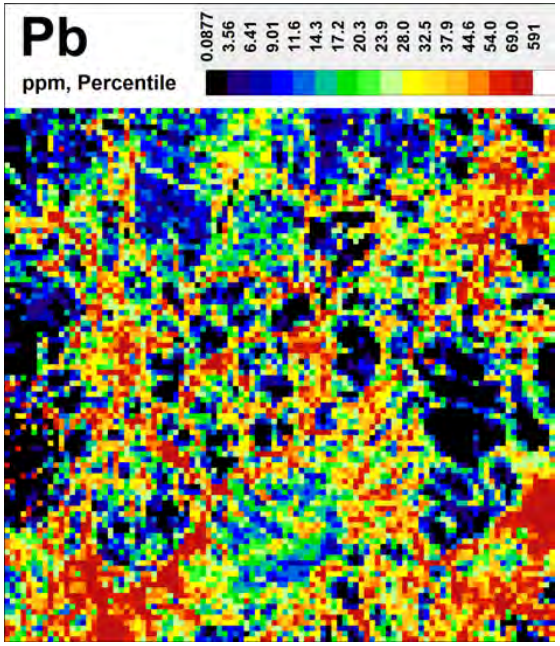
Pb
ppm, Percentile
0.0877
3.56
6.41
9.01
11.6
14.3
17.2
20.3
23.9
28.0
32.5
37.9
44.6
54.0
69.0
591

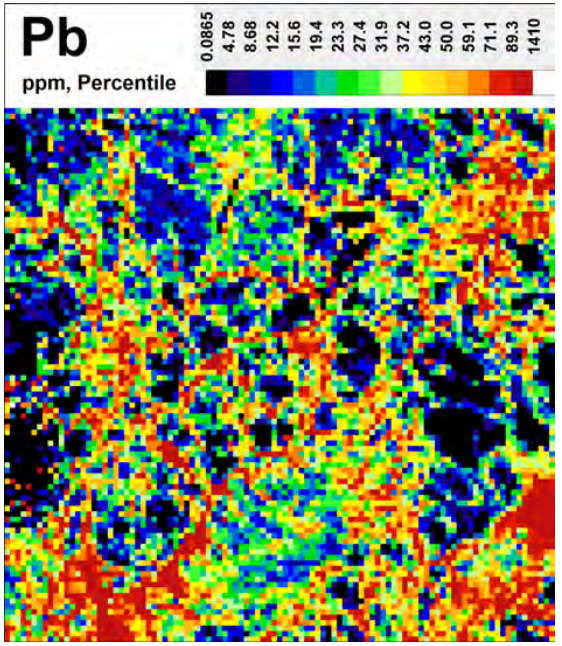
Pb
ppm, Percentile
0.0865
4.78
8.68
12.2
15.6
19.4
23.3
27.4
31.9
37.2
43.0
50.0
59.1
71.1
89.3
1410

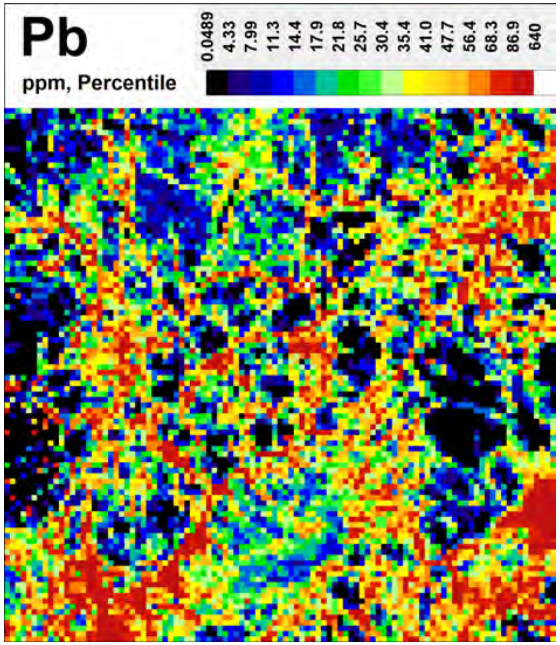
Pb
ppm, Percentile
0.0489
4.33
7.99
11.3
14.4
17.9
21.8
25.7
30.4
35.4
41.0
47.7
56.4
68.3
86.9
640

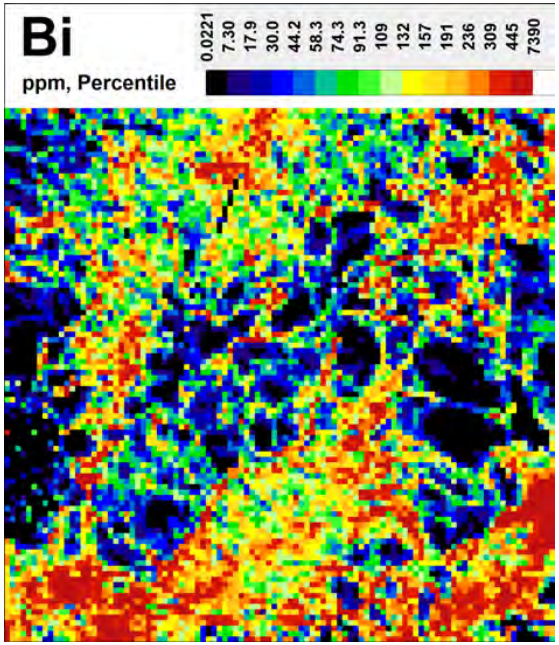
Bi
ppm, Percentile
0.0221
7.30
17.9
30.0
44.2
58.3
74.3
91.3
109
132
157
191
236
309
445
7390

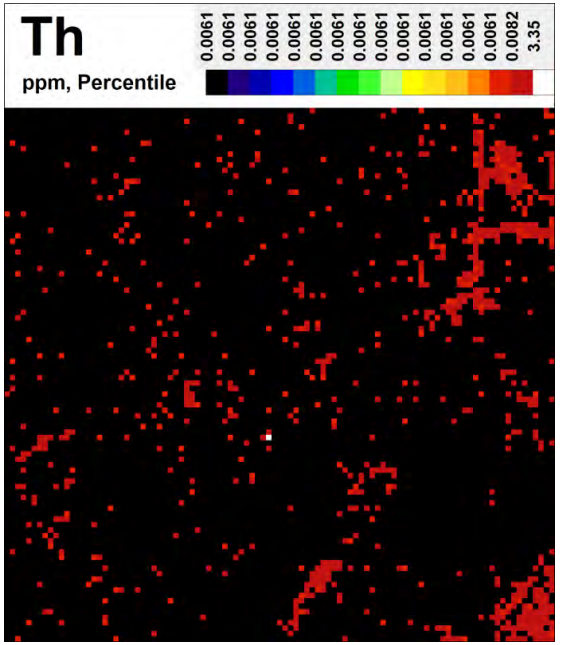
Th
ppm, Percentile
0.0061
0.0061
0.0061
0.0061
0.0061
0.0061
0.0061
0.0061
0.0061
0.0061
0.0061
0.0061
0.0061
0.0082
3.35

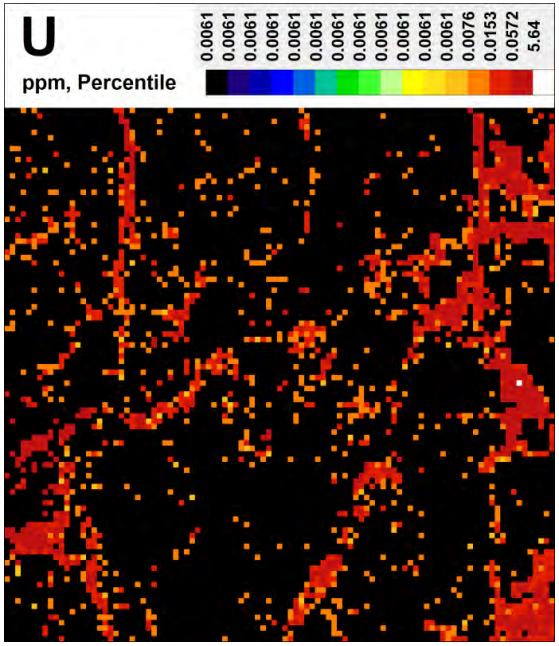
U
ppm, Percentile
0.0061 0.0061 0.0061 0.0061 0.0061 0.0061 0.0061 0.0061 0.0061 0.0061 0.0061 0.0076 0.0153 0.0572 5.64

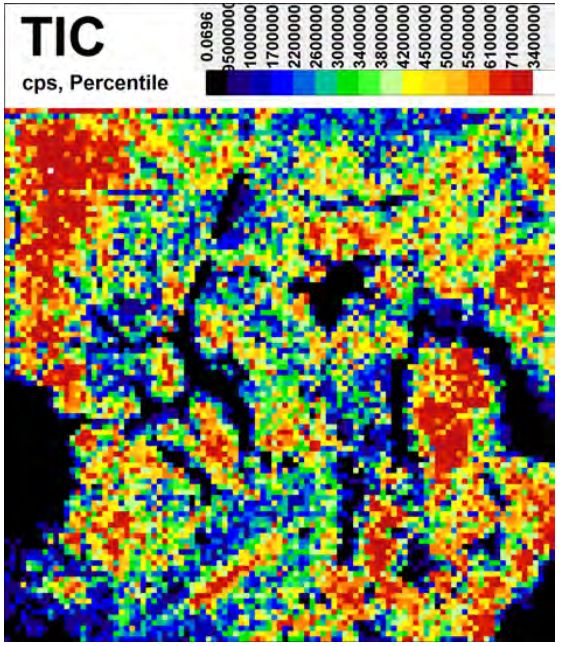
TIC
cps, Percentile
0.0696 1000000 1700000 2200000 2600000 3000000 3400000 3800000 4200000 4500000 5000000 5500000 6100000 7100000 3400000

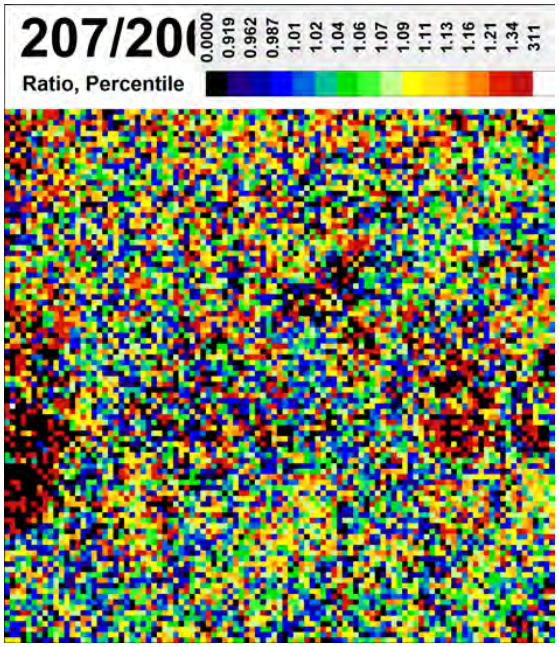
207/20(
Ratio, Percentile
0.0000 0.919 0.962 0.987 1.01 1.02 1.04 1.06 1.07 1.09 1.11 1.13 1.16 1.21 1.34 311

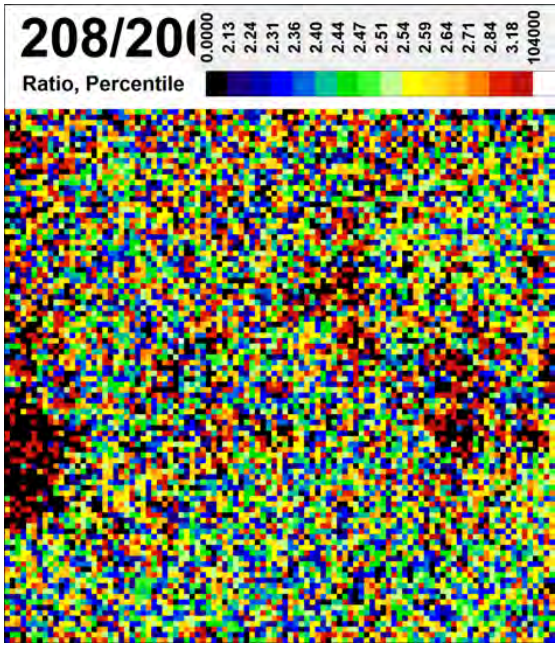
208/20(
Ratio, Percentile
0.0000 2.13 2.24 2.31 2.36 2.40 2.44 2.47 2.51 2.54 2.59 2.64 2.71 2.84 3.18 104000

Figure DR7. (pages 135–148) LA-ICP-MS results of amalgamated type-2a pyrite grains with poorly defined margins within a mafic volcanic sample (RD15-118-251) showing a reflected light photomicrograph of the mapping area and 32 major and trace maps. LA-ICP-MS maps reveal enrichment of transition metals, post-transition metals, metalloids, and lithophile elements (Mg-Mn-Al-Si-P-Na-K-Ca-Ti-Y-U-Th) at brittle fractures. Results from this domain are unclear due to small nature of the sample compared to the large laser spot size (10 μm).

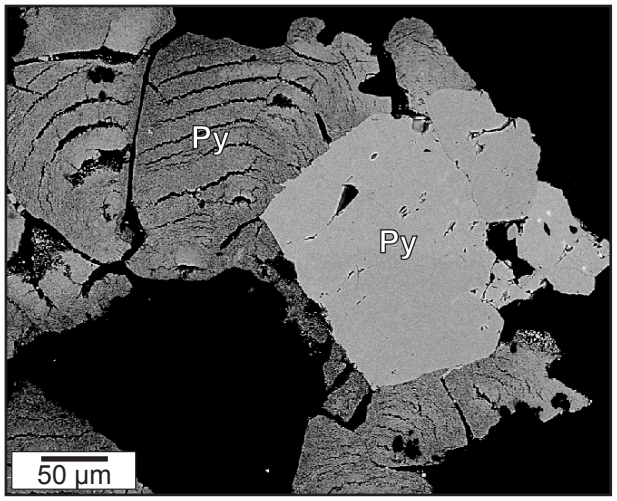
Py
Py
50 µm

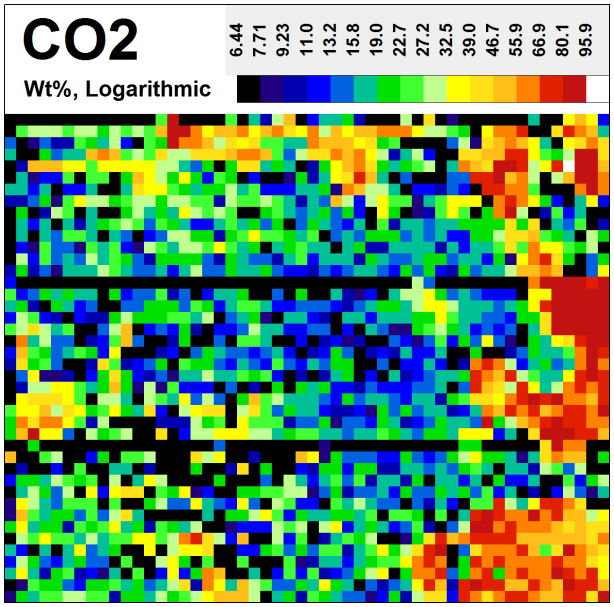
CO2
Wt%, Logarithmic
6.44 7.71 9.23 11.0 13.2 15.8 19.0 22.7 27.2 32.5 39.0 46.7 55.9 66.9 80.1 95.9

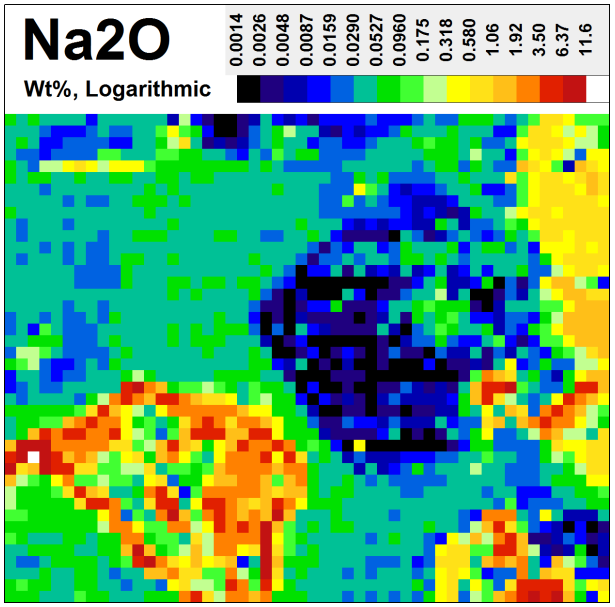
Na2O
Wt%, Logarithmic
0.0014 0.0026 0.0048 0.0087 0.0159 0.0290 0.0527 0.0960 0.175 0.318 0.580 1.06 1.92 3.50 6.37 11.6

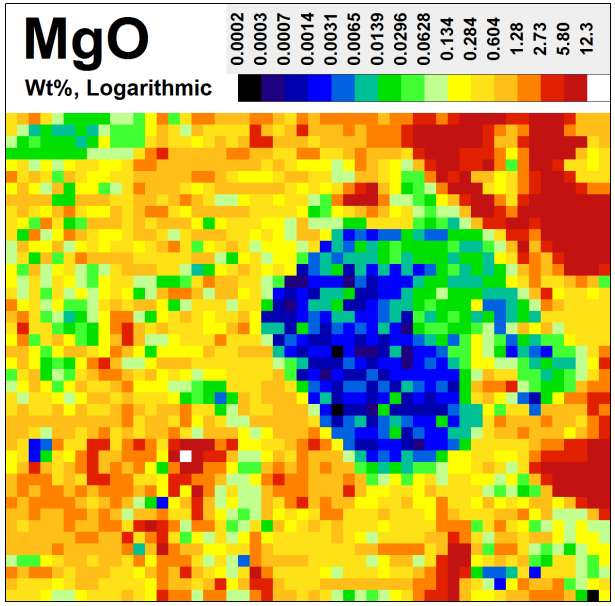
MgO
Wt%, Logarithmic
0.0002 0.0003 0.0007 0.0014 0.0031 0.0065 0.0139 0.0296 0.0628 0.134 0.284 0.604 1.28 2.73 5.80 12.3

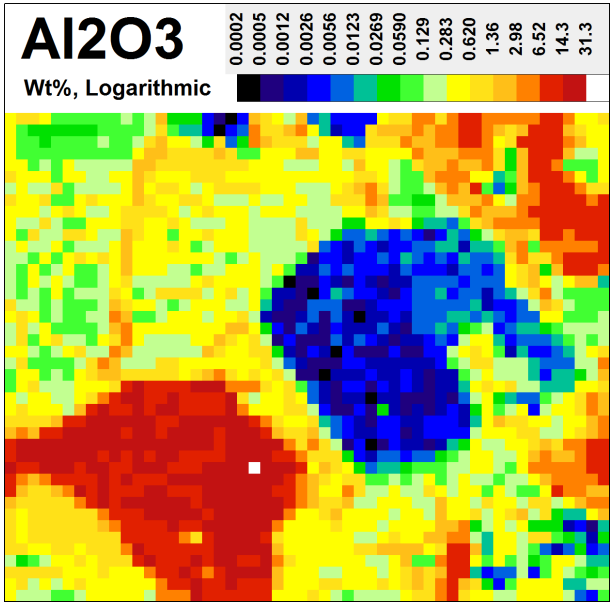
Al2O3
Wt%, Logarithmic
0.0002 0.0005 0.0012 0.0026 0.0056 0.0123 0.0269 0.0590 0.129 0.283 0.620 1.36 2.98 6.52 14.3 31.3

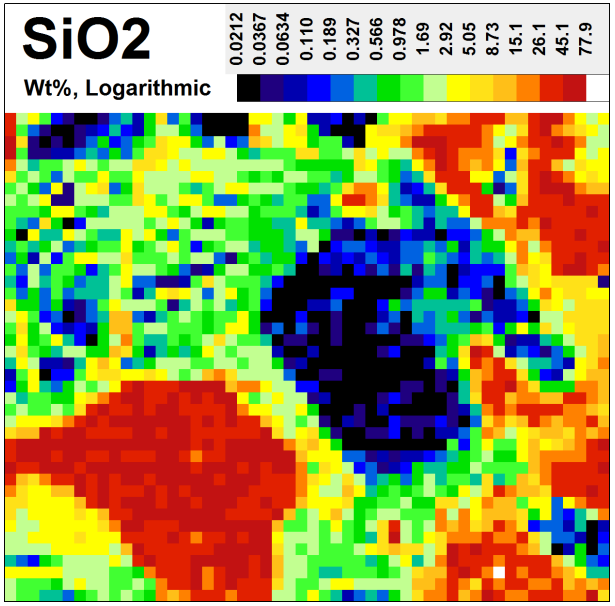
SiO2
Wt%, Logarithmic
0.0212 0.0367 0.0634 0.110 0.189 0.327 0.566 0.978 1.69 2.92 5.05 8.73 15.1 26.1 45.1 77.9

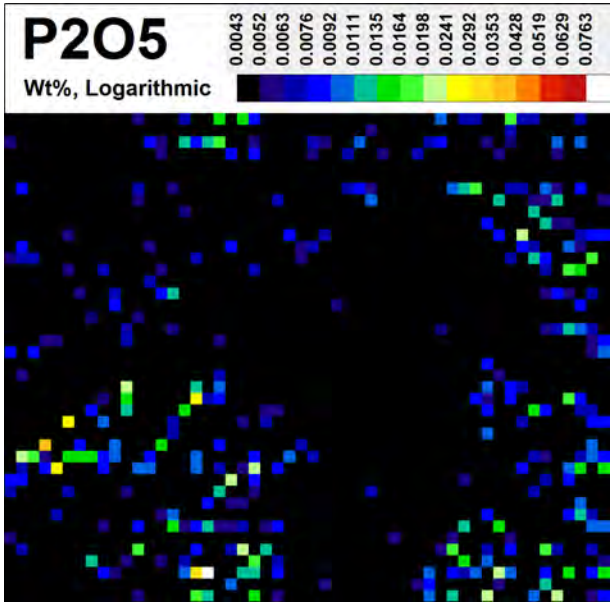
P2O5
Wt%, Logarithmic
0.0043 0.0052 0.0063 0.0076 0.0092 0.0111 0.0135 0.0164 0.0198 0.0241 0.0292 0.0353 0.0428 0.0519 0.0629 0.0763

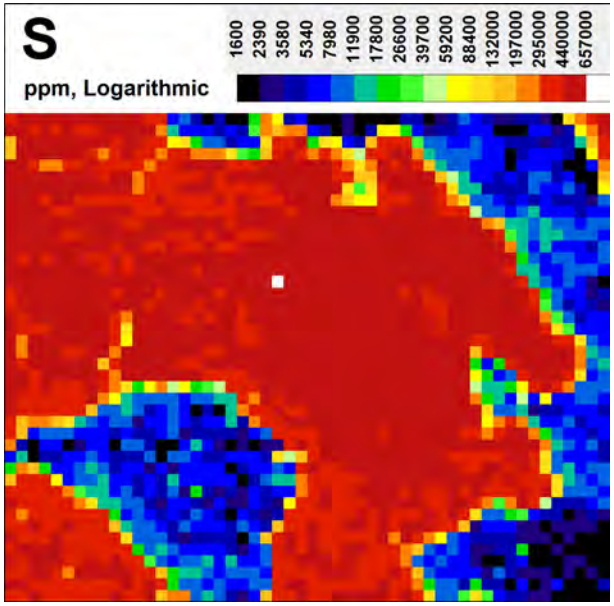
S
ppm, Logarithmic
1600 2390 3580 5340 7980 11900 17800 26600 39700 59200 88400 132000 197000 295000 440000 657000

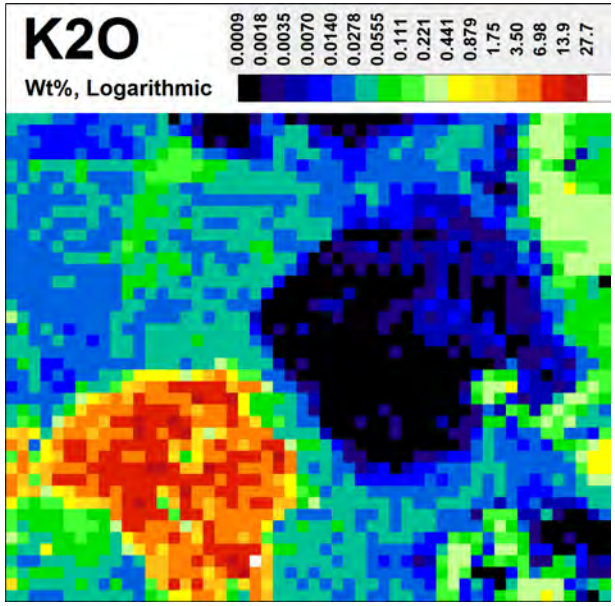
K2O
Wt%, Logarithmic
0.0009 0.0018 0.0035 0.0070 0.0140 0.0278 0.0555 0.111 0.221 0.441 0.879 1.75 3.50 6.98 13.9 27.7

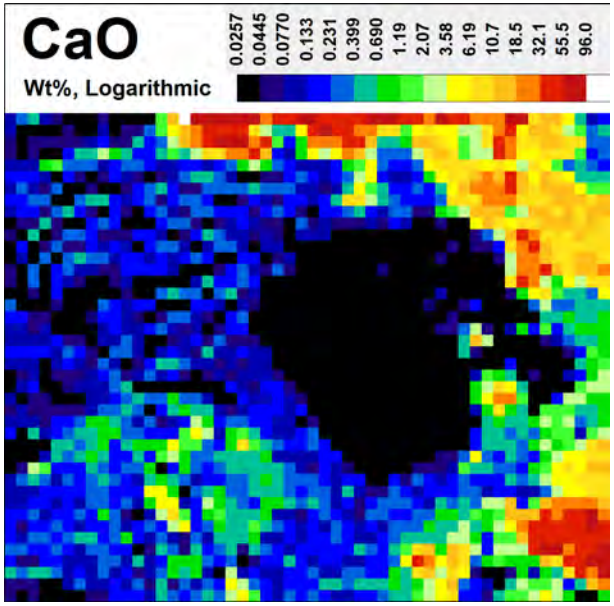
CaO
Wt%, Logarithmic
0.0257 0.0445 0.0770 0.133 0.231 0.399 0.690 1.19 2.07 3.58 6.19 10.7 18.5 32.1 55.5 96.0

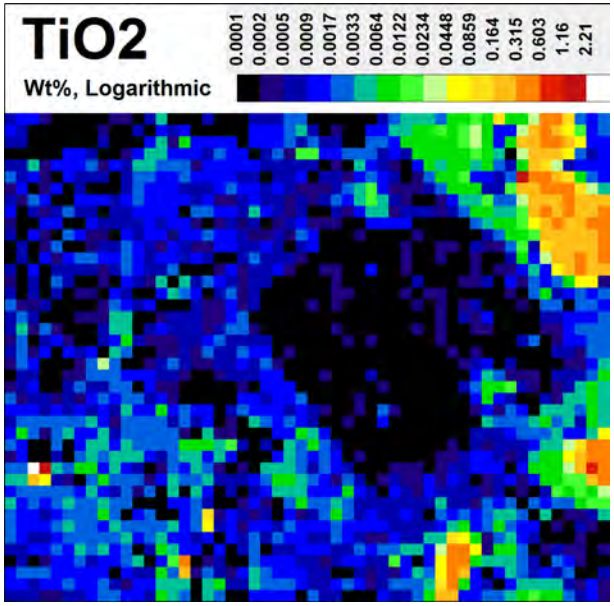
TiO2
Wt%, Logarithmic
0.0001 0.0002 0.0005 0.0009 0.0017 0.0033 0.0064 0.0122 0.0234 0.0448 0.0859 0.164 0.315 0.603 1.16 2.21

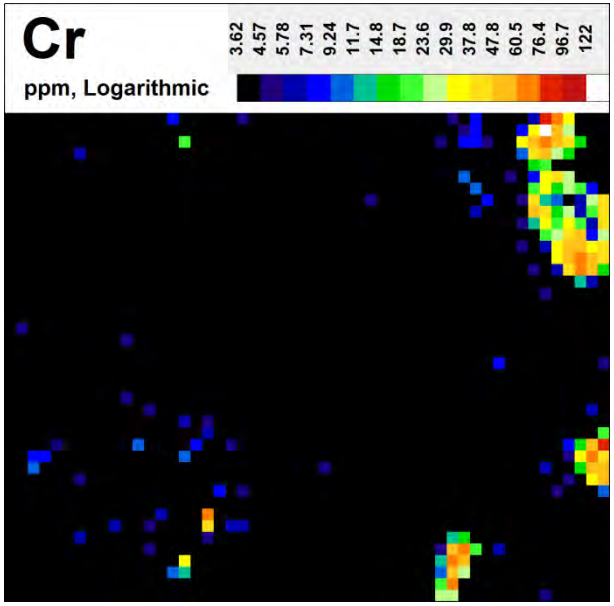
Cr
ppm, Logarithmic
3.62 4.57 5.78 7.31 9.24 11.7 14.8 18.7 23.6 29.9 37.8 47.8 60.5 76.4 96.7 122

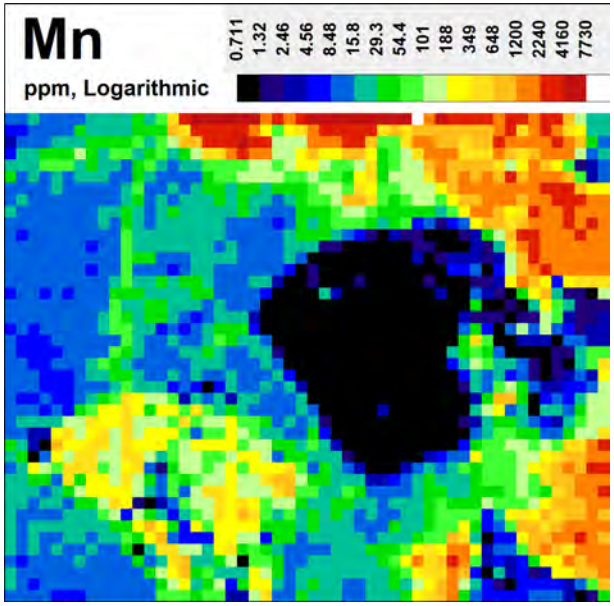
Mn
ppm, Logarithmic
0.711 1.32 2.46 4.56 8.48 15.8 29.3 54.4 101 188 349 648 1200 2240 4160 7730

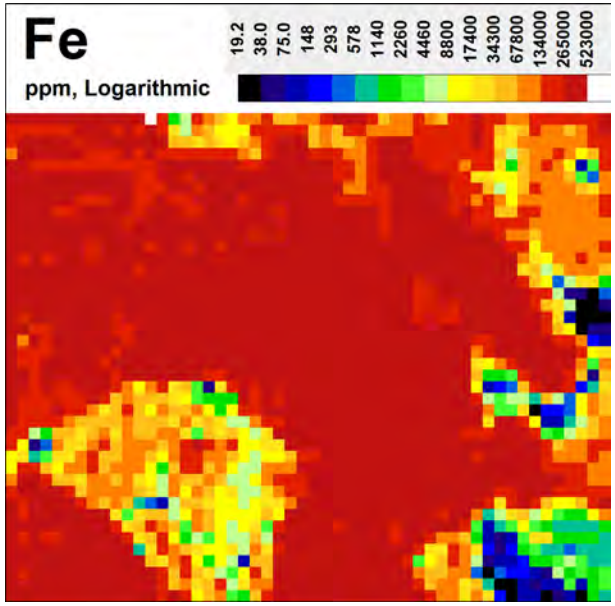
Fe
ppm, Logarithmic
19.2 38.0 75.0 148 293 578 1140 2260 4460 8800 17400 34300 67800 134000 265000 523000

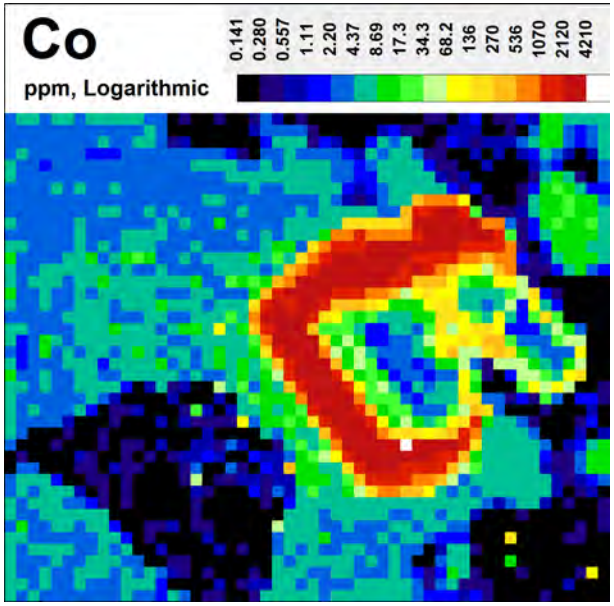
Co
ppm, Logarithmic
0.141 0.280 0.557 1.11 2.20 4.37 8.69 17.3 34.3 68.2 136 270 536 1070 2120 4210

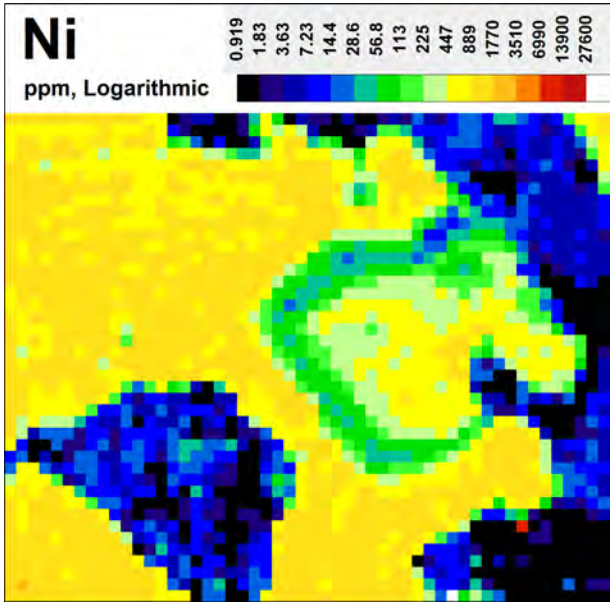
Ni
ppm, Logarithmic
0.919 1.83 3.63 7.23 14.4 28.6 56.8 113 225 447 889 1770 3510 6990 13900 27600

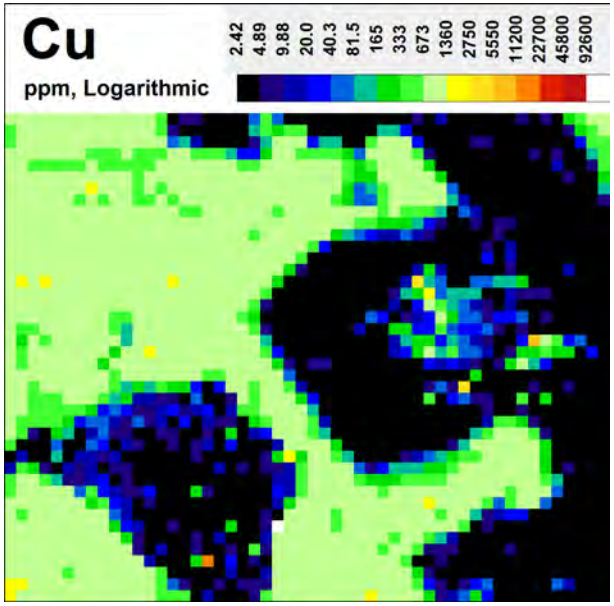
Cu
ppm, Logarithmic
2.42 4.89 9.88 20.0 40.3 81.5 165 333 673 1360 2750 5550 11200 22700 45800 92600

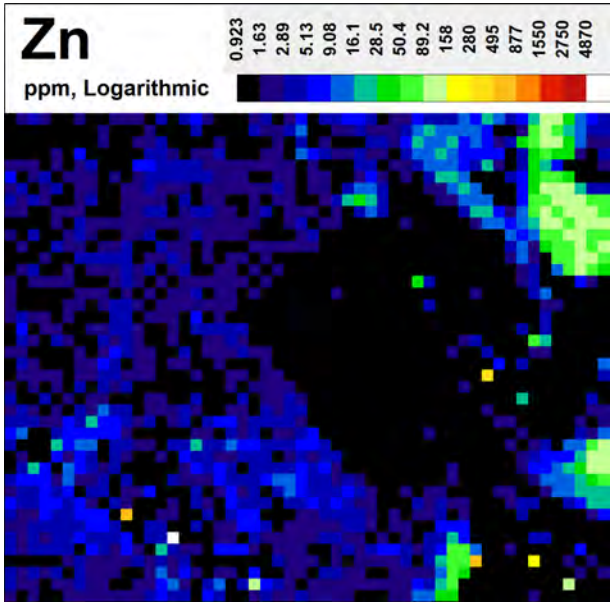
Zn
ppm, Logarithmic
0.923 1.63 2.89 5.13 9.08 16.1 28.5 50.4 89.2 158 280 495 877 1550 2750 4870

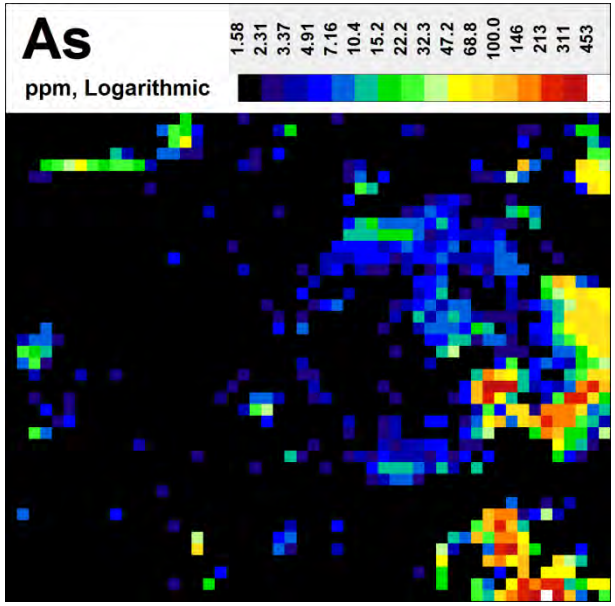
As
ppm, Logarithmic
1.58 2.31 3.37 4.91 7.16 10.4 15.2 22.2 32.3 47.2 68.8 100.0 146 213 311 453

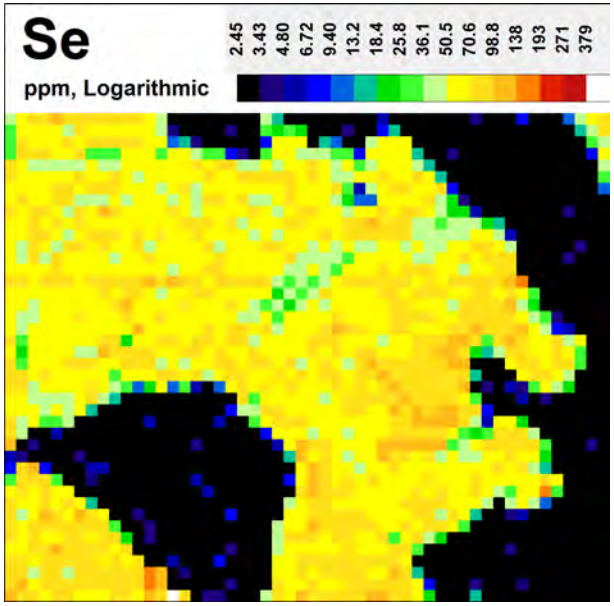
Se
ppm, Logarithmic
2.45 3.43 4.80 6.72 9.40 13.2 18.4 25.8 36.1 50.5 70.6 98.8 138 193 271 379

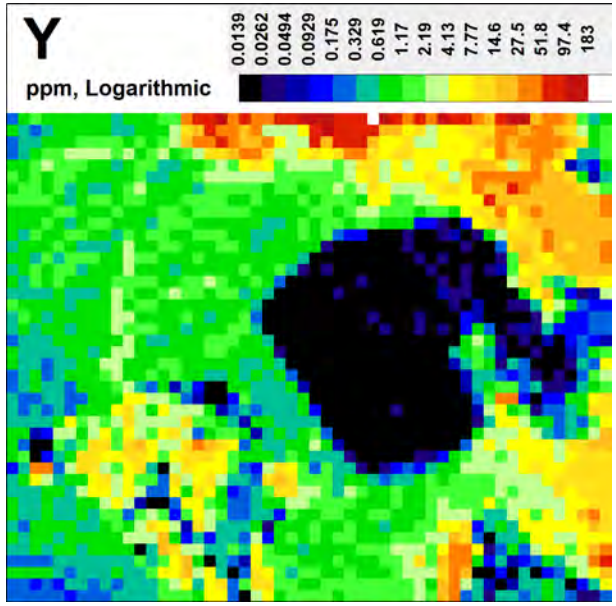
Y
ppm, Logarithmic
0.0139 0.0262 0.0494 0.0929 0.175 0.329 0.619 1.17 2.19 4.13 7.77 14.6 27.5 51.8 97.4 183

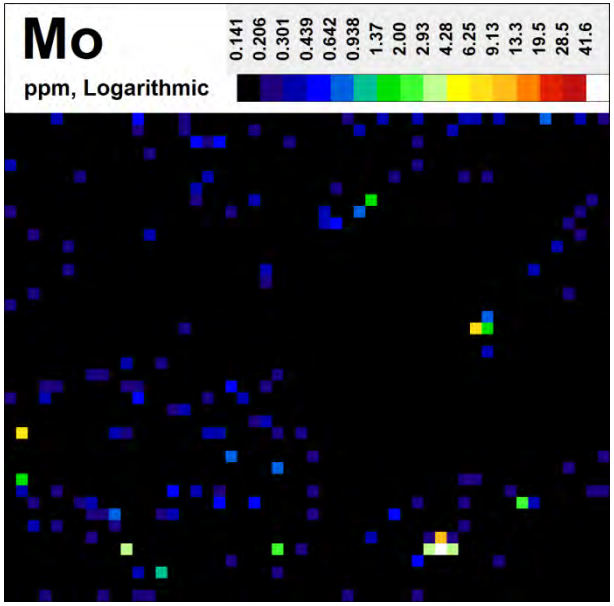
Mo
ppm, Logarithmic
0.141 0.206 0.301 0.439 0.642 0.938 1.37 2.00 2.93 4.28 6.25 9.13 13.3 19.5 28.5 41.6

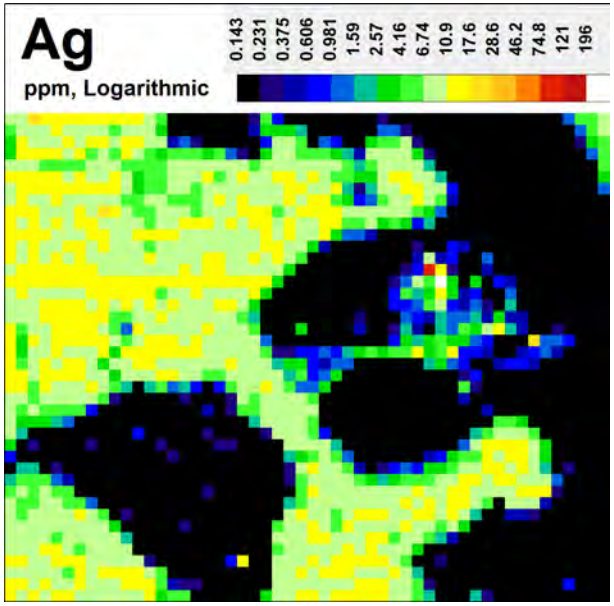
Ag
ppm, Logarithmic
0.143 0.231 0.375 0.606 0.981 1.59 2.57 4.16 6.74 10.9 17.6 28.6 46.2 74.8 121 196

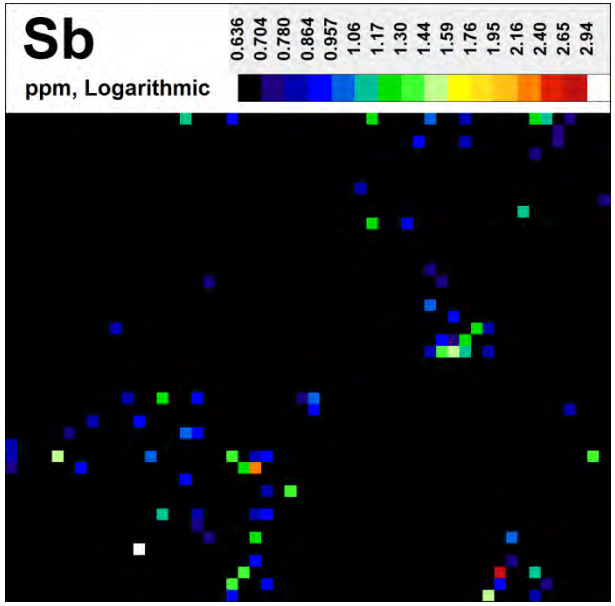
Sb
ppm, Logarithmic
0.636 0.704 0.780 0.864 0.957 1.06 1.17 1.30 1.44 1.59 1.76 1.95 2.16 2.40 2.65 2.94

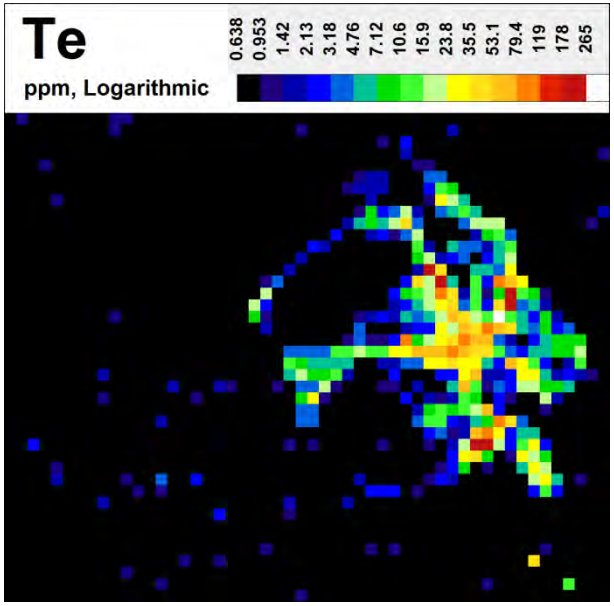
Te
ppm, Logarithmic
0.638 0.953 1.42 2.13 3.18 4.76 7.12 10.6 15.9 23.8 35.5 53.1 79.4 119 178 265

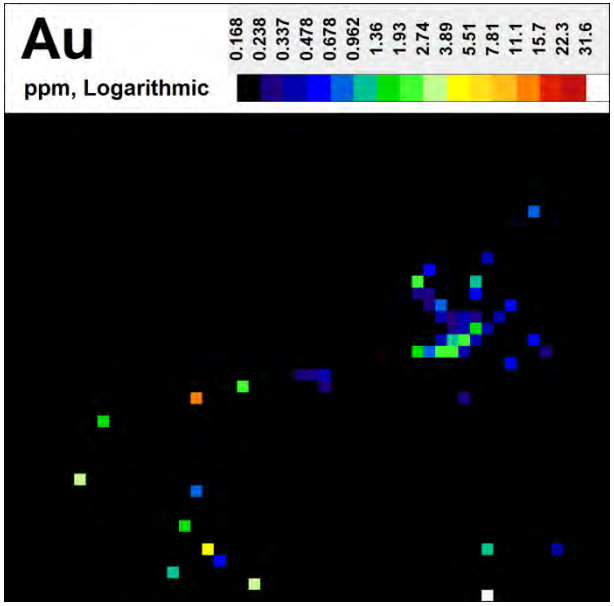
Au
ppm, Logarithmic
0.168 0.238 0.337 0.478 0.678 0.962 1.36 1.93 2.74 3.89 5.51 7.81 11.1 15.7 22.3 31.6

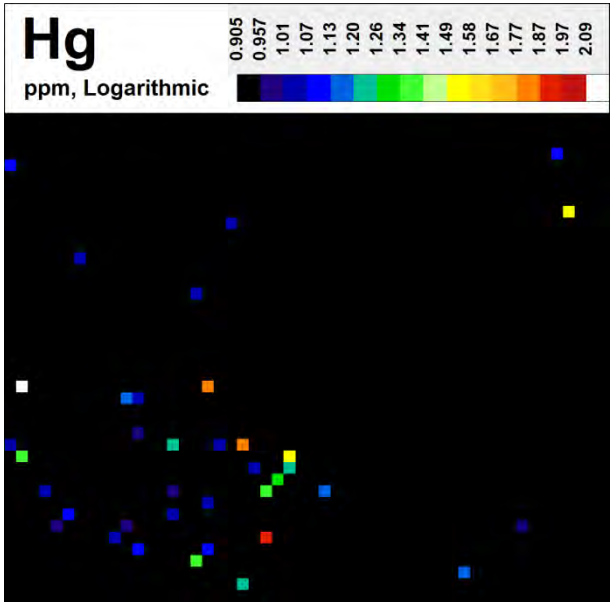
Hg
ppm, Logarithmic
0.905 0.957 1.01 1.07 1.13 1.20 1.26 1.34 1.41 1.49 1.58 1.67 1.77 1.87 1.97 2.09

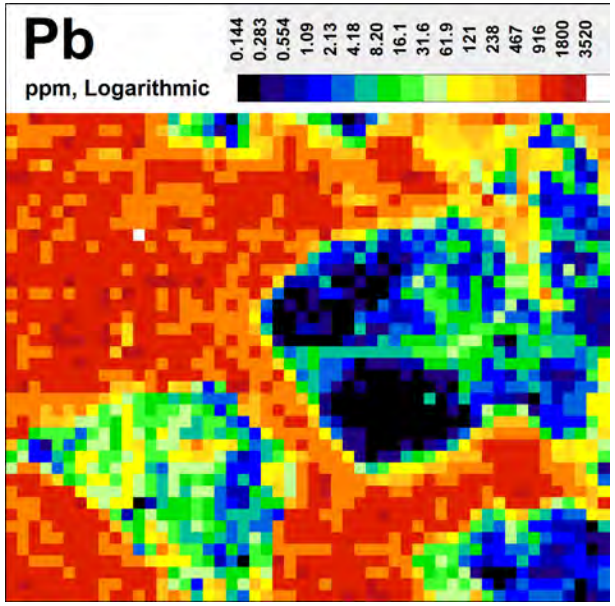
Pb
ppm, Logarithmic
0.144 0.283 0.554 1.09 2.13 4.18 8.20 16.1 31.6 61.9 121 238 467 916 1800 3520

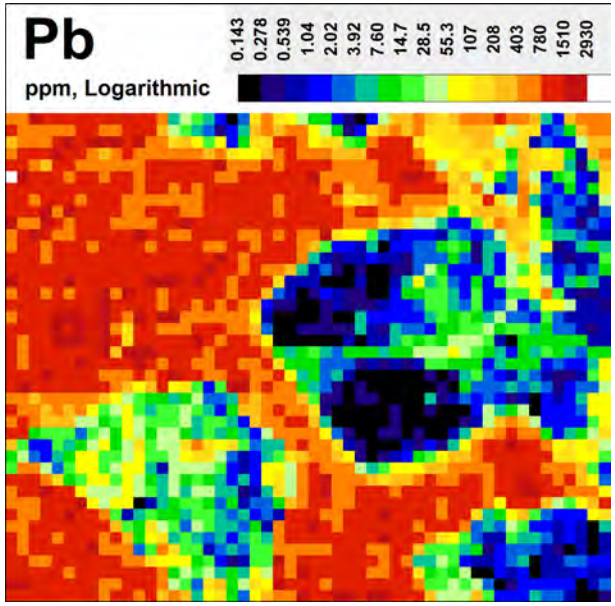
Pb
ppm, Logarithmic
0.143 0.278 0.539 1.04 2.02 3.92 7.60 14.7 28.5 55.3 107 208 403 780 1510 2930

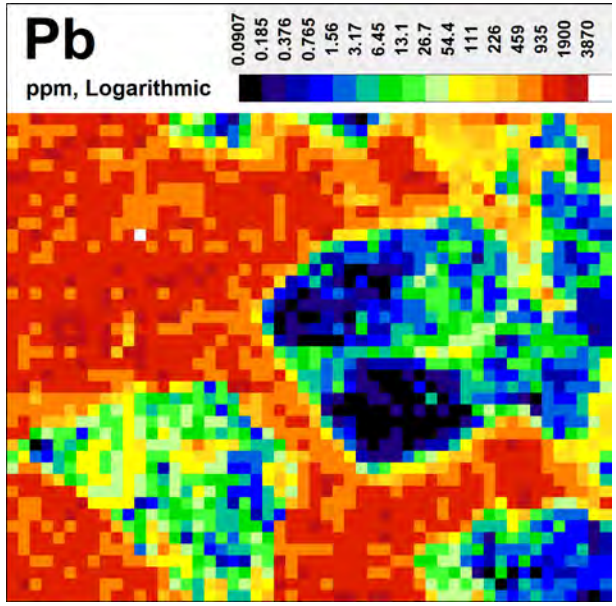
Pb
ppm, Logarithmic
0.0907 0.185 0.376 0.765 1.56 3.17 6.45 13.1 26.7 54.4 111 226 459 935 1900 3870

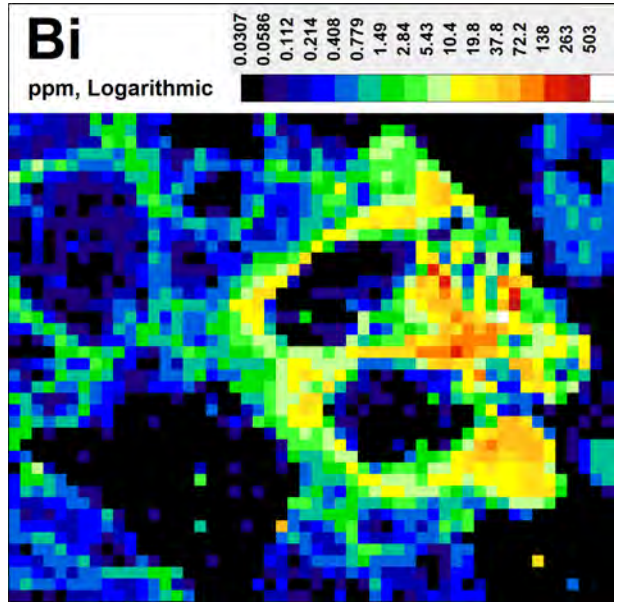
Bi
ppm, Logarithmic
0.0307 0.0586 0.112 0.214 0.408 0.779 1.49 2.84 5.43 10.4 19.8 37.8 72.2 138 263 503

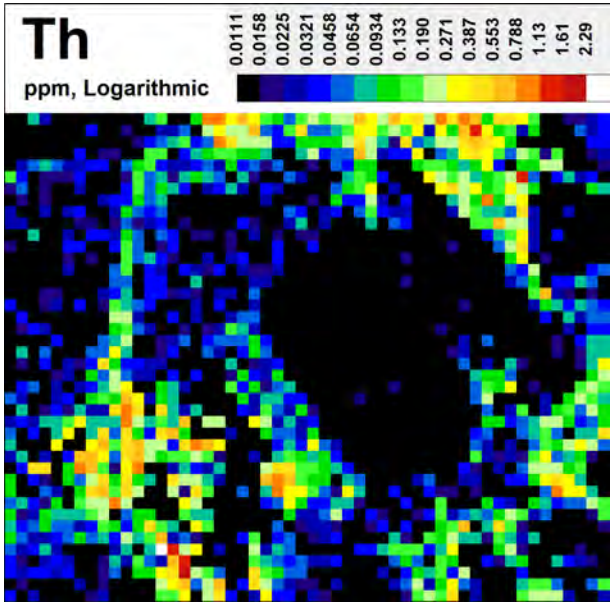
Th
ppm, Logarithmic
0.0111 0.0158 0.0225 0.0321 0.0458 0.0654 0.0934 0.133 0.190 0.271 0.387 0.553 0.788 1.13 1.61 2.29

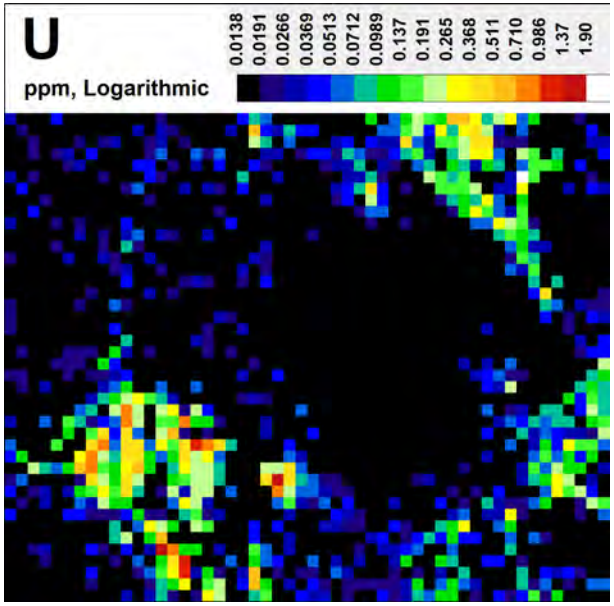
U
ppm, Logarithmic
0.0138 0.0191 0.0266 0.0369 0.0513 0.0712 0.0989 0.137 0.191 0.265 0.368 0.511 0.710 0.986 1.37 1.90

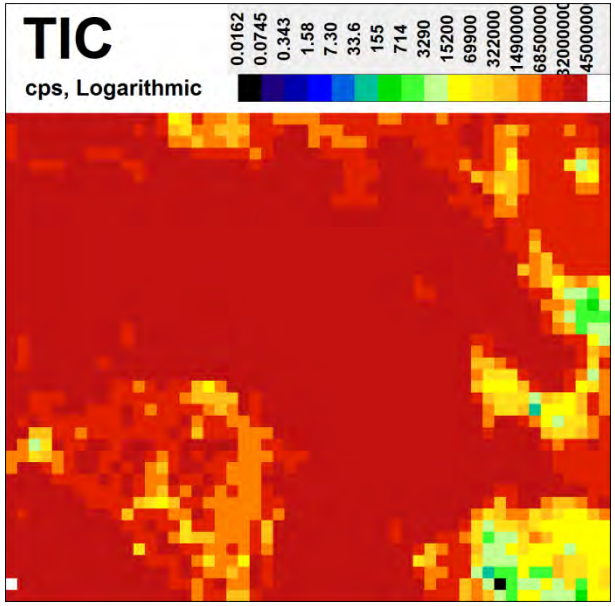
TIC
cps, Logarithmic
0.0162 0.0745 0.343 1.58 7.30 33.6 155 714 3290 15200 69900 322000 1490000 6850000 32000000 45000000

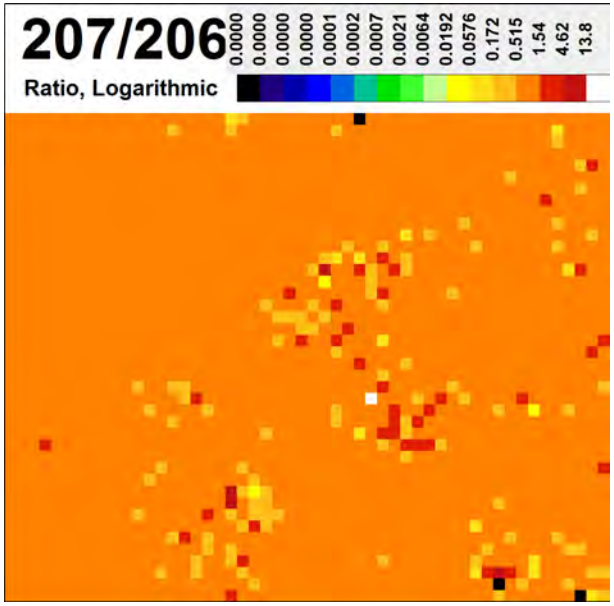
207/206
Ratio, Logarithmic
0.0000 0.0000 0.0000 0.0000 0.0000 0.0001 0.0002 0.0007 0.0021 0.0064 0.0192 0.0576 0.172 0.515 1.54 4.62 13.8

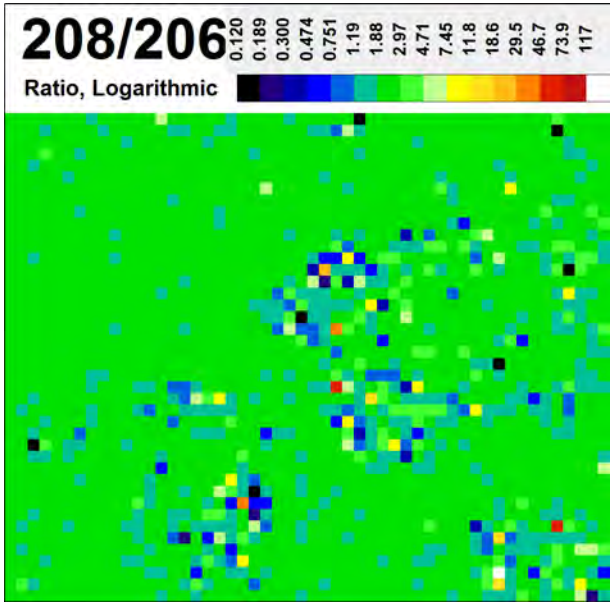
208/206
Ratio, Logarithmic
0.120 0.189 0.300 0.474 0.751 1.19 1.88 2.97 4.71 7.45 11.8 18.6 29.5 46.7 73.9 117

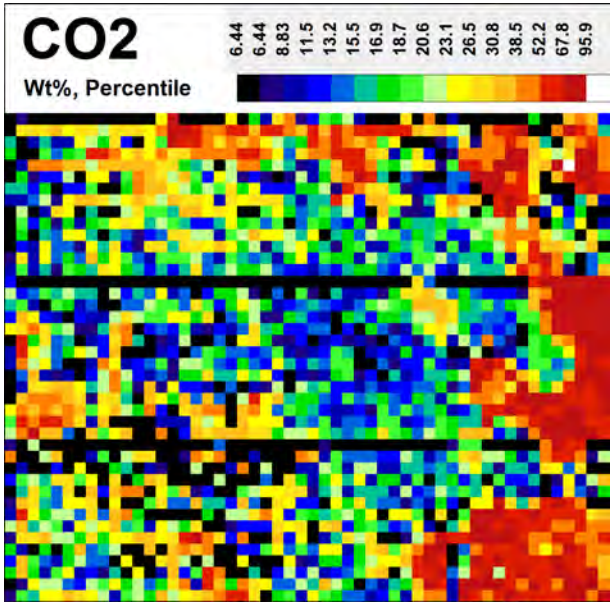
CO2
Wt%, Percentile
6.44
6.44
8.83
11.5
13.2
15.5
16.9
18.7
20.6
23.1
26.5
30.8
38.5
52.2
67.8
95.9

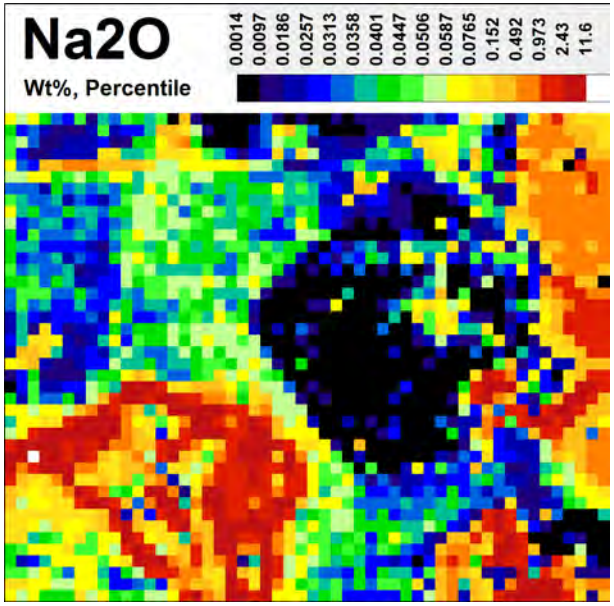
Na2O
Wt%, Percentile
0.0014
0.0097
0.0186
0.0257
0.0313
0.0358
0.0401
0.0447
0.0506
0.0587
0.0765
0.152
0.492
0.973
2.43
11.6

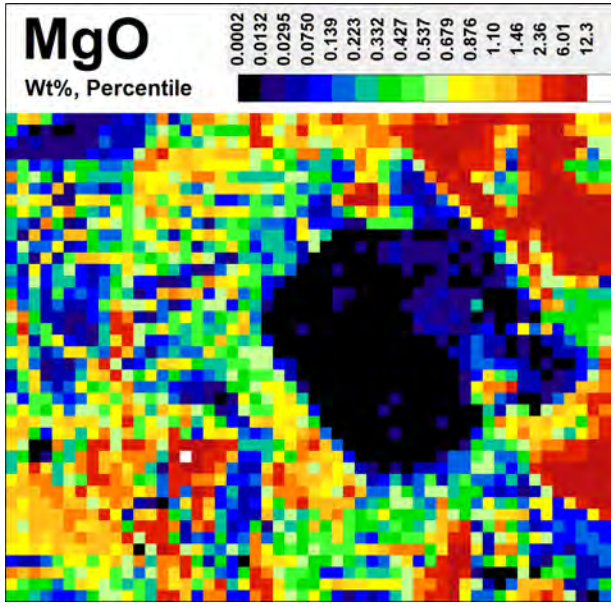
MgO
Wt%, Percentile
0.0002
0.0132
0.0295
0.0750
0.139
0.223
0.332
0.427
0.537
0.679
0.876
1.10
1.46
2.36
6.01
12.3

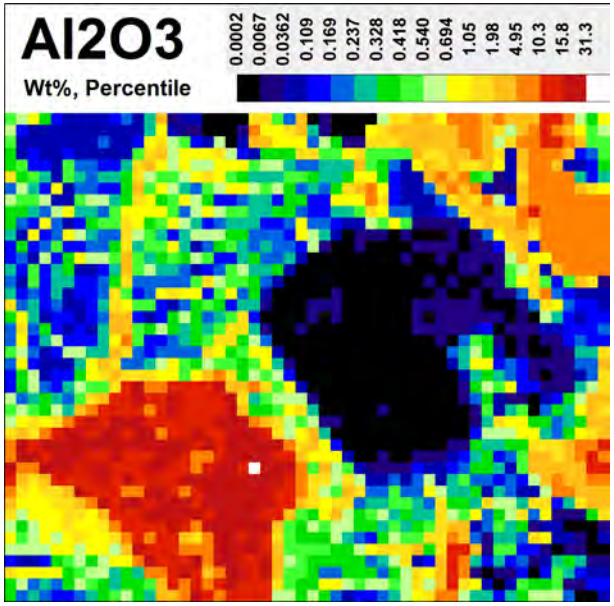
Al2O3
Wt%, Percentile
0.0002
0.0067
0.0362
0.109
0.169
0.237
0.328
0.418
0.540
0.694
1.05
1.98
4.95
10.3
15.8
31.3

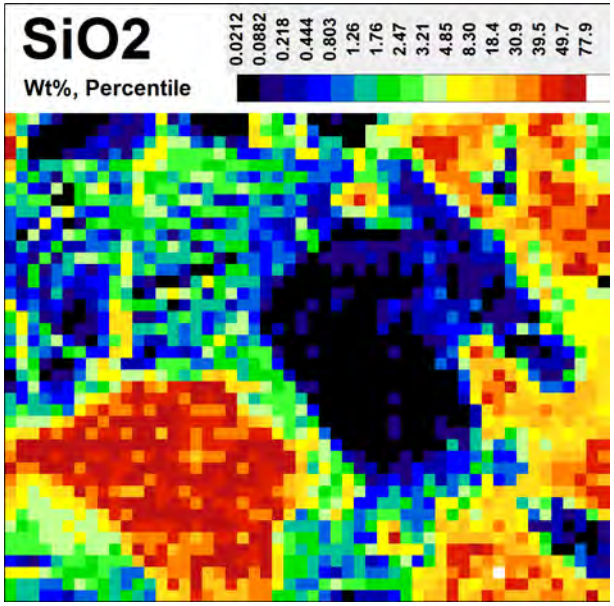
SiO2
Wt%, Percentile
0.0212
0.0882
0.218
0.444
0.803
1.26
1.76
2.47
3.21
4.85
8.30
18.4
30.9
39.5
49.7
77.9

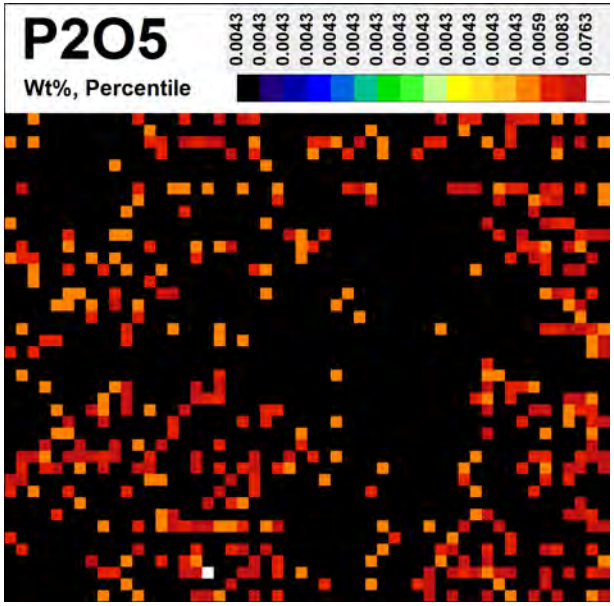
P2O5
Wt%, Percentile
0.0043 0.0043 0.0043 0.0043 0.0043 0.0043 0.0043 0.0043 0.0043 0.0043 0.0043 0.0059 0.0083 0.0763

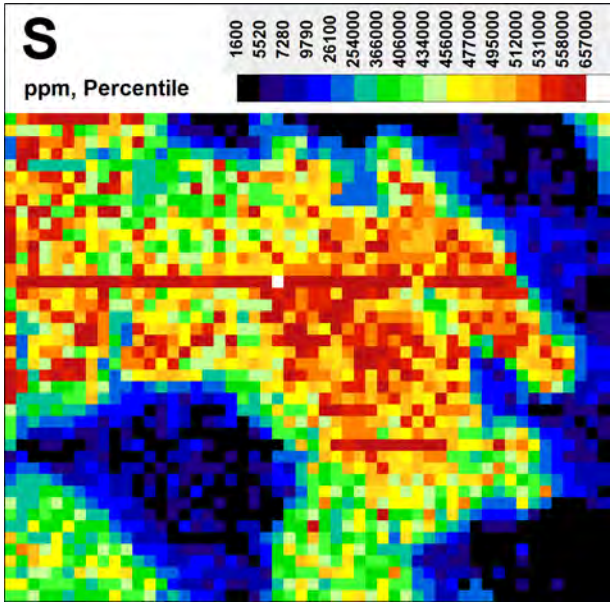
S
ppm, Percentile
1600 5520 7280 9790 26100 254000 366000 406000 434000 456000 477000 495000 512000 531000 558000 657000

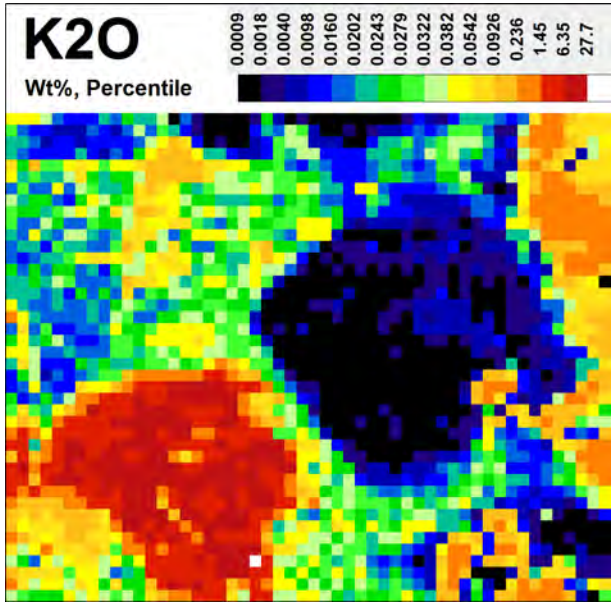
K2O
Wt%, Percentile
0.0009 0.0018 0.0040 0.0098 0.0160 0.0202 0.0243 0.0279 0.0322 0.0382 0.0542 0.0926 0.236 1.45 6.35 27.7

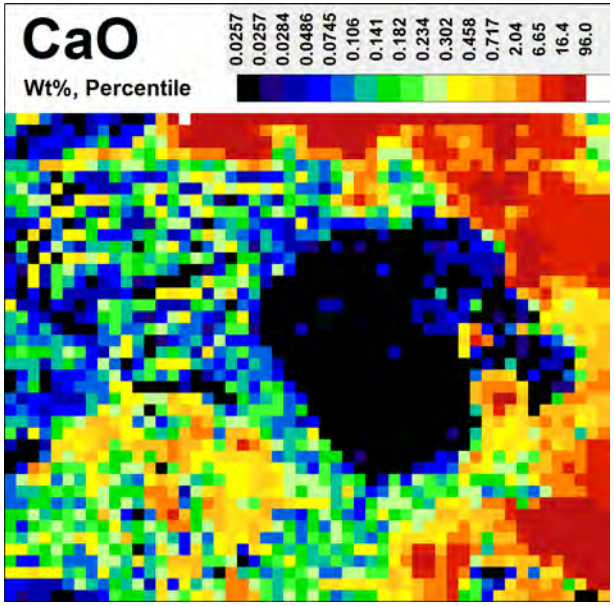
CaO
Wt%, Percentile
0.0257 0.0257 0.0284 0.0486 0.0745 0.106 0.141 0.182 0.234 0.302 0.458 0.717 2.04 6.65 16.4 96.0

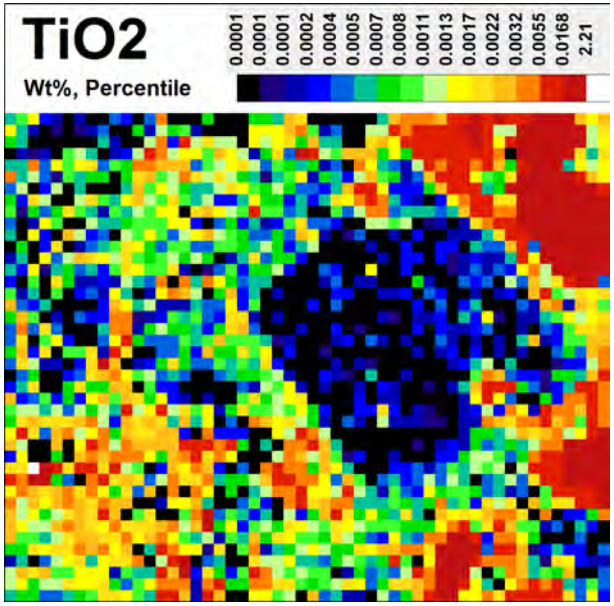
TiO2
Wt%, Percentile
0.0001 0.0001 0.0001 0.0002 0.0004 0.0005 0.0007 0.0008 0.0011 0.0013 0.0017 0.0022 0.0032 0.0055 0.0168 2.21

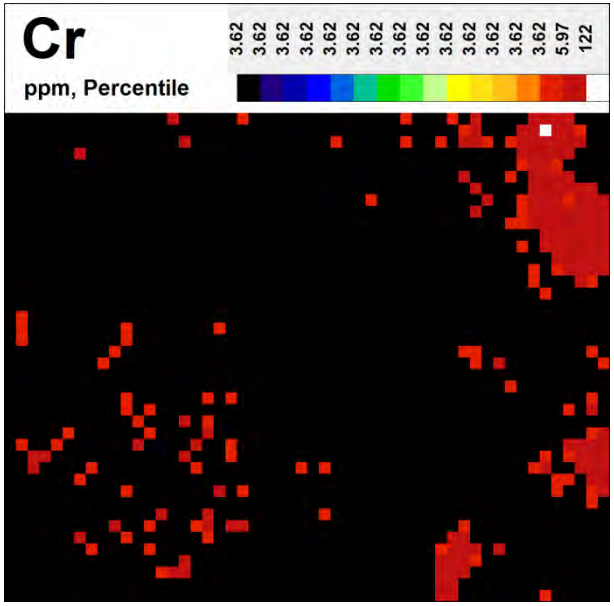
Cr
ppm, Percentile
3.62 3.62 3.62 3.62 3.62 3.62 3.62 3.62 3.62 3.62 3.62 3.62 5.97 122

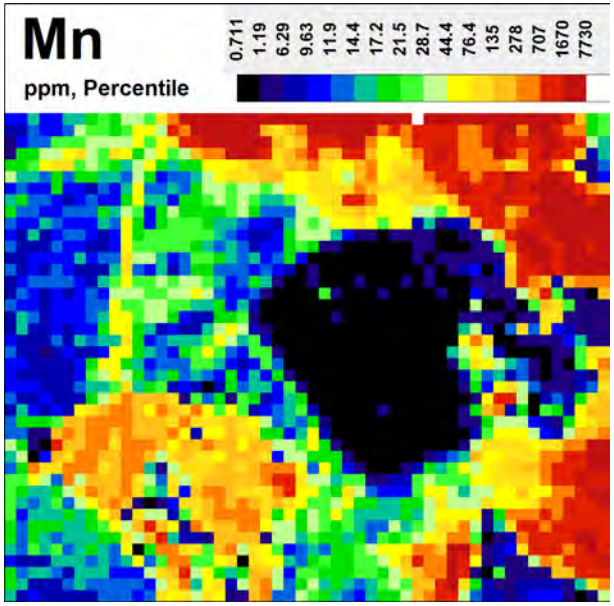
Mn
ppm, Percentile
0.711 1.19 6.29 9.63 11.9 14.4 17.2 21.5 28.7 44.4 76.4 135 278 707 1670 7730

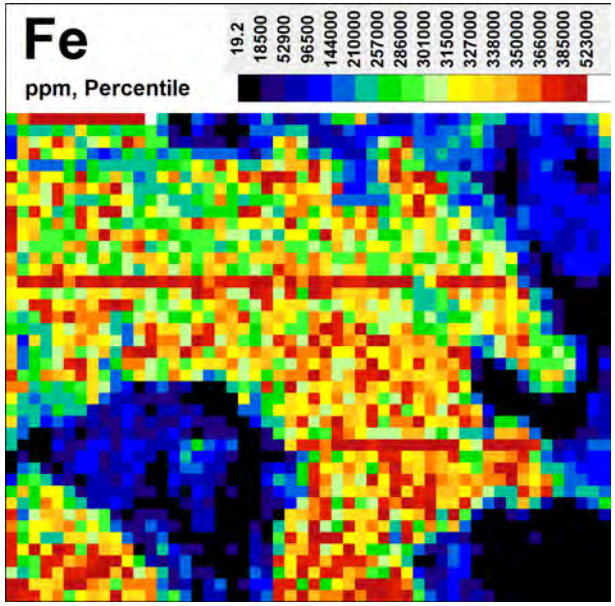
Fe
ppm, Percentile
19.2 18500 52900 96500 144000 210000 257000 286000 301000 315000 327000 338000 350000 366000 385000 523000

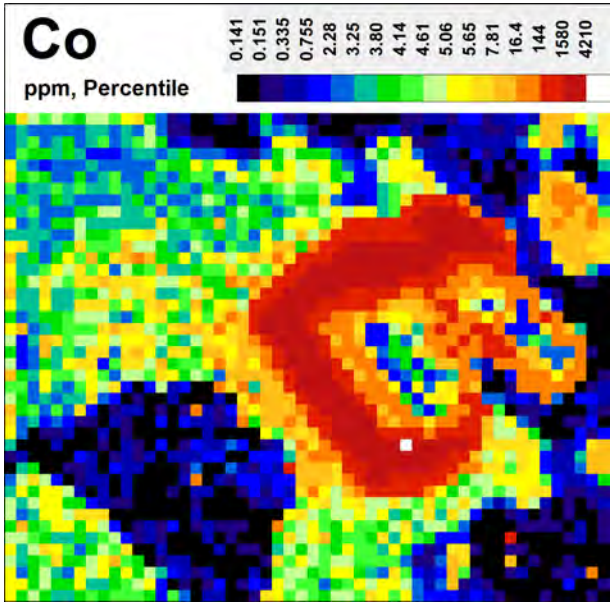
Co
ppm, Percentile
0.141 0.151 0.335 0.755 2.28 3.25 3.80 4.14 4.61 5.06 5.65 7.81 16.4 144 1580 4210

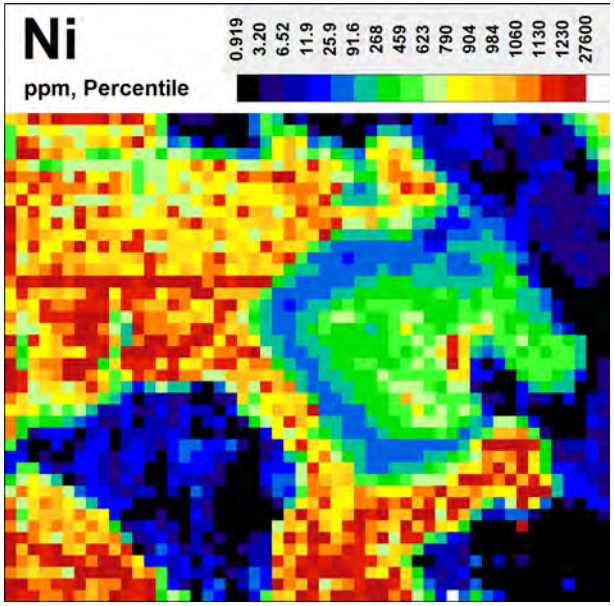
Ni
ppm, Percentile
0.919 3.20 6.52 11.9 25.9 91.6 268 459 623 790 904 984 1060 1130 1230 27600

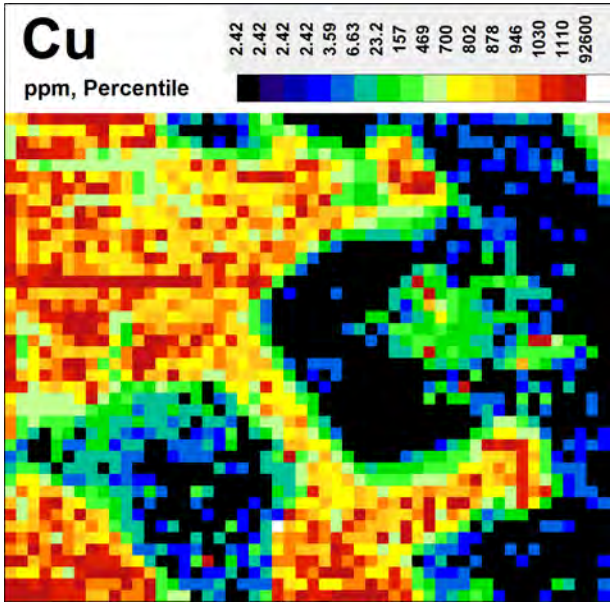
Cu
ppm, Percentile
2.42 2.42 2.42 2.42 3.59 6.63 23.2 157 469 700 802 878 946 1030 1110 92600

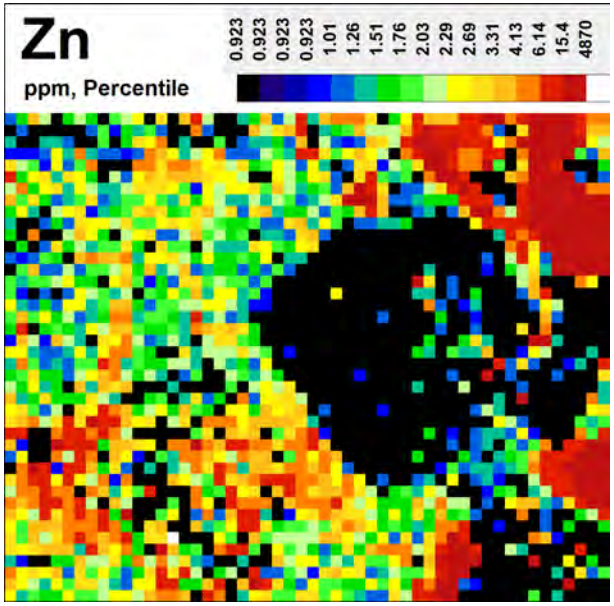
Zn
ppm, Percentile
0.923 0.923 0.923 0.923 1.01 1.26 1.51 1.76 2.03 2.29 2.69 3.31 4.13 6.14 15.4 4870

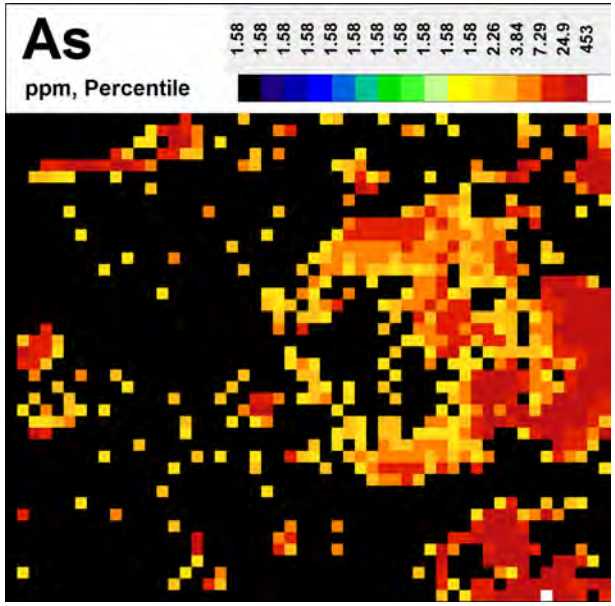
As
ppm, Percentile
1.58 1.58 1.58 1.58 1.58 1.58 1.58 1.58 1.58 1.58 2.26 3.84 7.29 24.9 453

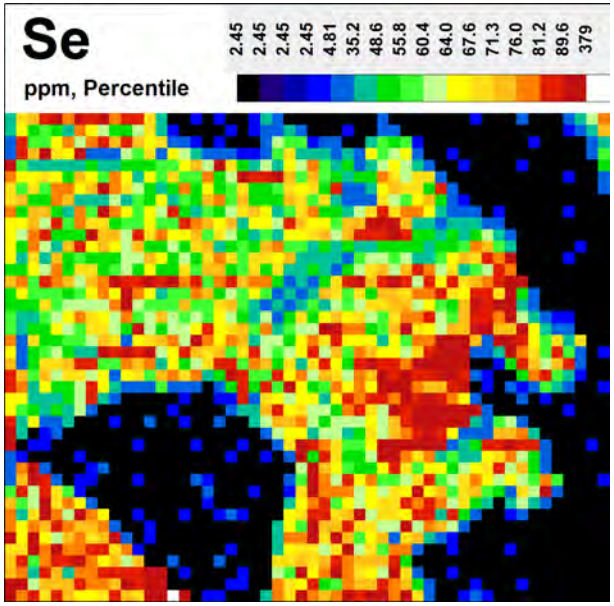
Se
ppm, Percentile
2.45 2.45 2.45 2.45 4.81 35.2 48.6 55.8 60.4 64.0 67.6 71.3 76.0 81.2 89.6 379

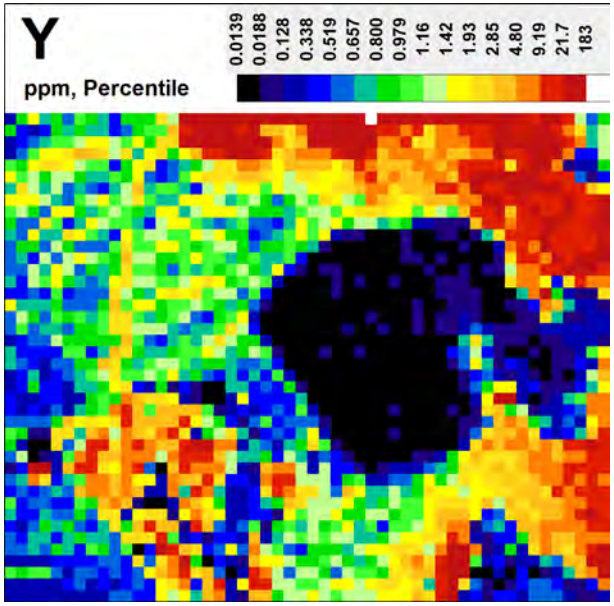
Y
ppm, Percentile
0.0139 0.0188 0.128 0.338 0.519 0.657 0.800 0.979 1.16 1.42 1.93 2.85 4.80 9.19 21.7 183

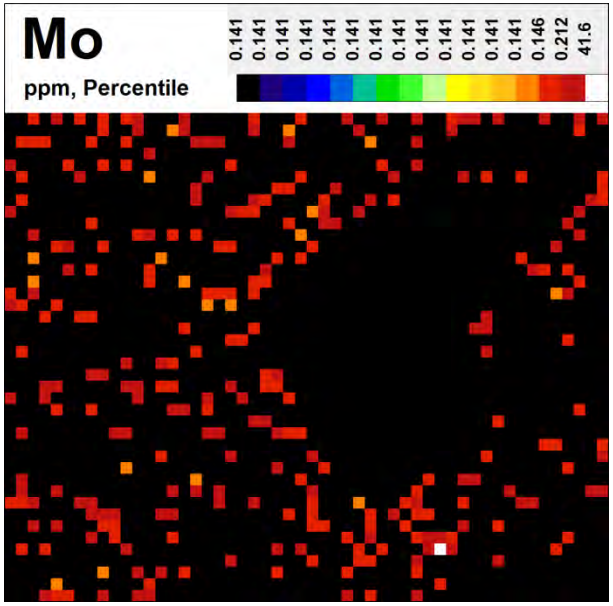
Mo
ppm, Percentile
0.141 0.141 0.141 0.141 0.141 0.141 0.141 0.141 0.141 0.141 0.141 0.146 0.212 41.6

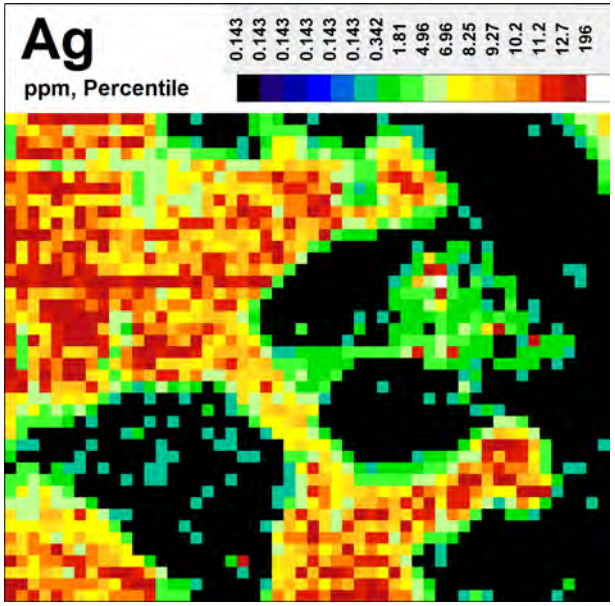
Ag
ppm, Percentile
0.143 0.143 0.143 0.143 0.143 0.342 1.81 4.96 6.96 8.25 9.27 10.2 11.2 12.7 196

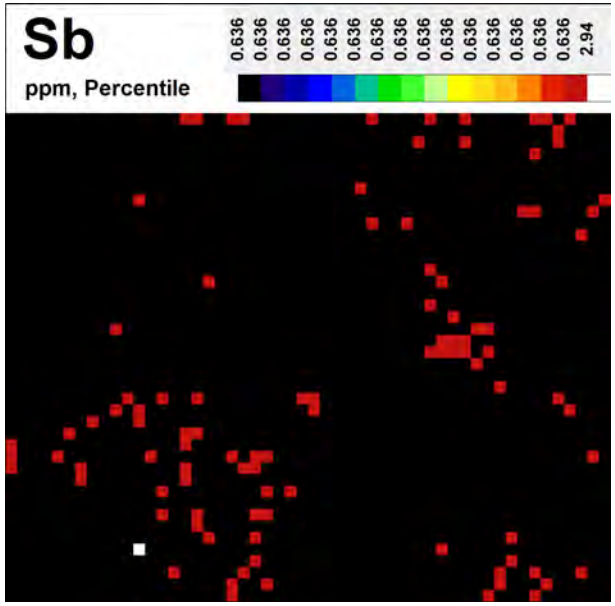
Sb
ppm, Percentile
0.636 0.636 0.636 0.636 0.636 0.636 0.636 0.636 0.636 0.636 0.636 0.636 0.636 2.94

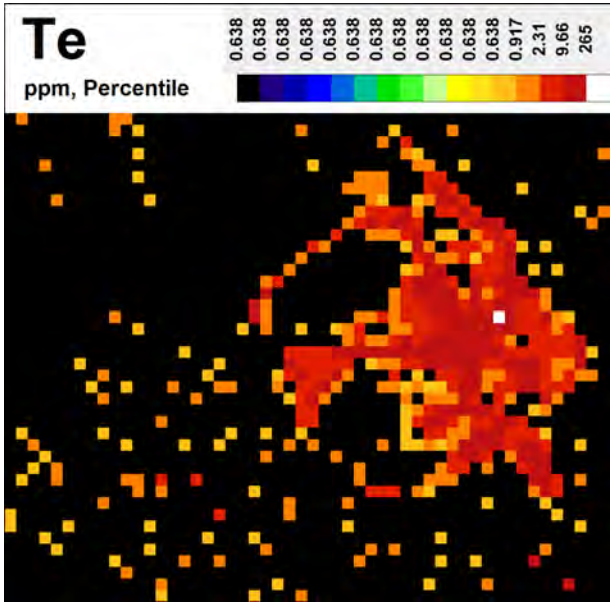
Te
ppm, Percentile
0.638 0.638 0.638 0.638 0.638 0.638 0.638 0.638 0.638 0.638 0.917 2.31 9.66 265

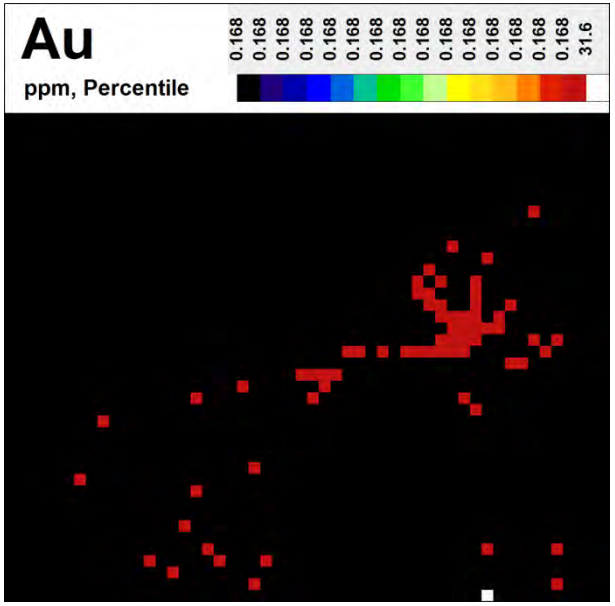
Au
ppm, Percentile
0.168 0.168 0.168 0.168 0.168 0.168 0.168 0.168 0.168 0.168 0.168 0.168 0.168 31.6

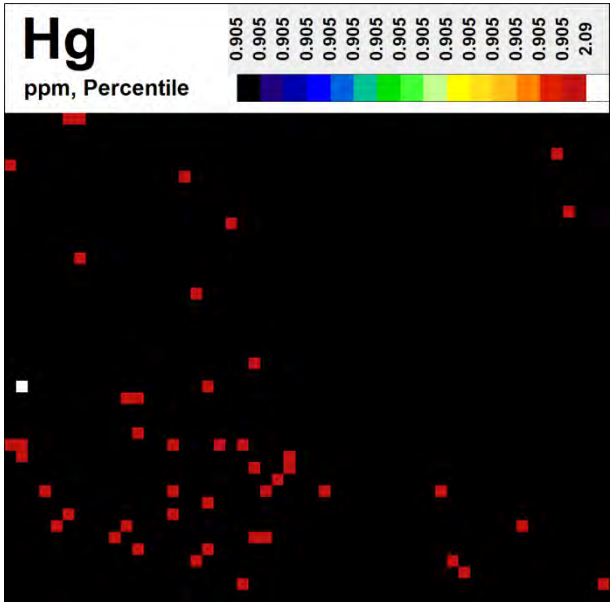
Hg
ppm, Percentile
0.905 0.905 0.905 0.905 0.905 0.905 0.905 0.905 0.905 0.905 0.905 0.905 0.905 2.09

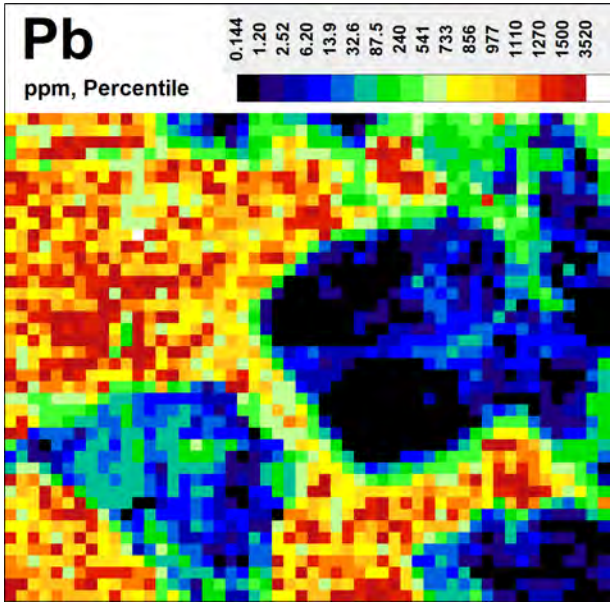
Pb
ppm, Percentile
0.144 1.20 2.52 6.20 13.9 32.6 87.5 240 541 733 856 977 1110 1270 1500 3520

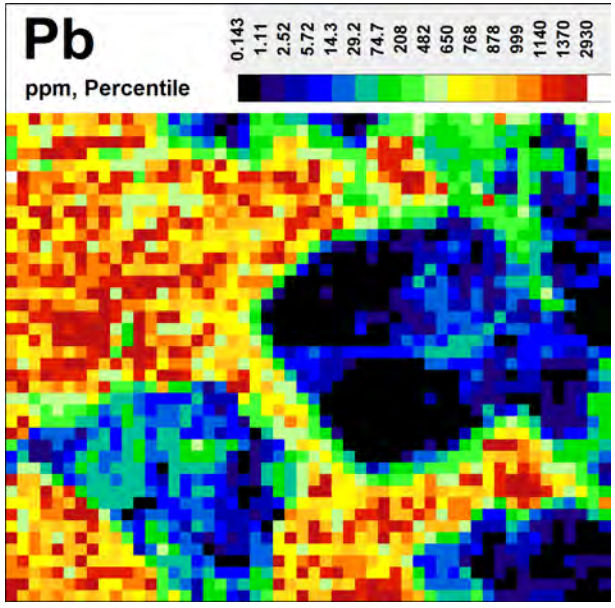
Pb
ppm, Percentile
0.143 1.11 2.52 5.72 14.3 29.2 74.7 208 482 650 768 878 999 1140 1370 2930

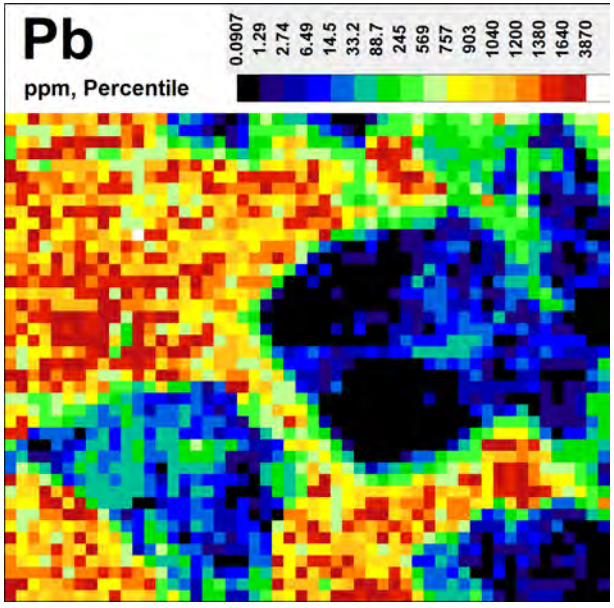
Pb
ppm, Percentile
0.0907 1.29 2.74 6.49 14.5 33.2 88.7 245 569 757 903 1040 1200 1380 1640 3870

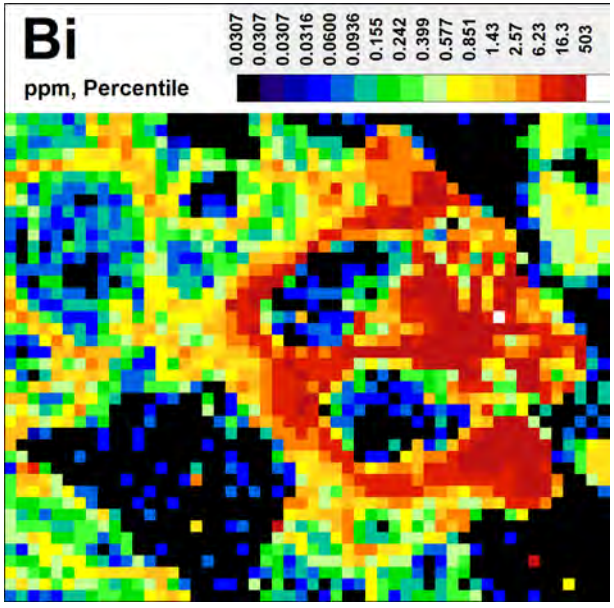
Bi
ppm, Percentile
0.0307 0.0307 0.0307 0.0316 0.0600 0.0936 0.155 0.242 0.399 0.577 0.851 1.43 2.57 6.23 16.3 503

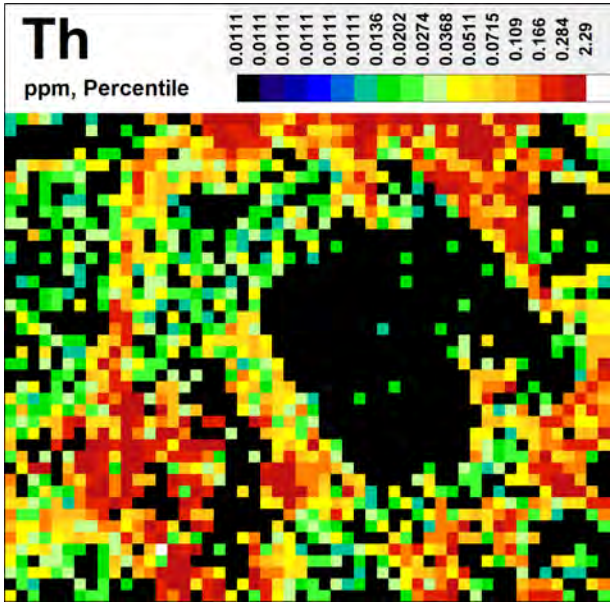
Th
ppm, Percentile
0.0111
0.0111
0.0111
0.0111
0.0111
0.0111
0.0136
0.0202
0.0274
0.0368
0.0511
0.0715
0.109
0.166
0.284
2.29

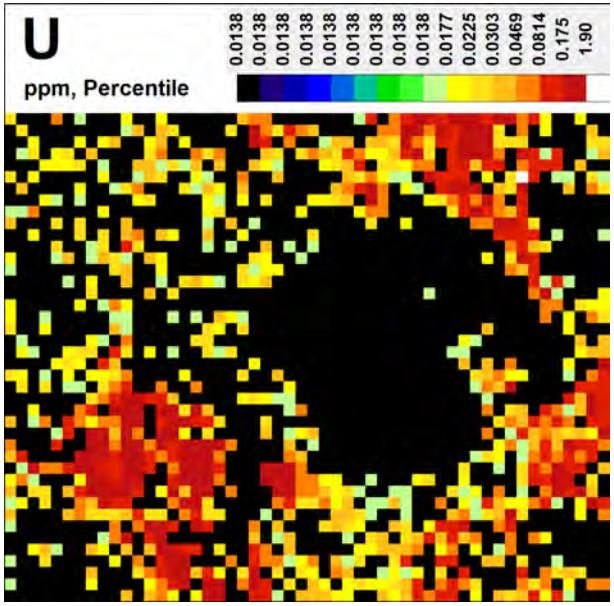
U
ppm, Percentile
0.0138
0.0138
0.0138
0.0138
0.0138
0.0138
0.0138
0.0138
0.0177
0.0225
0.0303
0.0469
0.0814
0.175
1.90

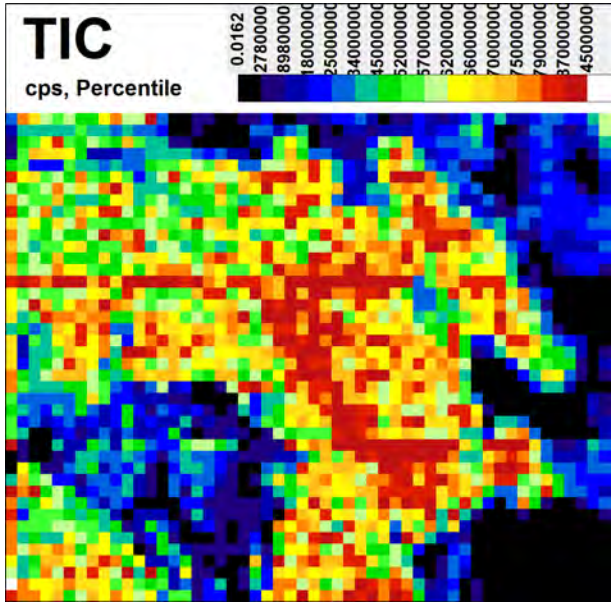
TIC
cps, Percentile
0.0162

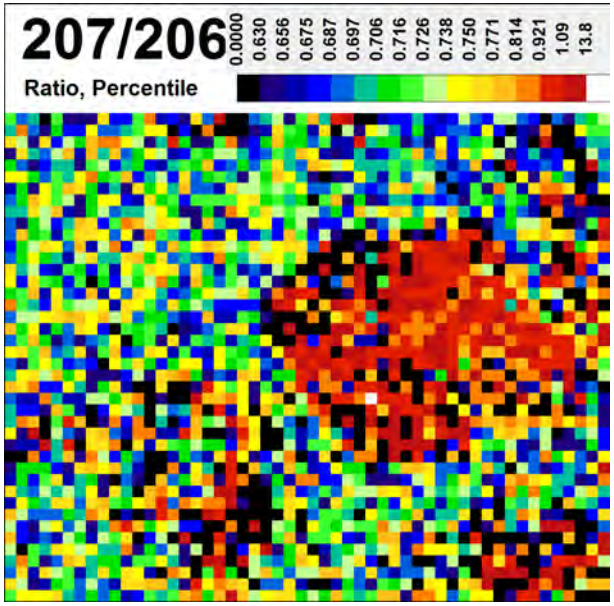
207/206
Ratio, Percentile
0.0000
0.630
0.656
0.675
0.687
0.697
0.706
0.716
0.726
0.738
0.750
0.771
0.814
0.921
1.09
13.8

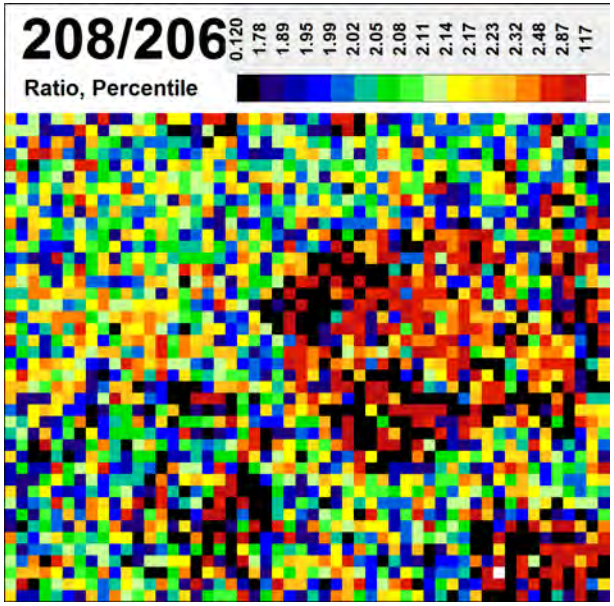
208/206
Ratio, Percentile
0.120
1.78
1.89
1.95
1.99
2.02
2.05
2.08
2.11
2.14
2.17
2.23
2.32
2.48
2.87
117

Figure DR8. (pages 150–163) LA-ICP-MS results of a euhedral type-2a pyrite porphyroblast overgrown by collorform bands of type-3 pyrite within a mafic volcanic sample (RD15-265-353) showing a BSE image of the mapping area and 32 major and trace maps. LA-ICP-MS maps reveal maps reveal trace element zonation, within the core of the early, type-2a pyrite porphyroblast, which is cut by Au-Ag-Te-Bi-rich a fracture and unusual Cu-Pb-Zn-Ag-rich concentrations that are devoid of Au within type-3 collform pyrite bands.

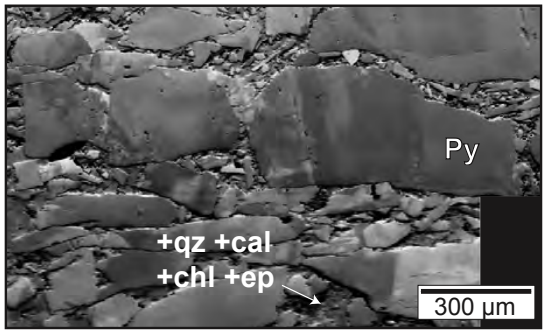
Py
+qz +cal
+chl +ep
300 µm

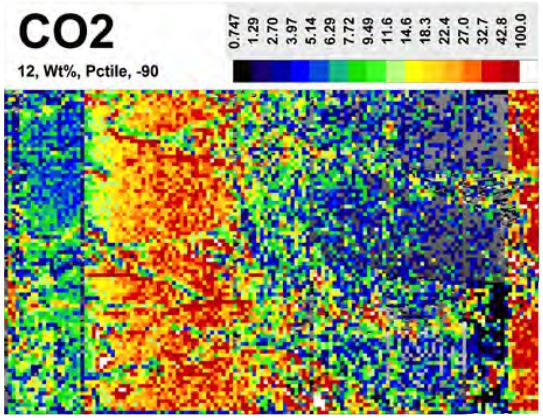
CO2
12, Wt%, Pctile, -90
0.747 1.29 2.70 3.97 5.14 6.29 7.72 9.49 11.6 14.6 18.3 22.4 27.0 32.7 42.8 100.0

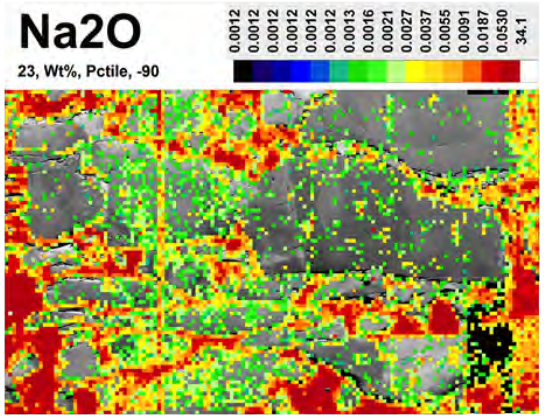
Na2O
23, Wt%, Pctile, -90
0.0012 0.0012 0.0012 0.0012 0.0012 0.0012 0.0013 0.0016 0.0021 0.0027 0.0037 0.0055 0.0091 0.0187 0.0530 34.1

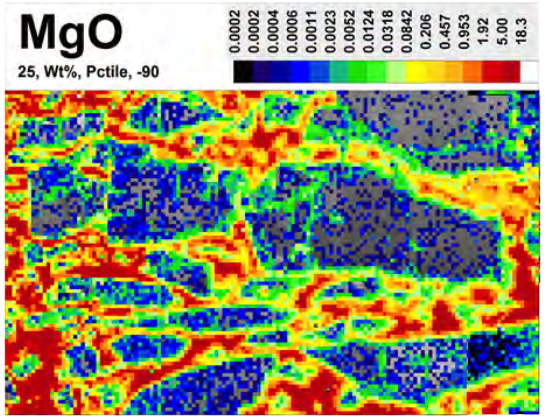
MgO
25, Wt%, Pctile, -90
0.0002 0.0002 0.0004 0.0006 0.0011 0.0023 0.0052 0.0124 0.0318 0.0842 0.206 0.457 0.953 1.92 5.00 18.3

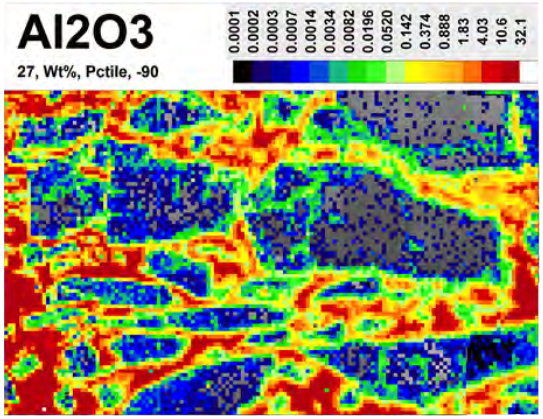
Al2O3
27, Wt%, Pctile, -90
0.0001 0.0002 0.0003 0.0007 0.0014 0.0034 0.0082 0.0196 0.0520 0.142 0.374 0.888 1.83 4.03 10.6 32.1

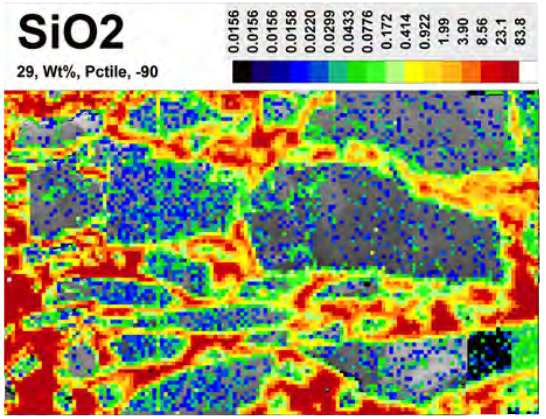
SiO2
29, Wt%, Pctile, -90
0.0156 0.0156 0.0156 0.0158 0.0220 0.0299 0.0433 0.0776 0.172 0.414 0.922 1.99 3.90 8.56 23.1 83.8

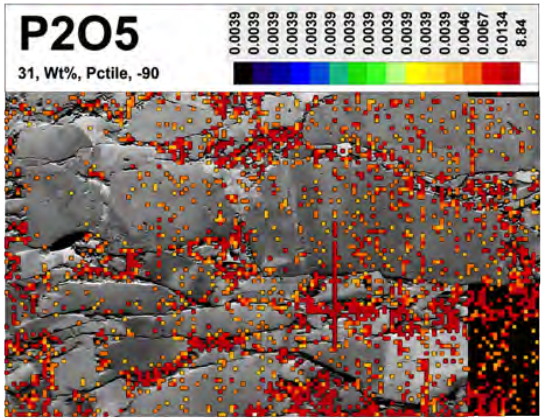
P2O5
31, Wt%, Pctile, -90
0.0039 0.0039 0.0039 0.0039 0.0039 0.0039 0.0039 0.0039 0.0039 0.0039 0.0046 0.0067 0.0134 8.84

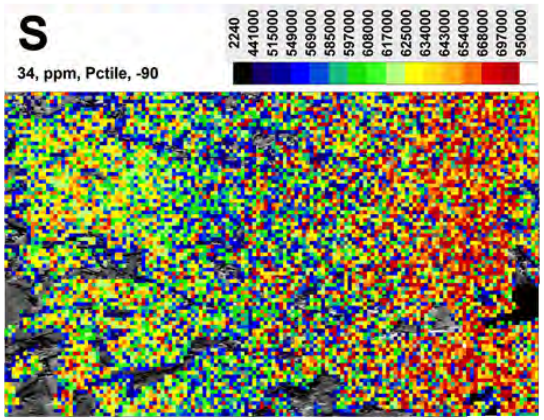
S
34, ppm, Pctile, -90
2240 441000 515000 549000 569000 585000 597000 608000 617000 625000 634000 643000 654000 668000 697000 950000

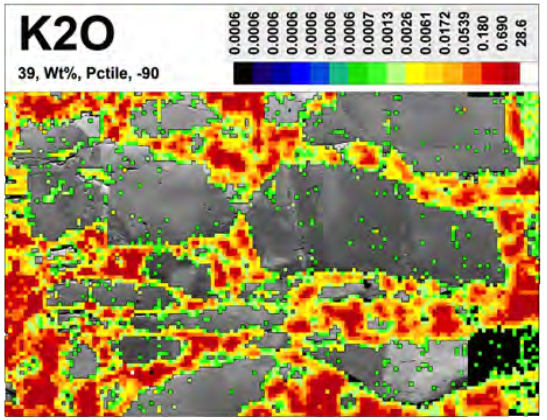
K2O
39, Wt%, Pctile, -90
0.0006 0.0006 0.0006 0.0006 0.0006 0.0006 0.0006 0.0007 0.0013 0.0026 0.0061 0.0172 0.0539 0.180 0.690 28.6

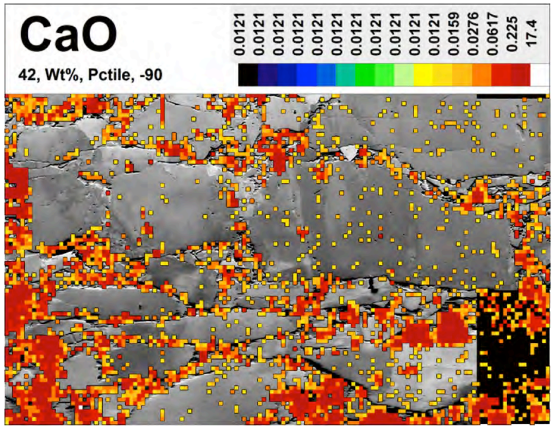
CaO
42, Wt%, Pctile, -90
0.0121 0.0121 0.0121 0.0121 0.0121 0.0121 0.0121 0.0121 0.0121 0.0121 0.0121 0.0159 0.0276 0.0617 0.225 17.4

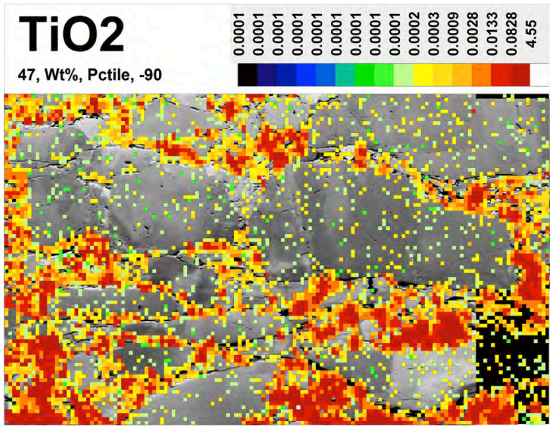
TiO2
47, Wt%, Pctile, -90
0.0001 0.0001 0.0001 0.0001 0.0001 0.0001 0.0001 0.0001 0.0002 0.0003 0.0009 0.0028 0.0133 0.0828 4.55

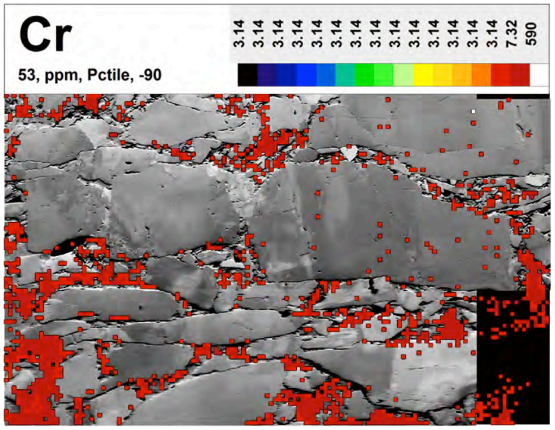
Cr
53, ppm, Pctile, -90
3.14 3.14 3.14 3.14 3.14 3.14 3.14 3.14 3.14 3.14 3.14 3.14 3.14 7.32 590

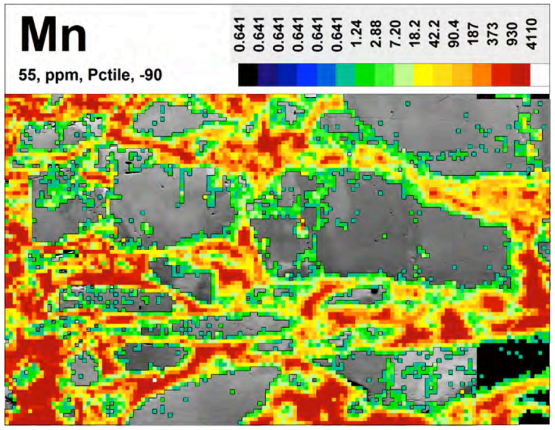
Mn
55, ppm, Pctile, -90
0.641 0.641 0.641 0.641 0.641 0.641 1.24 2.88 7.20 18.2 42.2 90.4 187 373 930 4110

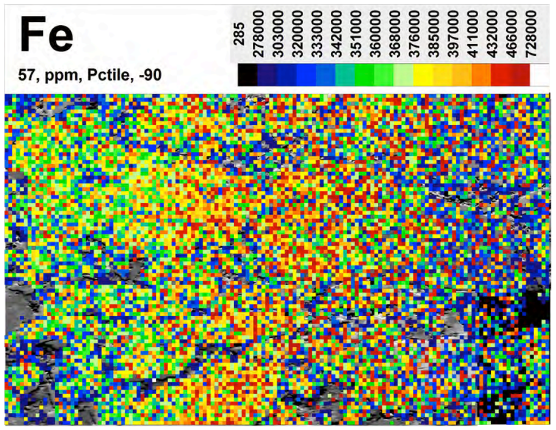
Fe
57, ppm, Pctile, -90
285 278000 303000 320000 333000 342000 351000 360000 368000 376000 385000 397000 411000 432000 466000 728000

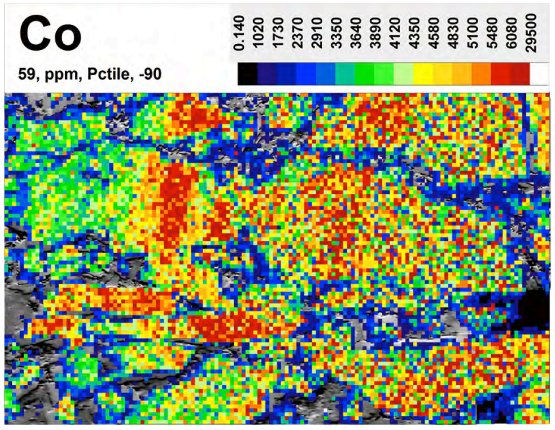
Co
59, ppm, Pctile, -90
0.140 1020 1730 2370 2910 3350 3640 3890 4120 4350 4580 4830 5100 5480 6080 29500

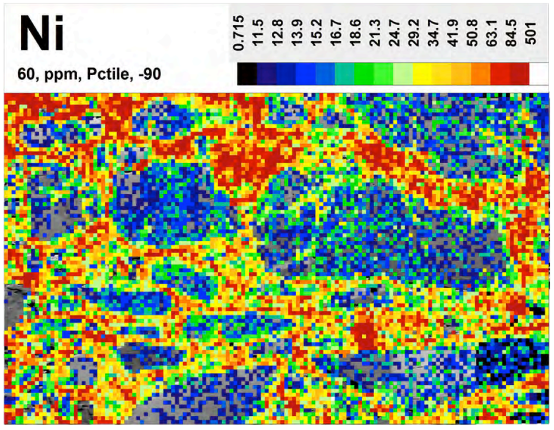
Ni
60, ppm, Pctile, -90
0.715 11.5 12.8 13.9 15.2 16.7 18.6 21.3 24.7 29.2 34.7 41.9 50.8 63.1 84.5 501

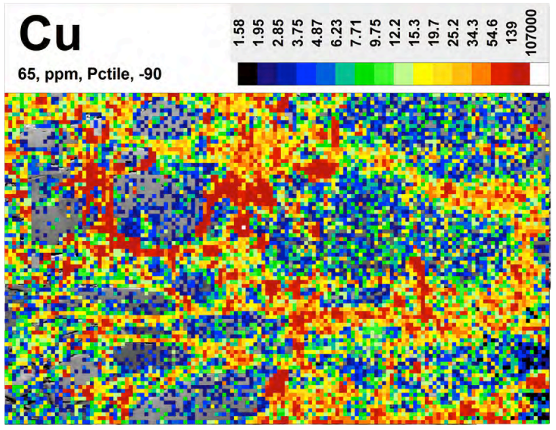
Cu
65, ppm, Pctile, -90
1.58 1.95 2.85 3.75 4.87 6.23 7.71 9.75 12.2 15.3 19.7 25.2 34.3 54.6 139 107000

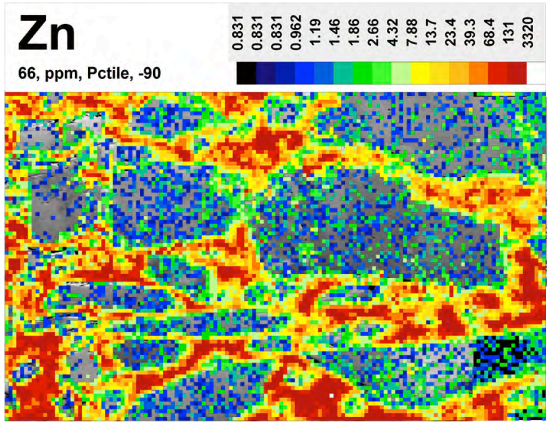
Zn
66, ppm, Pctile, -90
0.831 0.831 0.831 0.962 1.19 1.46 1.86 2.66 4.32 7.88 13.7 23.4 39.3 68.4 131 3320

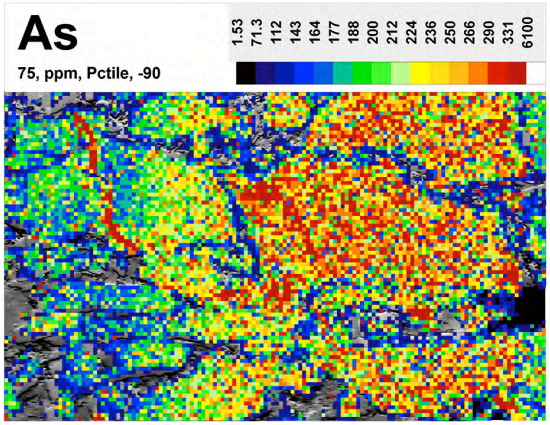
As
75, ppm, Pctile, -90
1.53 71.3 112 143 164 177 188 200 212 224 236 250 266 290 331 6100

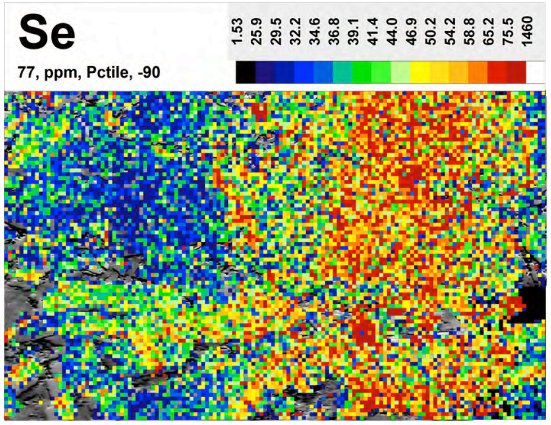
Se
77, ppm, Pctile, -90
1.53 25.9 29.5 32.2 34.6 36.8 39.1 41.4 44.0 46.9 50.2 54.2 58.8 65.2 75.5 1460

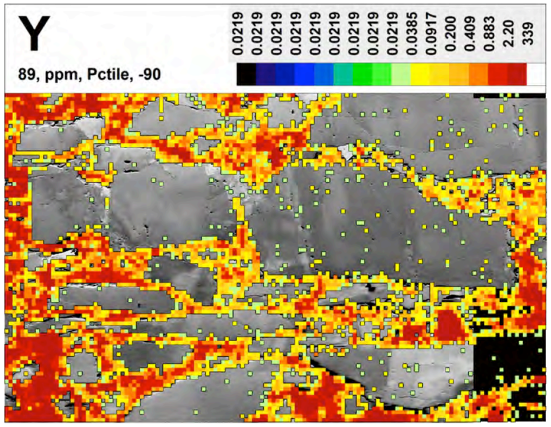
Y
89, ppm, Pctile, -90
0.0219 0.0219 0.0219 0.0219 0.0219 0.0219 0.0219 0.0219 0.0219 0.0385 0.0917 0.200 0.409 0.883 2.20 339

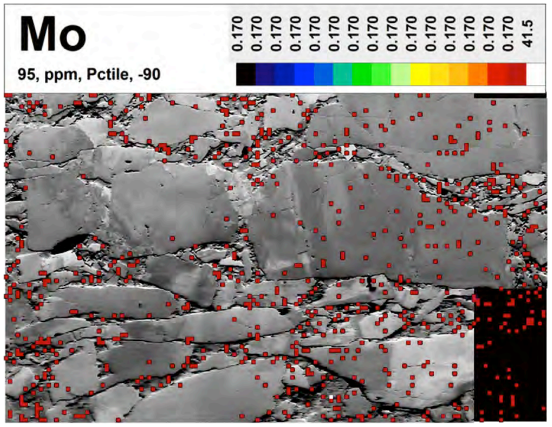
Mo
95, ppm, Pctile, -90
0.170 0.170 0.170 0.170 0.170 0.170 0.170 0.170 0.170 0.170 0.170 0.170 0.170 0.170 0.170 41.5

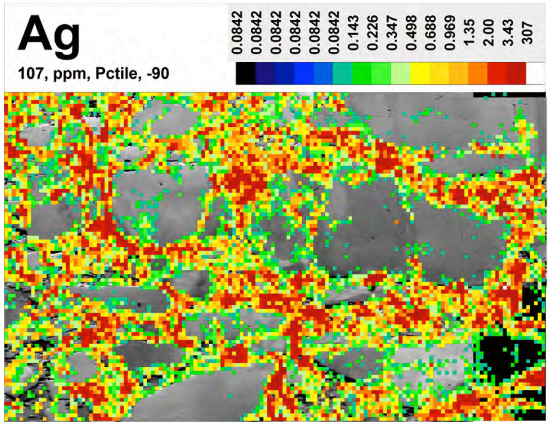
Ag
107, ppm, Pctile, -90
0.0842 0.0842 0.0842 0.0842 0.0842 0.0842 0.143 0.226 0.347 0.498 0.688 0.969 1.35 2.00 3.43 307

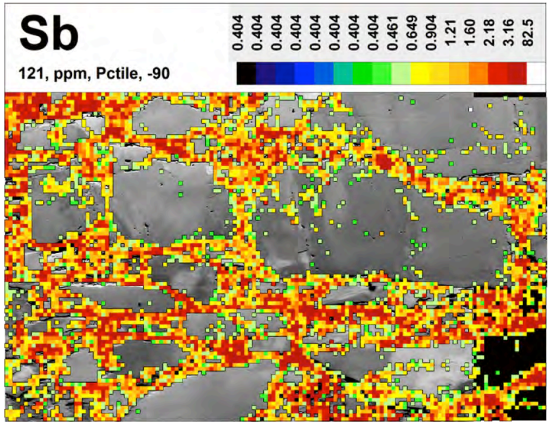
Sb
121, ppm, Pctile, -90
0.404 0.404 0.404 0.404 0.404 0.404 0.404 0.404 0.461 0.649 0.904 1.21 1.60 2.18 3.16 82.5

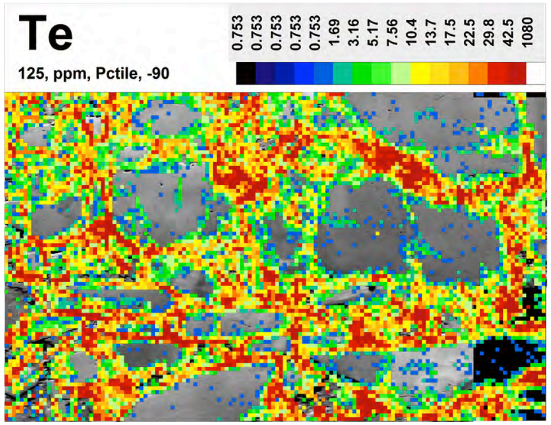
Te
125, ppm, Pctile, -90
0.753 0.753 0.753 0.753 0.753 1.69 3.16 5.17 7.56 10.4 13.7 17.5 22.5 29.8 42.5 1080

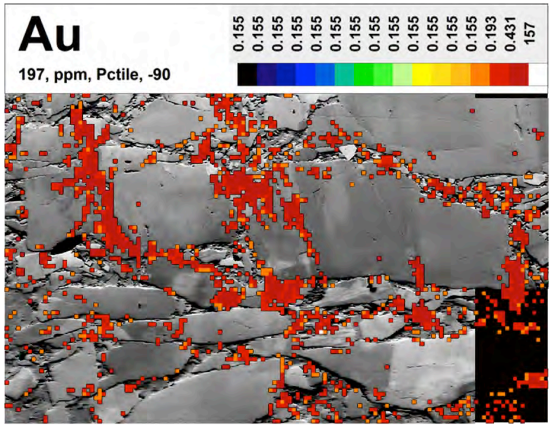
Au
197, ppm, Pctile, -90
0.155 0.155 0.155 0.155 0.155 0.155 0.155 0.155 0.155 0.155 0.155 0.155 0.193 0.431 157

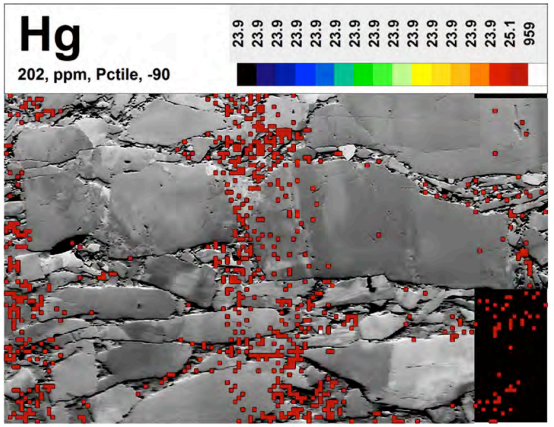
Hg
202, ppm, Pctile, -90
23.9 23.9 23.9 23.9 23.9 23.9 23.9 23.9 23.9 23.9 23.9 23.9 23.9 25.1 959

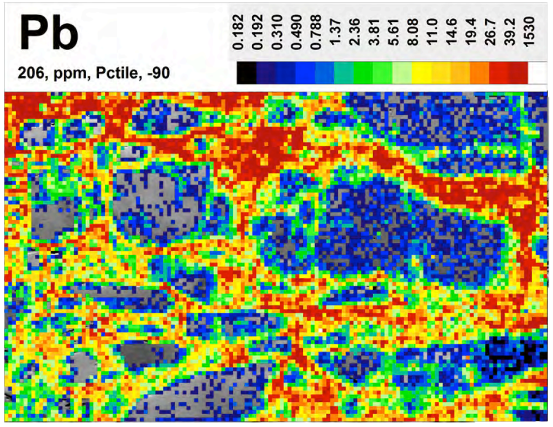
Pb
206, ppm, Pctile, -90
0.182 0.192 0.310 0.490 0.788 1.37 2.36 3.81 5.61 8.08 11.0 14.6 19.4 26.7 39.2 1530

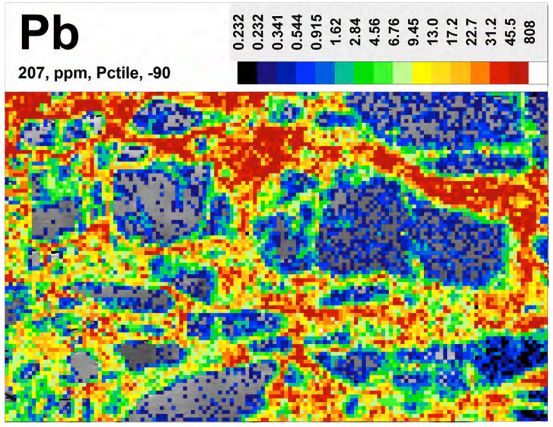
Pb
207, ppm, Pctile, -90
0.232 0.232 0.341 0.544 0.915 1.62 2.84 4.56 6.76 9.45 13.0 17.2 22.7 31.2 45.5 808

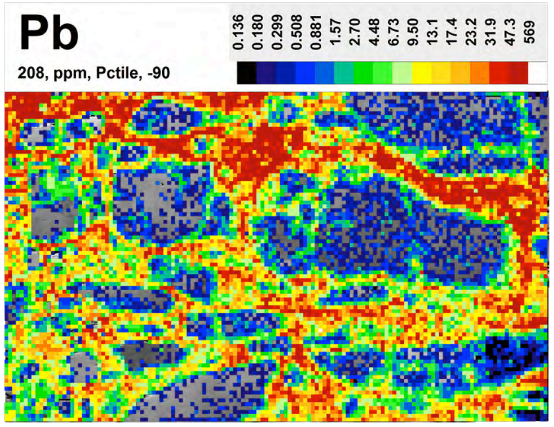
Pb
208, ppm, Pctile, -90
0.136 0.180 0.299 0.508 0.881 1.57 2.70 4.48 6.73 9.50 13.1 17.4 23.2 31.9 47.3 569

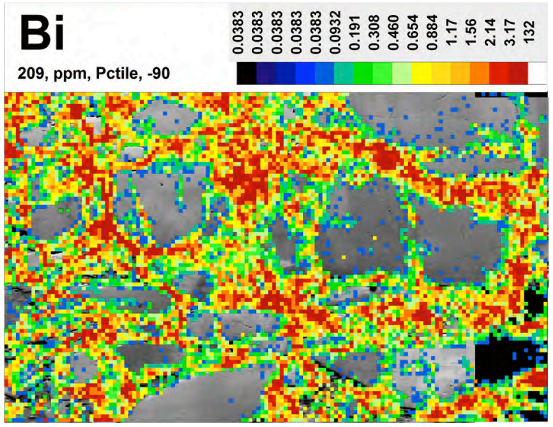
Bi
209, ppm, Pctile, -90
0.0383 0.0383 0.0383 0.0383 0.0383 0.0932 0.191 0.308 0.460 0.654 0.884 1.17 1.56 2.14 3.17 132

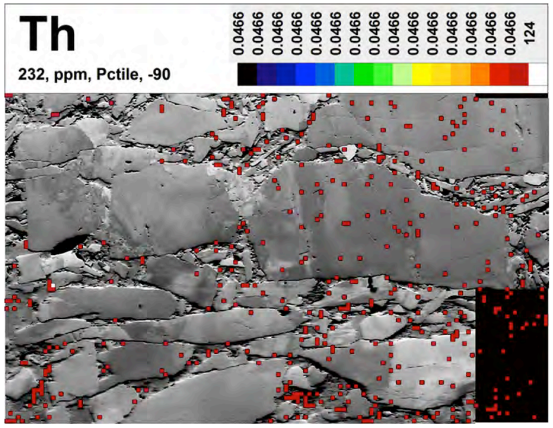
Th
232, ppm, Pctile, -90
0.0466 0.0466 0.0466 0.0466 0.0466 0.0466 0.0466 0.0466 0.0466 0.0466 0.0466 0.0466 0.0466 0.0466 124

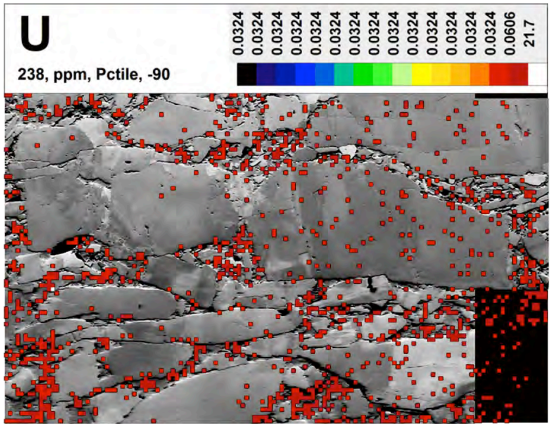
U
238, ppm, Pctile, -90
0.0324 0.0324 0.0324 0.0324 0.0324 0.0324 0.0324 0.0324 0.0324 0.0324 0.0324 0.0324 0.0324 0.0606 21.7

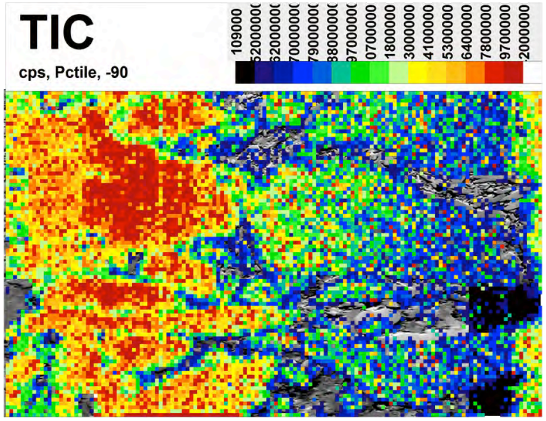
TIC
cps, Pctile, -90
109000
52000000
32000000
70000000
79000000
38000000
97000000
07000000
18000000
30000000
41000000
53000000
64000000
78000000
97000000
20000000

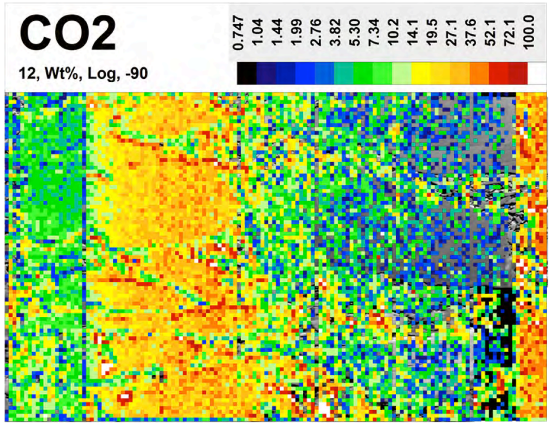
CO2
12, Wt%, Log, -90
0.747 1.04 1.44 1.99 2.76 3.82 5.30 7.34 10.2 14.1 19.5 27.1 37.6 52.1 72.1 100.0

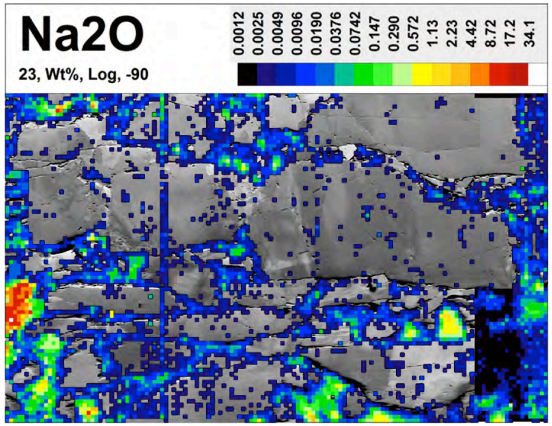
Na2O
23, Wt%, Log, -90
0.0012 0.0025 0.0049 0.0096 0.0190 0.0376 0.0742 0.147 0.290 0.572 1.13 2.23 4.42 8.72 17.2 34.1

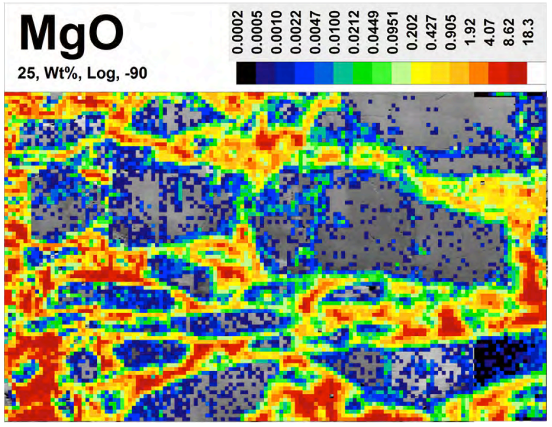
MgO
25, Wt%, Log, -90
0.0002 0.0005 0.0010 0.0022 0.0047 0.0100 0.0212 0.0449 0.0951 0.202 0.427 0.905 1.92 4.07 8.62 18.3

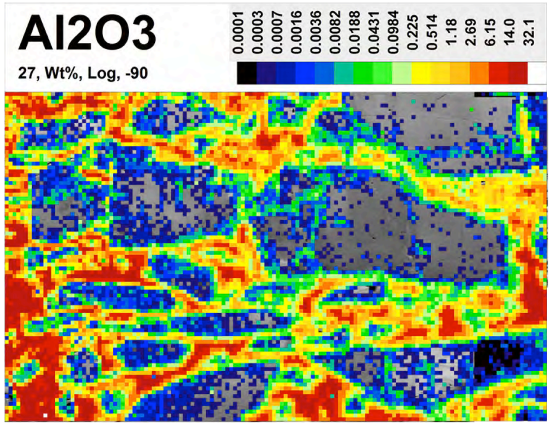
Al2O3
27, Wt%, Log, -90
0.0001 0.0003 0.0007 0.0016 0.0036 0.0082 0.0188 0.0431 0.0984 0.225 0.514 1.18 2.69 6.15 14.0 32.1

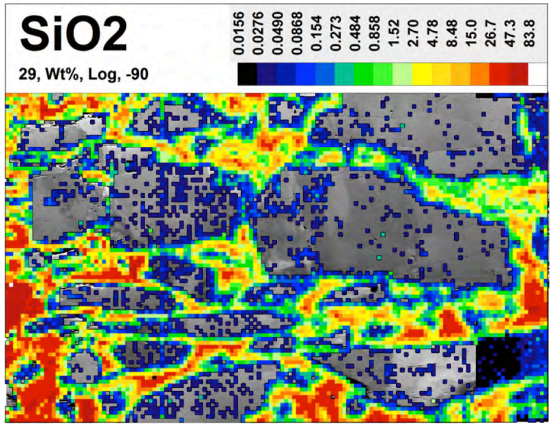
SiO2
29, Wt%, Log, -90
0.0156 0.0276 0.0490 0.0868 0.154 0.273 0.484 0.858 1.52 2.70 4.78 8.48 15.0 26.7 47.3 83.8

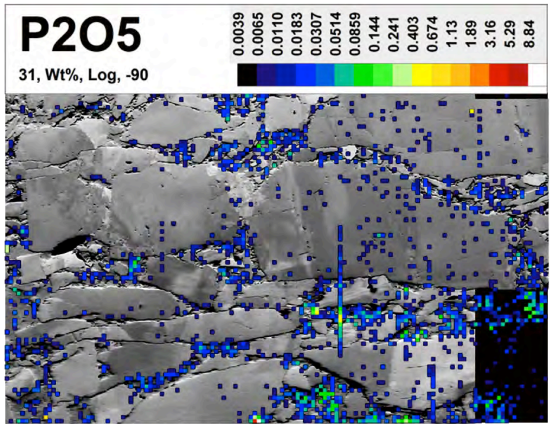
P2O5
31, Wt%, Log, -90
0.0039 0.0065 0.0110 0.0183 0.0307 0.0514 0.0859 0.144 0.241 0.403 0.674 1.13 1.89 3.16 5.29 8.84

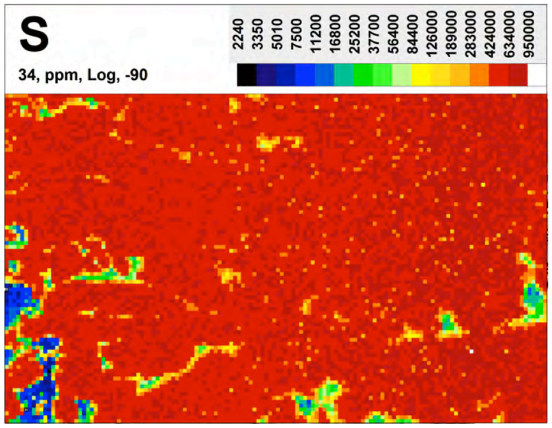
S
34, ppm, Log, -90
2240 3350 5010 7500 11200 16800 25200 37700 56400 84400 126000 189000 283000 424000 634000 950000

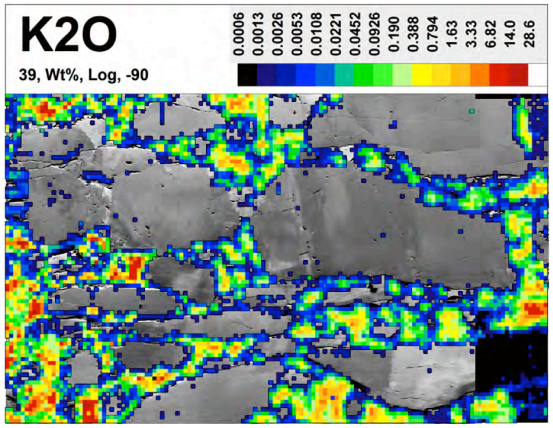
K2O
39, Wt%, Log, -90
0.0006 0.0013 0.0026 0.0053 0.0108 0.0221 0.0452 0.0926 0.190 0.388 0.794 1.63 3.33 6.82 14.0 28.6

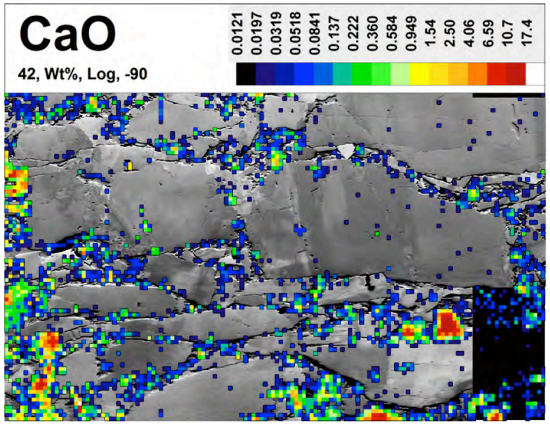
CaO
42, Wt%, Log, -90
0.0121 0.0197 0.0319 0.0518 0.0841 0.137 0.222 0.360 0.584 0.949 1.54 2.50 4.06 6.59 10.7 17.4

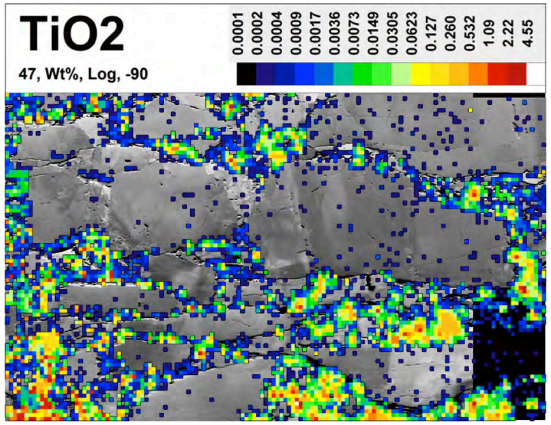
TiO2
47, Wt%, Log, -90
0.0001 0.0002 0.0004 0.0009 0.0017 0.0036 0.0073 0.0149 0.0305 0.0623 0.127 0.260 0.532 1.09 2.22 4.55

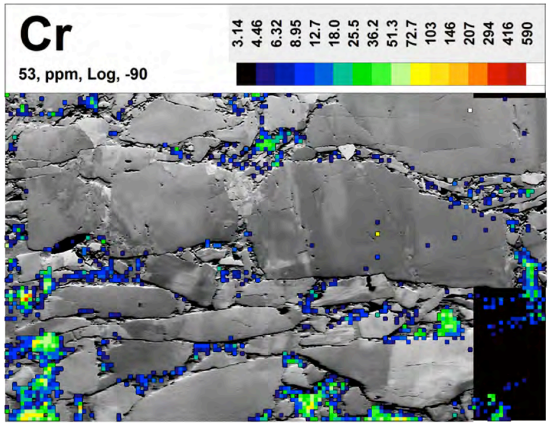
Cr
53, ppm, Log, -90
3.14 4.46 6.32 8.95 12.7 18.0 25.5 36.2 51.3 72.7 103 146 207 294 416 590

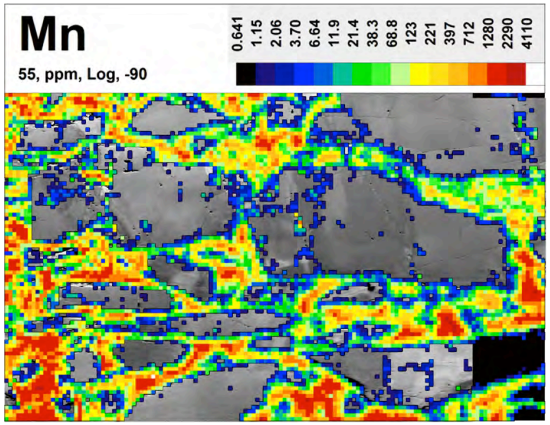
Mn
55, ppm, Log, -90
0.641 1.15 2.06 3.70 6.64 11.9 21.4 38.3 68.8 123 221 397 712 1280 2290 4110

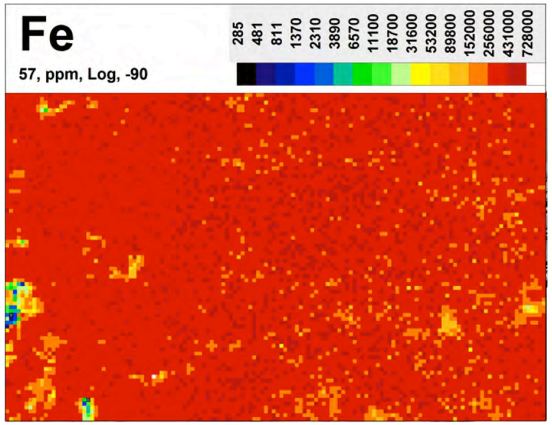
Fe
57, ppm, Log, -90
285 481 811 1370 2310 3890 6570 11100 18700 31600 53200 89800 152000 256000 431000 728000

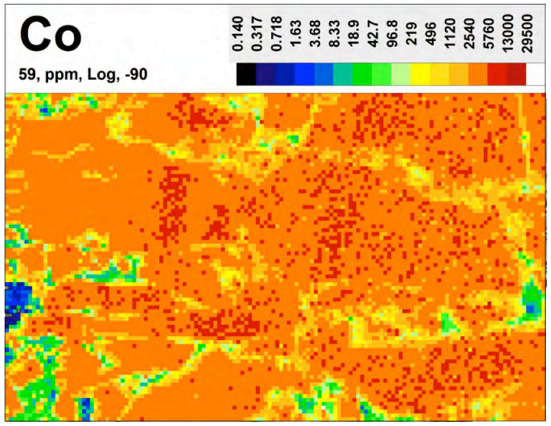
Co
59, ppm, Log, -90
0.140 0.317 0.718 1.63 3.68 8.33 18.9 42.7 96.8 219 496 1120 2540 5760 13000 29500

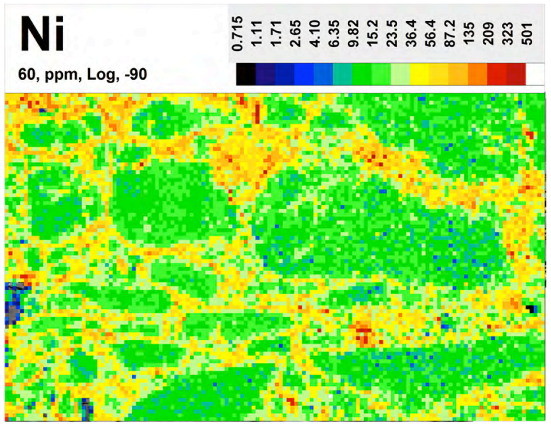
Ni
60, ppm, Log, -90
0.715 1.11 1.71 2.65 4.10 6.35 9.82 15.2 23.5 36.4 56.4 87.2 135 209 323 501

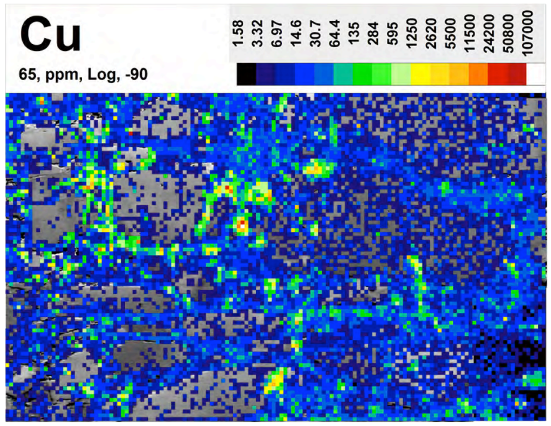
Cu
65, ppm, Log, -90
1.58 3.32 6.97 14.6 30.7 64.4 135 284 595 1250 2620 5500 11500 24200 50800 107000

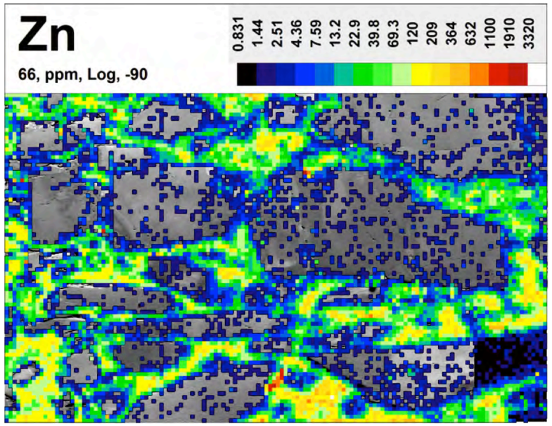
Zn
66, ppm, Log, -90
0.831 1.44 2.51 4.36 7.59 13.2 22.9 39.8 69.3 120 209 364 632 1100 1910 3320

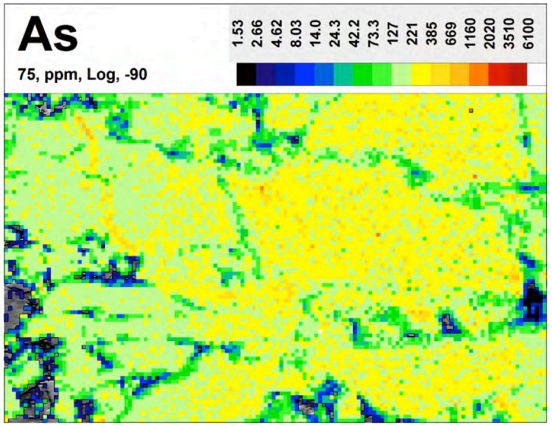
As
75, ppm, Log, -90
1.53 2.66 4.62 8.03 14.0 24.3 42.2 73.3 127 221 385 669 1160 2020 3510 6100

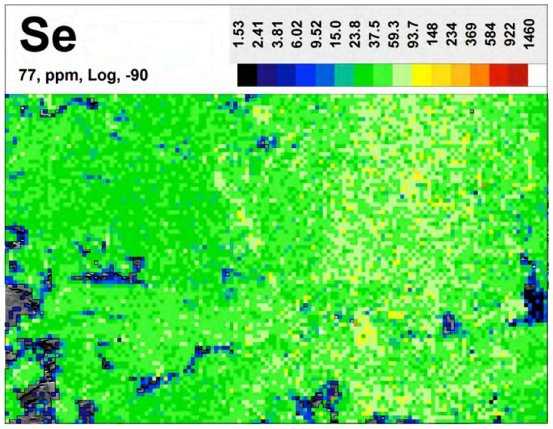
Se
77, ppm, Log, -90
1.53 2.41 3.81 6.02 9.52 15.0 23.8 37.5 59.3 93.7 148 234 369 584 922 1460

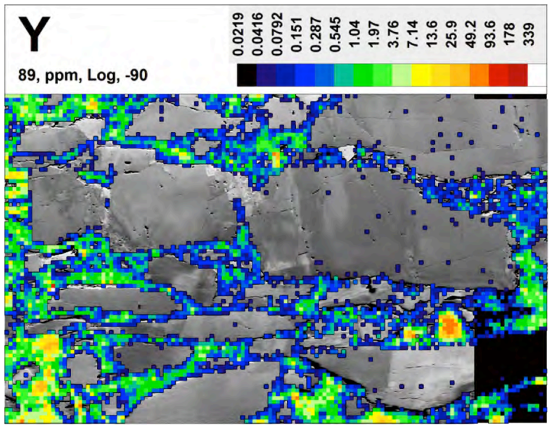
Y
89, ppm, Log, -90
0.0219 0.0416 0.0792 0.151 0.287 0.545 1.04 1.97 3.76 7.14 13.6 25.9 49.2 93.6 178 339

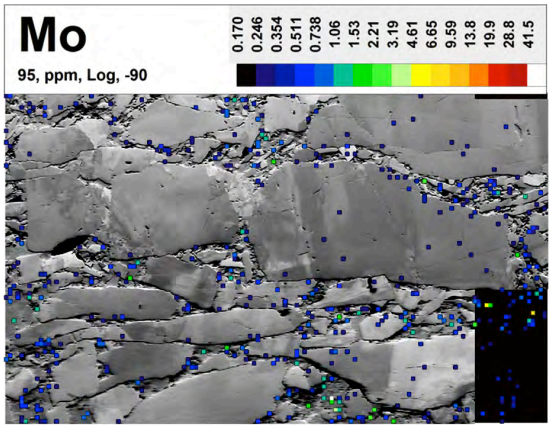
Mo
95, ppm, Log, -90
0.170 0.246 0.354 0.511 0.738 1.06 1.53 2.21 3.19 4.61 6.65 9.59 13.8 19.9 28.8 41.5

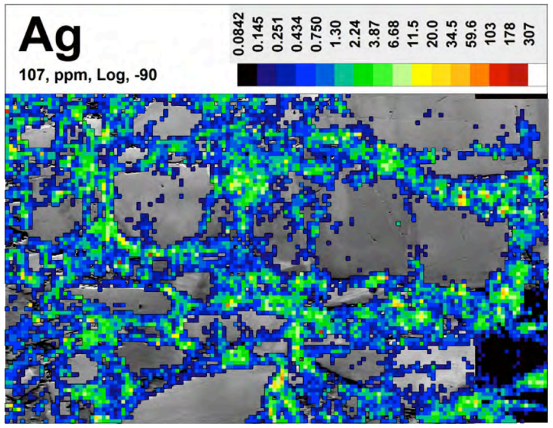
Ag
107, ppm, Log, -90
0.0842 0.145 0.251 0.434 0.750 1.30 2.24 3.87 6.68 11.5 20.0 34.5 59.6 103 178 307

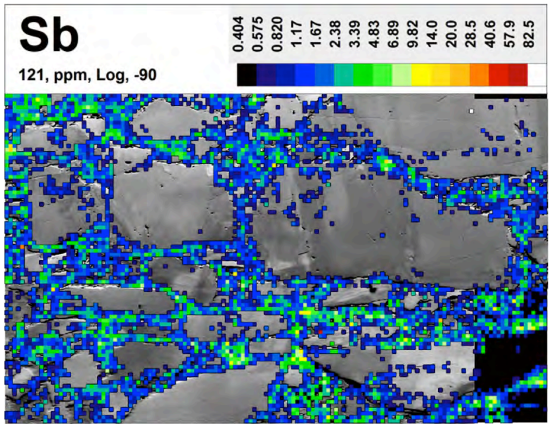
Sb
121, ppm, Log, -90
0.404 0.575 0.820 1.17 1.67 2.38 3.39 4.83 6.89 9.82 14.0 20.0 28.5 40.6 57.9 82.5

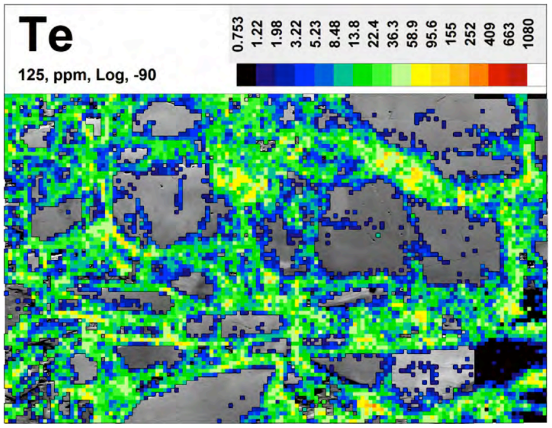
Te
125, ppm, Log, -90
0.753 1.22 1.98 3.22 5.23 8.48 13.8 22.4 36.3 58.9 95.6 155 252 409 663 1080

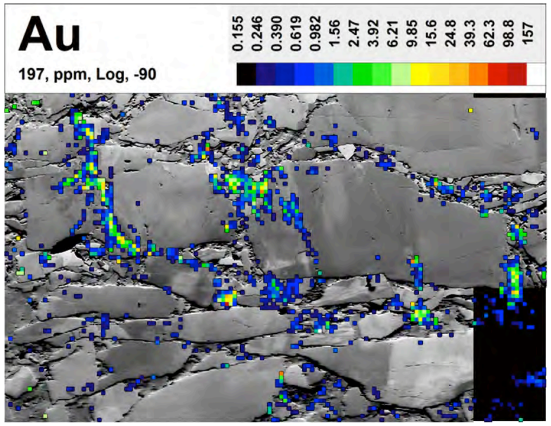
Au
197, ppm, Log, -90
0.155 0.246 0.390 0.619 0.982 1.56 2.47 3.92 6.21 9.85 15.6 24.8 39.3 62.3 98.8 157

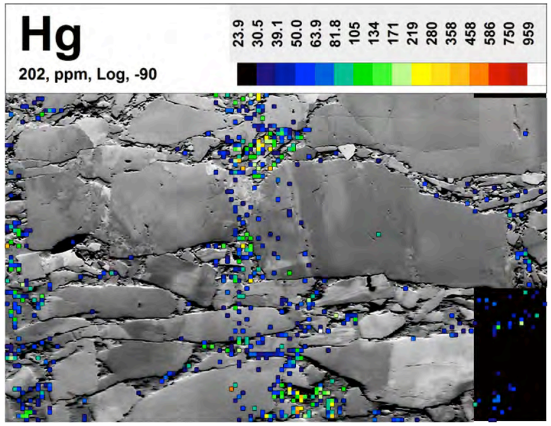
Hg
202, ppm, Log, -90
23.9 30.5 39.1 50.0 63.9 81.8 105 134 171 219 280 358 458 586 750 959

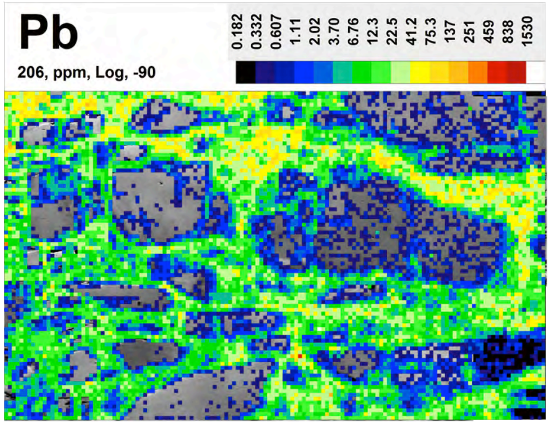
Pb
206, ppm, Log, -90
0.182 0.332 0.607 1.11 2.02 3.70 6.76 12.3 22.5 41.2 75.3 137 251 459 838 1530

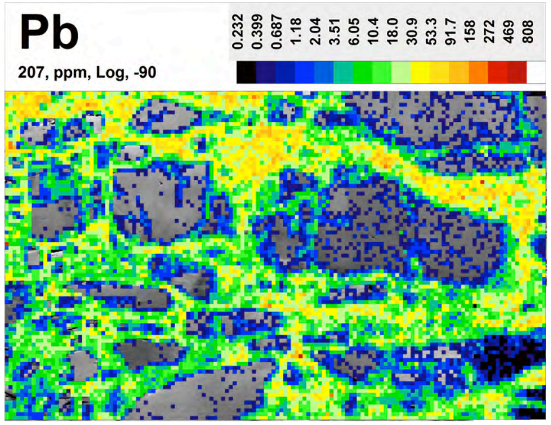
Pb
207, ppm, Log, -90
0.232 0.399 0.687 1.18 2.04 3.51 6.05 10.4 18.0 30.9 53.3 91.7 158 272 469 808

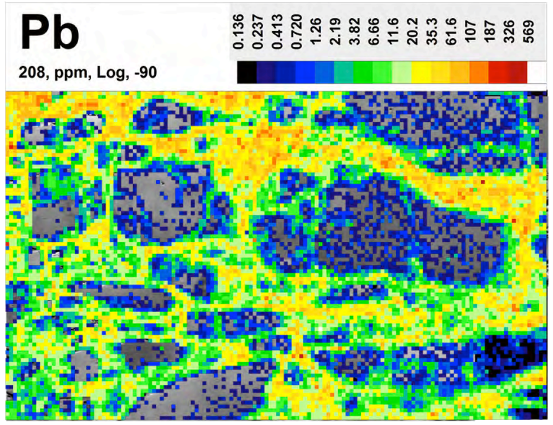
Pb
208, ppm, Log, -90
0.136 0.237 0.413 0.720 1.26 2.19 3.82 6.66 11.6 20.2 35.3 61.6 107 187 326 569

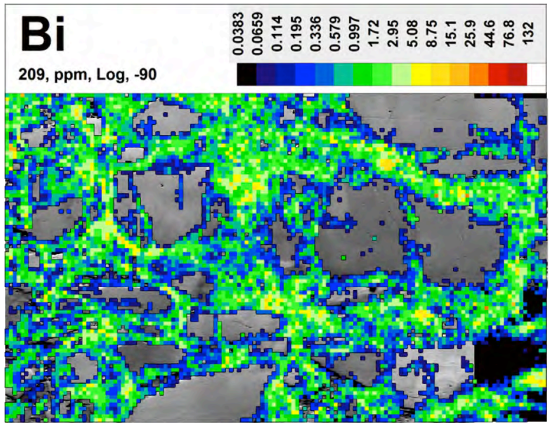
Bi
209, ppm, Log, -90
0.0383 0.0659 0.114 0.195 0.336 0.579 0.997 1.72 2.95 5.08 8.75 15.1 25.9 44.6 76.8 132

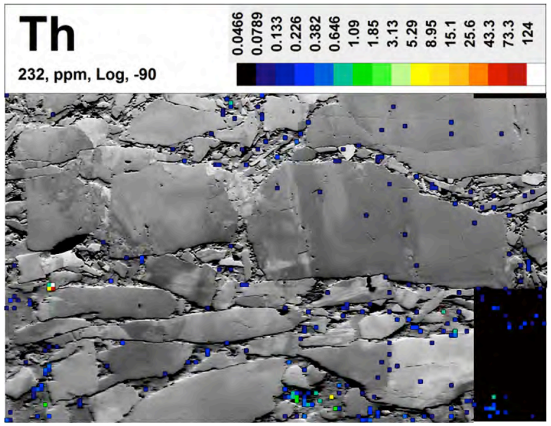
Th
232, ppm, Log, -90
0.0466 0.0789 0.133 0.226 0.382 0.646 1.09 1.85 3.13 5.29 8.95 15.1 25.6 43.3 73.3 124

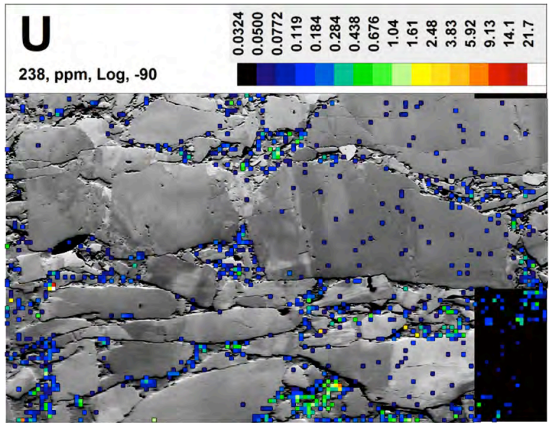
U
238, ppm, Log, -90
0.0324 0.0500 0.0772 0.119 0.184 0.284 0.438 0.676 1.04 1.61 2.48 3.83 5.92 9.13 14.1 21.7

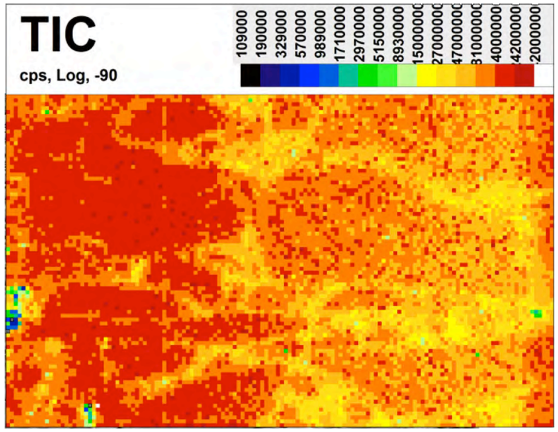
TIC
cps, Log, -90
109000
190000
329000
570000
989000
1710000
2970000
5150000
8930000

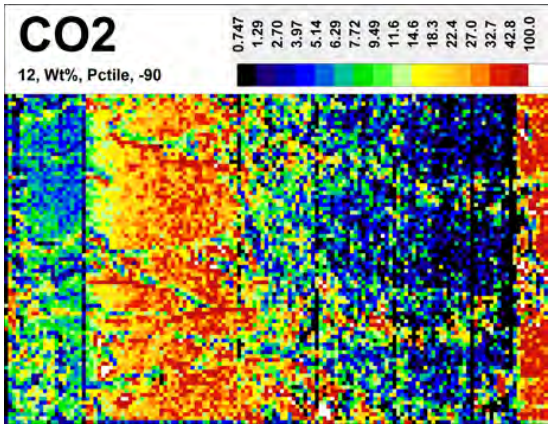
CO2
12, Wt%, Pctile, -90
0.747 1.29 2.70 3.97 5.14 6.29 7.72 9.49 11.6 14.6 18.3 22.4 27.0 32.7 42.8 100.0

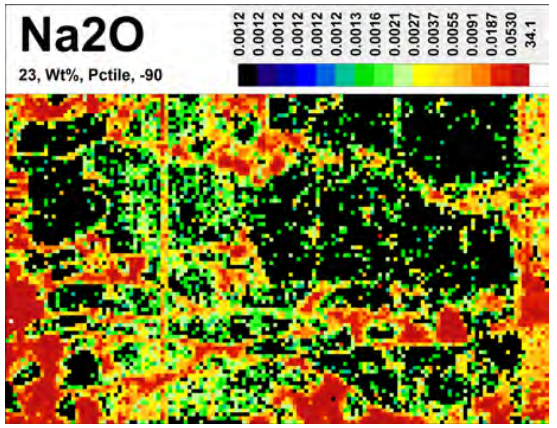
Na2O
23, Wt%, Pctile, -90
0.0012 0.0012 0.0012 0.0012 0.0012 0.0012 0.0013 0.0016 0.0021 0.0027 0.0037 0.0055 0.0091 0.0187 0.0530 34.1

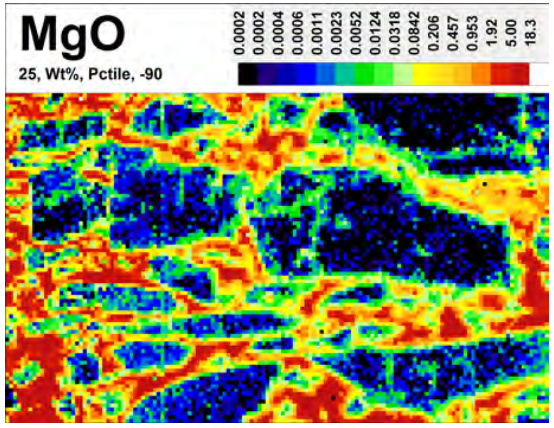
MgO
25, Wt%, Pctile, -90
0.0002 0.0002 0.0004 0.0006 0.0011 0.0023 0.0052 0.0124 0.0318 0.0842 0.206 0.457 0.953 1.92 5.00 18.3

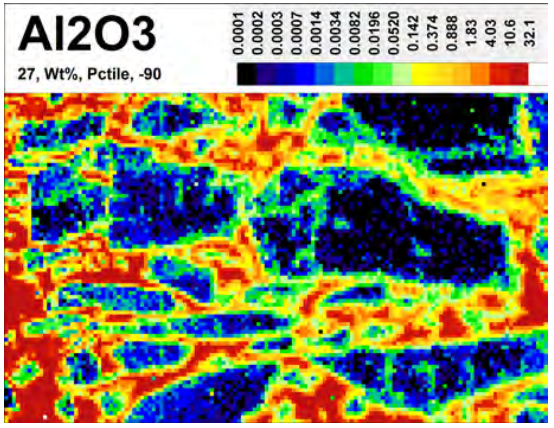
Al2O3
27, Wt%, Pctile, -90
0.0001 0.0002 0.0003 0.0007 0.0014 0.0034 0.0082 0.0196 0.0520 0.142 0.374 0.888 1.83 4.03 10.6 32.1

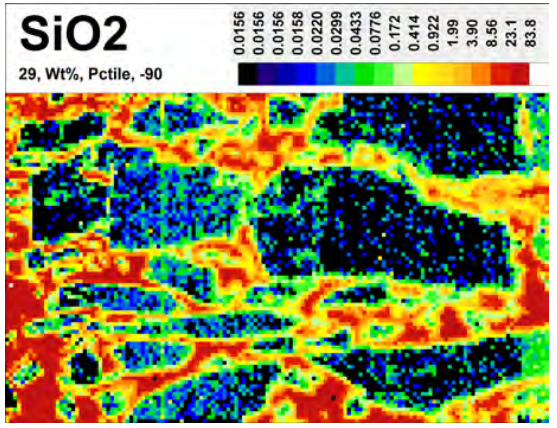
SiO2
29, Wt%, Pctile, -90
0.0156 0.0156 0.0156 0.0158 0.0220 0.0299 0.0433 0.0776 0.172 0.414 0.922 1.99 3.90 8.56 23.1 83.8

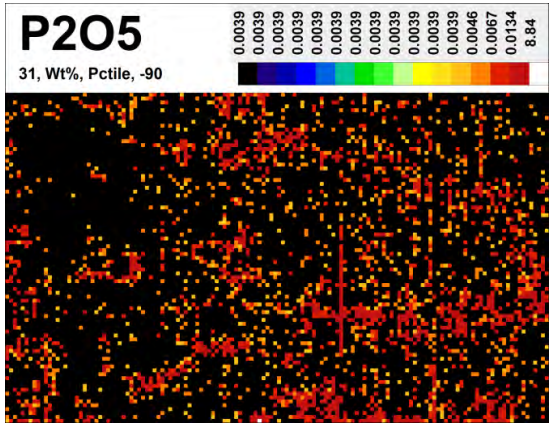
P2O5
31, Wt%, Pctile, -90
0.0039 0.0039 0.0039 0.0039 0.0039 0.0039 0.0039 0.0039 0.0039 0.0039 0.0039 0.0046 0.0067 0.0134 8.84

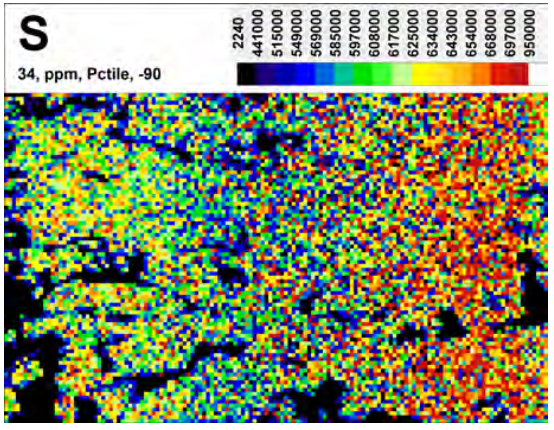
S
34, ppm, Pctile, -90
2240 441000 515000 549000 569000 585000 597000 608000 617000 625000 634000 643000 654000 668000 697000 950000

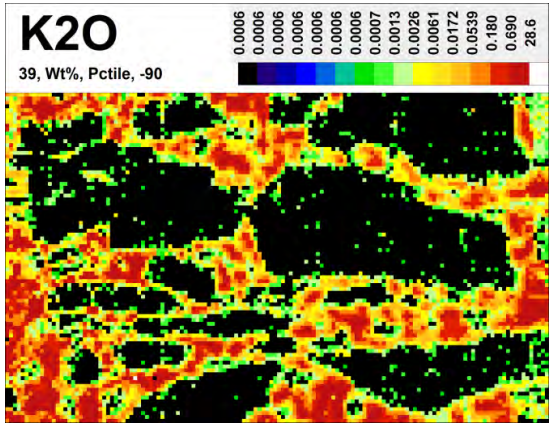
K2O
39, Wt%, Pctile, -90
0.0006 0.0006 0.0006 0.0006 0.0006 0.0006 0.0007 0.0013 0.0026 0.0061 0.0172 0.0539 0.180 0.690 28.6

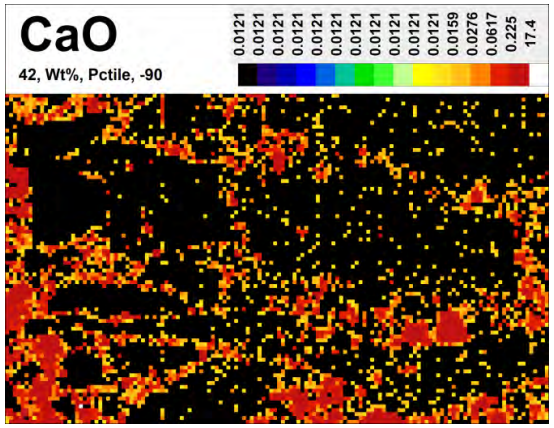
CaO
42, Wt%, Pctile, -90
0.0121 0.0121 0.0121 0.0121 0.0121 0.0121 0.0121 0.0121 0.0121 0.0121 0.0121 0.0159 0.0276 0.0617 0.225 17.4

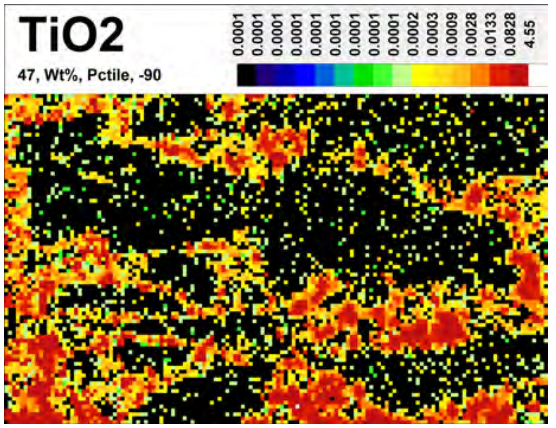
TiO2
47, Wt%, Pctile, -90
0.0001 0.0001 0.0001 0.0001 0.0001 0.0001 0.0001 0.0001 0.0001 0.0002 0.0003 0.0009 0.0028 0.0133 0.0828 4.55

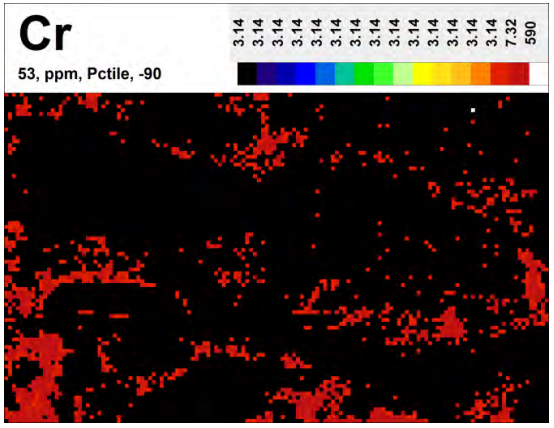
Cr
53, ppm, Pctile, -90
3.14 3.14 3.14 3.14 3.14 3.14 3.14 3.14 3.14 3.14 3.14 3.14 3.14 7.32 590

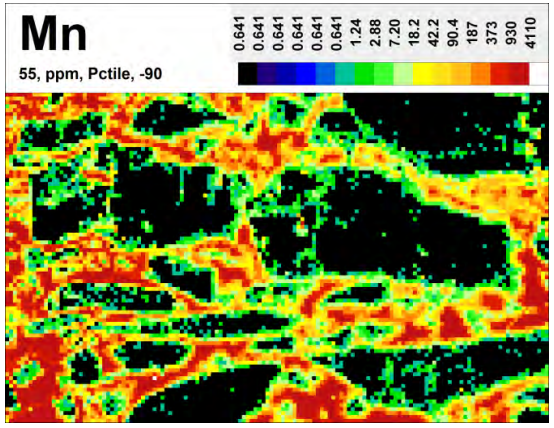
Mn
55, ppm, Pctile, -90
0.641 0.641 0.641 0.641 0.641 1.24 2.88 7.20 18.2 42.2 90.4 187 373 930 4110

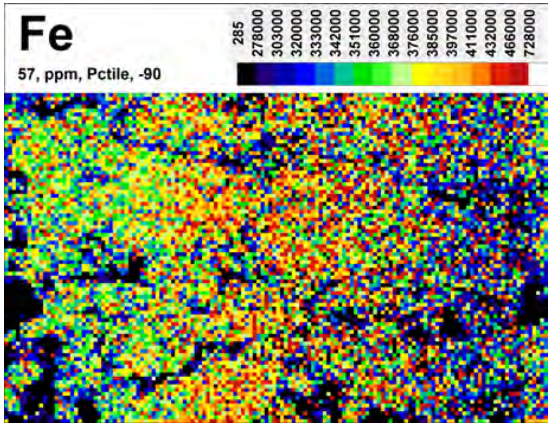
Fe
57, ppm, Pctile, -90
285 278000 303000 320000 333000 342000 351000 360000 368000 376000 385000 397000 411000 432000 466000 728000

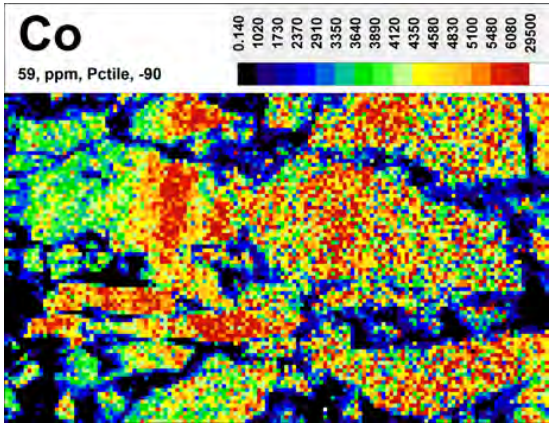
Co
59, ppm, Pctile, -90
0.140 1020 1730 2370 2910 3350 3640 3890 4120 4350 4580 4830 5100 5480 6080 29500

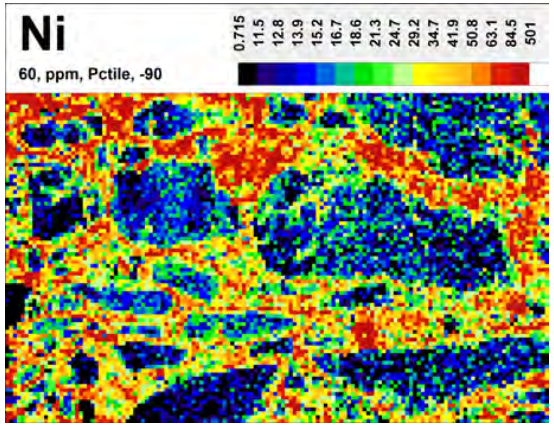
Ni
60, ppm, Pctile, -90
0.715 11.5 12.8 13.9 15.2 16.7 18.6 21.3 24.7 29.2 34.7 41.9 50.8 63.1 84.5 501

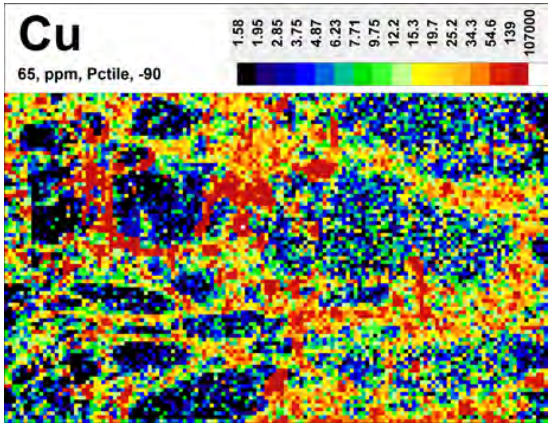
Cu
65, ppm, Pctile, -90
1.58 1.95 2.85 3.75 4.87 6.23 7.71 9.75 12.2 15.3 19.7 25.2 34.3 54.6 139 107000

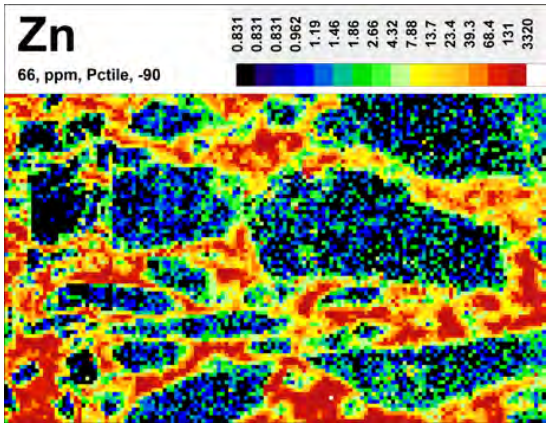
Zn
66, ppm, Pctile, -90
0.831 0.831 0.831 0.962 1.19 1.46 1.86 2.66 4.32 7.88 13.7 23.4 39.3 68.4 131 3320

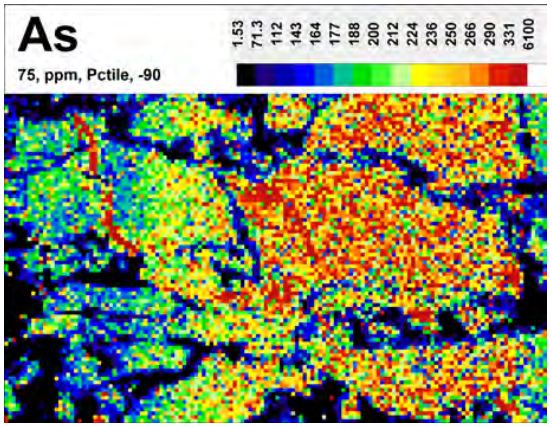
As
75, ppm, Pctile, -90
1.53 71.3 112 143 164 177 188 200 212 224 236 250 266 290 331 6100

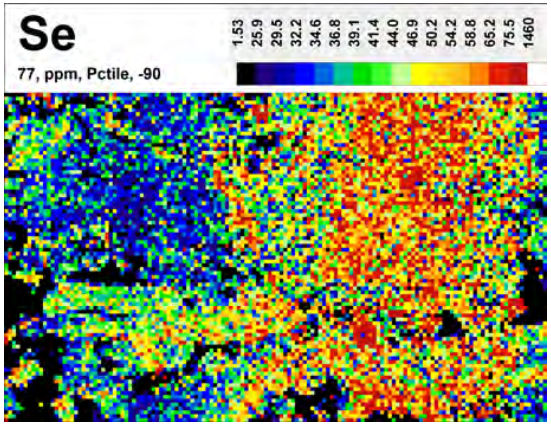
Se
77, ppm, Pctile, -90
1.53 25.9 29.5 32.2 34.6 36.8 39.1 41.4 44.0 46.9 50.2 54.2 58.8 65.2 75.5 1460

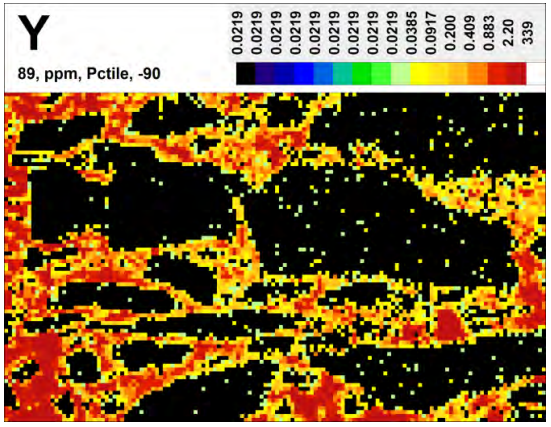
Y
89, ppm, Pctile, -90
0.0219 0.0219 0.0219 0.0219 0.0219 0.0219 0.0219 0.0219 0.0385 0.0917 0.200 0.409 0.883 2.20 339

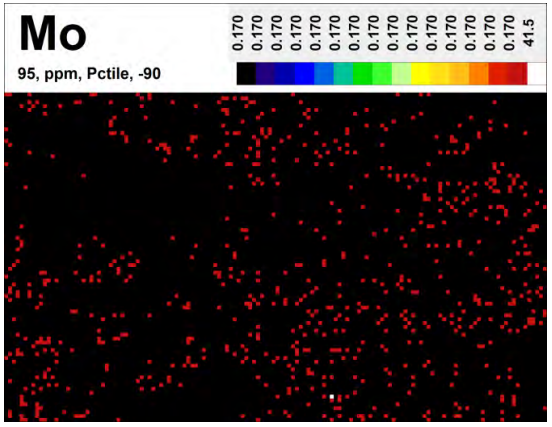
Mo
95, ppm, Pctile, -90
0.170 0.170 0.170 0.170 0.170 0.170 0.170 0.170 0.170 0.170 0.170 0.170 0.170 0.170 0.170 41.5

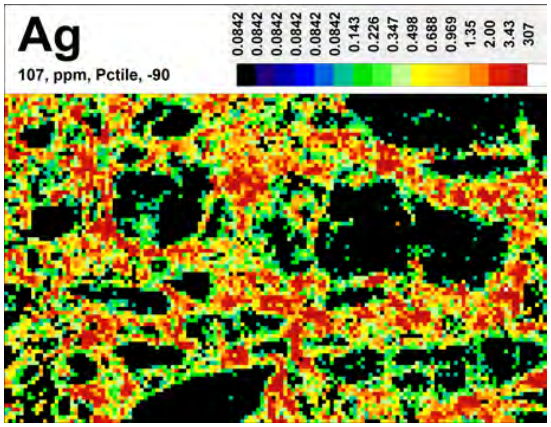
Ag
107, ppm, Pctile, -90
0.0842 0.0842 0.0842 0.0842 0.0842 0.0842 0.143 0.226 0.347 0.498 0.688 0.969 1.35 2.00 3.43 307

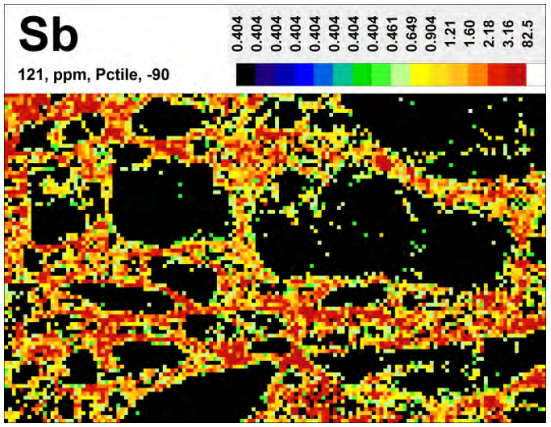
Sb
121, ppm, Pctile, -90
0.404 0.404 0.404 0.404 0.404 0.404 0.404 0.404 0.461 0.649 0.904 1.21 1.60 2.18 3.16 82.5

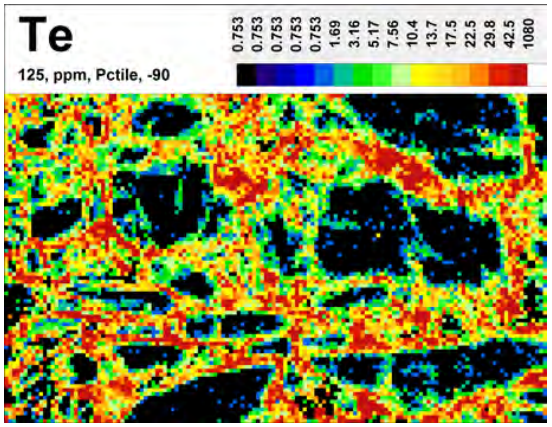
Te
125, ppm, Pctile, -90
0.753 0.753 0.753 0.753 0.753 1.69 3.16 5.17 7.56 10.4 13.7 17.5 22.5 29.8 42.5 1080

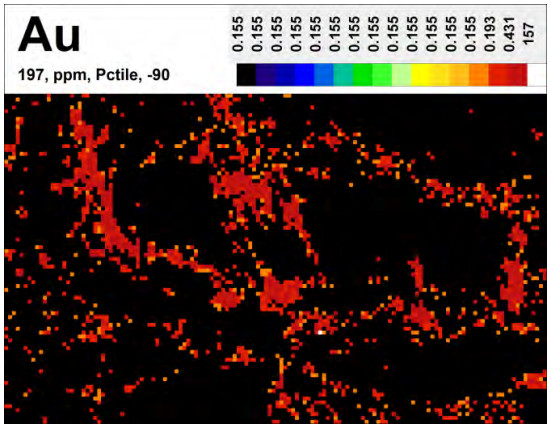
Au
197, ppm, Pctile, -90
0.155 0.155 0.155 0.155 0.155 0.155 0.155 0.155 0.155 0.155 0.155 0.193 0.431 157

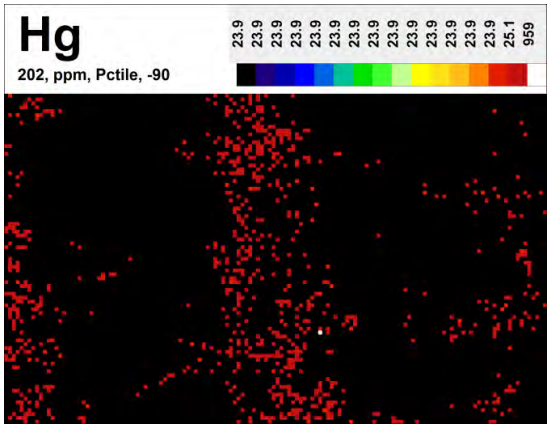
Hg
202, ppm, Pctile, -90
23.9 23.9 23.9 23.9 23.9 23.9 23.9 23.9 23.9 23.9 23.9 23.9 25.1 959

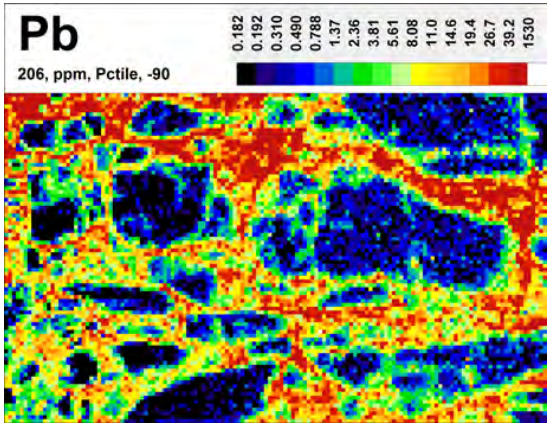
Pb
206, ppm, Pctile, -90
0.182 0.192 0.310 0.490 0.788 1.37 2.36 3.81 5.61 8.08 11.0 14.6 19.4 26.7 39.2 1530

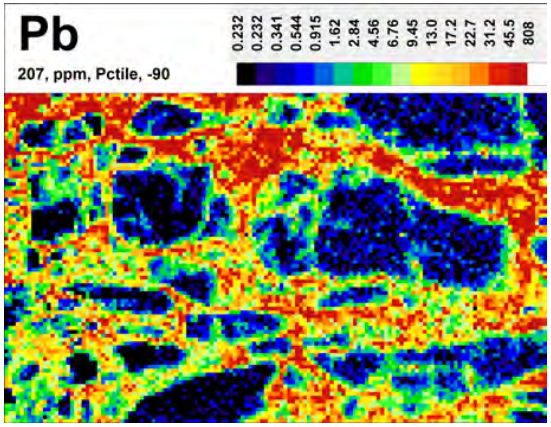
Pb
207, ppm, Pctile, -90
0.232 0.232 0.341 0.544 0.915 1.62 2.84 4.56 6.76 9.45 13.0 17.2 22.7 31.2 45.5 808

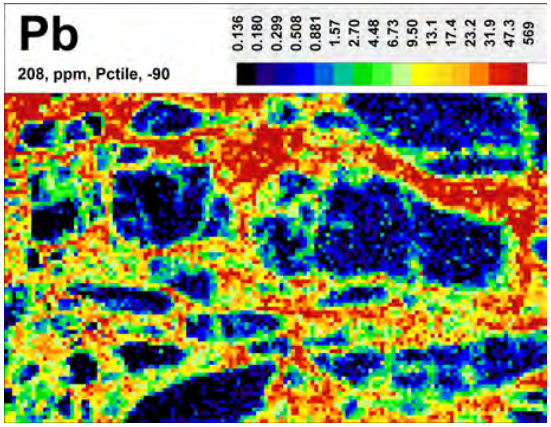
Pb
208, ppm, Pctile, -90
0.136 0.180 0.299 0.508 0.881 1.57 2.70 4.48 6.73 9.50 13.1 17.4 23.2 31.9 47.3 569

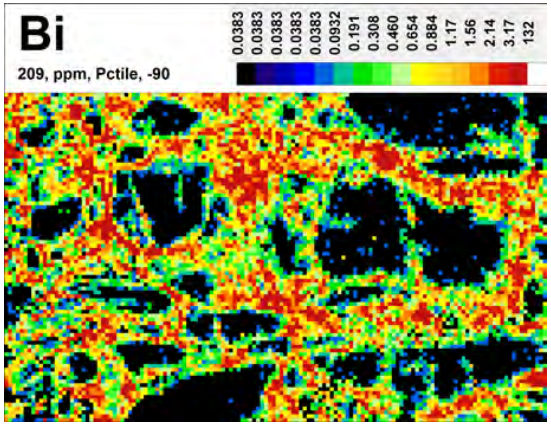
Bi
209, ppm, Pctile, -90
0.0383 0.0383 0.0383 0.0383 0.0383 0.0932 0.191 0.308 0.460 0.654 0.884 1.17 1.56 2.14 3.17 132

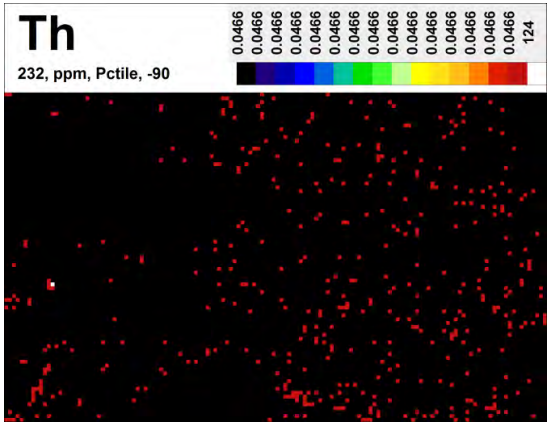
Th
232, ppm, Pctile, -90
0.0466 0.0466 0.0466 0.0466 0.0466 0.0466 0.0466 0.0466 0.0466 0.0466 0.0466 0.0466 0.0466 0.0466 0.0466 124

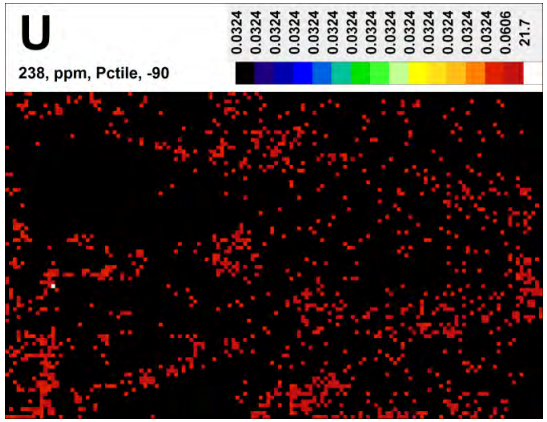
U
238, ppm, Pctile, -90
0.0324 0.0324 0.0324 0.0324 0.0324 0.0324 0.0324 0.0324 0.0324 0.0324 0.0324 0.0324 0.0324 0.0324 0.0606 21.7

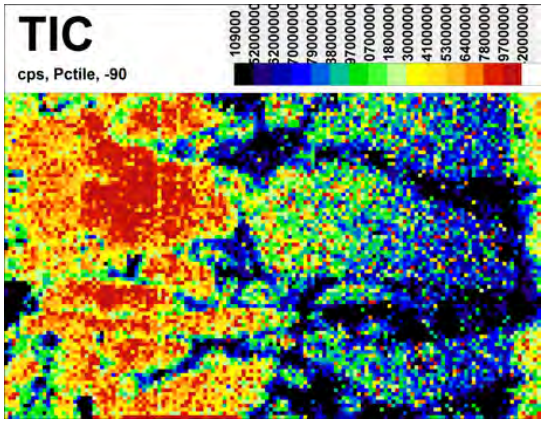
TIC
cps, Pctile, -90

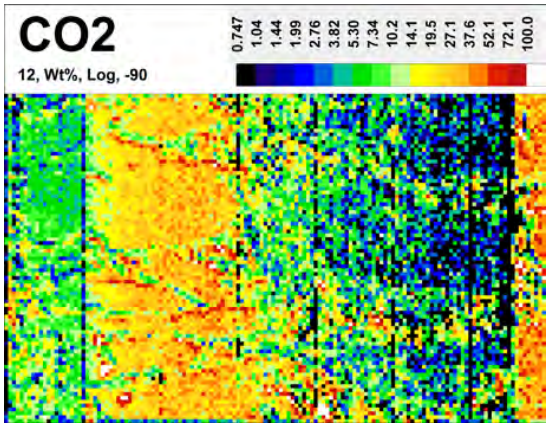
CO2
12, Wt%, Log, -90
0.747 1.04 1.44 1.99 2.76 3.82 5.30 7.34 10.2 14.1 19.5 27.1 37.6 52.1 72.1 100.0

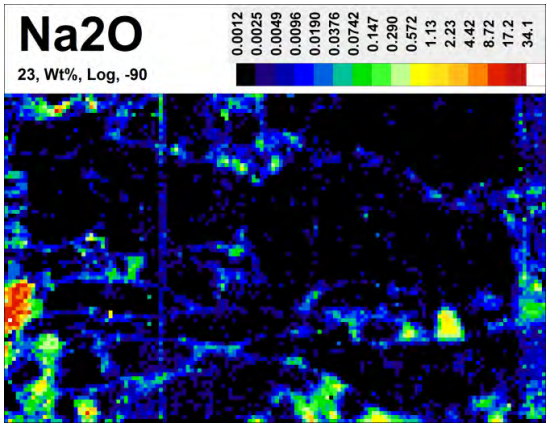
Na2O
23, Wt%, Log, -90
0.0012 0.0025 0.0049 0.0096 0.0190 0.0376 0.0742 0.147 0.290 0.572 1.13 2.23 4.42 8.72 17.2 34.1

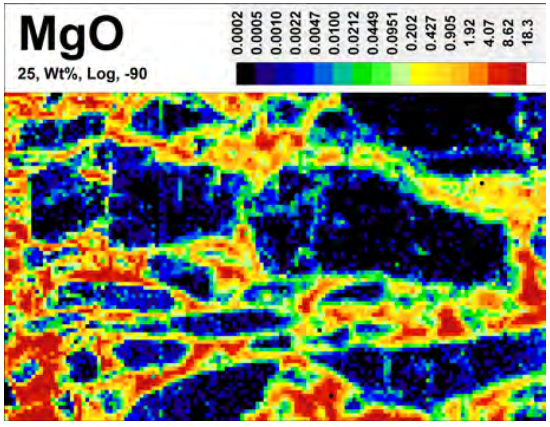
MgO
25, Wt%, Log, -90
0.0002 0.0005 0.0010 0.0022 0.0047 0.0100 0.0212 0.0449 0.0951 0.202 0.427 0.905 1.92 4.07 8.62 18.3

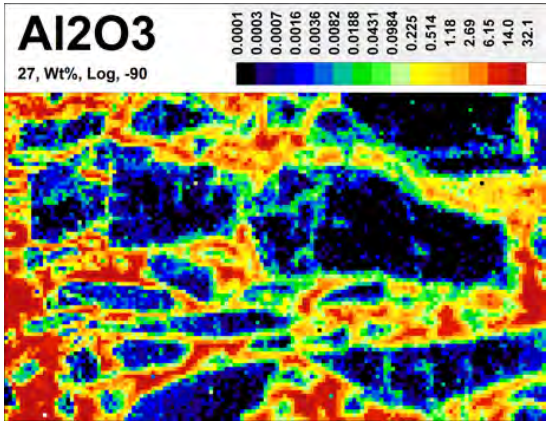
Al2O3
27, Wt%, Log, -90
0.0001 0.0003 0.0007 0.0016 0.0036 0.0082 0.0188 0.0431 0.0984 0.225 0.514 1.18 2.69 6.15 14.0 32.1

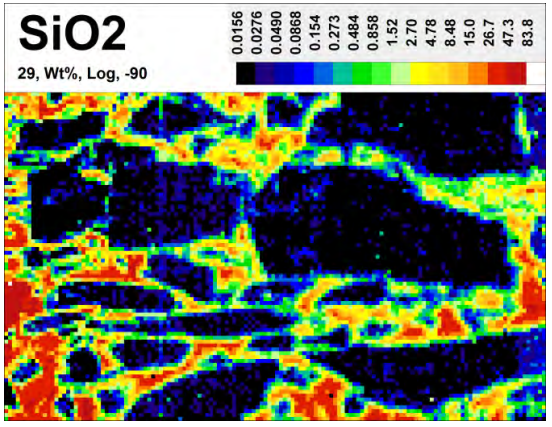
SiO2
29, Wt%, Log, -90
0.0156 0.0276 0.0490 0.0868 0.154 0.273 0.484 0.858 1.52 2.70 4.78 8.48 15.0 26.7 47.3 83.8

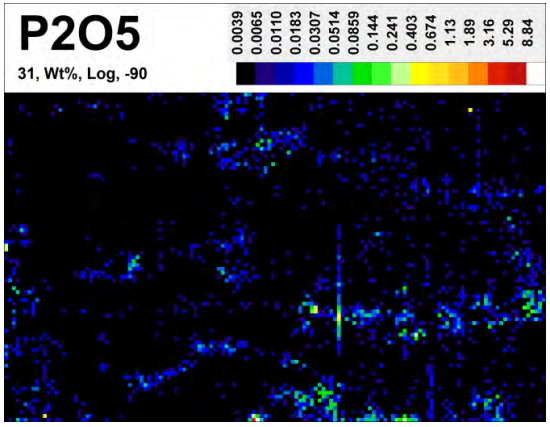
P2O5
31, Wt%, Log, -90
0.0039 0.0065 0.0110 0.0183 0.0307 0.0514 0.0859 0.144 0.241 0.403 0.674 1.13 1.89 3.16 5.29 8.84

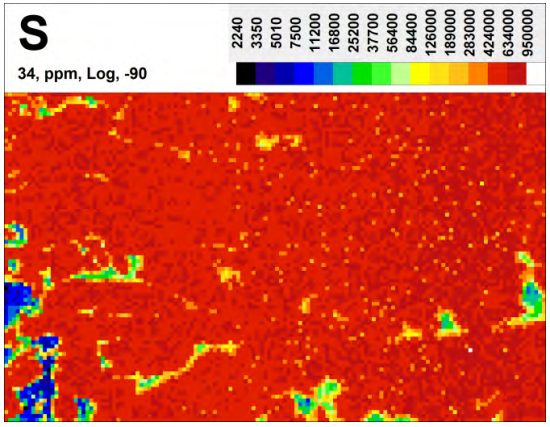
S
34, ppm, Log, -90
2240 3350 5010 7500 11200 16800 25200 37700 56400 84400 126000 189000 283000 424000 634000 950000

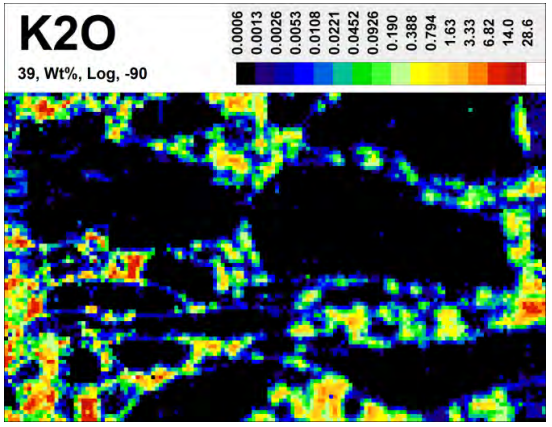
K2O
39, Wt%, Log, -90
0.0006 0.0013 0.0026 0.0053 0.0108 0.0221 0.0452 0.0926 0.190 0.388 0.794 1.63 3.33 6.82 14.0 28.6

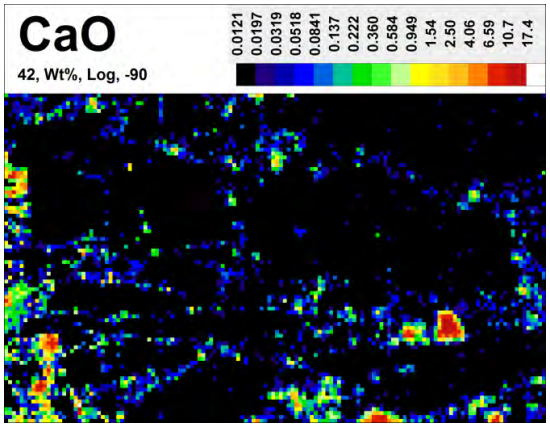
CaO
42, Wt%, Log, -90
0.0121 0.0197 0.0319 0.0518 0.0841 0.137 0.222 0.360 0.584 0.949 1.54 2.50 4.06 6.59 10.7 17.4

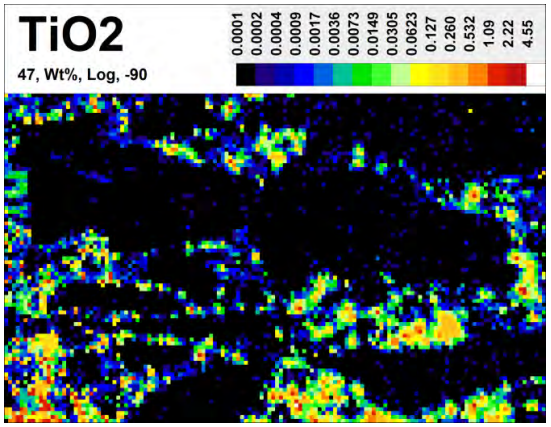
TiO2
47, Wt%, Log, -90
0.0001 0.0002 0.0004 0.0009 0.0017 0.0036 0.0073 0.0149 0.0305 0.0623 0.127 0.260 0.532 1.09 2.22 4.55

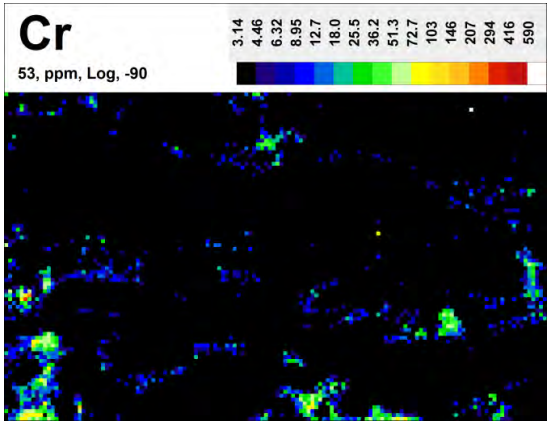
Cr
53, ppm, Log, -90
3.14 4.46 6.32 8.95 12.7 18.0 25.5 36.2 51.3 72.7 103 146 207 294 416 590

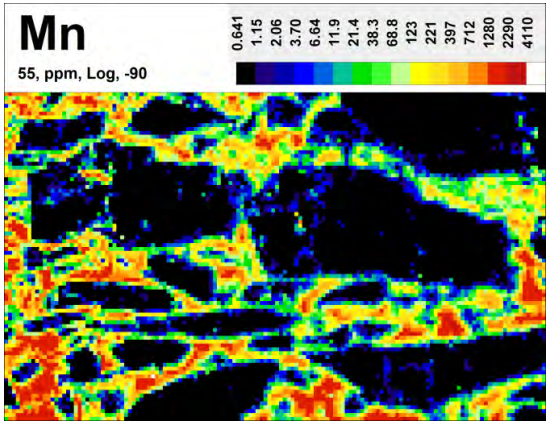
Mn
55, ppm, Log, -90
0.641 1.15 2.06 3.70 6.64 11.9 21.4 38.3 68.8 123 221 397 712 1280 2290 4110

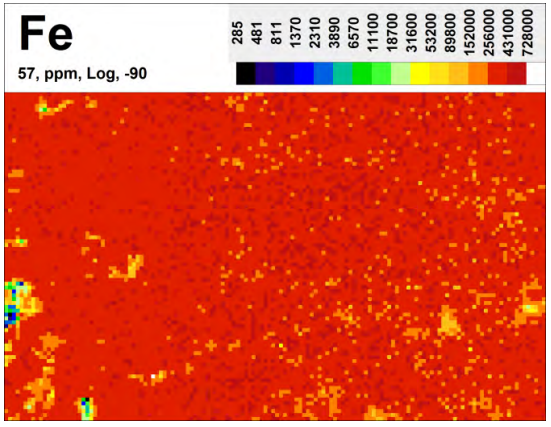
Fe
57, ppm, Log, -90
285 481 811 1370 2310 3890 6570 11100 18700 31600 53200 89800 152000 256000 431000 728000

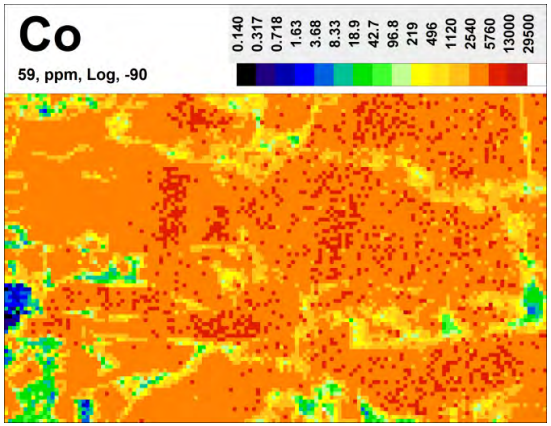
Co
59, ppm, Log, -90
0.140 0.317 0.718 1.63 3.68 8.33 18.9 42.7 96.8 219 496 1120 2540 5760 13000 29500

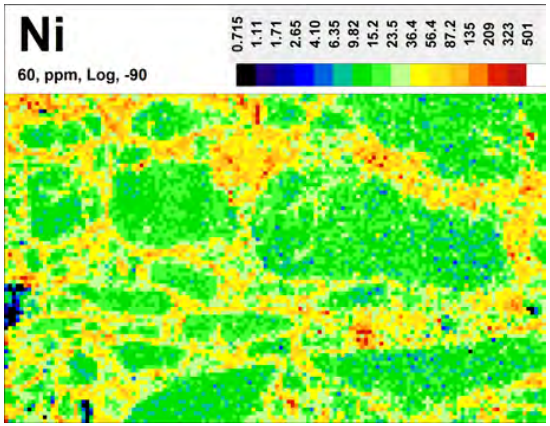
Ni
60, ppm, Log, -90
0.715 1.11 1.71 2.65 4.10 6.35 9.82 15.2 23.5 36.4 56.4 87.2 135 209 323 501

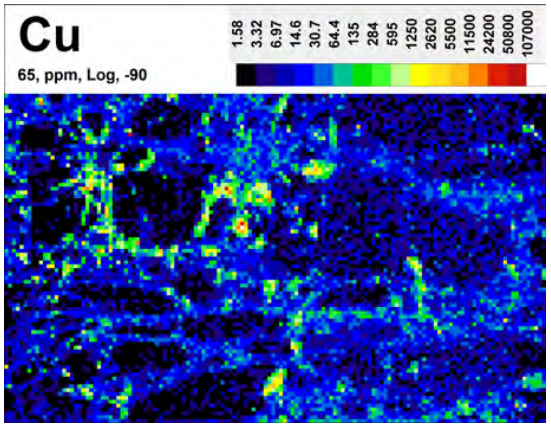
Cu
65, ppm, Log, -90
1.58 3.32 6.97 14.6 30.7 64.4 135 284 595 1250 2620 5500 11500 24200 50800 107000

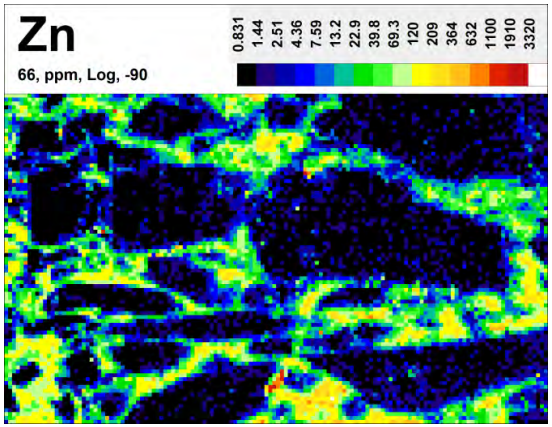
Zn
66, ppm, Log, -90
0.831 1.44 2.51 4.36 7.59 13.2 22.9 39.8 69.3 120 209 364 632 1100 1910 3320

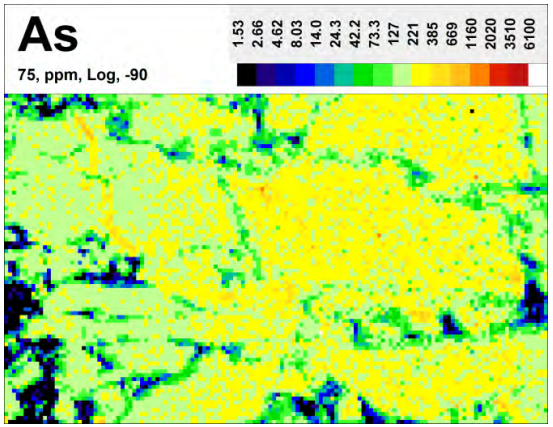
As
75, ppm, Log, -90
1.53 2.66 4.62 8.03 14.0 24.3 42.2 73.3 127 221 385 669 1160 2020 3510 6100

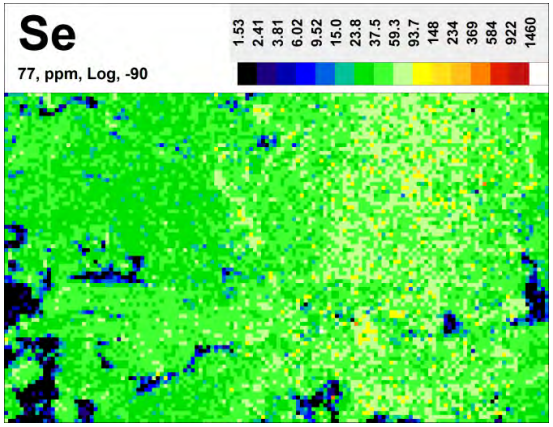
Se
77, ppm, Log, -90
1.53 2.41 3.81 6.02 9.52 15.0 23.8 37.5 59.3 93.7 148 234 369 584 922 1460

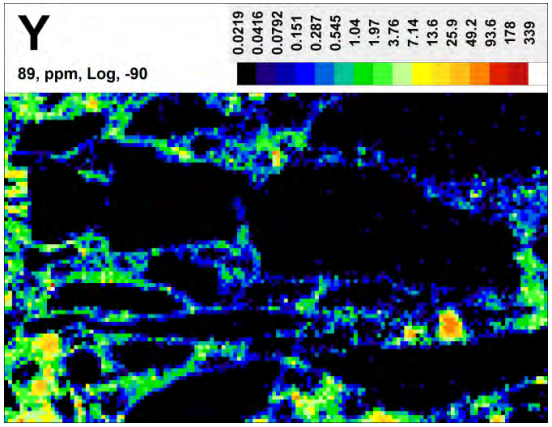
Y
89, ppm, Log, -90
0.0219 0.0416 0.0792 0.151 0.287 0.545 1.04 1.97 3.76 7.14 13.6 25.9 49.2 93.6 178 339

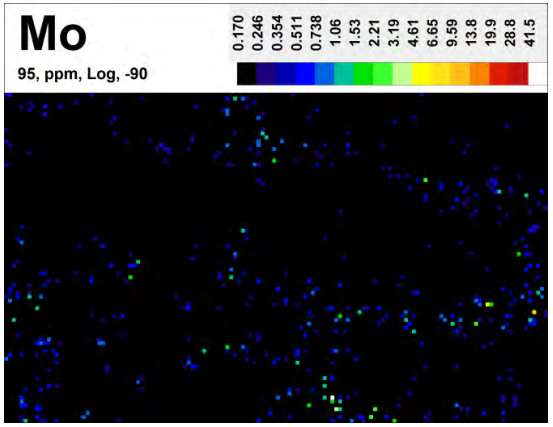
Mo
95, ppm, Log, -90
0.170 0.246 0.354 0.511 0.738 1.06 1.53 2.21 3.19 4.61 6.65 9.59 13.8 19.9 28.8 41.5

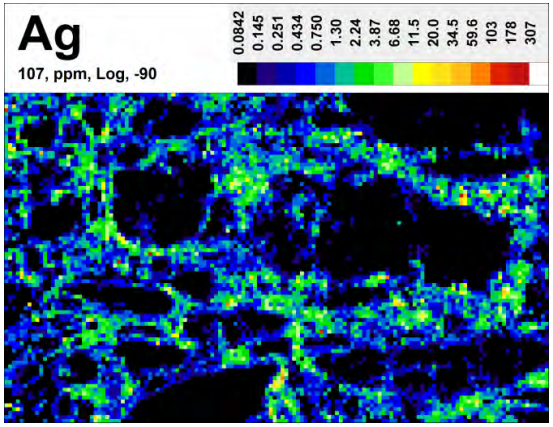
Ag
107, ppm, Log, -90
0.0842 0.145 0.251 0.434 0.750 1.30 2.24 3.87 6.68 11.5 20.0 34.5 59.6 103 178 307

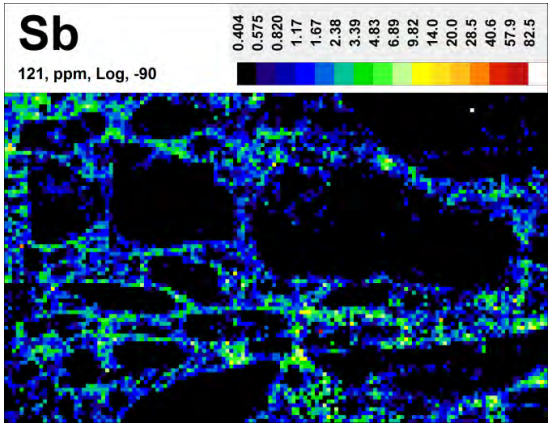
Sb
121, ppm, Log, -90
0.404 0.575 0.820 1.17 1.67 2.38 3.39 4.83 6.89 9.82 14.0 20.0 28.5 40.6 57.9 82.5

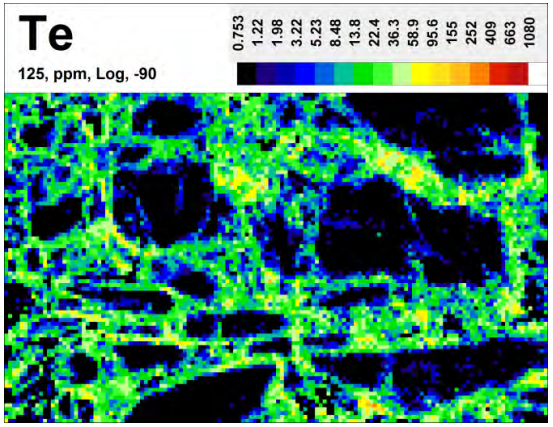
Te
125, ppm, Log, -90
0.753 1.22 1.98 3.22 5.23 8.48 13.8 22.4 36.3 58.9 95.6 155 252 409 663 1080

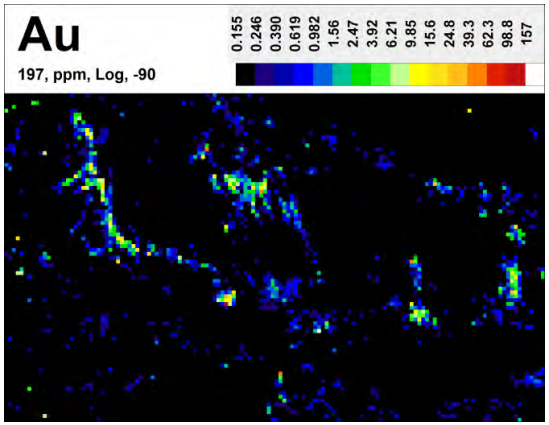
Au
197, ppm, Log, -90
0.155 0.246 0.390 0.619 0.982 1.56 2.47 3.92 6.21 9.85 15.6 24.8 39.3 62.3 98.8 157

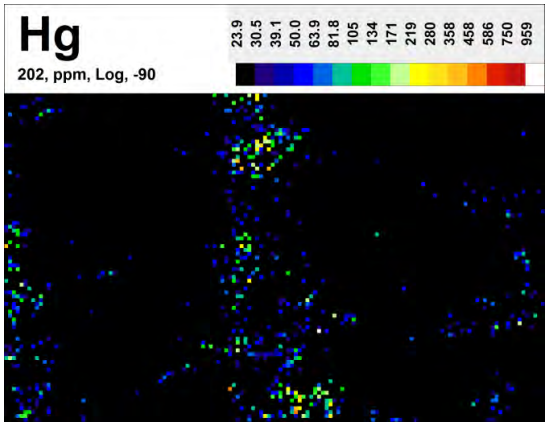
Hg
202, ppm, Log, -90
23.9 30.5 39.1 50.0 63.9 81.8 105 134 171 219 280 358 458 586 750 959

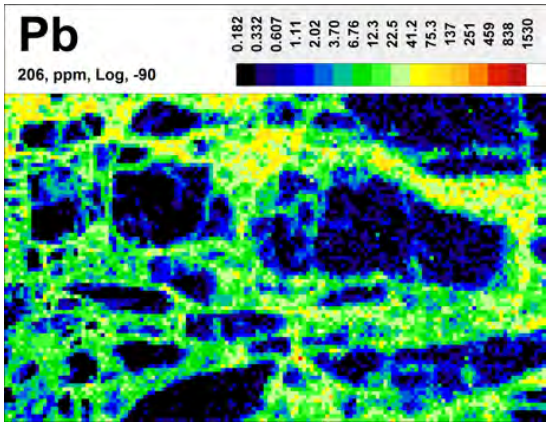
Pb
206, ppm, Log, -90
0.182 0.332 0.607 1.11 2.02 3.70 6.76 12.3 22.5 41.2 75.3 137 251 459 838 1530

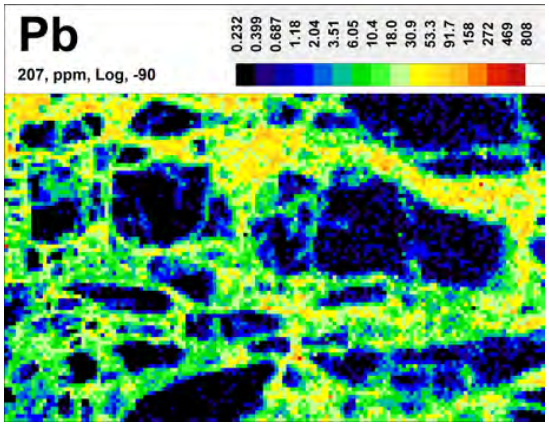
Pb
207, ppm, Log, -90
0.232 0.399 0.687 1.18 2.04 3.51 6.05 10.4 18.0 30.9 53.3 91.7 158 272 469 808

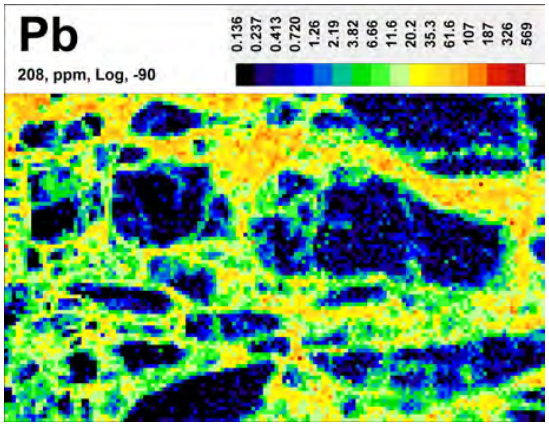
Pb
208, ppm, Log, -90
0.136 0.237 0.413 0.720 1.26 2.19 3.82 6.66 11.6 20.2 35.3 61.6 107 187 326 569

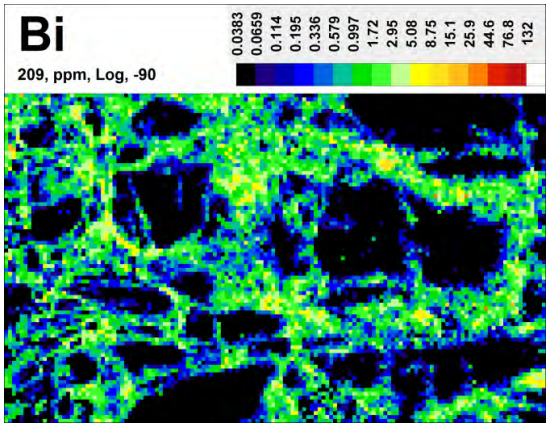
Bi
209, ppm, Log, -90
0.0383 0.0659 0.114 0.195 0.336 0.579 0.997 1.72 2.95 5.08 8.75 15.1 25.9 44.6 76.8 132

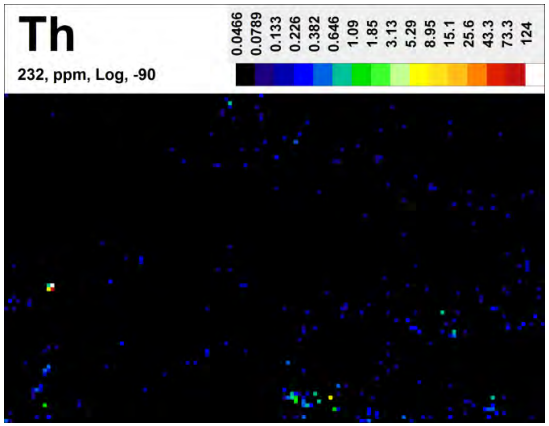
Th
232, ppm, Log, -90
0.0466 0.0789 0.133 0.226 0.382 0.646 1.09 1.85 3.13 5.29 8.95 15.1 25.6 43.3 73.3 124

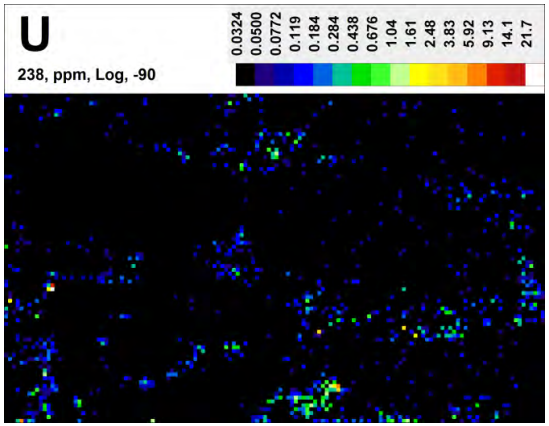
U
238, ppm, Log, -90
0.0324 0.0500 0.0772 0.119 0.184 0.284 0.438 0.676 1.04 1.61 2.48 3.83 5.92 9.13 14.1 21.7

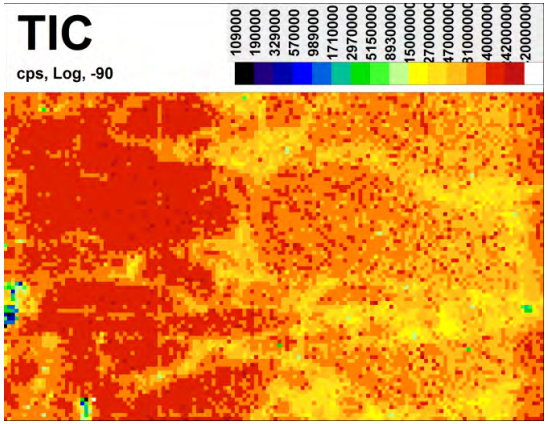

Figure DR9. (pages 165–184) LA-ICP-MS results of a brecciated and boudinaged pyrite domain within a mafic volcanic sample (MV-20) showing an orientation contrast image of the mapping area and 32 major and trace maps overlapped on the OC image. OC image reveals a complex misorientation pattern through gray-scale variations at boudin necks. LA-ICP-MS maps reveal Au and other trace elements (Ag-Bi-Te) enrichement at low-angle grain boundaries and brittle fractures. Note, grain boundaries within this sample are devoid of Au. LA-ICP-MS maps without OC underlays are also added.

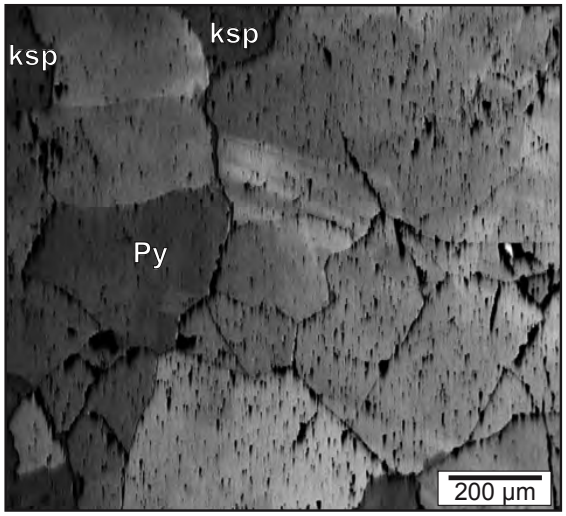
ksp
ksp
Py
200 µm

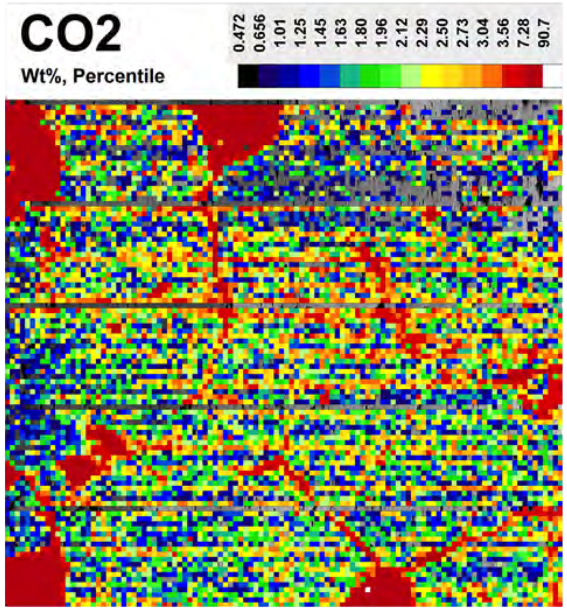
CO2
Wt%, Percentile
0.472 0.656 1.01 1.25 1.45 1.63 1.80 1.96 2.12 2.29 2.50 2.73 3.04 3.56 7.28 90.7

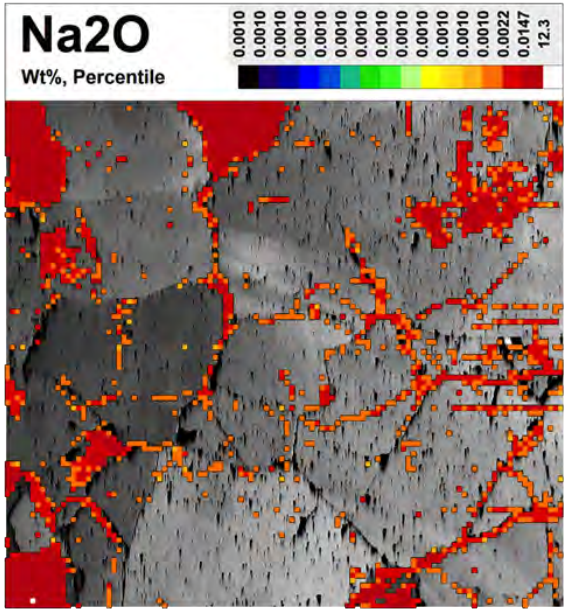
Na2O
Wt%, Percentile
0.0010 0.0010 0.0010 0.0010 0.0010 0.0010 0.0010 0.0010 0.0010 0.0010 0.0010 0.0010 0.0022 0.0147 12.3

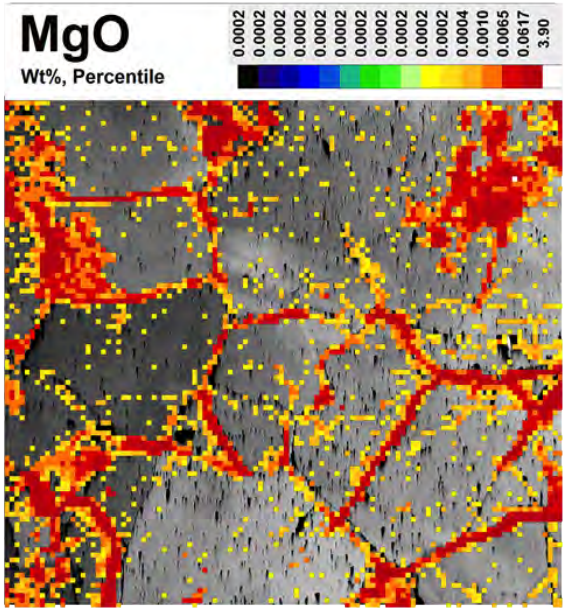
MgO
Wt%, Percentile
0.0002 0.0002 0.0002 0.0002 0.0002 0.0002 0.0002 0.0002 0.0002 0.0002 0.0004 0.0010 0.0065 0.0617 3.90

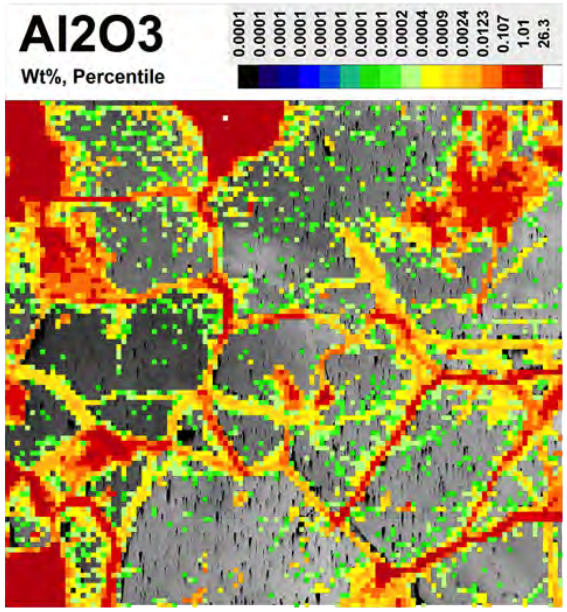
Al2O3
Wt%, Percentile
0.0001 0.0001 0.0001 0.0001 0.0001 0.0001 0.0001 0.0001 0.0002 0.0004 0.0009 0.0024 0.0123 0.107 1.01 26.3

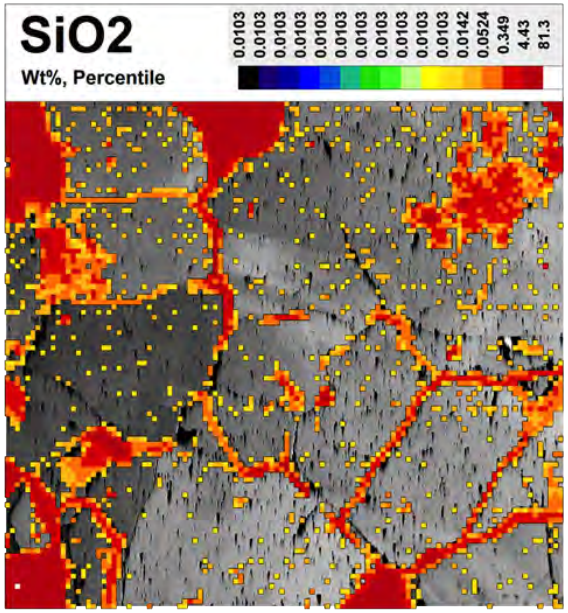
SiO2
Wt%, Percentile
0.0103 0.0103 0.0103 0.0103 0.0103 0.0103 0.0103 0.0103 0.0103 0.0103 0.0142 0.0524 0.349 4.43 81.3

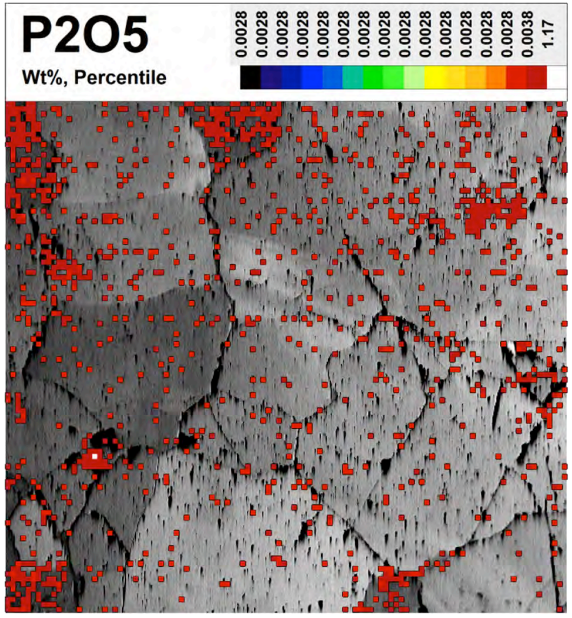
P2O5
Wt%, Percentile
0.0028 0.0028 0.0028 0.0028 0.0028 0.0028 0.0028 0.0028 0.0028 0.0028 0.0028 0.0028 0.0028 0.0038 1.17

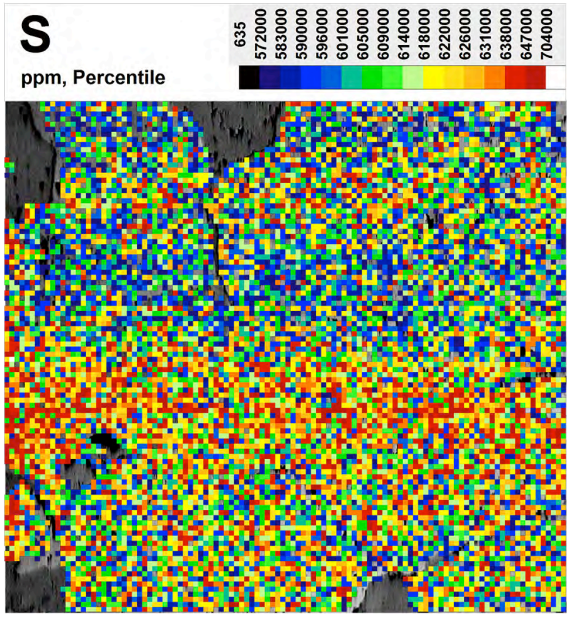
S
ppm, Percentile
635 572000 583000 590000 596000 601000 605000 609000 614000 618000 622000 626000 631000 638000 647000 704000

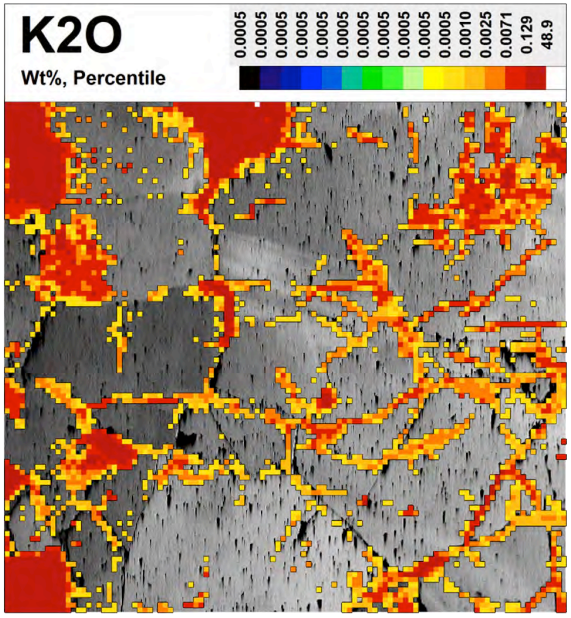
K2O
Wt%, Percentile
0.0005 0.0005 0.0005 0.0005 0.0005 0.0005 0.0005 0.0005 0.0005 0.0005 0.0010 0.0025 0.0071 0.129 48.9

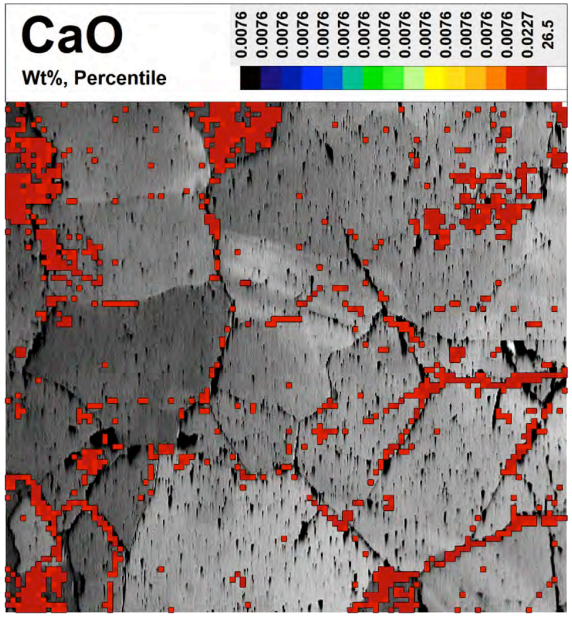
CaO
Wt%, Percentile
0.0076 0.0076 0.0076 0.0076 0.0076 0.0076 0.0076 0.0076 0.0076 0.0076 0.0076 0.0076 0.0227 26.5

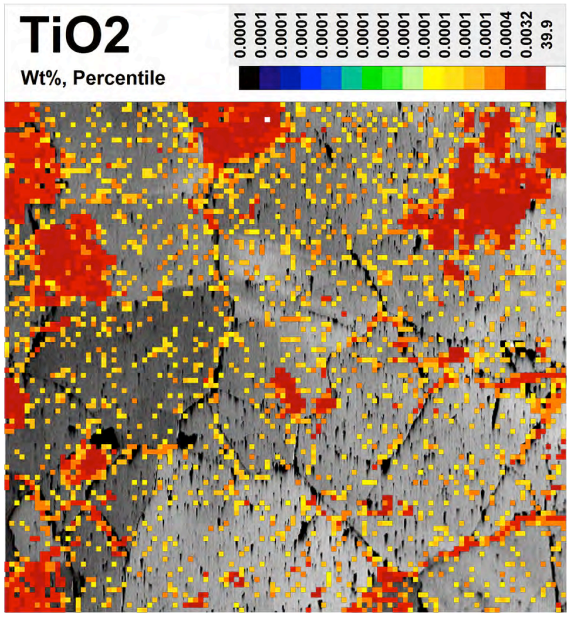
TiO2
Wt%, Percentile
0.0001 0.0001 0.0001 0.0001 0.0001 0.0001 0.0001 0.0001 0.0001 0.0001 0.0001 0.0001 0.0001 0.0004 0.0032 39.9

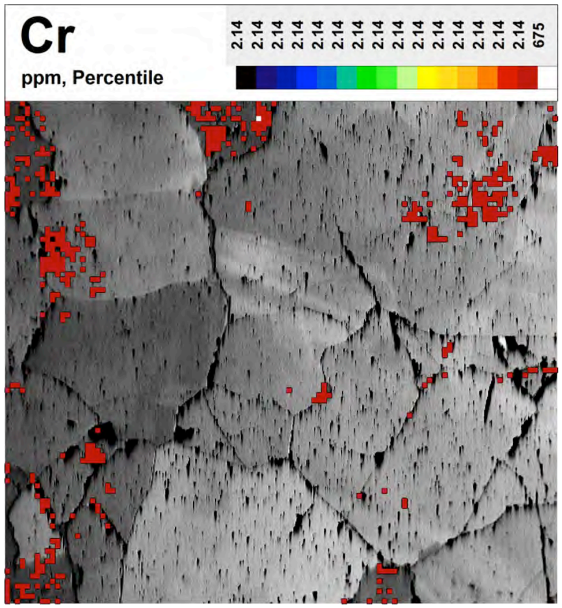
Cr
ppm, Percentile
2.14 2.14 2.14 2.14 2.14 2.14 2.14 2.14 2.14 2.14 2.14 2.14 2.14 2.14 675

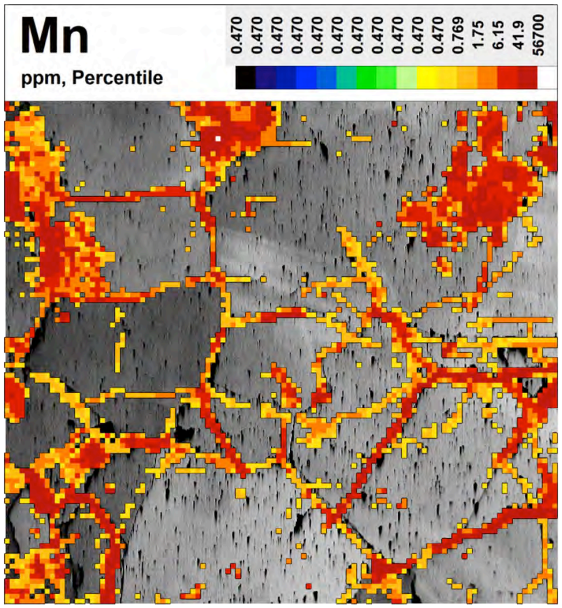
Mn
ppm, Percentile
0.470 0.470 0.470 0.470 0.470 0.470 0.470 0.470 0.470 0.470 0.769 1.75 6.15 41.9 56700

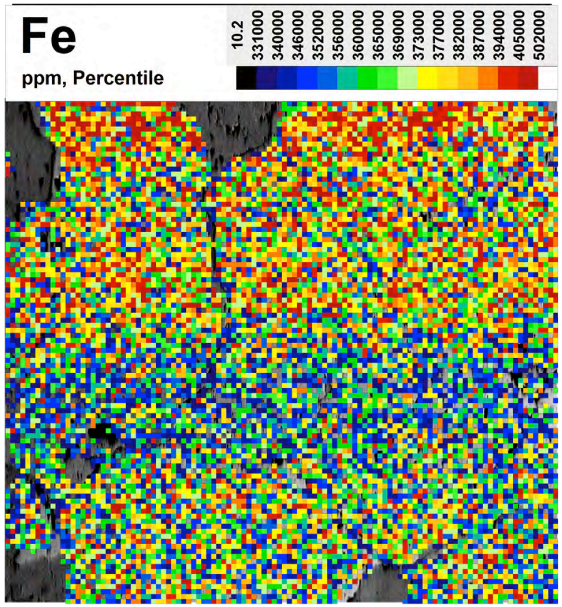
Fe
ppm, Percentile
10.2 331000 340000 346000 352000 356000 360000 365000 369000 373000 377000 382000 387000 394000 405000 502000

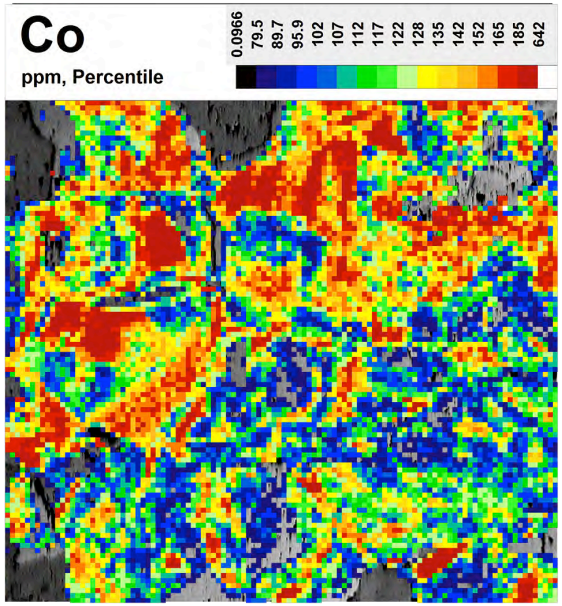
Co
ppm, Percentile
0.0966 79.5 89.7 95.9 102 107 112 117 122 128 135 142 152 165 185 642

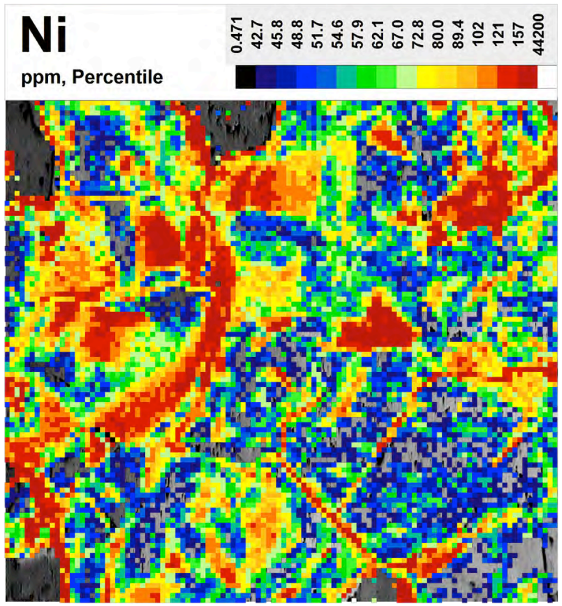
Ni
ppm, Percentile
0.471 42.7 45.8 48.8 51.7 54.6 57.9 62.1 67.0 72.8 80.0 89.4 102 121 157 44200

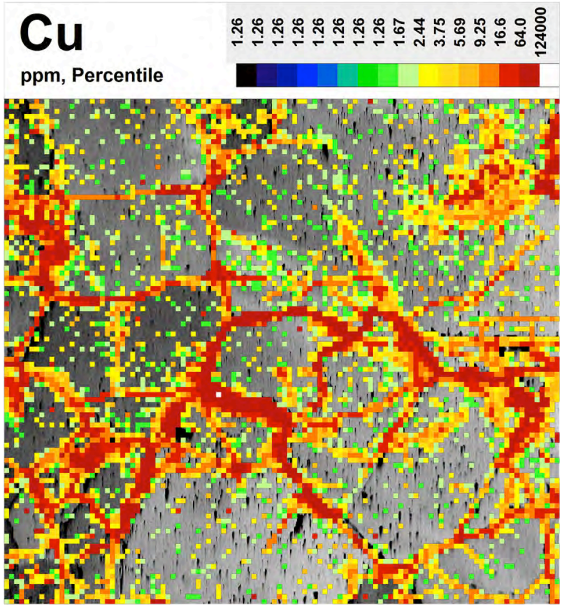
Cu
ppm, Percentile
1.26 1.26 1.26 1.26 1.26 1.26 1.26 1.67 2.44 3.75 5.69 9.25 16.6 64.0 124000

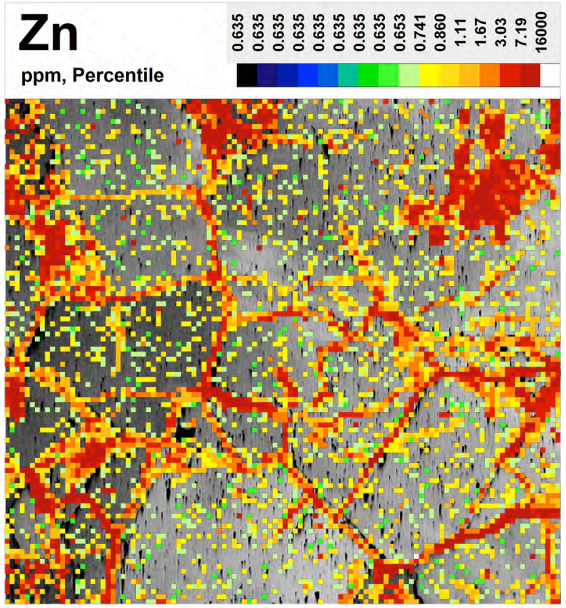
Zn
ppm, Percentile
0.635 0.635 0.635 0.635 0.635 0.635 0.635 0.653 0.741 0.860 1.11 1.67 3.03 7.19 16000

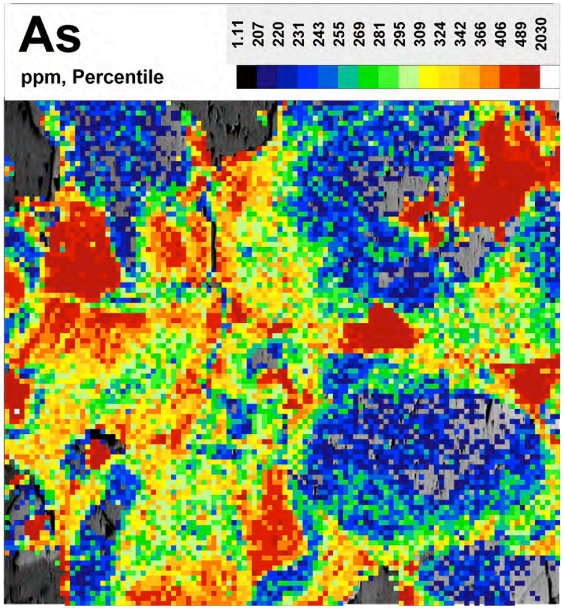
As
ppm, Percentile
1.11 207 220 231 243 255 269 281 295 309 324 342 366 406 489 2030

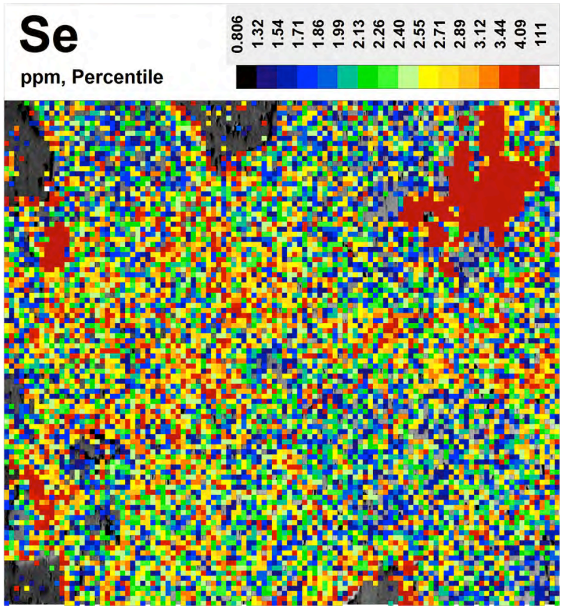
Se
ppm, Percentile
0.806 1.32 1.54 1.71 1.86 1.99 2.13 2.26 2.40 2.55 2.71 2.89 3.12 3.44 4.09 111

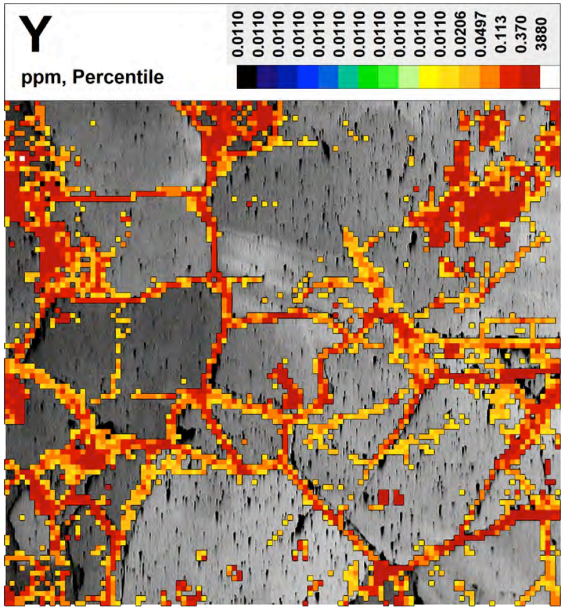
Y
ppm, Percentile
0.0110 0.0110 0.0110 0.0110 0.0110 0.0110 0.0110 0.0110 0.0110 0.0110 0.0110 0.0206 0.0497 0.113 0.370 3880

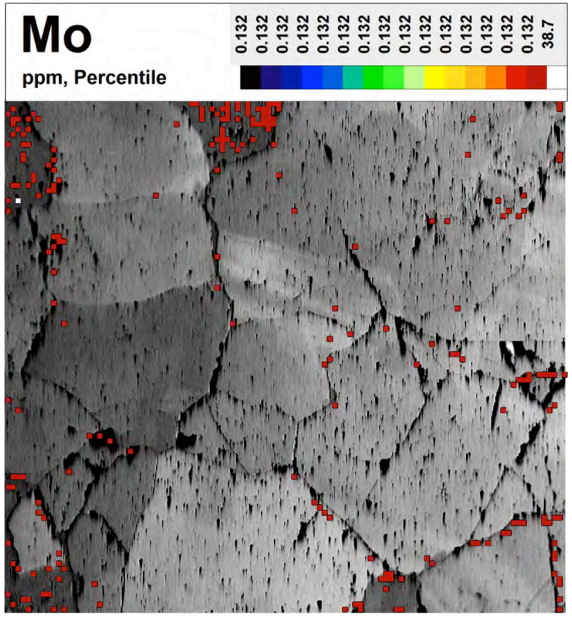
Mo
ppm, Percentile
0.132 0.132 0.132 0.132 0.132 0.132 0.132 0.132 0.132 0.132 0.132 0.132 0.132 38.7

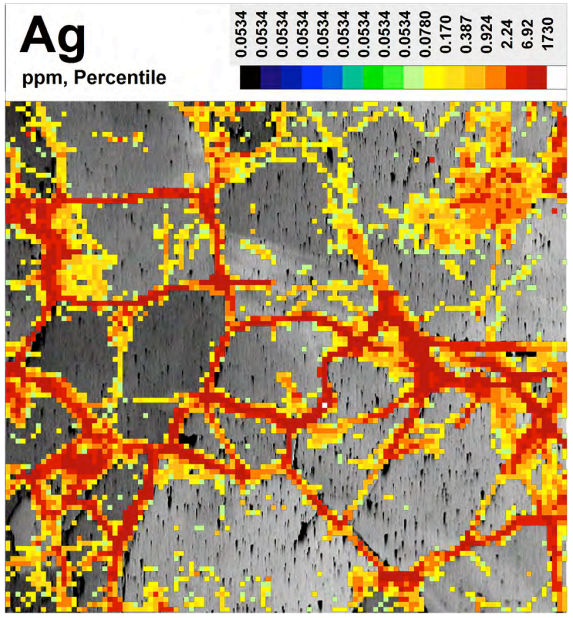
Ag
ppm, Percentile
0.0534 0.0534 0.0534 0.0534 0.0534 0.0534 0.0534 0.0534 0.0780 0.170 0.387 0.924 2.24 6.92 1730

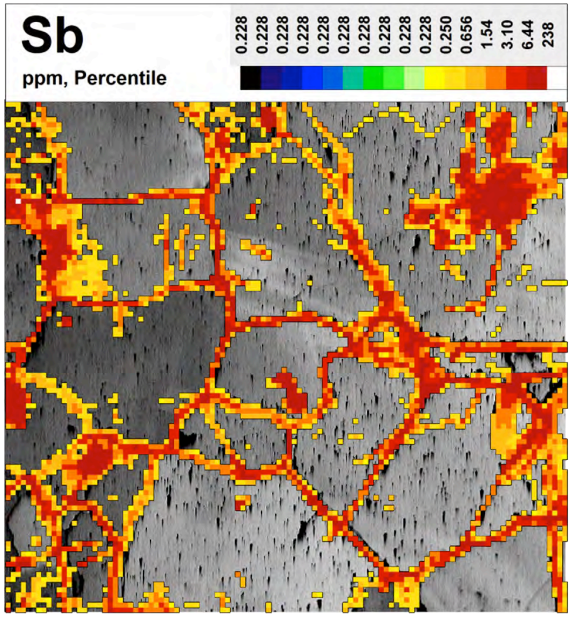
Sb
ppm, Percentile
0.228 0.228 0.228 0.228 0.228 0.228 0.228 0.228 0.228 0.250 0.656 1.54 3.10 6.44 238

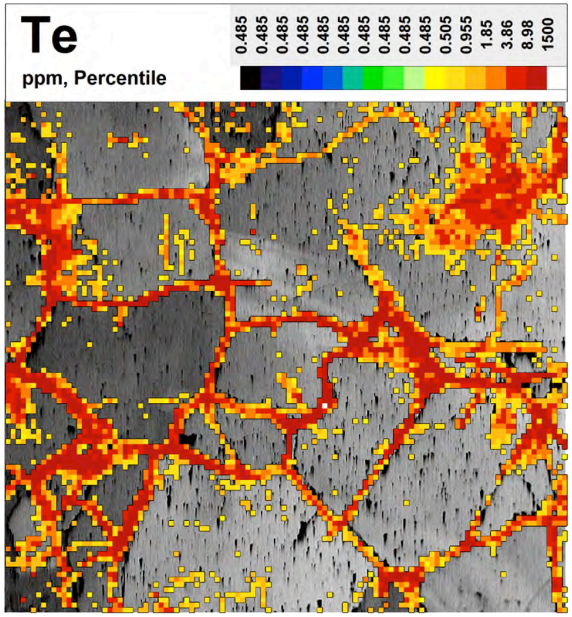
Te
ppm, Percentile
0.485 0.485 0.485 0.485 0.485 0.485 0.485 0.485 0.485 0.505 0.955 1.85 3.86 8.98 1500

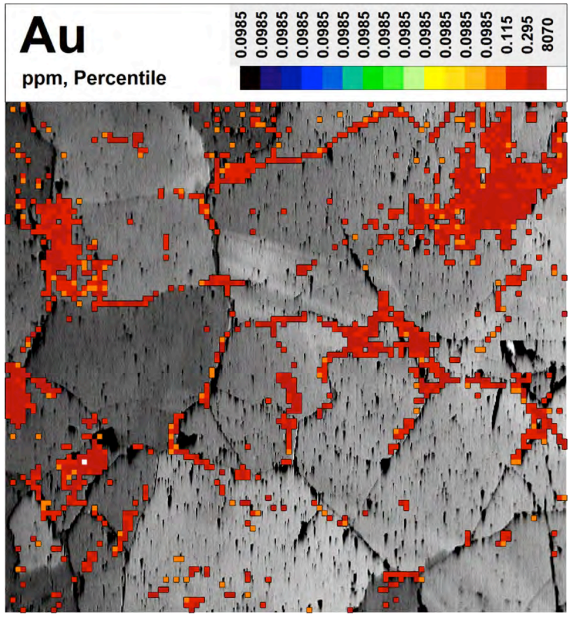
Au
ppm, Percentile
0.0985 0.0985 0.0985 0.0985 0.0985 0.0985 0.0985 0.0985 0.0985 0.0985 0.0985 0.115 0.295 8070

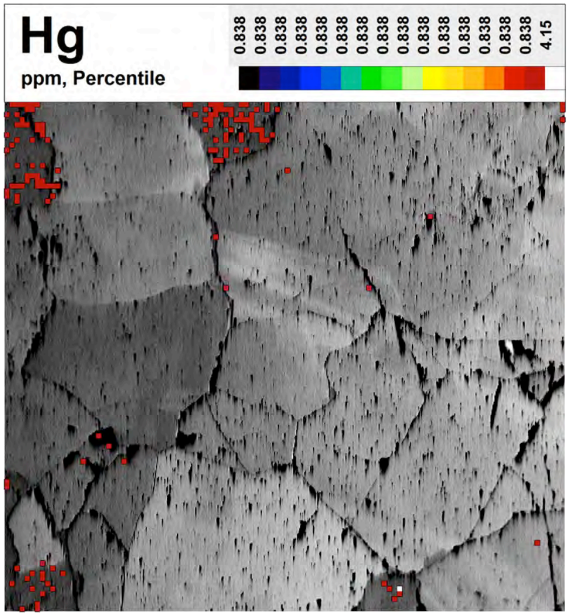
Hg
ppm, Percentile
0.838 0.838 0.838 0.838 0.838 0.838 0.838 0.838 0.838 0.838 0.838 0.838 0.838 4.15

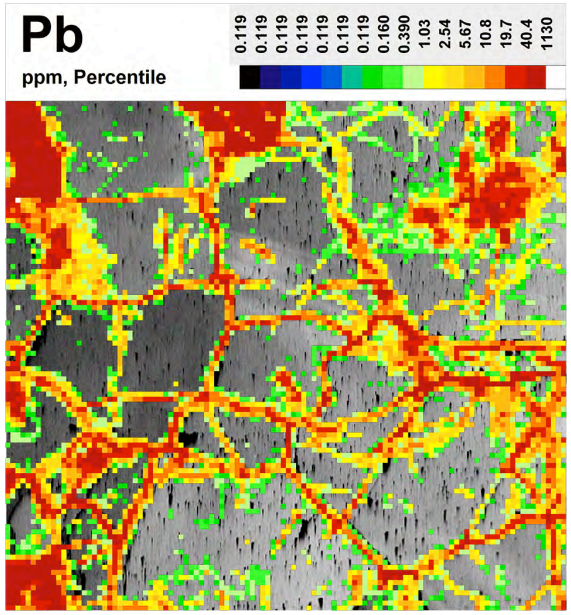
Pb
ppm, Percentile
0.119 0.119 0.119 0.119 0.119 0.119 0.160 0.390 1.03 2.54 5.67 10.8 19.7 40.4 1130

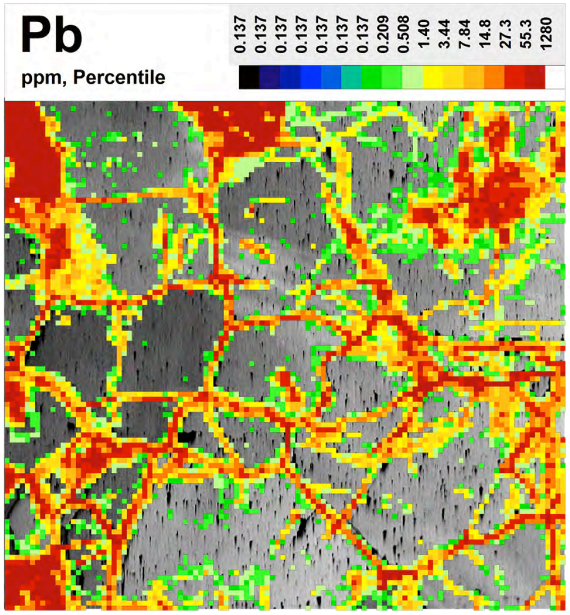
Pb
ppm, Percentile
0.137 0.137 0.137 0.137 0.137 0.137 0.209 0.508 1.40 3.44 7.84 14.8 27.3 55.3 1280

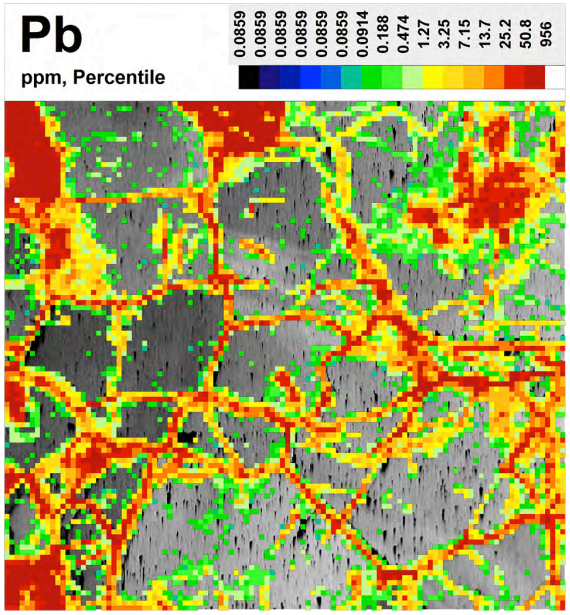
Pb
ppm, Percentile
0.0859 0.0859 0.0859 0.0859 0.0859 0.0859 0.0914 0.188 0.474 1.27 3.25 7.15 13.7 25.2 50.8 956

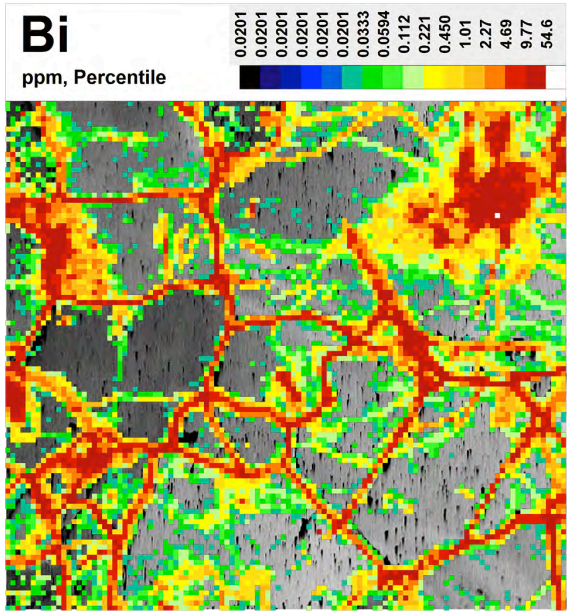
Bi
ppm, Percentile
0.0201 0.0201 0.0201 0.0201 0.0201 0.0201 0.0333 0.0594 0.112 0.221 0.450 1.01 2.27 4.69 9.77 54.6

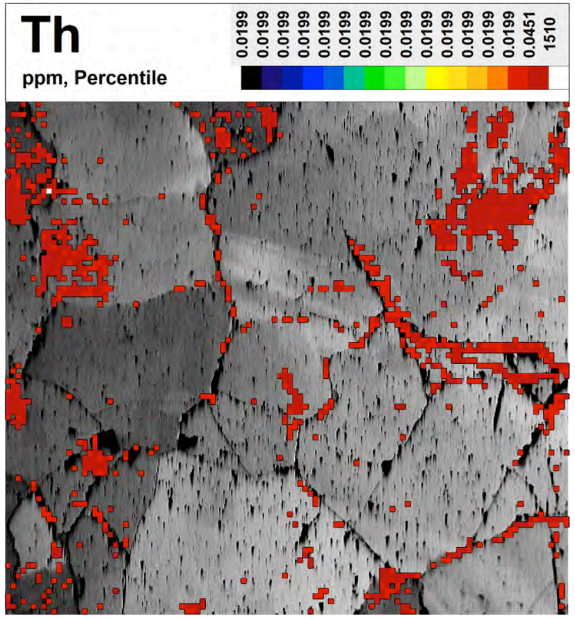
Th
ppm, Percentile
0.0199
0.0199
0.0199
0.0199
0.0199
0.0199
0.0199
0.0199
0.0199
0.0199
0.0199
0.0199
0.0199
0.0451
1510

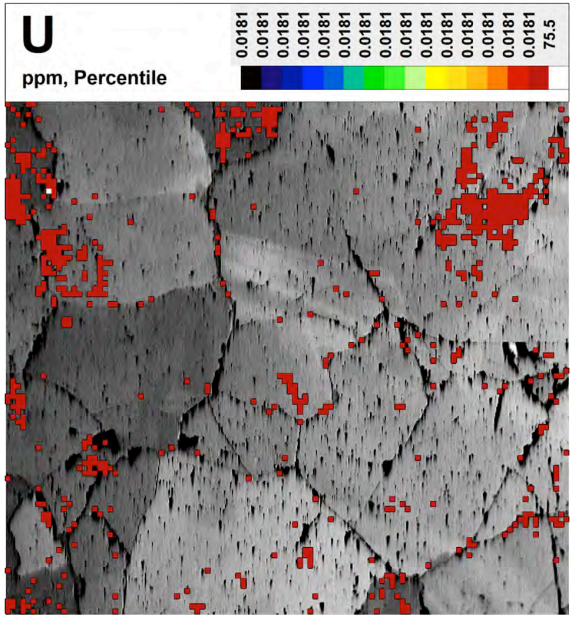
U
ppm, Percentile
0.0181
0.0181
0.0181
0.0181
0.0181
0.0181
0.0181
0.0181
0.0181
0.0181
0.0181
0.0181
0.0181
0.0181
75.5

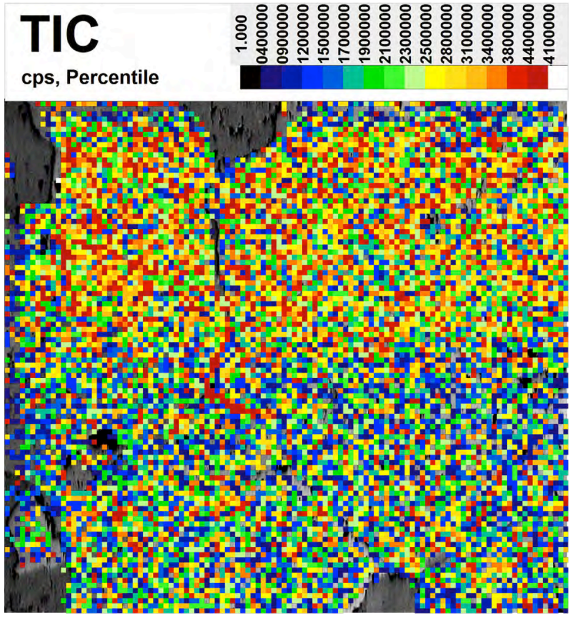
TIC
cps, Percentile
1.000
0400000
0900000
1200000
1500000
1700000
1900000
2100000
2300000
2500000
2800000
3100000
3400000
3800000
4400000
4100000

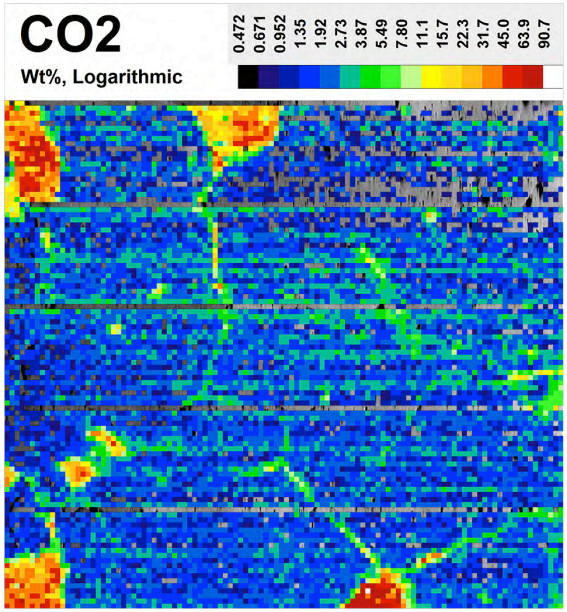
CO2
Wt%, Logarithmic
0.472 0.671 0.952 1.35 1.92 2.73 3.87 5.49 7.80 11.1 15.7 22.3 31.7 45.0 63.9 90.7

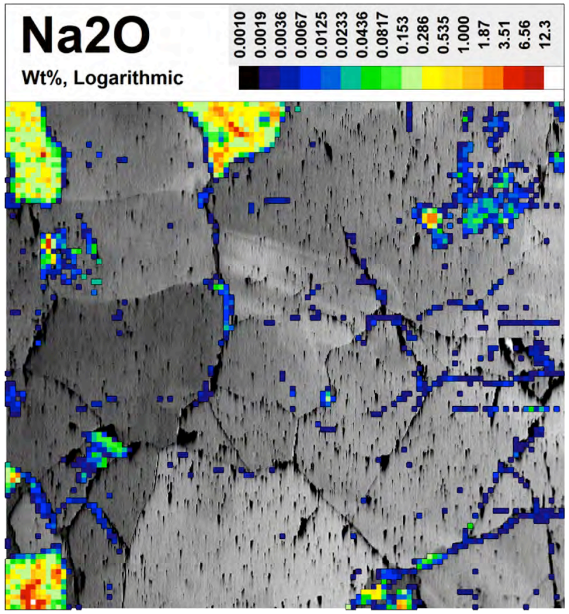
Na2O
Wt%, Logarithmic
0.0010 0.0019 0.0036 0.0067 0.0125 0.0233 0.0436 0.0817 0.153 0.286 0.535 1.000 1.87 3.51 6.56 12.3

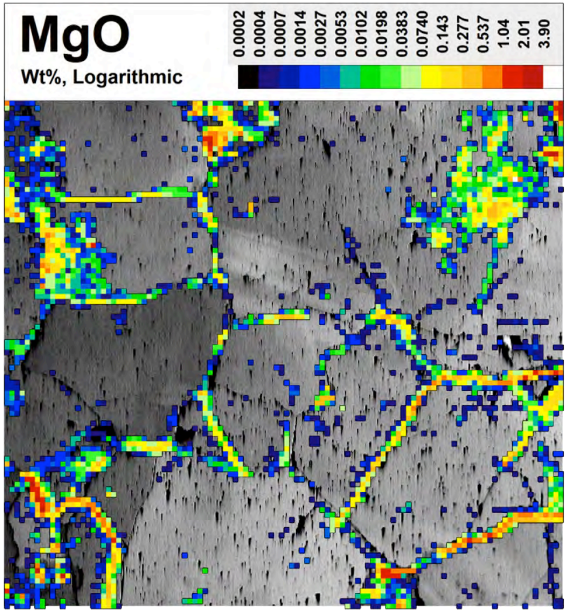
MgO
Wt%, Logarithmic
0.0002 0.0004 0.0007 0.0014 0.0027 0.0053 0.0102 0.0198 0.0383 0.0740 0.143 0.277 0.537 1.04 2.01 3.90

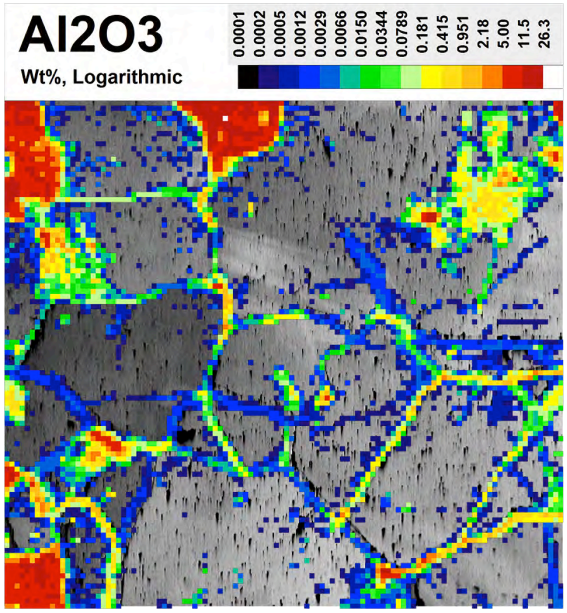
Al2O3
Wt%, Logarithmic
0.0001 0.0002 0.0005 0.0012 0.0029 0.0066 0.0150 0.0344 0.0789 0.181 0.415 0.951 2.18 5.00 11.5 26.3

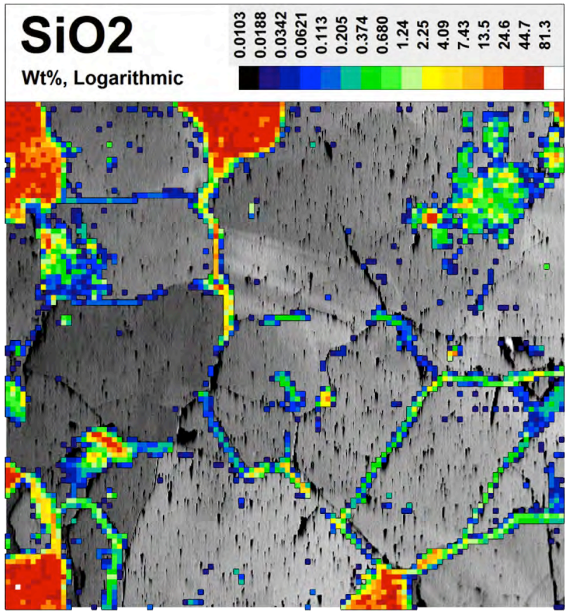
SiO2
Wt%, Logarithmic
0.0103 0.0188 0.0342 0.0621 0.113 0.205 0.374 0.680 1.24 2.25 4.09 7.43 13.5 24.6 44.7 81.3

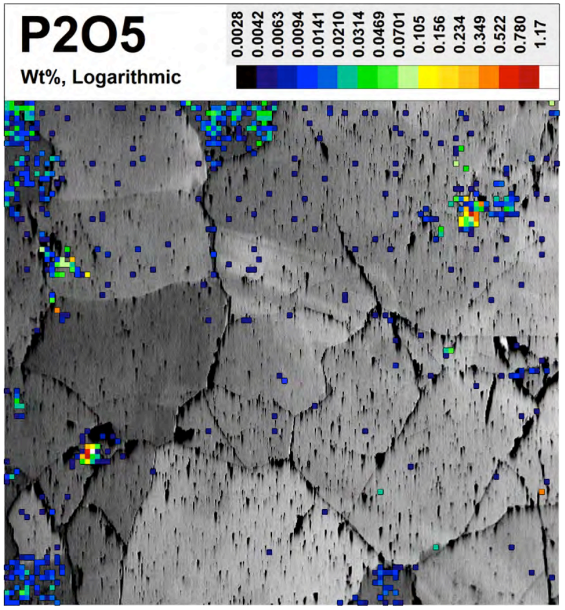
P2O5
Wt%, Logarithmic
0.0028 0.0042 0.0063 0.0094 0.0141 0.0210 0.0314 0.0469 0.0701 0.105 0.156 0.234 0.349 0.522 0.780 1.17

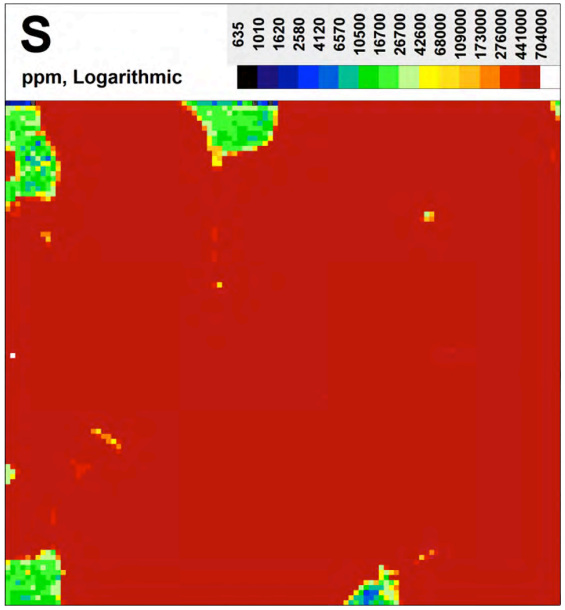
S
ppm, Logarithmic
635 1010 1620 2580 4120 6570 10500 16700 26700 42600 68000 109000 173000 276000 441000 704000

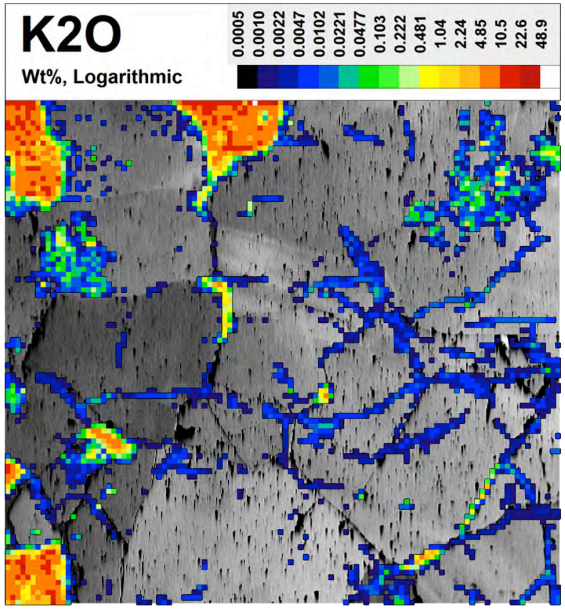
K2O
Wt%, Logarithmic
0.0005 0.0010 0.0022 0.0047 0.0102 0.0221 0.0477 0.103 0.222 0.481 1.04 2.24 4.85 10.5 22.6 48.9

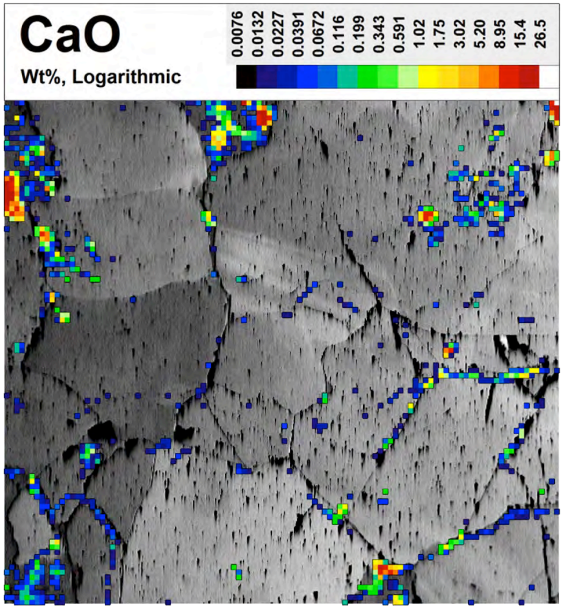
CaO
Wt%, Logarithmic
0.0076 0.0132 0.0227 0.0391 0.0672 0.116 0.199 0.343 0.591 1.02 1.75 3.02 5.20 8.95 15.4 26.5

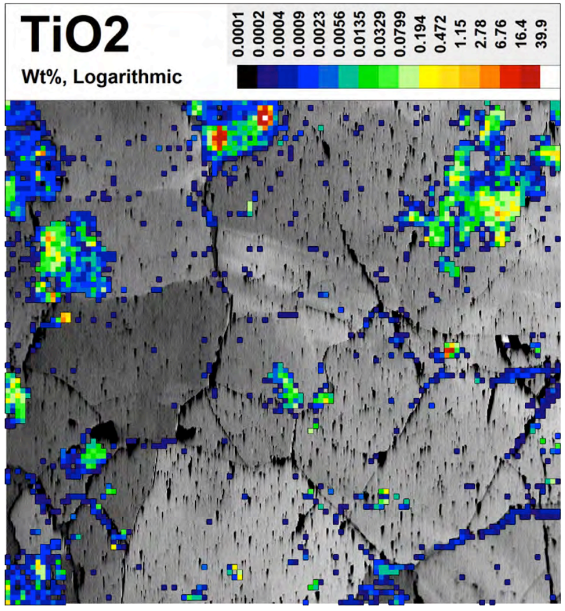
TiO2
Wt%, Logarithmic
0.0001 0.0002 0.0004 0.0009 0.0023 0.0056 0.0135 0.0329 0.0799 0.194 0.472 1.15 2.78 6.76 16.4 39.9

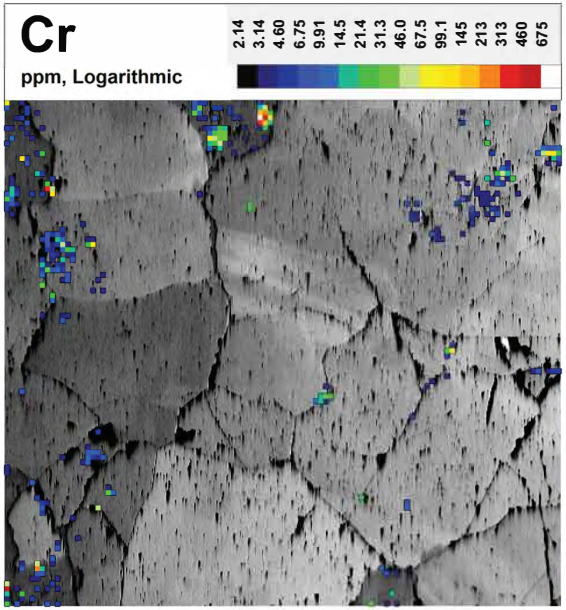
Cr
ppm, Logarithmic
2.14 3.14 4.60 6.75 9.91 14.5 21.4 31.3 46.0 67.5 99.1 145 213 313 460 675

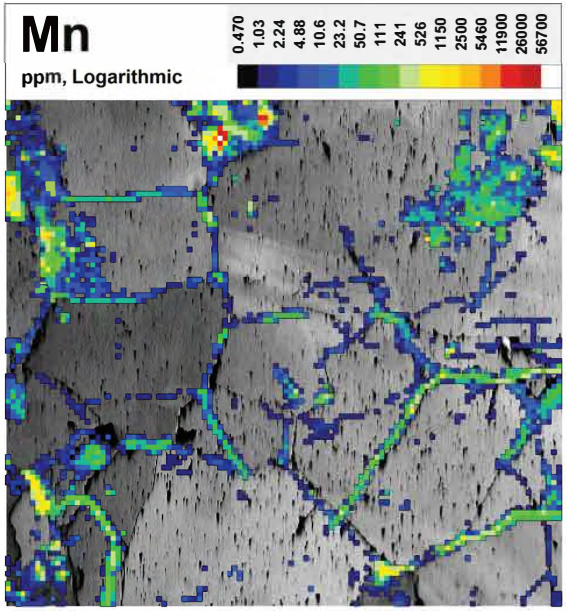
Mn
ppm, Logarithmic
0.470 1.03 2.24 4.88 10.6 23.2 50.7 111 241 526 1150 2500 5460 11900 26000 56700

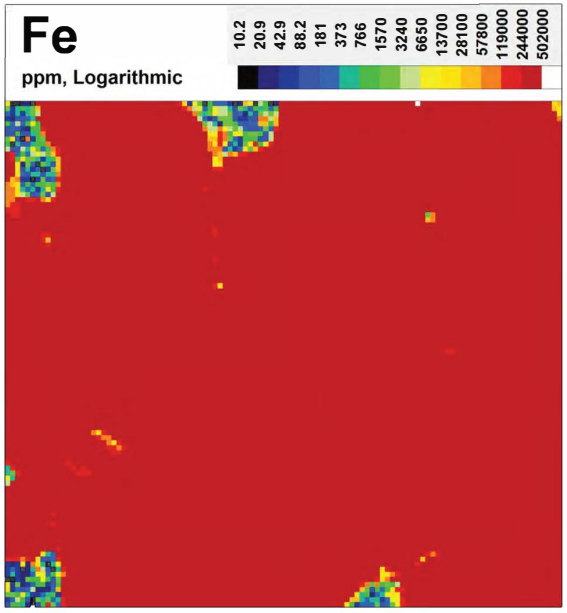
Fe
ppm, Logarithmic
10.2 20.9 42.9 88.2 181 373 766 1570 3240 6650 13700 28100 57800 119000 244000 502000

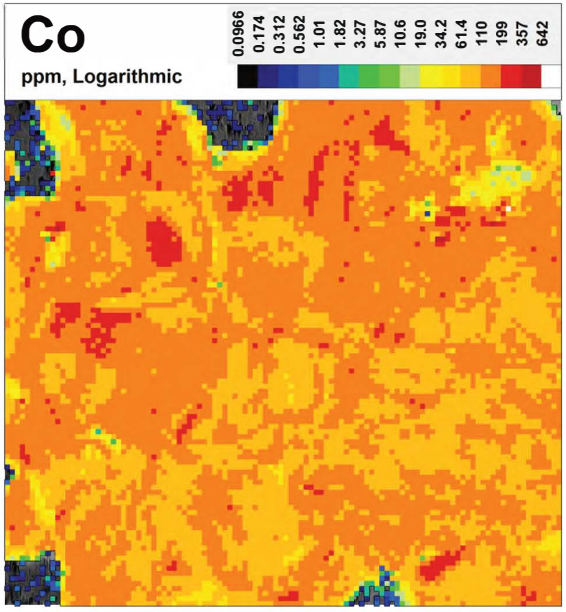
Co
ppm, Logarithmic
0.0966 0.174 0.312 0.562 1.01 1.82 3.27 5.87 10.6 19.0 34.2 61.4 110 199 357 642

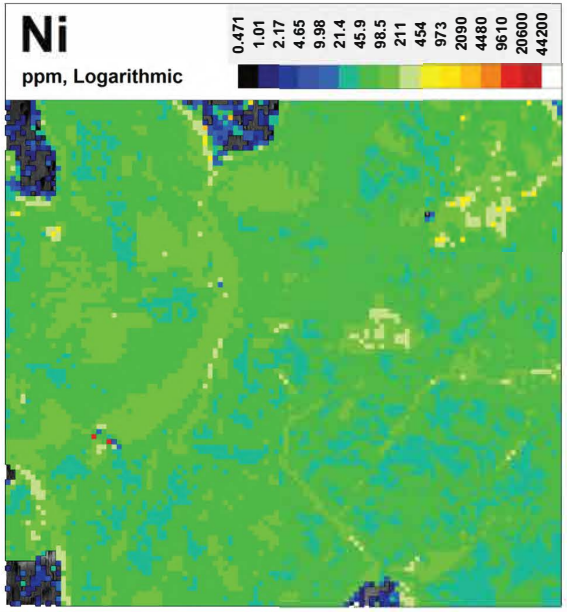
Ni
ppm, Logarithmic
0.471 1.01 2.17 4.65 9.98 21.4 45.9 98.5 211 454 973 2090 4480 9610 20600 44200

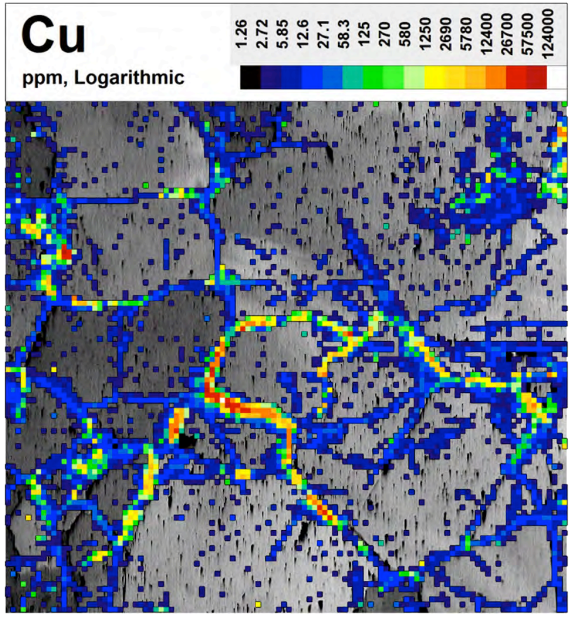
Cu
ppm, Logarithmic
1.26 2.72 5.85 12.6 27.1 58.3 125 270 580 1250 2690 5780 12400 26700 57500 124000

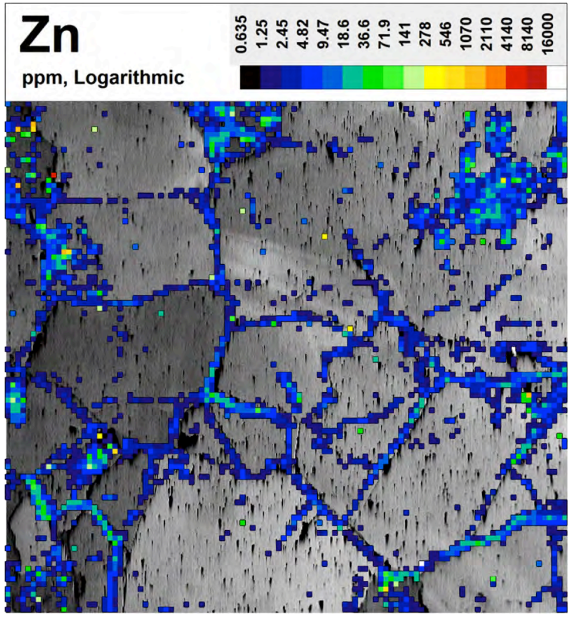
Zn
ppm, Logarithmic
0.635 1.25 2.45 4.82 9.47 18.6 36.6 71.9 141 278 546 1070 2110 4140 8140 16000

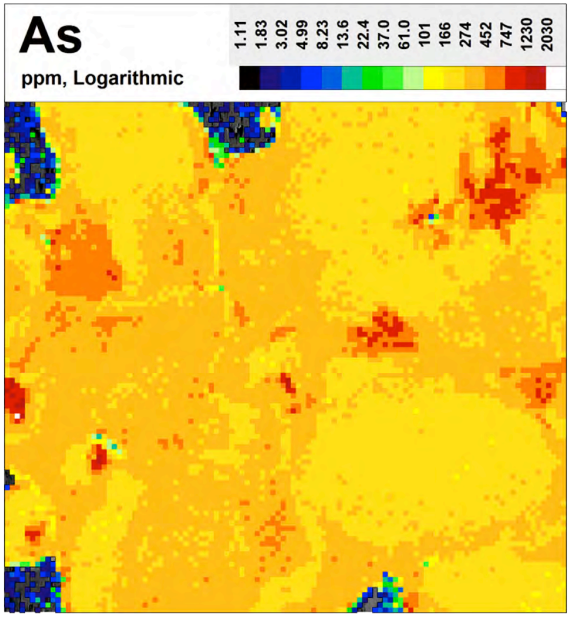
As
ppm, Logarithmic
1.11 1.83 3.02 4.99 8.23 13.6 22.4 37.0 61.0 101 166 274 452 747 1230 2030

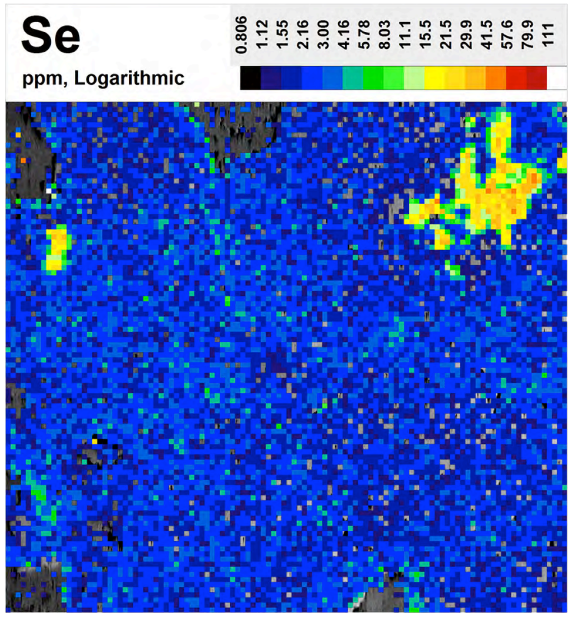
Se
ppm, Logarithmic
0.806 1.12 1.55 2.16 3.00 4.16 5.78 8.03 11.1 15.5 21.5 29.9 41.5 57.6 79.9 111

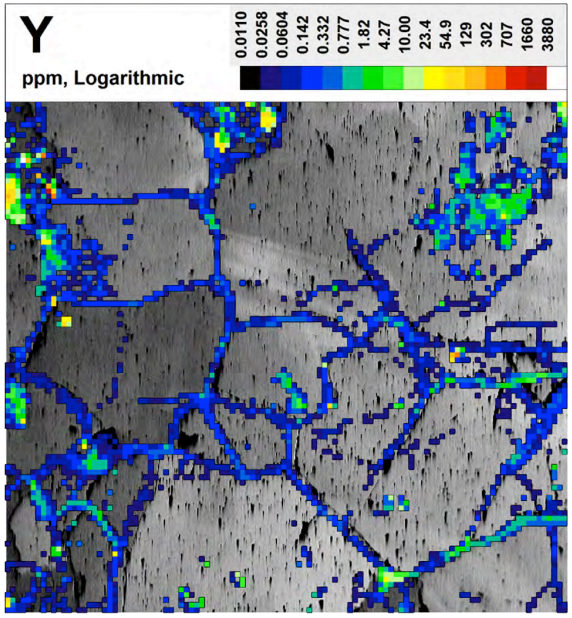
Y
ppm, Logarithmic
0.0110 0.0258 0.0604 0.142 0.332 0.777 1.82 4.27 10.00 23.4 54.9 129 302 707 1660 3880

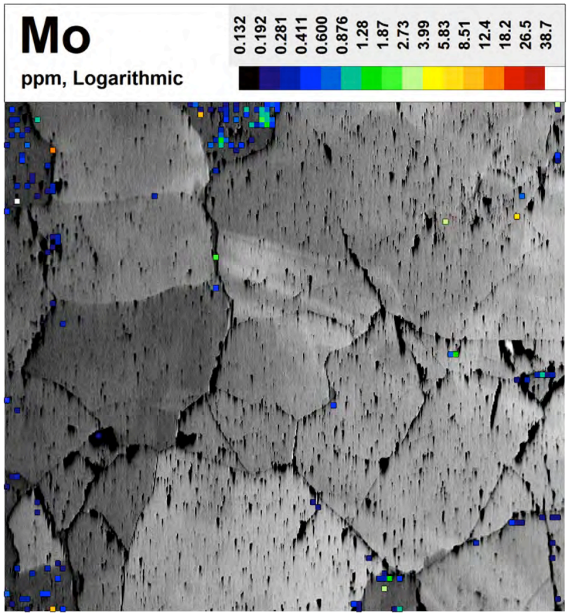
Mo
ppm, Logarithmic
0.132 0.192 0.281 0.411 0.600 0.876 1.28 1.87 2.73 3.99 5.83 8.51 12.4 18.2 26.5 38.7

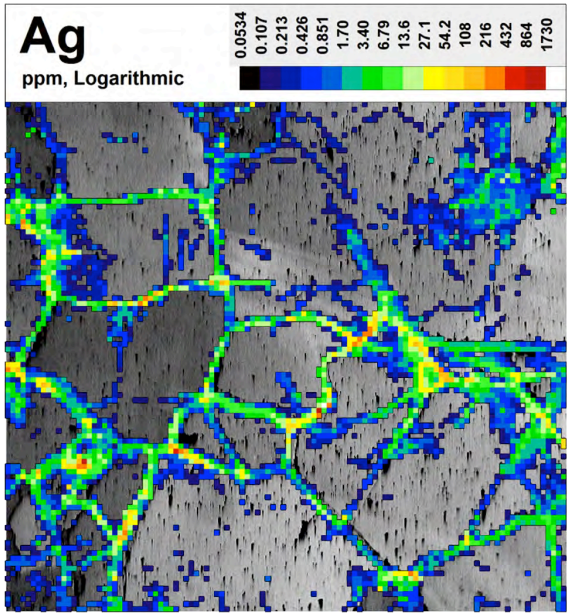
Ag
ppm, Logarithmic
0.0534 0.107 0.213 0.426 0.851 1.70 3.40 6.79 13.6 27.1 54.2 108 216 432 864 1730

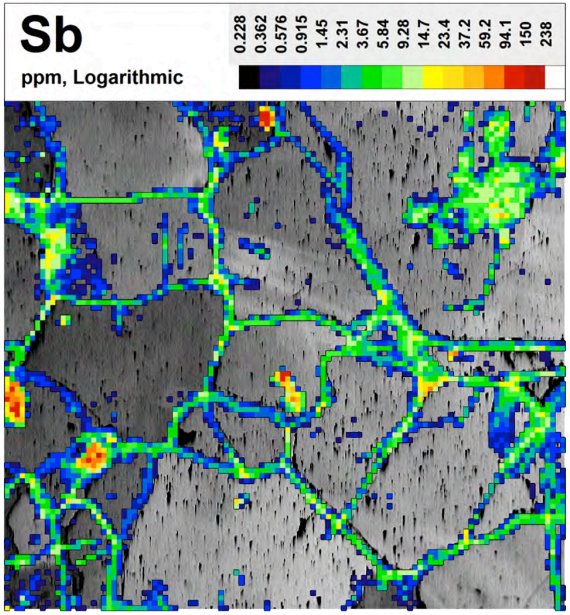
Sb
ppm, Logarithmic
0.228 0.362 0.576 0.915 1.45 2.31 3.67 5.84 9.28 14.7 23.4 37.2 59.2 94.1 150 238

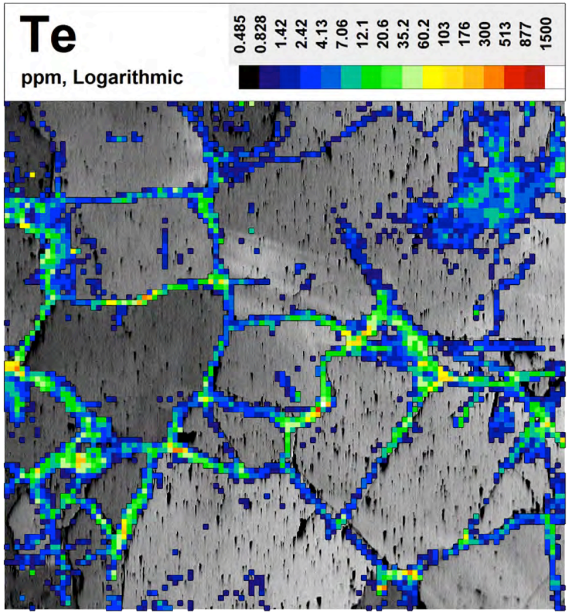
Te
ppm, Logarithmic
0.485 0.828 1.42 2.42 4.13 7.06 12.1 20.6 35.2 60.2 103 176 300 513 877 1500

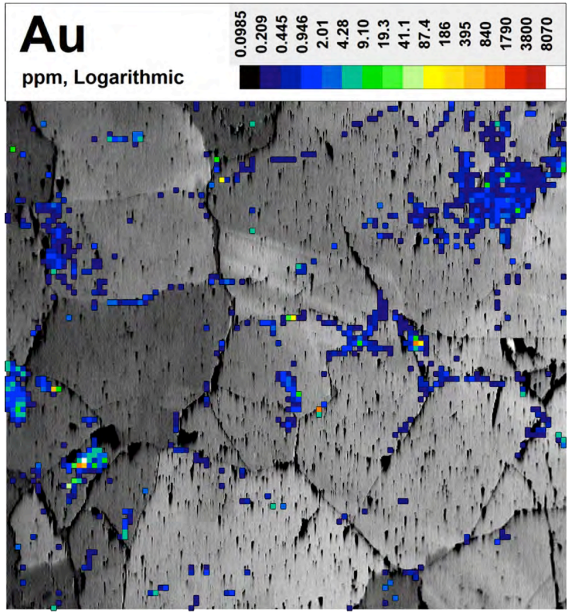
Au
ppm, Logarithmic
0.0985 0.209 0.445 0.946 2.01 4.28 9.10 19.3 41.1 87.4 186 395 840 1790 3800 8070

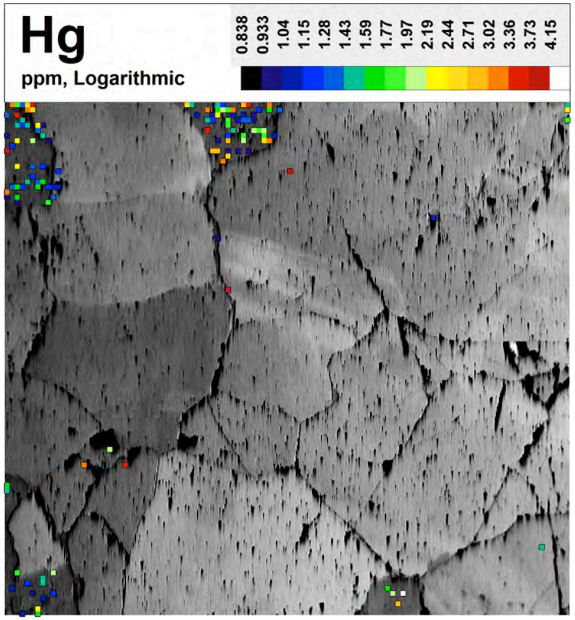
Hg
ppm, Logarithmic
0.838 0.933 1.04 1.15 1.28 1.43 1.59 1.77 1.97 2.19 2.44 2.71 3.02 3.36 3.73 4.15

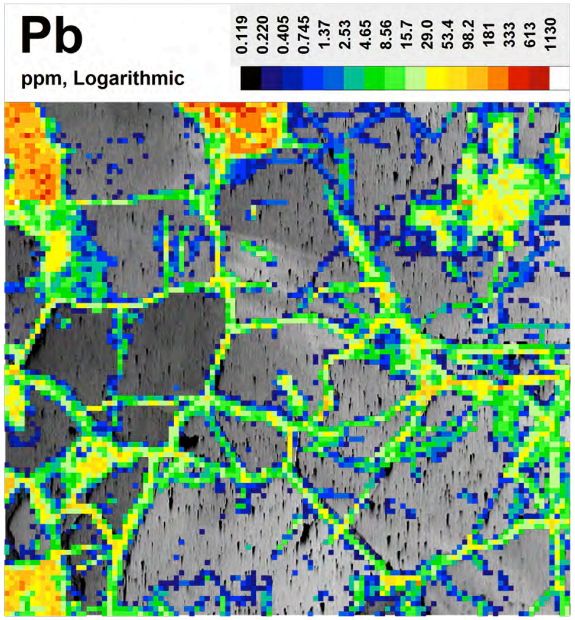
Pb
ppm, Logarithmic
0.119 0.220 0.405 0.745 1.37 2.53 4.65 8.56 15.7 29.0 53.4 98.2 181 333 613 1130

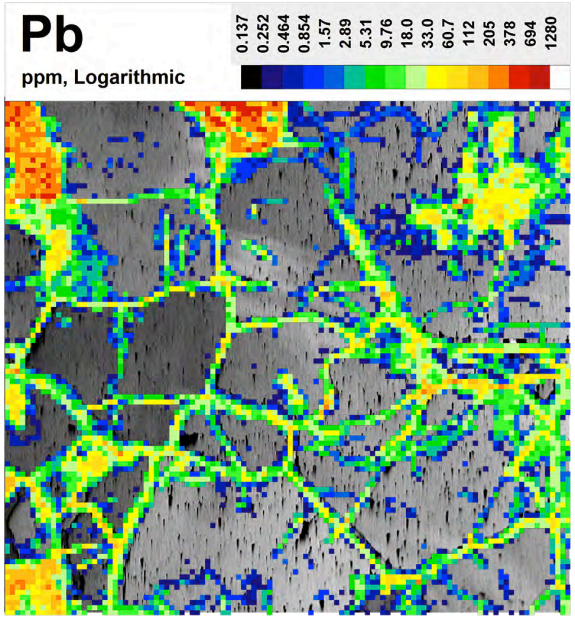
Pb
ppm, Logarithmic
0.137 0.252 0.464 0.854 1.57 2.89 5.31 9.76 18.0 33.0 60.7 112 205 378 694 1280

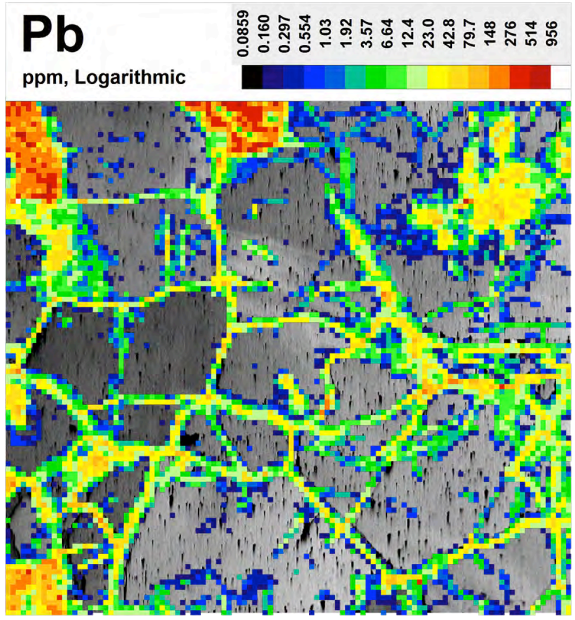
Pb
ppm, Logarithmic
0.0859 0.160 0.297 0.554 1.03 1.92 3.57 6.64 12.4 23.0 42.8 79.7 148 276 514 956

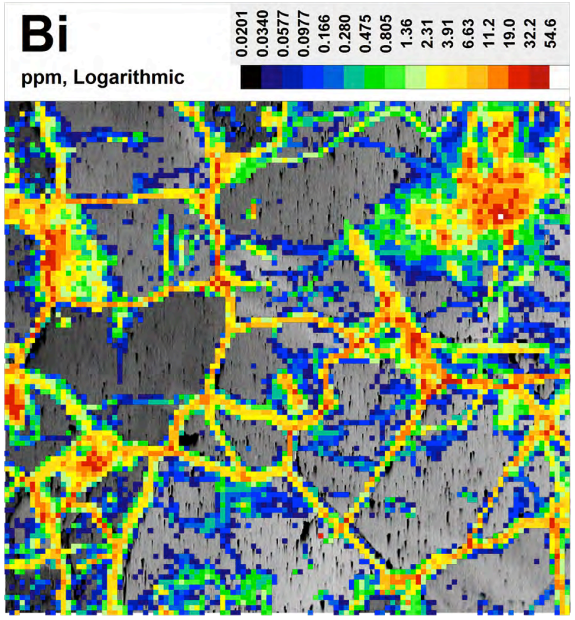
Bi
ppm, Logarithmic
0.0201 0.0340 0.0577 0.0977 0.166 0.280 0.475 0.805 1.36 2.31 3.91 6.63 11.2 19.0 32.2 54.6

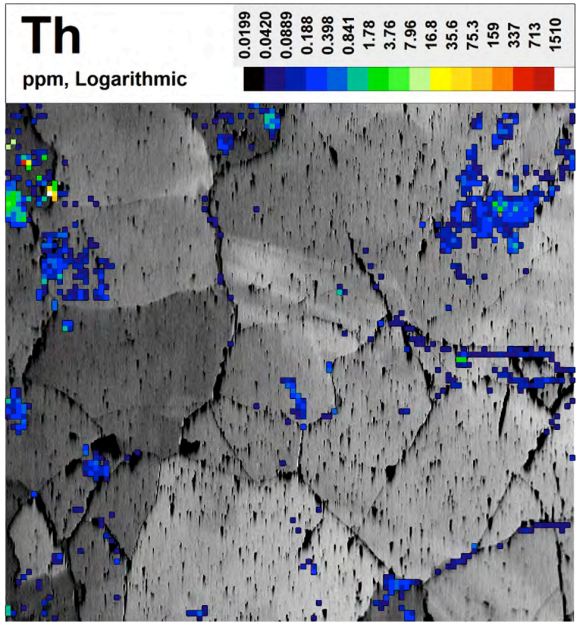
Th
ppm, Logarithmic
0.0199
0.0420
0.0889
0.188
0.398
0.841
1.78
3.76
7.96
16.8
35.6
75.3
159
337
713
1510

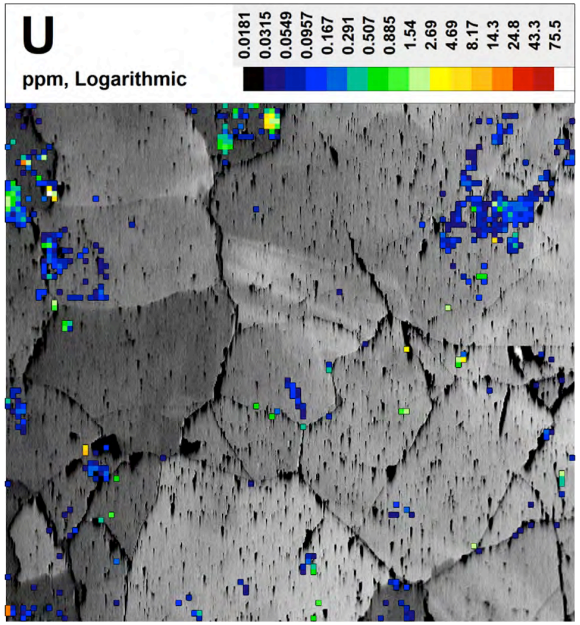
U
ppm, Logarithmic
0.0181
0.0315
0.0549
0.0957
0.167
0.291
0.507
0.885
1.54
2.69
4.69
8.17
14.3
24.8
43.3
75.5

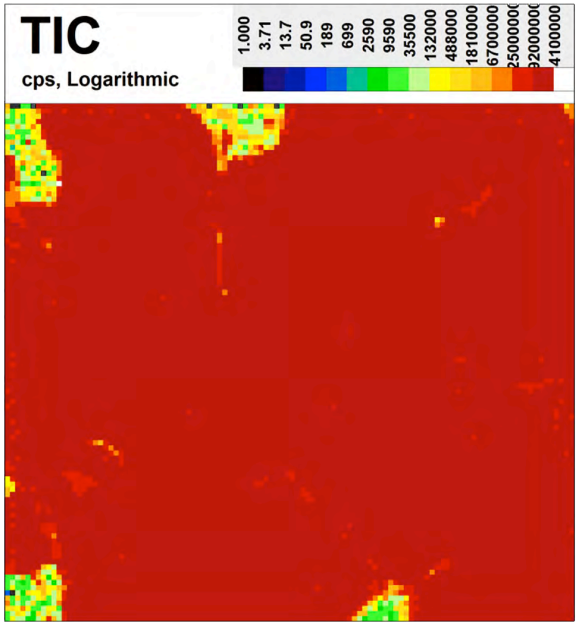
TIC
cps, Logarithmic
1.000
3.71
13.7
50.9
189
699
2590
9590
35500
132000
488000
1810000
6700000

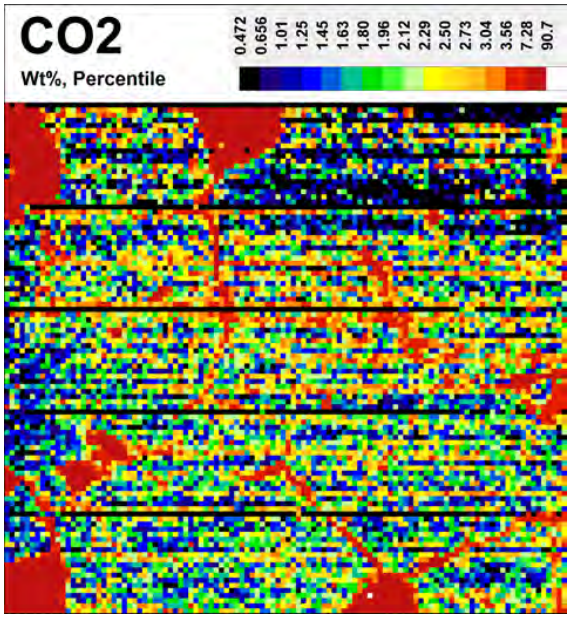
CO2
Wt%, Percentile
0.472
0.656
1.01
1.25
1.45
1.63
1.80
1.96
2.12
2.29
2.50
2.73
3.04
3.56
7.28
90.7

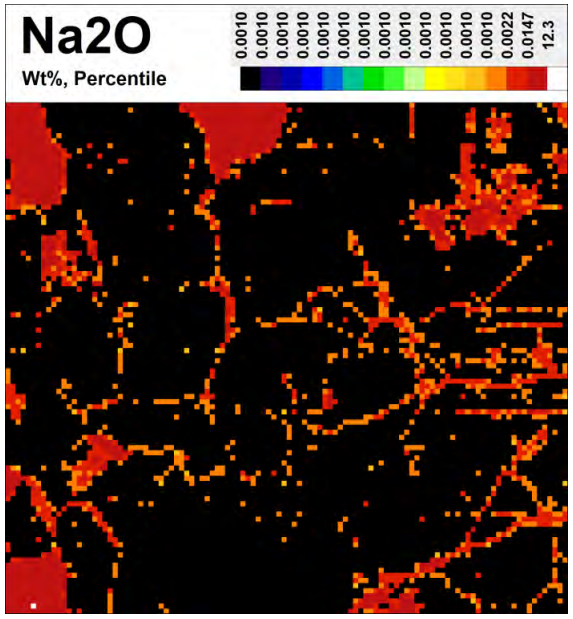
Na2O
Wt%, Percentile
0.0010
0.0010
0.0010
0.0010
0.0010
0.0010
0.0010
0.0010
0.0010
0.0010
0.0010
0.0010
0.0010
0.0022
0.0147
12.3

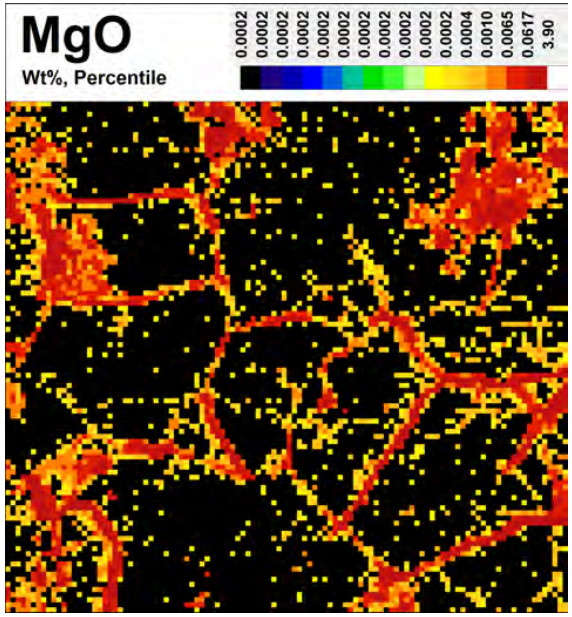
MgO
Wt%, Percentile
0.0002
0.0002
0.0002
0.0002
0.0002
0.0002
0.0002
0.0002
0.0002
0.0002
0.0004
0.0010
0.0065
0.0617
3.90

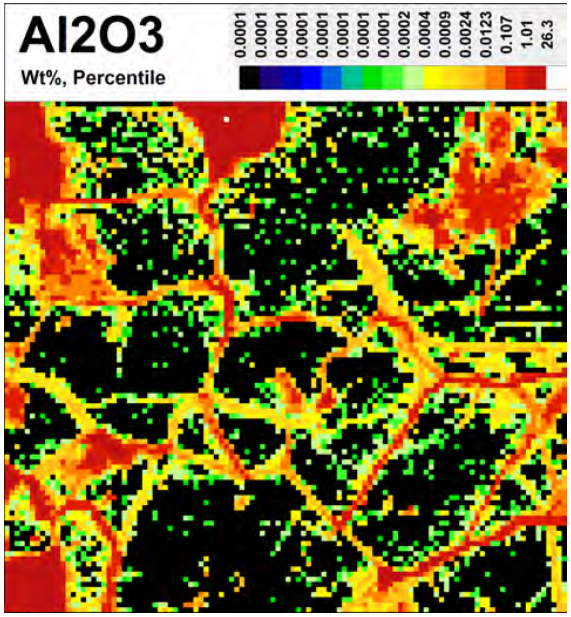
Al2O3
Wt%, Percentile
0.0001
0.0001
0.0001
0.0001
0.0001
0.0001
0.0001
0.0002
0.0004
0.0009
0.0024
0.0123
0.107
1.01
26.3

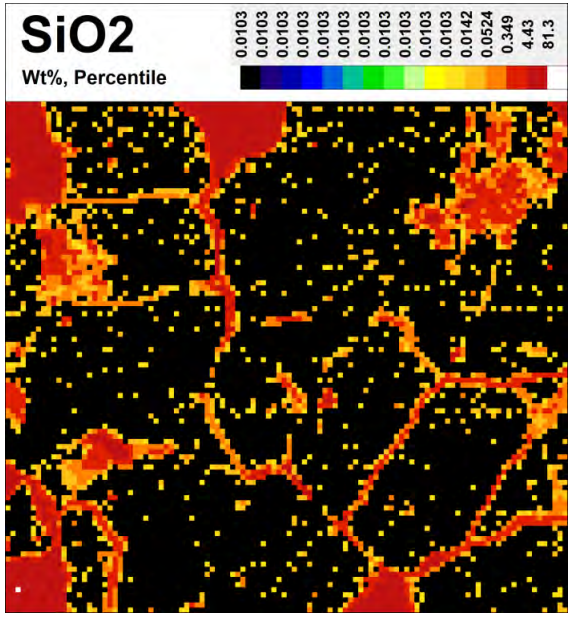
SiO2
Wt%, Percentile
0.0103
0.0103
0.0103
0.0103
0.0103
0.0103
0.0103
0.0103
0.0103
0.0103
0.0142
0.0524
0.349
4.43
81.3

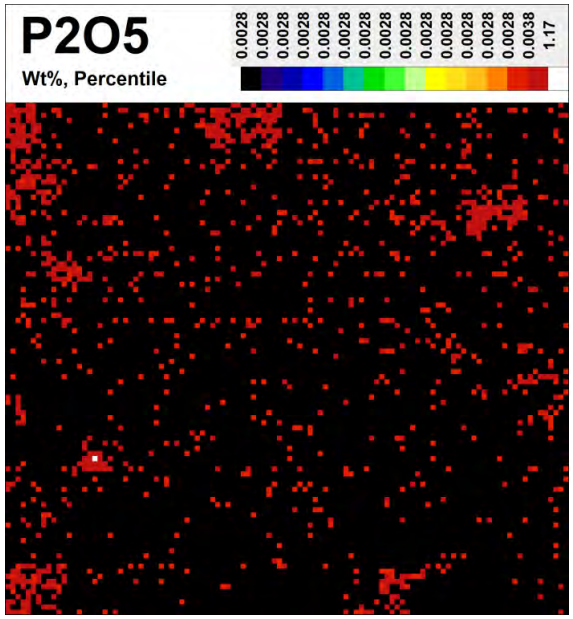
P2O5
Wt%, Percentile
0.0028 0.0028 0.0028 0.0028 0.0028 0.0028 0.0028 0.0028 0.0028 0.0028 0.0028 0.0028 0.0038 1.17

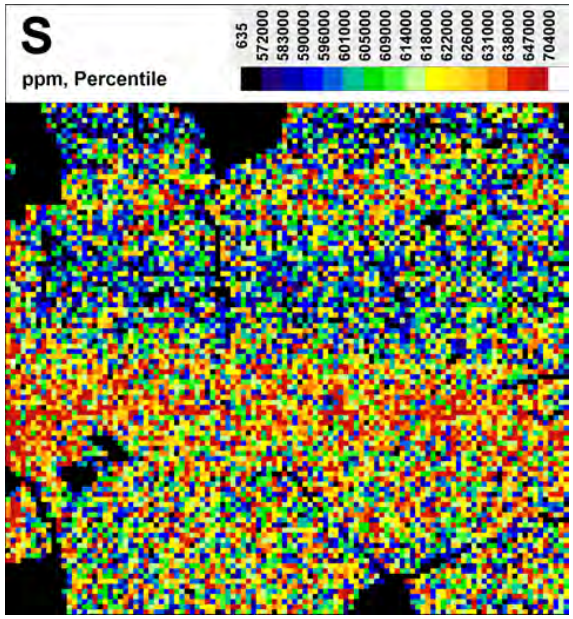
S
ppm, Percentile
635 572000 583000 590000 596000 601000 605000 609000 614000 618000 622000 626000 631000 638000 647000 704000

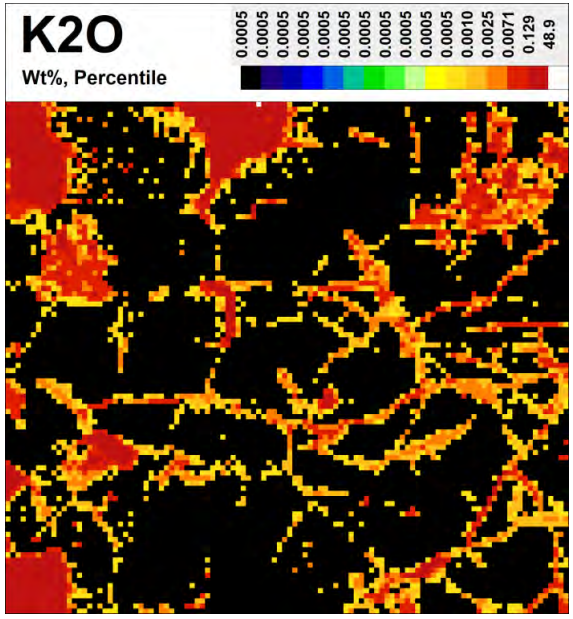
K2O
Wt%, Percentile
0.0005 0.0005 0.0005 0.0005 0.0005 0.0005 0.0005 0.0005 0.0005 0.0005 0.0010 0.0025 0.0071 0.129 48.9

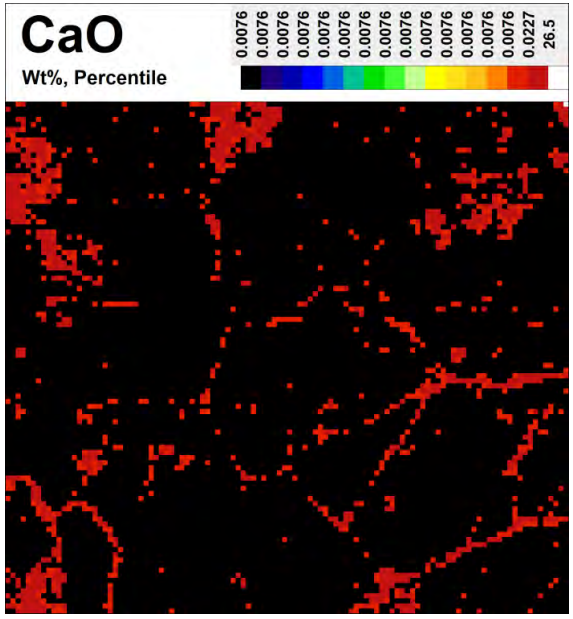
CaO
Wt%, Percentile
0.0076 0.0076 0.0076 0.0076 0.0076 0.0076 0.0076 0.0076 0.0076 0.0076 0.0076 0.0076 0.0227 26.5

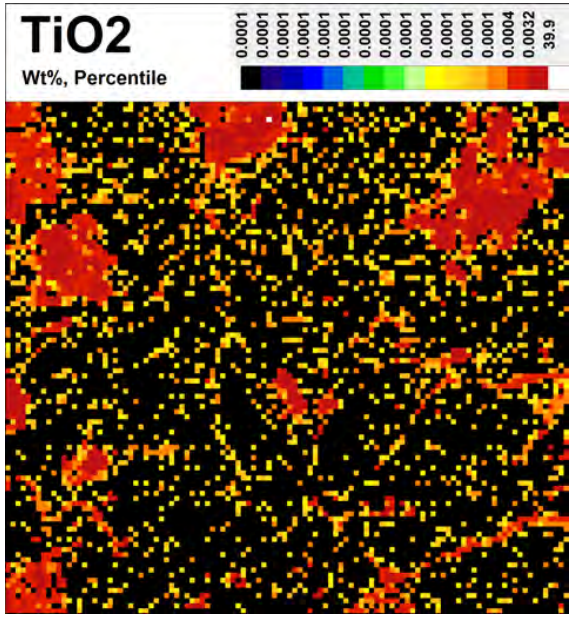
TiO2
Wt%, Percentile
0.0001 0.0001 0.0001 0.0001 0.0001 0.0001 0.0001 0.0001 0.0001 0.0001 0.0001 0.0001 0.0004 0.0032 39.9

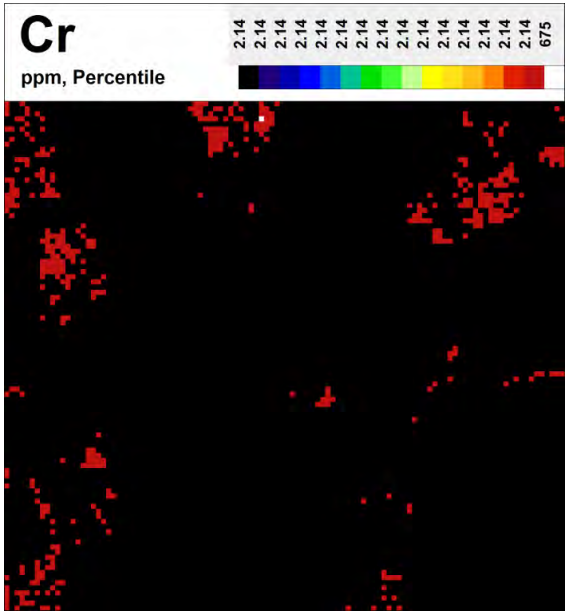
Cr
ppm, Percentile
2.14 2.14 2.14 2.14 2.14 2.14 2.14 2.14 2.14 2.14 2.14 2.14 2.14 675

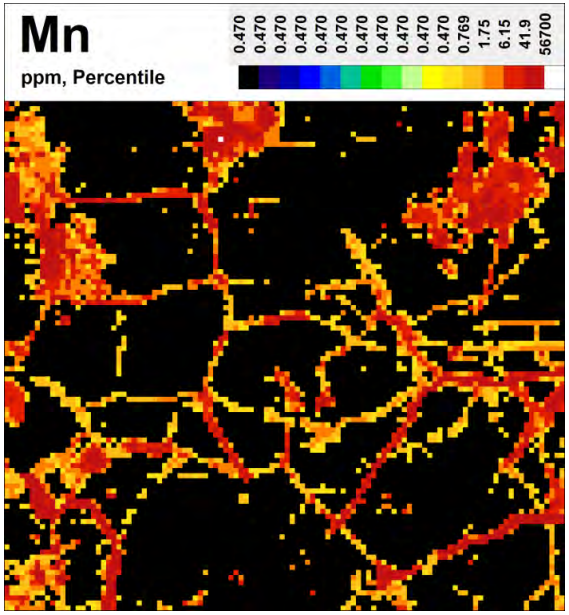
Mn
ppm, Percentile
0.470 0.470 0.470 0.470 0.470 0.470 0.470 0.470 0.470 0.470 0.769 1.75 6.15 41.9 56700

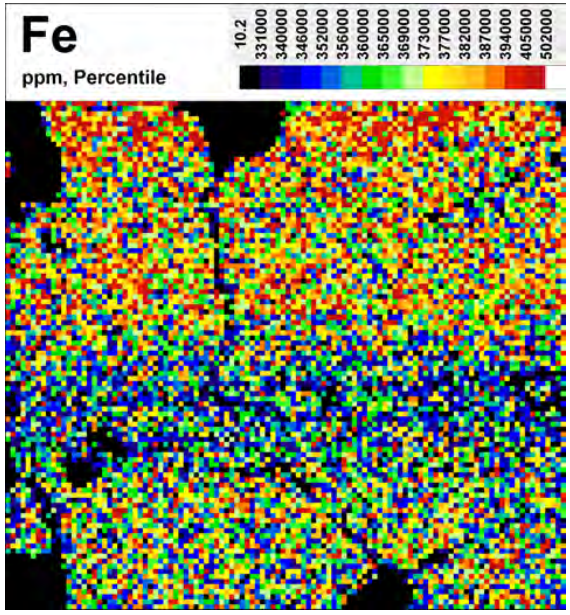
Fe
ppm, Percentile
10.2 331000 340000 346000 352000 356000 360000 365000 369000 373000 377000 382000 387000 394000 405000 502000

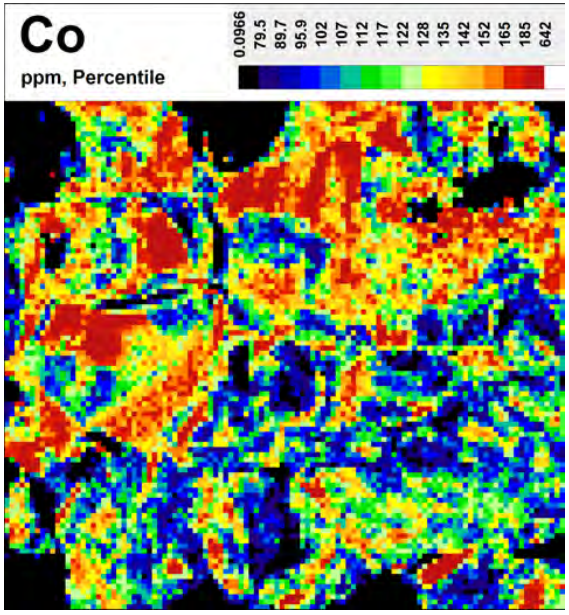
Co
ppm, Percentile
0.0966 79.5 89.7 95.9 102 107 112 117 122 128 135 142 152 165 185 642

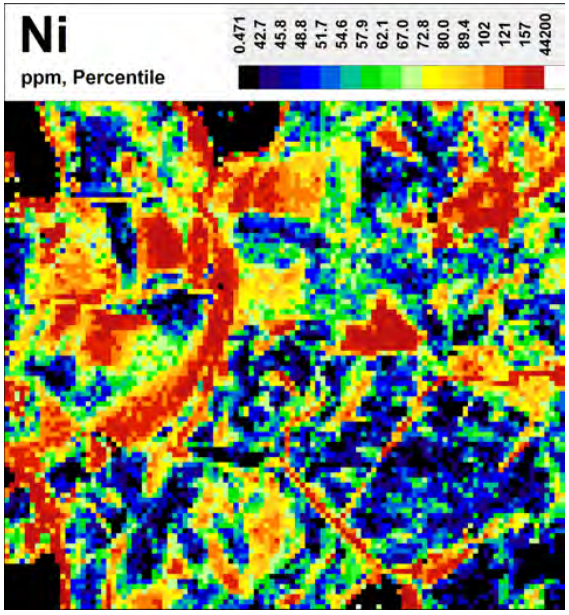
Ni
ppm, Percentile
0.471 42.7 45.8 48.8 51.7 54.6 57.9 62.1 67.0 72.8 80.0 89.4 102 121 157 44200

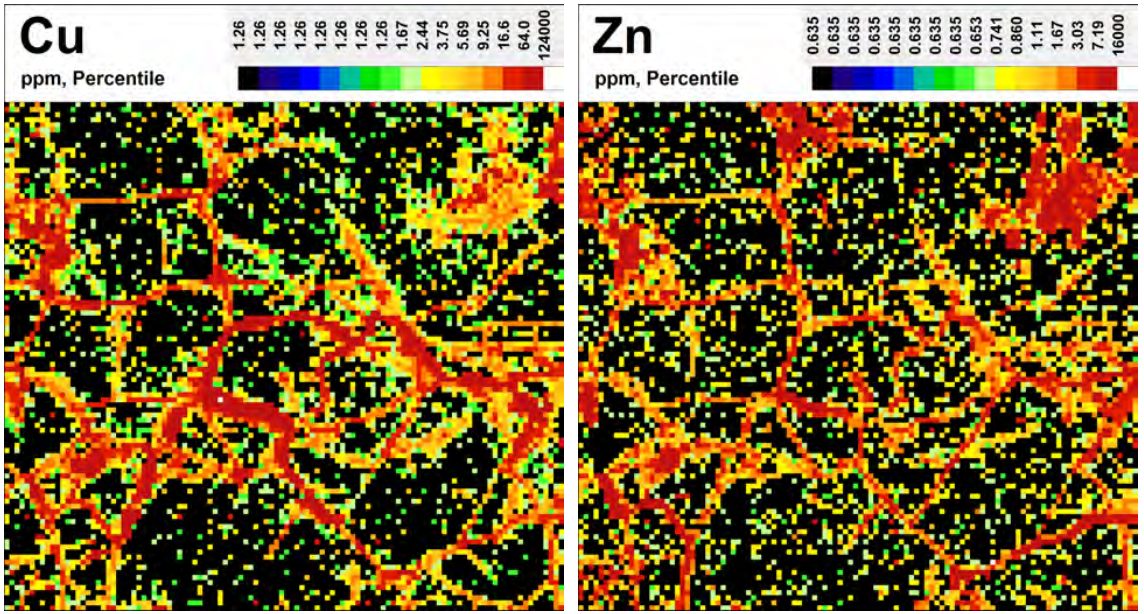
Cu
ppm, Percentile
1.26 1.26 1.26 1.26 1.26 1.26 1.26 1.67 2.44 3.75 5.69 9.25 16.6 64.0 124000
Zn
ppm, Percentile
0.635 0.635 0.635 0.635 0.635 0.635 0.635 0.653 0.741 0.860 1.11 1.67 3.03 7.19 16000

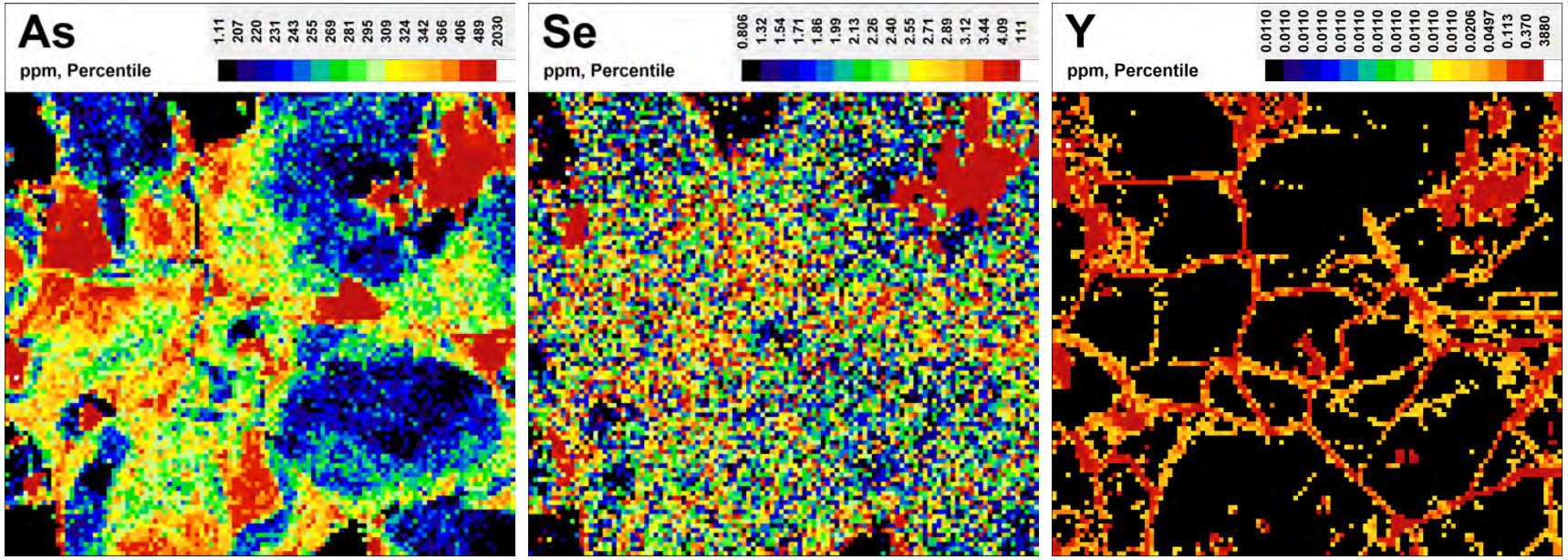
As
ppm, Percentile
1.11 207 220 231 243 255 269 281 295 309 324 342 366 406 489 2030
Se
ppm, Percentile
0.806 1.32 1.54 1.71 1.86 1.99 2.13 2.26 2.40 2.55 2.71 2.89 3.12 3.44 4.09 111
Y
ppm, Percentile
0.0110 0.0110 0.0110 0.0110 0.0110 0.0110 0.0110 0.0110 0.0110 0.0110 0.0206 0.0497 0.113 0.370 3880

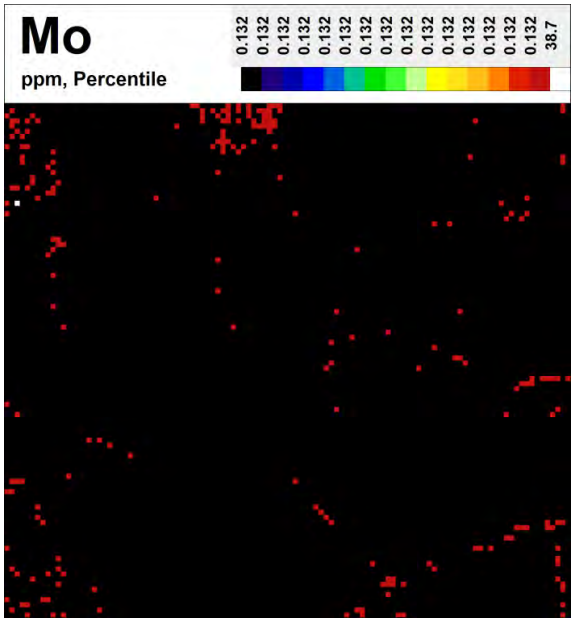
Mo
ppm, Percentile
0.132 0.132 0.132 0.132 0.132 0.132 0.132 0.132 0.132 0.132 0.132 0.132 0.132 38.7

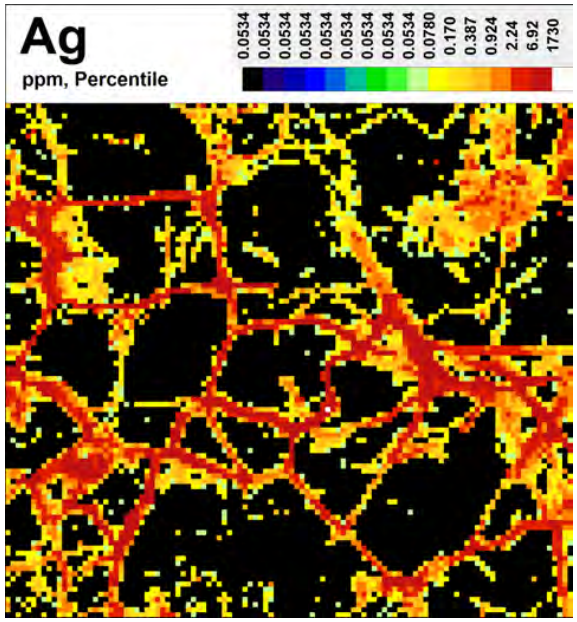
Ag
ppm, Percentile
0.0534 0.0534 0.0534 0.0534 0.0534 0.0534 0.0534 0.0534 0.0780 0.170 0.387 0.924 2.24 6.92 1730

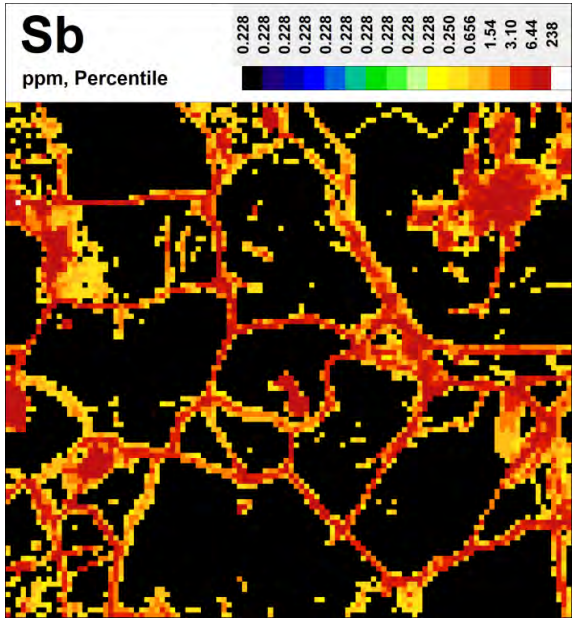
Sb
ppm, Percentile
0.228 0.228 0.228 0.228 0.228 0.228 0.228 0.228 0.228 0.250 0.656 1.54 3.10 6.44 238

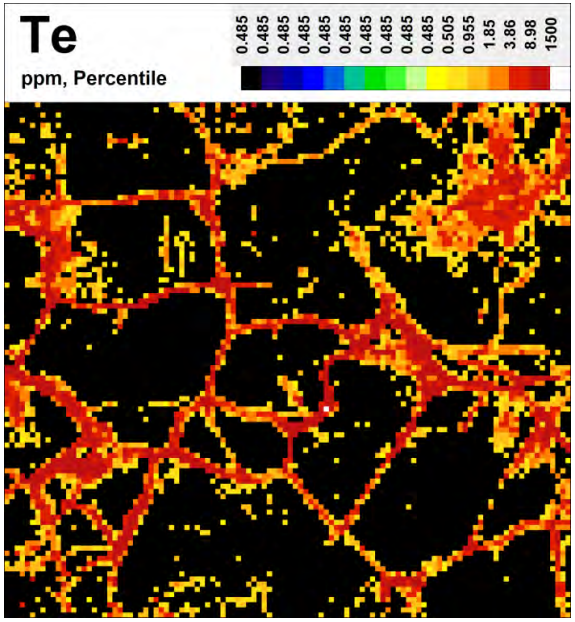
Te
ppm, Percentile
0.485 0.485 0.485 0.485 0.485 0.485 0.485 0.485 0.485 0.505 0.955 1.85 3.86 8.98 1500

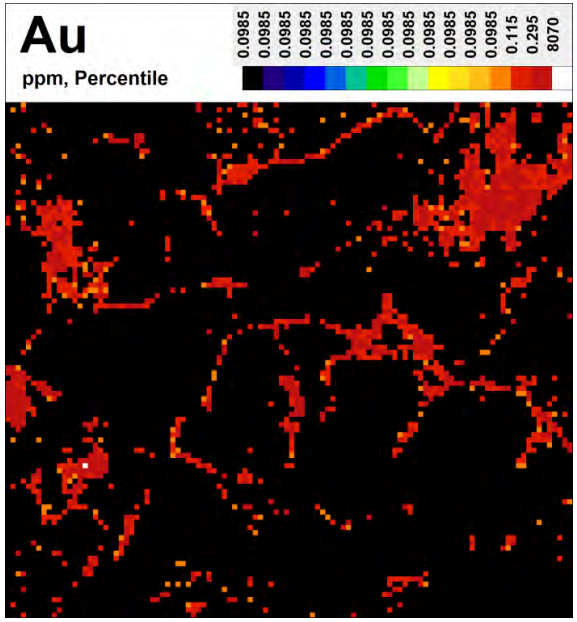
Au
ppm, Percentile
0.0985 0.0985 0.0985 0.0985 0.0985 0.0985 0.0985 0.0985 0.0985 0.0985 0.0985 0.115 0.295 8070

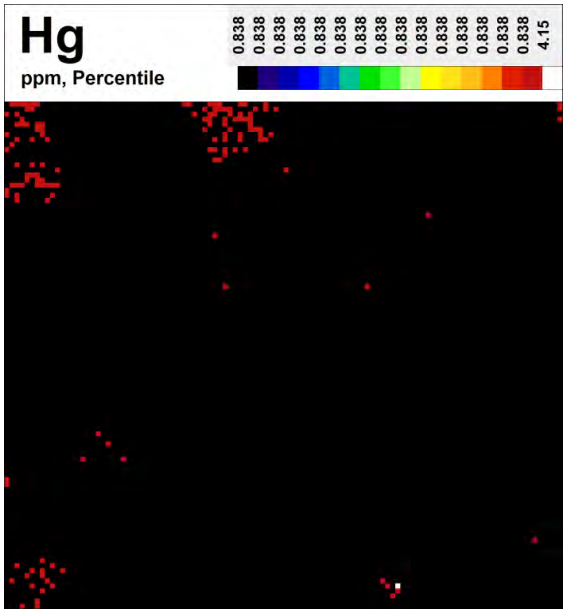
Hg
ppm, Percentile
0.838 0.838 0.838 0.838 0.838 0.838 0.838 0.838 0.838 0.838 0.838 0.838 0.838 4.15

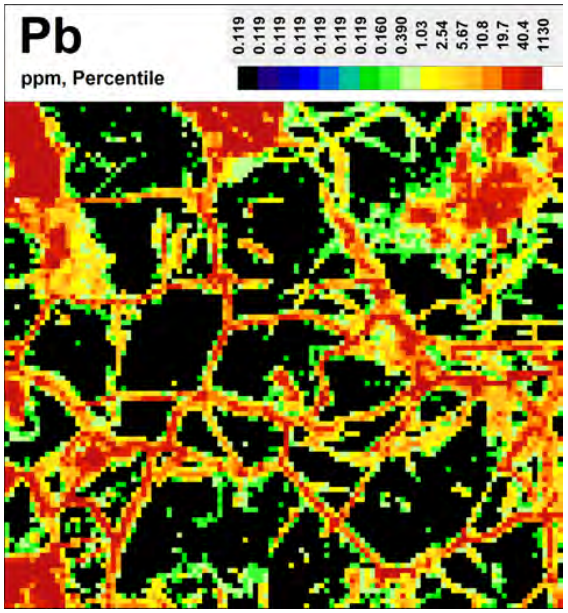
Pb
ppm, Percentile
0.119 0.119 0.119 0.119 0.119 0.119 0.160 0.390 1.03 2.54 5.67 10.8 19.7 40.4 1130

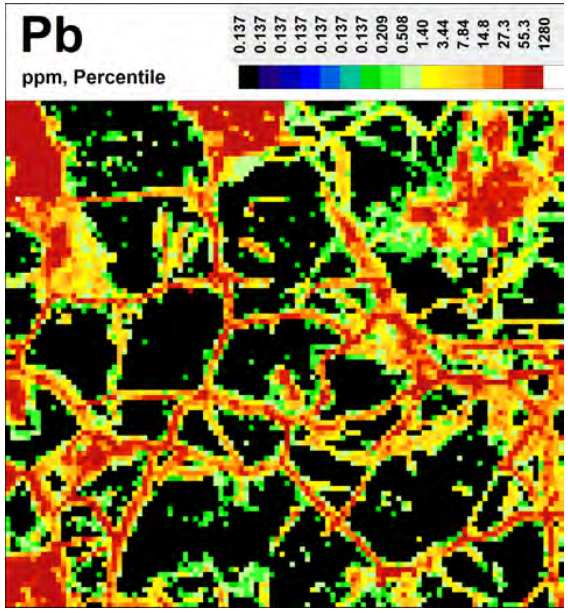
Pb
ppm, Percentile
0.137 0.137 0.137 0.137 0.137 0.137 0.209 0.508 1.40 3.44 7.84 14.8 27.3 55.3 1280

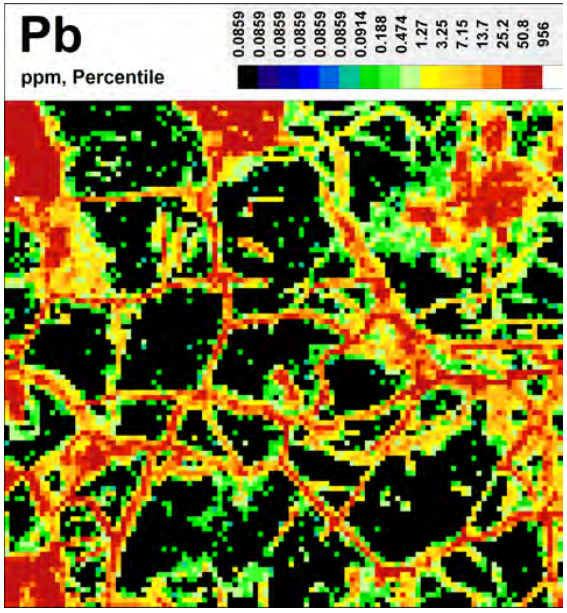
Pb
ppm, Percentile
0.0859 0.0859 0.0859 0.0859 0.0859 0.0859 0.0914 0.188 0.474 1.27 3.25 7.15 13.7 25.2 50.8 956

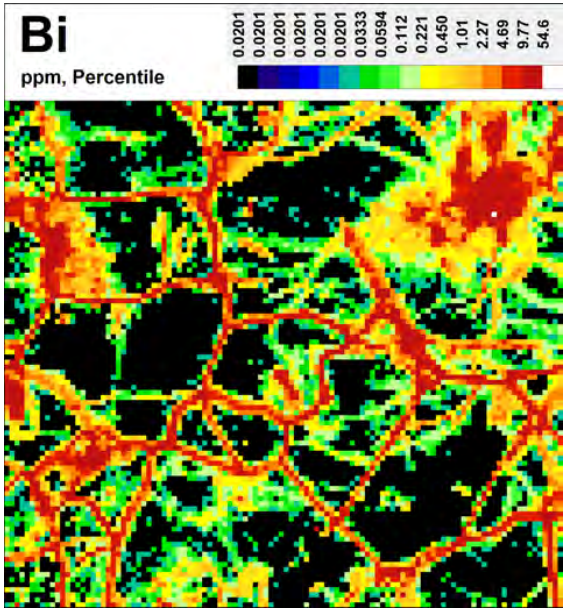
Bi
ppm, Percentile
0.0201 0.0201 0.0201 0.0201 0.0201 0.0201 0.0333 0.0594 0.112 0.221 0.450 1.01 2.27 4.69 9.77 54.6

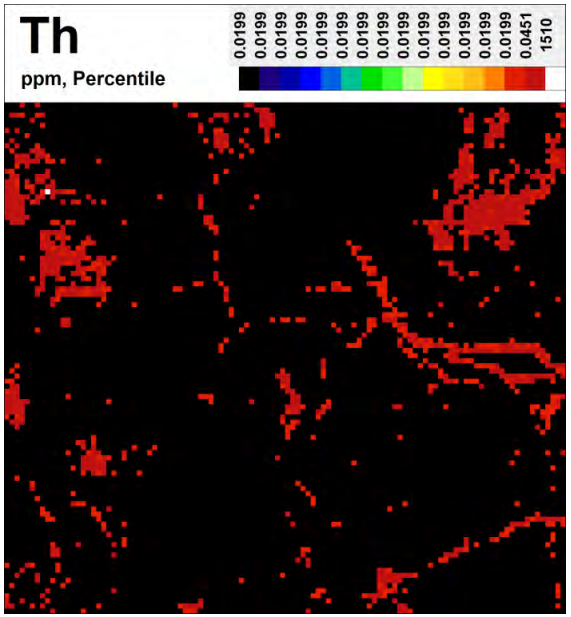
Th
ppm, Percentile
0.0199
0.0199
0.0199
0.0199
0.0199
0.0199
0.0199
0.0199
0.0199
0.0199
0.0199
0.0199
0.0199
0.0451
1510

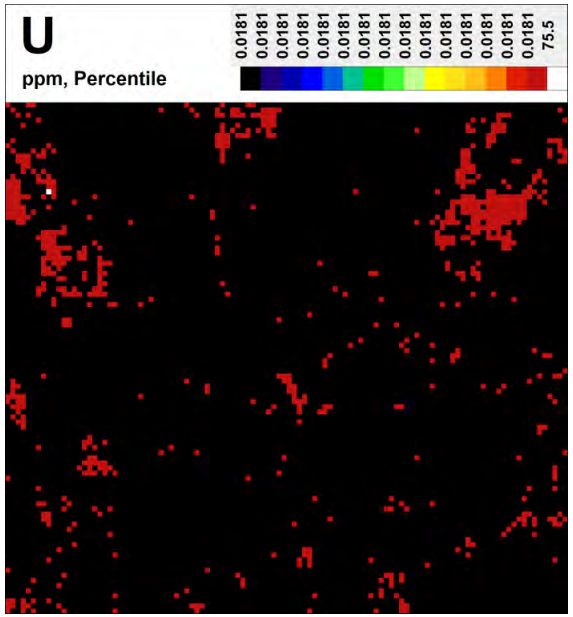
U
ppm, Percentile
0.0181
0.0181
0.0181
0.0181
0.0181
0.0181
0.0181
0.0181
0.0181
0.0181
0.0181
0.0181
0.0181
75.5

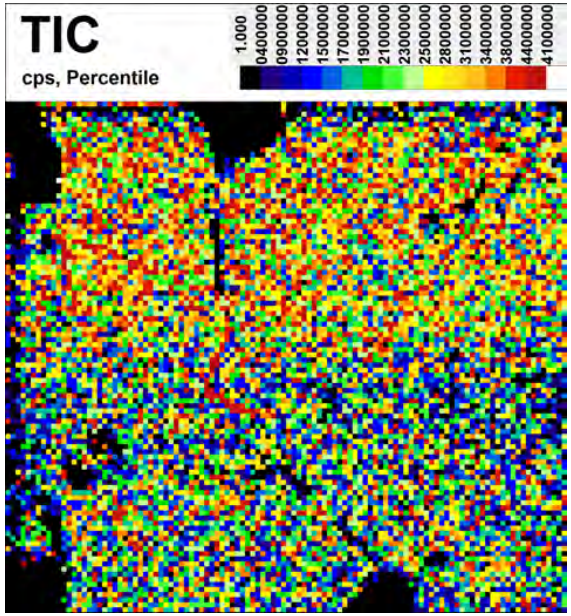
TIC
cps, Percentile
1.000
0400000
0900000
1200000
1500000
1700000
1900000
2100000
2300000
2500000
2800000
3100000
3400000
3800000
4400000
4100000

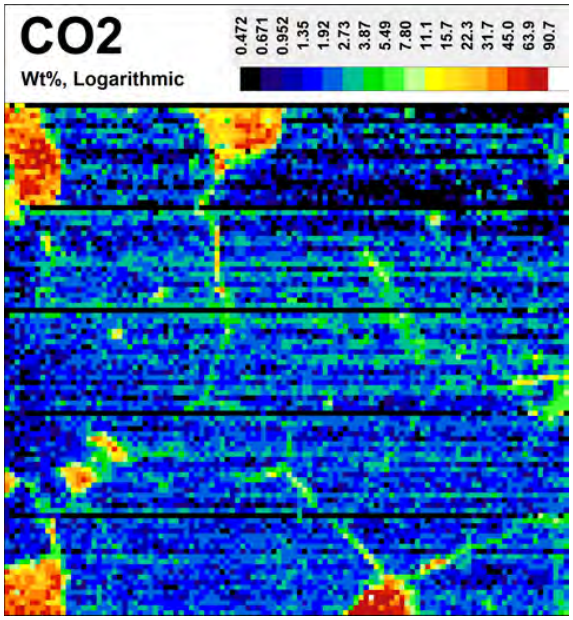
CO2
Wt%, Logarithmic
0.472 0.671 0.952 1.35 1.92 2.73 3.87 5.49 7.80 11.1 15.7 22.3 31.7 45.0 63.9 90.7

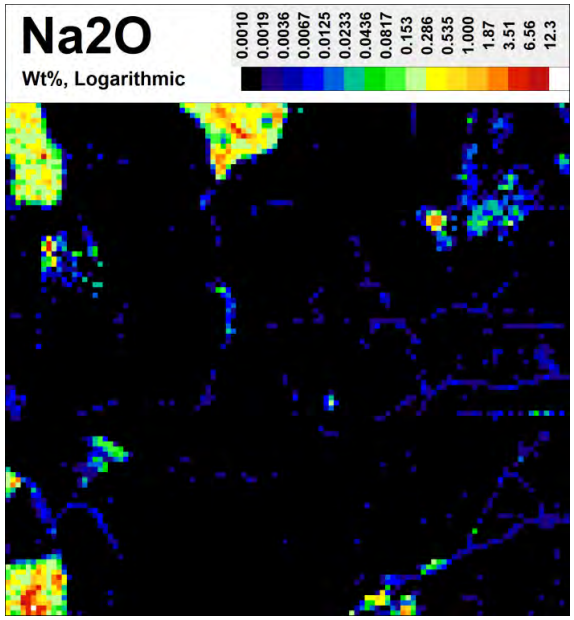
Na2O
Wt%, Logarithmic
0.0010 0.0019 0.0036 0.0067 0.0125 0.0233 0.0436 0.0817 0.153 0.286 0.535 1.000 1.87 3.51 6.56 12.3

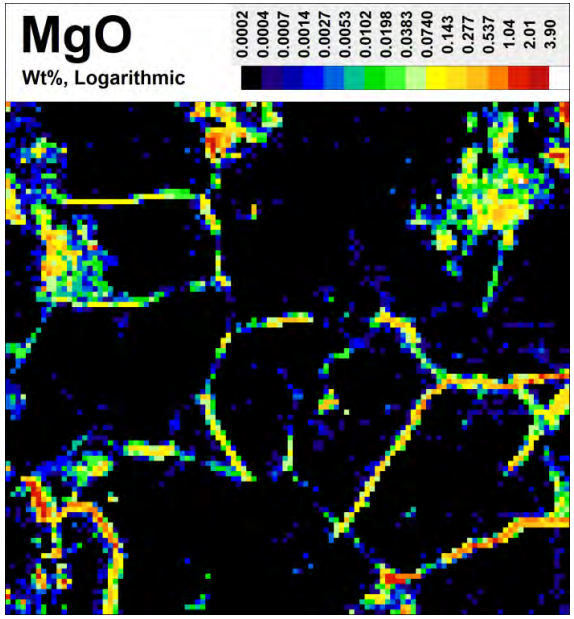
MgO
Wt%, Logarithmic
0.0002 0.0004 0.0007 0.0014 0.0027 0.0053 0.0102 0.0198 0.0383 0.0740 0.143 0.277 0.537 1.04 2.01 3.90

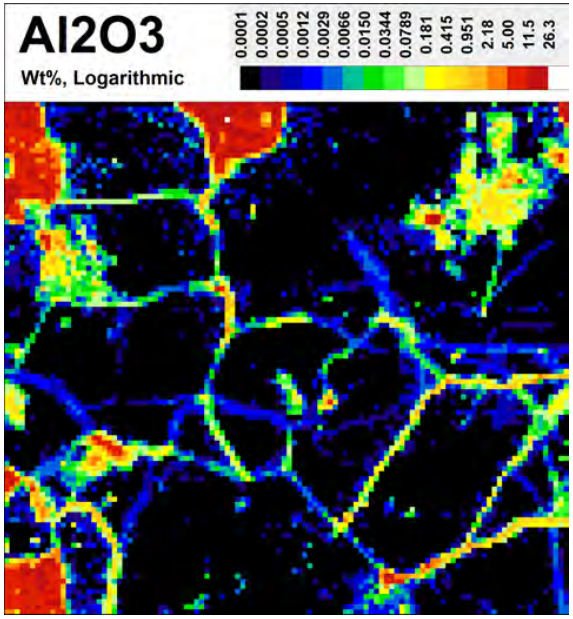
Al2O3
Wt%, Logarithmic
0.0001 0.0002 0.0005 0.0012 0.0029 0.0066 0.0150 0.0344 0.0789 0.181 0.415 0.951 2.18 5.00 11.5 26.3

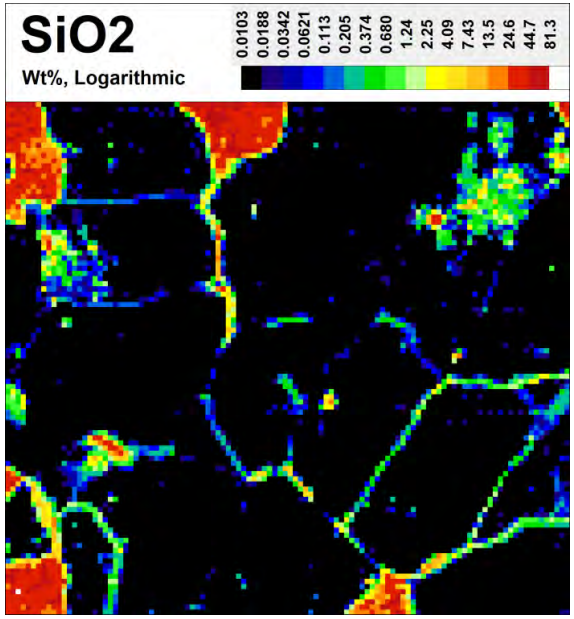
SiO2
Wt%, Logarithmic
0.0103 0.0188 0.0342 0.0621 0.113 0.205 0.374 0.680 1.24 2.25 4.09 7.43 13.5 24.6 44.7 81.3

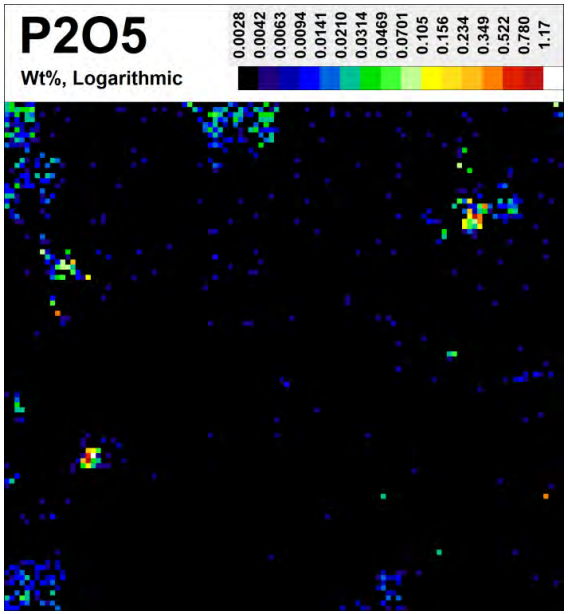
P2O5
Wt%, Logarithmic
0.0028 0.0042 0.0063 0.0094 0.0141 0.0210 0.0314 0.0469 0.0701 0.105 0.156 0.234 0.349 0.522 0.780 1.17

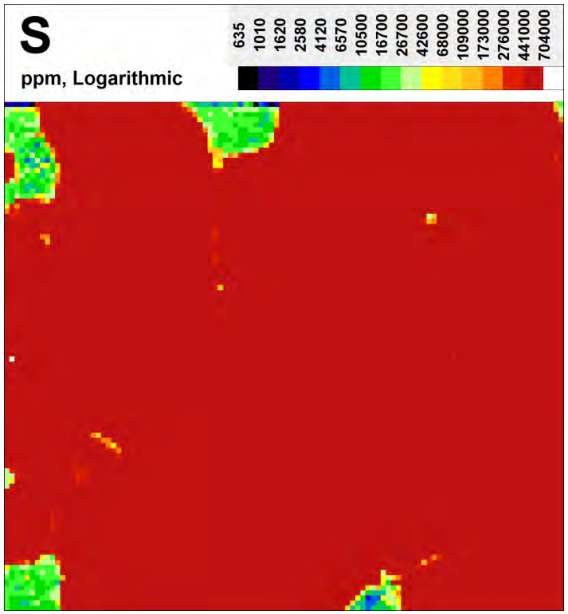
S
ppm, Logarithmic
635 1010 1620 2580 4120 6570 10500 16700 26700 42600 68000 109000 173000 276000 441000 704000

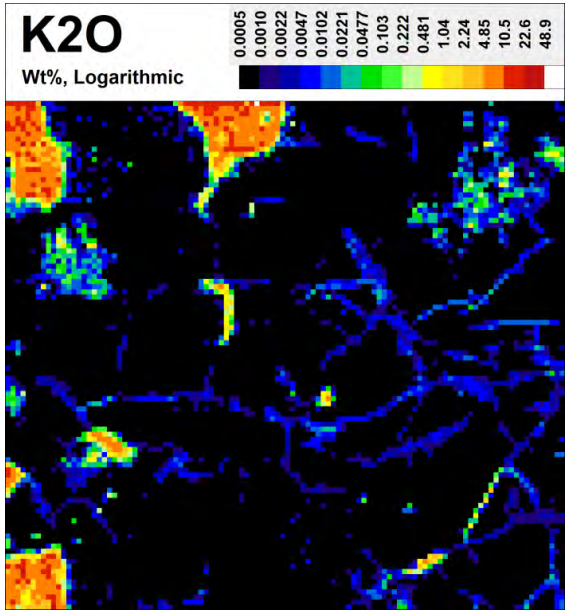
K2O
Wt%, Logarithmic
0.0005 0.0010 0.0022 0.0047 0.0102 0.0221 0.0477 0.103 0.222 0.481 1.04 2.24 4.85 10.5 22.6 48.9

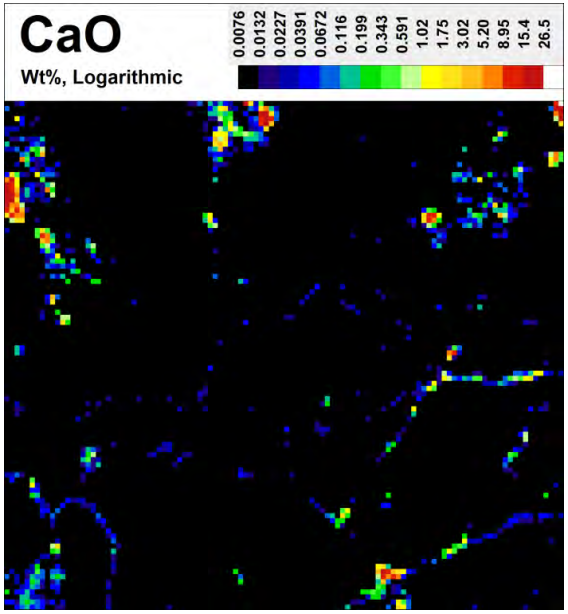
CaO
Wt%, Logarithmic
0.0076 0.0132 0.0227 0.0391 0.0672 0.116 0.199 0.343 0.591 1.02 1.75 3.02 5.20 8.95 15.4 26.5

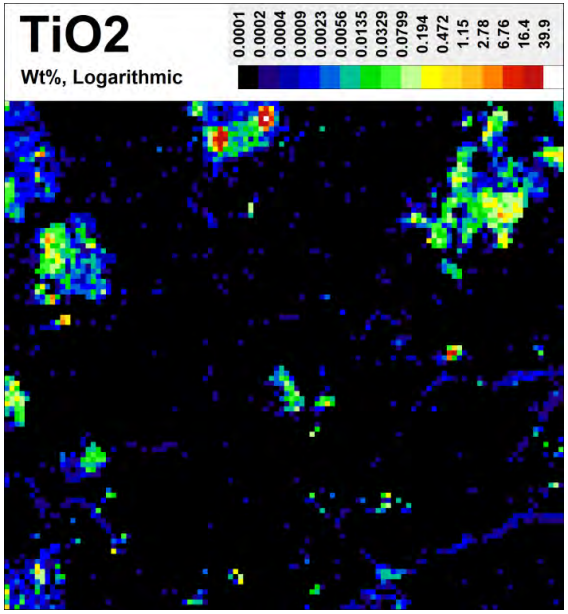
TiO2
Wt%, Logarithmic
0.0001 0.0002 0.0004 0.0009 0.0023 0.0056 0.0135 0.0329 0.0799 0.194 0.472 1.15 2.78 6.76 16.4 39.9

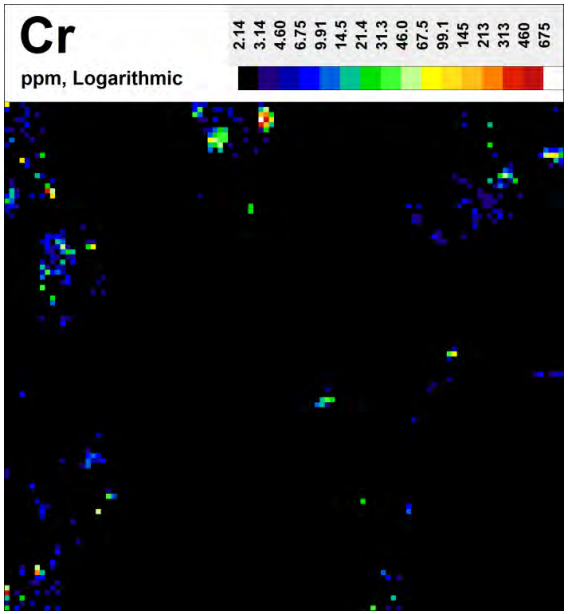
Cr
ppm, Logarithmic
2.14 3.14 4.60 6.75 9.91 14.5 21.4 31.3 46.0 67.5 99.1 145 213 313 460 675

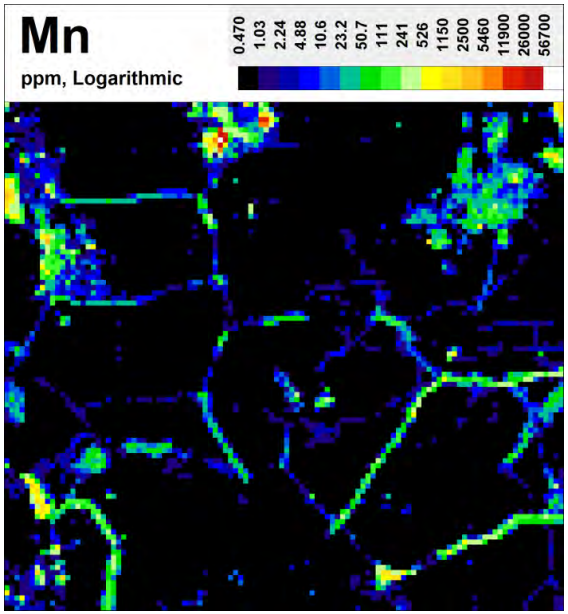
Mn
ppm, Logarithmic
0.470 1.03 2.24 4.88 10.6 23.2 50.7 111 241 526 1150 2500 5460 11900 26000 56700

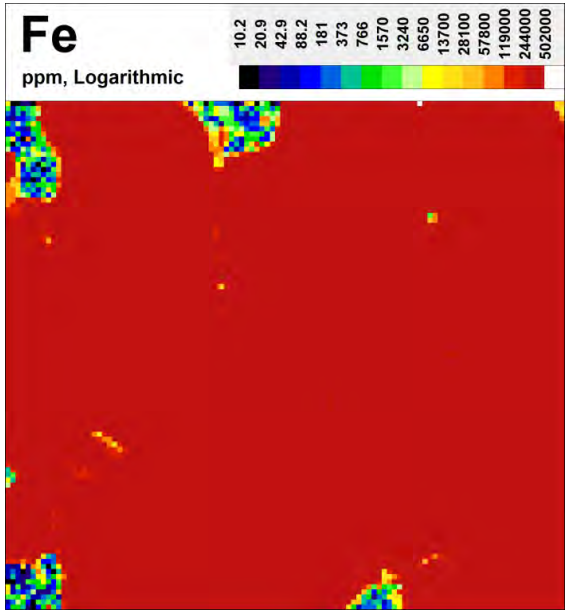
Fe
ppm, Logarithmic
10.2 20.9 42.9 88.2 181 373 766 1570 3240 6650 13700 28100 57800 119000 244000 502000

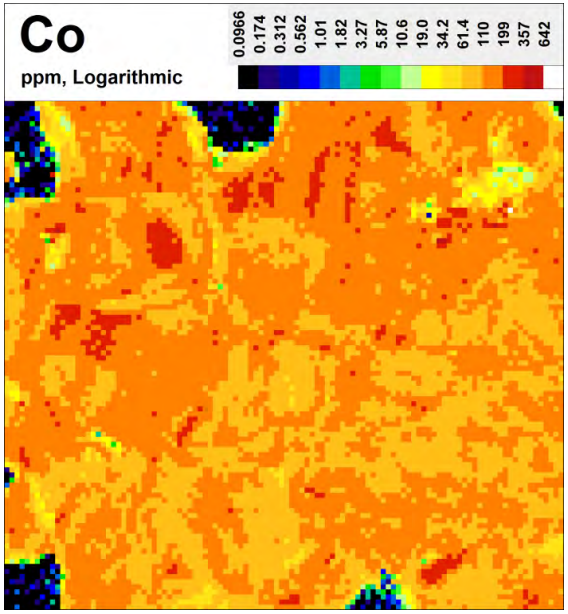
Co
ppm, Logarithmic
0.0966 0.174 0.312 0.562 1.01 1.82 3.27 5.87 10.6 19.0 34.2 61.4 110 199 357 642

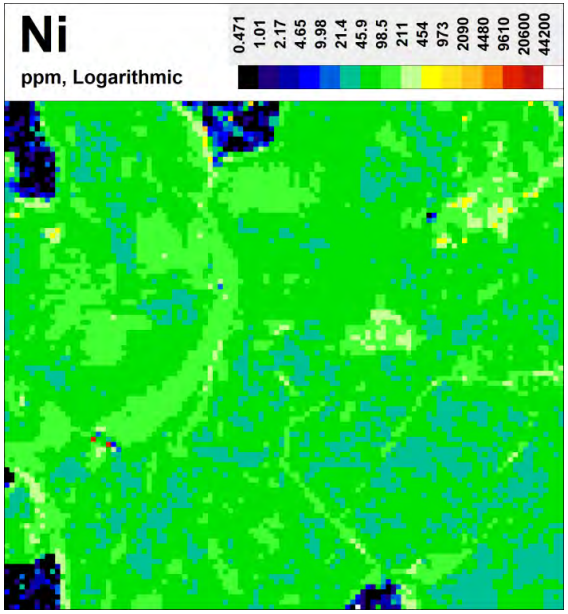
Ni
ppm, Logarithmic
0.471 1.01 2.17 4.65 9.98 21.4 45.9 98.5 211 454 973 2090 4480 9610 20600 44200

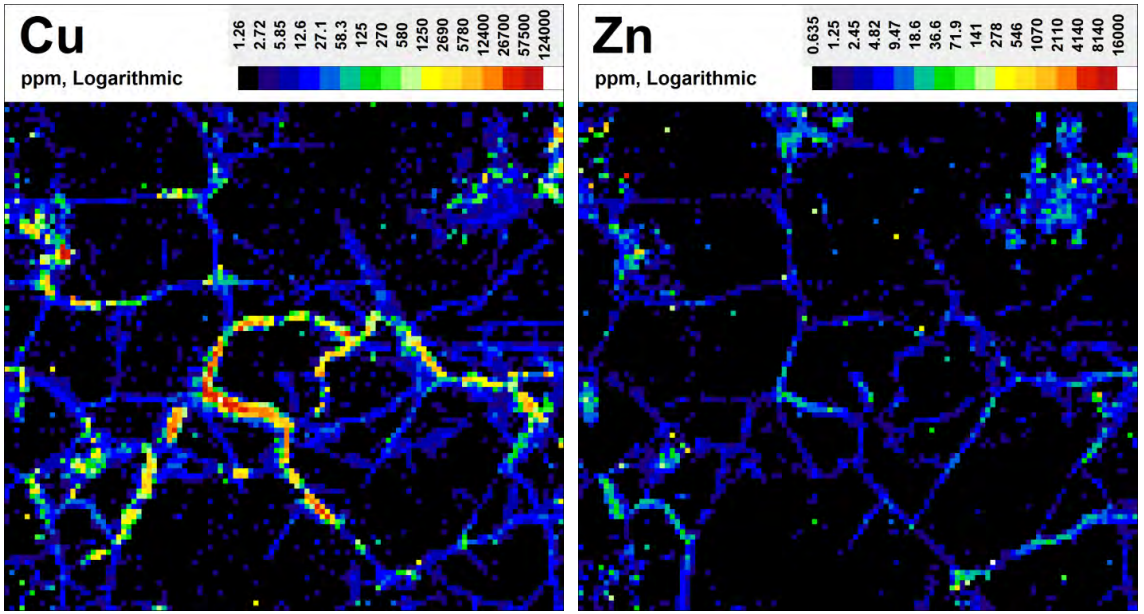
Cu
ppm, Logarithmic
1.26 2.72 5.85 12.6 27.1 58.3 125 270 580 1250 2690 5780 12400 26700 57500 124000

Zn
ppm, Logarithmic
0.635 1.25 2.45 4.82 9.47 18.6 36.6 71.9 141 278 546 1070 2110 4140 8140 16000

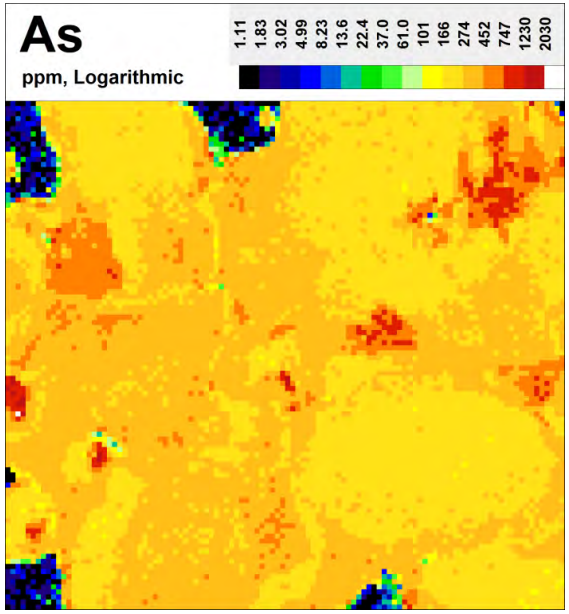
As
ppm, Logarithmic
1.11 1.83 3.02 4.99 8.23 13.6 22.4 37.0 61.0 101 166 274 452 747 1230 2030

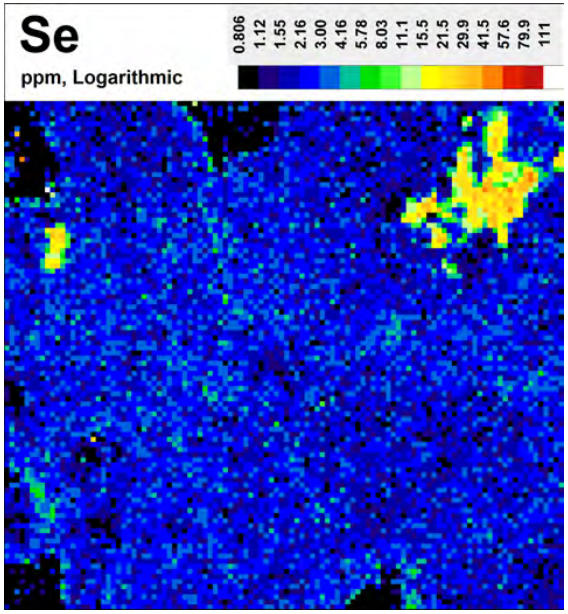
Se
ppm, Logarithmic
0.806 1.12 1.55 2.16 3.00 4.16 5.78 8.03 11.1 15.5 21.5 29.9 41.5 57.6 79.9 111

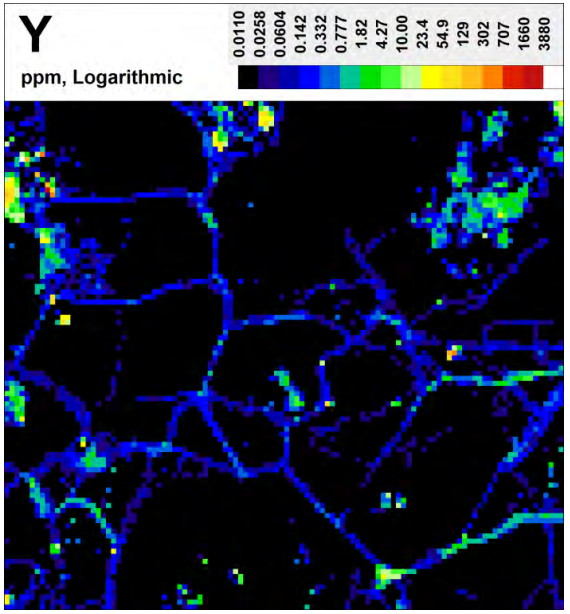
Y
ppm, Logarithmic
0.0110 0.0258 0.0604 0.142 0.332 0.777 1.82 4.27 10.00 23.4 54.9 129 302 707 1660 3880

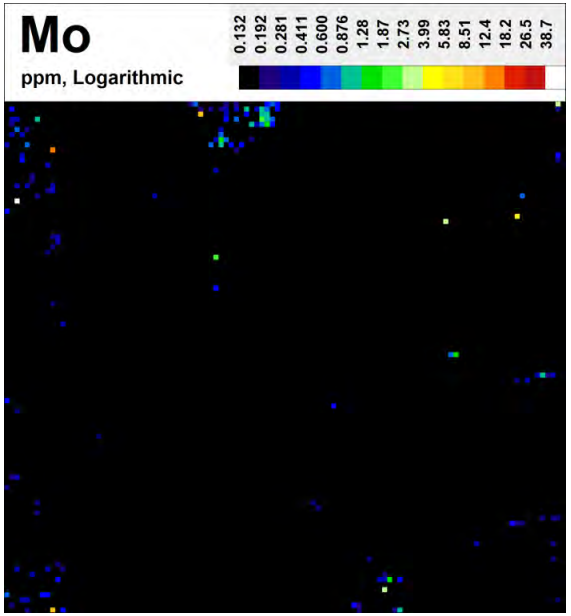
Mo
ppm, Logarithmic
0.132 0.192 0.281 0.411 0.600 0.876 1.28 1.87 2.73 3.99 5.83 8.51 12.4 18.2 26.5 38.7

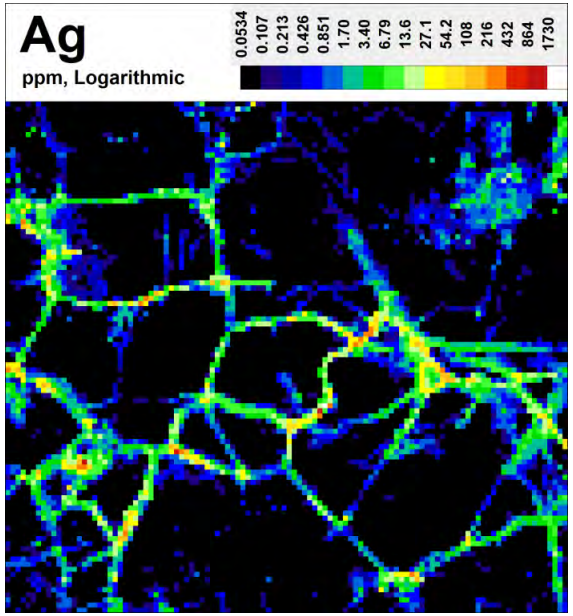
Ag
ppm, Logarithmic
0.0534 0.107 0.213 0.426 0.851 1.70 3.40 6.79 13.6 27.1 54.2 108 216 432 864 1730

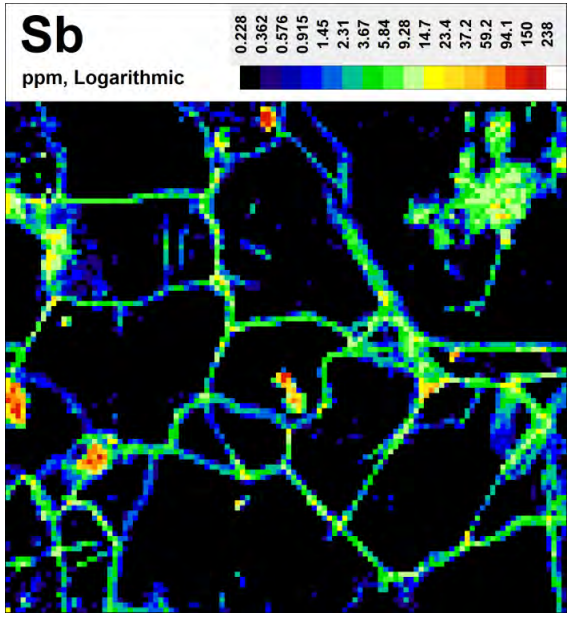
Sb
ppm, Logarithmic
0.228 0.362 0.576 0.915 1.45 2.31 3.67 5.84 9.28 14.7 23.4 37.2 59.2 94.1 150 238

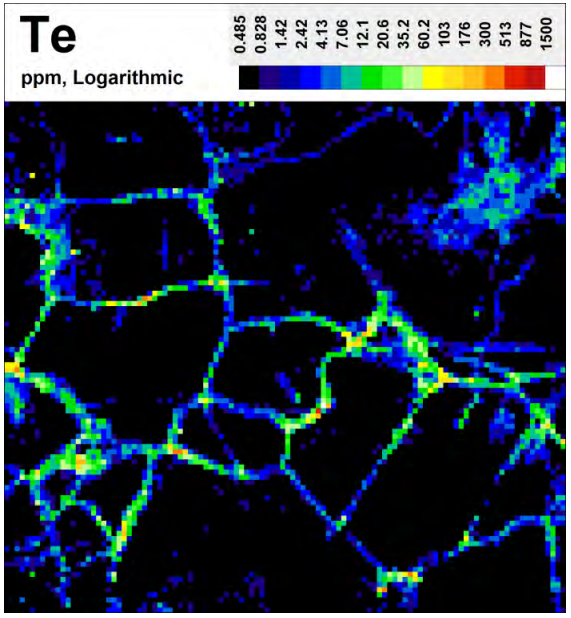
Te
ppm, Logarithmic
0.485 0.828 1.42 2.42 4.13 7.06 12.1 20.6 35.2 60.2 103 176 300 513 877 1500

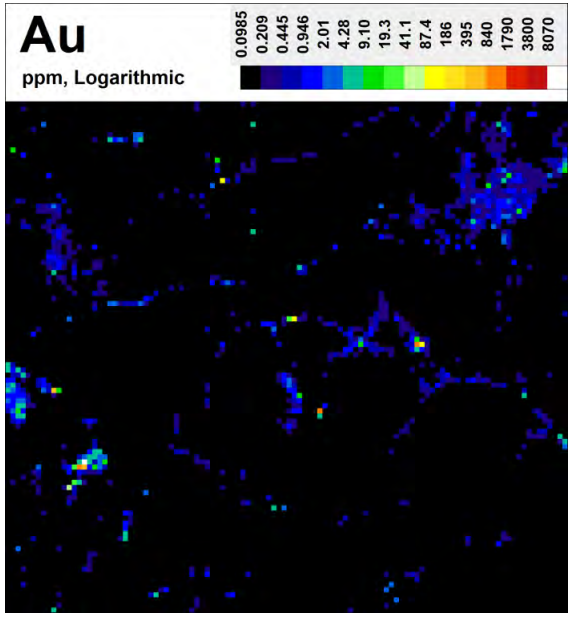
Au
ppm, Logarithmic
0.0985 0.209 0.445 0.946 2.01 4.28 9.10 19.3 41.1 87.4 186 395 840 1790 3800 8070

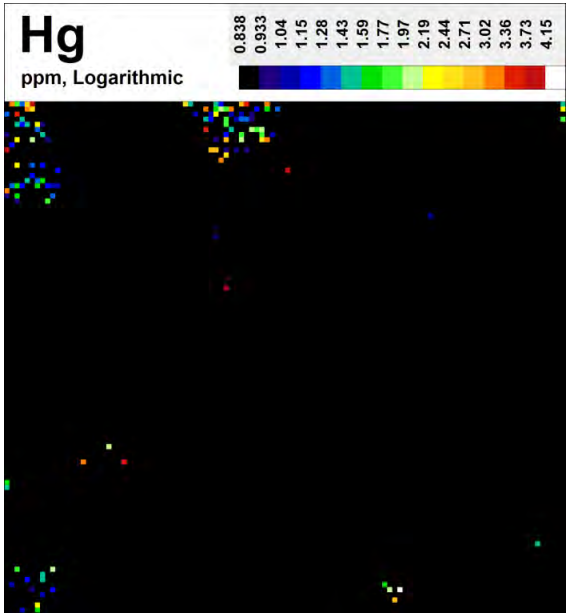
Hg
ppm, Logarithmic
0.838 0.933 1.04 1.15 1.28 1.43 1.59 1.77 1.97 2.19 2.44 2.71 3.02 3.36 3.73 4.15

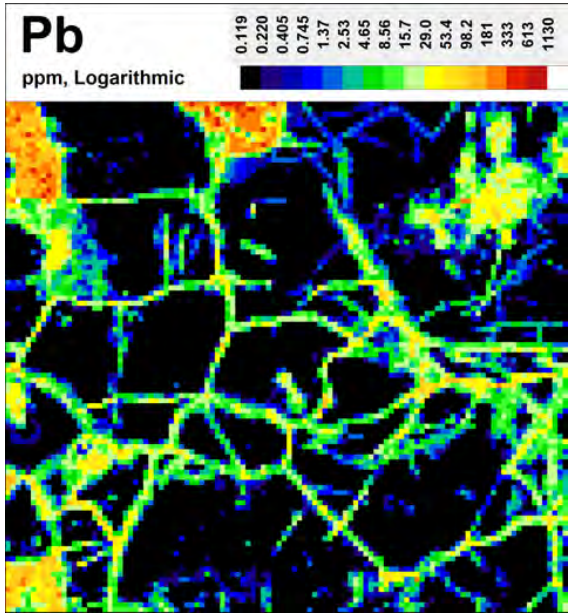
Pb
ppm, Logarithmic
0.119 0.220 0.405 0.745 1.37 2.53 4.65 8.56 15.7 29.0 53.4 98.2 181 333 613 1130

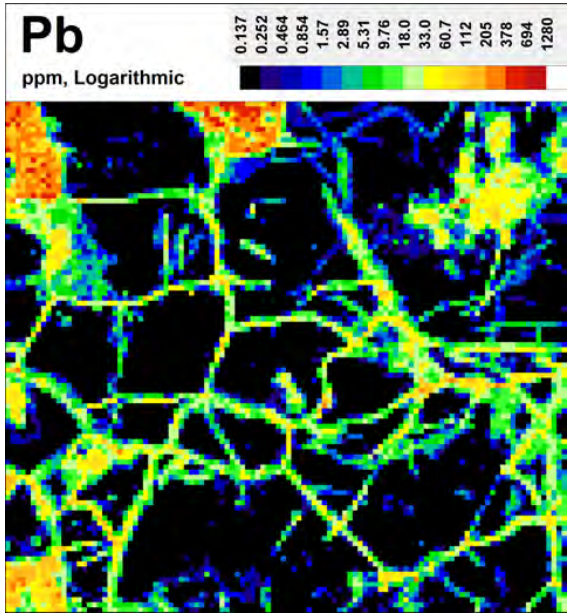
Pb
ppm, Logarithmic
0.137 0.252 0.464 0.854 1.57 2.89 5.31 9.76 18.0 33.0 60.7 112 205 378 694 1280

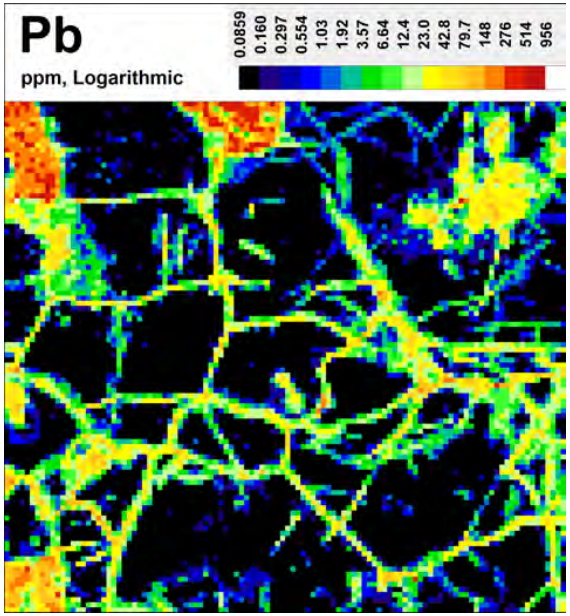
Pb
ppm, Logarithmic
0.0859 0.160 0.297 0.554 1.03 1.92 3.57 6.64 12.4 23.0 42.8 79.7 148 276 514 956

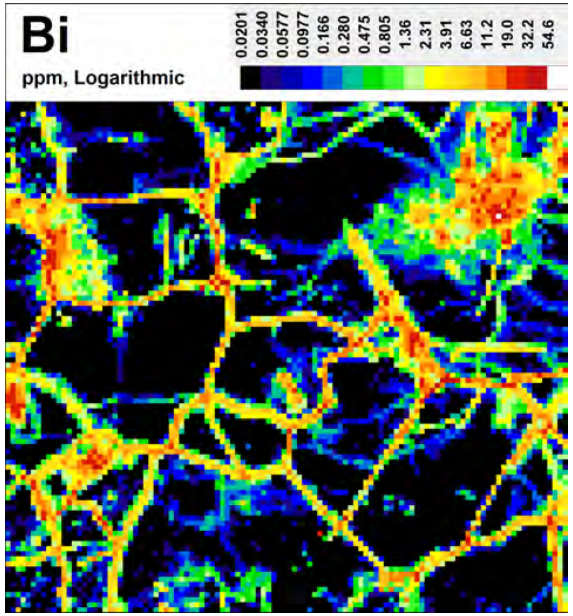
Bi
ppm, Logarithmic
0.0201 0.0340 0.0577 0.0977 0.166 0.280 0.475 0.805 1.36 2.31 3.91 6.63 11.2 19.0 32.2 54.6

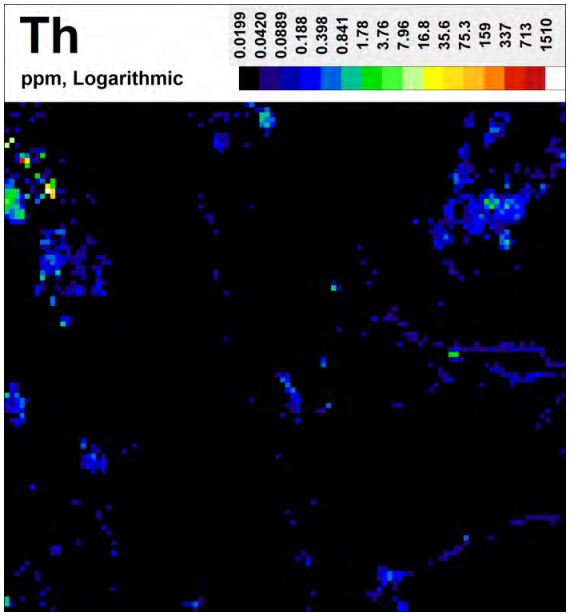
Th
ppm, Logarithmic
0.0199
0.0420
0.0889
0.188
0.398
0.841
1.78
3.76
7.96
16.8
35.6
75.3
159
337
713
1510

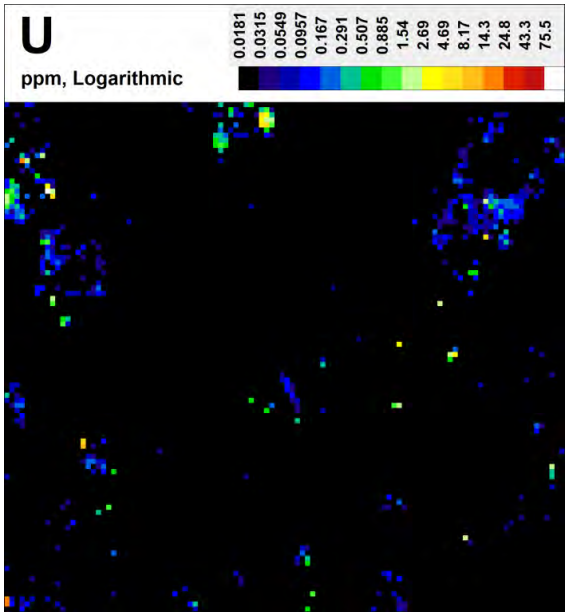
U
ppm, Logarithmic
0.0181
0.0315
0.0549
0.0957
0.167
0.291
0.507
0.885
1.54
2.69
4.69
8.17
14.3
24.8
43.3
75.5

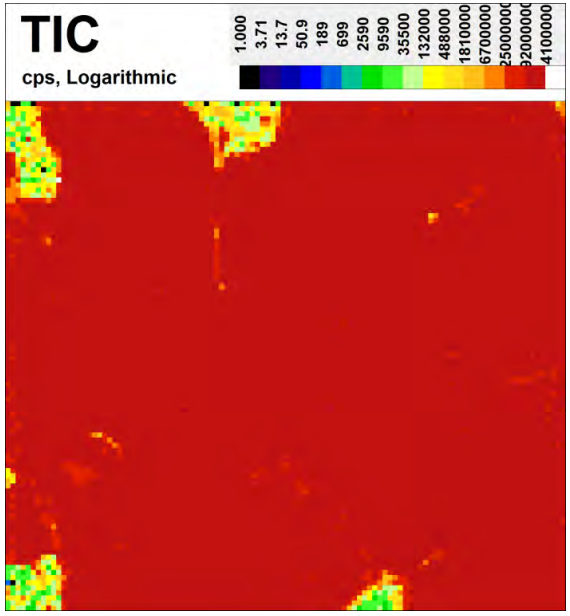
TIC
cps, Logarithmic
1.000
3.71
13.7
50.9
189
699
2590
9590
35500
132000
488000
1810000
6700000

Figure DR10. (pages 185–212) LA-ICP-MS results of an apparently annealed (foam-textured) pyrite domain with triple junctions within a mafic volcanic sample (RD16-H) showing an orientation contrast image of the mapping area and 32 major and trace maps overlapped on the OC image. OC image reveals minor plastic strain through a linear misorientation pattern. LA-ICP-MS maps reveal first-row transition metals (Co-Ni), metalloids (As) and Au enrichment at grain boundaries. LA-ICP-MS maps without OC underlays are also added.

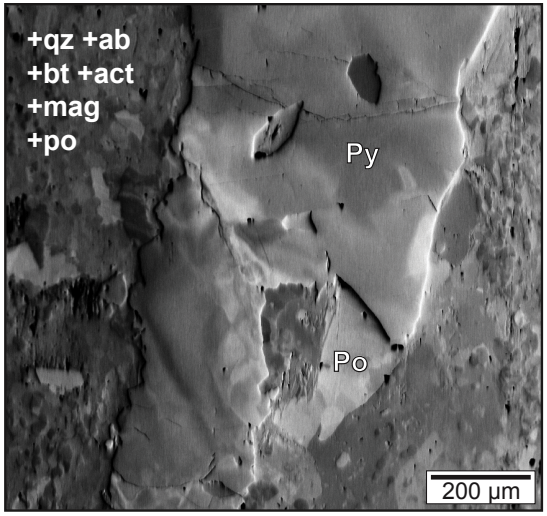
+qz +ab
+bt +act
+mag
+po
Py
Po
200 µm

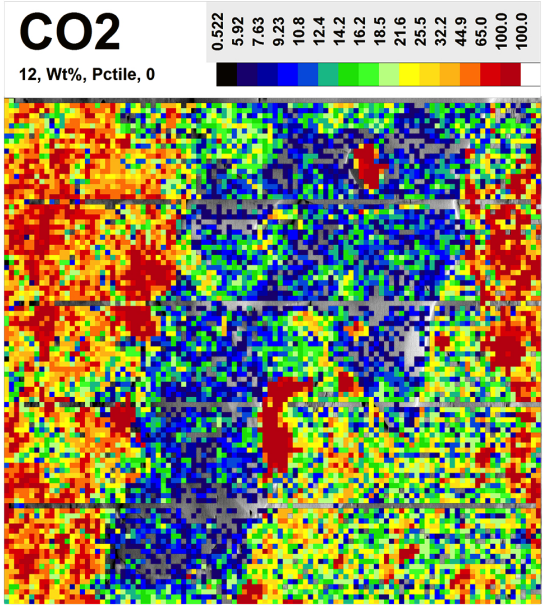
CO2
12, Wt%, Pctile, 0
0.522 5.92 7.63 9.23 10.8 12.4 14.2 16.2 18.5 21.6 25.5 32.2 44.9 65.0 100.0 100.0

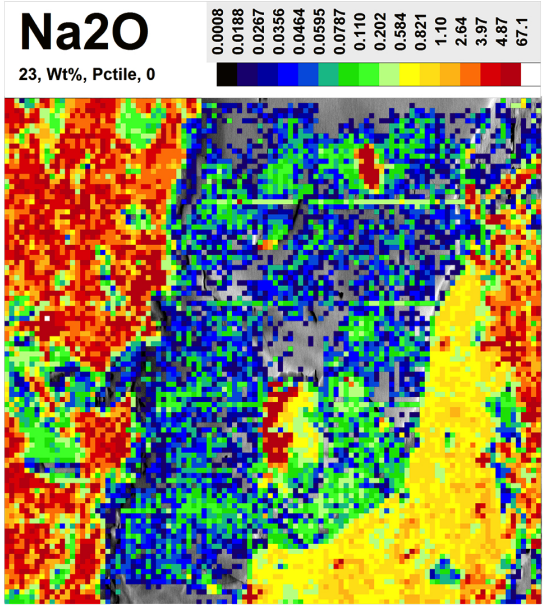
Na2O
23, Wt%, Pctile, 0
0.0008 0.0188 0.0267 0.0356 0.0464 0.0595 0.0787 0.110 0.202 0.584 0.821 1.10 2.64 3.97 4.87 67.1

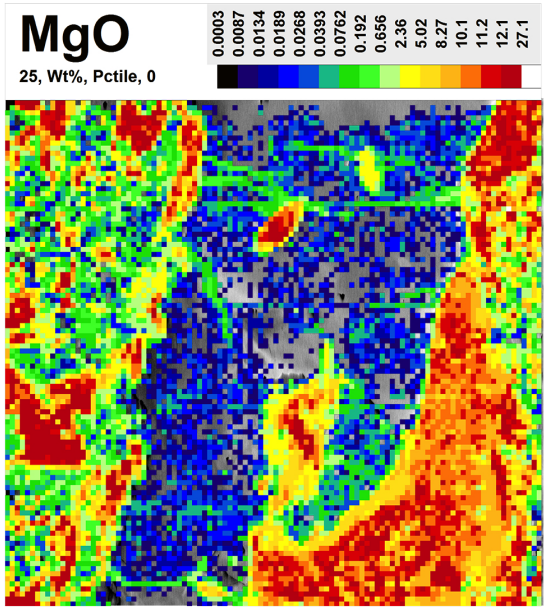
MgO
25, Wt%, Pctile, 0
0.0003 0.0087 0.0134 0.0189 0.0268 0.0393 0.0762 0.192 0.656 2.36 5.02 8.27 10.1 11.2 12.1 27.1

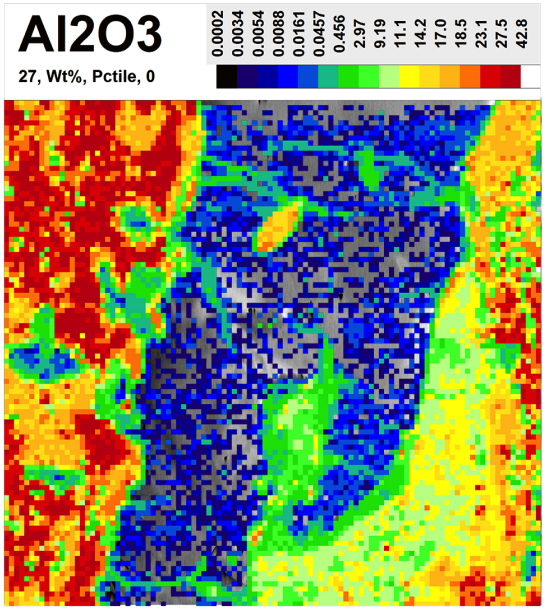
Al2O3
27, Wt%, Pctile, 0
0.0002 0.0034 0.0054 0.0088 0.0161 0.0457 0.456 2.97 9.19 11.1 14.2 17.0 18.5 23.1 27.5 42.8

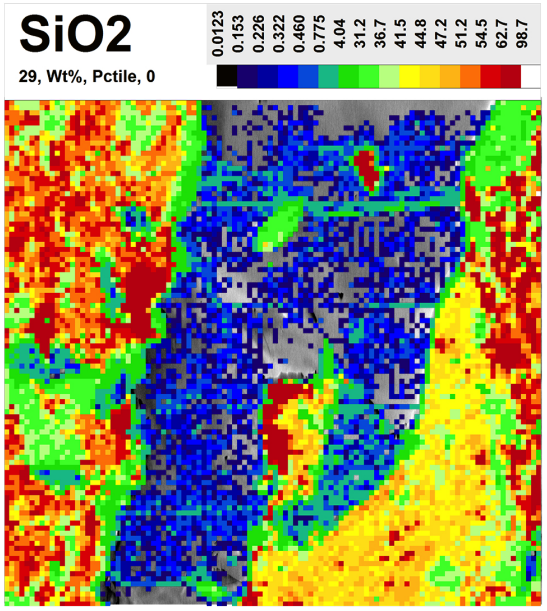
SiO2
29, Wt%, Pctile, 0
0.0123 0.153 0.226 0.322 0.460 0.775 4.04 31.2 36.7 41.5 44.8 47.2 51.2 54.5 62.7 98.7

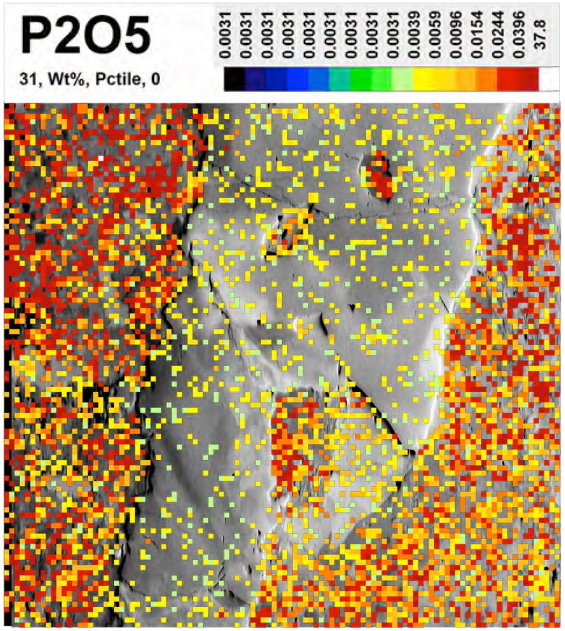
P2O5
31, Wt%, Pctile, 0
0.0031 0.0031 0.0031 0.0031 0.0031 0.0031 0.0031 0.0031 0.0039 0.0059 0.0096 0.0154 0.0244 0.0396 37.8

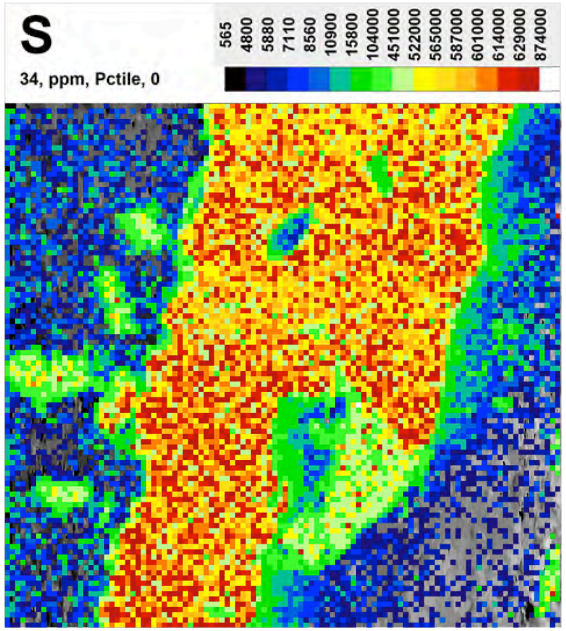
S
34, ppm, Pctile, 0
565 4800 5880 7110 8560 10900 15800 104000 451000 522000 565000 587000 601000 614000 629000 874000

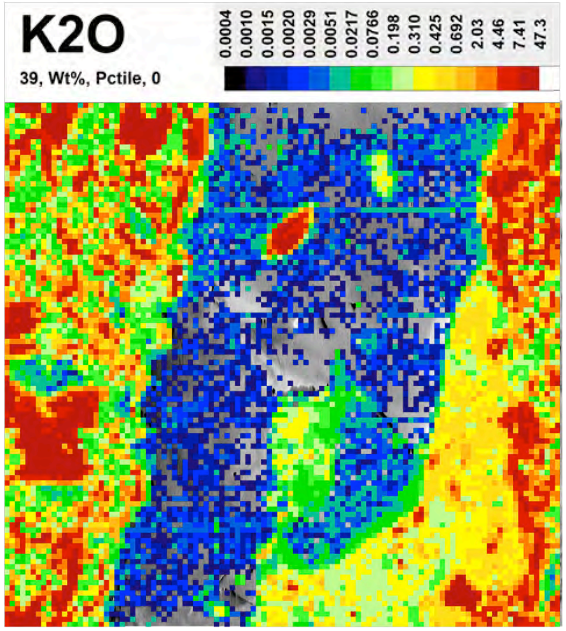
K2O
39, Wt%, Pctile, 0
0.0004 0.0010 0.0015 0.0020 0.0029 0.0051 0.0217 0.0766 0.198 0.310 0.425 0.692 2.03 4.46 7.41 47.3

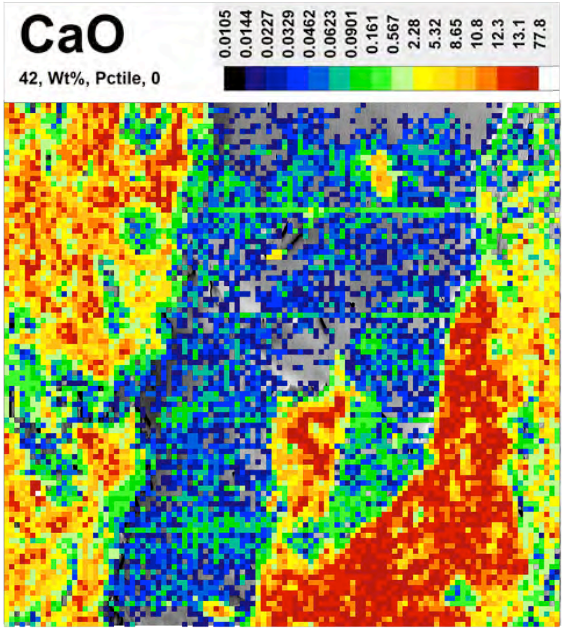
CaO
42, Wt%, Pctile, 0
0.0105 0.0144 0.0227 0.0329 0.0462 0.0623 0.0901 0.161 0.567 2.28 5.32 8.65 10.8 12.3 13.1 77.8

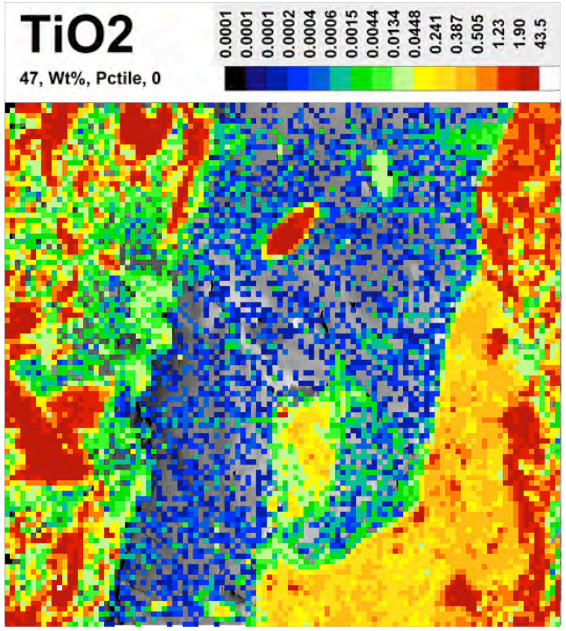
TiO2
47, Wt%, Pctile, 0
0.0001 0.0001 0.0001 0.0002 0.0004 0.0006 0.0015 0.0044 0.0134 0.0448 0.241 0.387 0.505 1.23 1.90 43.5

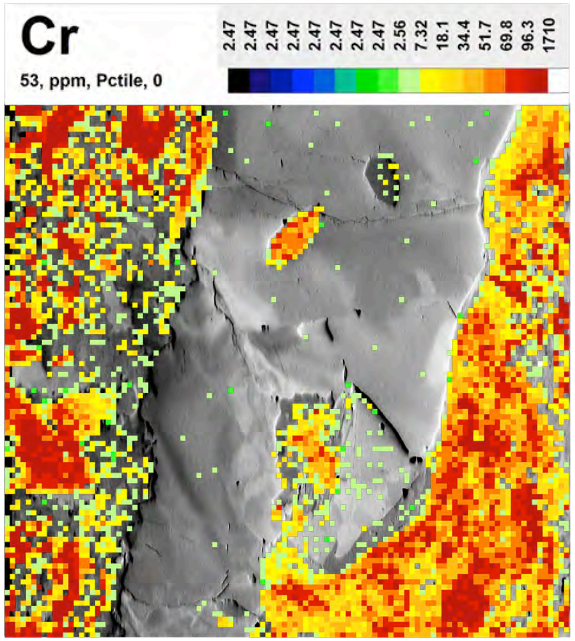
Cr
53, ppm, Pctile, 0
2.47 2.47 2.47 2.47 2.47 2.47 2.47 2.56 7.32 18.1 34.4 51.7 69.8 96.3 1710

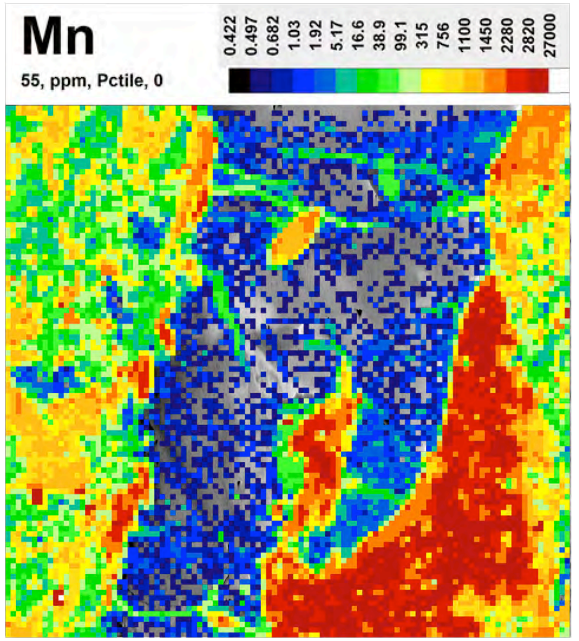
Mn
55, ppm, Pctile, 0
0.422 0.497 0.682 1.03 1.92 5.17 16.6 38.9 99.1 315 756 1100 1450 2280 2820 27000

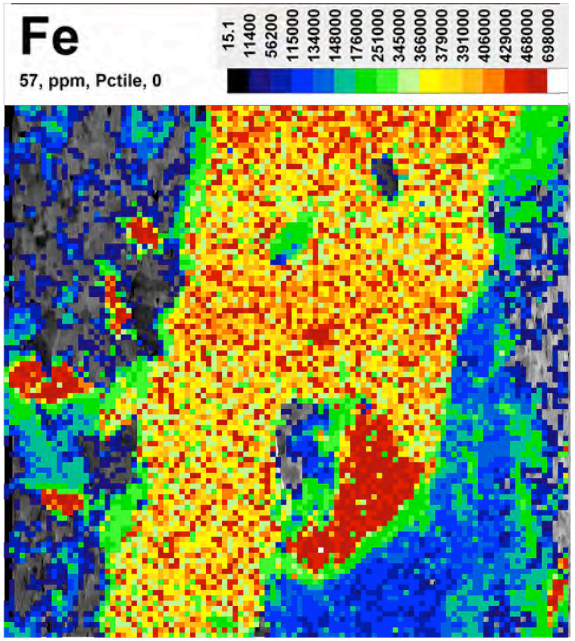
Fe
57, ppm, Pctile, 0
15.1 11400 56200 115000 134000 148000 176000 251000 345000 366000 379000 391000 406000 429000 468000 698000

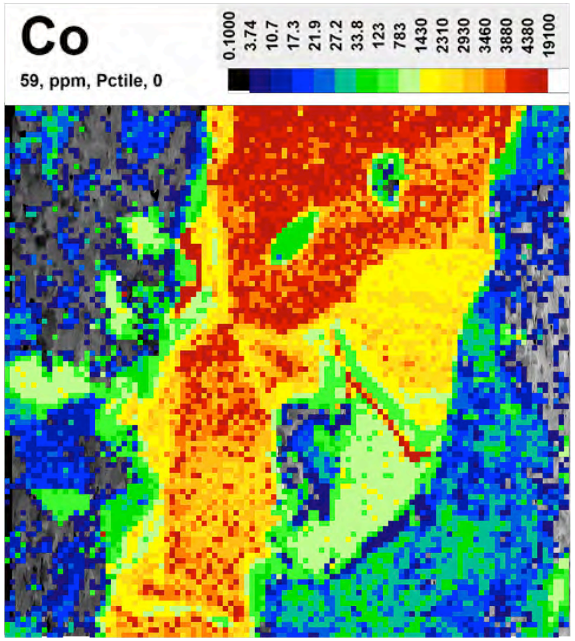
Co
59, ppm, Pctile, 0
0.1000 3.74 10.7 17.3 21.9 27.2 33.8 123 783 1430 2310 2930 3460 3880 4380 19100

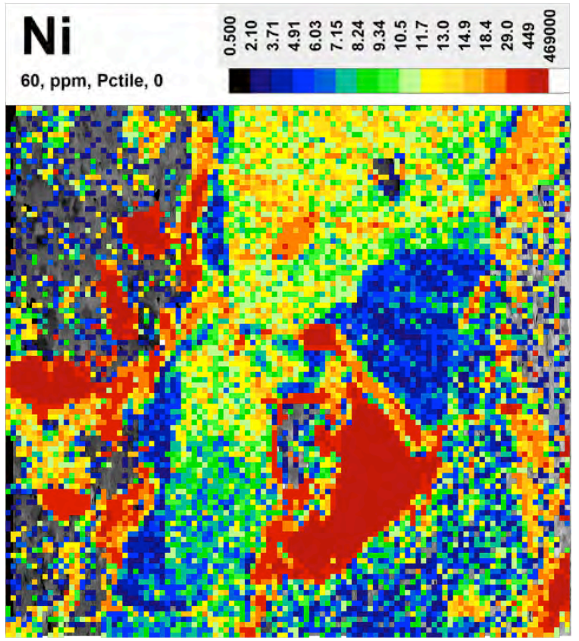
Ni
60, ppm, Pctile, 0
0.500 2.10 3.71 4.91 6.03 7.15 8.24 9.34 10.5 11.7 13.0 14.9 18.4 29.0 449 469000

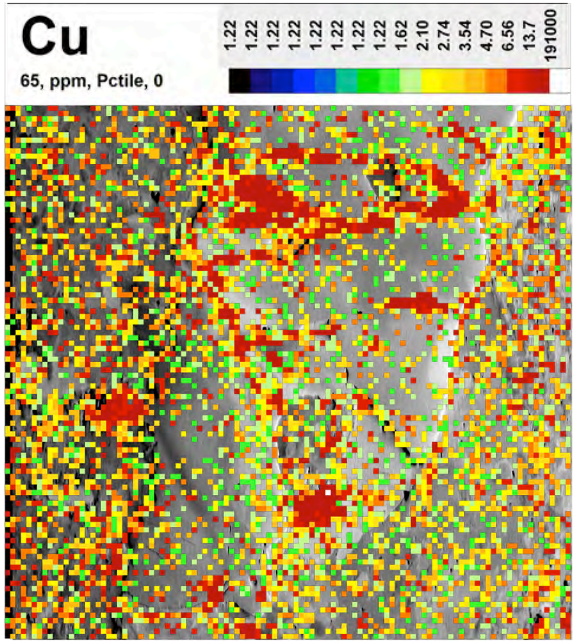
Cu
65, ppm, Pctile, 0
1.22 1.22 1.22 1.22 1.22 1.22 1.22 1.62 2.10 2.74 3.54 4.70 6.56 13.7 191000

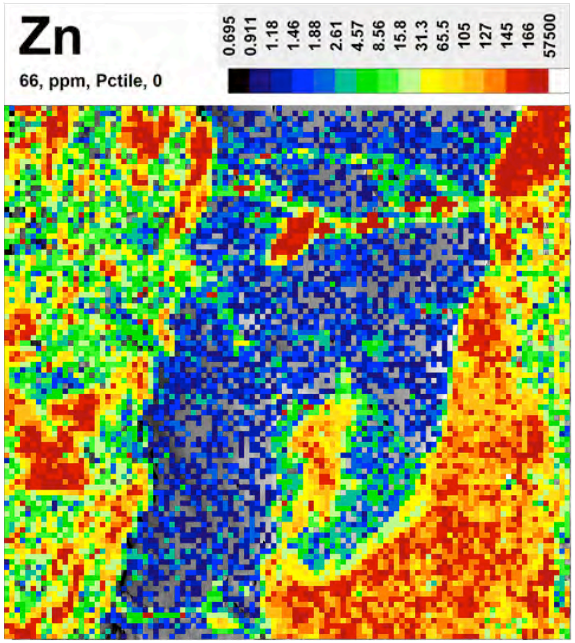
Zn
66, ppm, Pctile, 0
0.695 0.911 1.18 1.46 1.88 2.61 4.57 8.56 15.8 31.3 65.5 105 127 145 166 57500

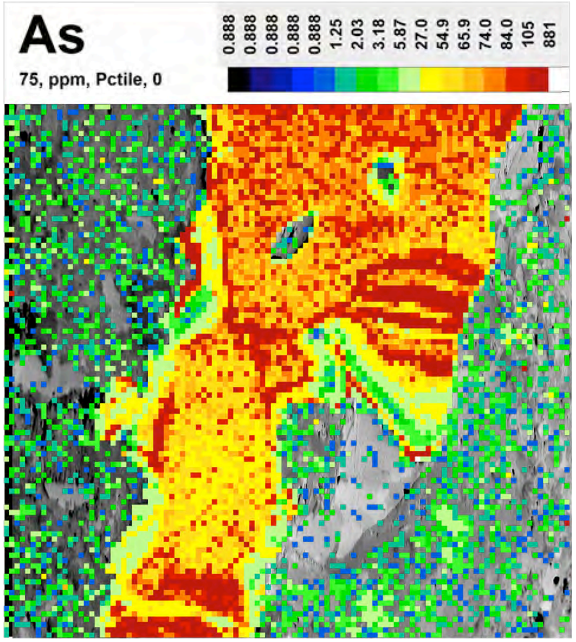
As
75, ppm, Pctile, 0
0.888 0.888 0.888 0.888 0.888 1.25 2.03 3.18 5.87 27.0 54.9 65.9 74.0 84.0 105 881

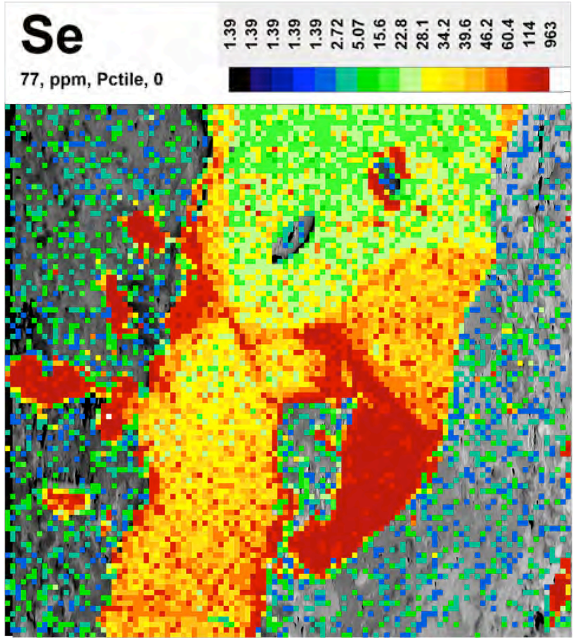
Se
77, ppm, Pctile, 0
1.39 1.39 1.39 1.39 1.39 2.72 5.07 15.6 22.8 28.1 34.2 39.6 46.2 60.4 114 963

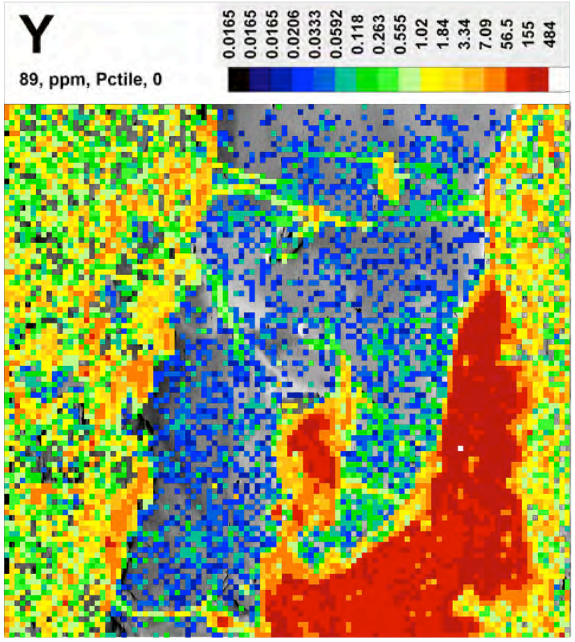
Y
89, ppm, Pctile, 0
0.0165 0.0165 0.0165 0.0206 0.0333 0.0592 0.118 0.263 0.555 1.02 1.84 3.34 7.09 56.5 155 484

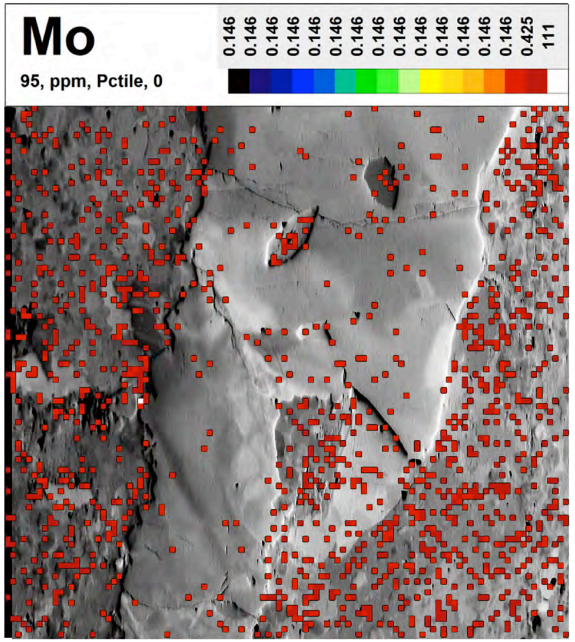
Mo
95, ppm, Pctile, 0
0.146 0.146 0.146 0.146 0.146 0.146 0.146 0.146 0.146 0.146 0.146 0.146 0.425 111

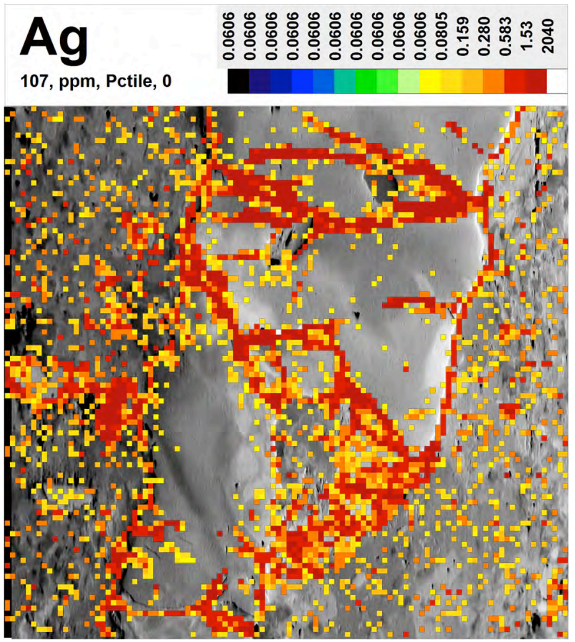
Ag
107, ppm, Pctile, 0
0.0606 0.0606 0.0606 0.0606 0.0606 0.0606 0.0606 0.0606 0.0606 0.0606 0.0805 0.159 0.280 0.583 1.53 2040

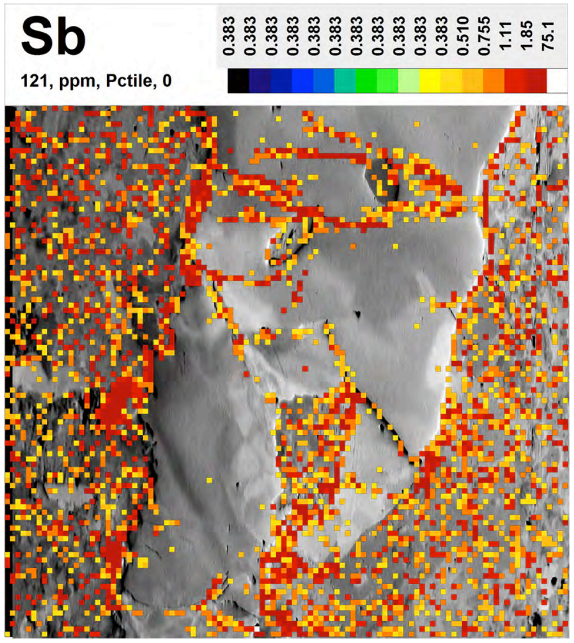
Sb
121, ppm, Pctile, 0
0.383 0.383 0.383 0.383 0.383 0.383 0.383 0.383 0.383 0.383 0.510 0.755 1.11 1.85 75.1

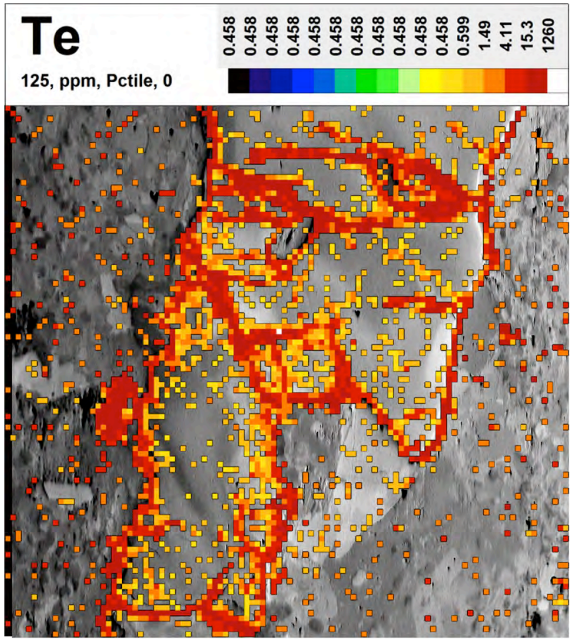
Te
125, ppm, Pctile, 0
0.458 0.458 0.458 0.458 0.458 0.458 0.458 0.458 0.458 0.458 0.599 1.49 4.11 15.3 1260

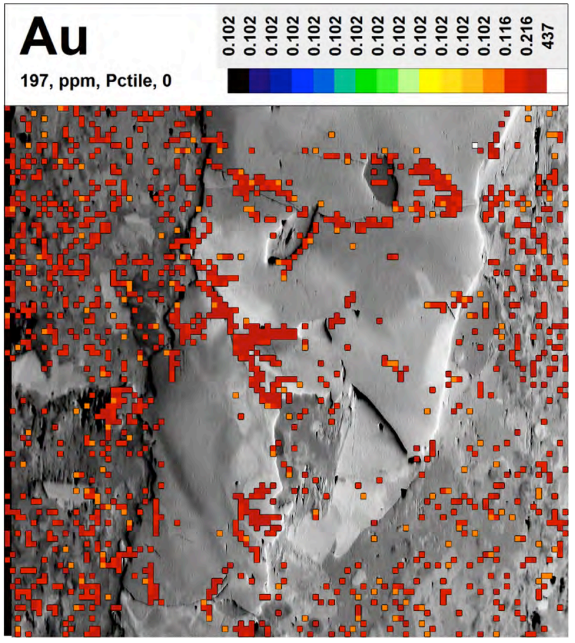
Au
197, ppm, Pctile, 0
0.102 0.102 0.102 0.102 0.102 0.102 0.102 0.102 0.102 0.102 0.102 0.102 0.102 0.116 0.216 437

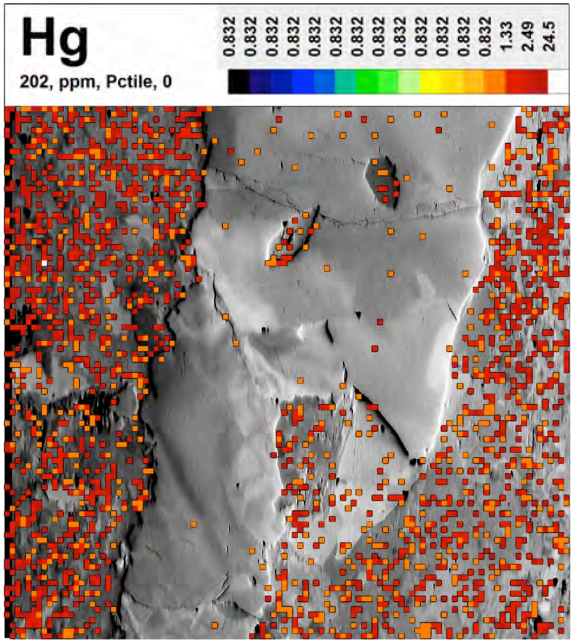
Hg
202, ppm, Pctile, 0
0.832 0.832 0.832 0.832 0.832 0.832 0.832 0.832 0.832 0.832 0.832 1.33 2.49 24.5

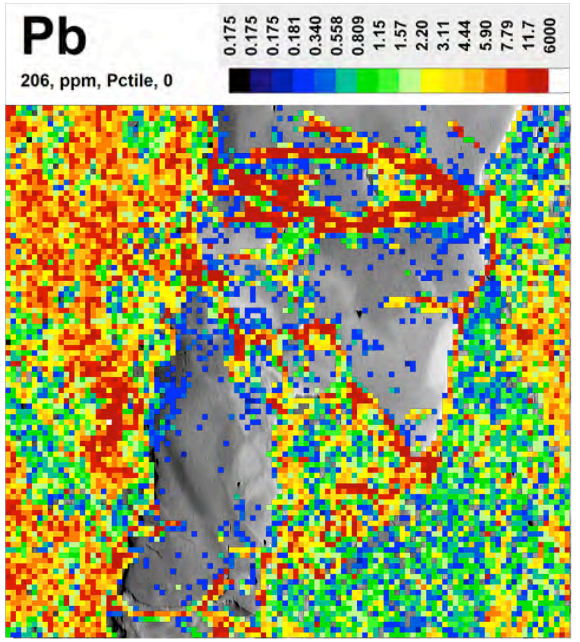
Pb
206, ppm, Pctile, 0
0.175 0.175 0.175 0.181 0.340 0.558 0.809 1.15 1.57 2.20 3.11 4.44 5.90 7.79 11.7 6000

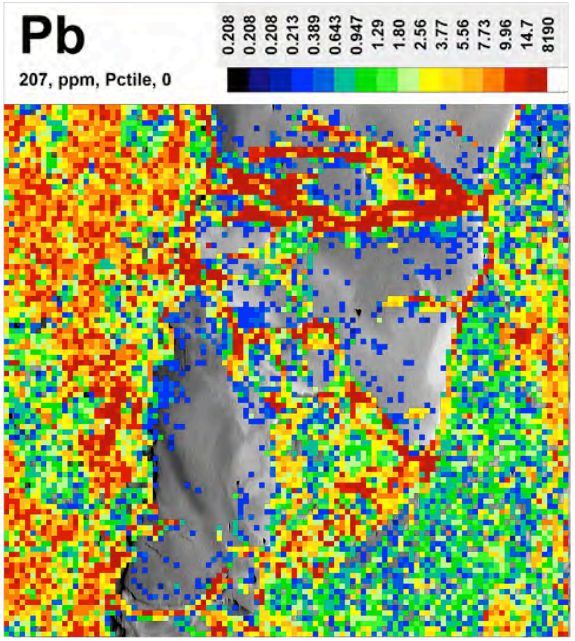
Pb
207, ppm, Pctile, 0
0.208 0.208 0.208 0.213 0.389 0.643 0.947 1.29 1.80 2.56 3.77 5.56 7.73 9.96 14.7 8190

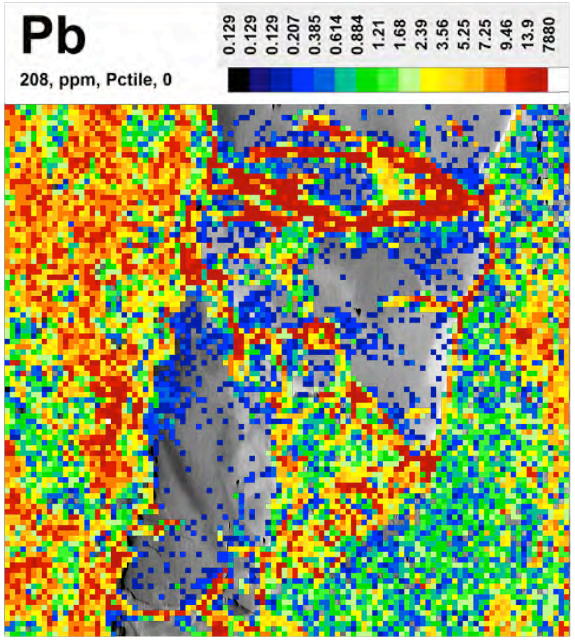
Pb
208, ppm, Pctile, 0
0.129 0.129 0.129 0.207 0.385 0.614 0.884 1.21 1.68 2.39 3.56 5.25 7.25 9.46 13.9 7880

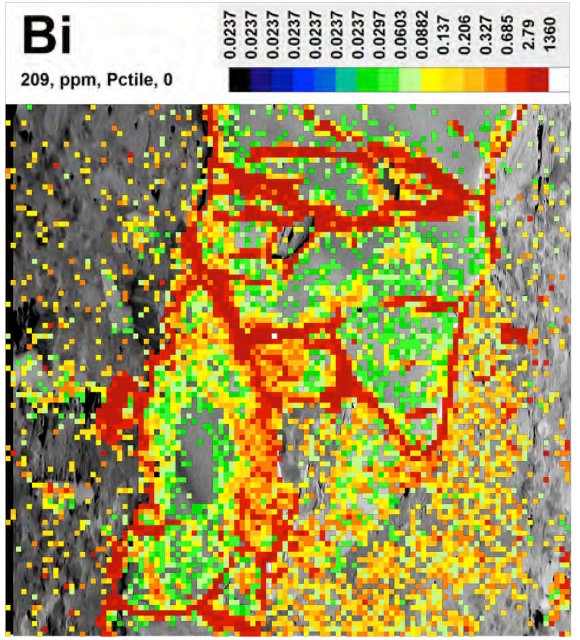
Bi
209, ppm, Pctile, 0
0.0237 0.0237 0.0237 0.0237 0.0237 0.0237 0.0237 0.0297 0.0603 0.0882 0.137 0.206 0.327 0.685 2.79 1360

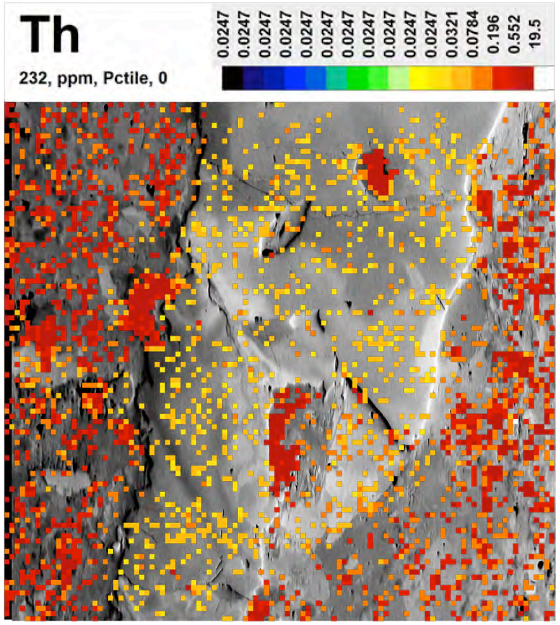
Th
232, ppm, Pctile, 0
0.0247
0.0247
0.0247
0.0247
0.0247
0.0247
0.0247
0.0247
0.0247
0.0247
0.0321
0.0784
0.196
0.552
19.5

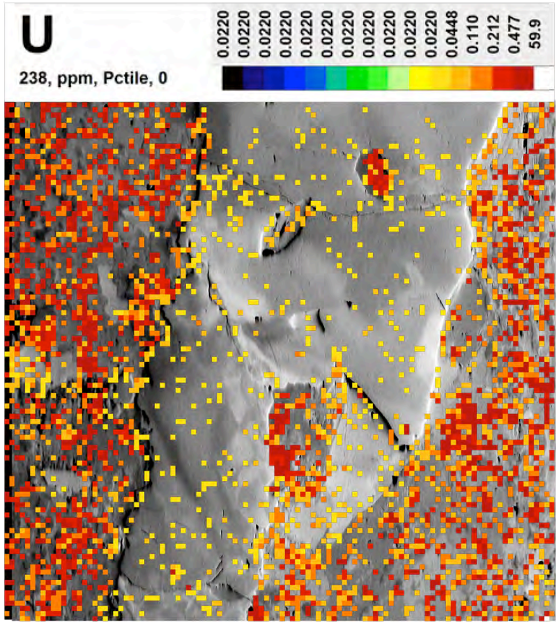
U
238, ppm, Pctile, 0
0.0220
0.0220
0.0220
0.0220
0.0220
0.0220
0.0220
0.0220
0.0220
0.0220
0.0448
0.110
0.212
0.477
59.9

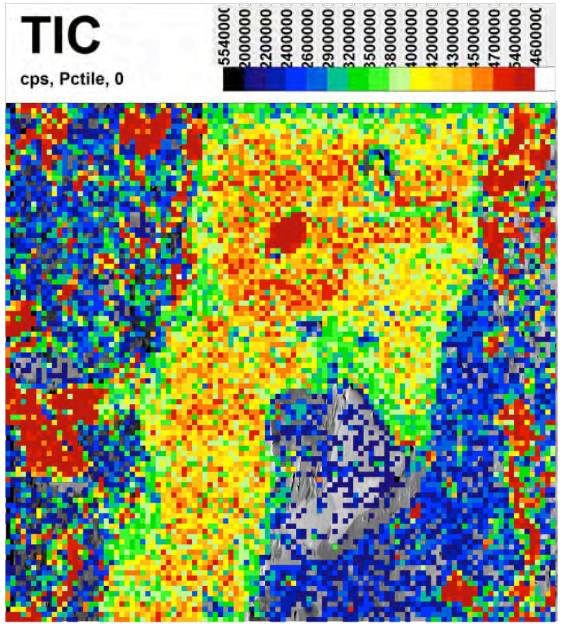
TIC
cps, Pctile, 0

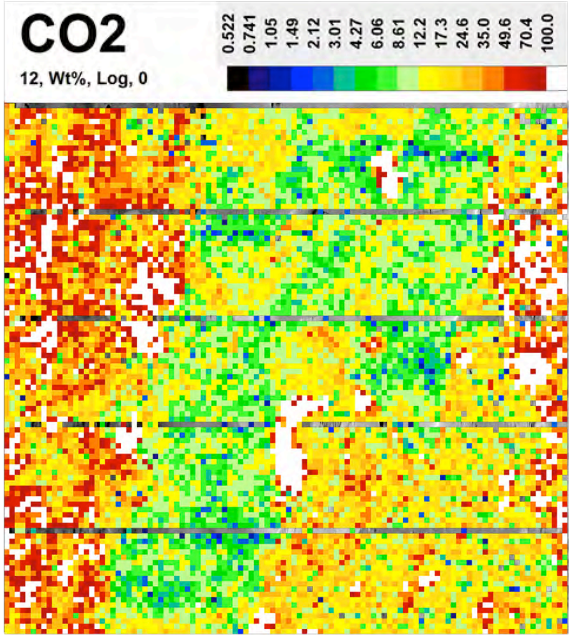
CO2
12, Wt%, Log, 0
0.522
0.741
1.05
1.49
2.12
3.01
4.27
6.06
8.61
12.2
17.3
24.6
35.0
49.6
70.4
100.0

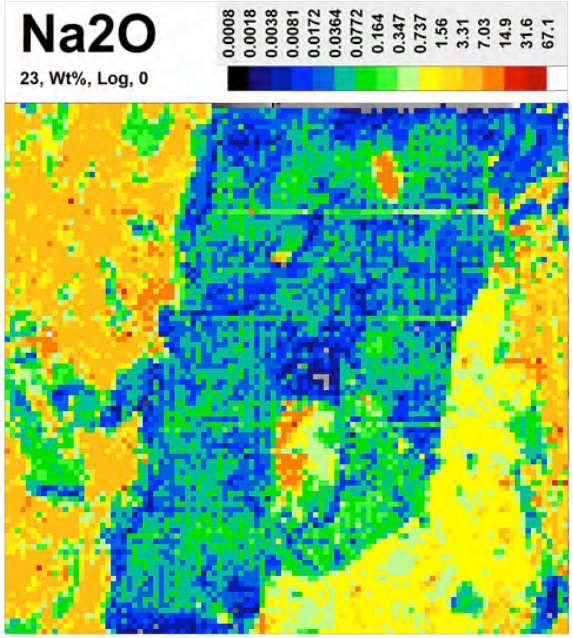
Na2O
23, Wt%, Log, 0
0.0008
0.0018
0.0038
0.0081
0.0172
0.0364
0.0772
0.164
0.347
0.737
1.56
3.31
7.03
14.9
31.6
67.1

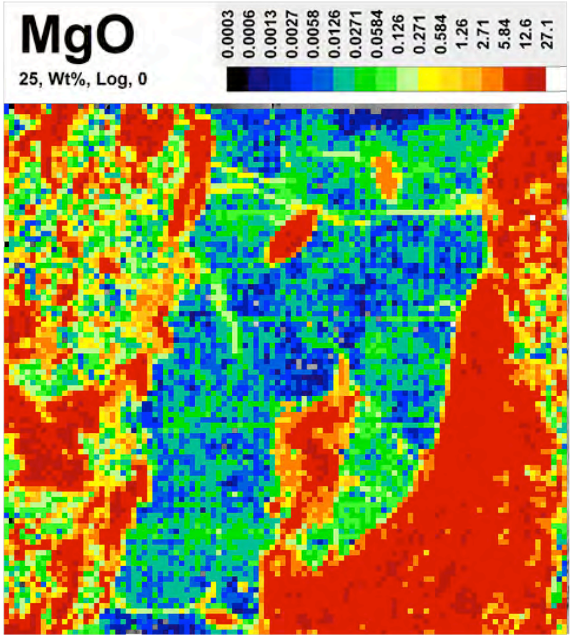
MgO
25, Wt%, Log, 0
0.0003
0.0006
0.0013
0.0027
0.0058
0.0126
0.0271
0.0584
0.126
0.271
0.584
1.26
2.71
5.84
12.6
27.1

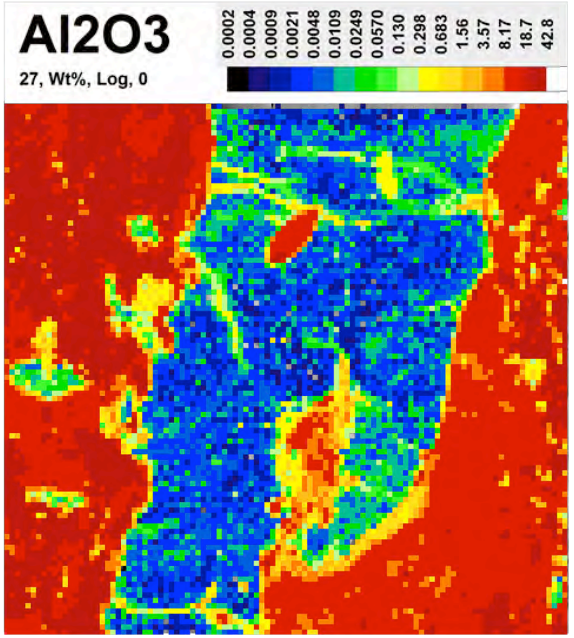
Al2O3
27, Wt%, Log, 0
0.0002
0.0004
0.0009
0.0021
0.0048
0.0109
0.0249
0.0570
0.130
0.298
0.683
1.56
3.57
8.17
18.7
42.8

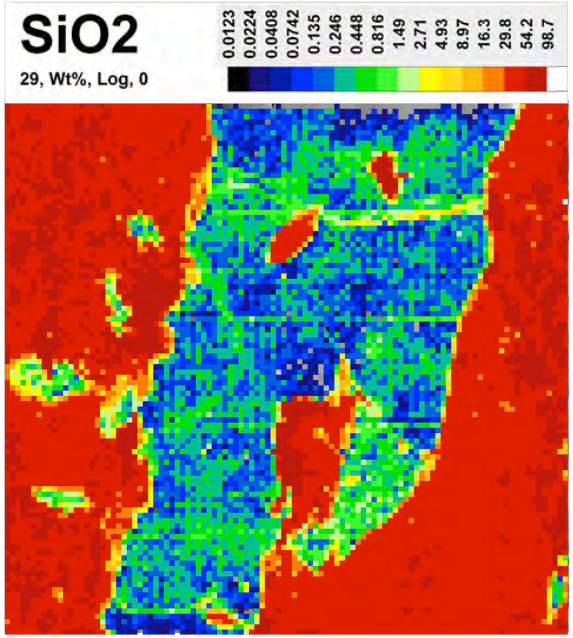
SiO2
29, Wt%, Log, 0
0.0123
0.0224
0.0408
0.0742
0.135
0.246
0.448
0.816
1.49
2.71
4.93
8.97
16.3
29.8
54.2
98.7

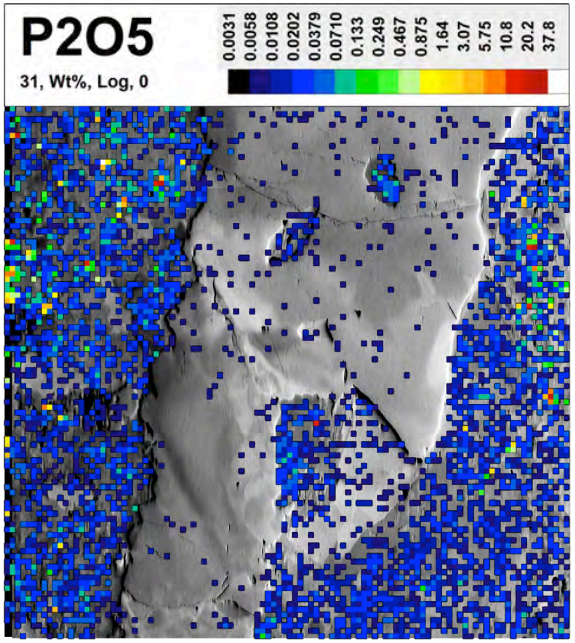
P2O5
31, Wt%, Log, 0
0.0031
0.0058
0.0108
0.0202
0.0379
0.0710
0.133
0.249
0.467
0.875
1.64
3.07
5.75
10.8
20.2
37.8

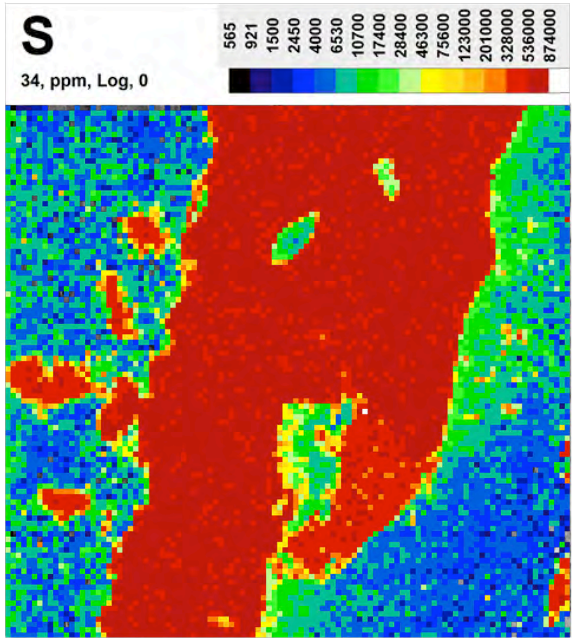
S
34, ppm, Log, 0
565
921
1500
2450
4000
6530
10700
17400
28400
46300
75600
123000
201000
328000
536000
874000

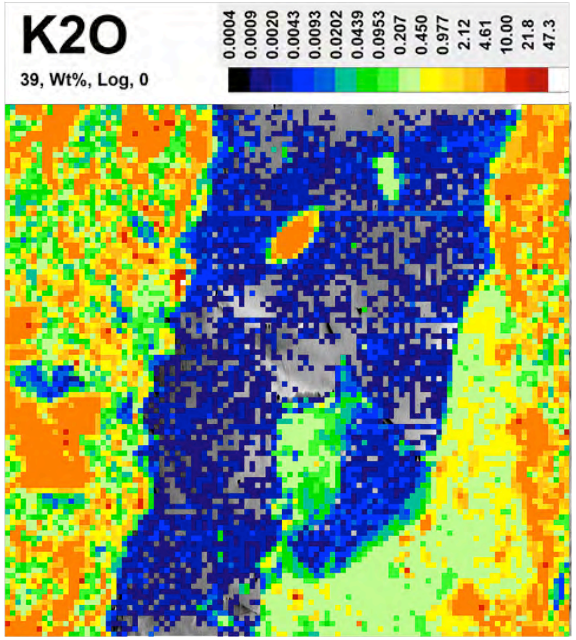
K2O
39, Wt%, Log, 0
0.0004
0.0009
0.0020
0.0043
0.0093
0.0202
0.0439
0.0953
0.207
0.450
0.977
2.12
4.61
10.00
21.8
47.3

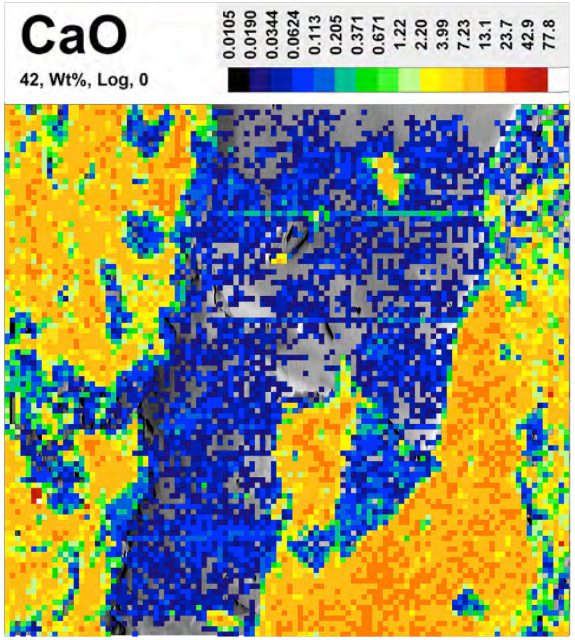
CaO
42, Wt%, Log, 0
0.0105
0.0190
0.0344
0.0624
0.113
0.205
0.371
0.671
1.22
2.20
3.99
7.23
13.1
23.7
42.9
77.8

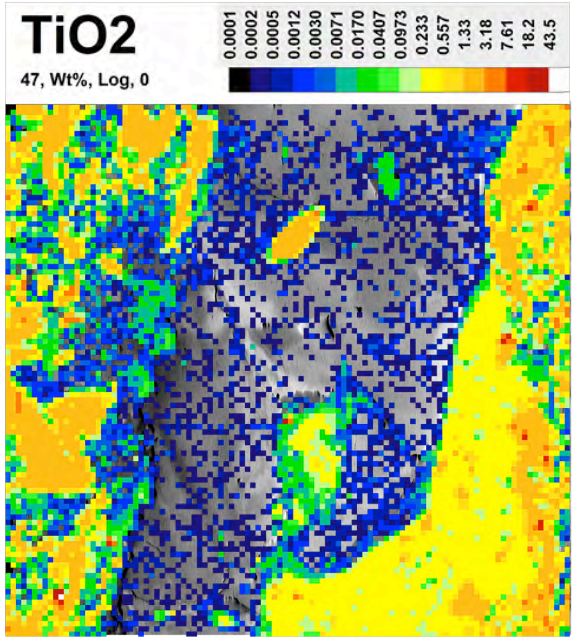
TiO2
47, Wt%, Log, 0
0.0001
0.0002
0.0005
0.0012
0.0030
0.0071
0.0170
0.0407
0.0973
0.233
0.557
1.33
3.18
7.61
18.2
43.5

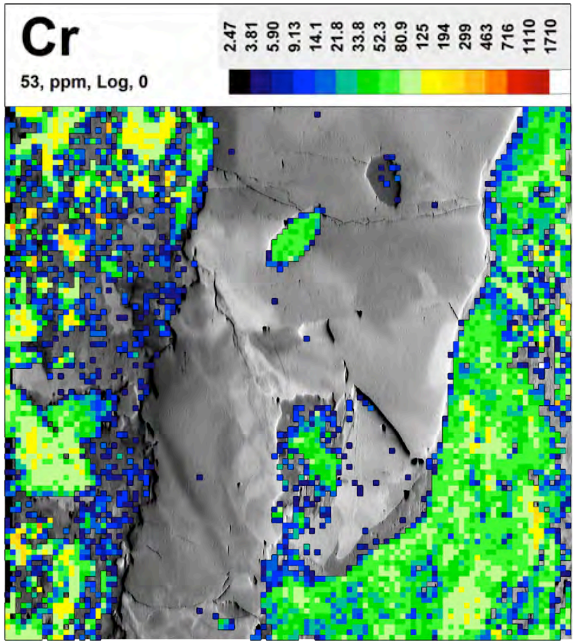
Cr
53, ppm, Log, 0
2.47 3.81 5.90 9.13 14.1 21.8 33.8 52.3 80.9 125 194 299 463 716 1110 1710

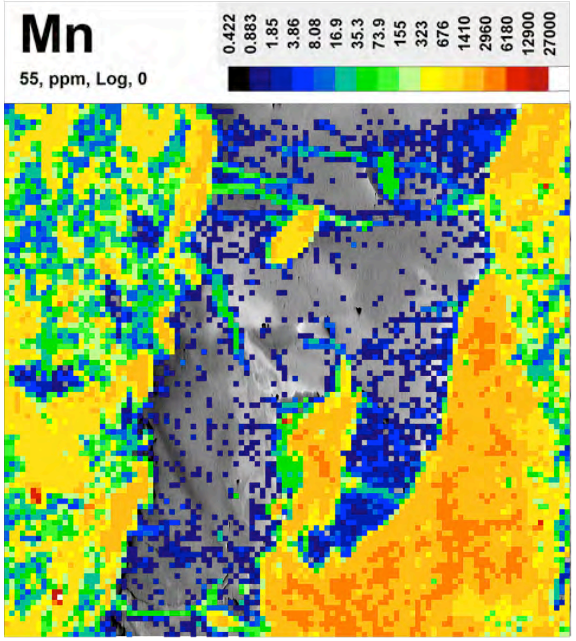
Mn
55, ppm, Log, 0
0.422 0.883 1.85 3.86 8.08 16.9 35.3 73.9 155 323 676 1410 2960 6180 12900 27000

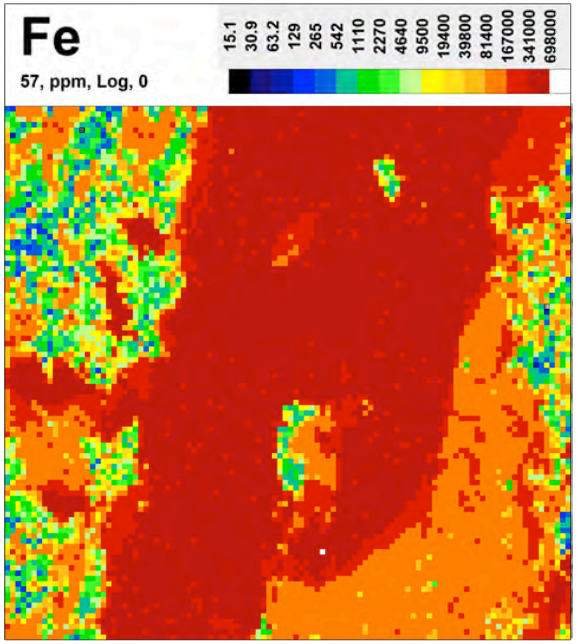
Fe
57, ppm, Log, 0
15.1 30.9 63.2 129 265 542 1110 2270 4640 9500 19400 39800 81400 167000 341000 698000

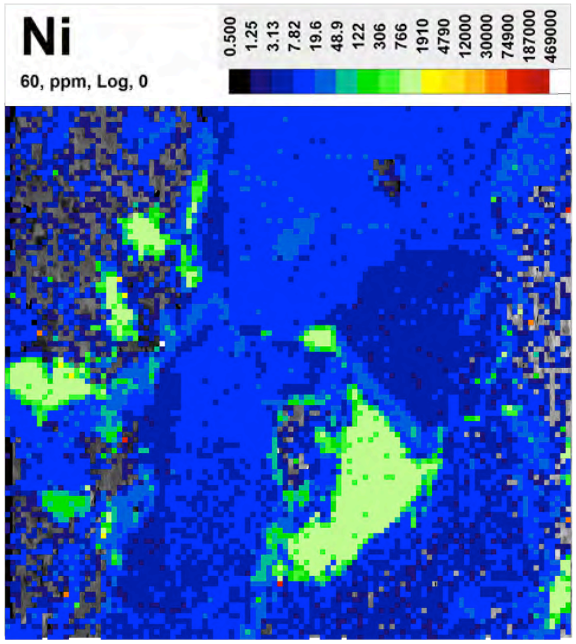
Ni
60, ppm, Log, 0
0.500 1.25 3.13 7.82 19.6 48.9 122 306 766 1910 4790 12000 30000 74900 187000 469000

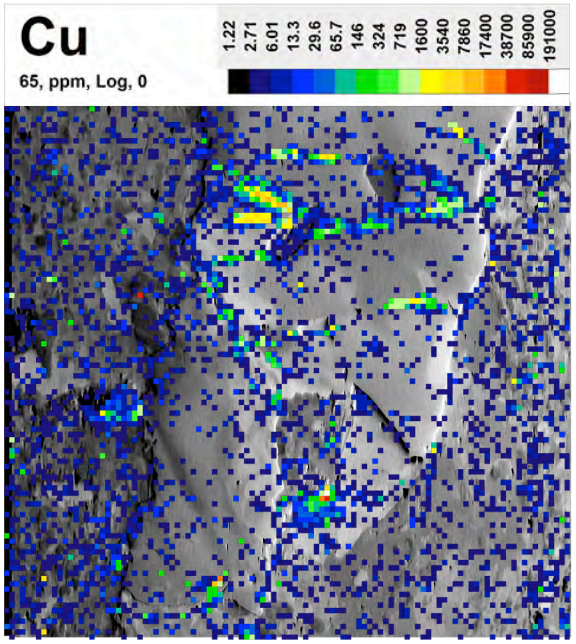
Cu
65, ppm, Log, 0
1.22 2.71 6.01 13.3 29.6 65.7 146 324 719 1600 3540 7860 17400 38700 85900 191000

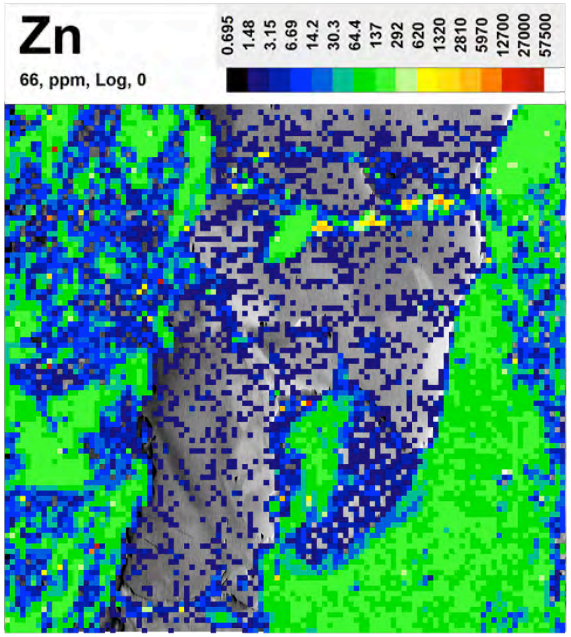
Zn
66, ppm, Log, 0
0.695 1.48 3.15 6.69 14.2 30.3 64.4 137 292 620 1320 2810 5970 12700 27000 57500

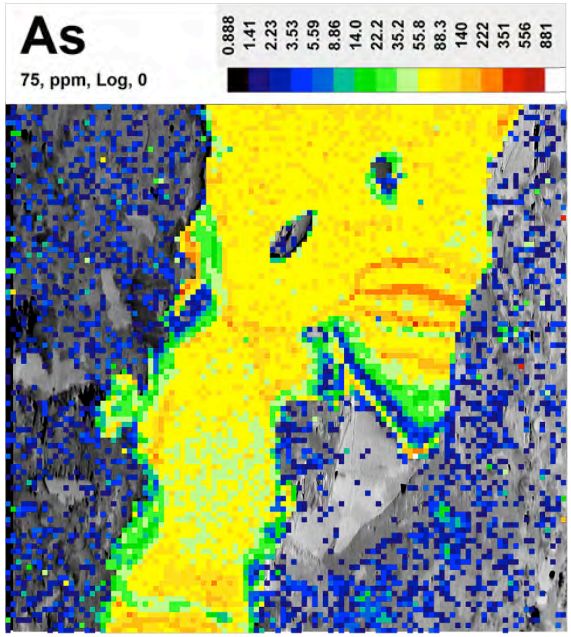
As
75, ppm, Log, 0
0.888 1.41 2.23 3.53 5.59 8.86 14.0 22.2 35.2 55.8 88.3 140 222 351 556 881

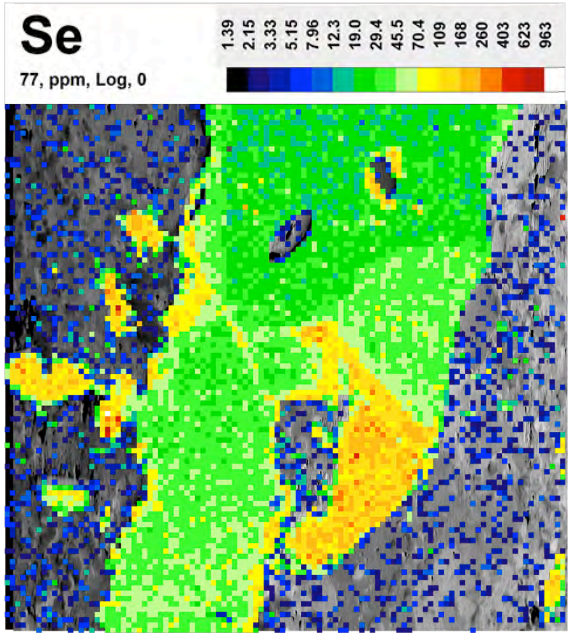
Se
77, ppm, Log, 0
1.39 2.15 3.33 5.15 7.96 12.3 19.0 29.4 45.5 70.4 109 168 260 403 623 963

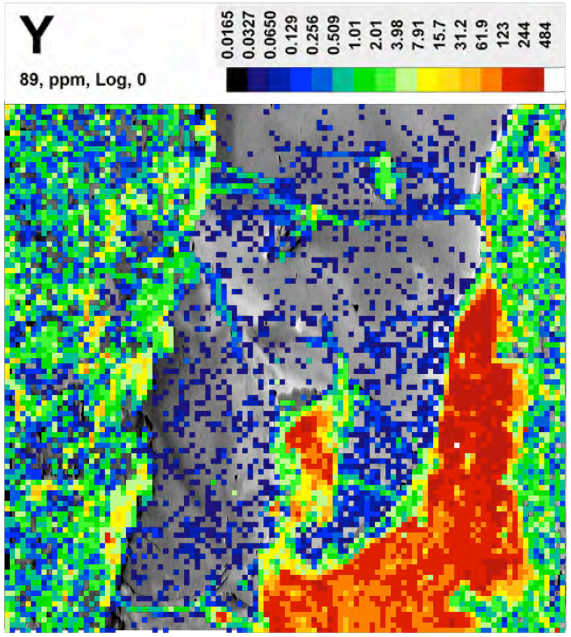
Y
89, ppm, Log, 0
0.0165 0.0327 0.0650 0.129 0.256 0.509 1.01 2.01 3.98 7.91 15.7 31.2 61.9 123 244 484

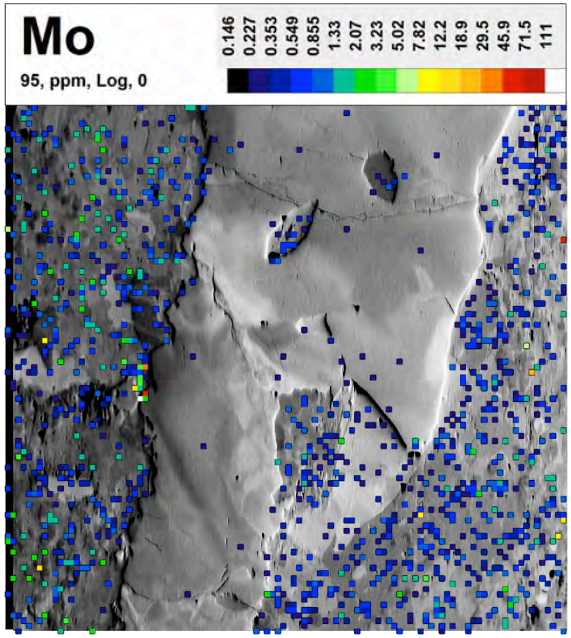
Mo
95, ppm, Log, 0
0.146 0.227 0.353 0.549 0.855 1.33 2.07 3.23 5.02 7.82 12.2 18.9 29.5 45.9 71.5 111

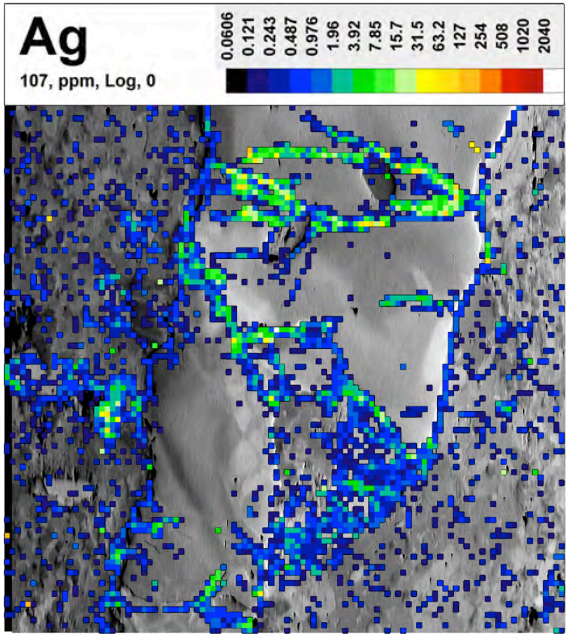
Ag
107, ppm, Log, 0
0.0606 0.121 0.243 0.487 0.976 1.96 3.92 7.85 15.7 31.5 63.2 127 254 508 1020 2040

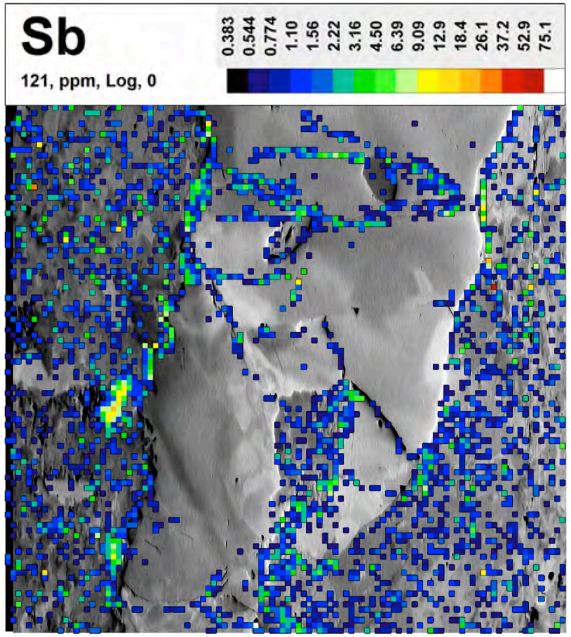
Sb
121, ppm, Log, 0
0.383 0.544 0.774 1.10 1.56 2.22 3.16 4.50 6.39 9.09 12.9 18.4 26.1 37.2 52.9 75.1

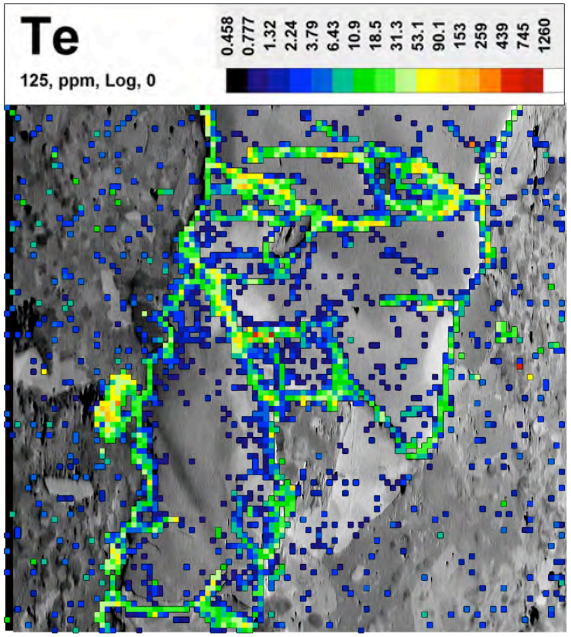
Te
125, ppm, Log, 0
0.458 0.777 1.32 2.24 3.79 6.43 10.9 18.5 31.3 53.1 90.1 153 259 439 745 1260

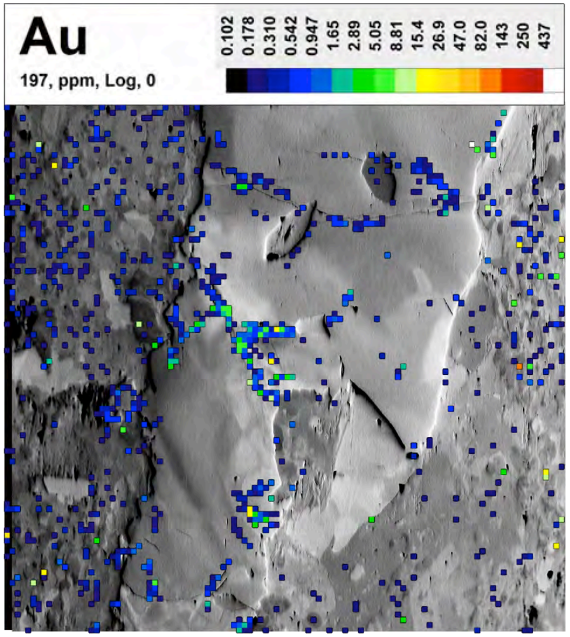
Au
197, ppm, Log, 0
0.102 0.178 0.310 0.542 0.947 1.65 2.89 5.05 8.81 15.4 26.9 47.0 82.0 143 250 437

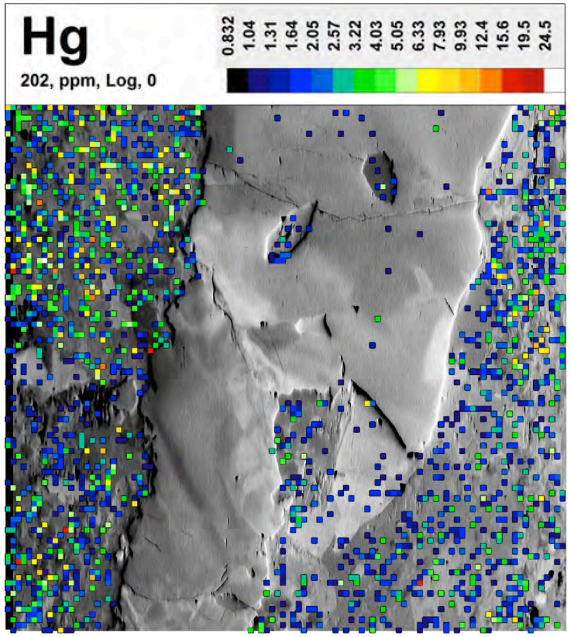
Hg
202, ppm, Log, 0
0.832 1.04 1.31 1.64 2.05 2.57 3.22 4.03 5.05 6.33 7.93 9.93 12.4 15.6 19.5 24.5

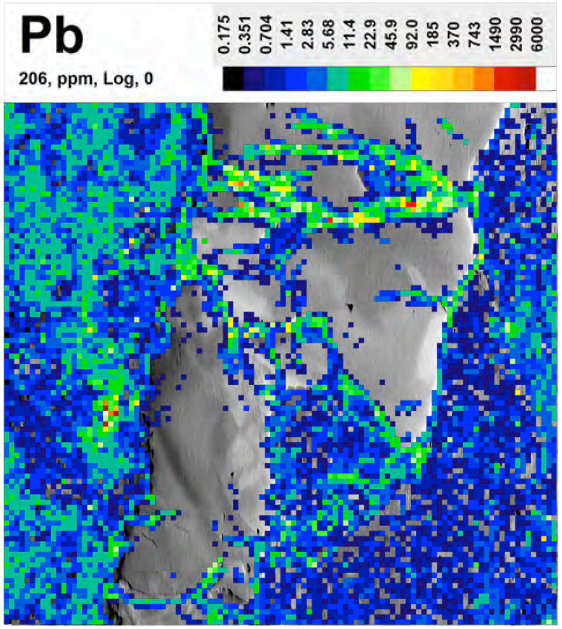
Pb
206, ppm, Log, 0
0.175 0.351 0.704 1.41 2.83 5.68 11.4 22.9 45.9 92.0 185 370 743 1490 2990 6000

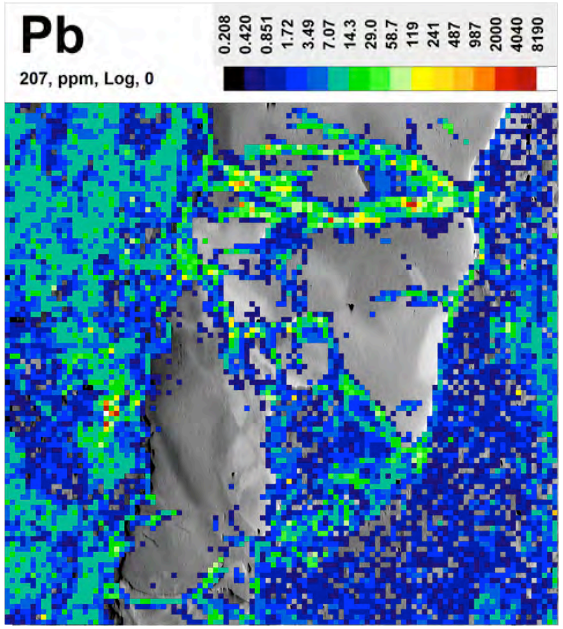
Pb
207, ppm, Log, 0
0.208 0.420 0.851 1.72 3.49 7.07 14.3 29.0 58.7 119 241 487 987 2000 4040 8190

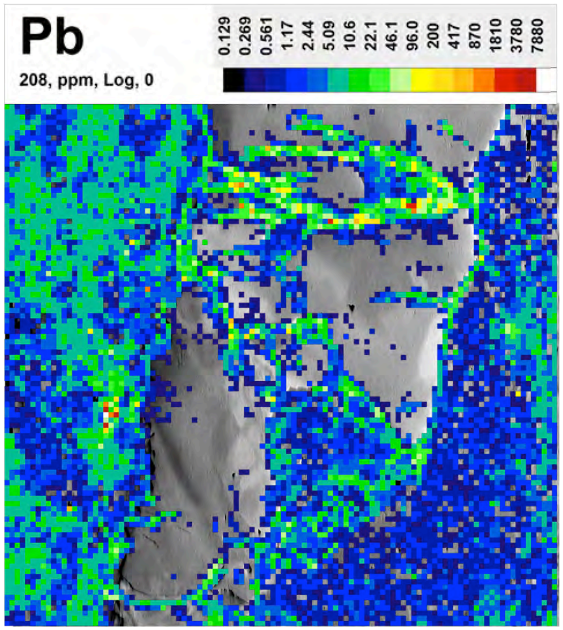
Pb
208, ppm, Log, 0
0.129 0.269 0.561 1.17 2.44 5.09 10.6 22.1 46.1 96.0 200 417 870 1810 3780 7880

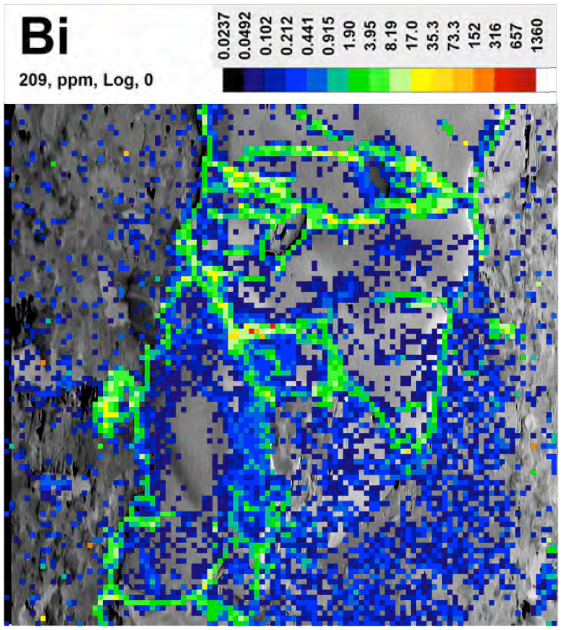
Bi
209, ppm, Log, 0
0.0237 0.0492 0.102 0.212 0.441 0.915 1.90 3.95 8.19 17.0 35.3 73.3 152 316 657 1360

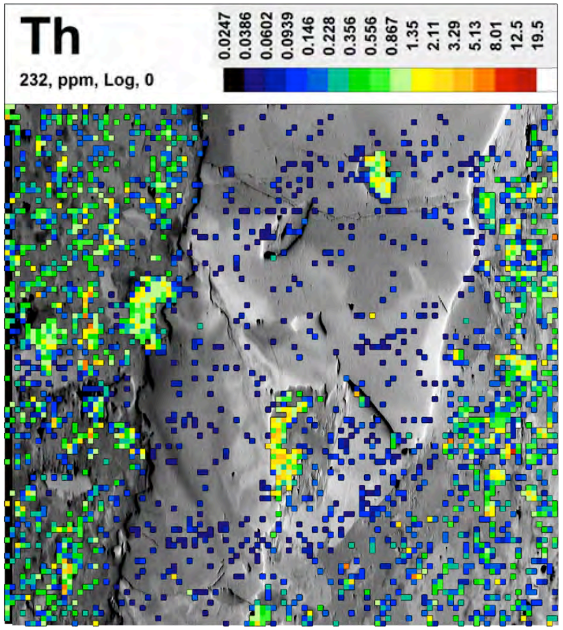
Th
232, ppm, Log, 0
0.0247 0.0386 0.0602 0.0939 0.146 0.228 0.356 0.556 0.867 1.35 2.11 3.29 5.13 8.01 12.5 19.5

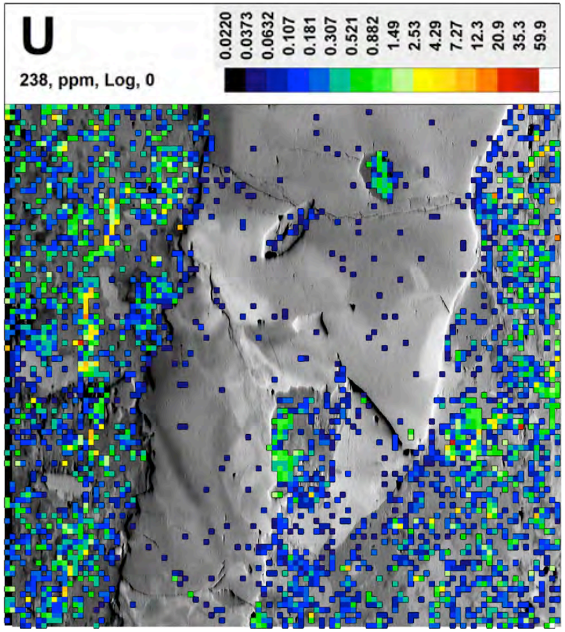
U
238, ppm, Log, 0
0.0220
0.0373
0.0632
0.107
0.181
0.307
0.521
0.882
1.49
2.53
4.29
7.27
12.3
20.9
35.3
59.9

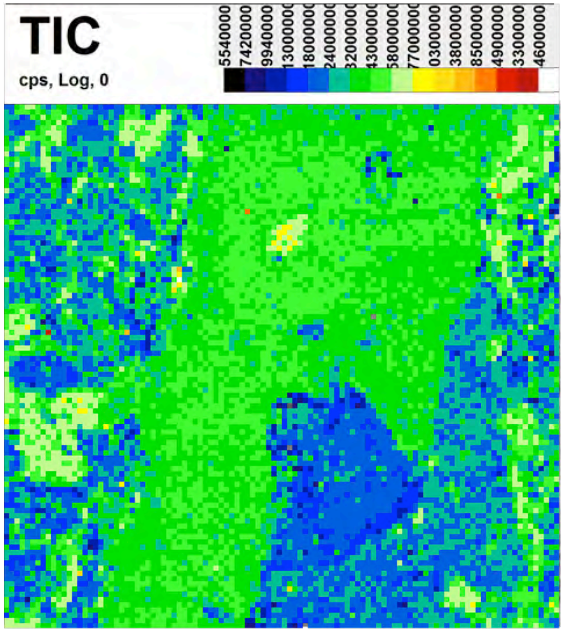
TIC
cps, Log, 0

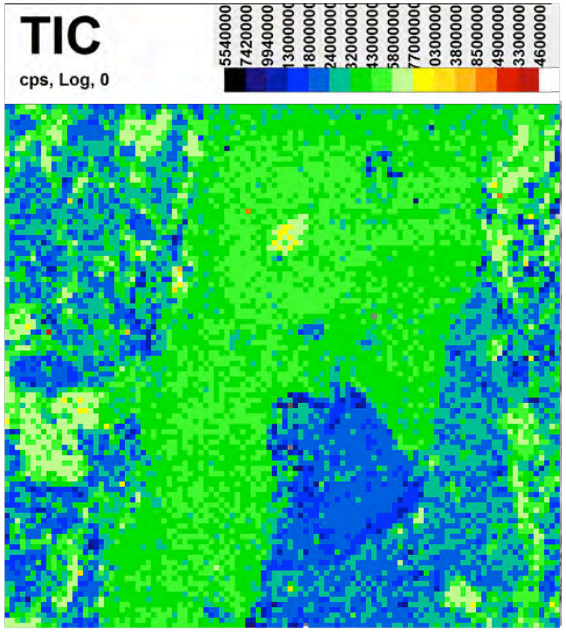
TIC
cps, Log, 0

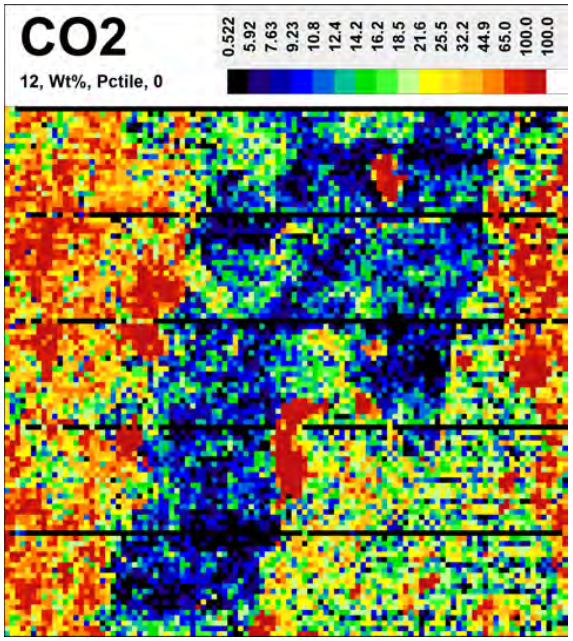
CO2
12, Wt%, Pctile, 0
0.522
5.92
7.63
9.23
10.8
12.4
14.2
16.2
18.5
21.6
25.5
32.2
44.9
65.0
100.0
100.0

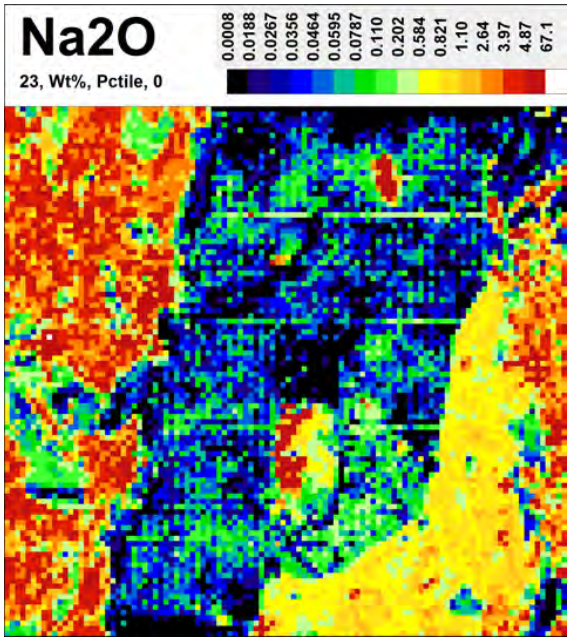
Na2O
23, Wt%, Pctile, 0
0.0008
0.0188
0.0267
0.0356
0.0464
0.0595
0.0787
0.110
0.202
0.584
0.821
1.10
2.64
3.97
4.87
67.1

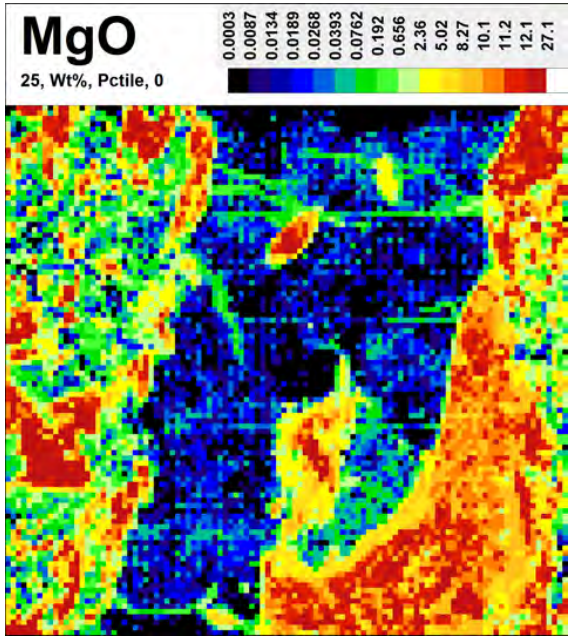
MgO
25, Wt%, Pctile, 0
0.0003
0.0087
0.0134
0.0189
0.0268
0.0393
0.0762
0.192
0.656
2.36
5.02
8.27
10.1
11.2
12.1
27.1

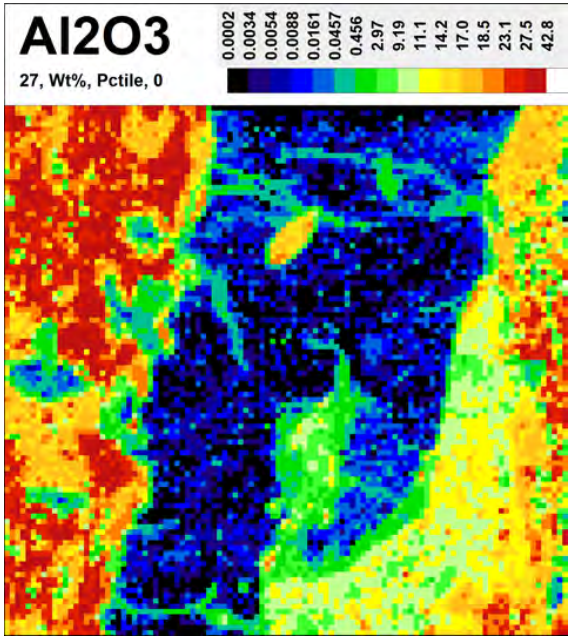
Al2O3
27, Wt%, Pctile, 0
0.0002
0.0034
0.0054
0.0088
0.0161
0.0457
0.456
2.97
9.19
11.1
14.2
17.0
18.5
23.1
27.5
42.8

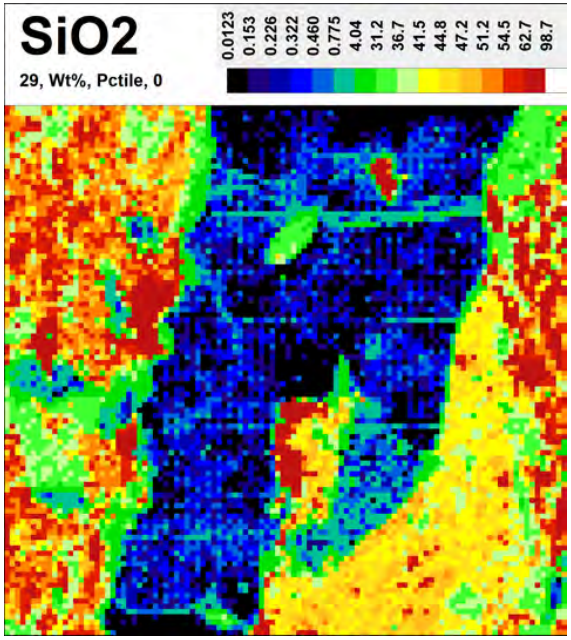
SiO2
29, Wt%, Pctile, 0
0.0123
0.153
0.226
0.322
0.460
0.775
4.04
31.2
36.7
41.5
44.8
47.2
51.2
54.5
62.7
98.7

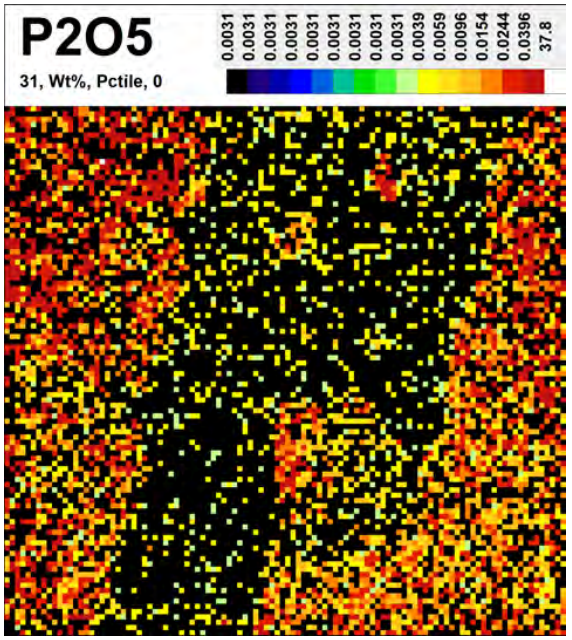
P2O5
31, Wt%, Pctile, 0
0.0031 0.0031 0.0031 0.0031 0.0031 0.0031 0.0031 0.0031 0.0039 0.0059 0.0096 0.0154 0.0244 0.0396 37.8

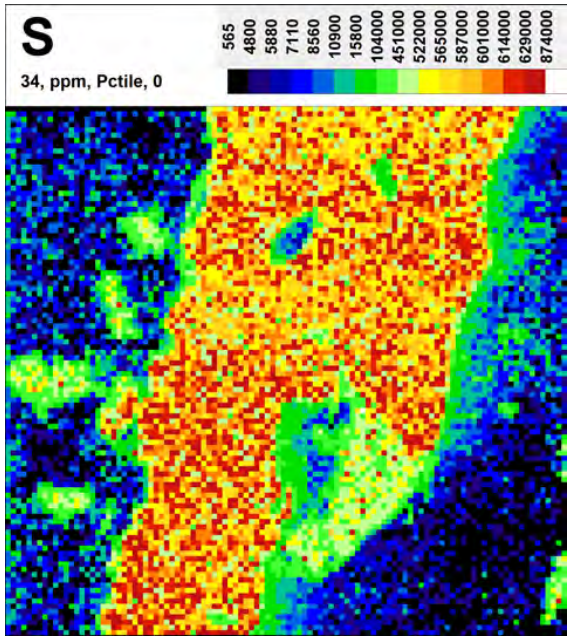
S
34, ppm, Pctile, 0
565 4800 5880 7110 8560 10900 15800 104000 451000 522000 565000 587000 601000 614000 629000 874000

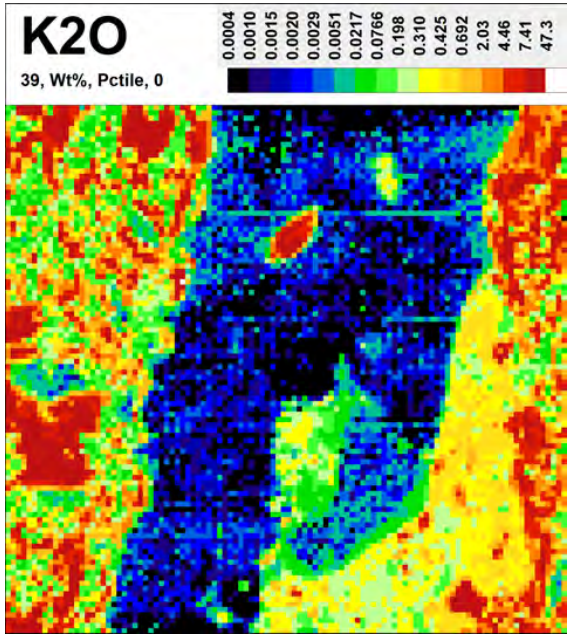
K2O
39, Wt%, Pctile, 0
0.0004 0.0010 0.0015 0.0020 0.0029 0.0051 0.0217 0.0766 0.198 0.310 0.425 0.692 2.03 4.46 7.41 47.3

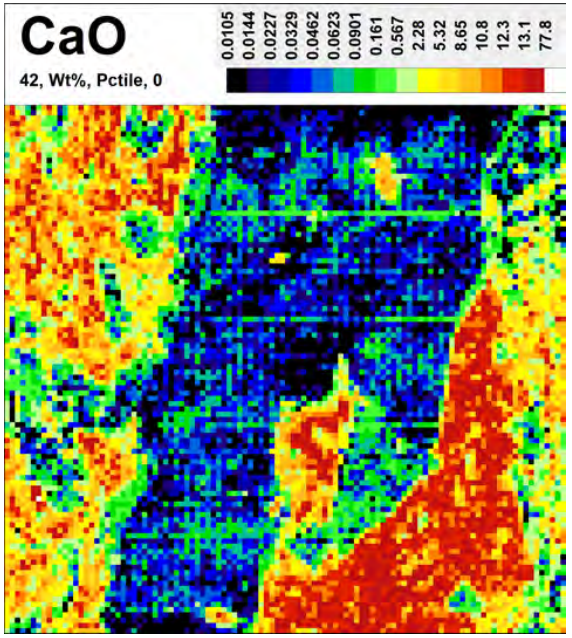
CaO
42, Wt%, Pctile, 0
0.0105 0.0144 0.0227 0.0329 0.0462 0.0623 0.0901 0.161 0.567 2.28 5.32 8.65 10.8 12.3 13.1 77.8

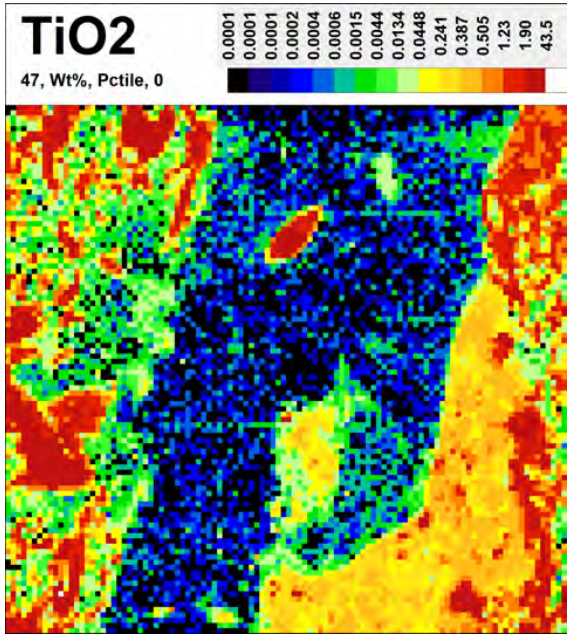
TiO2
47, Wt%, Pctile, 0
0.0001 0.0001 0.0001 0.0002 0.0004 0.0006 0.0015 0.0044 0.0134 0.0448 0.241 0.387 0.505 1.23 1.90 43.5

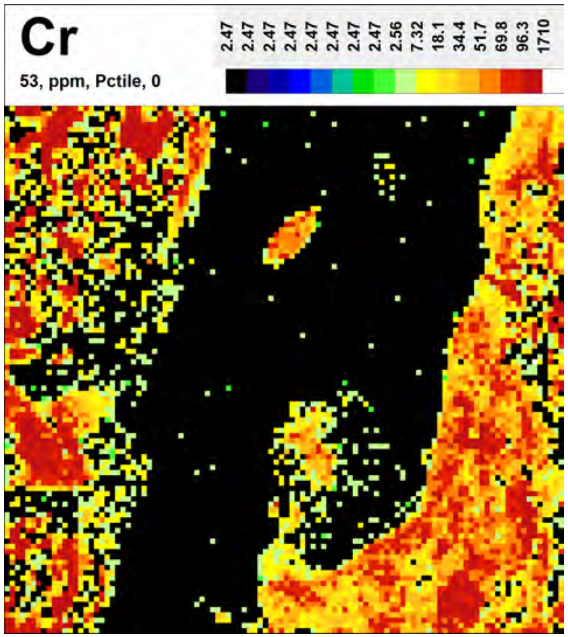
Cr
53, ppm, Pctile, 0
2.47 2.47 2.47 2.47 2.47 2.47 2.47 2.56 7.32 18.1 34.4 51.7 69.8 96.3 1710

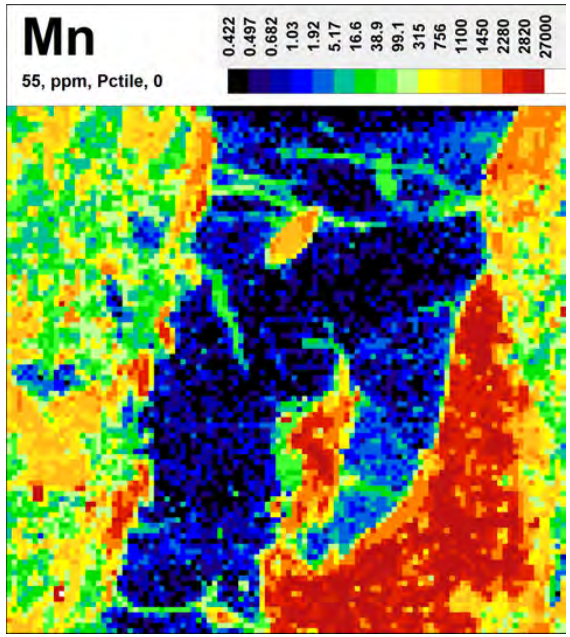
Mn
55, ppm, Pctile, 0
0.422 0.497 0.682 1.03 1.92 5.17 16.6 38.9 99.1 315 756 1100 1450 2280 2820 27000

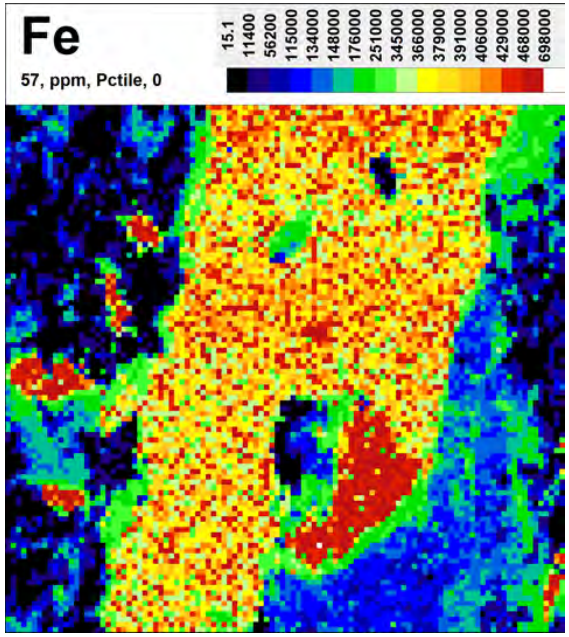
Fe
57, ppm, Pctile, 0
15.1 11400 56200 115000 134000 148000 176000 251000 345000 366000 379000 391000 406000 429000 468000 698000

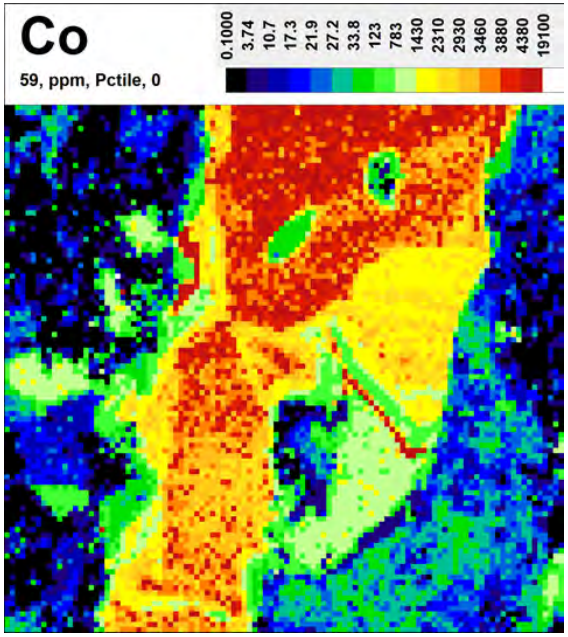
Co
59, ppm, Pctile, 0
0.1000 3.74 10.7 17.3 21.9 27.2 33.8 123 783 1430 2310 2930 3460 3880 4380 19100

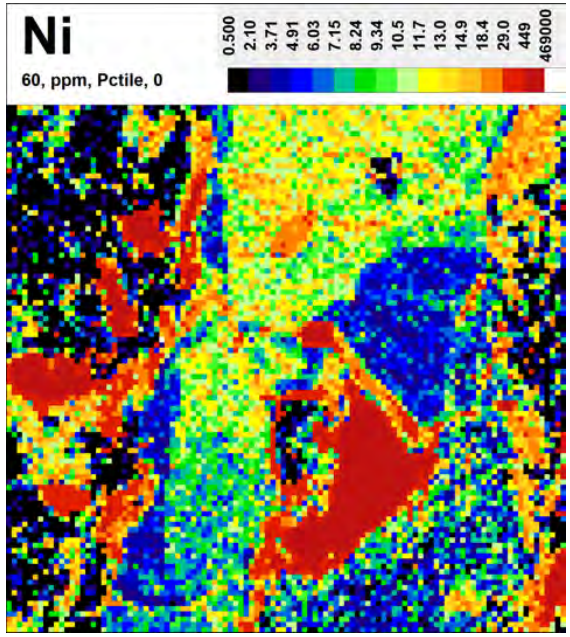
Ni
60, ppm, Pctile, 0
0.500 2.10 3.71 4.91 6.03 7.15 8.24 9.34 10.5 11.7 13.0 14.9 18.4 29.0 449 469000

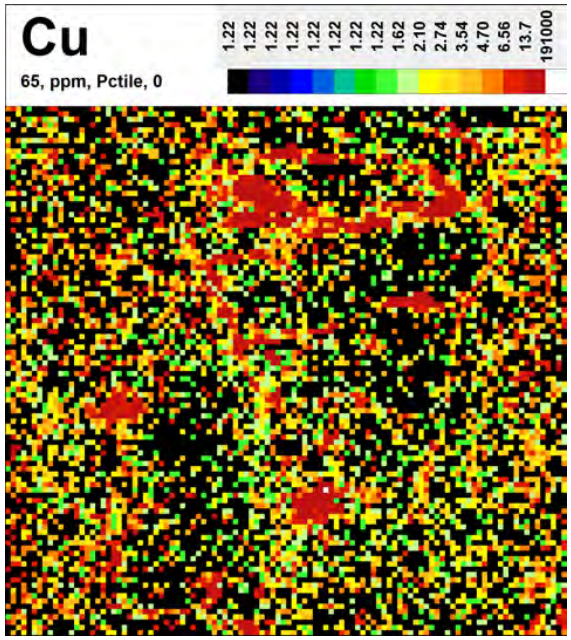
Cu
65, ppm, Pctile, 0
1.22 1.22 1.22 1.22 1.22 1.22 1.22 1.62 2.10 2.74 3.54 4.70 6.56 13.7 191000

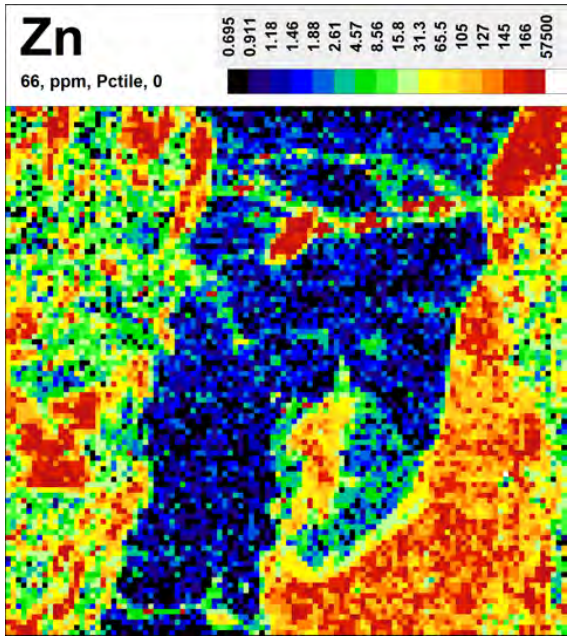
Zn
66, ppm, Pctile, 0
0.695 0.911 1.18 1.46 1.88 2.61 4.57 8.56 15.8 31.3 65.5 105 127 145 166 57500

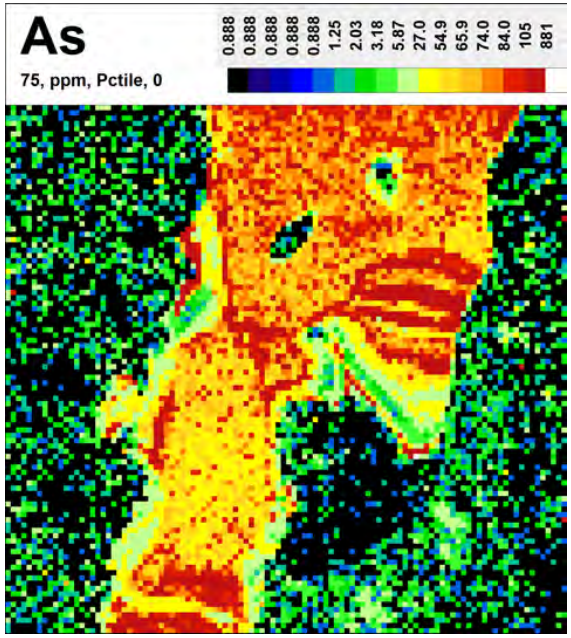
As
75, ppm, Pctile, 0
0.888 0.888 0.888 0.888 0.888 1.25 2.03 3.18 5.87 27.0 54.9 65.9 74.0 84.0 105 881

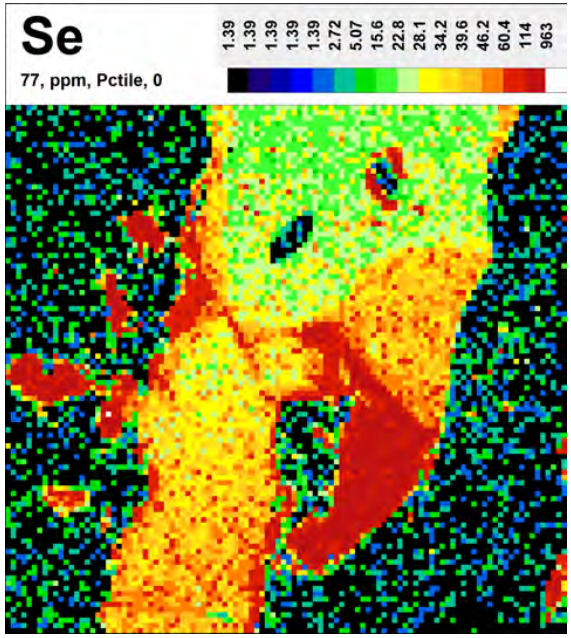
Se
77, ppm, Pctile, 0
1.39 1.39 1.39 1.39 1.39 2.72 5.07 15.6 22.8 28.1 34.2 39.6 46.2 60.4 114 963

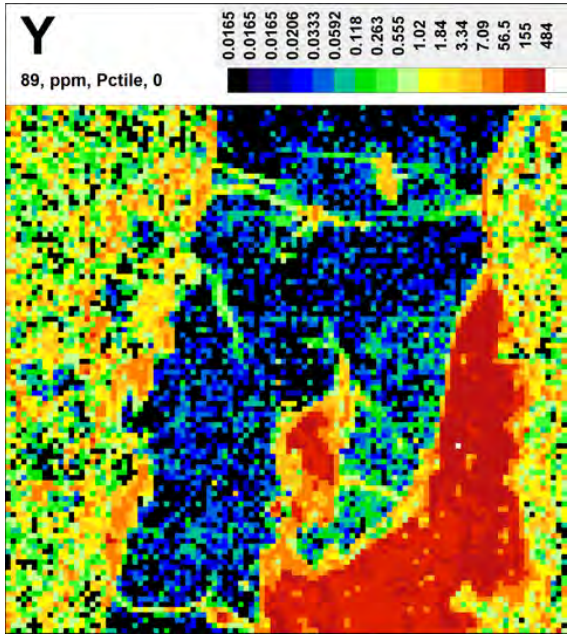
Y
89, ppm, Pctile, 0
0.0165 0.0165 0.0165 0.0206 0.0333 0.0592 0.118 0.263 0.555 1.02 1.84 3.34 7.09 56.5 155 484

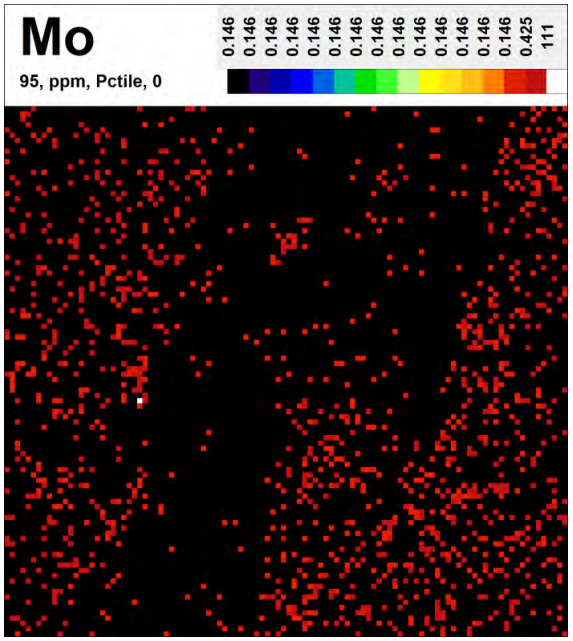
Mo
95, ppm, Pctile, 0
0.146 0.146 0.146 0.146 0.146 0.146 0.146 0.146 0.146 0.146 0.146 0.146 0.425 111

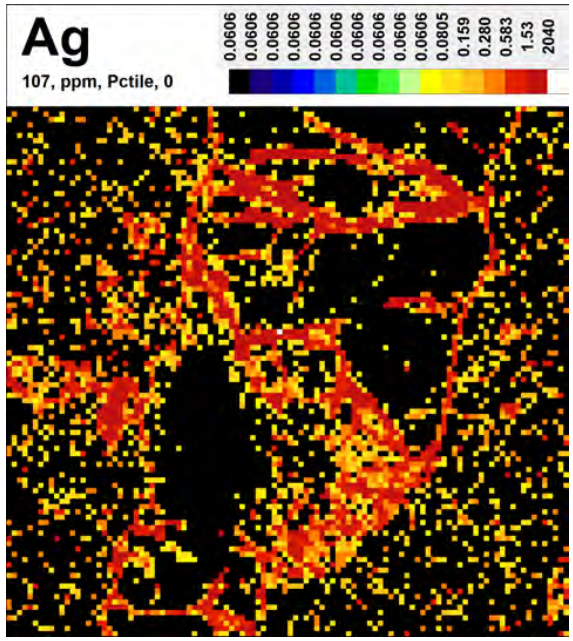
Ag
107, ppm, Pctile, 0
0.0606 0.0606 0.0606 0.0606 0.0606 0.0606 0.0606 0.0606 0.0606 0.0805 0.159 0.280 0.583 1.53 2040

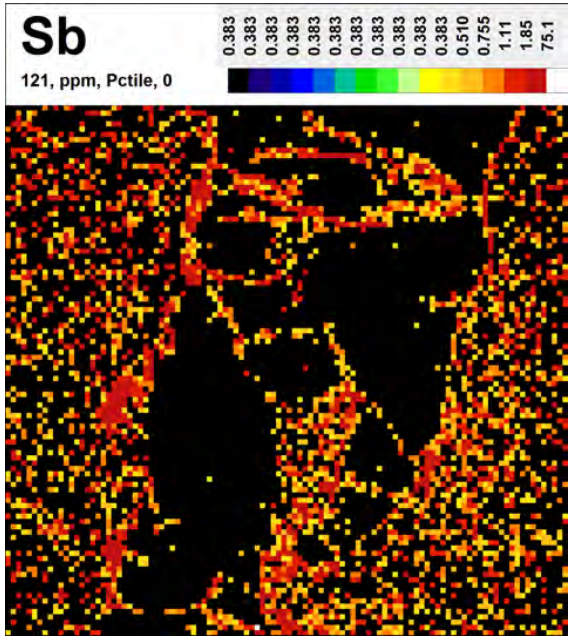
Sb
121, ppm, Pctile, 0
0.383 0.383 0.383 0.383 0.383 0.383 0.383 0.383 0.383 0.383 0.510 0.755 1.11 1.85 75.1

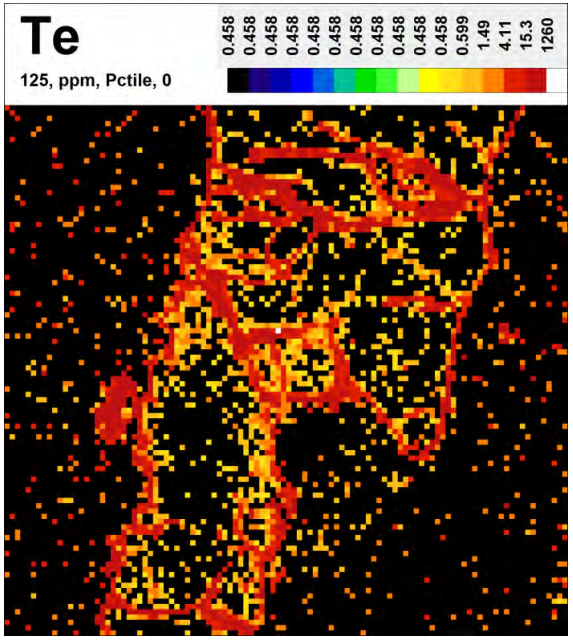
Te
125, ppm, Pctile, 0
0.458 0.458 0.458 0.458 0.458 0.458 0.458 0.458 0.458 0.458 0.599 1.49 4.11 15.3 1260

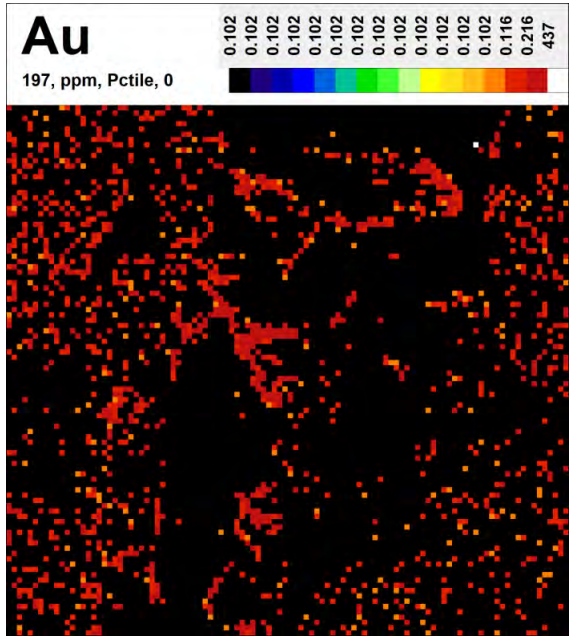
Au
197, ppm, Pctile, 0
0.102 0.102 0.102 0.102 0.102 0.102 0.102 0.102 0.102 0.102 0.102 0.102 0.116 0.216 437

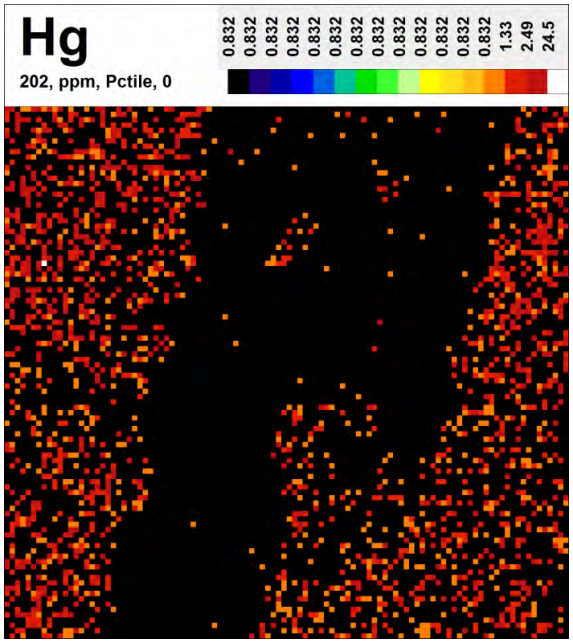
Hg
202, ppm, Pctile, 0
0.832 0.832 0.832 0.832 0.832 0.832 0.832 0.832 0.832 0.832 0.832 1.33 2.49 24.5

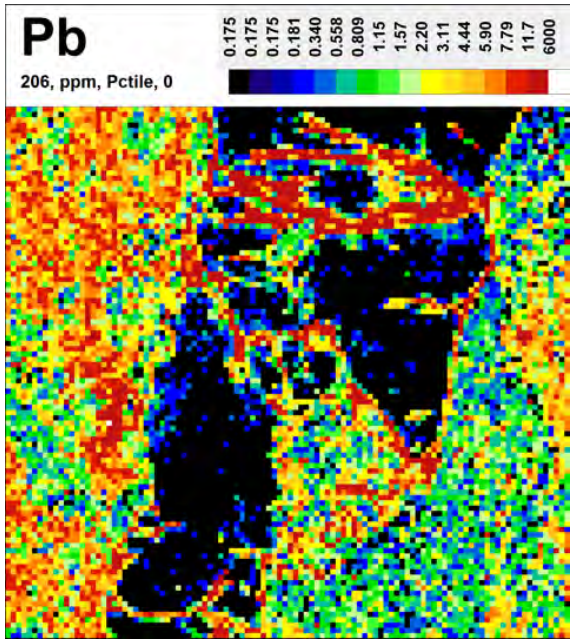
Pb
206, ppm, Pctile, 0
0.175 0.175 0.175 0.181 0.340 0.558 0.809 1.15 1.57 2.20 3.11 4.44 5.90 7.79 11.7 6000

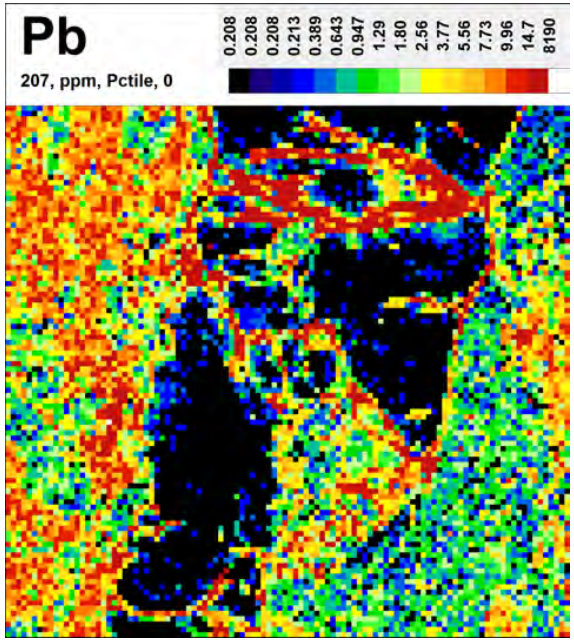
Pb
207, ppm, Pctile, 0
0.208 0.208 0.208 0.213 0.389 0.643 0.947 1.29 1.80 2.56 3.77 5.56 7.73 9.96 14.7 8190

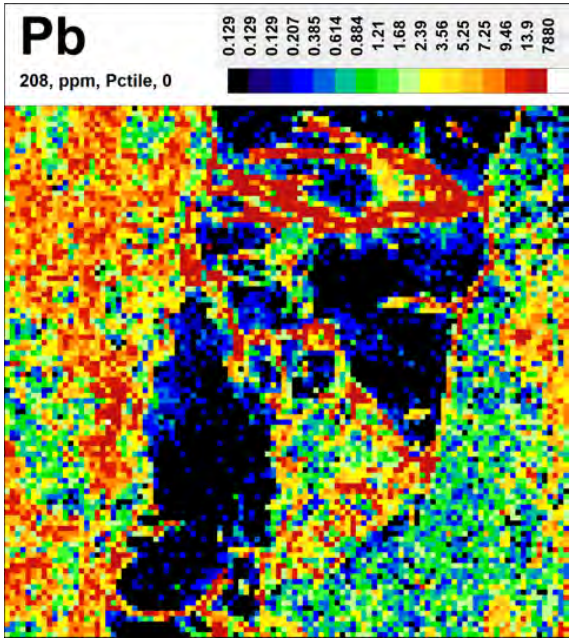
Pb
208, ppm, Pctile, 0
0.129 0.129 0.129 0.207 0.385 0.614 0.884 1.21 1.68 2.39 3.56 5.25 7.25 9.46 13.9 7880

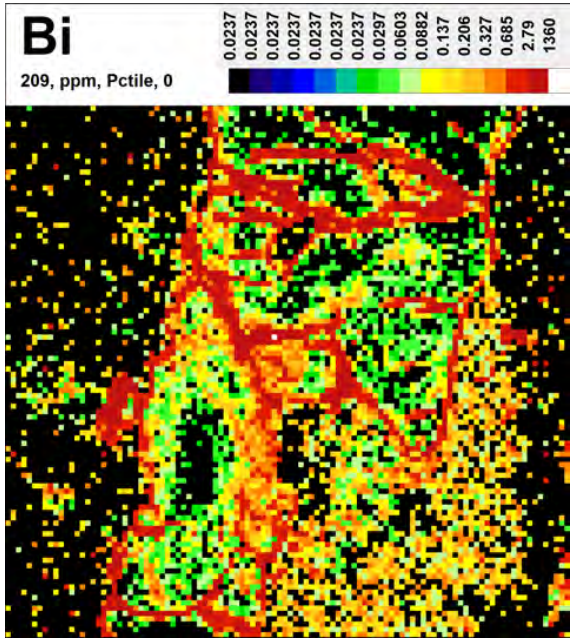
Bi
209, ppm, Pctile, 0
0.0237 0.0237 0.0237 0.0237 0.0237 0.0237 0.0297 0.0603 0.0882 0.137 0.206 0.327 0.685 2.79 1360

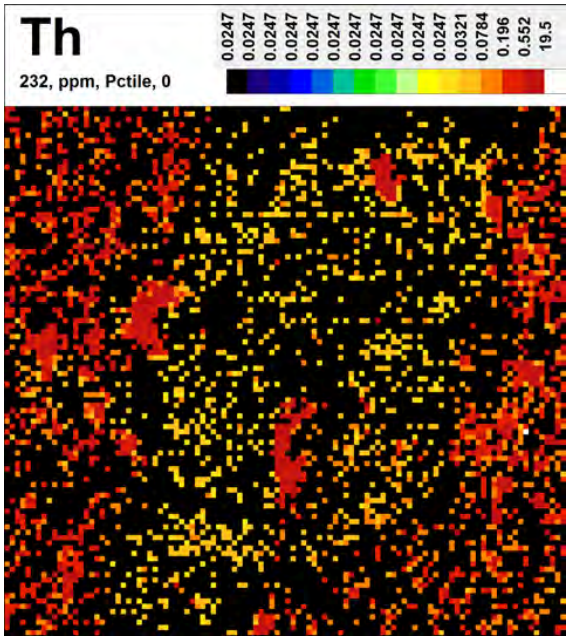
Th
232, ppm, Pctile, 0
0.0247 0.0247 0.0247 0.0247 0.0247 0.0247 0.0247 0.0247 0.0247 0.0247 0.0321 0.0784 0.196 0.552 19.5

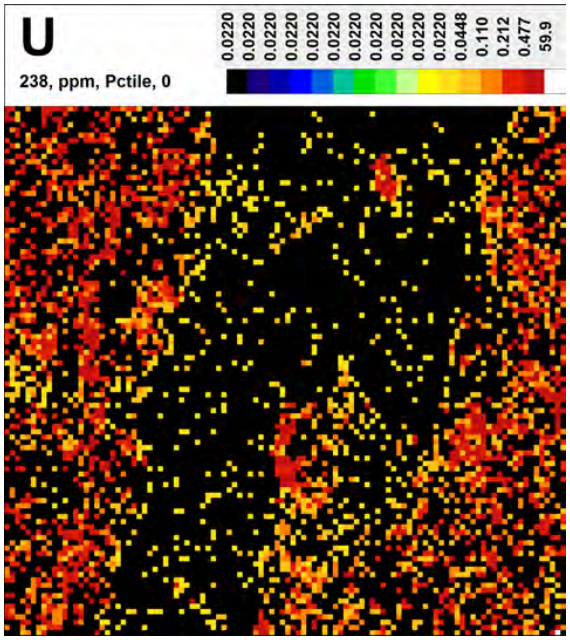
U
238, ppm, Pctile, 0
0.0220 0.0220 0.0220 0.0220 0.0220 0.0220 0.0220 0.0220 0.0220 0.0220 0.0448 0.110 0.212 0.477 59.9

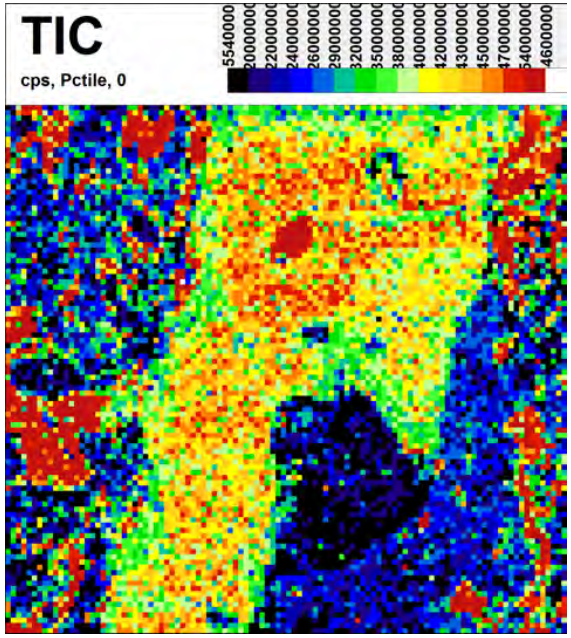
TIC
cps, Pctile, 0

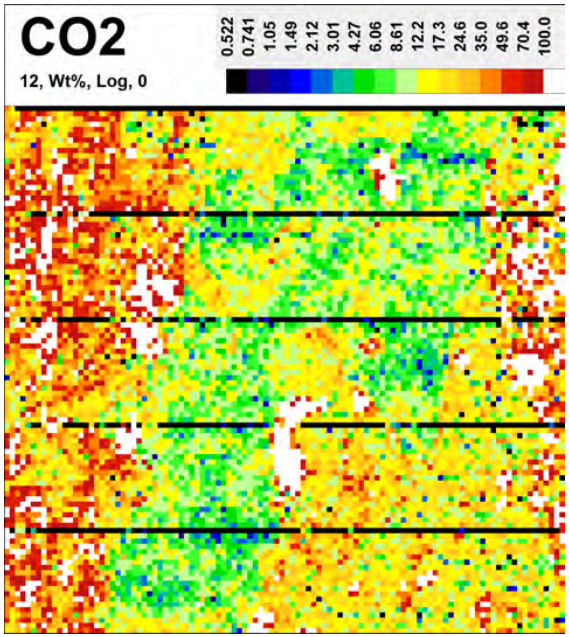
CO2
12, Wt%, Log, 0
0.522 0.741 1.05 1.49 2.12 3.01 4.27 6.06 8.61 12.2 17.3 24.6 35.0 49.6 70.4 100.0

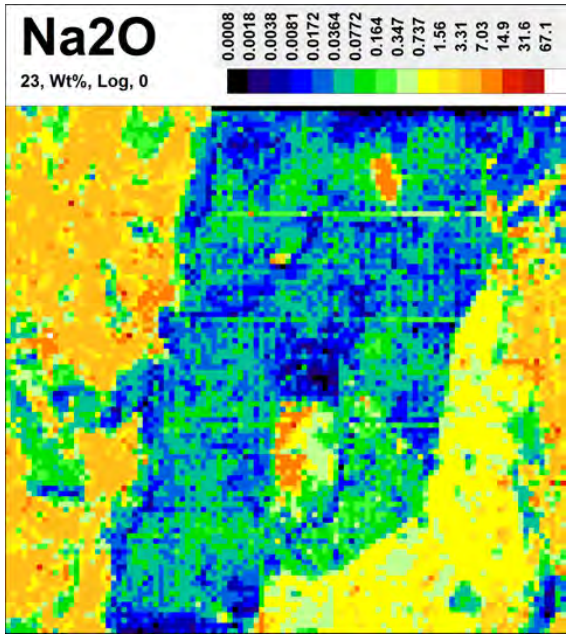
Na2O
23, Wt%, Log, 0
0.0008 0.0018 0.0038 0.0081 0.0172 0.0364 0.0772 0.164 0.347 0.737 1.56 3.31 7.03 14.9 31.6 67.1

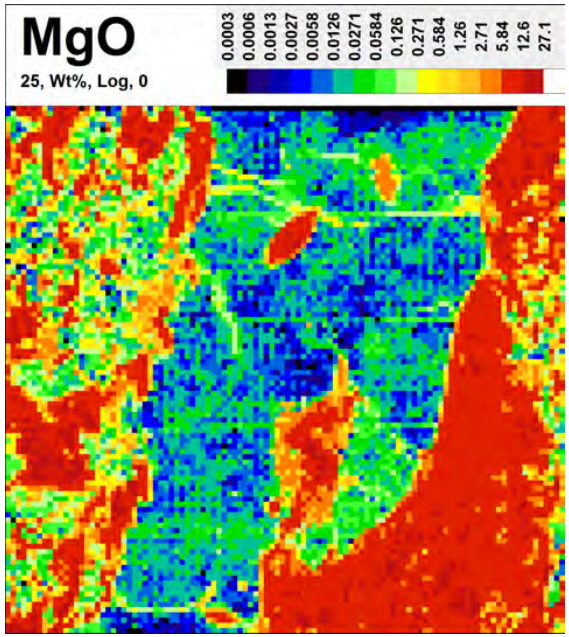
MgO
25, Wt%, Log, 0
0.0003 0.0006 0.0013 0.0027 0.0058 0.0126 0.0271 0.0584 0.126 0.271 0.584 1.26 2.71 5.84 12.6 27.1

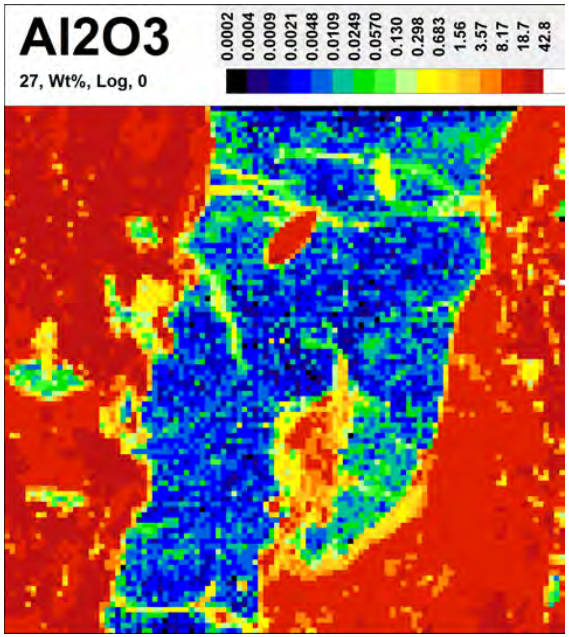
Al2O3
27, Wt%, Log, 0
0.0002 0.0004 0.0009 0.0021 0.0048 0.0109 0.0249 0.0570 0.130 0.298 0.683 1.56 3.57 8.17 18.7 42.8

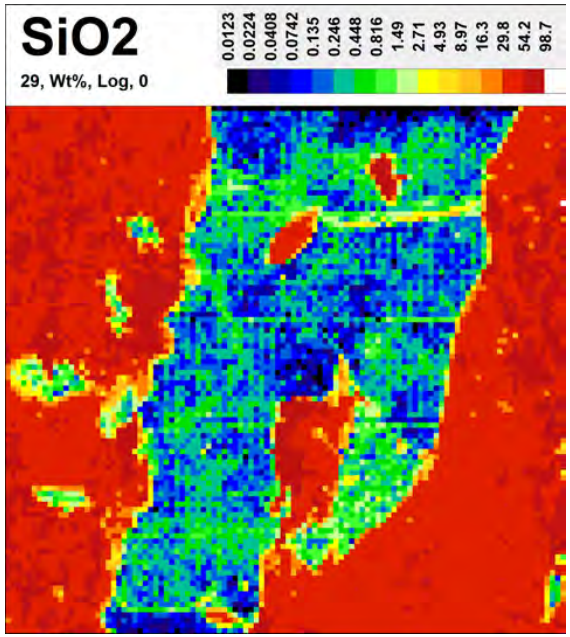
SiO2
29, Wt%, Log, 0
0.0123 0.0224 0.0408 0.0742 0.135 0.246 0.448 0.816 1.49 2.71 4.93 8.97 16.3 29.8 54.2 98.7

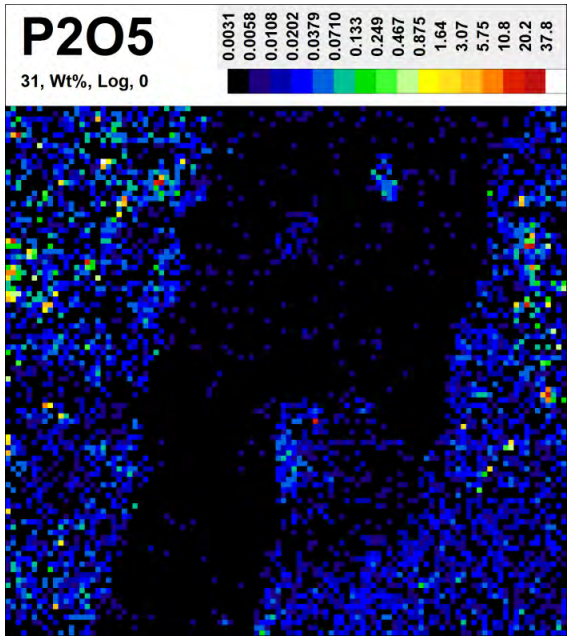
P2O5
31, Wt%, Log, 0
0.0031 0.0058 0.0108 0.0202 0.0379 0.0710 0.133 0.249 0.467 0.875 1.64 3.07 5.75 10.8 20.2 37.8

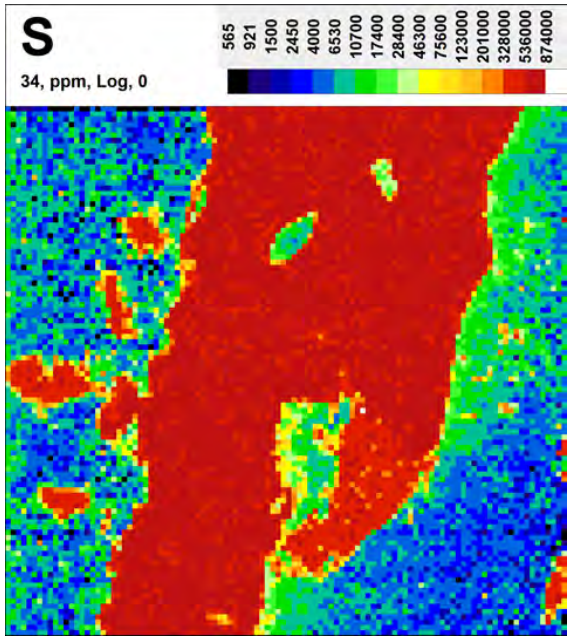
S
34, ppm, Log, 0
565 921 1500 2450 4000 6530 10700 17400 28400 46300 75600 123000 201000 328000 536000 874000

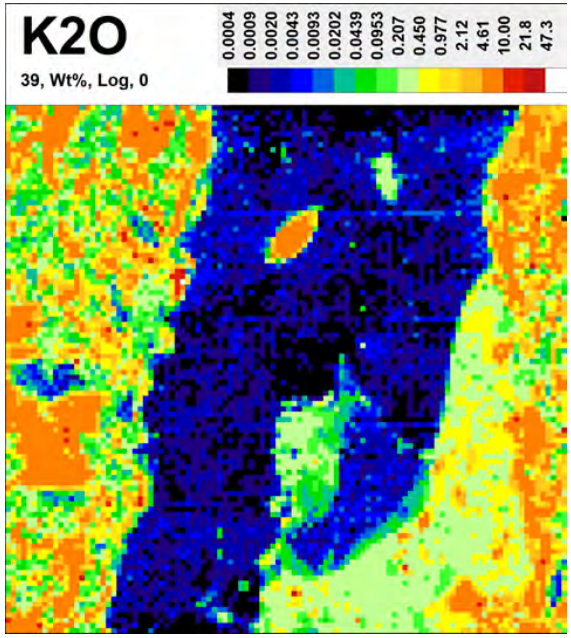
K2O
39, Wt%, Log, 0
0.0004 0.0009 0.0020 0.0043 0.0093 0.0202 0.0439 0.0953 0.207 0.450 0.977 2.12 4.61 10.00 21.8 47.3

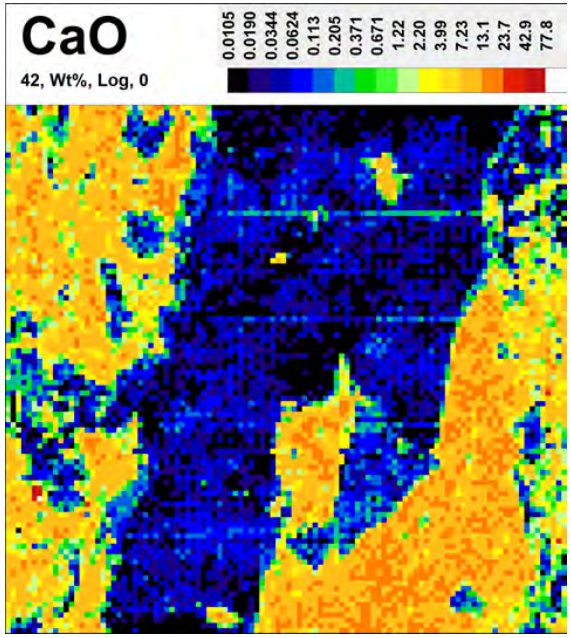
CaO
42, Wt%, Log, 0
0.0105 0.0190 0.0344 0.0624 0.113 0.205 0.371 0.671 1.22 2.20 3.99 7.23 13.1 23.7 42.9 77.8

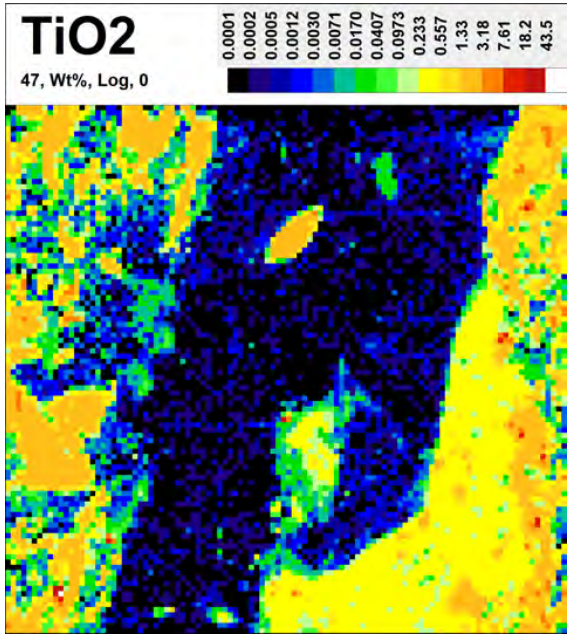
TiO2
47, Wt%, Log, 0
0.0001 0.0002 0.0005 0.0012 0.0030 0.0071 0.0170 0.0407 0.0973 0.233 0.557 1.33 3.18 7.61 18.2 43.5

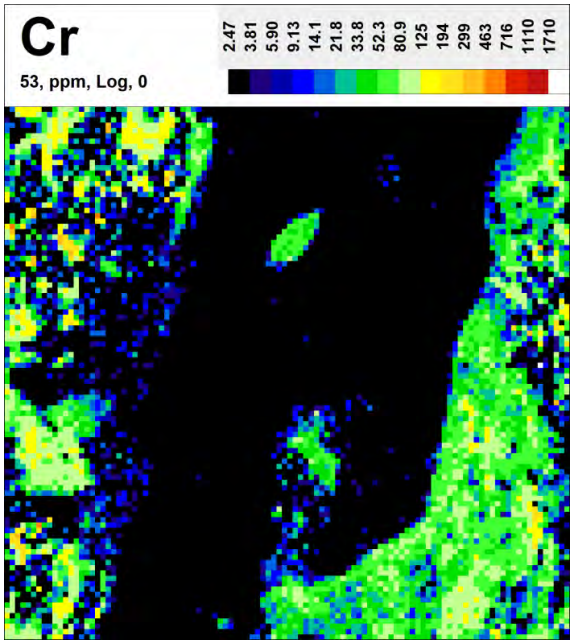
Cr
53, ppm, Log, 0
2.47 3.81 5.90 9.13 14.1 21.8 33.8 52.3 80.9 125 194 299 463 716 1110 1710

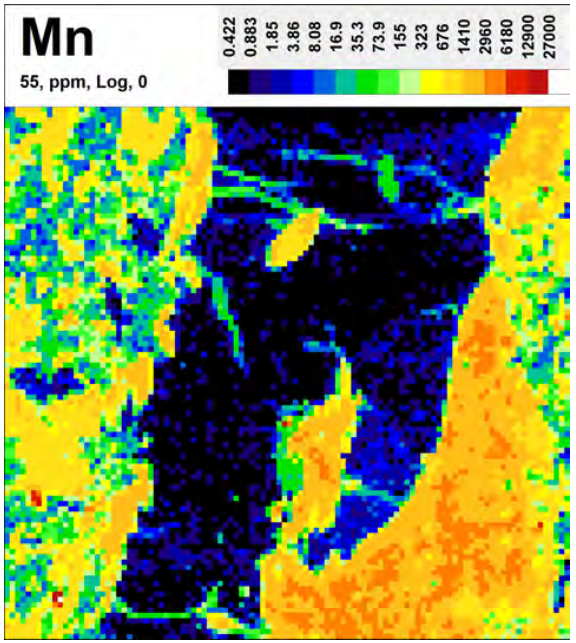
Mn
55, ppm, Log, 0
0.422 0.883 1.85 3.86 8.08 16.9 35.3 73.9 155 323 676 1410 2960 6180 12900 27000

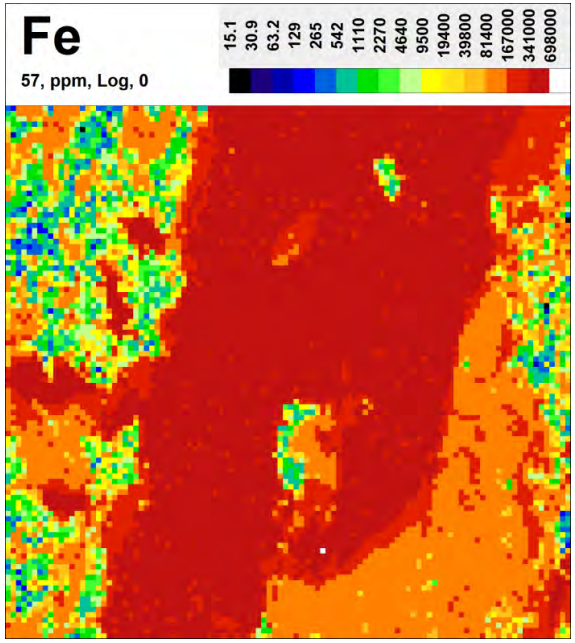
Fe
57, ppm, Log, 0
15.1 30.9 63.2 129 265 542 1110 2270 4640 9500 19400 39800 81400 167000 341000 698000

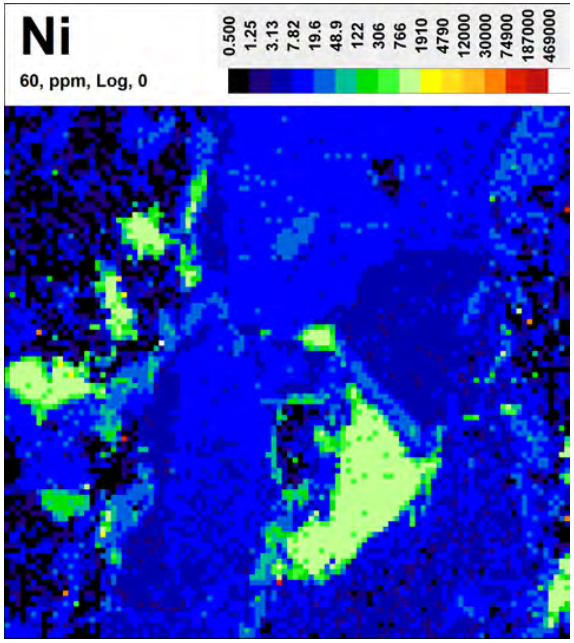
Ni
60, ppm, Log, 0
0.500 1.25 3.13 7.82 19.6 48.9 122 306 766 1910 4790 12000 30000 74900 187000 469000

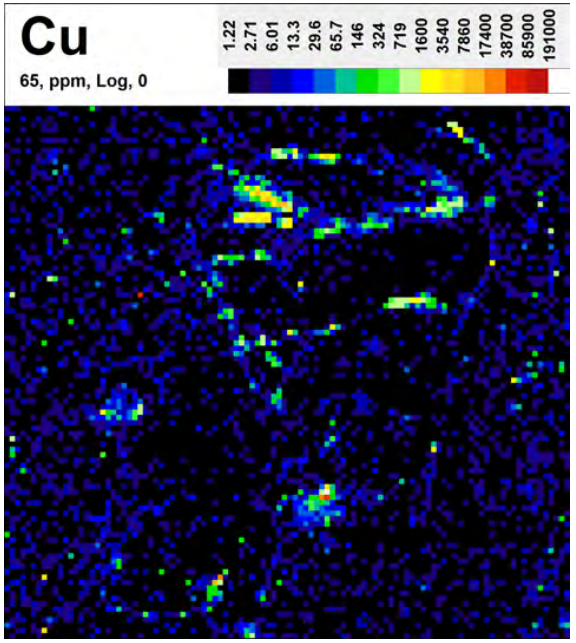
Cu
65, ppm, Log, 0
1.22 2.71 6.01 13.3 29.6 65.7 146 324 719 1600 3540 7860 17400 38700 85900 191000

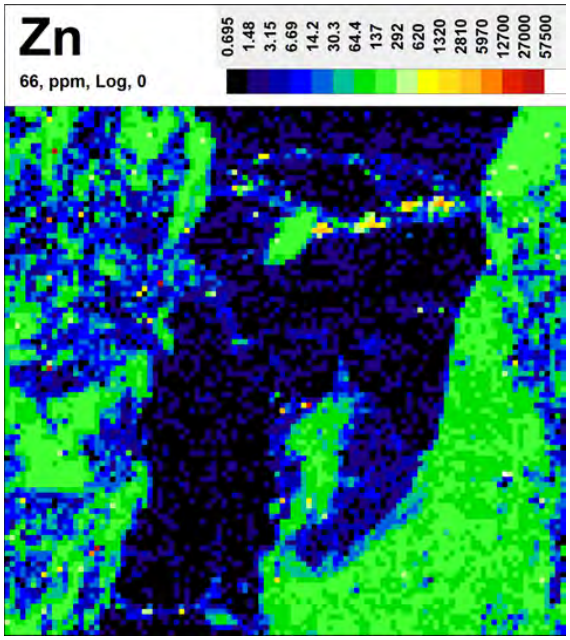
Zn
66, ppm, Log, 0
0.695 1.48 3.15 6.69 14.2 30.3 64.4 137 292 620 1320 2810 5970 12700 27000 57500

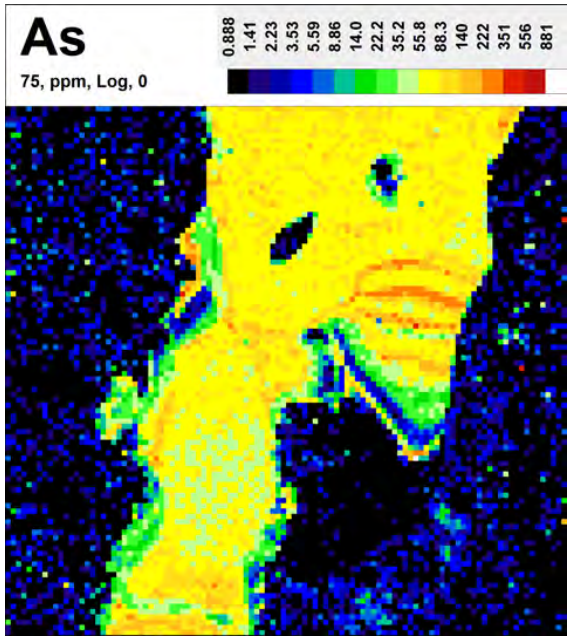
As
75, ppm, Log, 0
0.888 1.41 2.23 3.53 5.59 8.86 14.0 22.2 35.2 55.8 88.3 140 222 351 556 881

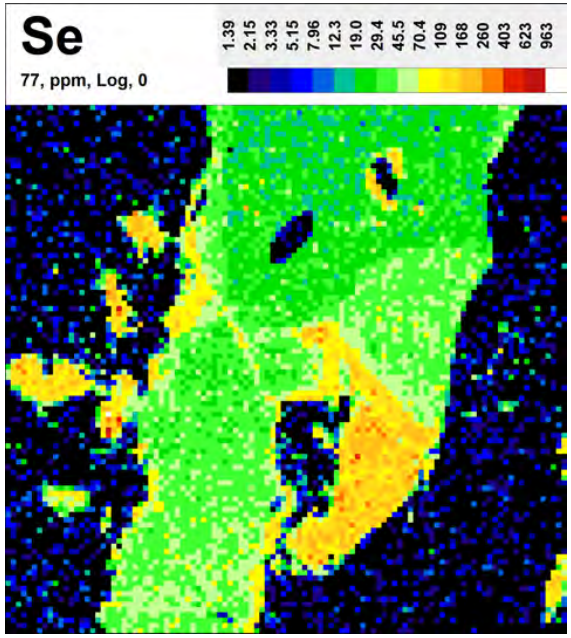
Se
77, ppm, Log, 0
1.39 2.15 3.33 5.15 7.96 12.3 19.0 29.4 45.5 70.4 109 168 260 403 623 963

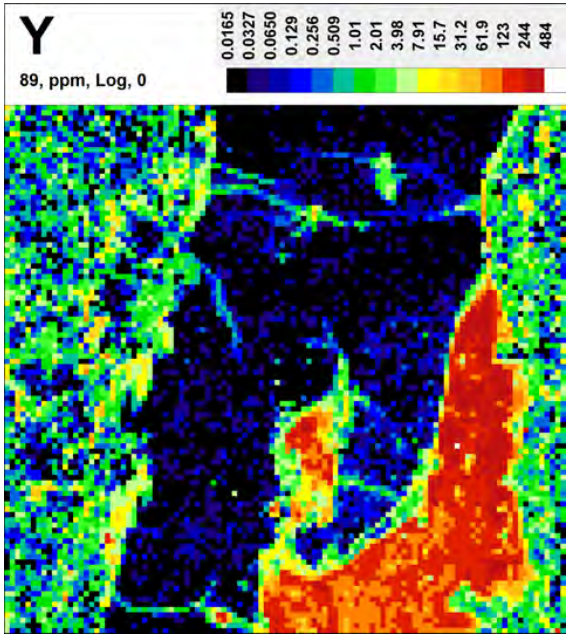
Y
89, ppm, Log, 0
0.0165 0.0327 0.0650 0.129 0.256 0.509 1.01 2.01 3.98 7.91 15.7 31.2 61.9 123 244 484

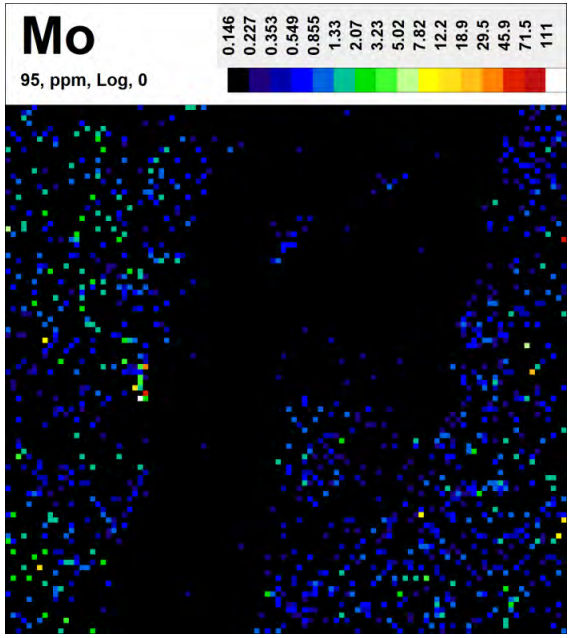
Mo
95, ppm, Log, 0
0.146 0.227 0.353 0.549 0.855 1.33 2.07 3.23 5.02 7.82 12.2 18.9 29.5 45.9 71.5 111

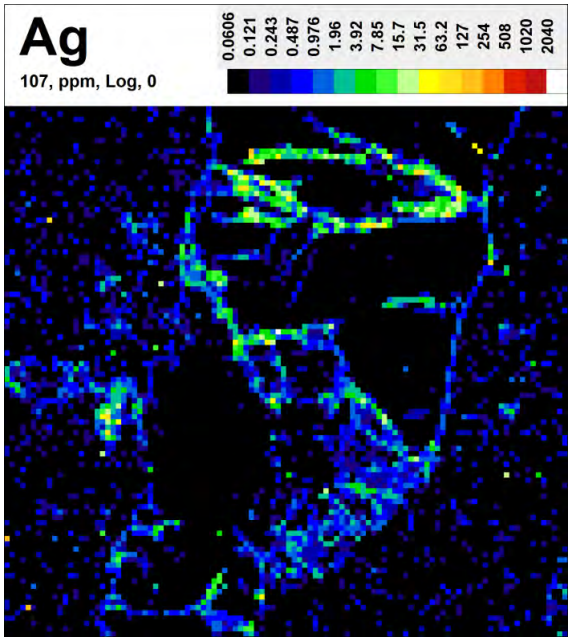
Ag
107, ppm, Log, 0
0.0606 0.121 0.243 0.487 0.976 1.96 3.92 7.85 15.7 31.5 63.2 127 254 508 1020 2040

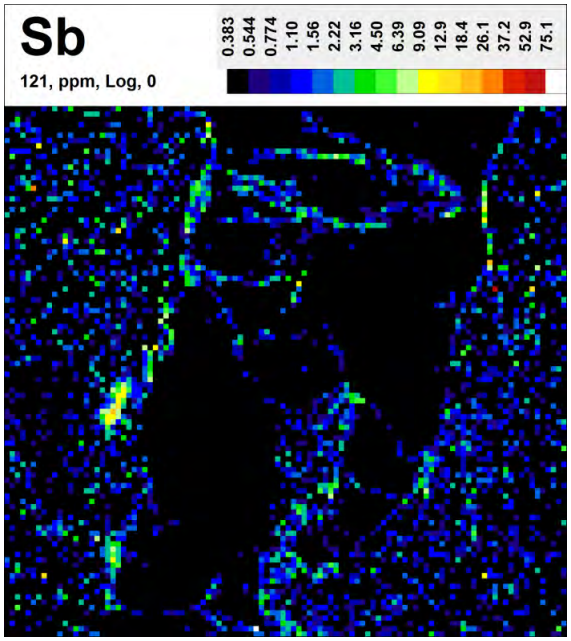
Sb
121, ppm, Log, 0
0.383 0.544 0.774 1.10 1.56 2.22 3.16 4.50 6.39 9.09 12.9 18.4 26.1 37.2 52.9 75.1

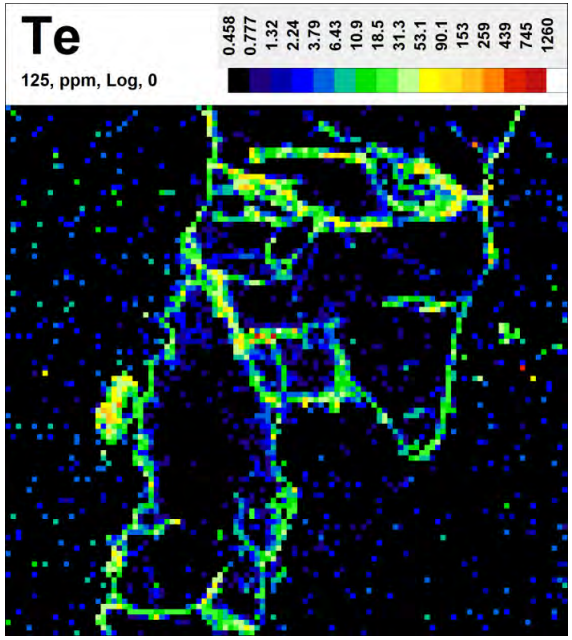
Te
125, ppm, Log, 0
0.458 0.777 1.32 2.24 3.79 6.43 10.9 18.5 31.3 53.1 90.1 153 259 439 745 1260

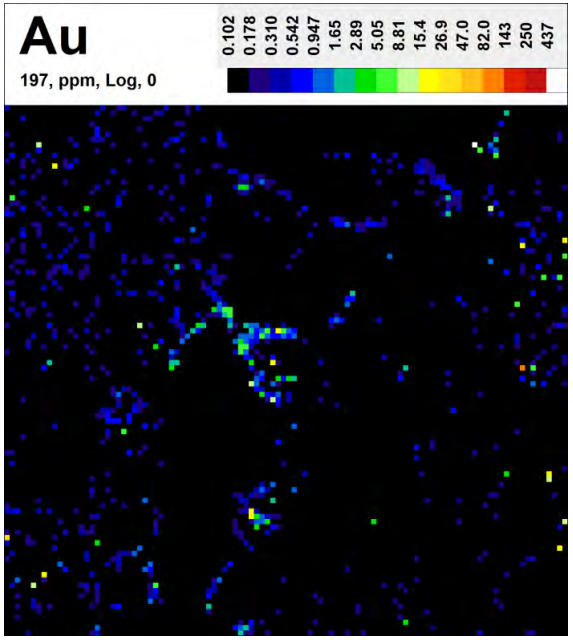
Au
197, ppm, Log, 0
0.102 0.178 0.310 0.542 0.947 1.65 2.89 5.05 8.81 15.4 26.9 47.0 82.0 143 250 437

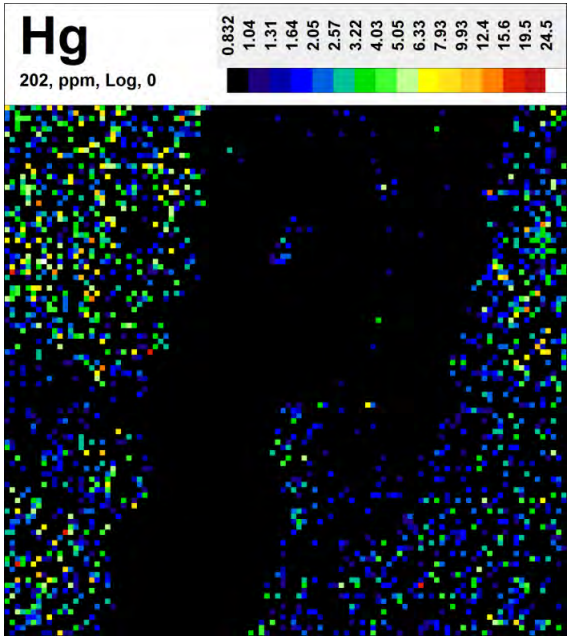
Hg
202, ppm, Log, 0
0.832 1.04 1.31 1.64 2.05 2.57 3.22 4.03 5.05 6.33 7.93 9.93 12.4 15.6 19.5 24.5

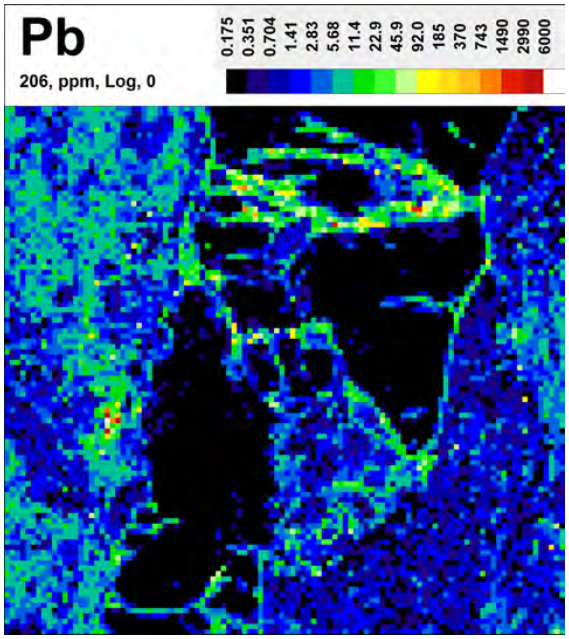
Pb
206, ppm, Log, 0
0.175 0.351 0.704 1.41 2.83 5.68 11.4 22.9 45.9 92.0 185 370 743 1490 2990 6000

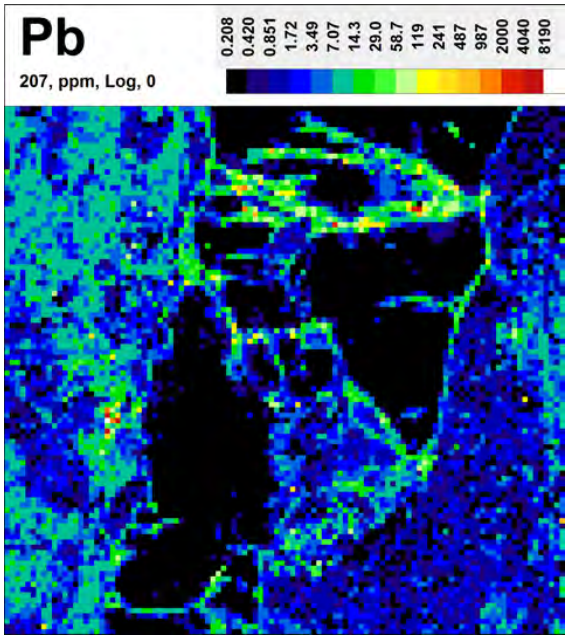
Pb
207, ppm, Log, 0
0.208 0.420 0.851 1.72 3.49 7.07 14.3 29.0 58.7 119 241 487 987 2000 4040 8190

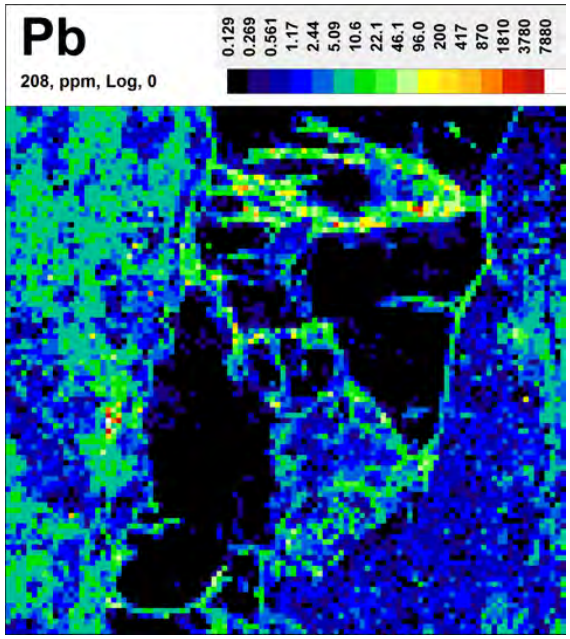
Pb
208, ppm, Log, 0
0.129 0.269 0.561 1.17 2.44 5.09 10.6 22.1 46.1 96.0 200 417 870 1810 3780 7880

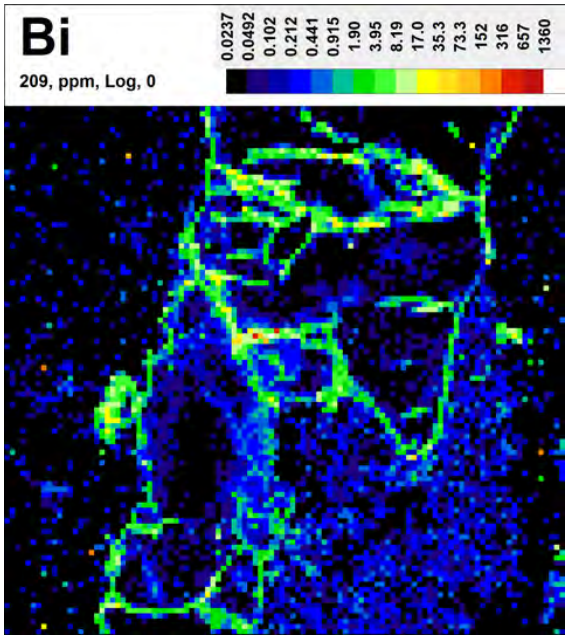
Bi
209, ppm, Log, 0
0.0237 0.0492 0.102 0.212 0.441 0.915 1.90 3.95 8.19 17.0 35.3 73.3 152 316 657 1360

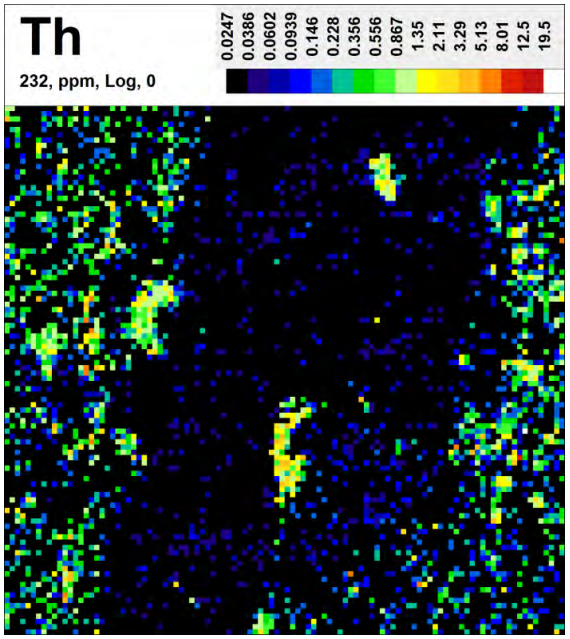
Th
232, ppm, Log, 0
0.0247 0.0386 0.0602 0.0939 0.146 0.228 0.356 0.556 0.867 1.35 2.11 3.29 5.13 8.01 12.5 19.5

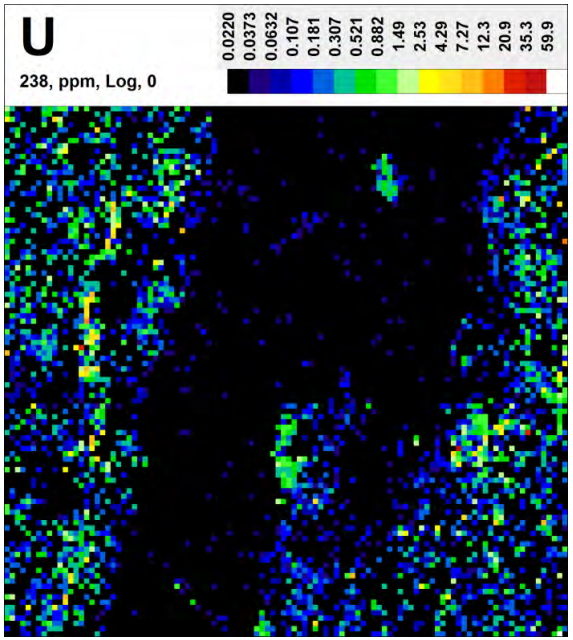
U
238, ppm, Log, 0
0.0220
0.0373
0.0632
0.107
0.181
0.307
0.521
0.882
1.49
2.53
4.29
7.27
12.3
20.9
35.3
59.9

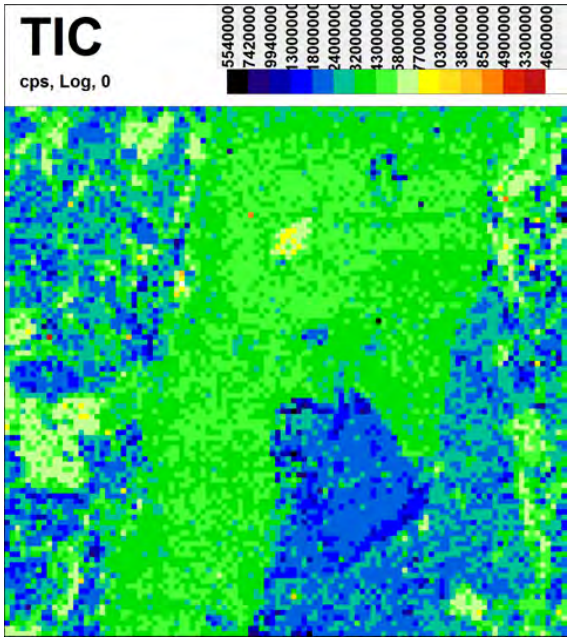
TIC
cps, Log, 0

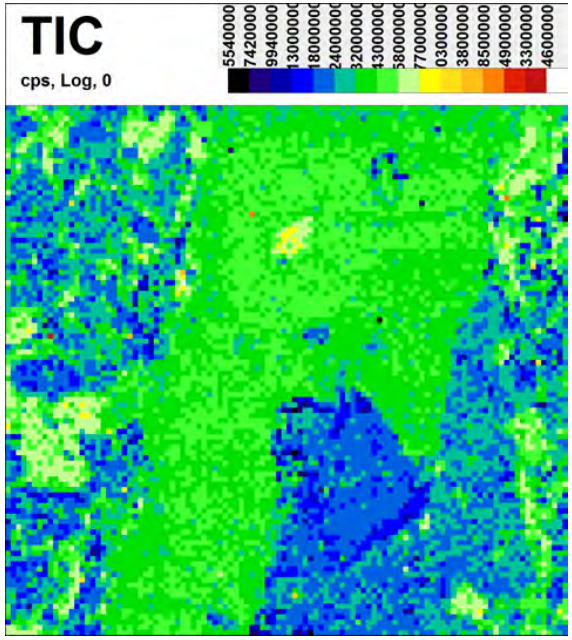
TIC
cps, Log, 0

Figure DR11. (pages 213–241) LA-ICP-MS results of a pinch and swell pyrite domain within a mafic volcanic sample (RD16-I) showing an orientation contrast image of the mapping area and 32 major and trace maps overlapped on the OC image. OC image reveals plastic strain through a complex misorientation pattern overprinted by a brittle fracture. LA-ICP-MS maps reveal Au and other trace elements (Ag-Bi-Te) enrichement at low-angle grain boundaries and brittle fractures. Note, grain boundaries within this sample are devoid of Au. LA-ICP-MS maps without OC underlays are also added.

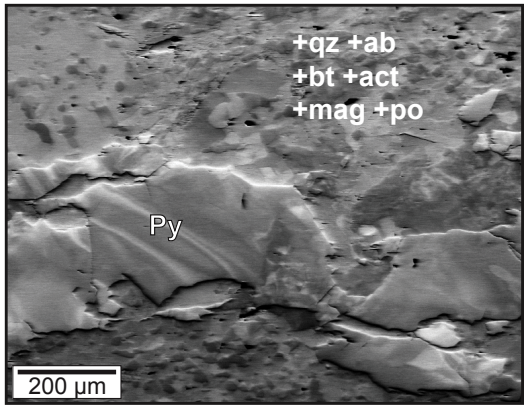
+qz +ab
+bt +act
+mag +po
Py
200 µm

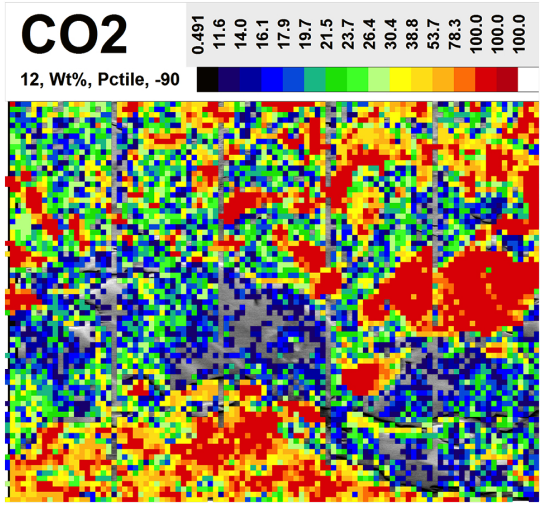
CO2
0.491 11.6 14.0 16.1 17.9 19.7 21.5 23.7 26.4 30.4 38.8 53.7 78.3 100.0 100.0 100.0
12, Wt%, Pctile, -90

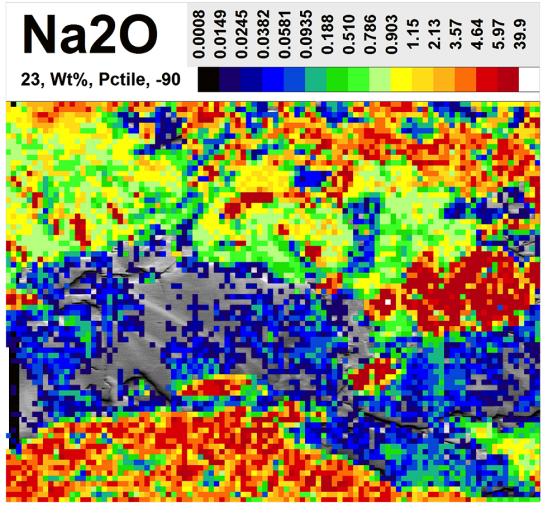
Na2O
0.0008 0.0149 0.0245 0.0382 0.0581 0.0935 0.188 0.510 0.786 0.903 1.15 2.13 3.57 4.64 5.97 39.9
23, Wt%, Pctile, -90

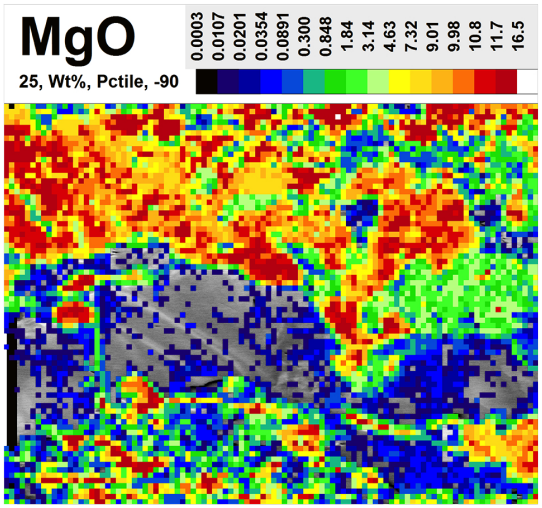
MgO
0.0003 0.0107 0.0201 0.0354 0.0891 0.300 0.848 1.84 3.14 4.63 7.32 9.01 9.98 10.8 11.7 16.5
25, Wt%, Pctile, -90

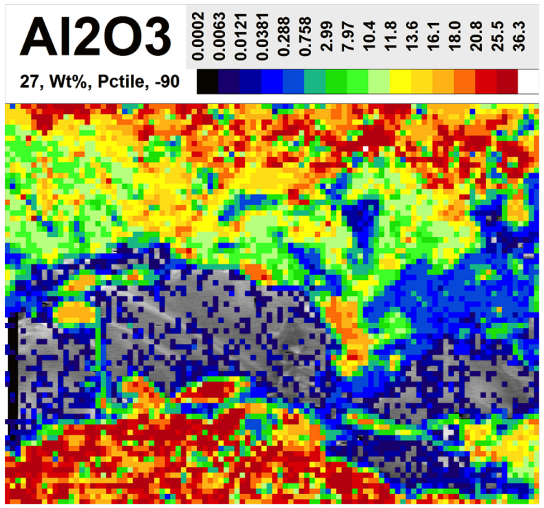
Al2O3
0.0002 0.0063 0.0121 0.0381 0.288 0.758 2.99 7.97 10.4 11.8 13.6 16.1 18.0 20.8 25.5 36.3
27, Wt%, Pctile, -90

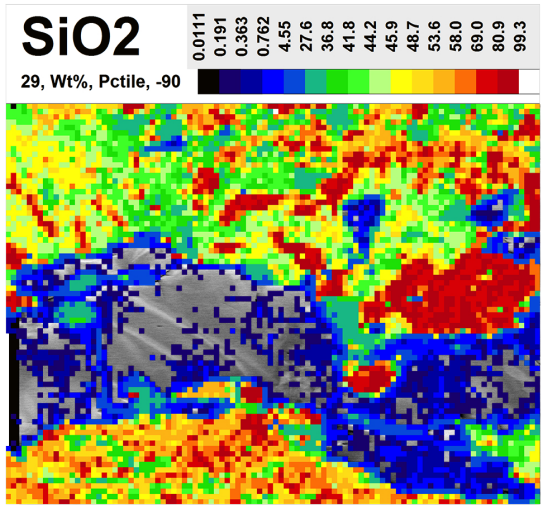
SiO2
0.0111 0.191 0.363 0.762 4.55 27.6 36.8 41.8 44.2 45.9 48.7 53.6 58.0 69.0 80.9 99.3
29, Wt%, Pctile, -90

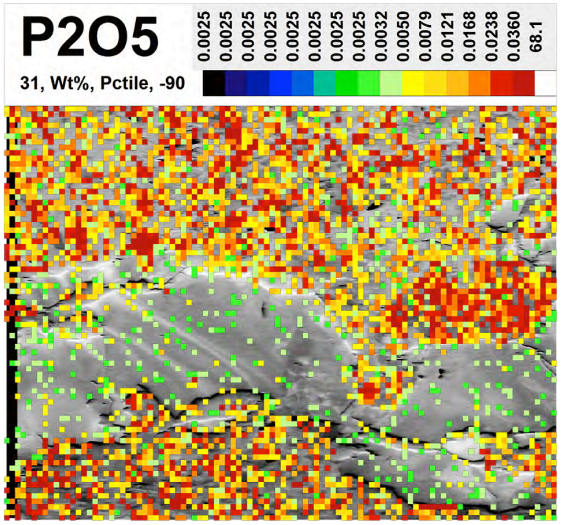
P2O5
0.0025 0.0025 0.0025 0.0025 0.0025 0.0025 0.0025 0.0025 0.0032 0.0050 0.0079 0.0121 0.0168 0.0238 0.0360 68.1
31, Wt%, Pctile, -90

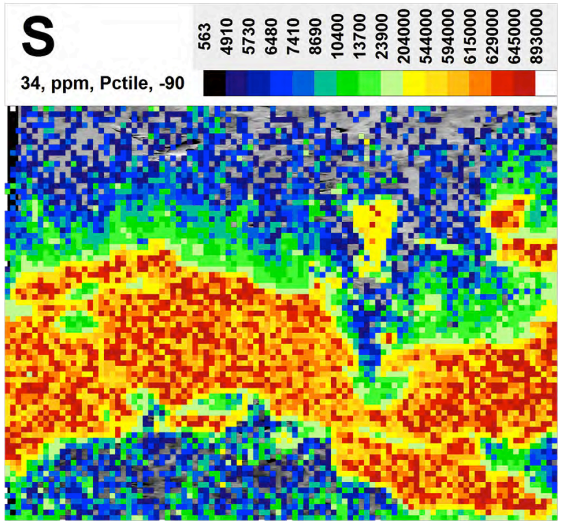
S
563 4910 5730 6480 7410 8690 10400 13700 23900 204000 544000 594000 615000 629000 645000 893000
34, ppm, Pctile, -90

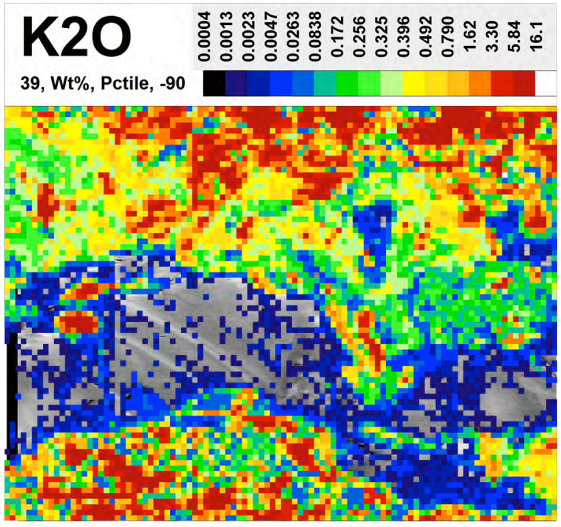
K2O
0.0004 0.0013 0.0023 0.0047 0.0263 0.0838 0.172 0.256 0.325 0.396 0.492 0.790 1.62 3.30 5.84 16.1
39, Wt%, Pctile, -90

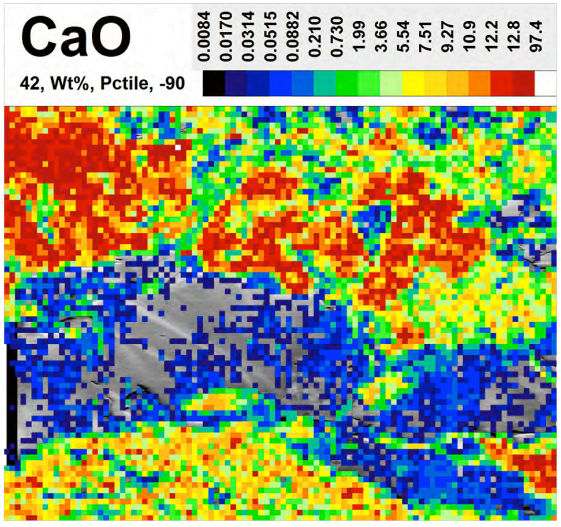
CaO
0.0084 0.0170 0.0314 0.0515 0.0882 0.210 0.730 1.99 3.66 5.54 7.51 9.27 10.9 12.2 12.8 97.4
42, Wt%, Pctile, -90

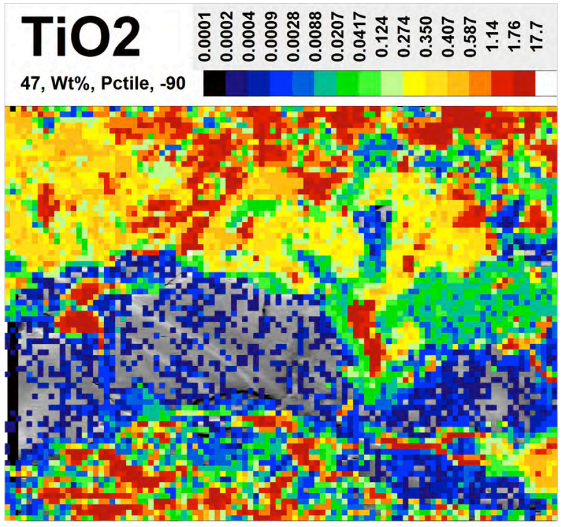
TiO2
0.0001 0.0002 0.0004 0.0009 0.0028 0.0088 0.0207 0.0417 0.124 0.274 0.350 0.407 0.587 1.14 1.76 17.7
47, Wt%, Pctile, -90

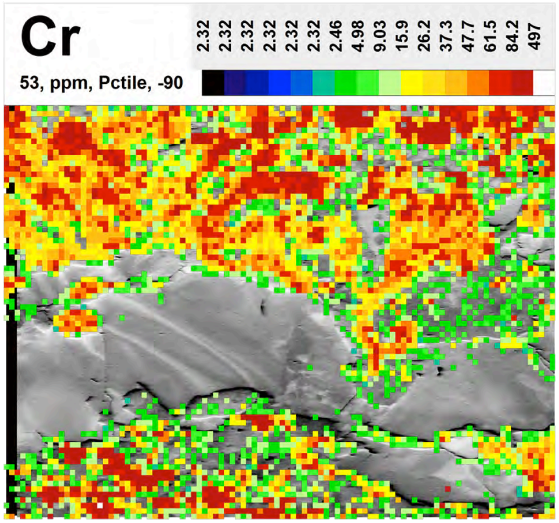
Cr
2.32 2.32 2.32 2.32 2.32 2.46 4.98 9.03 15.9 26.2 37.3 47.7 61.5 84.2 497
53, ppm, Pctile, -90

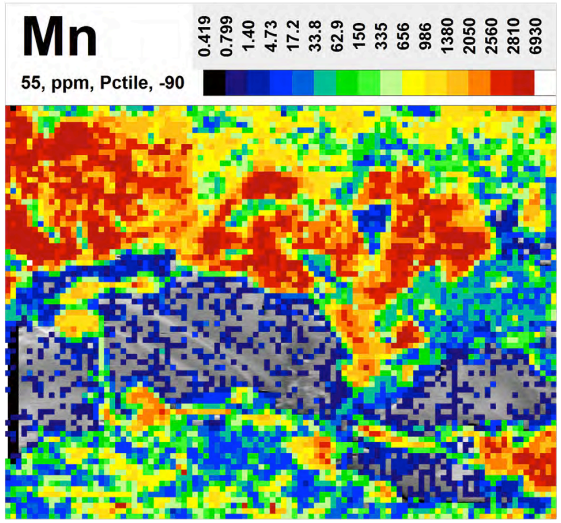
Mn
0.419 0.799 1.40 4.73 17.2 33.8 62.9 150 335 656 986 1380 2050 2560 2810 6930
55, ppm, Pctile, -90

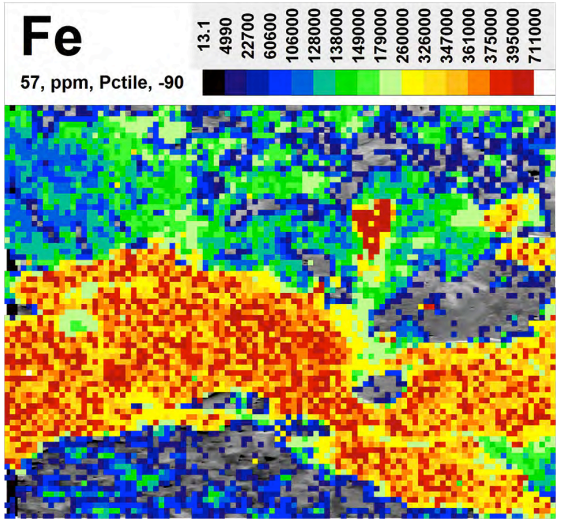
Fe
13.1 4990 22700 60600 106000 128000 138000 149000 179000 260000 326000 347000 361000 375000 395000 711000
57, ppm, Pctile, -90

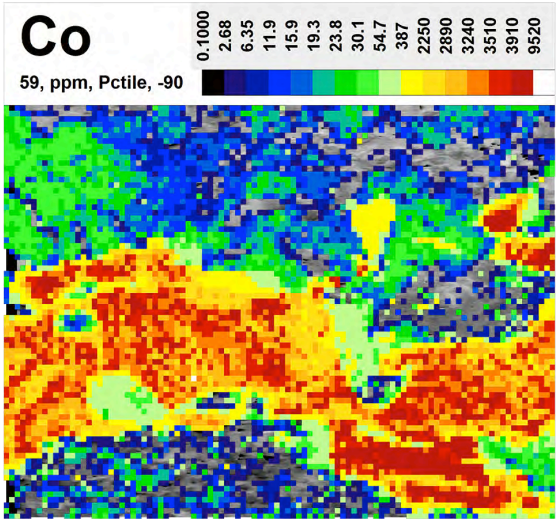
Co
0.1000 2.68 6.35 11.9 15.9 19.3 23.8 30.1 54.7 387 2250 2890 3240 3510 3910 9520
59, ppm, Pctile, -90

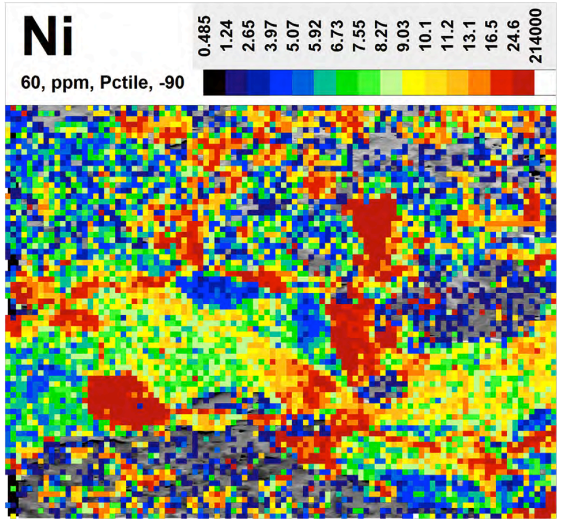
Ni
0.485 1.24 2.65 3.97 5.07 5.92 6.73 7.55 8.27 9.03 10.1 11.2 13.1 16.5 24.6 214000
60, ppm, Pctile, -90

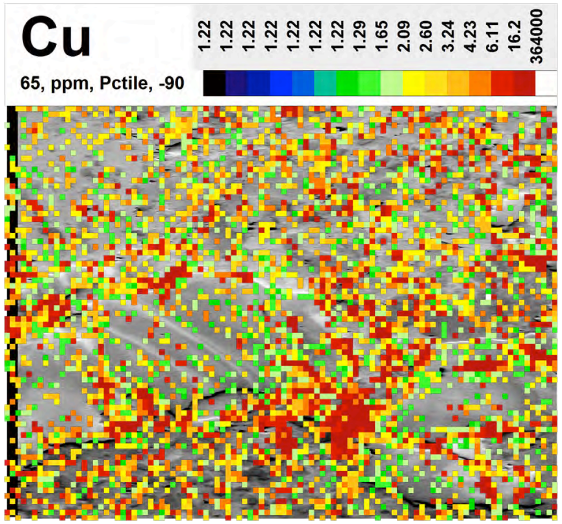
Cu
65, ppm, Pctile, -90
1.22 1.22 1.22 1.22 1.22 1.22 1.22 1.29 1.65 2.09 2.60 3.24 4.23 6.11 16.2 364000

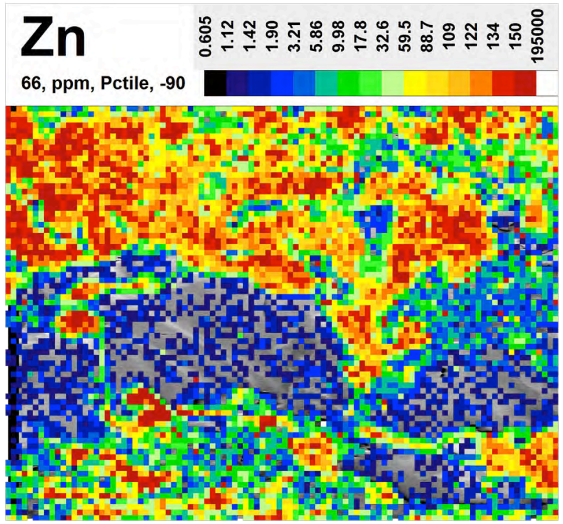
Zn
66, ppm, Pctile, -90
0.605 1.12 1.42 1.90 3.21 5.86 9.98 17.8 32.6 59.5 88.7 109 122 134 150 195000

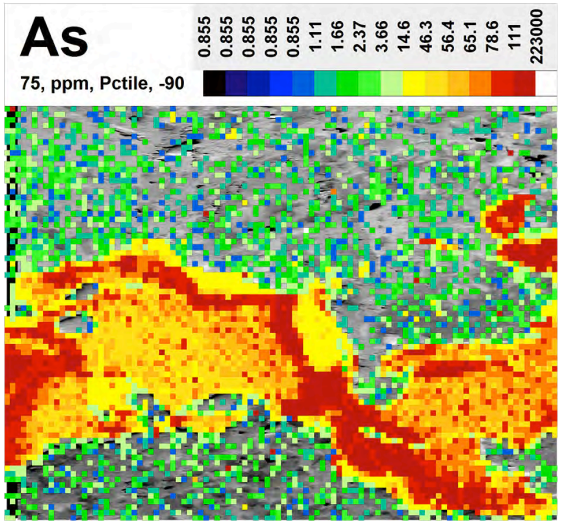
As
75, ppm, Pctile, -90
0.855 0.855 0.855 0.855 0.855 1.11 1.66 2.37 3.66 14.6 46.3 56.4 65.1 78.6 111 223000

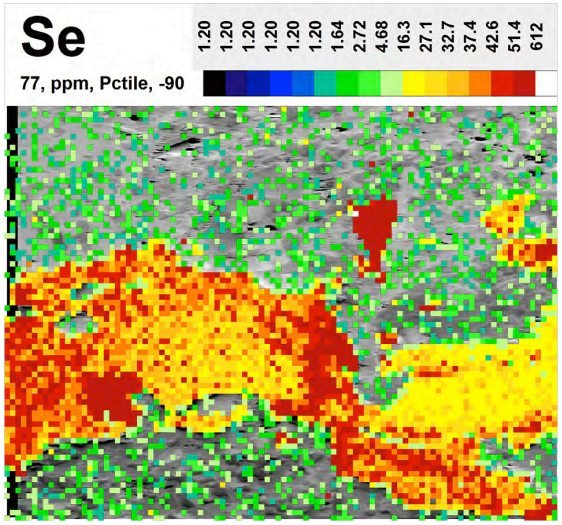
Se
77, ppm, Pctile, -90
1.20 1.20 1.20 1.20 1.20 1.20 1.64 2.72 4.68 16.3 27.1 32.7 37.4 42.6 51.4 612

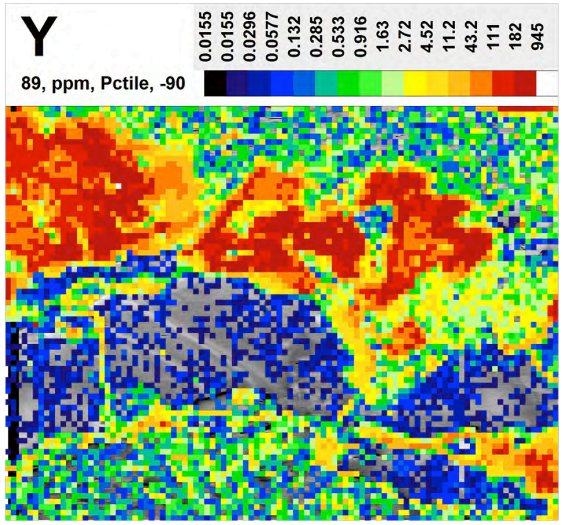
Y
89, ppm, Pctile, -90
0.0155 0.0155 0.0296 0.0577 0.132 0.285 0.533 0.916 1.63 2.72 4.52 11.2 43.2 111 182 945

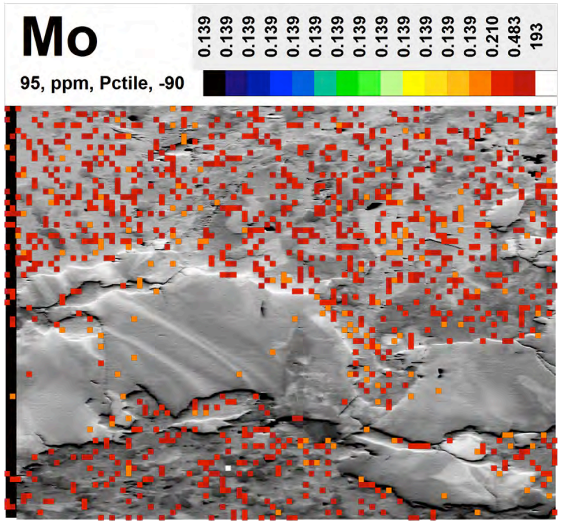
Mo
0.139 0.139 0.139 0.139 0.139 0.139 0.139 0.139 0.139 0.139 0.139 0.139 0.210 0.483 193
95, ppm, Pctile, -90

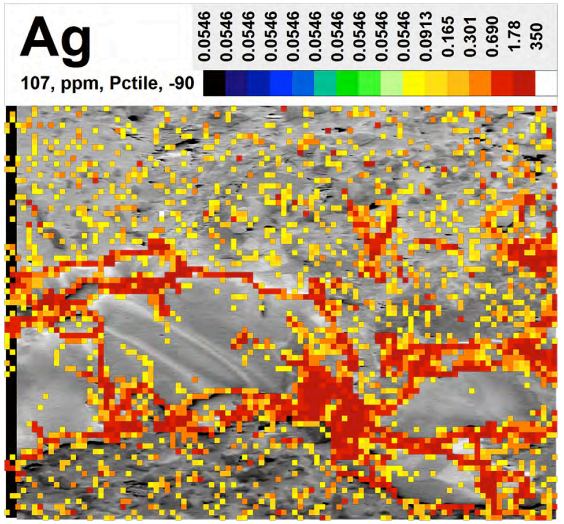
Ag
0.0546 0.0546 0.0546 0.0546 0.0546 0.0546 0.0546 0.0546 0.0546 0.0546 0.0913 0.165 0.301 0.690 1.78 350
107, ppm, Pctile, -90

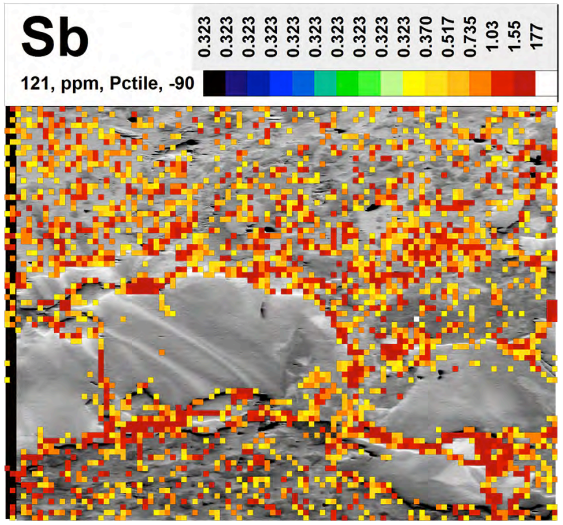
Sb
0.323 0.323 0.323 0.323 0.323 0.323 0.323 0.323 0.323 0.323 0.370 0.517 0.735 1.03 1.55 177
121, ppm, Pctile, -90

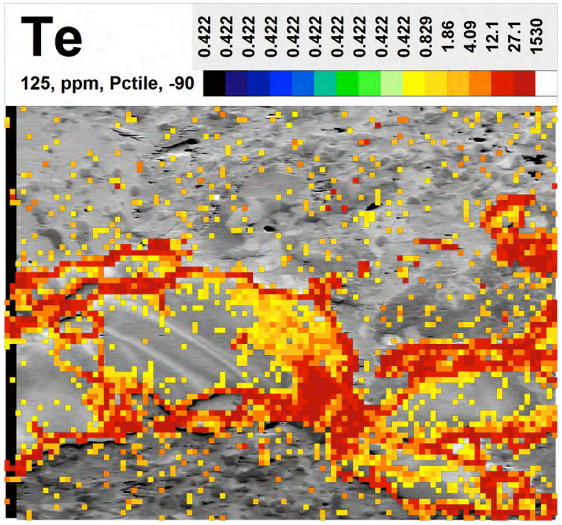
Te
0.422 0.422 0.422 0.422 0.422 0.422 0.422 0.422 0.422 0.422 0.829 1.86 4.09 12.1 27.1 1530
125, ppm, Pctile, -90

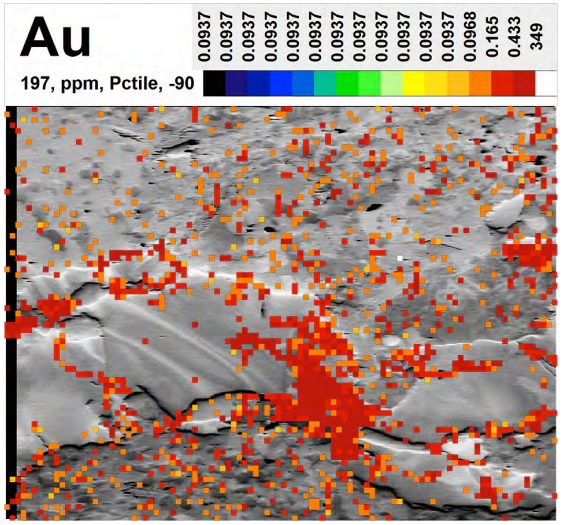
Au
0.0937 0.0937 0.0937 0.0937 0.0937 0.0937 0.0937 0.0937 0.0937 0.0937 0.0937 0.0968 0.165 0.433 349
197, ppm, Pctile, -90

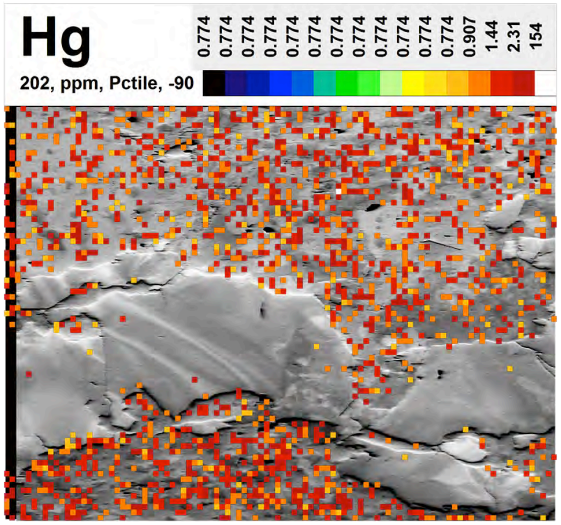
Hg
202, ppm, Pctile, -90
0.774 0.774 0.774 0.774 0.774 0.774 0.774 0.774 0.774 0.774 0.774 0.907 1.44 2.31 154

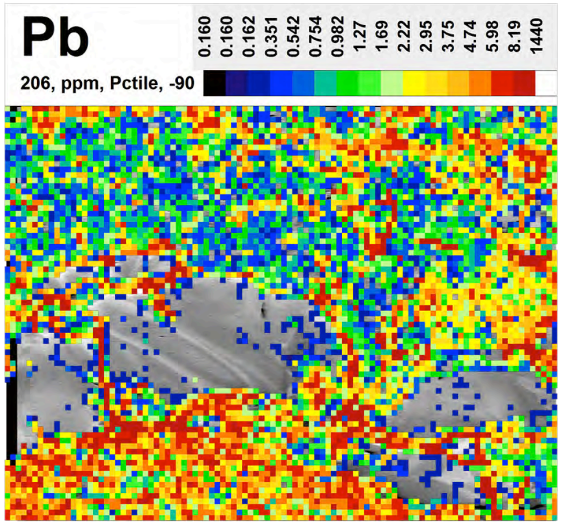
Pb
206, ppm, Pctile, -90
0.160 0.160 0.162 0.351 0.542 0.754 0.982 1.27 1.69 2.22 2.95 3.75 4.74 5.98 8.19 1440

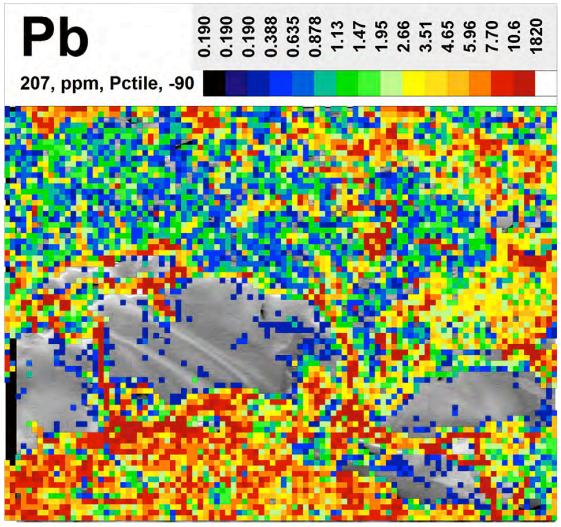
Pb
207, ppm, Pctile, -90
0.190 0.190 0.190 0.388 0.635 0.878 1.13 1.47 1.95 2.66 3.51 4.65 5.96 7.70 10.6 1820

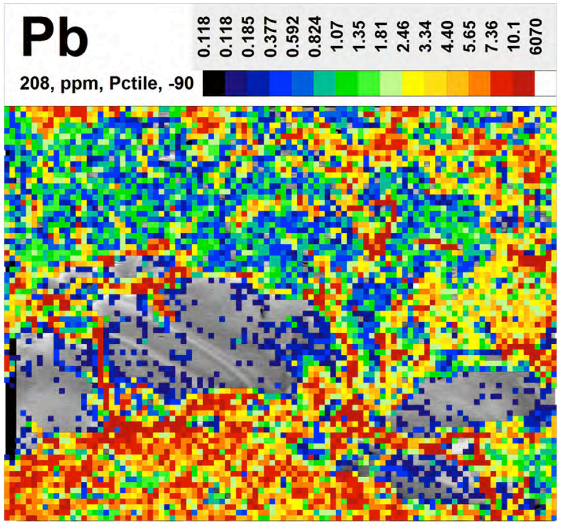
Pb
208, ppm, Pctile, -90
0.118 0.118 0.185 0.377 0.592 0.824 1.07 1.35 1.81 2.46 3.34 4.40 5.65 7.36 10.1 6070

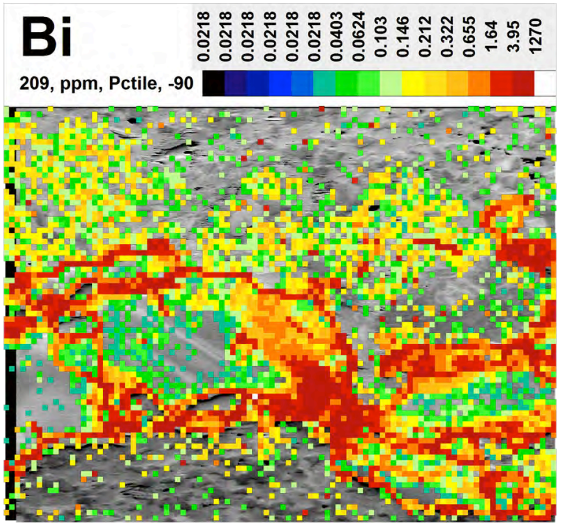
Bi
209, ppm, Pctile, -90
0.0218 0.0218 0.0218 0.0218 0.0218 0.0218 0.0403 0.0624 0.103 0.146 0.212 0.322 0.655 1.64 3.95 1270

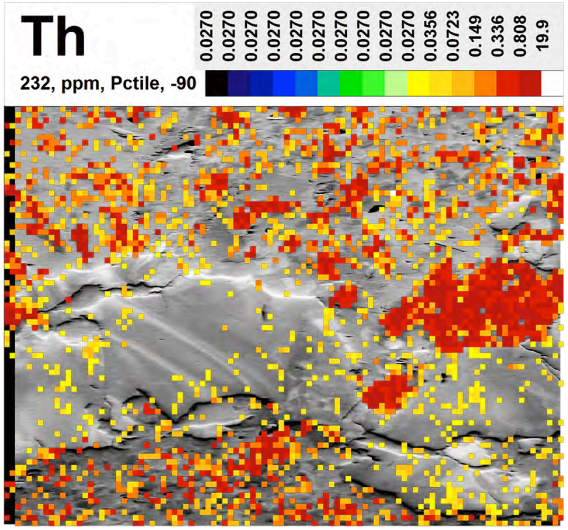
Th
232, ppm, Pctile, -90
0.0270
0.0270
0.0270
0.0270
0.0270
0.0270
0.0270
0.0270
0.0270
0.0356
0.0723
0.149
0.336
0.808
19.9

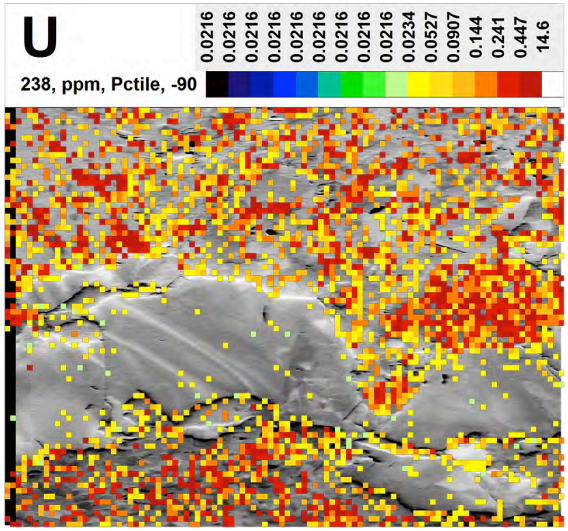
U
238, ppm, Pctile, -90
0.0216
0.0216
0.0216
0.0216
0.0216
0.0216
0.0216
0.0216
0.0234
0.0527
0.0907
0.144
0.241
0.447
14.6

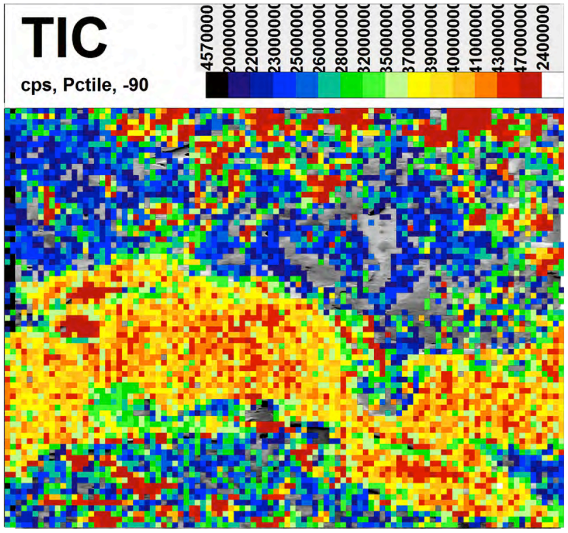
TIC
cps, Pctile, -90

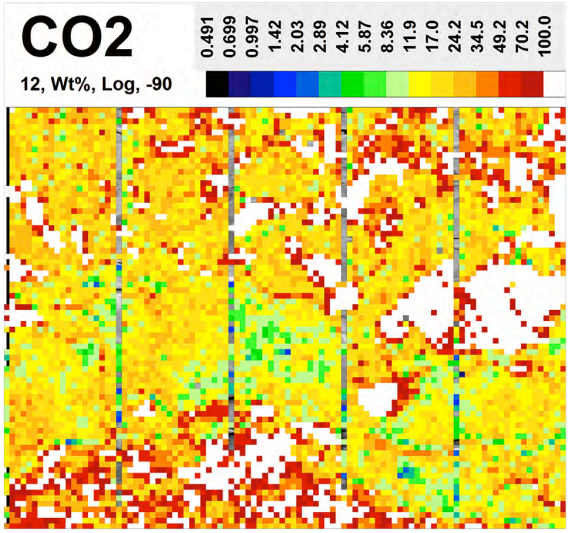
CO2
12, Wt%, Log, -90
0.491 0.699 0.997 1.42 2.03 2.89 4.12 5.87 8.36 11.9 17.0 24.2 34.5 49.2 70.2 100.0

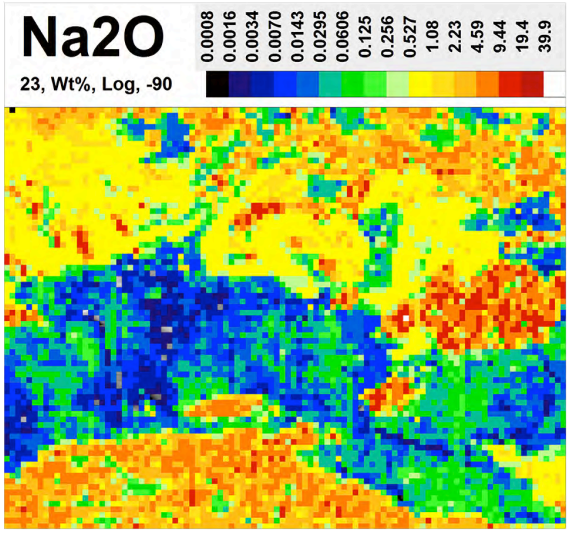
Na2O
23, Wt%, Log, -90
0.0008 0.0016 0.0034 0.0070 0.0143 0.0295 0.0606 0.125 0.256 0.527 1.08 2.23 4.59 9.44 19.4 39.9

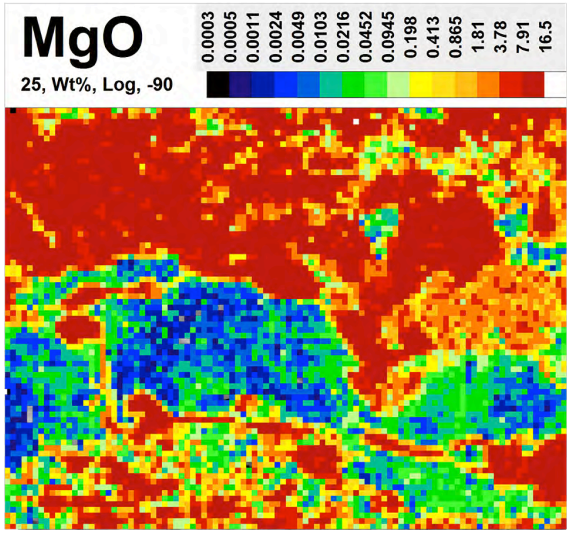
MgO
25, Wt%, Log, -90
0.0003 0.0005 0.0011 0.0024 0.0049 0.0103 0.0216 0.0452 0.0945 0.198 0.413 0.865 1.81 3.78 7.91 16.5

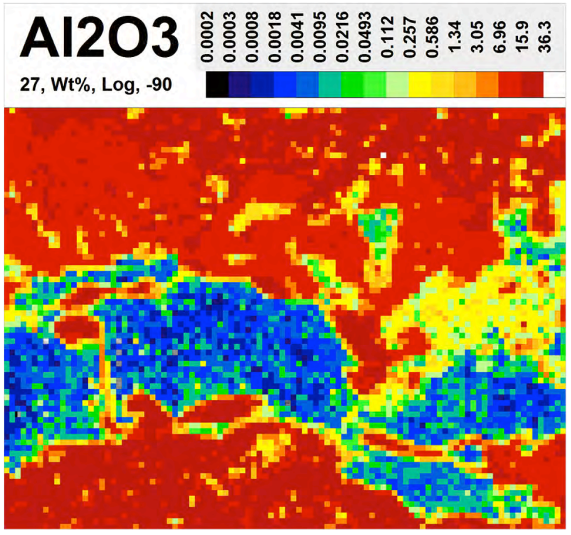
Al2O3
27, Wt%, Log, -90
0.0002 0.0003 0.0008 0.0018 0.0041 0.0095 0.0216 0.0493 0.112 0.257 0.586 1.34 3.05 6.96 15.9 36.3

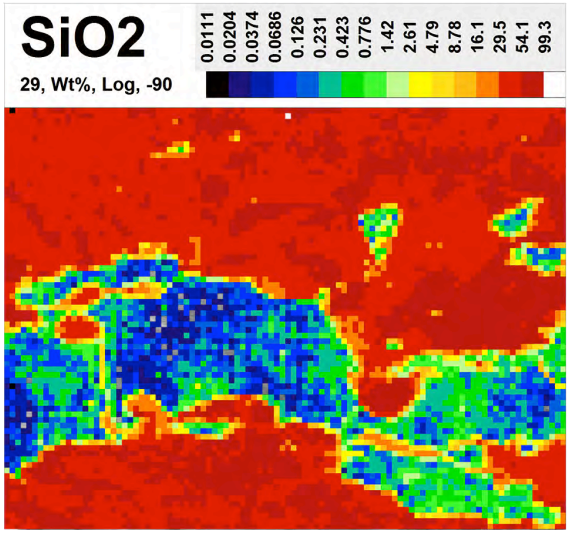
SiO2
29, Wt%, Log, -90
0.0111 0.0204 0.0374 0.0686 0.126 0.231 0.423 0.776 1.42 2.61 4.79 8.78 16.1 29.5 54.1 99.3

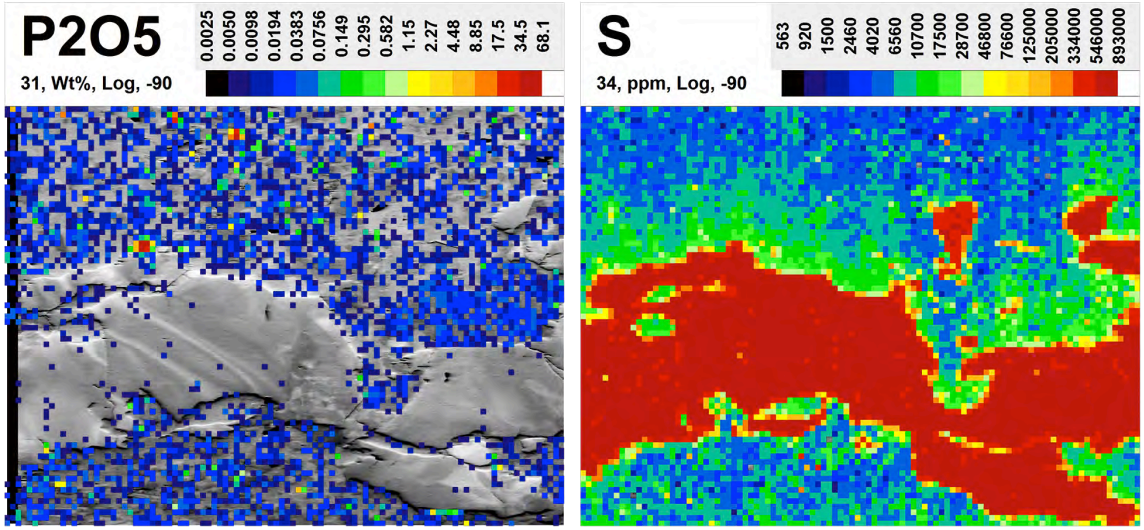
P2O5
31, Wt%, Log, -90
0.0025 0.0050 0.0098 0.0194 0.0383 0.0756 0.149 0.295 0.582 1.15 2.27 4.48 8.85 17.5 34.5 68.1
S
34, ppm, Log, -90
563 920 1500 2460 4020 6560 10700 17500 28700 46800 76600 125000 205000 334000 546000 893000

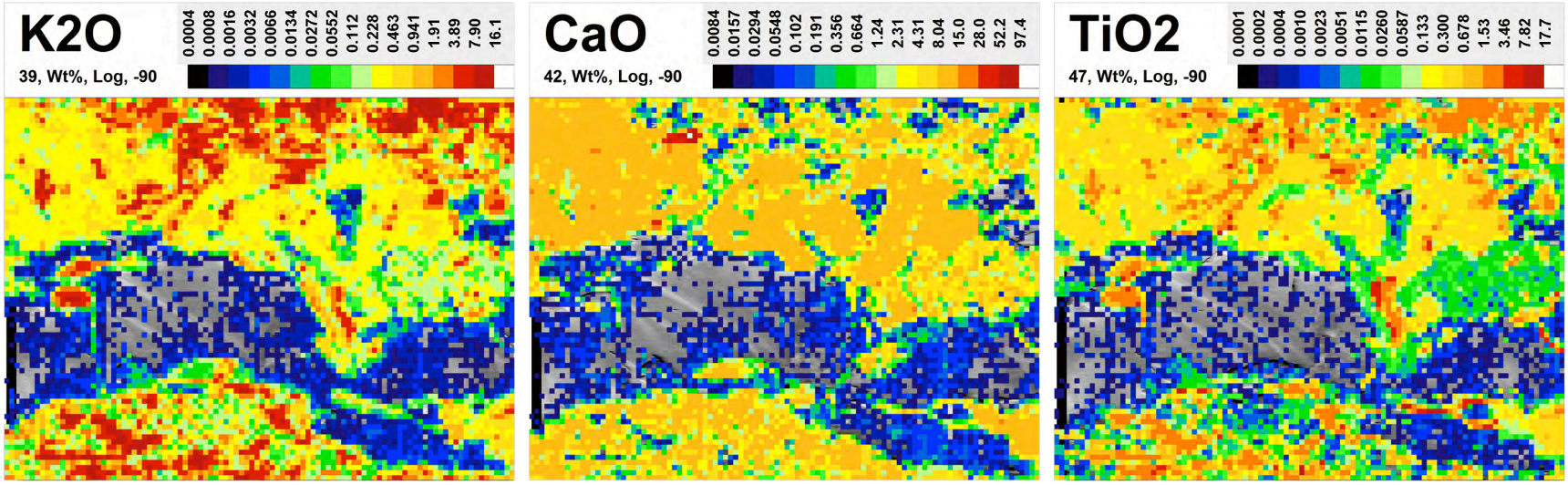
K2O
39, Wt%, Log, -90
0.0004 0.0008 0.0016 0.0032 0.0066 0.0134 0.0272 0.0552 0.112 0.228 0.463 0.941 1.91 3.89 7.90 16.1
CaO
42, Wt%, Log, -90
0.0084 0.0157 0.0294 0.0548 0.102 0.191 0.356 0.664 1.24 2.31 4.31 8.04 15.0 28.0 52.2 97.4
TiO2
47, Wt%, Log, -90
0.0001 0.0002 0.0004 0.0010 0.0023 0.0051 0.0115 0.0260 0.0587 0.133 0.300 0.678 1.53 3.46 7.82 17.7

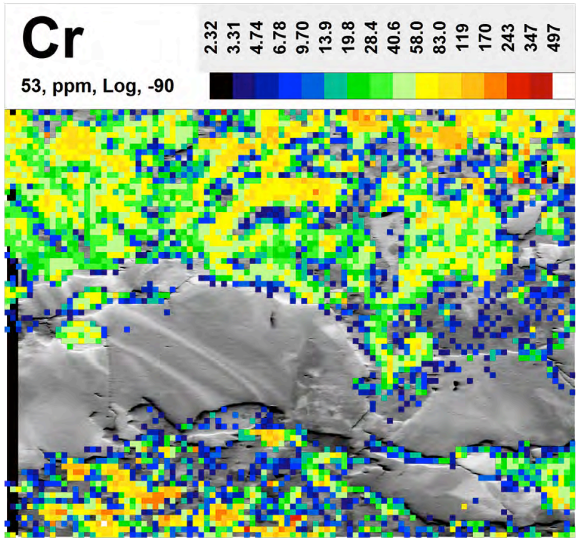
Cr
53, ppm, Log, -90
2.32 3.31 4.74 6.78 9.70 13.9 19.8 28.4 40.6 58.0 83.0 119 170 243 347 497

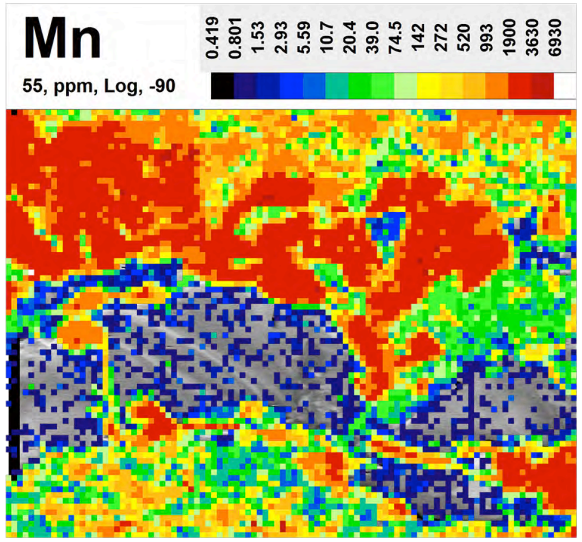
Mn
55, ppm, Log, -90
0.419 0.801 1.53 2.93 5.59 10.7 20.4 39.0 74.5 142 272 520 993 1900 3630 6930

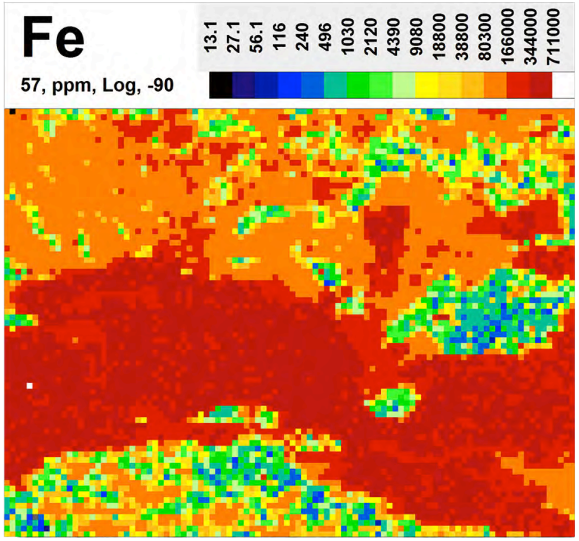
Fe
57, ppm, Log, -90
13.1 27.1 56.1 116 240 496 1030 2120 4390 9080 18800 38800 80300 166000 344000 711000

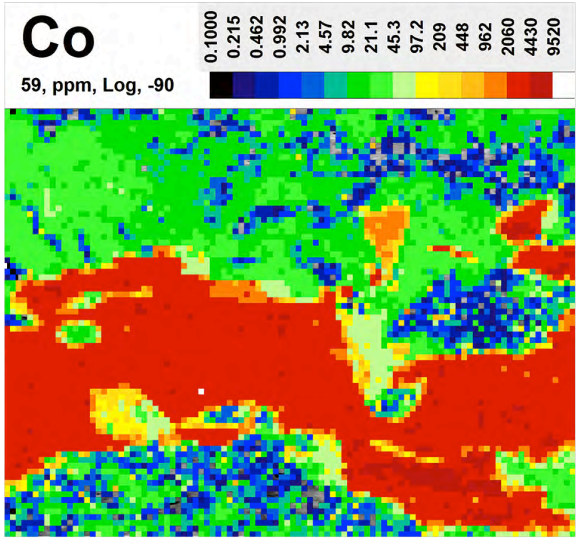
Co
59, ppm, Log, -90
0.1000 0.215 0.462 0.992 2.13 4.57 9.82 21.1 45.3 97.2 209 448 962 2060 4430 9520

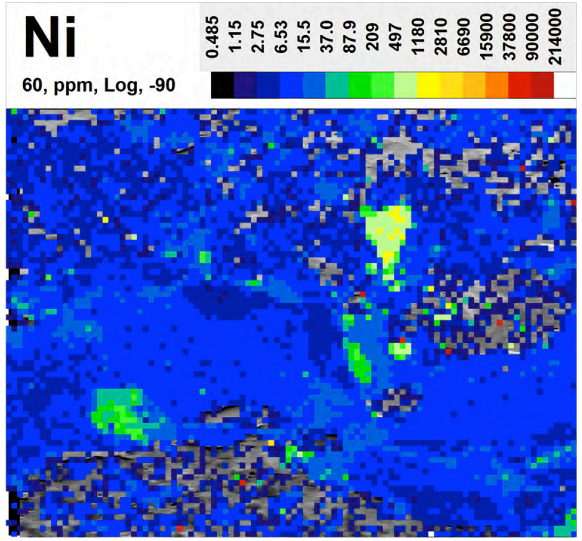
Ni
60, ppm, Log, -90
0.485 1.15 2.75 6.53 15.5 37.0 87.9 209 497 1180 2810 6690 15900 37800 90000 214000

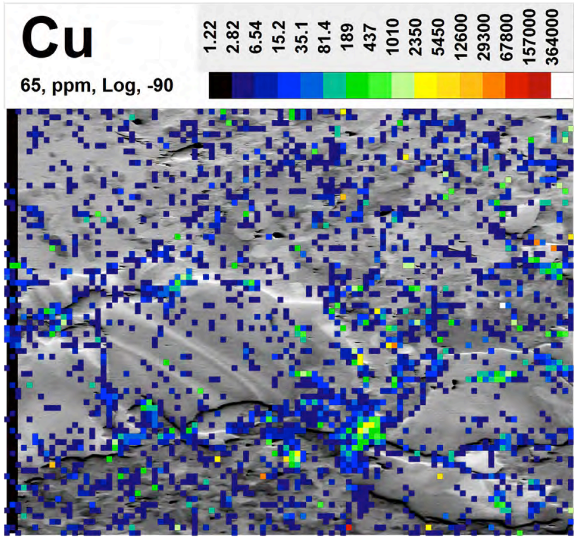
Cu
65, ppm, Log, -90
1.22 2.82 6.54 15.2 35.1 81.4 189 437 1010 2350 5450 12600 29300 67800 157000 364000

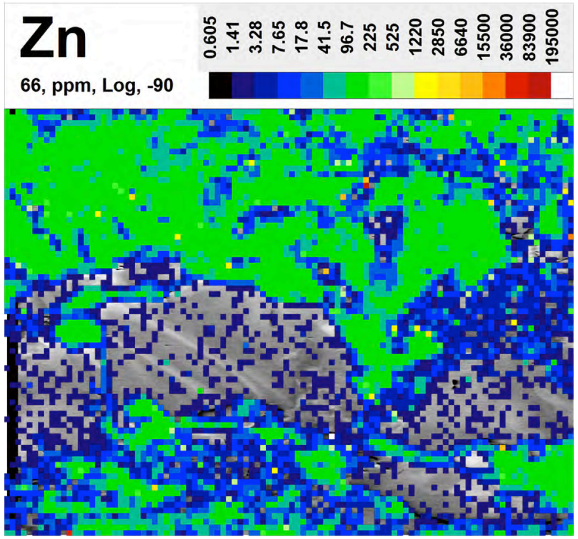
Zn
66, ppm, Log, -90
0.605 1.41 3.28 7.65 17.8 41.5 96.7 225 525 1220 2850 6640 15500 36000 83900 195000

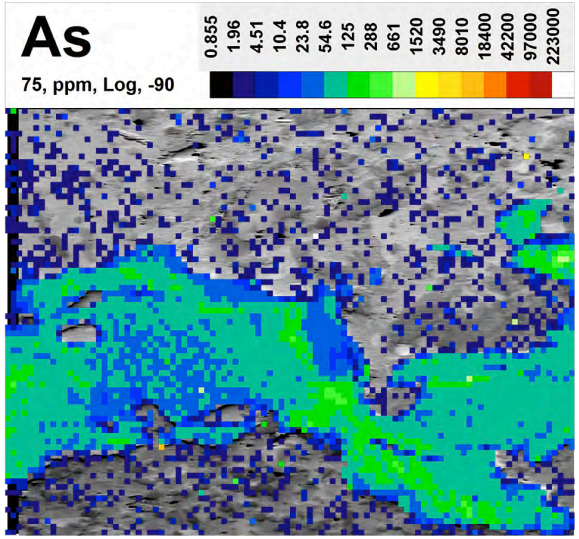
As
75, ppm, Log, -90
0.855 1.96 4.51 10.4 23.8 54.6 125 288 661 1520 3490 8010 18400 42200 97000 223000

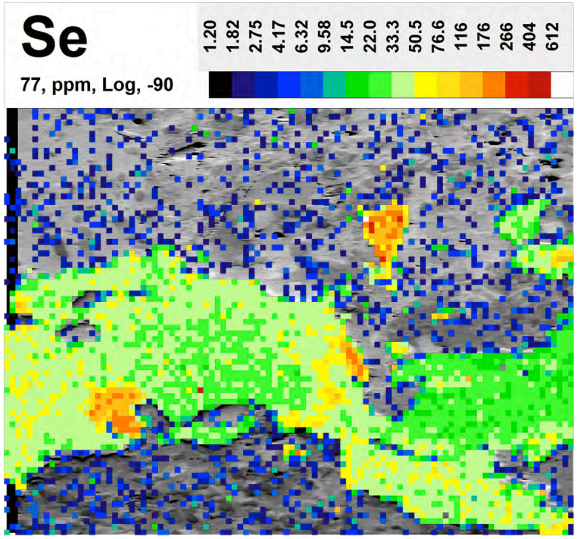
Se
77, ppm, Log, -90
1.20 1.82 2.75 4.17 6.32 9.58 14.5 22.0 33.3 50.5 76.6 116 176 266 404 612

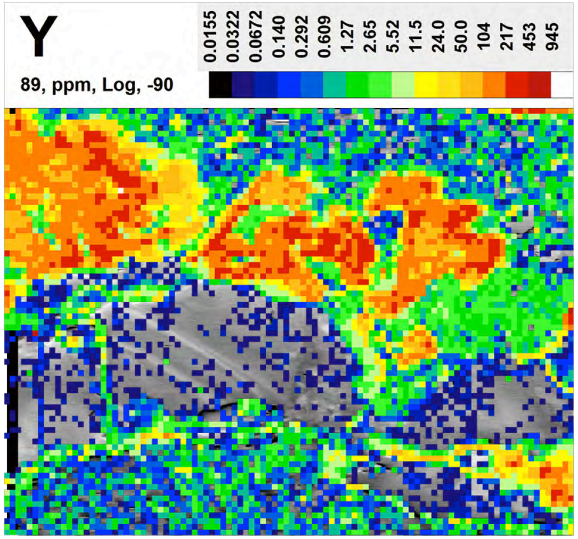
Y
89, ppm, Log, -90
0.0155 0.0322 0.0672 0.140 0.292 0.609 1.27 2.65 5.52 11.5 24.0 50.0 104 217 453 945

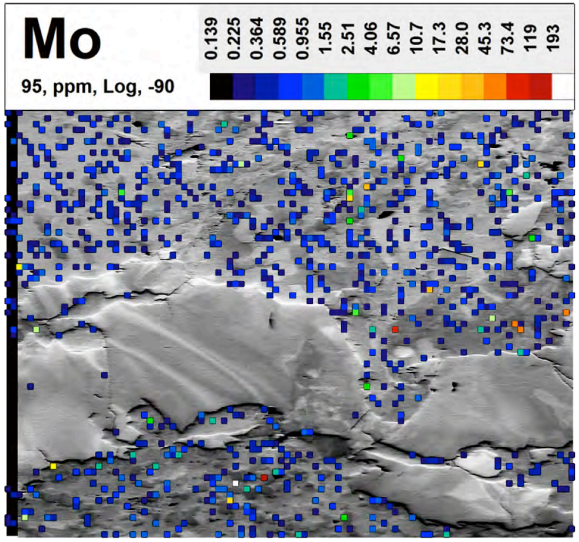
Mo
95, ppm, Log, -90
0.139 0.225 0.364 0.589 0.955 1.55 2.51 4.06 6.57 10.7 17.3 28.0 45.3 73.4 119 193

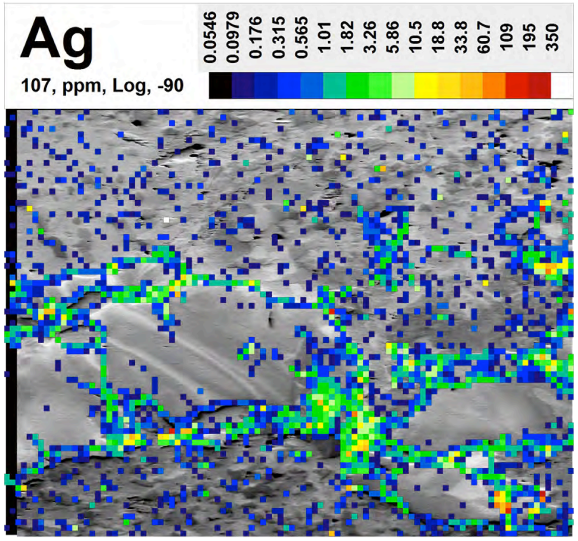
Ag
107, ppm, Log, -90
0.0546 0.0979 0.176 0.315 0.565 1.01 1.82 3.26 5.86 10.5 18.8 33.8 60.7 109 195 350

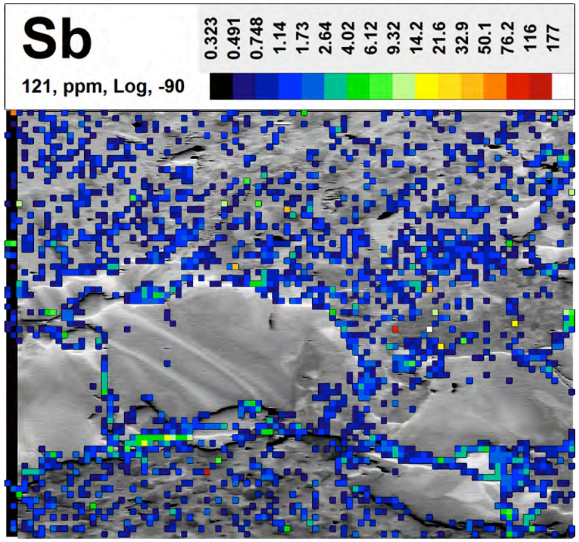
Sb
121, ppm, Log, -90
0.323 0.491 0.748 1.14 1.73 2.64 4.02 6.12 9.32 14.2 21.6 32.9 50.1 76.2 116 177

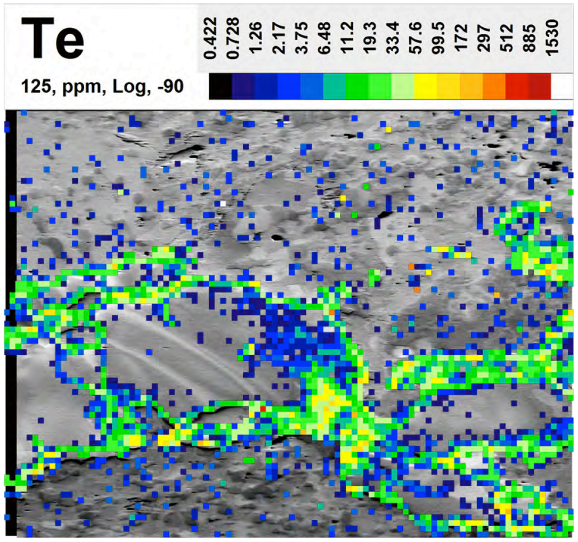
Te
125, ppm, Log, -90
0.422 0.728 1.26 2.17 3.75 6.48 11.2 19.3 33.4 57.6 99.5 172 297 512 885 1530

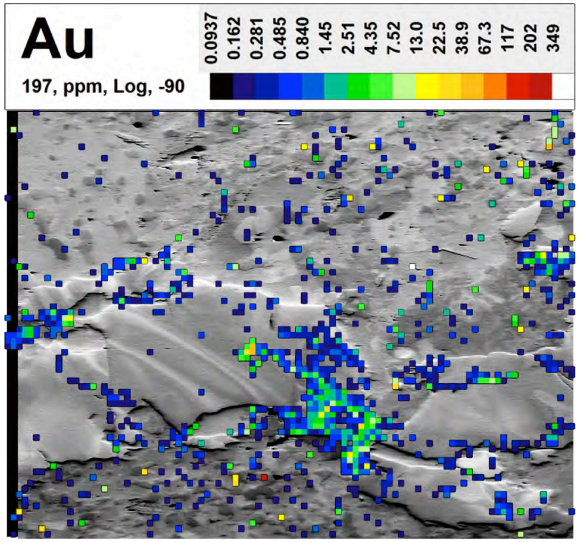
Au
197, ppm, Log, -90
0.0937 0.162 0.281 0.485 0.840 1.45 2.51 4.35 7.52 13.0 22.5 38.9 67.3 117 202 349

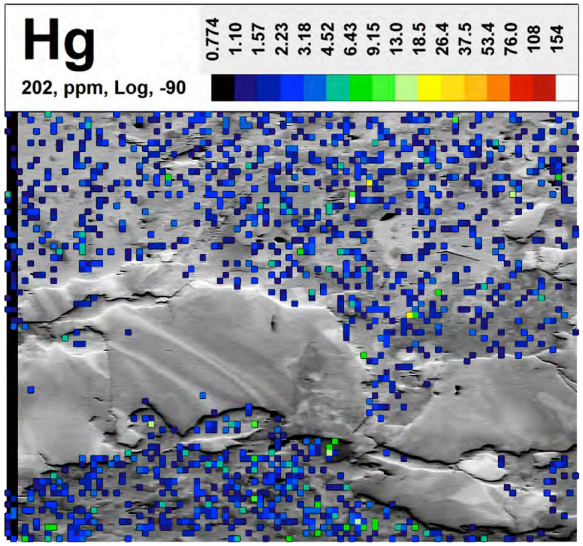
Hg
202, ppm, Log, -90
0.774
1.10
1.57
2.23
3.18
4.52
6.43
9.15
13.0
18.5
26.4
37.5
53.4
76.0
108
154

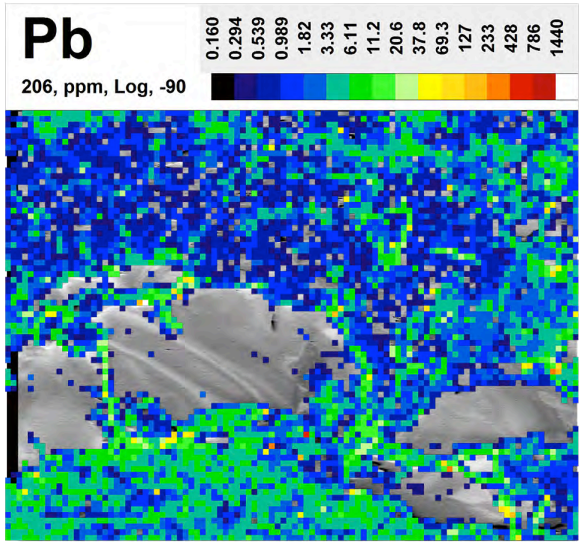
Pb
206, ppm, Log, -90
0.160
0.294
0.539
0.989
1.82
3.33
6.11
11.2
20.6
37.8
69.3
127
233
428
786
1440

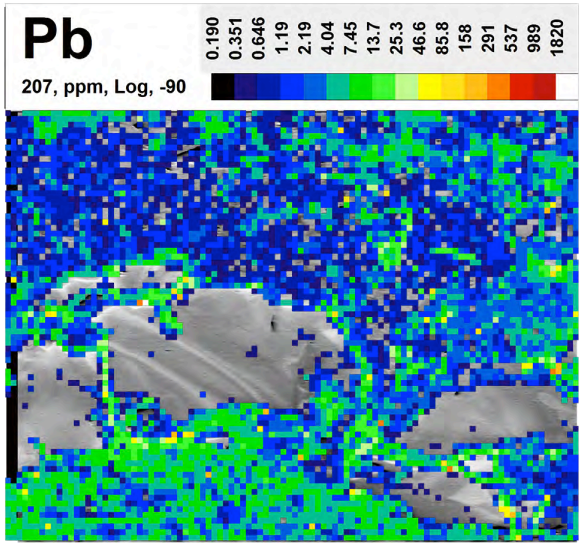
Pb
207, ppm, Log, -90
0.190
0.351
0.646
1.19
2.19
4.04
7.45
13.7
25.3
46.6
85.8
158
291
537
989
1820

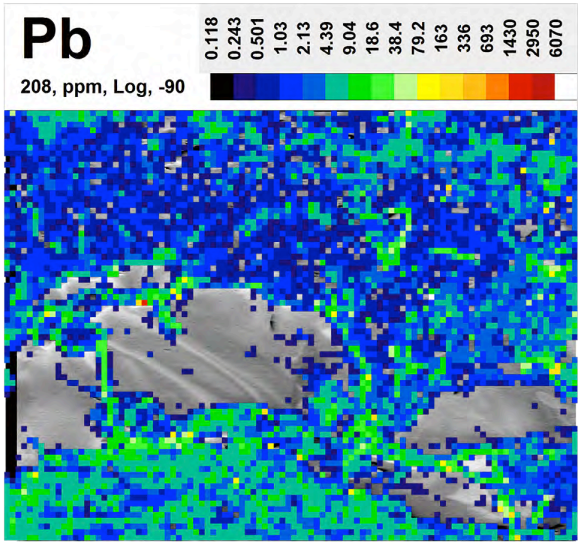
Pb
208, ppm, Log, -90
0.118
0.243
0.501
1.03
2.13
4.39
9.04
18.6
38.4
79.2
163
336
693
1430
2950
6070

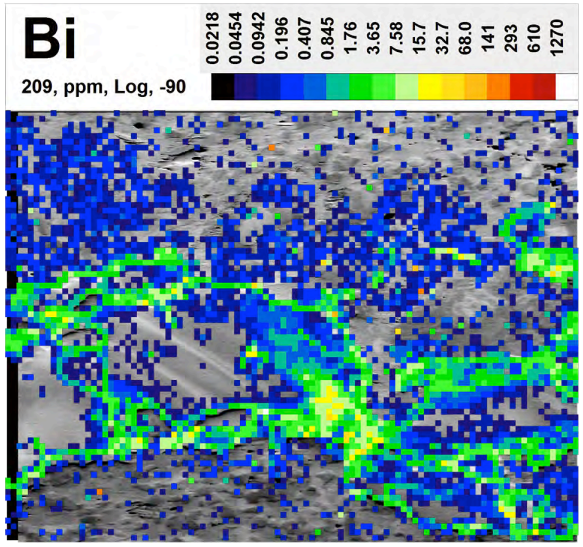
Bi
209, ppm, Log, -90
0.0218
0.0454
0.0942
0.196
0.407
0.845
1.76
3.65
7.58
15.7
32.7
68.0
141
293
610
1270

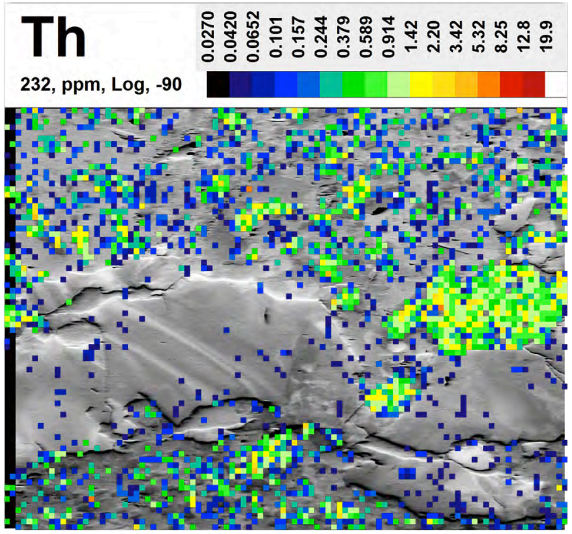
Th
232, ppm, Log, -90
0.0270
0.0420
0.0652
0.101
0.157
0.244
0.379
0.589
0.914
1.42
2.20
3.42
5.32
8.25
12.8
19.9

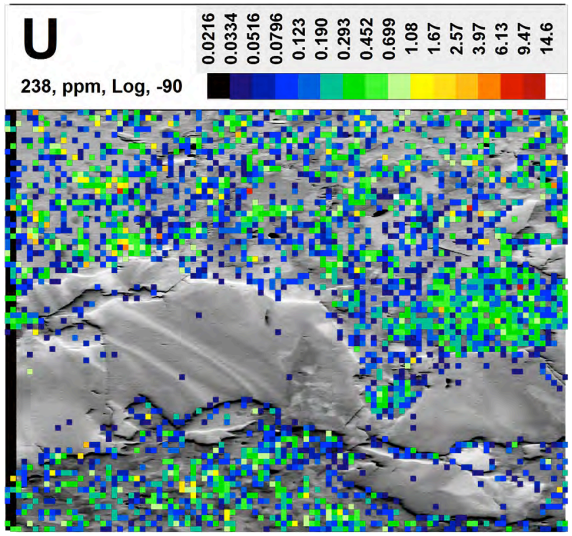
U
238, ppm, Log, -90
0.0216
0.0334
0.0516
0.0796
0.123
0.190
0.293
0.452
0.699
1.08
1.67
2.57
3.97
6.13
9.47
14.6

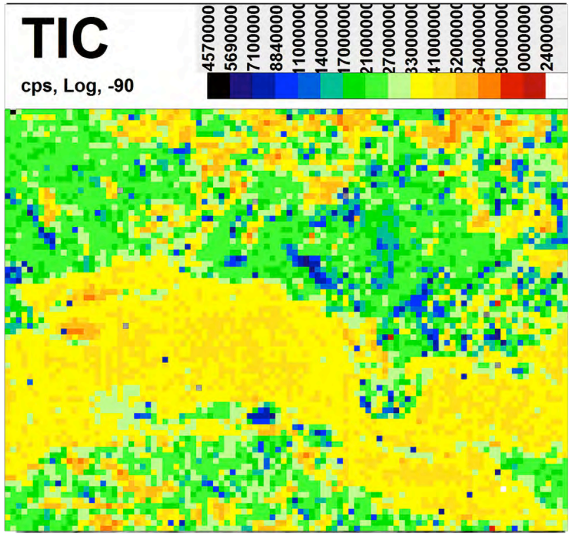
TIC
cps, Log, -90

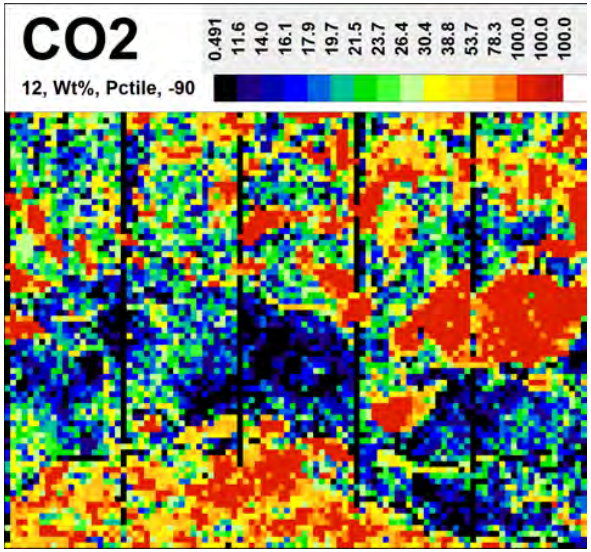
CO2
0.491 11.6 14.0 16.1 17.9 19.7 21.5 23.7 26.4 30.4 38.8 53.7 78.3 100.0 100.0 100.0
12, Wt%, Pctile, -90

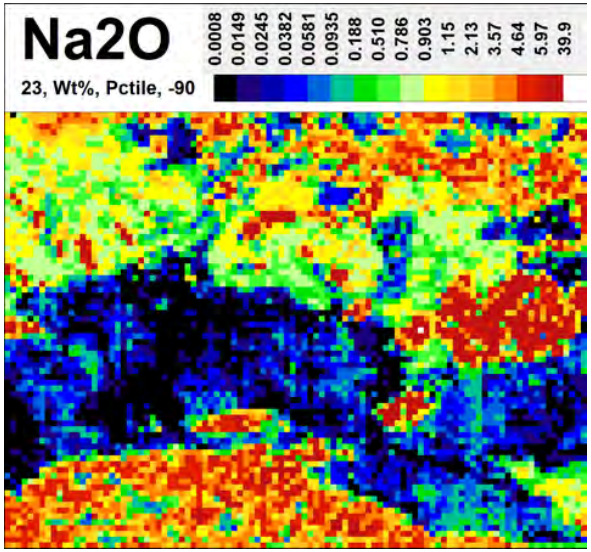
Na2O
0.0008 0.0149 0.0245 0.0382 0.0581 0.0935 0.188 0.510 0.786 0.903 1.15 2.13 3.57 4.64 5.97 39.9
23, Wt%, Pctile, -90

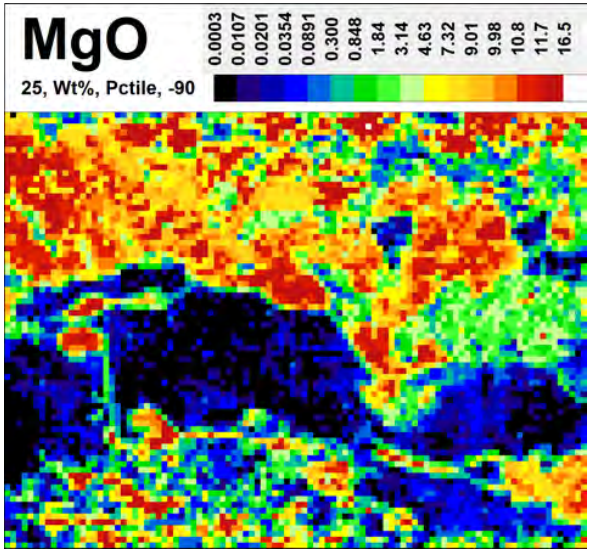
MgO
0.0003 0.0107 0.0201 0.0354 0.0891 0.300 0.848 1.84 3.14 4.63 7.32 9.01 9.98 10.8 11.7 16.5
25, Wt%, Pctile, -90

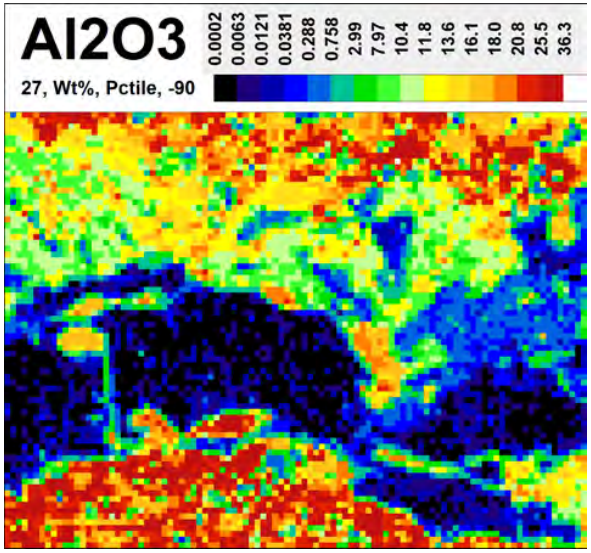
Al2O3
0.0002 0.0063 0.0121 0.0381 0.288 0.758 2.99 7.97 10.4 11.8 13.6 16.1 18.0 20.8 25.5 36.3
27, Wt%, Pctile, -90

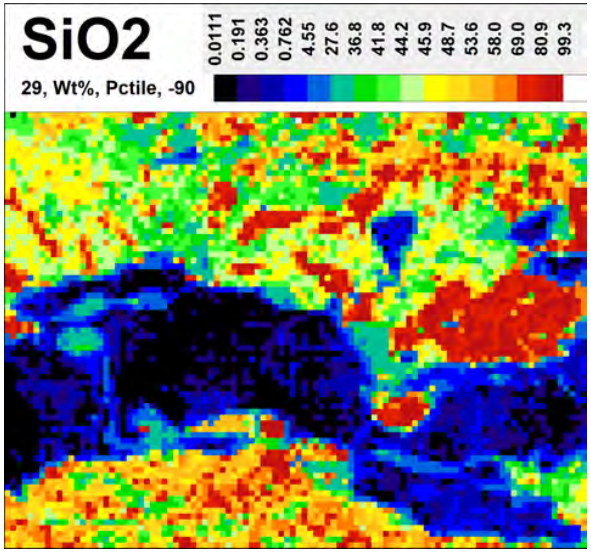
SiO2
0.0111 0.191 0.363 0.762 4.55 27.6 36.8 41.8 44.2 45.9 48.7 53.6 58.0 69.0 80.9 99.3
29, Wt%, Pctile, -90

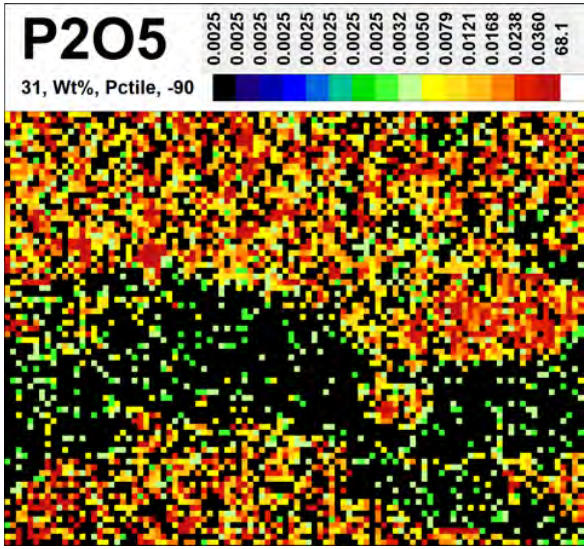
P2O5
0.0025 0.0025 0.0025 0.0025 0.0025 0.0025 0.0025 0.0025 0.0032 0.0050 0.0079 0.0121 0.0168 0.0238 0.0360 68.1
31, Wt%, Pctile, -90

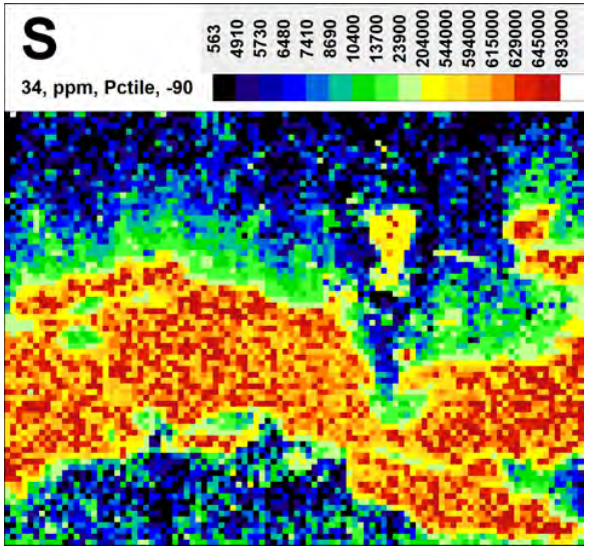
S
563 4910 5730 6480 7410 8690 10400 13700 23900 204000 544000 594000 615000 629000 645000 893000
34, ppm, Pctile, -90

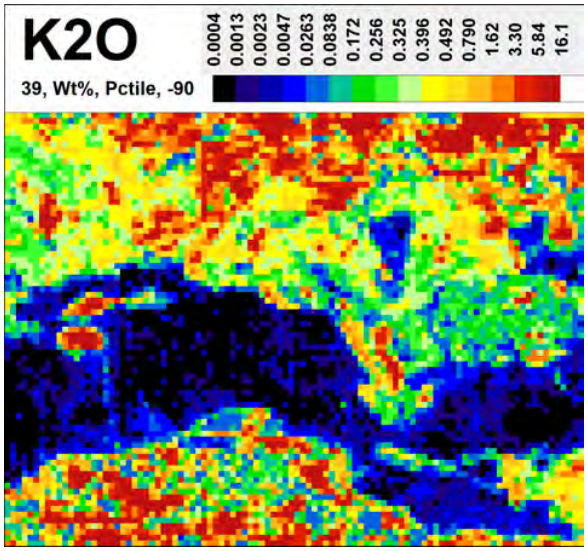
K2O
0.0004 0.0013 0.0023 0.0047 0.0263 0.0838 0.172 0.256 0.325 0.396 0.492 0.790 1.62 3.30 5.84 16.1
39, Wt%, Pctile, -90

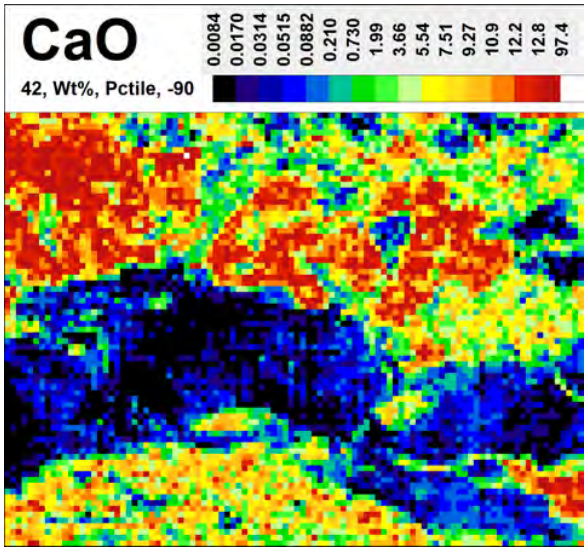
CaO
0.0084 0.0170 0.0314 0.0515 0.0882 0.210 0.730 1.99 3.66 5.54 7.51 9.27 10.9 12.2 12.8 97.4
42, Wt%, Pctile, -90

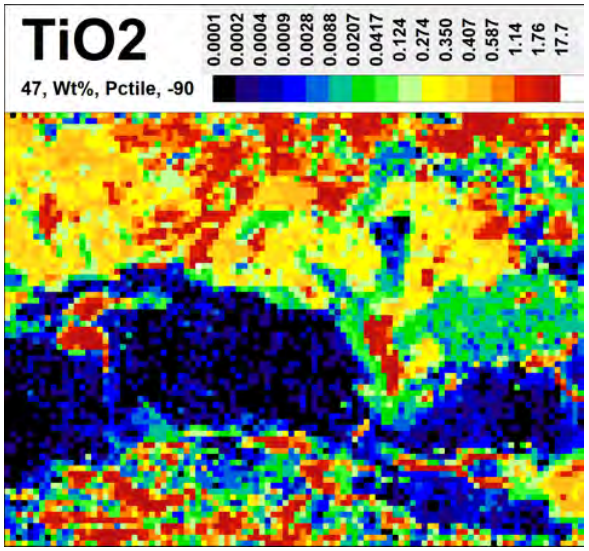
TiO2
0.0001 0.0002 0.0004 0.0009 0.0028 0.0088 0.0207 0.0417 0.124 0.274 0.350 0.407 0.587 1.14 1.76 17.7
47, Wt%, Pctile, -90

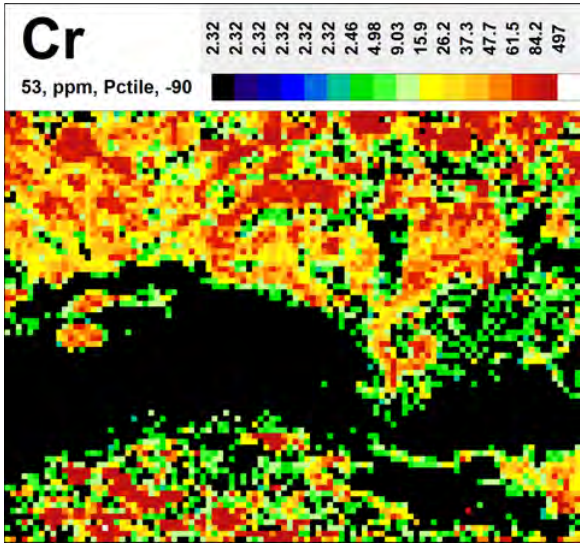
Cr
2.32 2.32 2.32 2.32 2.32 2.32 2.46 4.98 9.03 15.9 26.2 37.3 47.7 61.5 84.2 497
53, ppm, Pctile, -90

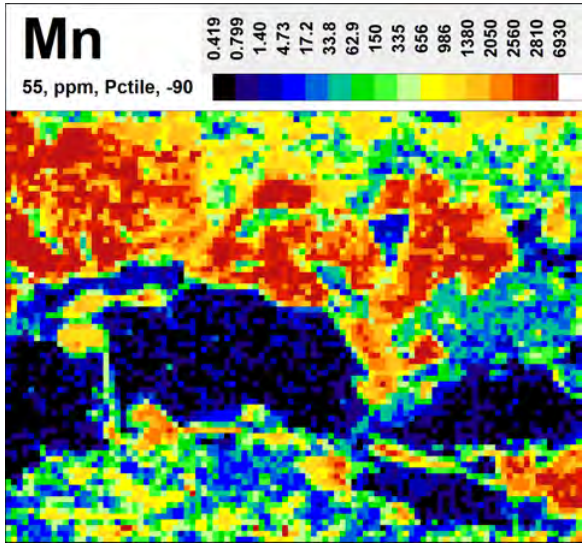
Mn
0.419 0.799 1.40 4.73 17.2 33.8 62.9 150 335 656 986 1380 2050 2560 2810 6930
55, ppm, Pctile, -90

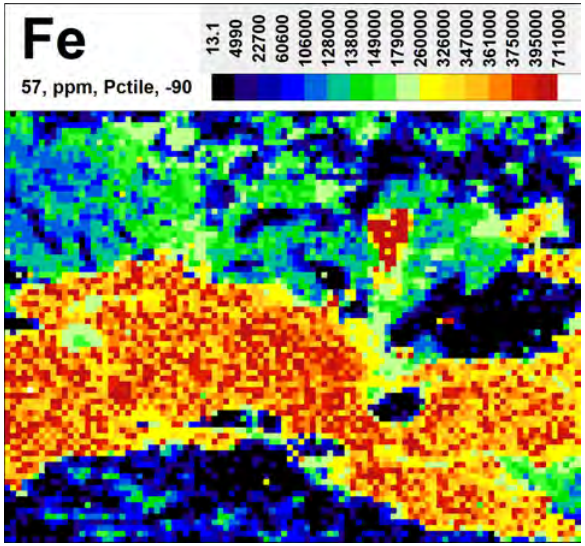
Fe
13.1 4990 22700 60600 106000 128000 138000 149000 179000 260000 326000 347000 361000 375000 395000 711000
57, ppm, Pctile, -90

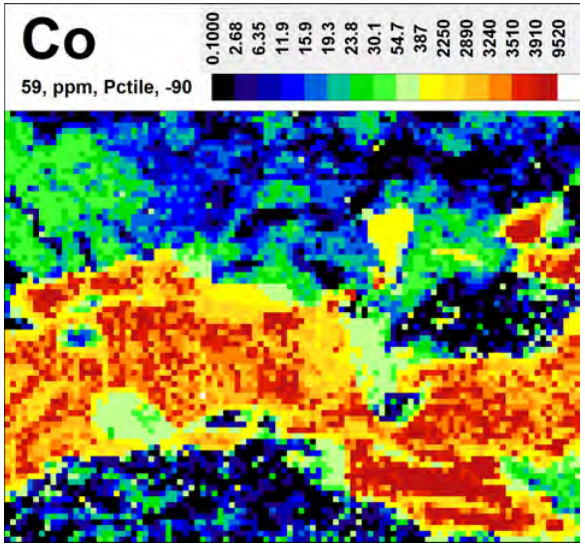
Co
0.1000 2.68 6.35 11.9 15.9 19.3 23.8 30.1 54.7 387 2250 2890 3240 3510 3910 9520
59, ppm, Pctile, -90

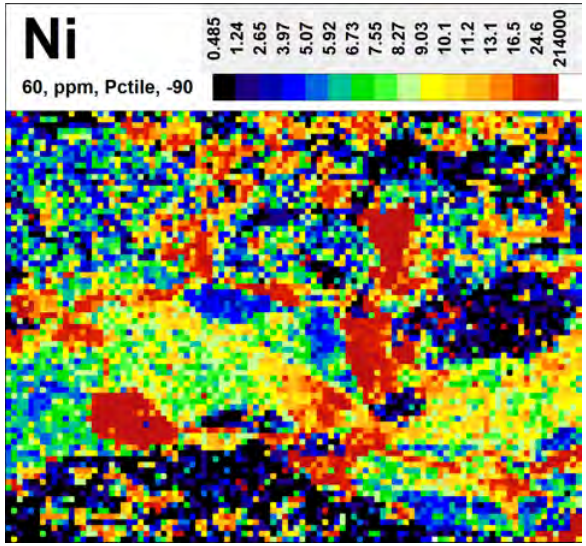
Ni
0.485 1.24 2.65 3.97 5.07 5.92 6.73 7.55 8.27 9.03 10.1 11.2 13.1 16.5 24.6 214000
60, ppm, Pctile, -90

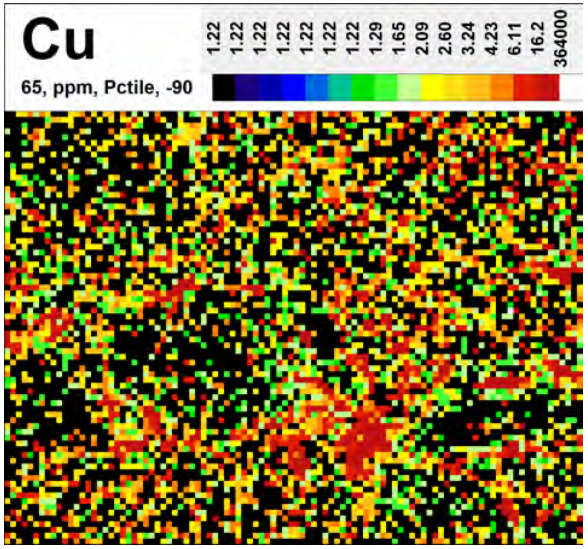
Cu
65, ppm, Pctile, -90
1.22 1.22 1.22 1.22 1.22 1.22 1.22 1.29 1.65 2.09 2.60 3.24 4.23 6.11 16.2 364000

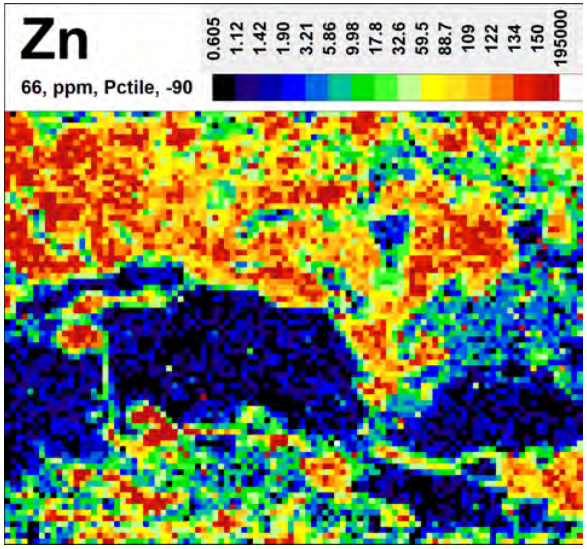
Zn
66, ppm, Pctile, -90
0.605 1.12 1.42 1.90 3.21 5.86 9.98 17.8 32.6 59.5 88.7 109 122 134 150 195000

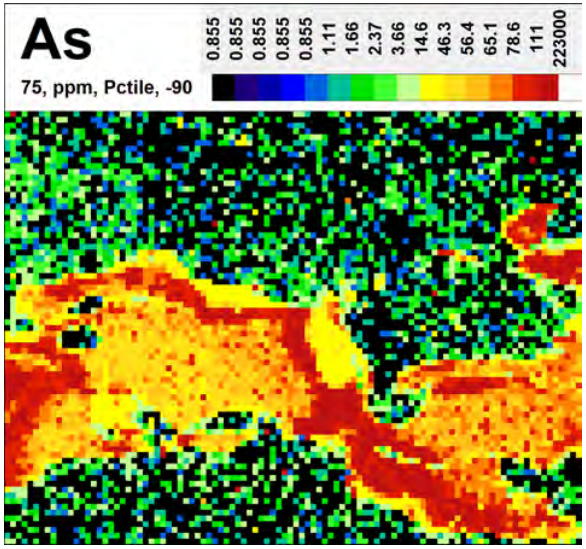
As
75, ppm, Pctile, -90
0.855 0.855 0.855 0.855 0.855 1.11 1.66 2.37 3.66 14.6 46.3 56.4 65.1 78.6 111 223000

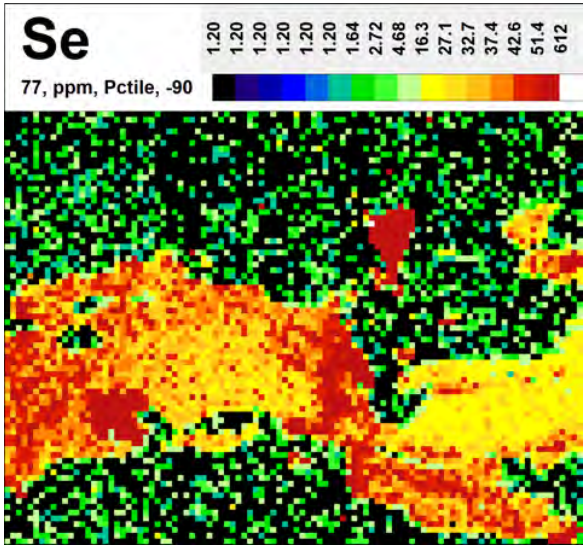
Se
77, ppm, Pctile, -90
1.20 1.20 1.20 1.20 1.20 1.20 1.64 2.72 4.68 16.3 27.1 32.7 37.4 42.6 51.4 612

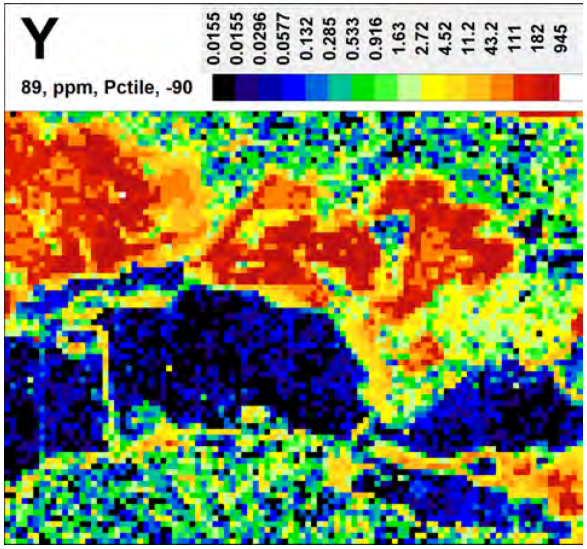
Y
89, ppm, Pctile, -90
0.0155 0.0155 0.0296 0.0577 0.132 0.285 0.533 0.916 1.63 2.72 4.52 11.2 43.2 111 182 945

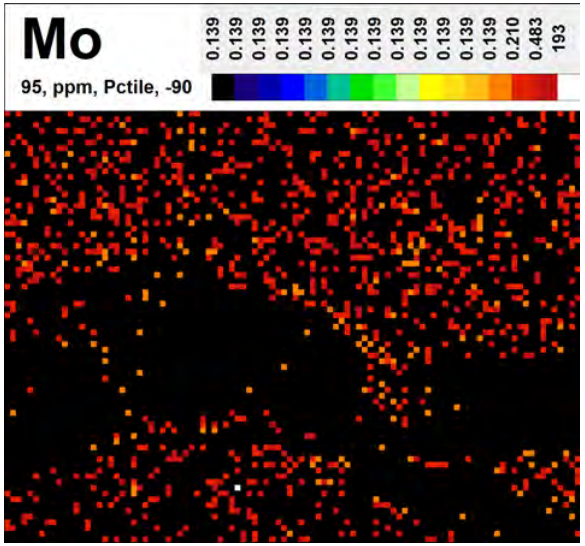
Mo
95, ppm, Pctile, -90
0.139 0.139 0.139 0.139 0.139 0.139 0.139 0.139 0.139 0.139 0.139 0.210 0.483 193

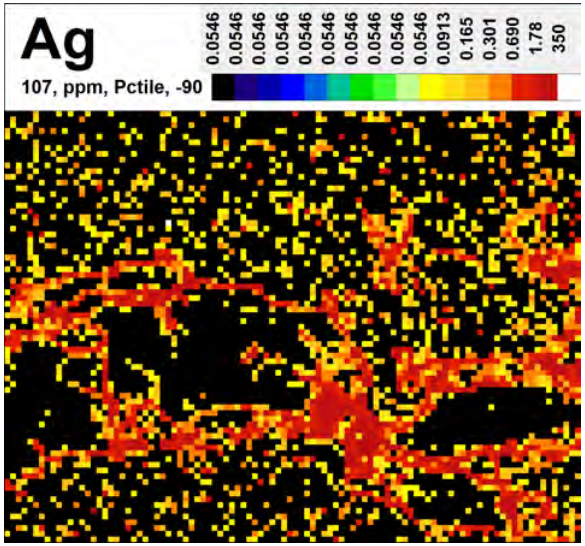
Ag
107, ppm, Pctile, -90
0.0546 0.0546 0.0546 0.0546 0.0546 0.0546 0.0546 0.0546 0.0546 0.0913 0.165 0.301 0.690 1.78 350

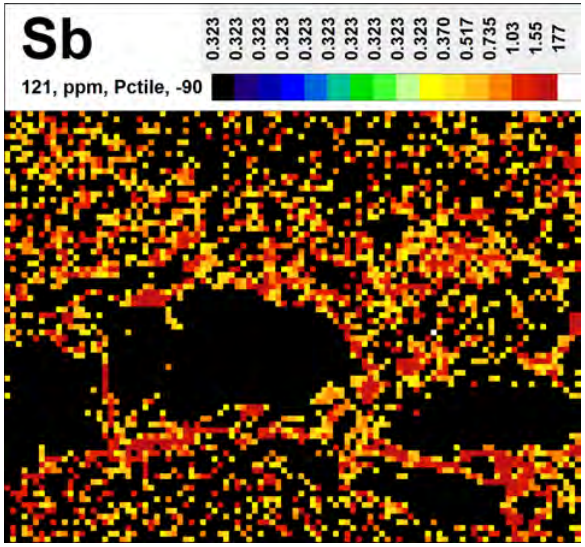
Sb
121, ppm, Pctile, -90
0.323 0.323 0.323 0.323 0.323 0.323 0.323 0.323 0.323 0.370 0.517 0.735 1.03 1.55 177

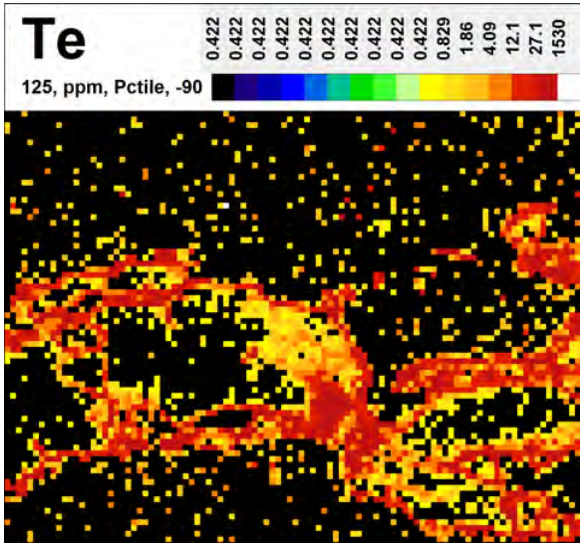
Te
125, ppm, Pctile, -90
0.422 0.422 0.422 0.422 0.422 0.422 0.422 0.422 0.422 0.422 0.829 1.86 4.09 12.1 27.1 1530

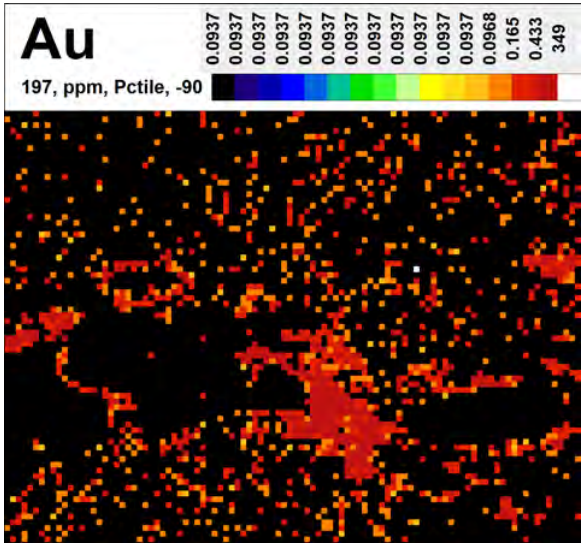
Au
197, ppm, Pctile, -90
0.0937 0.0937 0.0937 0.0937 0.0937 0.0937 0.0937 0.0937 0.0937 0.0937 0.0937 0.0968 0.165 0.433 349

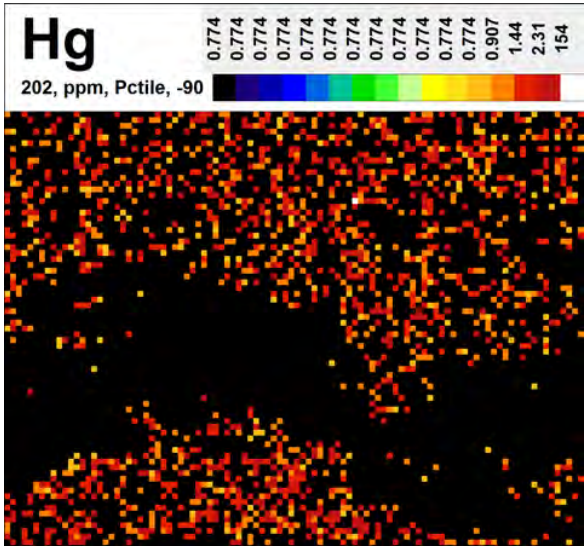
Hg
202, ppm, Pctile, -90
0.774 0.774 0.774 0.774 0.774 0.774 0.774 0.774 0.774 0.774 0.774 0.907 1.44 2.31 154

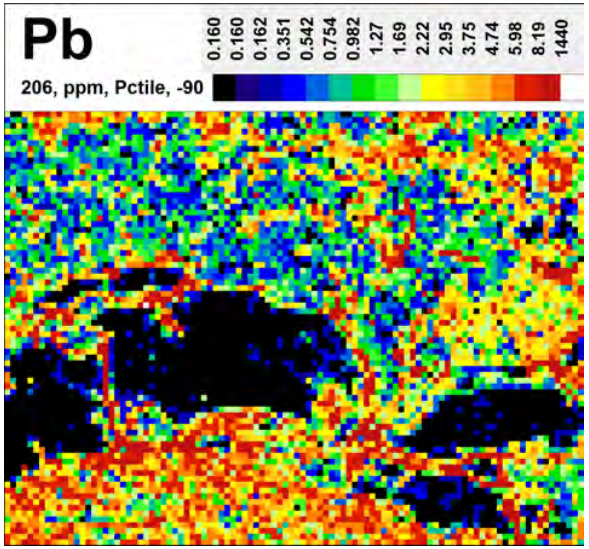
Pb
206, ppm, Pctile, -90
0.160 0.160 0.162 0.351 0.542 0.754 0.982 1.27 1.69 2.22 2.95 3.75 4.74 5.98 8.19 1440

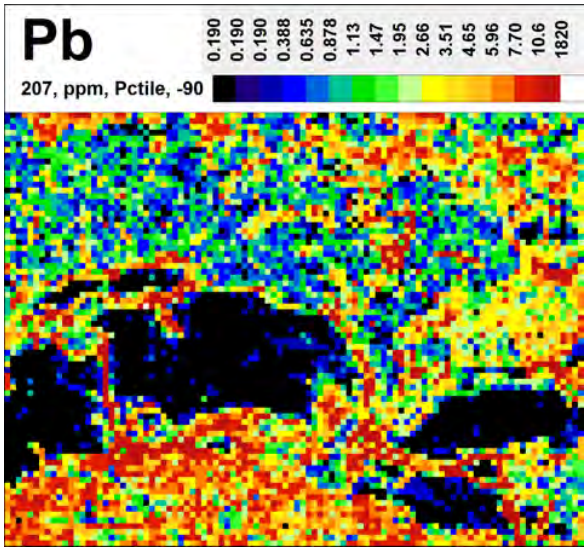
Pb
207, ppm, Pctile, -90
0.190 0.190 0.190 0.388 0.635 0.878 1.13 1.47 1.95 2.66 3.51 4.65 5.96 7.70 10.6 1820

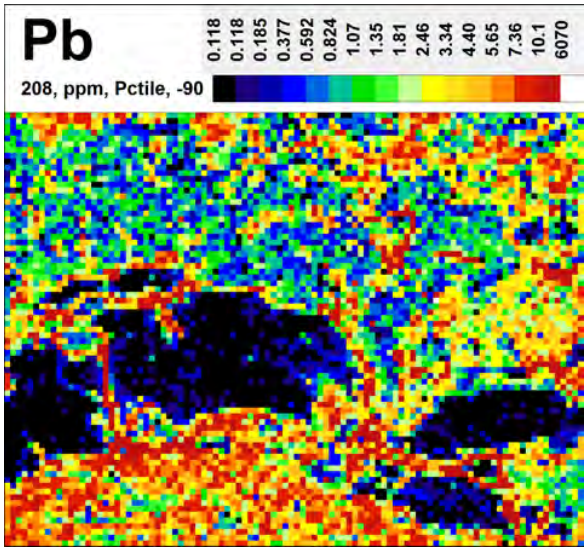
Pb
208, ppm, Pctile, -90
0.118 0.118 0.185 0.377 0.592 0.824 1.07 1.35 1.81 2.46 3.34 4.40 5.65 7.36 10.1 6070

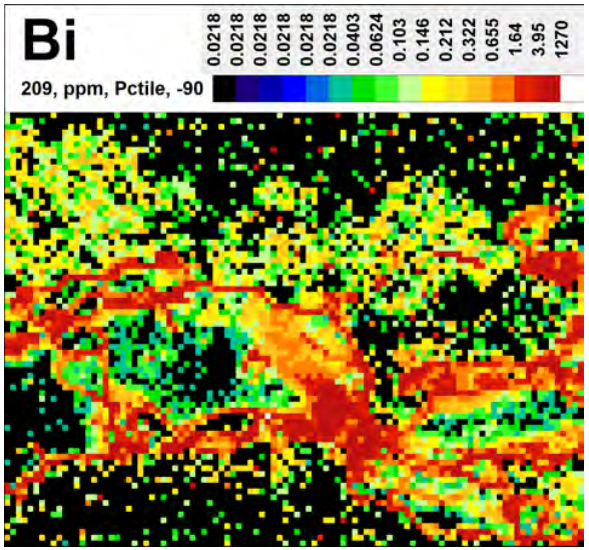
Bi
209, ppm, Pctile, -90
0.0218 0.0218 0.0218 0.0218 0.0218 0.0218 0.0403 0.0624 0.103 0.146 0.212 0.322 0.655 1.64 3.95 1270

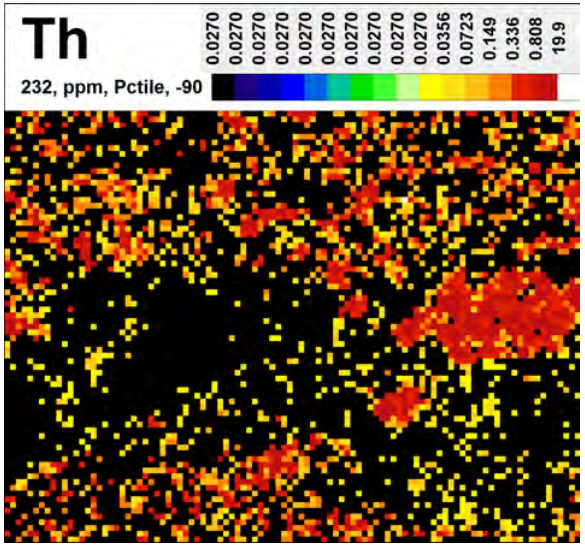
Th
232, ppm, Pctile, -90
0.0270
0.0270
0.0270
0.0270
0.0270
0.0270
0.0270
0.0270
0.0270
0.0356
0.0723
0.149
0.336
0.808
19.9

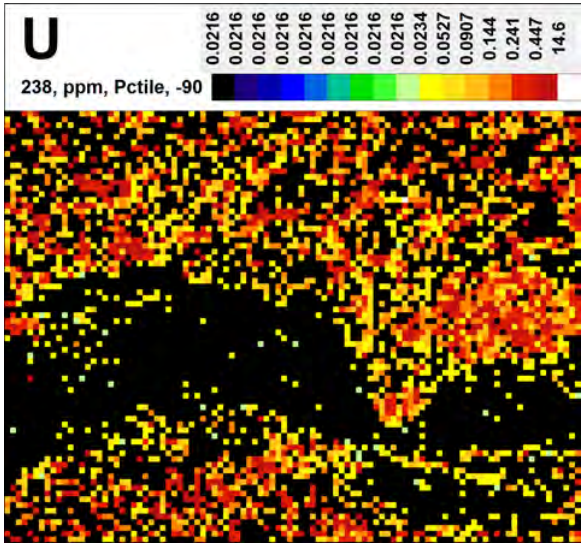
U
238, ppm, Pctile, -90
0.0216
0.0216
0.0216
0.0216
0.0216
0.0216
0.0216
0.0216
0.0216
0.0234
0.0527
0.0907
0.144
0.241
0.447
14.6

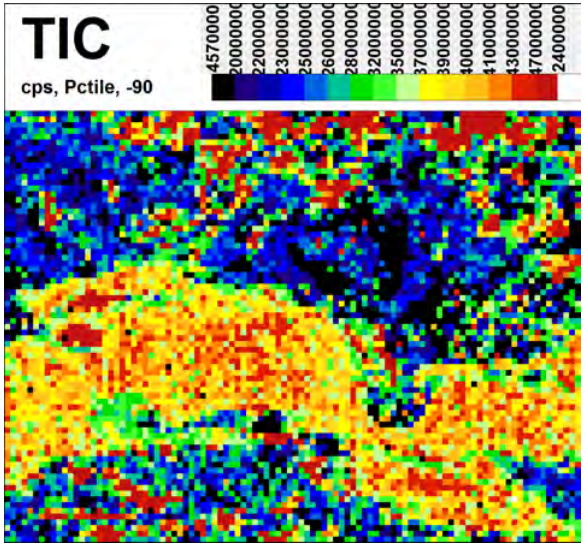
TIC
cps, Pctile, -90

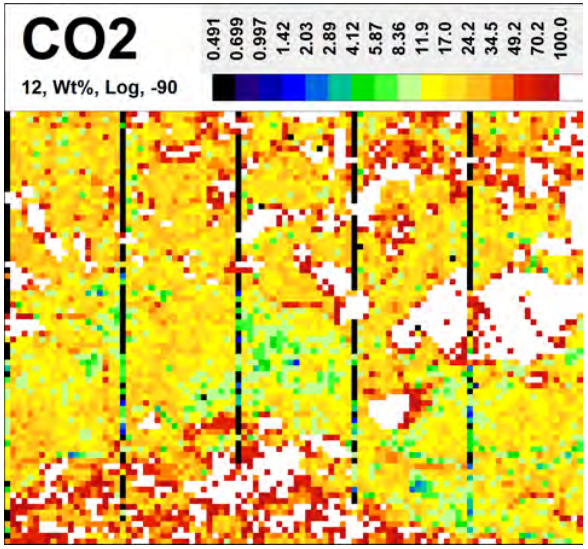
CO2
12, Wt%, Log, -90
0.491
0.699
0.997
1.42
2.03
2.89
4.12
5.87
8.36
11.9
17.0
24.2
34.5
49.2
70.2
100.0

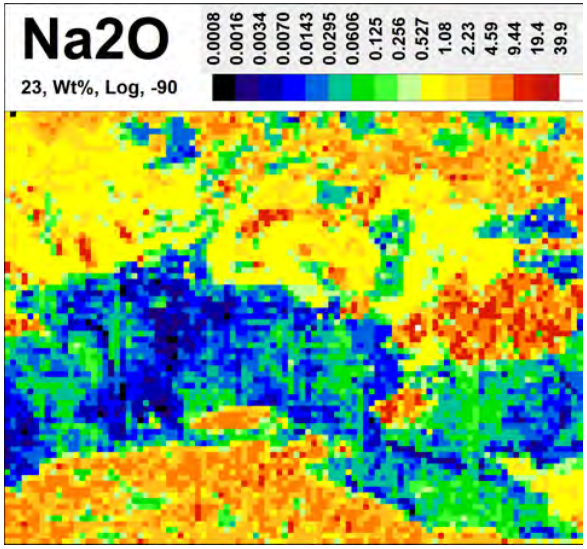
Na2O
23, Wt%, Log, -90
0.0008
0.0016
0.0034
0.0070
0.0143
0.0295
0.0606
0.125
0.256
0.527
1.08
2.23
4.59
9.44
19.4
39.9

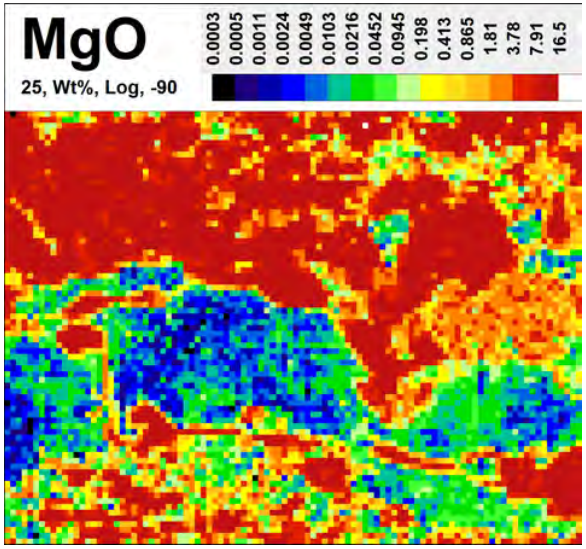
MgO
25, Wt%, Log, -90
0.0003
0.0005
0.0011
0.0024
0.0049
0.0103
0.0216
0.0452
0.0945
0.198
0.413
0.865
1.81
3.78
7.91
16.5

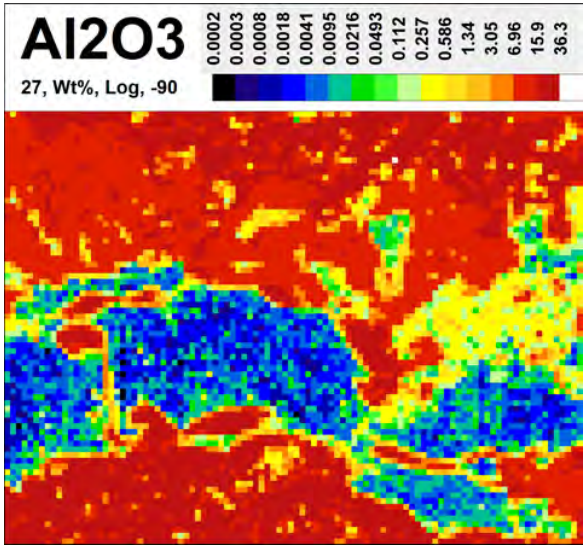
Al2O3
27, Wt%, Log, -90
0.0002
0.0003
0.0008
0.0018
0.0041
0.0095
0.0216
0.0493
0.112
0.257
0.586
1.34
3.05
6.96
15.9
36.3

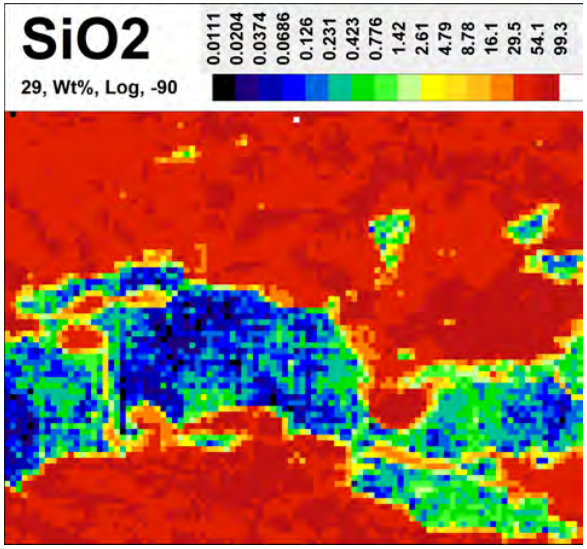
SiO2
29, Wt%, Log, -90
0.0111
0.0204
0.0374
0.0686
0.126
0.231
0.423
0.776
1.42
2.61
4.79
8.78
16.1
29.5
54.1
99.3

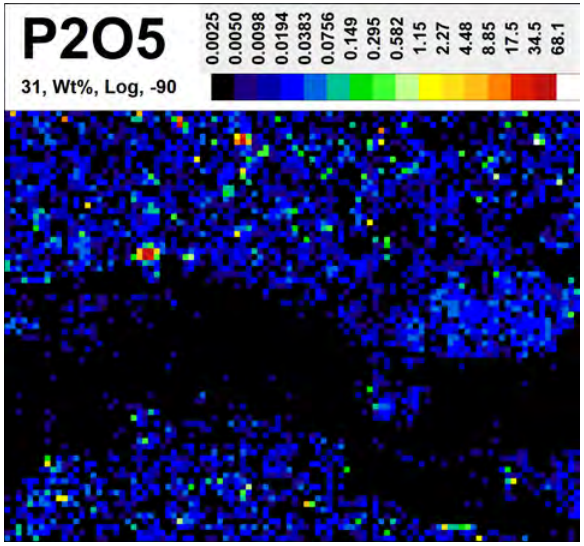
P2O5
31, Wt%, Log, -90
0.0025 0.0050 0.0098 0.0194 0.0383 0.0756 0.149 0.295 0.582 1.15 2.27 4.48 8.85 17.5 34.5 68.1

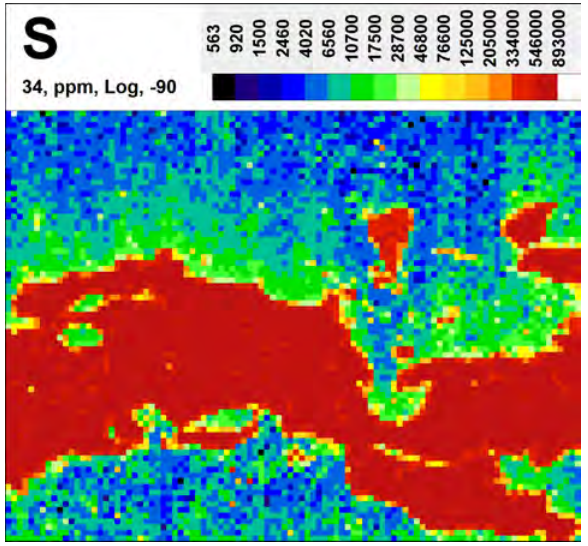
S
34, ppm, Log, -90
563 920 1500 2460 4020 6560 10700 17500 28700 46800 76600 125000 205000 334000 546000 893000

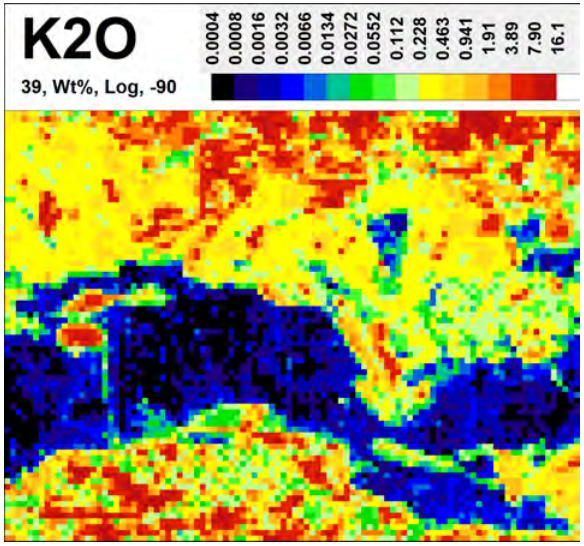
K2O
39, Wt%, Log, -90
0.0004 0.0008 0.0016 0.0032 0.0066 0.0134 0.0272 0.0552 0.112 0.228 0.463 0.941 1.91 3.89 7.90 16.1

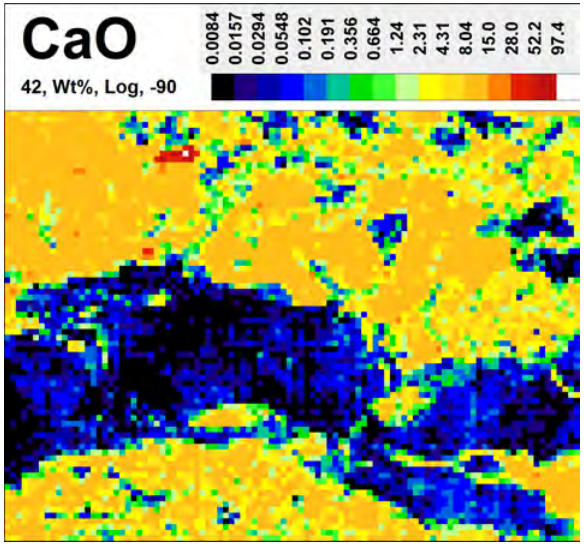
CaO
42, Wt%, Log, -90
0.0084 0.0157 0.0294 0.0548 0.102 0.191 0.356 0.664 1.24 2.31 4.31 8.04 15.0 28.0 52.2 97.4

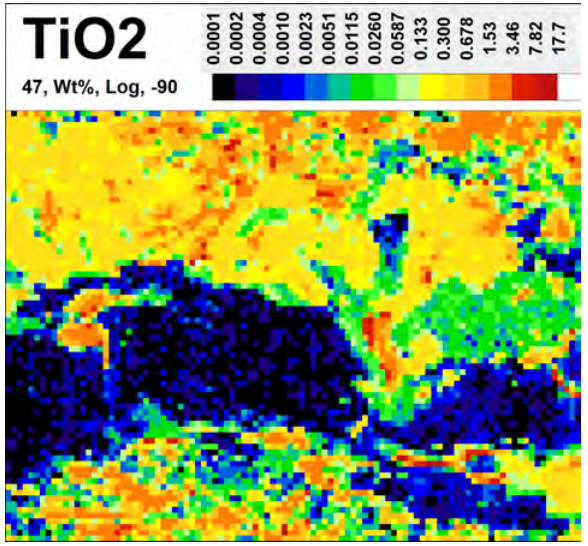
TiO2
47, Wt%, Log, -90
0.0001 0.0002 0.0004 0.0010 0.0023 0.0051 0.0115 0.0260 0.0587 0.133 0.300 0.678 1.53 3.46 7.82 17.7

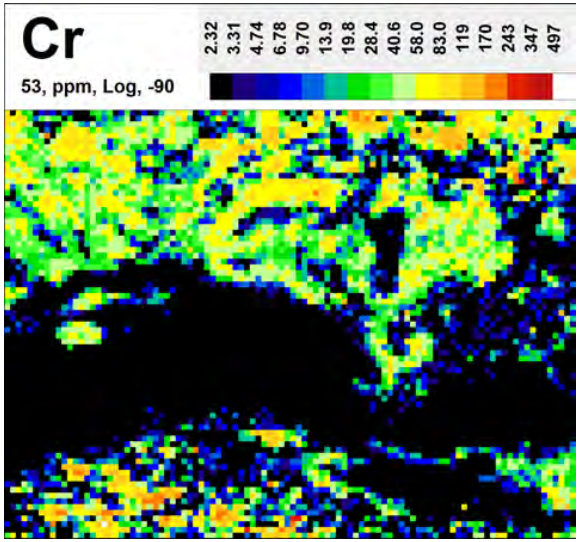
Cr
53, ppm, Log, -90
2.32 3.31 4.74 6.78 9.70 13.9 19.8 28.4 40.6 58.0 83.0 119 170 243 347 497

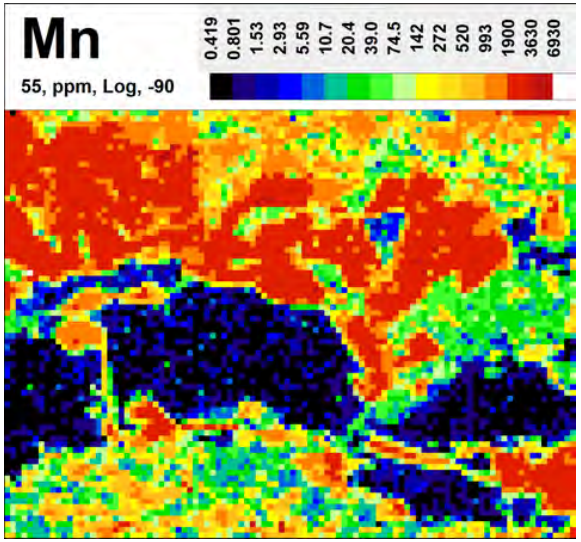
Mn
55, ppm, Log, -90
0.419 0.801 1.53 2.93 5.59 10.7 20.4 39.0 74.5 142 272 520 993 1900 3630 6930

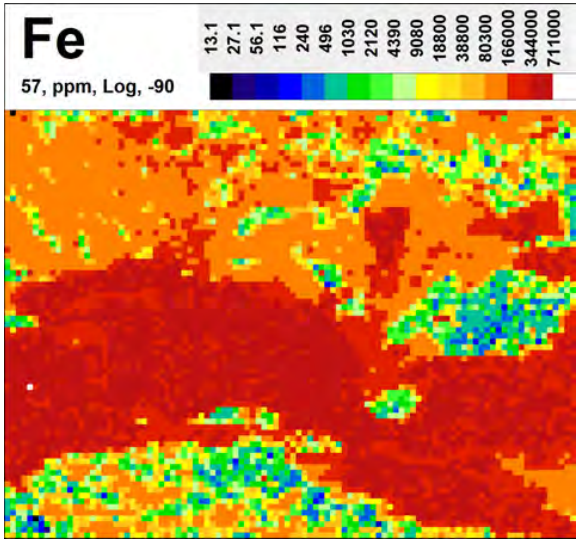
Fe
57, ppm, Log, -90
13.1 27.1 56.1 116 240 496 1030 2120 4390 9080 18800 38800 80300 166000 344000 711000

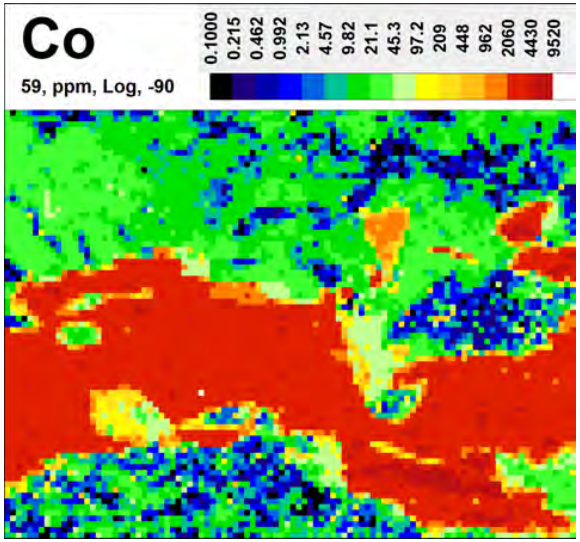
Co
59, ppm, Log, -90
0.1000 0.215 0.462 0.992 2.13 4.57 9.82 21.1 45.3 97.2 209 448 962 2060 4430 9520

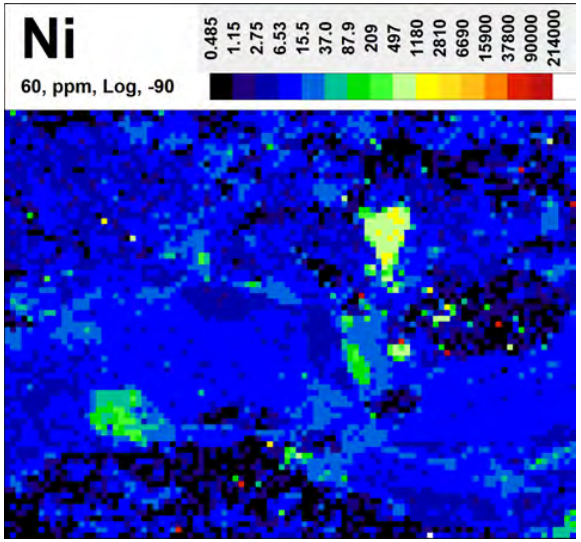
Ni
60, ppm, Log, -90
0.485 1.15 2.75 6.53 15.5 37.0 87.9 209 497 1180 2810 6690 15900 37800 90000 214000

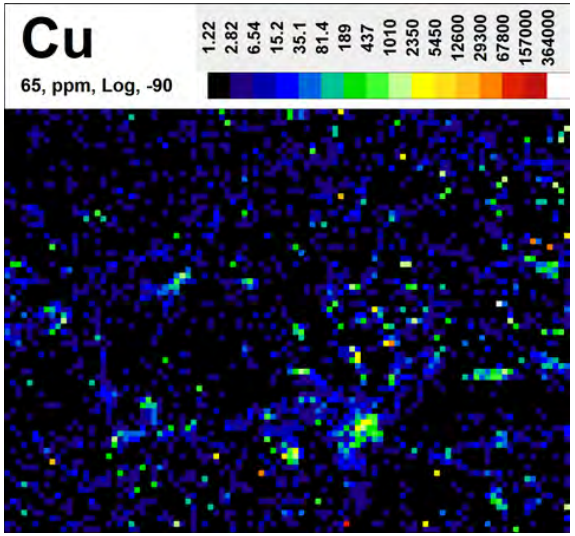
Cu
65, ppm, Log, -90
1.22
2.82
6.54
15.2
35.1
81.4
189
437
1010
2350
5450
12600
29300
67800
157000
364000

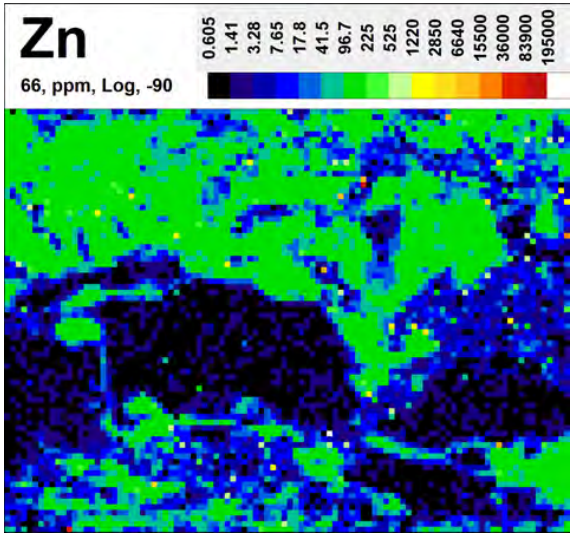
Zn
66, ppm, Log, -90
0.605
1.41
3.28
7.65
17.8
41.5
96.7
225
525
1220
2850
6640
15500
36000
83900
195000

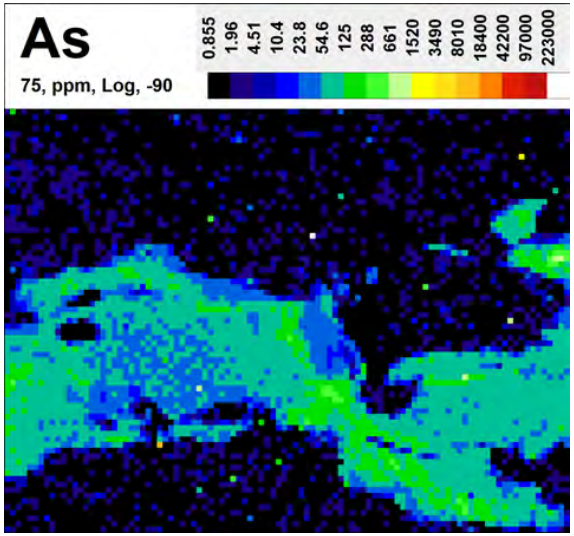
As
75, ppm, Log, -90
0.855
1.96
4.51
10.4
23.8
54.6
125
288
661
1520
3490
8010
18400
42200
97000
223000

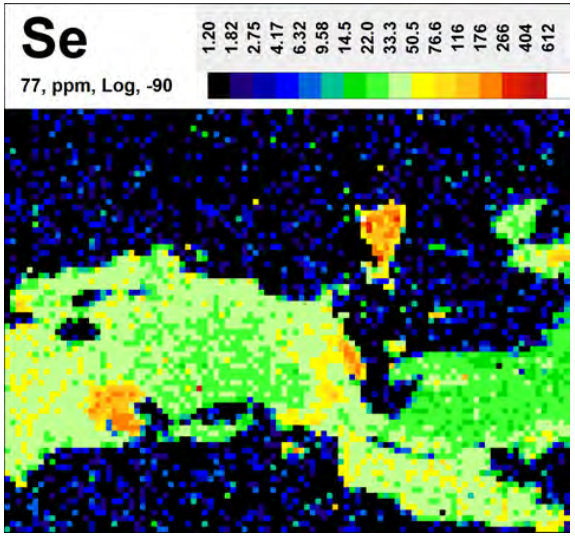
Se
77, ppm, Log, -90
1.20
1.82
2.75
4.17
6.32
9.58
14.5
22.0
33.3
50.5
76.6
116
176
266
404
612

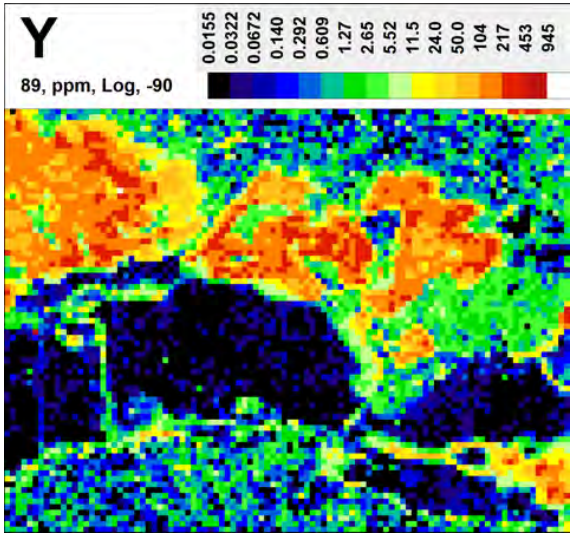
Y
89, ppm, Log, -90
0.0155
0.0322
0.0672
0.140
0.292
0.609
1.27
2.65
5.52
11.5
24.0
50.0
104
217
453
945

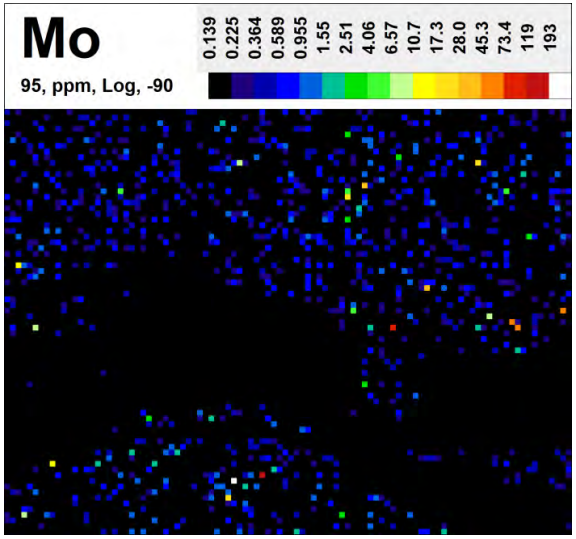
Mo
95, ppm, Log, -90
0.139 0.225 0.364 0.589 0.955 1.55 2.51 4.06 6.57 10.7 17.3 28.0 45.3 73.4 119 193

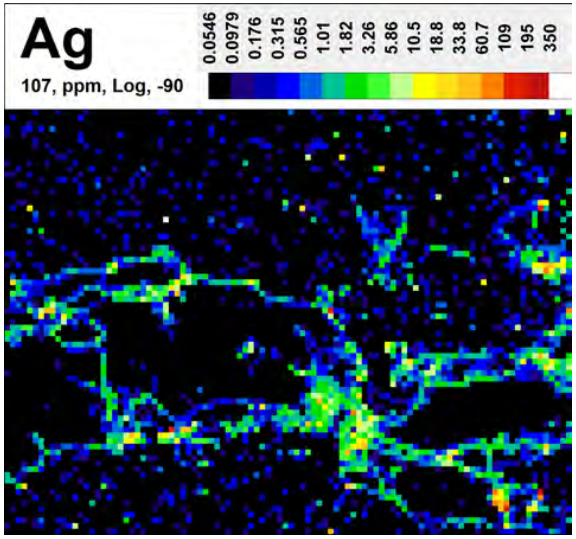
Ag
107, ppm, Log, -90
0.0546 0.0979 0.176 0.315 0.565 1.01 1.82 3.26 5.86 10.5 18.8 33.8 60.7 109 195 350

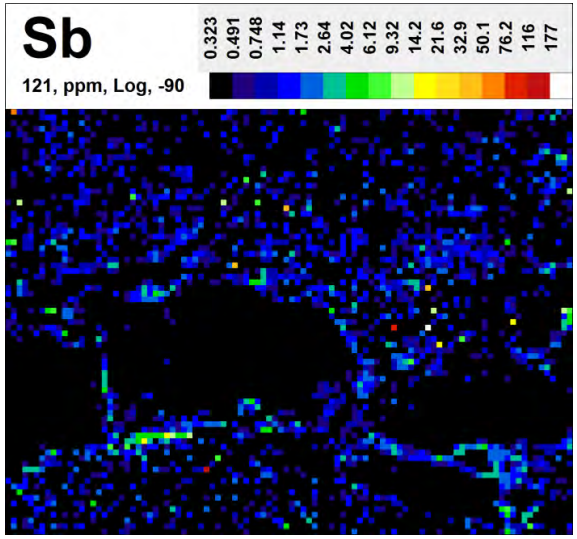
Sb
121, ppm, Log, -90
0.323 0.491 0.748 1.14 1.73 2.64 4.02 6.12 9.32 14.2 21.6 32.9 50.1 76.2 116 177

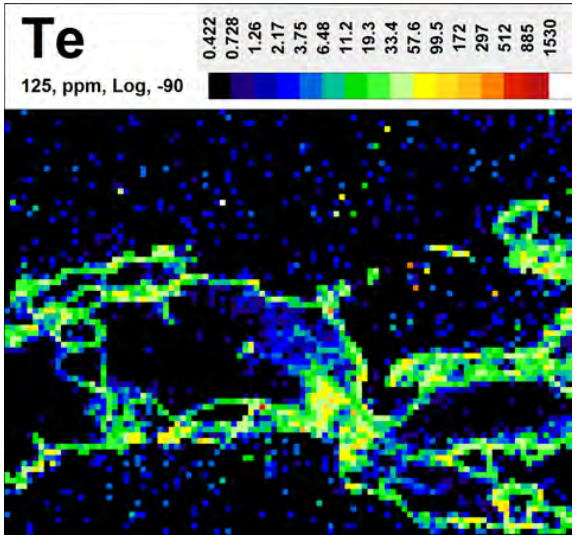
Te
125, ppm, Log, -90
0.422 0.728 1.26 2.17 3.75 6.48 11.2 19.3 33.4 57.6 99.5 172 297 512 885 1530

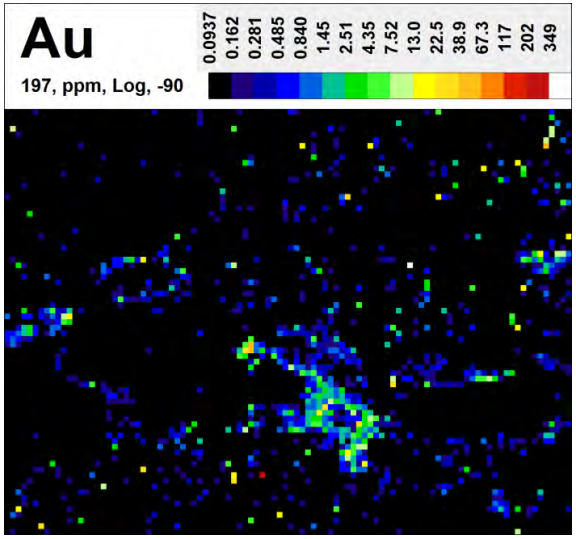
Au
197, ppm, Log, -90
0.0937 0.162 0.281 0.485 0.840 1.45 2.51 4.35 7.52 13.0 22.5 38.9 67.3 117 202 349

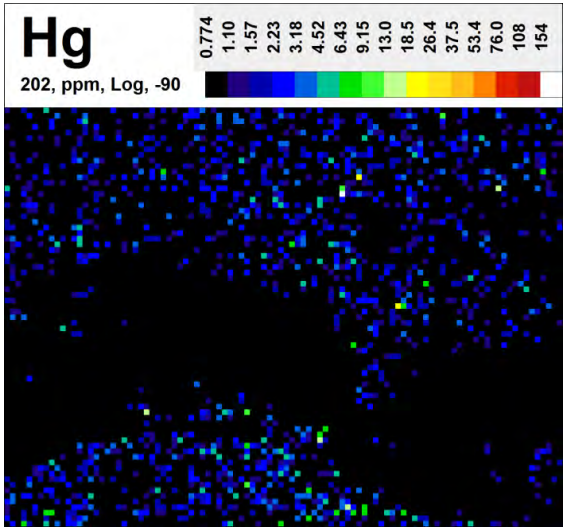
Hg
202, ppm, Log, -90
0.774 1.10 1.57 2.23 3.18 4.52 6.43 9.15 13.0 18.5 26.4 37.5 53.4 76.0 108 154

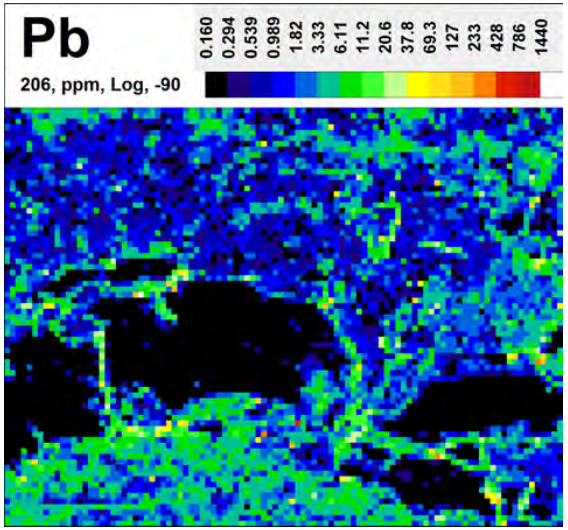
Pb
206, ppm, Log, -90
0.160 0.294 0.539 0.989 1.82 3.33 6.11 11.2 20.6 37.8 69.3 127 233 428 786 1440

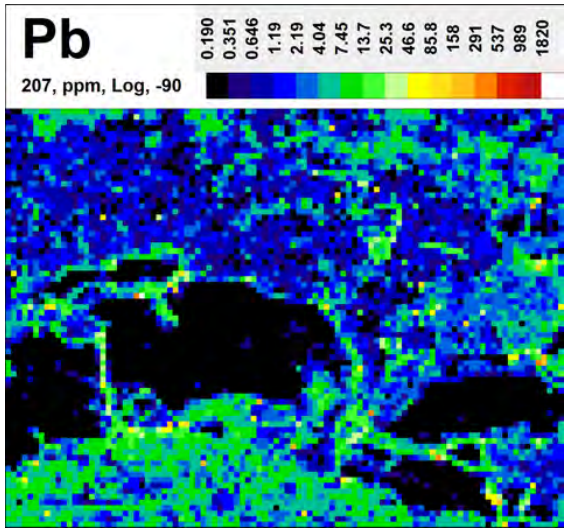
Pb
207, ppm, Log, -90
0.190 0.351 0.646 1.19 2.19 4.04 7.45 13.7 25.3 46.6 85.8 158 291 537 989 1820

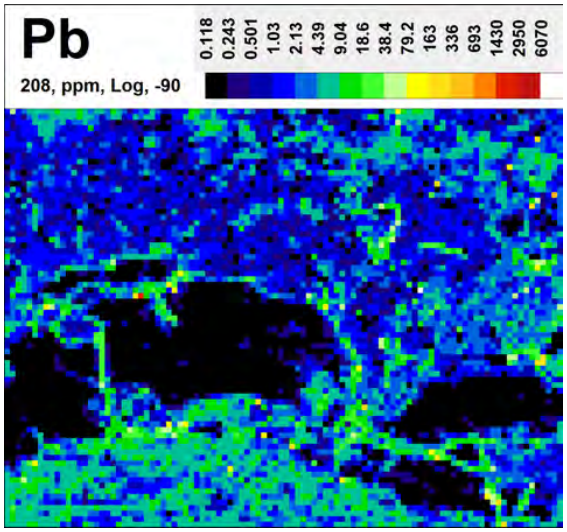
Pb
208, ppm, Log, -90
0.118 0.243 0.501 1.03 2.13 4.39 9.04 18.6 38.4 79.2 163 336 693 1430 2950 6070

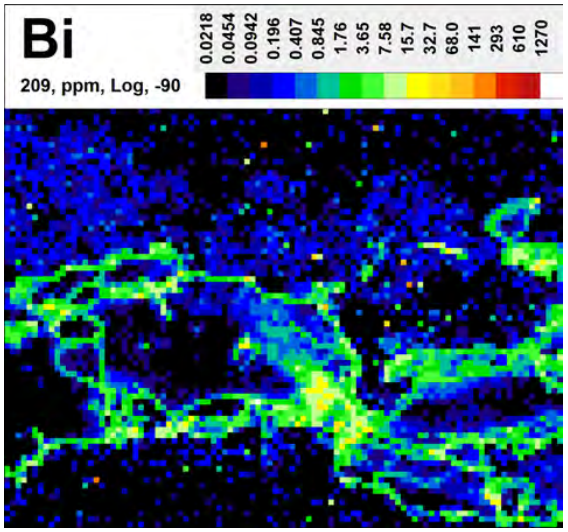
Bi
209, ppm, Log, -90
0.0218 0.0454 0.0942 0.196 0.407 0.845 1.76 3.65 7.58 15.7 32.7 68.0 141 293 610 1270

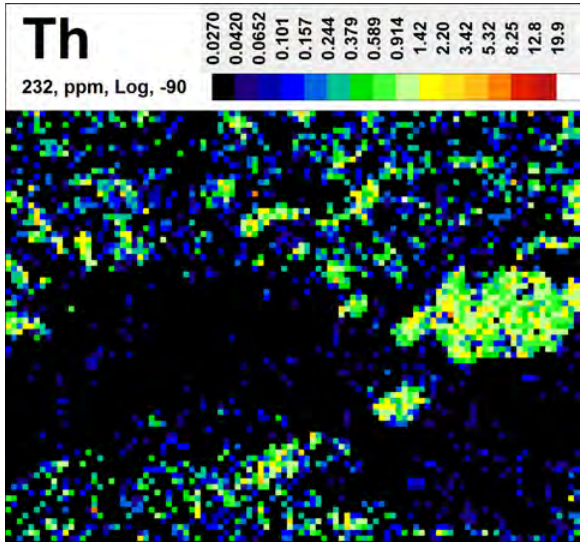
Th
232, ppm, Log, -90
0.0270
0.0420
0.0652
0.101
0.157
0.244
0.379
0.589
0.914
1.42
2.20
3.42
5.32
8.25
12.8
19.9

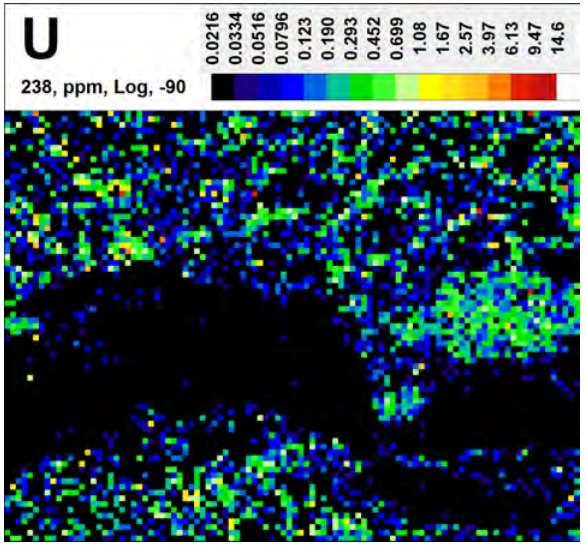
U
238, ppm, Log, -90
0.0216
0.0334
0.0516
0.0796
0.123
0.190
0.293
0.452
0.699
1.08
1.67
2.57
3.97
6.13
9.47
14.6

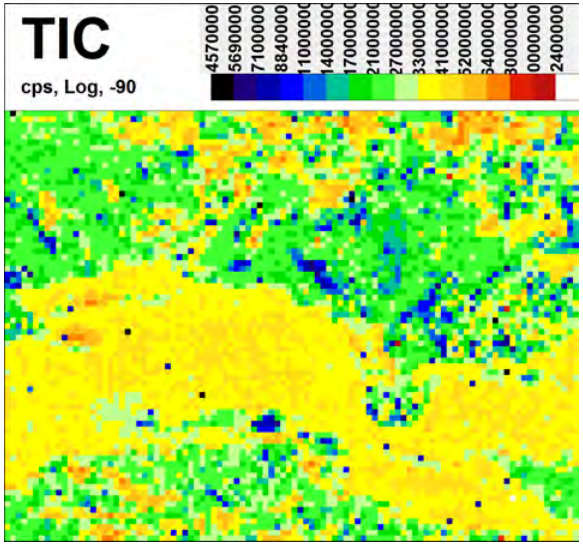
TIC
cps, Log, -90

Figure DR12. (pages 243–270) LA-ICP-MS results of another pinch and swell pyrite domain within a mafic volcanic sample (RD16-I) showing an orientation contrast image of the mapping area and 32 major and trace maps overlapped on the OC image. OC image reveals plastic strain through a complex misorientation pattern. LA-ICP-MS maps reveal Au and other trace elements (Ag-Bi-Te) enrichement at low-angle grain boundaries and brittle fractures. Note, grain boundaries within this sample are devoid of Au. LA-ICP-MS maps without OC underlays are also added.

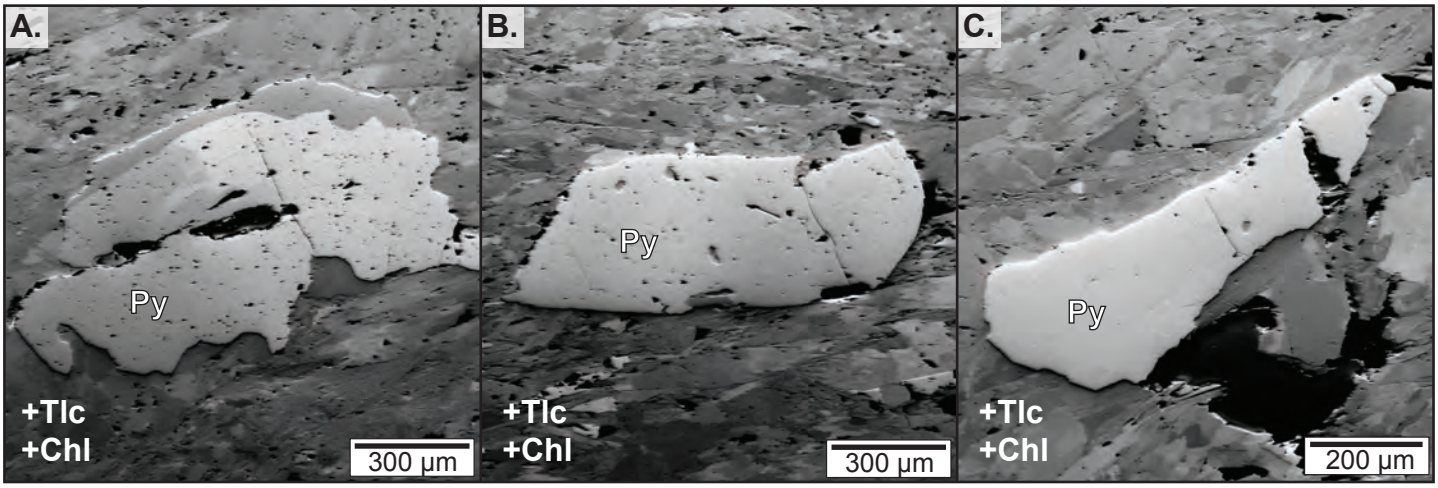

Figure DR13. A–C. Orientation contrast image of pyrite porphyroblasts within a talc-chlorite matrix of an ultramafic volcanic sample (TC-06) showing little to no evidence of intracrystalline plastic strain through gray-scale variations.